Petroleum and Coal

Article **Open Access**

PRACTICAL METHODS TO DETERMINE THE THERMAL STABILITY OF MOTOR OILS

Tirapote Rattana-amron and Chuleekorn Chotsuwan*

National Nanotechnology Center (NANOTEC), National Science and Technology Development Agency (NSTDA), Pathum Thani 12120, Thailand

Received October 4, 2018; Accepted December 21, 2018

Abstract

A performance of motor oil is influenced by base oil types and additives. Many ingredients such as antioxidants, viscosity index improvers, detergents, and antiwear agents are added to lubricants in order to improve its performances. Stability of motor oil is a concerned factor and widely used to measure performance of automotive lubricants. Therefore, understanding the stability of motor oil products is an initial step for improving the quality of lubricants. In this study, practical thermal analysis methods of conventional differential scanning calorimetry (DSC) and thermal gravimetric analysis (TGA) were used to evaluate the stability of 20 commercial motorcycle oils in 5 American Petroleum Institute (API) grades. Oxidation induction time (OIT), oxidation onset temperature (OOT), volatility loss and activation energy were used as stability indicators to determine performances in thermal degradation process at 100°C for 8 weeks. The OIT and OOT were employed to evaluate oxidation stability. It was found that the latest API groups (SJ and SL) were more stable than the previous categories such as SC, SF, and SG. Volatility and apparent activation energies were used to determine thermal stability by TGA instrument. Stability of motor oils had no correlation with the API category. Significant variation of OIT, OOT, volatility and the activation energy within the same API category were observed during thermal degradation.

***Keywords**: thermal stability; degradation; oil oxidation; activation energy of motor oils.*

1. Introduction

A lubricant market is driven by the growing automotive industry. Total lubricant demand is estimated to be 2.5 billion liters per year in 2015 and projects to reach 3.2 billion liters per year in 2020 [1]. In addition, motorcycles have always been a dominant market. A number of motorcycles on the roads have been growing by approximately 18 million units per year. The high demand for lubricant products in developing countries come with several problems such as counterfeit lubricants, reusing lube oil without appropriate re-refining processes and mixing lubricants with poor quality oils. Using these low quality lubricants not only impacts engine performances but also generates hazardous chemical vapors to the environment. These chemicals contribute to chronic hazards including mutagenicity and carcinogenicity, which are very toxic to humans [2]. Oxidation stability and volatility are important factors to be considered as indicators on the quality and performance of lubricants. Poor quality motor oils express a high level of volatility and low oxidation stability. These properties directly affect the physical and chemical properties of lubricants, for example, volatility relates to the fire and flash point of the lubricating fluid in high-temperature conditions [3]. Oxidation property of a lubricant can lead to several undesirable results, such as increased oil viscosity, the formation of corrosive acids, and sludge buildups, which accelerating engine corrosion [4].

Thermal stability determination of lubricant by thermal analysis techniques are important for the modern engine lubricants. Pressurized differential scanning calorimetry (PDSC) instrument is used to determine the oxidative stability of engine oils such as OIT and OOT under isothermal and dynamic conditions [5-8]. This technique offers fast analysis (within an hour),

high sensitivity, less waste sample after testing and reproducibility of measurements [9]. However, the PDSC instrument is not as common as the conventional DSC. In general thermal analysis laboratories, the conventional TGA and DSC are widely used for numerous applications for a variety of materials. Many studies have reported that the conventional DSC could be used as a tool to classify and evaluate the effectiveness of oxidative inhibitors, which added to hydrocarbon products [10-12]. In addition, the evaporation loss of lubricating oil is also important in engine oil lubrication. It contributes to oil consumption in an engine and can lead to a change in the properties of the oil, which could produce air pollution [13]. Therefore, volatility of lubricant is an important factor that impacts the performances of formulated engine oil. TGA technique is a common method for investigating weight loss of a sample while the temperature is changed over time [14]. The ASTM D 6375 standard test method is used for determining evaporation loss of lubricating oils by the thermogravimetric analyzer. Specifically, Noack method gives useful volatility information in order to evaluate the volatility properties of motor oils [15]. Following this standard, a lubricant sample is quickly heated to 249°C in the dynamic section then held isothermally. A TGA curve provides a percent mass loss versus time, as shown in Fig. 1. For evaluation of oxidative stability by using the conventional DSC instrument, the oxidation induction time (OIT) and oxidation onset temperature (OOT) can be used to assess oil stability [16]. A typical OIT measurement is a plot of heat flow (mw/mg) versus time (min). The OIT technique indicates the time from the beginning that oil is exposed to oxygen gas in the isothermal condition until onset temperature peak occurs as shown in Fig. 2.

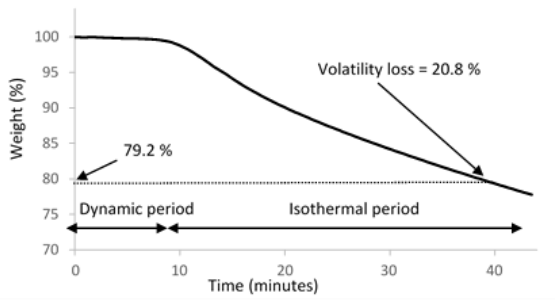

Fig. 1. Thermogravimetric analysis determination of the evaporation loss (Noack volatility)

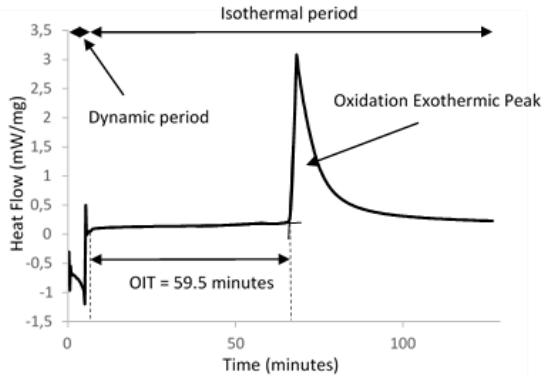

Fig. 2. Differential scanning calorimetry curve for the oxidation induction time (OIT) determination

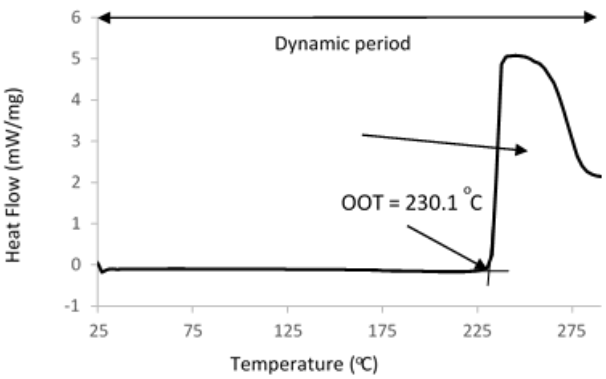

Fig. 3. Differential scanning calorimetry curve for the oxidation onset temperature (OOT) determination

This test method is standardized by the ASTM E 1858 standard [17]. The OOT is also using to evaluate the oxidative stability of lubricant. This method measures the oxidation onset temperature, which is standardized by the ASTM E 2009. In the beginning, a sample is heated with a constant heating rate. Simultaneously, one atmosphere of oxygen is filled in until the exothermic peak emerges. The OOT value is defined as the temperature at the onset of the exothermic oxidation peak [18] as shown in Fig. 3.

Moreover, activation energy is another indicator utilizing kinetic analysis to determine the stability of lubricant. This application of TGA is based on the iso-conversional method of kinetic

analysis under non-isothermal conditions, which is frequently used to determine the activation energy of oxidative degradation study in oils [19-20]. It can be used as an analytical device for accurately measuring weight change of a material subjected to a temperature history. The weight loss information is used to determine the activation energy of lubricant samples. The high quality motor oil depends on the type of base oil as well as additives [21]. It should have good stability and volatility properties because these factors lead to serious damages to the engine. Determination of performances in an automotive lubricant through conventional thermal analysis techniques are beneficial for the formulation of lubricant before a full-scale engine testing, which is expensive and takes a longtime. Therefore, these practical methods can be utilized for improving the thermal performance of base oils and additives. In addition, thermal stability information should be provided to customers, they could identify performances of lubricants and select high performance lubricant without any influences of false commercials.

In this work, we have investigated the thermal stability of 20 motorcycle oils during thermal degradation for 8 weeks by using practical thermal analysis methods to obtain values of OOT, OIT, volatility loss and activation energy. The change of quality in lubricants were estimated by a correlation of a trend in thermal stability.

2. Materials and methods

2.1. Motor oils

Twenty conventional motorcycle oils were obtained from 20 brands commonly available in local lubricant markets. The tested lubricants consisted of international brands and local brands, which were suitable for 4-stroke motorcycle engines. In this investigation, viscosity grade of all samples were Society of Automotive Engineers (SAE) 40 of which 5 brands in SC category; 5 in SF; 4 in SG; 3 in SJ and 3 in SL category. About 30 mL of each lubricant fluid was filled in a glass cylinder container (2.5 cm diameter and 9.5 cm height) without closing a lid and stored at 100°C for 8 weeks. Every 2 weeks, 2 mL of each sample was collected for determination of volatility loss, OIT and OOT in order to observe changes of performances.

2.2. Oxidation onset temperature (OOT) analysis according to the ASTM E 2009

According to the ASTM E 2009 standard for the OOT test, approximately 3 mg of lubricant samples were heated at a constant rate of 10°C/min from 25°C to 100°C in an oxygen atmosphere with constant flow rate of 50 mL/min. The oxidation onset temperature was specified from its DSC curves of the exothermic process.

2.3. Oxidation induction time (OIT) analysis according to the ASTM E 1858

Thermal stability of lubricants was analyzed in term of OIT test according to the ASTM E 1858 standard. Approximately 3 mg of sample was placed into an uncovered aluminum pan and were held initially at 25°C under nitrogen flow of 50 mL/min. The temperature was increased to 210°C with a heating rate of 40°C/min, still under the same nitrogen flow. When reaching the defined temperature, hold for 5 min and switched nitrogen to oxygen gas at 50 mL/min then held at 210°C (isothermal) for 60 min. The OIT was measured by DSC signal when an exothermic reaction onset was observed.

2.4. Volatility analysis according to the ASTM D 6375

The procedure followed the ASTM D 6375, using 61 ± 3 mg of lubricant samples in an opened aluminum crucible with an internal diameter of 0.56 cm. The temperature was increased from 50°C to 220°C with a heating rate of 100°C/min and followed by heating to 249°C at 10°C/min. The isothermal period was held at 249°C for 30 min with air purge at a total flow rate of 80 mL/min. The percentage of evaporation loss of lubricants was determined by the TGA curve of the sample at 30 min after isothermal period. The TGA results were used to compare the volatility of samples for performance evaluation.

2.5. Determination of activation energy

The conventional TGA was used to evaluate the kinetics of motor oils. Non-isothermal thermogravimetry has been applied to determine activation energy. Approximately 5.0 mg of selected sample was filled in a 70 µL alumina crucible and placed into TGA instrument. Samples were heated from the ambient temperature to 600°C under a nitrogen atmosphere with a flow rate of 100 mL/min. The experiments were conducted at 4 constant heating rates of 5, 10, 20 and 30°C/min as shown in Fig. 4 at percent conversion of 10, 20, 30, 40, 50, 60, 70, 80 and 90% were utilized to determine the activation energy. The decomposition of oil samples was evaluated to quantify the rate of aging of oils at different conditions. The kinetic models are based on the following fundamental rate equations [22].

$$\frac{d\alpha}{dt} = Aexp\left(-\frac{E}{RT}\right)f(\alpha) \quad (1)$$

where E is the activation energy of the kinetic process; A is the Arrhenius parameter also called the pre-exponential factor and R the universal gas constant. The conversion dependent function, $f(\alpha)$ is assumed that the degradation reaction is a simple nth-order reaction.

The conversion dependent term can be expressed as

$$f(\alpha) = (1-\alpha)^n \quad (2)$$

where n is the order of the kinetics, which is characterized by the first order kinetics $n = 1$ for decomposition of oil [23].

The integral form of the equation (1) can be written as:

$$g(x) = \int_0^x \frac{dx}{f(x)} = \frac{A}{\beta}\int_{T_0}^{T} exp\left(-\frac{E}{RT}\right)dT = \frac{AE}{\beta R}p\left(\frac{E}{RT}\right) \quad (3)$$

where β denotes the heating rate of ethe xperiment.

Kissinger-Akahira-Sunose (KAS) method is based on the Coats, and Redfern approximation [24], which has been employed and the function of the integral isoconventional KAS method is given by [25].

$$\ln\left(\frac{\beta}{T^2}\right) = \ln\left(\frac{AR}{Eg(x)}\right) - \frac{E}{RT} \quad (4)$$

Equation (3), temperatures at various chosen values of conversions are determined at different heating rates. The activation energy can be obtained from the slope of the strength-line by plotting $\ln(\beta/T^2)$ on y-the axis versus $1/T$ on x-the axis at a given level of the conversion as shown in Fig. 5.

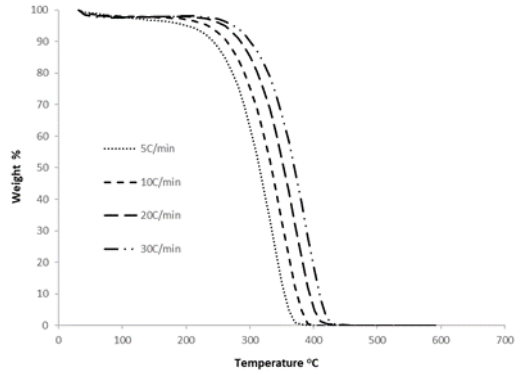

Fig 4. Typical TGA curves for weight loss profiles at different heating rates of SC1

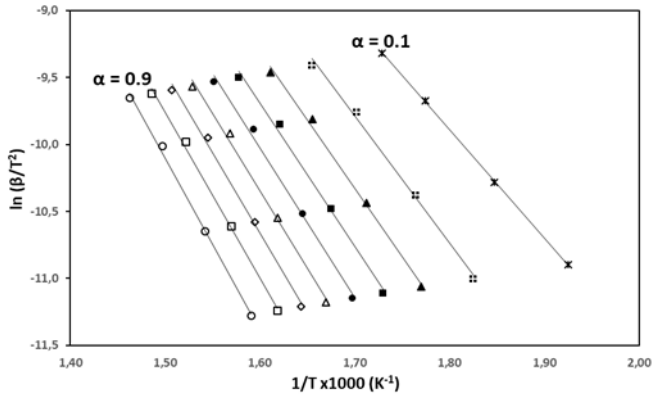

Fig 5. The Kissinger-Akahira-Sunose (KAS) plots for thermal degradation of lubricant at different rates and conversion level (α) : 0.1-0.9

3. Results and discussion

3.1. Initial product performances

Twenty commercial motor oils having the same SAE viscosity grade at number 40 were investigated to determine the oxidative stability and volatility before thermal degradation test. They

were in 5 categories including SC, SF, SG, SJ, and SL. These engine oil samples were analyzed according to the three ASTM standards and the results of volatility loss, OIT and OOT are shown in Table 1.

Table 1. The initial volatility loss (%), oxidation onset temperature (OOT, °C) and oxidation induction time (OIT, min) of twenty lubricants having the following API: SC, SF, SG, SJ, and SL categories

Lubricants API	Volatility loss (%)	OIT (min)	OOT (°C)	Lubricants	Volatility loss (%)	OIT (min)	OOT (°C)
SC01	8.3	9.4	246.2	SG01	19.0	15.0	248.0
SC02	4.7	7.7	235.1	SG02	17.8	55.1	266.4
SC03	4.8	8.3	236.7	SG03	14.1	59.8	276.5
SC04	6.8	5.2	228.1	SG04	11.5	48.7	263.9
SC05	5.6	8.3	230.4	SJ01	10.2	58.0	272.0
SF01	15.0	23.4	257.0	SJ02	11.8	66.2	282.7
SF02	11.8	16.0	248.5	SJ03	20.8	57.9	271.3
SF03	8.5	17.9	249.7	SL01	21.2	65.0	279.0
SF04	8.0	8.7	238.8	SL02	13.5	115.0	293.9
SF05	6.3	17.1	250.2	SL03	6.6	92.7	287.8

Stable motor oil should have high oxidation temperature (OOT) and long oxidation time (OIT) value. The results revealed that the average of OOT value for each API category increased from 235°C to 287°C and got better in the alphabetical order of the oil categories. There was a gap between the minimum and maximum of OOT values within each category. The range for SC, SF, SG, SJ, and SL were 18.1, 18.2, 28.5, 11.4 and 14.9, respectively, and these ranges reflected the quality of motor oils within the group. A narrow range implied that members of the same API had almost the same quality while there was quite a different oxidative stability in the group with a large range. The relationship of the API categories and the oxidative stability evaluated by OOT also showed that the lubricants in the latest API service category (SL) was more stable than the previous category oils (SC, SF, SG, and SJ). The mean of the OOT was in the following order from the lowest to the highest: SC (235.3°C), SF (248.8°C), SG (263.7°C), SJ (275.3°C) and SL (286.9°C). The OOT value was a suitable tool to identify a poor oxidative oil in a category. For example, in SF category, SF04 had the lowest OOT of approximately 239°C, which was significantly lower than the OOT mean of 248.8°C. Therefore, the OOT values could be used as an indicator to evaluate the thermal stability of motor oils. The stability of the 5 API categories was also determined by OIT showing that the OIT of lubricants in each API category was in good agreement with the OOT data. Increasing the OIT accompanied with a higher oxidation temperature. Note that the two motor oils (SC3 and SC5) in SC group had a similar OIT value (8.3 mins), but the results of OOT were different: 230.4°C and 236.7°C, respectively. For the most stable oil, SL02 had the longest OIT (115 mins) while OOT was the highest value (293.3°C) among all investigated motor oils. The volatility property provided by the Noack volatility test of the 20 lubricant fluids are shown in Table 1. There were 6 oils including SF01, SG01, SG02, SG03, SJ03 and SL01 whose evaporative loss were more than 14%, especially, SJ03 and SL01 had more than 20% of volatilization while SC2 and SC3 were good volatility oils having the lowest volatility. Therefore, the volatility rate is also an important factor for lubricants. A high volatile oil should be considered when using these oils.

In this study, there was no significant correlation between volatility loss and the API category. For this set of commercial lubricants, it was found that there was also no direct relationship between SAE viscosity grade and volatility because all samples were in the same SAE viscosity grade, but they had different volatility properties. Moreover, the SAE viscosity grade was not a good indicator for providing the volatility information to the customers. The API category was also not a good indicator to determine the volatility of each motor oil, and there was no volatility trend when API category change from SC to SL. However, there was a good correlation between the API category and oxidative stability that the later API category such as SJ and SL was more stable than the previous categories (SC, SF, and SG).

3.2. Thermal stability during degradation

Twenty motor oils were degraded at 100°C for 8 weeks, and samples were collected every 2 weeks during the degradation test period. The oxidative stability and volatility results were obtained using DSC and TGA instruments.

Stability of motor oils during thermal degradation were determined in terms of OIT (mins), OOT (°C) and volatility (%) over 8 weeks of aging test at 100°C. The data of 5 lubricants in the API SC category was taken every 2 weeks and plotted as shown in Fig. 6 (a) for OOT (°C) using the left axis, and for OIT (mins) using the right axis. Fig. 6 (b) was volatility of the 5 lubricants in SC grade. The OOT values of the 5 motor oils showed that SC5 was quite a high oxidative stability motor oil to fight against an oxidation because its OOT values of 230°C remained almost unchanged during 8 weeks.

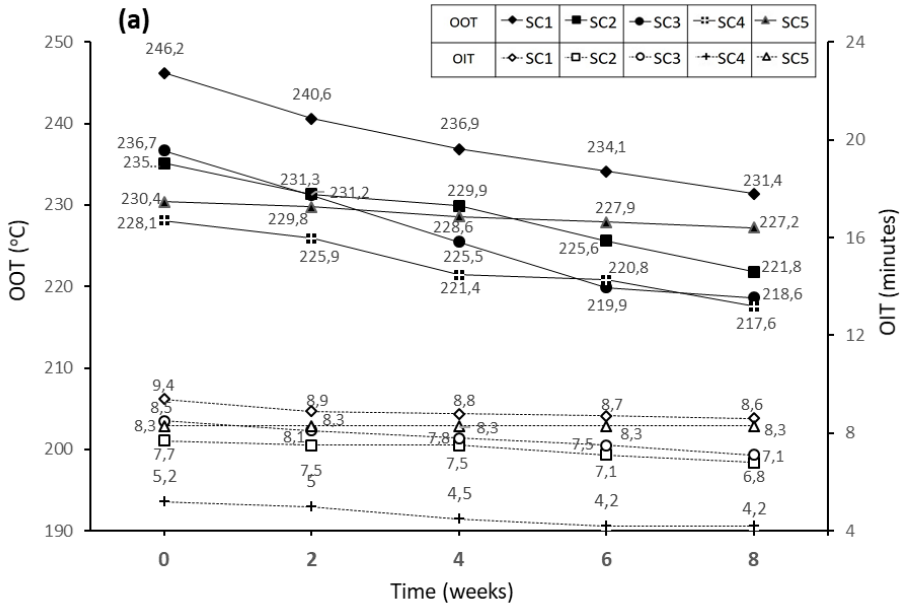

Fig. 6 (a) Values of OOT (°C) shown on the left axis for the upper group of data and OIT (min) shown on the right axis for the lower group of the five lubricants within the API SC grade tested over eight weeks of heating at 100°C

In contrast, OOT of SC1, SC2, SC3 and SC4 degraded over the testing period. Specifically, SC1 showed the highest OOT but degraded from 246.2°C to 231.4°C after 8 weeks. For SC2, SC3, SC4 and SC5, OOT results revealed that before degradation test (0 week), SC3 had higher OOT than SC2, SC4 and SC5. However, 8 weeks later, SC5 was more stable than SC2, SC3, SC4 and SC2 was more stable than SC3 and SC4, which had the lowest OOT of 217-218°C. For oxidative stability determined by time of oxidation at isothermal methods, so called OIT values, the 5 motor oils had similar oxidative stability trend. Their OIT values slightly decreased over the period, except SC5, which remained unchanged at 8.3 mins. SC1 had the highest OIT values (9.4 mins) over 8 weeks which only slightly decreased by 0.8 mins at the end of the test. For SC2 at the beginning of the test, it had lower OIT than SC3. However, after 8 weeks their OIT values were almost the same at approximately 7 mins. The lowest stability in SC group was SC4. It had the shortest OIT value at every oxidation point. These OIT values were significantly lower than the others.

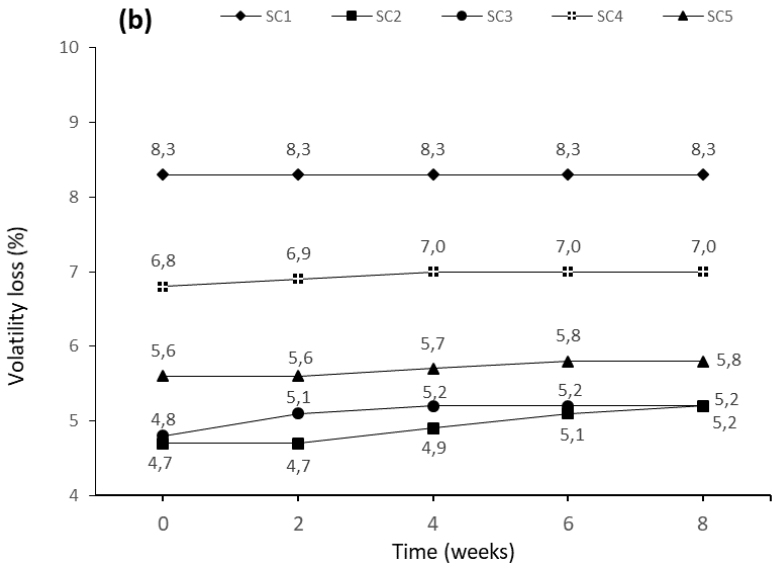

Fig. 6 (b) Volatility loss (%) of the five lubricants within the API SC grade tested after eight weeks of heating at 100°C

Fig.6 (b) showed volatility loss (%) of 5 motor oils in SC grades. Over 8 weeks of thermal degradation at 100°C, the volatility loss changed only slightly from no loss for SC1 to maximum of 0.4% for SC2. It was noted that these motor oils did not volatile much in 8 weeks. Moreover, volatility loss revealed that SC2 and SC3 had almost the same volatility loss of stock condition at two weeks. SC3 increased volatility loss but SC2 still unchanged. After two weeks, SC3 volatility remained steady while SC2 volatility slowly increased. Both SC2 and SC3 had similar volatility loss of 5.2% at the end of the degradation period. From the data shown in Fig. 6 (a and b) it could be concluded that SC5 was a good stable motor oil. It had quite high oxidative stability and volatility although it did not have the best OIT, OOT and volatility properties. In contrast, SC1 showed the best oxidative stabilities in term of OOT and OIT but its evaporation was very high. Therefore, SC1 was not a good motor oil in this group.

The oxidative stability test for 8 weeks at 100°C for SF group were shown in Fig 7 (a). The trend of OOT for the SF 5 motor oils decreased over the testing period. SF1 had the highest OOT values throughout 8 weeks while SF4 had the lowest OOT value. For SF2, SF3, and SF5, they had almost the same OOT value in the fresh condition. After two weeks, the OOT of SF3 was higher than that of SF5 and SF2; all three motor oils declined slowly to an almost similar value (234-235°C) at the end of the degradation test. In SF group, OIT of all 5 samples decreased within 8 weeks. SF1 was the most stable motor oil, and its OIT values were the highest during the degradation period. In contrast, SF4 had very low stability when compared with the others although its OIT was almost unchanged. Moreover, the OIT results reveal that the oxidation property trends of SF2, SF3, and SF5 went down over the period. After 4 weeks, SF2 expressed quite high stability because its OIT remained unchanged and it was higher than that of SF3 and SF5. However, the OIT decreased after that, and it was the same as SF3 at the end of the testing while SF5 had higher OIT than SF2 and SF3.

Volatility loss (%) of all oils was shown in Fig 7 (b). There were 4 motor oils including SF1, SF2, SF3, and SF5 that did not change their volatility property while SF4 increased its volatility loss by 0.8% during 6 weeks and stayed constant at 8.8% until the end of the degradation test. The volatility property of all aged oil samples after 8 weeks showed that SF3 and SF4 had almost similar volatility loss of approximately 9% while SF1 and SF2 had high volatility approximately 15% and 12%, respectively. By comparison, SF5 was the best oil in term of volatilization in this group because of the lowest volatility loss of about 6%. According to the oxidation property and volatility loss, it was obvious that SF2, SF3, and SF5 had good oxidative

stability. However, when considered volatility property, SF5 had the best oxidation and volatility property. In contrast, SF1 was the best in terms of oxidative stability but poor volatility. A high performance lubricant requires high oxidative stability and low volatility rating.

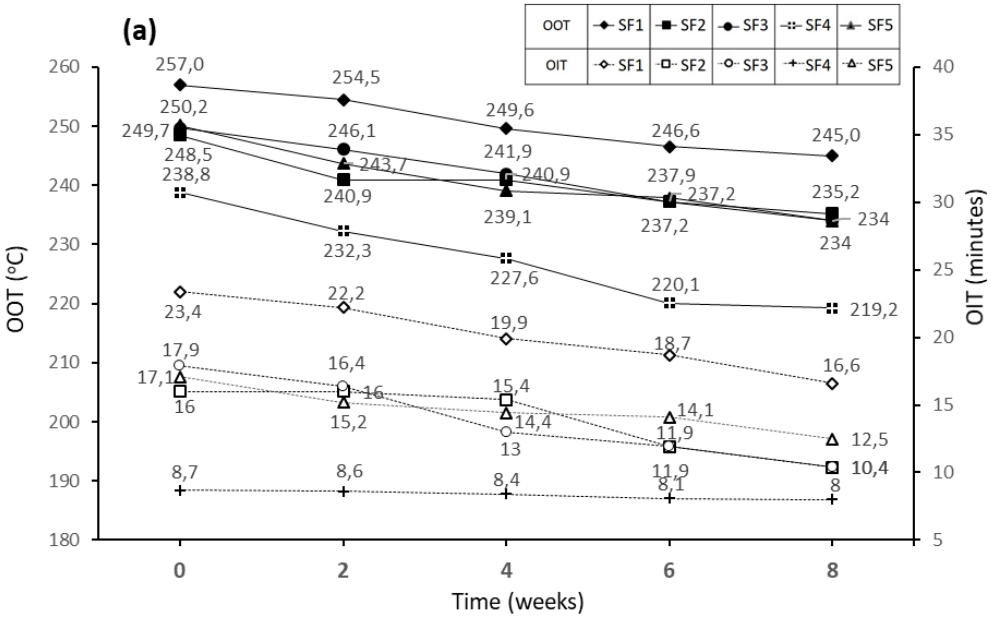

Fig. 7 (a) Values of OOT (°C) shown on the left axis for the upper group of data and OIT (min) shown on the right axis for the lower group of the five lubricants within the API SF grade tested over eight weeks of heating at 100°C

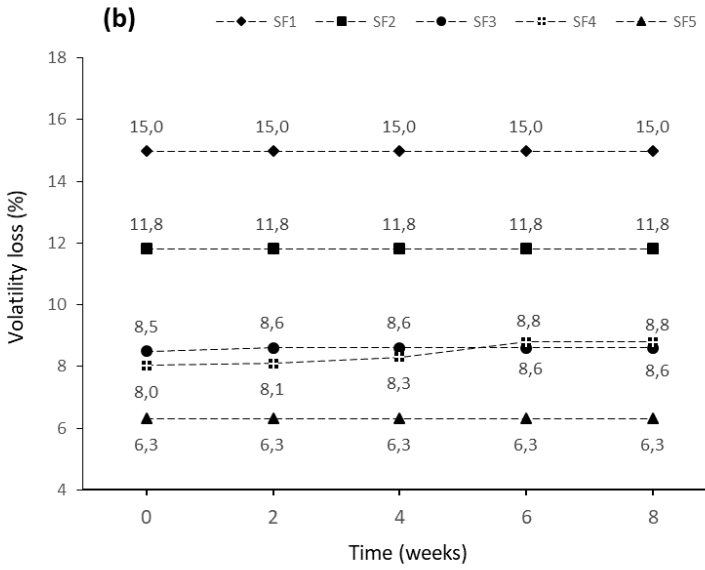

Fig. 7 (b) Volatility loss (%) of the five lubricants within the API SF grade tested after eight weeks of heating at 100°C

Differences of the thermal stability of four motor oils in the SG group was determined by dynamic OOT (°C) and isothermal OIT (min) and were shown in Fig. 8 (a). The oxidative stability property in terms of OOT showed that SG3 had the highest OOT and stayed relatively constant during the degradation test. This behavior indicated that SG3 had good oxidative stability compared with the rest. SG2 performed slightly better than SG4 within 6 weeks. After that, the OOT oxidative stability of both oils was nearly the same at approximately 259°C. SG1

had the lowest OOT over the degradation test. At the end of the degradation test, OOT of SG1 decreased by 12.5°C while the other lubricants such as SG2 SG3 and SG4 had smaller changes of 7.4, 5.7 and 5.4, respectively. For this reason, it was concluded that SG1 had the lowest oxidative stability in SG group. OIT test of four SG motor oils revealed that throughout the degradation test, SG2 and SG3 were the most stable oils for SG group.

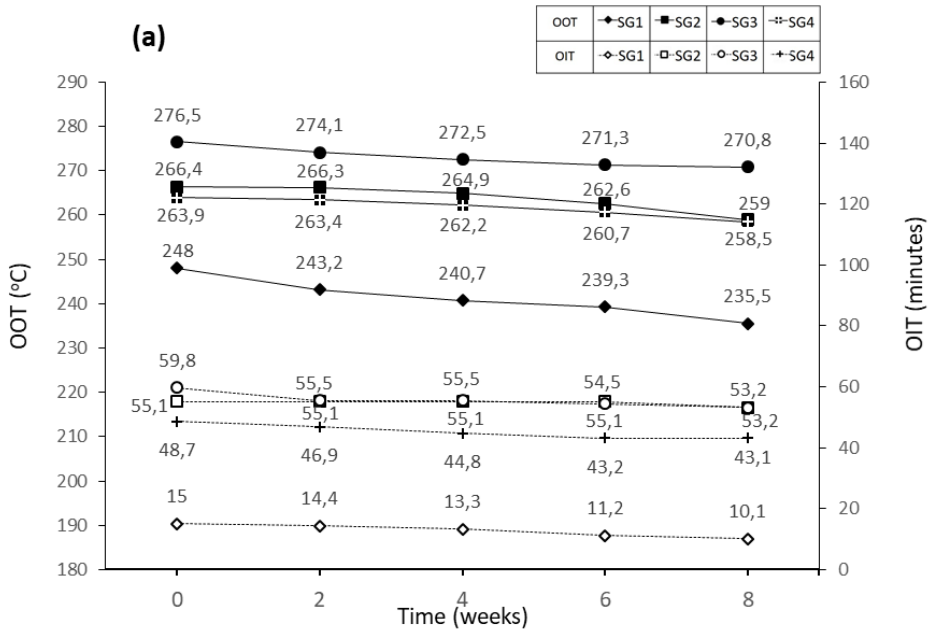

Fig. 8 (a) Values of OOT (°C) on the left axis (the upper group) and OIT (min) on the right axis (the lower group) of the five lubricants within the API SG grade tested over eight weeks of heating at 100°C

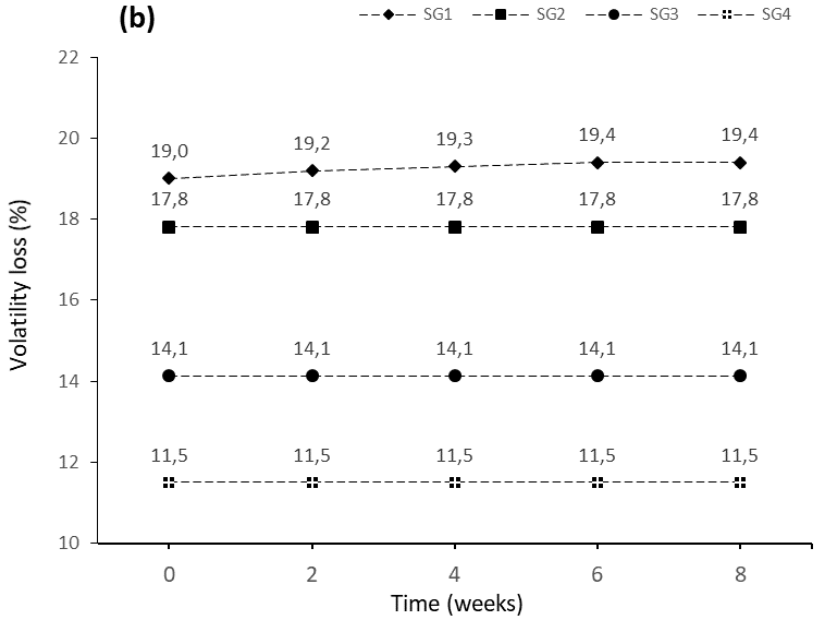

Fig. 8 (b) Thermal degradation test in eight weeks in terms of volatility loss (%) of the five lubricants within the API SG grade tested after eight weeks of heating at 100°C

The OIT results of both oils were the same after 2 weeks. At the end of the degradation test, SG2 and SG3 had OIT at 53.2 mins, which was the highest oxidation time in this SG

group. SG4 was more stable than SG1 but its oxidation time was not as good as that of SG2 and SG3. Therefore, SG1 was the least stable when considered OIT and OOT values.

Fig. 8 (b) showed volatility loss (%) by TGA of four motor oils in SG group. The overall volatility trends of SG2, SG3, and SG4 stayed relatively constant at 17.8, 14.1 and 11.5%, respectively. Only SG1 oil had a different volatility behavior. It was the highest volatile oil in SG category and at the end of degradation, the volatility increased by 0.4%. The results from Fig. 8 (a and b) showed that SG3 was the most dominant in the oxidation properties. It had the highest OOT and OIT during the degradation test. However, SG3 evaporated more than SG4 by 2.6%. This small difference was not significant. Therefore, SG3 had the best performance in SG group.

The results for SJ group were illustrated in Fig. 9 (a). The oxidative stability of three motor oils showed that OOT of all motor oils were reduced with increasing incubation time. SJ2 was more stable than SJ1 and SJ3. Before the degradation process, SJ2 was oxidized at approximately 283°C. After 8 weeks, the oxidative stability decreased by approximately 8°C. The OIT result revealed that stability of SJ1 was higher than SJ3. These 2 oils had almost the same oxidation temperature before the degradation test. Over the period, they had similar oxidation trends. However, SJ1 had better stability than SJ3 because its OOT value was higher. At the end of the degradation process, SJ1 OOT was reduced by only 6.4°C while SJ3 OOT was reduced by 10°C. The OIT results showed the same oxidation trend as the OOT results. SJ2 was the most stable oil in this group because its OIT was the longest while SJ1 and SJ3 had almost the same oxidation induction time. Fig. 9 (b) presented the difference of volatility property (%) over 8 weeks of three oils in SJ category. SJ1 maintained low volatility property and stayed constant in volatility loss over the degradation test. This volatile behavior indicated that SJ1was a good quality motor oil. For volatility loss of the others, there was a small change of 0.1% volatility for SJ2 while SJ3 had the highest volatility loss of 21%. The order of volatilization of 3 oils was SJ3 > SJ2 > SJ1. The thermal stability of SJ group shown in Fig. 9 (a and b) indicated that SJ2 had a better performance in the oxidative stability and volatility than the others.

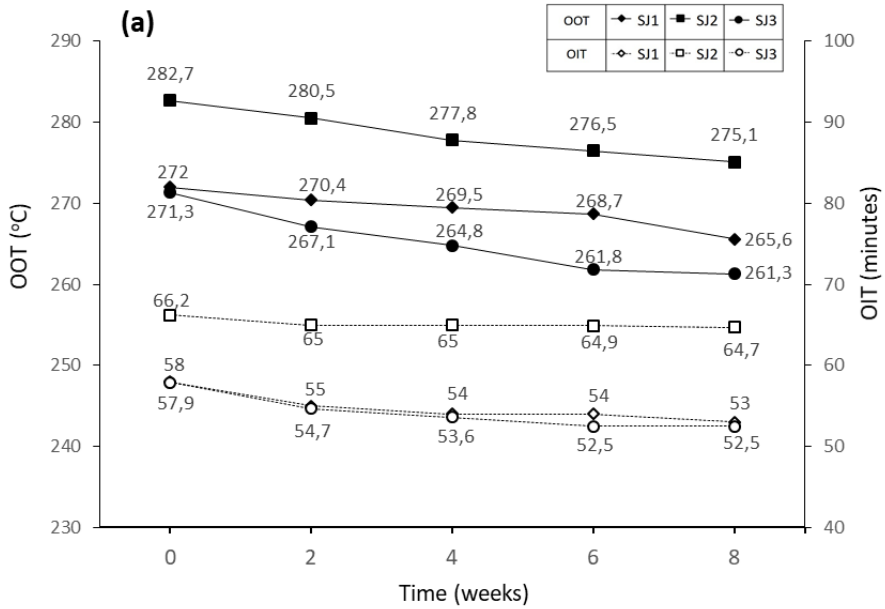

Fig. 9 (a) Values of OOT (°C) on the left axis (the upper group) and OIT (min) on the right axis (the lower group) of the five lubricants within the API SJ grade tested over eight weeks of heating at 100 °C

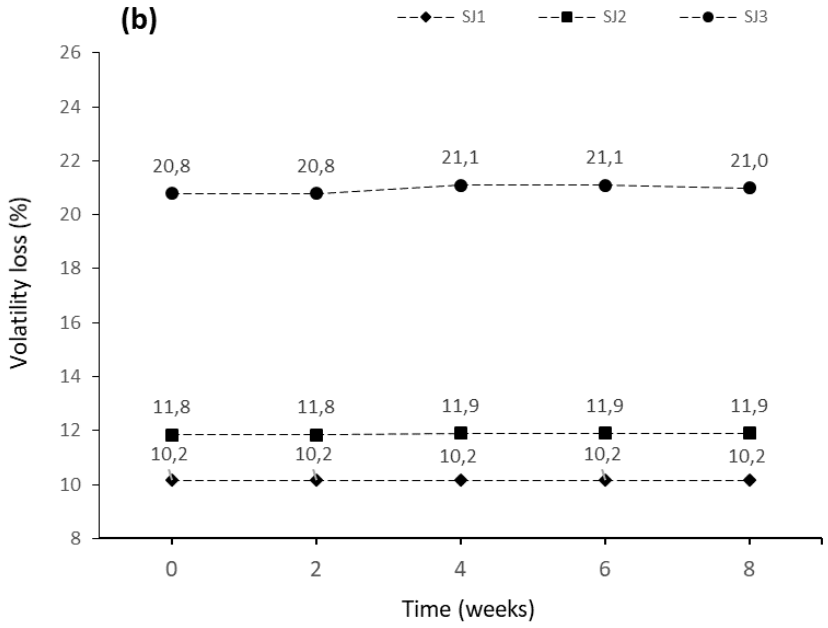

Fig. 9 (b) Thermal degradation test in eight weeks in terms of volatility loss (%) of the five lubricants within the API SJ grade tested after eight weeks of heating at 100°C

The oxidative stability properties of motor oils in SL category were shown in Fig 10 (a). All OOT values were reduced after the thermal degradation process. It was noted that SL2 had the highest OOT before the aging test then reduced by 12.5°C after 8 weeks. The OOT of SL1 and SL3 were lower at 287.8°C and 279°C and decreased by 6.2 and 7.1°C at the end of the degradation test. Although SL2 had the highest oxidative stability that reached 294°C, after 8 weeks the OOT decreased sharply to 281.4°C, which was almost the same temperature as that of SL3. For this reason, SL3 should be identified as a high performance motor oil in SL group. The OIT result showed the oxidation time of SL motor oils in Fig 10 (a).

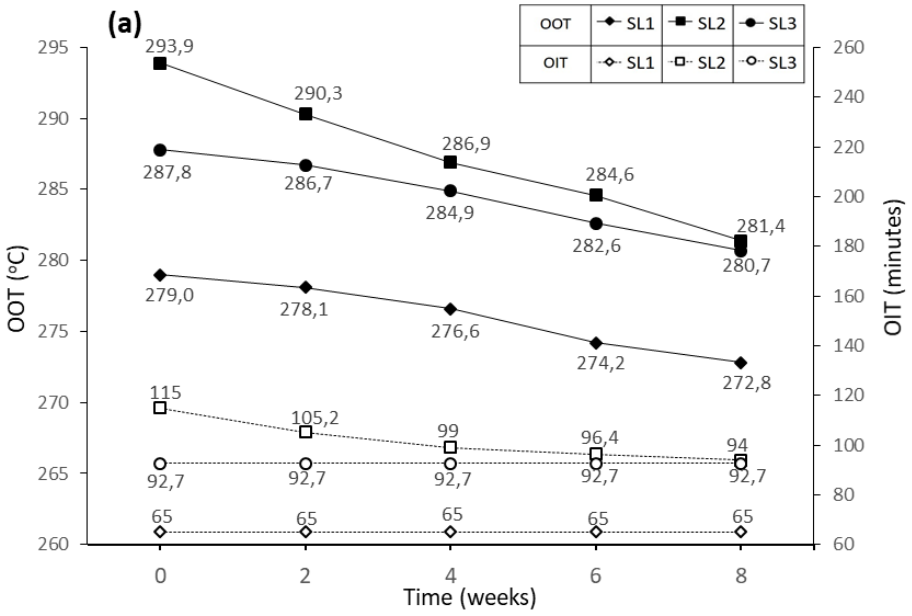

Fig. 10 (a) Values of OOT (°C) on the left axis (the upper group) and OIT (min) on the right axis (the lower group) of the five lubricants within the API SL grade tested over eight weeks of heating at 100°C

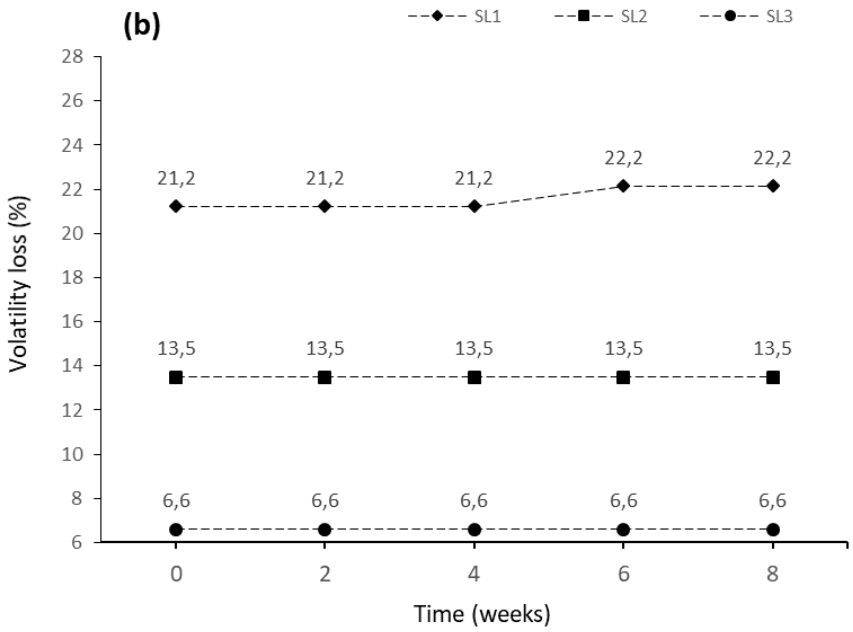

Fig. 10 (b) Thermal degradation test in eight weeks in terms of volatility loss (%) of the five lubricants within the API SL grade tested after eight weeks of heating at 100°C

It could be observed that SL2 oil had the same trend as its OOT results, its OIT reduced by 21 mins over 8 weeks. For SL1 and SL3, OIT results had no change in oxidation time at 65 and 93 mins, respectively. A good stable oil should have constant OIT value and take a long time to be oxidized. The OIT results showed that SL3 was the most stable oil in this group. The volatilization of three motor oils was evaluated and showed in Fig. 10 (b). SL1 had the highest volatility at 21.2% and increased slightly to 22.2% at the end of the test. However, SL3 had better volatility than SL2. The volatility property of SL2 was 13.5% while SL3 was 6.6%. The volatility loss of both oils remained constant over 8 weeks. The results indicated that SL3 had the best volatile property (lowest loss) and remained unchanged. SL3 also had the best oxidative stability in SL group.

The OOT and OIT results were provided by the conventional DSC, which was very useful tool for characterizing the oxidative stability of commercial motor oils. An exothermic peak from DSC output signal expressed the hydrocarbon chains that were oxidized by a free radical mechanism [26]. It expressed level of resistance of a motor oil to oxidation reaction during the testing period [27]. In the analysis of OOT and OIT results, it was observed that there was a good correlation between the latest service API category and oxidative stability. The newer API category showed higher oxidative stability than the old category. This was a clear indication of the latest API standard accompanies with better anti-oxidation properties of the lubricants [28]. The rate of oxidation of lubricant was influenced by the quality and type of base oil as well as the antioxidant additives. Antioxidants played an important role to protect the lubricant in service by limiting the chemical changes and degradation [29]. Moreover, OOT and OIT applications were widely used for assessing the improvement of oxidative stability of lubricants [30-32]. Both OOT and OIT are good for quality identification and should be provided to customers. TGA Noack application was a good method for evaluating the volatility of lubricant. It was useful for estimation of volatility oil at high temperature condition such as engine operating temperature. Rate of volatility depended on the differences in molecular structure of base oil and additives [33]. The results of TGA Noack indicated that increase of volatility in oil was not influenced by the SAE viscosity grades and the API service categories. The differences of volatility in individual motor oil exhibited the lubricant's tendency to vaporize. The high volatility motor oil was not recommended because there may not have enough lubricant to

lubricate and reduced the heat generated between surfaces in the engine. Moreover, high volatility lubricants had a chance to be consumed more than low volatility oil at the normal operating temperature of the engine. It caused several serious problems of engines such as oil starvation, which would generate friction, wear and raise temperature of engines [34]. As shown in this study, volatility testing data should be added to product labels in order to better inform customers of the critical information of motor oils. The results of the oxidative stability and volatility during the thermal degradation process revealed useful information about performance of several API grades.

3.3. Kinetics of thermal decomposition

Kinetics of thermal decomposition in motor oils were determined using data obtained from TGA result. The temperature ranges were shifted to higher temperatures when heating rate was increased. In addition. Following the KAS method plotted of 1/T versus ln (β/T^2) at 9 conversion levels (α) at 0.1-0.9, all plots had a strong linear relationship ($r^2 > 0.98$). The apparent activation energies (E_a) were calculated from the slope of the linear regression equation at different conversion levels. Table 2-6 are lists of the apparent activation energies of fresh and aged lubricants in SC, SF, SG, SJ and SL category, respectively. It was clearly shown that the trends of apparent activation energy increased from low to high conversion levels because long chain hydrocarbons remained in the base oil degraded at high activation energy [35]. Moreover, the average of the apparent activation energy of 5 categories in all fresh motor oils was higher than the aged lubricants. This showed that fresh lubricants are more stable than aged lubricants because chemical structures of base oils change from long chain hydrocarbons to aromatic compound during long exposure to high temperature for long period. Moreover, straight chains are substituted by aromatic rings and decrease the oxidative stability of lubricants [36-37].

Table 2. Activation energies determined of fresh and aged lubricants using Kissinger-Akahira-Sunose method in the API SC grade

Conversion	Activation energy (kJ/mol)									
	SC1		SC2		SC3		SC4		SC5	
	fresh	aged	fresh	aged	fresh	aged	fresh	aged	fresh	aged
0.1	91.98	90.43	78.81	74.87	89.79	80.39	86.12	83.84	77.67	75.04
0.2	92.04	88.94	78.77	76.62	99.40	89.61	98.77	87.04	87.97	84.56
0.3	93.57	90.99	80.95	79.26	105.91	98.35	100.05	95.92	95.81	88.84
0.4	92.48	89.08	83.12	82.61	104.56	96.63	99.58	97.13	98.20	92.56
0.5	98.85	95.07	85.58	84.08	106.85	99.40	105.66	102.79	102.38	99.34
0.6	97.28	96.23	88.49	87.36	115.48	107.92	106.22	104.76	104.05	98.83
0.7	100.57	99.77	91.02	88.64	113.49	105.34	107.58	106.73	107.69	103.28
0.8	103.21	102.94	94.46	91.04	116.18	109.10	112.96	110.62	112.95	107.06
0.9	107.99	106.79	98.65	96.13	119.19	113.43	114.62	113.12	118.99	114.41
Mean	97.55	95.58	86.65	84.51	107.87	100.02	103.51	100.22	100.63	95.99

Table 3. Activation energies determined of fresh and aged lubricants using Kissinger-Akahira-Sunose method in the API SF grade

Conversion	Activation energy (kJ/mol)									
	SF1		SF2		SF3		SF4		SF5	
	fresh	aged	fresh	aged	fresh	aged	fresh	aged	fresh	aged
0.1	84.59	79.61	75.38	72.27	85.35	78.04	82.22	74.52	85.08	78.40
0.2	96.90	92.50	83.62	79.99	93.71	86.64	89.01	87.94	94.39	86.97
0.3	97.03	95.48	87.35	84.48	97.91	90.75	91.33	86.02	99.89	91.85
0.4	100.60	97.90	90.18	87.41	106.98	94.99	93.42	89.02	103.17	95.88
0.5	104.80	101.20	93.08	90.38	105.17	98.69	96.48	91.29	106.74	98.51
0.6	107.80	103.70	96.20	92.34	109.12	101.32	100.95	93.77	110.14	103.26
0.7	110.80	106.80	98.65	95.14	112.72	109.67	101.56	97.09	115.71	107.84
0.8	115.40	110.10	100.92	98.84	116.67	108.43	104.76	99.73	122.91	120.76
0.9	118.20	114.90	104.57	102.33	121.33	113.14	108.37	103.04	137.86	134.84
Mean	104.01	100.24	92.22	89.24	105.44	97.96	96.46	91.38	108.43	102.03

Table 4. Activation energies determined of fresh and aged lubricants using Kissinger-Akahira-Sunose method in the API SG grade

Con-version	Activation energy (kJ/mol)							
	SG1		SG2		SG3		SG4	
	fresh	aged	fresh	aged	fresh	aged	fresh	aged
0.1	74.86	75.94	76.89	69.72	82.15	79.4	79.64	73.37
0.2	80.83	80.78	82.55	77.18	89.53	87.23	89.56	86.88
0.3	83.32	82.15	84.64	79.72	92.47	90.91	94.45	85.47
0.4	85.41	83.54	86.60	84.03	94.87	92.39	98.35	89.36
0.5	88.40	84.94	89.53	82.61	96.55	94.90	102.51	95.15
0.6	92.06	86.13	91.45	84.05	98.80	96.12	105.80	98.79
0.7	95.94	87.29	96.24	85.57	100.93	98.84	108.78	100.04
0.8	100.71	89.09	97.54	86.56	102.59	100.74	112.55	99.73
0.9	105.28	91.02	100.24	88.29	105.44	102.70	117.14	107.57
Mean	89.65	84.54	89.52	81.97	95.93	93.69	100.98	92.93

Table 2 showed activation energy results of SC group. SC3 and SC4 were the most stable oils in this group. At the initial condition, the average apparent activation energy of SC3 and SC4 were 107.87 and 103.51 kJmol^{-1}, respectively. After the degradation period, the average apparent activation energy of these 2 motor oils drops by approximately 8 and 3 kJmol^{-1}, respectively. SC1, SC2 had activation energy below 100 kJmol^{-1} before the ageing period. After 8 weeks, activation energy decreased by approximately 2 kJmol^{-1}. SC5 decreased activation energy by approximately 5 kJmol^{-1}. After thermal degradation test, its activation energy was almost the same as that of the SC1.The apparent activation energy results indicate that a motor oil having higher activation energy is more stable than that with a lower average apparent activation energy [35]. Table 3 clearly indicated that SF5 was the most stable motor oil in SF group. The average apparent activation energy reached 108.43 kJmol^{-1} at the fresh condition and dropped to 102.03 kJmol^{-1} after 8 weeks of ageing test. SF1 and SF3 had quite a high activation energy at 104.01 and 105.44 kJmol^{-1}, respectively. However, the activation energy of SF2 and SF3 were not over 100 kJmol^{-1}. Especially, SF3 was the lowest stability in SF group. Table 4 showed the average apparent activation energy of SG grade. It indicted that after degradation test, SG3 and SG4 had the highest activation energy (93-94 kJmol^{-1}). However, when compared activation energy results at the fresh condition of 2 motors. SG4 had a significantly greater value than SG3 by approximately 5 kJmol^{-1}. This shows that SG3 was the most stable motor oil in SG group. The apparent activation energy of SJ and SL grades were listed in Table 5 and 6, respectively.

Table 5. Activation energies determined of fresh and aged lubricants using Kissinger-Akahira-Sunose method in the API SJ grad

Con-version	Activation energy (kJ/mol)					
	SJ1		SJ2		SJ3	
	fresh	aged	fresh	aged	fresh	aged
0.1	84.02	79.82	81.66	75.73	82.37	78.31
0.2	89.83	83.87	89.03	83.06	88.67	82.98
0.3	95.93	88.74	94.51	88.55	91.66	84.05
0.4	102.23	92.38	100.39	91.94	94.18	85.91
0.5	108.28	97.92	104.69	99.32	95.90	87.63
0.6	113.86	103.62	109.19	103.16	98.28	89.94
0.7	120.25	107.42	117.58	108.41	100.25	91.98
0.8	128.72	112.92	117.58	114.87	104.38	95.19
0.9	136.93	121.98	122.41	121.18	110.86	101.22
Mean	108.89	98.74	104.12	98.47	96.28	88.58

SJ1 and SJ2 were more stable than SJ3 for fresh motor oil. After degradation, they had a similar average apparent activation energy of 98-99 kJmol^{-1}. However, at fresh condition SJ1 had higher average apparent activation energy than SJ2 by approximately 5 kJmol^{-1}. In SL group, ageing condition of SL3 exhibited the most stable lubricant in this group and showed

the highest activation energy among 19 motor oils (average activation energy = 104.2 kJmol^{-1}). In fresh condition, the activation energy of SL3 was very high (108.92 kJmol^{-1}) while SL1 and SL2 were 103.72 and 106.08 kJmol^{-1}, respectively. After the degradation period, SL3 decreased its average activation energy only by 4 kJmol^{-1} while SL1 and SL2 lost activation energy by approximately 8 and 21 kJmol^{-1}.

Table 6. Activation energies determined of fresh and aged lubricants using Kissinger-Akahira-Sunose method in the API SL grade

Con-version	Activation energy (kJ/mol)					
	SL1		SL2		SL3	
	fresh	aged	fresh	aged	fresh	aged
0.1	79.68	72.92	82.25	66.78	95.18	90.26
0.2	84.06	80.09	92.46	75.38	98.88	95.01
0.3	95.57	86.78	97.75	78.98	100.56	97.23
0.4	99.92	91.45	102.22	83.07	103.88	99.97
0.5	104.69	97.21	107.29	85.61	107.05	105.56
0.6	108.12	98.61	112.29	89.09	112.31	109.25
0.7	113.83	103.18	116.79	92.68	118.31	114.59
0.8	119.56	111.77	120.52	95.70	120.79	116.51
0.9	128.09	118.18	123.12	98.41	123.33	119.39
Mean	103.72	95.58	106.08	85.08	108.92	105.31

The activation energy analysis of fresh and aged motor oils can be used to characterize the stability of lubricants. This study showed that there was no correlation between the activation energy and lubricant grades. The differences of the apparent activation energy depend on a formulation of base oils and additives present in motor oil. These variations can be attributed to the complex organic transformations occurring during degradation of the motor oil [35]. These components such as base oil, antioxidants, detergent, corrosion inhibitors, viscosity index improvers, anti-wear agents, and anti-foaming agents are important factors and impact to the changes in the apparent activation energy of motor oils. Determination of stability by using the apparent activation energy during thermal degradation process provide a better understanding in physiochemical properties of motor oils.

4. Conclusions

The results of these studies can be used to characterize the performance of motor oils. Good oxidative stability of lubricants had high OOT, OIT, and the activation energy while volatility loss was low. Using the common DSC to determine OIT and OOT were very useful for evaluation of the oxidative stability in lubricants. The TGA Noack test provided valuable information on volatilities of lubricant. It simulated real life conditions, which lubricant exposed to a high temperature and air. Volatility measured by Noack did not correlate well with the SAE viscosity and the API categories. Moreover, mass loss data of TGA can be used to calculate the apparent activation energy. This is an important tool for stability study.

These lubricant properties shown from this work are practical and powerful indicators for characterization performance of lubricant products in the market.

- Oxidative degradation was critical information to determine a performance of motor oils.
- The SAE viscosity and the API category were not good factors to determine the volatility of commercial motor oils.
- The latest API category (SL) were more stable than the previous categories (SC, SF, SG, and SJ).
- Lubricants with the same SAE viscosity and API category could show significant differences in their oxidative stability and volatility.
- Stability of lubricant can also be evaluated in term of the activation energy, and there is no correlation between the activation energy and API grades.

- The ageing test is important to physiochemical degradation study of motor oils. These thermal analysis applications such as OIT, OOT, volatility and the activation energy can be used for stability determination.

Acknowledgement

The authors are grateful and acknowledge discussions with Professor Supapan Saraphin. Funding support by the Nanotec research fund grant number P1752632 greatly appreciated

References

[1] Ng W, Law H. The New Lubricant Trade in ASEAN. Ipsos Business Consulting. 2015; 1-9.
[2] Madanhire I, Mbohwa C. Mitigating Environmental Impact of Petroleum Lubricants, Springer; 2016; Chapter 2; 17-34.
[3] Stepina V, Vesely V. Lubricants and special Fluids, 1st ed.; Elsevier; 1992; Chapter 2; 63-68.
[4] Ebert LB. Chemistry of Engine Combustion Deposits, L.B. Ebert., Ed.; Springer: Boston, 1985; Chapter 17; 289-302.
[5] Kök MV, Sztatisz J, Pokol G. High-Pressure DSC Applications on Crude Oil Combustion. Energy & Fuels 1997; 11(6): 1137-1142.
[6] Perez JM. Oxidative properties of lubricants using thermal analysis. Thermochimica Acta 2000; 357–358: 47–56.
[7] Gamlin CD, Dutta NK, Choudhury NR, Kehoe D, Matisons J. Evaluation of kinetic parameters of thermal and oxidative decomposition of base oils by conventional, isothermal and modulated TGA and pressure DSC. Thermochimica. Acta 2002; 392–393: 357–369.
[8] Crnkovic PM, Leiva CRM, dos Santos AM, Milioli FE. Kinetic study of the oxidative degradation of Brazilian fuel oils. Energy Fuels 2007; 21(6): 3415–3419.
[9] Blaine LR. Thermal analytical characterization of oils and lubricants. American Laboratory 1994; 18(1): 18–20.
[10] Peltzer M, Jiménez A. Determination of oxidation parameters by DSC for polypropylene stabilized with hydroxytyrosol (3,4-dihydroxy-phenylethanol). Journal of Thermal Analysis and Calorimetry 2009; 96(1): 243–248.
[11] Volponi, JE, Mei LHI, Rosa DS. Use of oxidation onset temperature measurements for evaluating the oxidative degradation of isotatic polypropylene. Journal of Polymers and the Environment 2004; 12(1): 11–16.
[12] Tarrío-Saavedra J, Naya S, López-Beceiro J, Gracia-Fernández C, Artiaga R. Thermooxidative properties of biodiesels and other biological fuels. Biodiesel- Quality, Emissions and By-Products, 1st ed.; InTech, 2011; Chapter 3; 55-59.
[13] Pirjola L, Karjalainen P, Heikkilä J, Saari S, Tzamkiozis T, Ntziachristos L, Kulmala,K, Keskinen J, and Rönkkö T. Effects of Fresh Lubricant Oils on Particle Emissions Emitted by a Modern Gasoline Direct Injection Passenger Car. Environmental Science & Technology 2015; 49(6): 3644-3652.
[14] Zinbo M, Skewes LM. Determination of engine oil volatility by thermogravimetry. Thermochimica Acta 1989; 154(2): 367-376.
[15] Standard Test Method for Evaporation Loss of Lubricating Oils by Thermogravimetric Analyzer (TGA) Noack Method. ASTM D6375-09
[16] Focke WW, Westhuizen IVD, Grobler ABL, Nshoane K.T, Reddy J.K, Luyt A.S. The effect of synthetic antioxidants on the oxidative stability of biodiesel. Fuel 2012; 94: 227-233.
[17] Standard Test Methods for Determining Oxidation Induction Time of Hydrocarbons by Differential Scanning Calorimetry. ASTM E1858-00
[18] Standard Test Methods for Oxidation Onset Temperature of Hydrocarbons by Differential Scanning Calorimetry. ASTM E2009-08
[19] Kök MV, Pamir MR. Non-Isothermal Pyrolysis and Kinetics of Oil Shales. Journal of Thermal Analysis and Calorimetry 1999; 56(2): 953-958.
[20] Crnkovic PM, Leiva CRM, dos Santos AM, Milioli FE. Kinetic study of the oxidative degradation of Brazilian fuel oils. Energy & Fuels 2007; 21(6): 3415-3419.
[21] Ichiro M. Molecular Science of Lubricant Additives. Applied Sciences 2017; 7(5): 445.
[22] Vyazovkin S, Burnham AK, Criado JM, Pérez-Maqueda L.A, Popescu C, Sbirrazzuoli, N. ICTAC Kinetics Committee recommendations for performing kinetic computations on thermal analysis data. Thermochim. Acta 2011; 520(1-2): 1–19.

[23] Santos JCO, dos Santos IMG, Souza AG, Sobrinho EV, Fernandes VJ, Silva AJN. Thermoanalytical and rheological characterization of automotive mineral lubricants after thermal degradation, Fuel 2004; 83(17–18): 2393-2399.
[24] Lim ACR, Chin BLF, Jawad ZA, Hii KL. Kinetic Analysis of Rice Husk Pyrolysis Using Kissinger-Akahira-Sunose (KAS) Method. Procedia Engineering 2016; 148: 1247-1251.
[25] Vyazovkin S, Burnham A.K, Criado J.M, Pérez-Maqueda LA, Popescu C, Sbirrazzuoli N. ICTAC Kinetics Committee recommendations for performing kinetic computations on thermal analysis data. Thermochim. Acta 2011; 520: 1–19.
[26] Mayo FR. Free radical autoxidations of hydrocarbons. Accounts of Chemical Research 1968; 1(7): 193-201.
[27] Černý J, Zelinka M. Oxidative stability of Lubricants Measured by a PDSC Technique. Pet Coal 2004; 46: 56-62.
[28] Fox MF. Chemistry and Technology of Lubricants, Mortier R, Fox M, Orszulik S.; Ed., Springer, 2010; Chapter 17; 512-527.
[29] Aguilar G, Mazzamaro G, Rasberger M. Chemistry and Technology of Lubricants, Mortier R, Fox M, Orszulik S.; Ed., Springer, 2010; Chapter 4; 140-146.
[30] Adamczewska J, Love C. Oxidative stability of lubricants measured by PDSC CEC L-85-T-99 test procedure. Journal of Thermal Analysis and Calorimetry 2005; 80(3): 753–759.
[31] Wu Y, Weimin L, Zhanga M, Wang X. Improvement of oxidative stability of trimethylolpropane trioleate lubricant. Thermochimica Acta 2013; 569: 112-118.
[32] Salih N, Salimon J, Yousif E, Abdullah BM. Biolubricant basestocks from chemically modified plant oils: ricinoleic acid based-tetraesters. Chemistry Central Journal 2013; **7**: 128-141.
[33] Rudnick LR. Additives for industrial lubricant applications, 2nd ed,; CRC Press, 2009; Chapter 26; 493-506.
[31] Rudnick LR, Buchanan RP, Medina F. Evaluation of oxidation-mediated volatility of hydrocarbon lubricant base fluids, Synthetic Lubrication 2006; 23(1): 11–26.
[35] Tripathi AK, Vinu R. Characterization of thermal stability of synthetic and semi-synthetic engine oils. Lubricants 2015; 3(1): 54-79.
[36] Adhvaryu A, Perez JM, Singh ID. Application of quantitative NMR spectroscopy to oxidation kinetics of base oils using a pressurized differential scanning calorimetry technique. Energy Fuels 1999; 13(2): 493–498.
[37] Vinu R, Broadbelt LJ. Unraveling reaction pathways and specifying reaction kinetics for complex systems. Annual review of chemical and biomolecular engineering. 2012; 3: 29–54.

To whom correspondence should be addressed: Dr. Tirapote Rattana-amron, National Nanotechnology Center (NANOTEC), National Science and Technology Development Agency (NSTDA), Pathum Thani 12120, Thailand

Petroleum and Coal

Article **Open Access**

EFFECT OF ASPHALT MIXTURE AGGREGATE ON TIRE SLIP ON THE WET SURFACE OF ASPHALT PAVEMENTS

Mohammad Hosein Dehnad, Abolfazl Arezoomand*

Department of Civil Engineering, Engineering Faculty, University of Qom, Qom, Iran

Received October 5, 2018; Accepted December 21, 2018

Abstract

The existence of any liquid on the pavement surface causes a decrease in skid resistance. Heavy rain storm or improper surface grading leave a water film on the pavement surface. By increasing water film and vehicle velocity, there is a moment in which hydroplaning phenomenon can occur and causes the vehicle linear speed to become disproportionate to wheel rotational speed. In this study, a new laboratory-scale simulator is designed and manufactured that can simulate the occurrence of hydroplaning on asphalt pavements, facilitating the study of different parameters on the occurrence of this phenomenon such as vehicle speed, water film thickness, tire thread, pavement surface physical properties, etc. The lack of proportion between the linear movement of vehicle shaft and wheel rotation was considered as an important principle in designing of this machine. The designed apparatus involved electrical, mechanical, water transfer and asphalt mixture parts. The obtained results showed that the ratio of wheel rotational speed to its longitudinal speed is a proper index for identifying hydroplaning threshold. The results showed that by increasing frequency from 27.5 to 35 Hz, the ratio of wheel rotation to axle rotation in rpm is reduced by almost 10% in wet condition and hydroplaning occurred.

***Keywords**: Laboratory-Scale machine; Friction; Hydroplaning; Asphalt Pavement; AUT Simulator.*

1. Introduction

One of the important issues in road safety is friction between the vehicle tire and road surface. When the road surface is exposed to rain, a thin water film is established on the pavement surface. Water film performs as a lubricant and having the obvious result of decreasing skid resistance. The downfall in the level of skid resistance establishes dangerous situation for vehicles. On the one hand, pavement macrotexture is as the most important factor in skid resistance and present micro drainage capacity in the pavement surface. In a way that current protrusions on road surface and distance between rough stones cause to decrease water film thickness which is formed between pavement and tire. In another hand, vehicles traffic on the road, decrease pavement macro texture gradually. At high speeds and intensive rainfalls, tire tread can't scatter accumulated water between tire and pavement and a water film is formed between tire and pavement, totally eliminating any direct contact between the tire and the pavement surface [1]. This phenomenon is called hydroplaning which is affected by various related factors to vehicle tire pressure and thread, fluid and pavement surface [2].

The fluid thickness and its density are effective parameters which are related to the fluid. According to Ong *et al.*, when the thickness of water film increases to 0.1 to 2 mm, hydroplaning speed decreases drastically [3]. Micro-texture and macro-texture of pavement surfaces are important related factors in road surface which are influential in hydroplaning occurrence. According to the studies of Ong *et al.*, if the mean texture depth is in the range of 0.2 to 0.5mm pavement micro-texture can postpone hydroplaning through increasing hydroplaning

speed by up to 20% [3]. In another study, Yager used sand patch test to identify the level of texture depth and its relation to the potential of hydroplaning for various pavement surface [4].

2. Background

According to Figure 1, contact surface between tire and pavement composed of 3 areas [1]: Area (A): (sinkage zone), there isn't any contact between the tire and the pavement in this area. The tire floats on a wedge of water.

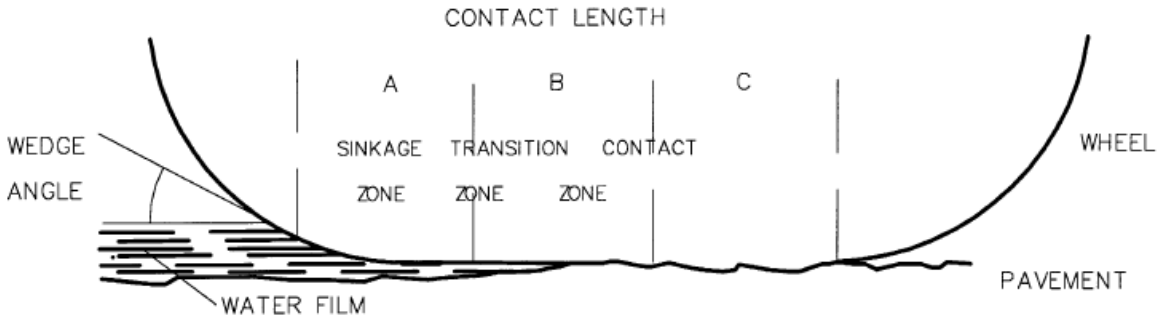

Figure 1. Contact surface between pavement and tire

Area (B): (transition zone), in this area water film being cut in some parts by some aggregates and friction force could develop due to existing micro-texture on coarse aggregates. Connection to aggregates resulted in tire deformation in this area.

Area (C): (tractive zone), there isn't any contact between tire and water layer in this area, and the whole micro-texture of the surface is active to increase friction.

By increasing vehicle speed, accessible time decreases to escape water from the interface between pavement and tire and increase the lubricating effect of water. According to previous studies, by increasing speed of the vehicle, area C would be small. Both areas A and B would be larger proportionally. If the tractive area is equal to zero and formed layer under tire wouldn't be interrupted, the contact between tire and pavement are removed completely. In this situation, the vehicle slide on the water. In this case, the hydroplaning phenomenon occurs.

Cerezo *et al.* are proposed a hydroplaning speed model calculating the water-film thickness by using road characteristics measurements [2].

If a tire is in full contact with the pavement surface and can roll freely, the relative speed between tire circumference and pavement which is called slip speed is equal to zero. The mathematical relationship for slip speed is as follows [5]:

$$S = V - V_p = V - (20.73 \times \omega \times r) \quad (1)$$

where, S = Slip speed km/h; V = Vehicle speed km/h; V_p = Average peripheral Speed of the tire km/h; ω = Angular velocity of tirthe e, radians /sec; r = Average radius of the tire, cm.

In the state of free tire roll, V_p is equals to vehicle speed and S is zero. For a fully locked wheel, V_p is equals to zero and slip speed is equals to vehicle speed. Slip ratio (SR) can be calculated from Equation 2 [5]:

$$SR = \frac{V - V_p}{V} \times 100 = \frac{S}{V} \times 100 \quad (2)$$

In another research in the university of Texas A&M, a study is performed on the relationship between wheel slip ratio and hydroplaning. The main finding of this research was that if the level of slip ratio is more than 10%, a considerable reduction in friction will occur and hydroplaning will happen [6].

A review of the present literature did not reveal the existence of any lab-scale apparatus for studying hydroplaning. Most studies are based on field tests and apparatus that are used for testing skid resistance and surface texture in the field [2,7]. For example, NCHRP has introduced outflow meter (ASTM E 2380) which is used for measuring macro texture surface as

hydroplaning evaluator apparatus [8]. One of the tire manufacturing companies, designed and invented a lab-scale apparatus with the aim of studying the effects of different tire thread patterns on hydroplaning initiation [9]. The advantage of this apparatus is a simple mechanism in its performance, low cost, the possibility of performing the test in short time and controlled environmental. On the other hand, the performance of the apparatus is contrary to what actually happens in a real situation. In a way that in a real situation, vehicle move in high speed on fluid. While in this apparatus, water move under fixed wheel by high pressure. One of the disadvantages of this apparatus is that the lack of wheel is moving on the surface by different velocities. For this reason, hydroplaning occurrence speed can't be measured.

Another machine called Skid Resistance Interface Testing Machine has been designed and built by TU-Delft University in the framework of the SKIDSAFE project to study the effect of the various phenomena occurring at the tire and pavement interface. This machine enables various combinations of slip velocity and pressure to be applied with concurrent measurement of temperature in the interface regions. With this device, it is also possible to study the raveling resistance of a surfacing material [10].

In another study Hichri et al. are developed a laboratory test method to reproduce the deposit of contaminant particles on the road surface and measure the friction coefficient on dry and wet contaminated surfaces [11].

3. Methodology

In the designed apparatus, which is named AUT Simulator, one wheel with linear suspension system and defined vertical load is connected to a central shaft through a crank, and it moves with an electromotor. Water splash operation performs with a definite pressure to the surface between wheel and asphalt mixture through water nozzle which is mounted in front of the wheel. With the use of a compactor on another crank, asphalt mixture has been compacted. By using a tachometer which is installed on the wheel and central shaft, the slipperiness of wheels and the part of a wheel rolling that is transferred to wheel skid are identified, and the hydroplaning phenomenon is evaluated in different conditions.

One magnetic brake is connected to wheel shaft to apply different friction factor and make negative torsion which has the ability of continuous range operation of brake changes. Also, for the observation of apparatus outputs, the software was used which can show the amounts of wheels revolution per minute (rpm) and central shaft on display machine momently by setting revolution frequency and apparatus speed in definite intervals.

By using AUT simulator, it is possible to compact different asphalt mixtures in the mold and evaluate the impact of pavement surface texture on hydroplaning initiation. Asphalt mixture is compacted in the molds using a similar procedure to ensure a constant mix void ratio and compaction percentage [12].

The number of revolutions is registered by two tachometers momently. By comparing these amounts in dry and wet conditions of the pavement surface, one can predict the occurrence of hydroplaning. In other words, the lack of proportion between a number of wheel rotation and the amount of wheel longitudinal movement is identified as the occurrence of this phenomenon. This is similar to the slide of moving car which doesn't roll its wheel the same amount of space which has moved and some part of rolling has transferred to wheel skid. Also, with designing and manufacturing of this apparatus, different tests can be done for evaluating tire air pressure impact, wheel load and water film thickness on hydroplaning speed. The schematic drawing of the machine is shown in Figure 2.

4. Material and manufacturing process

In this part, designing and manufacturing process of apparatus are described by separating mechanical, electrical, water transfer and asphalt mixture properties.

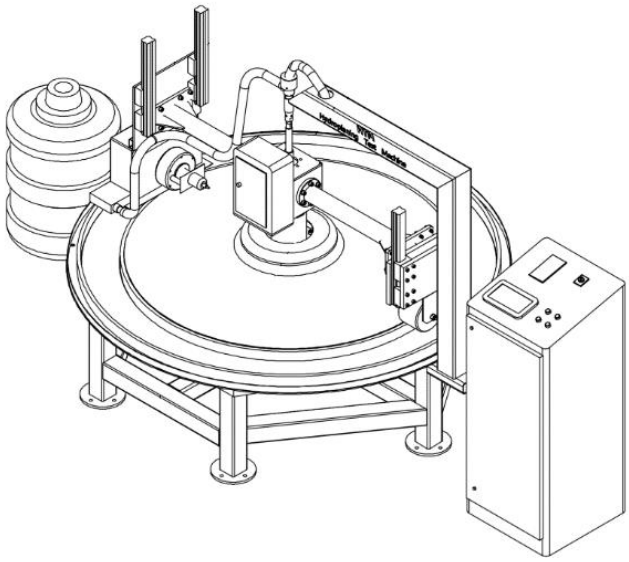

Figure 2. Schematic drawing of the AUT Simulator

4.1. Mechanical parts

The platform that asphalt layer is constructed on has a circular shape. In this structure, there is the possibility of continuous movement on a circular route and this to some extent is the nearest case to the real life situation. In previous apparatuses for assimilating the skid of the wheel, the wheel has been fixed, and fluid crosses under it with pressure [9] or two drams which are connected together, have been used. For ease of pouring and removing asphalt materials from the mold, the aluminum mold was constructed in many segments. A pneumatic tire with 24 cm diameter and 8 cm width was used in this apparatus. Also, to decrease tire thread impact on the hydroplaning phenomenon, a tire without thread has been used. Linear Motion Guide (LM-Guide) suspension was used for smooth circular rotation of the wheel. Mechanical components of the apparatus are shown in Figure 3.

Figure 3. General view of components of apparatus

4.2. Electrical parts

For providing apparatus propellant, one gear electromotor AC has been used. To have a smooth wheel operation at the start and end of the movement and also speed control, one inverter is connected to electromotor which has engine driver role. For connecting electromotor to the central shaft and transferring monotonous speed of the engine to the shaft, timing belt with lateral cogs with high accuracy has been used. In this device for exact rpm counting, the optical rotatory encoder has been used. They produce 2000 ppt in one revolution. Laser line emits on a circular glass plane as black and white continuously, and the rotational speed is identified. For transmitting electronic data, one electronic board has been placed on the apparatus central shaft. A rotary guide was used to establish electrical connections. Since in this device, data frequency from encoder has been high and pulsed to voltage proportion has been low, data is transferred wireless to the board. Microcontroller module that is inside the box acts as receptor and sender. Microcontroller read encoder in two phases and then receive and save them in the module.

4.3. Water transfer

Water nozzle is mounted on the device. For changing the water pressure, one ballast pump is connected to the water reservoir. For controlling water volumetric flow rate in the nozzle, one bypass hose is connected to the pump that can return back the extra water to the on board water reservoir. Water reaches the apparatus central shaft through a flexible hose with a definite pressure. On top of the central shaft, one Rotary Joint is placed which has the responsibility of water supply from the reservoir to the rotating wheel. From another side of Rotary Joint, another flexible tube leads water to a point just in front of the wheel (Figure 4). The front plate of water nozzle pond has the possibility of movement as sliding and exhausting of water with different thicknesses.

Figure 4. Water transfer between tire and asphalt mixture

4.4. Asphalt mixture

For compacting asphalt mixture in the molds, steel compactor has been placed on the other side of the wheel arm symmetrically, as can be seen in Figure 5. To facilitate the movement and making one monotonous surface, there is one suspension system similar to wheel for the compactor. Also, compactor height is changeable with two buckles. When apparatus is performing the test, the compactor is in upper height, and it has no contact with the surface, and

when the mixture should be compacted, the compactor is on asphalt mixture and wheel has no connection to surface anymore. All samples were compacted with the same number of wheel rotation to prepare similar samples.

Figure 5. Asphalt mixture compaction

5. Results

Performance grade bitumen PG58-16 was mixed with aggregate to produce asphalt mixtures. The softening point of used bitumen is 51 ℃, the penetration at 25℃ is 6.8 mm and its ductility is over 100 cm. The aggregate used had a grading in accordance with Iran national code of practice No. 234 as shown in Table 1.

Table 1. The grading used in asphalt samples preparation

Sieve Size	Mix Types		Sieve Size	Mix Types	
	Mix A	Mix B		Mix A	Mix B
	Percent Passing			Percent Passing	
19	-	100	# 16	92.5	-
12.5	-	95	# 30	82.5	-
9.5	-	-	# 50	60	13
# 4	100	59	# 100	30	-
# 8	97.5	43	# 200	14.5	6

To evaluate the introduced apparatus, 2 types of asphalt mixture, namely A and B with different grading are prepared according to national standards and optimum bitumen content.

Asphalt mixture is poured in molds and compactor which is connected to crank machine, compacts asphalt mixture with definite speed and cycle number. Then asphalt mixture texture is measured by sand patch method (ASTM E965). The wheel is on asphalt mixture surface and compactor is fixed at its higher location 10 cm above pavement surface. At first, the test is done in a dry condition of the surface at 15 to 35 Hz frequency with rising steps of 2.5. In each frequency, 150 complete cycle of wheel crosses on asphalt mixture surface. Secondly, the test is done in a wet condition of asphalt mixture surface. Water is sprinkled with specified pressure and thickness of 1 mm between wheel and surface through the nozzle. Similar to the previous mode, wheel and axle rotation in rpm are registered momently. Obtained results for one asphalt mixture with 0.49 mm depth surface texture is presented in Table 2.

Table 2. Tests result in dry and wet conditions in Mix A

Frequency (Hz)	Condition	MTD (mm)	Number of Cycles	Thickness of water film (mm)	Rotation of axle	Rotation of wheel	Ratio
15	Dry	0.49	150	0	29548	171879	5.817
20	Dry	0.49	150	0	34198	199272	5.827
25	Dry	0.49	150	0	49031	285409	5.821
27.5	Dry	0.49	150	0	55411	322989	5.829
30	Dry	0.49	150	0	58727	342262	5.828
32.5	Dry	0.49	150	0	61918	361046	5.831
35	Dry	0.49	150	0	67040	391176	5.835
15	Wet	0.49	150	1	32785	190186	5.801
20	Wet	0.49	150	1	35623	206328	5.792
25	Wet	0.49	150	1	48921	266375	5.445
27.5	Wet	0.49	150	1	55749	299707	5.376
30	Wet	0.49	150	1	58612	314219	5.361
32.5	Wet	0.49	150	1	62073	331966	5.348
35	Wet	0.49	150	1	67052	354638	5.289

As it can be seen in Table 2, in dry surface condition, with an increase of frequency, the shaft rpm ratio to wheel rpm increases slightly so that it can be regarded as constant in different frequencies. In wet conditions of the surface until the frequency of 20 Hz with little difference, almost this ratio is similar to dry surface conditions, but for the frequency of 25 Hz and higher speeds, more differences are observed in this ratio as can be seen in Figure 6. In this case, the surface connection between wheel and surface is slight because of water intercepting and amount of wheel rpm is less than the dry surface mode. In fact, this position is hydroplaning occurrence threshold. Some references call this case partial hydroplaning. When the speed increases, there is not enough time for water to escape from the contact surface between wheel and asphalt mixture and it reduces the wheel contact area with the surface. In the 35 Hz frequency, the ratio of shaft rpm to wheel rpm has been decreased by 10 percent compared with the dry mode.

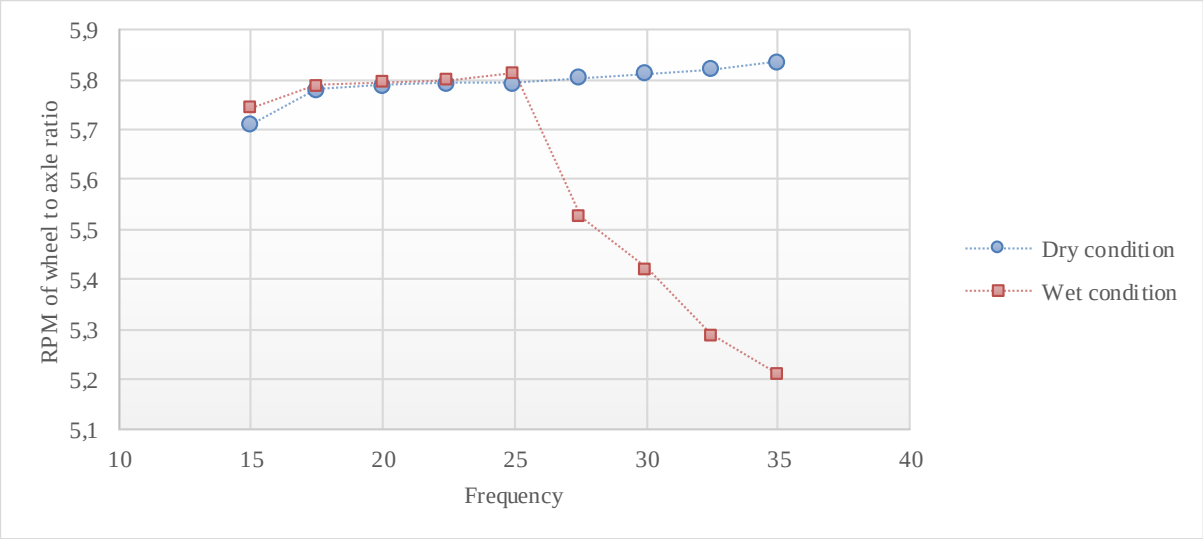

Figure 6. Rotation of wheel to axle ratio in wet and dry conditions

Moreover, rotation of the wheel to axle ratio in wet and dry conditions in Mix B at different frequencies is showed in Figure 6. In this mixture, MTD value is equal to 1.38 mm. The partial transition is observed in this ratio in Mix B up to 30 Hz. But in the frequency of 32.5 Hz, this proportion decreased about 5% in comparison to 30 Hz. Transition in this proportion results

from hydroplaning occurrence. Obtained results demonstrated that hydroplaning occurrence potential is declined by increasing pavement surface texture.

6. Conclusion and future work

This paper refers to the process of designing and making new testing apparatus for identifying hydroplaning occurrence. Difference between longitudinal speed and the rotational speed of wheel has been considered as an index for determining the hydroplaning threshold in this apparatus. The result showed that this ratio is a proper index for evaluating a hydroplaning phenomenon. Also, results demonstrated that hydroplaning occurrence potential is declined by increasing pavement surface texture. The designed machine has the following abilities which can be used in future researches to evaluate various parameters affecting this phenomenon.

- The ability of a comparative study for selecting proper grading and a minimum depth of surface texture to be used in asphalt mixtures for better surface draining and improved safety in high speed.
- The possibility of creating different types of asphalt pavements with different texture and materials.
- Evaluating the impact of different tire thread on sliding and hydroplaning.
- Examination of effects of different fluids viscosity on pavement surface on sliding.

References

[1] Kokkalis AG, Panagouli OK. Fractal evaluation of pavement skid resistance variations. I: surface wetting. Chaos, Solitons & Fractals, 1998;9(11): 1875-90.

[2] Cerezo V, Gothié M, Menissier M, Gibrat T. Hydroplaning speed and infrastructure characteristics. Proceedings of the Institution of Mechanical Engineers, Part J: Journal of Engineering Tribology, 2010;224(9): 891-8.

[3] Ong G, Fwa T, Guo J. Modeling hydroplaning and effects of pavement microtexture Transportation Research Record: Journal of the Transportation Research Board, 2005(1905):166-76.

[4] Yager TJ. Factors influencing aircraft ground handling performance. 1983.

[5] Meyer WE. Synthesis of frictional requirements research. NASA STI/Recon Technical Report N., 1982;83:29466.

[6] Martinez JE, Lewis JM, Stocker A. A Study of Variables Associated with Wheel Spin-down and Hydroplaning. Highway Research Record, 1972 (396).

[7] Metz J, Amarasiri S, Gunaratne M, editors. Comparative analytical and experimental investigation of pavement hydroplaning predictive methods. Transportation Research Board 92nd Annual Meeting, 2013.

[8] Hall JW, Smith KL, Titus-Glover L, Wambold JC, Yager TJ, Rado Z. 2009. (Guide for pavement friction: National Cooperative Highway Research Program, Transportation Research Board of the National Academies)

[9] Yurjevich MA. Indoor hydroplaning test apparatus and method. Google Patents; 2003.

[10] Villani M, Scarpas A, de Bondt A, Khedoe R, Artamendi I. Application of fractal analysis for measuring the effects of rubber polishing on the friction of asphalt concrete mixtures. Wear, 2014;320:179-88.

[11] Hichri Y, Cerezo V, Do MT. Friction on road surfaces contaminated by fine particles: Some new experimental evidences. Proceedings of the Institution of Mechanical Engineers, Part J: Journal of Engineering Tribology, 2016:1350650117704345.

[12] Dehnad M, Khodaii A. Evaluating the effect of different asphalt mixtures on hydroplaning using a new lab-scale apparatus. Petroleum Science and Technology, 2016; 34(20):1726-33.

To whom correspondence should be addressed: Dr. Mohammad Hosein Dehnad, Department of Civil Engineering, Engineering Faculty, University of Qom, Qom, Iran, m.dehnad@qom.ac.ir

Petroleum and Coal

Article **Open Access**

MAPPING OF HYDROCARBON PROLIFIC AREAS WITHIN THE CENOZOIC NIGER DELTA BASIN: OBSERVATIONS FROM HIGH-RESOLUTION POTENTIAL FIELD DATA

Leonard N. Onuba

Department of Geology, Chukwuemeka Odumegwu Ojukwu University PMB 02, Uli, Nigeria

Received November 29, 2018; Accepted January 18, 2019

Abstract

This study explores a very simple means to map hydrocarbon prolific areas within the onshore Cenozoic Niger Delta Basin using high-resolution potential field data. This was achieved by identifying and superimposing the map of gravity lows on the map of magnetic lows. About six (6) major sub-basins were recognised, namely: the Onuba sub-basin, the Udeonu sub-basin, Ahoada sub-basin, Aba sub-basin, Owerri sub-basin, and Okigwe sub-basin. Among the six sub-basins recognised, Onuba and Udeonu sub-basins are larger than the other sub-basins. The Udeonu sub-basin lies mainly within the central delta cutting across the Greater Ughelli depobelt, the Northern depobelt and the Central Swamps (I and II) depobelts (Early Eocene to Middle Miocene). The Onuba sub-basin lies within the distal delta cutting across the Central Swamp II, the Coastal Swamps (I and II) and the Offshore depobelts (Middle Miocene to Pliocene). The six sub-basins were suggested to lie within the hydrocarbon prolific areas. Out of the major onshore Niger Delta depobelts, the Coastal Swamps (I and II) are the most productive. By implication, the distal part of the delta that lies within the Onuba sub-basin is more productive than the central part of the delta.

Keywords: *Niger Delta Basin; potential field data; sub-basins; and hydrocarbon prolific areas.*

1. Introduction

A sedimentary basin may be described as an area of the Earth's crust dominated by subsidence that allows the net accumulation of sediment [1]. They can range in small size of hundreds of metres to as large as the ocean basin (not necessarily basinal in shape) with essentially two vital elements: a source of sediment supply and an area of sediment deposition. A basin may register the tectonic evolution of the lithosphere that contains numerous Earth resources like fossil fuel, minerals, water resources and may as well be the location of possible environmental challenges like earthquakes, volcanoes, etc. Within a basin or sub-basin, a depocentre can be described as the place where maximum thickness of sediment accumulation is observed over a particular period [1-2]. In a hydrocarbon province, sub-basins are generally attributed to higher net-to-gross reservoir properties depending on sediment provenance and delivery mechanisms [3]. The hydrocarbon columns are controlled not only by the structural geometry and the fault sealing capacity but also by seal distribution, reservoir characteristics and fluid properties. All these represent necessary parameters for evaluating hydrocarbon accumulations [4].

Basement faulting affects delta development and its sediment thickness distribution [5]. This may be dependent on the balance between the rates of subsidence and sediment supply [6]. The sedimentary pattern generated by this balance may have been affected by the tectonics of the basement and its structural configuration [7].

Prior to this study, various hydrocarbons' prolific areas have been established in the extensional part of the onshore Niger Delta that cuts across the depobelts [7-10]. However, it is not very clear if the prolific areas coincide with the sub-basins within the study area. In this study,

a simple comparative study was made to map various hydrocarbon prolific areas of the onshore Niger Delta. This was attained using potential field data with the scope to image full scale crustal signal variability for density and iron content in previously identified hydrocarbon prolific areas. This was achieved by identifying and mapping the ''depocentres'' within a sedimentary basin. Since depocentres are generally regarded as areas of maximum thickness of sediment accumulation, we expect to recognize them by identifying areas with relatively low density and low magnetic properties.

This study illustrates a very qualitative means of how potential field data could be employed to map sub-basins and hydrocarbon prolific areas using the Cenozoic Niger Delta Basin as a case study. This study involves identifying gravity lows and magnetic lows from the data and superimposing one on the other in order to identify the sub-basins within the Niger Delta. The major sub-basins identified were compared with previously established hydrocarbon prolific centres/belts in the same region.

2. Geological setting of the Cenozoic Niger Delta Basin (CNDB)

According to Daly [11], the petroleum potential of the African continent can be grouped into four main provinces, namely: offshore Mesozoic rifted passive margins; large Cenozoic delta systems; onshore Phanerozoic continental rifts and Palaeozoic cratonic basins. A major portion of the Phanerozoic petroleum potential of the African continent is associated with rift settings [12]. These include, for example, the Jurassic Yemen-Somalia rifts, the Permo-Triassic Karoo system, the Neocomian rift zone at the initiation of the Gondwana breakup, the Cretaceous basins controlled by the West and Central Africa Shear Zone and the Tertiary East Africa rift zone. In Nigeria, the West and Central Africa Shear Zones divide the continental margins into individual basins forming boundary faults of Cretaceous Benue-Abakaliki Trough that cuts across the West African shield [10]. The Benue-Abakaliki Trough represents a failed arm of a rift triple junction that failed to develop during the separation of African plate from South American plate and this lasted from the Albian to the Santonian [13]. The other arms that developed are characterised by the South Atlantic and the Gulf of Guinea in the Equatorial Atlantic.

The Niger Delta Basin is a structural depression linked to the tectonic evolution of the Benue Trough of Nigeria. This depression was formed within the basement complex of the African craton [15]. In Nigeria, the basement complex consisting mainly of granite and gneisses covering half of the landmass with extensive schist belt in the west [16]. The basement complex was subjected to two metamorphic events. The first event occurred at about 2000 ($\pm$250) Ma and the second was at about 600 ($\pm$150) Ma. The first is associated with a pre-Pan-African orogeny while the second is associated Pan-African orogeny [16-17].

The Niger Delta is a coastal basin attributed to the post-rift stage in the Cenozoic times of the passive continental margin. The post-rift stage was characterized mainly by sea-level eustatic change, uplifting and tilting of the African plate, formation, and deposition of clastic rocks and turbidites [18]. The coastal sedimentary basin of Nigeria passed through three depositional cycles, and the first two cycles form the basic framework on which the Niger Delta was built [15]. Sediment deposition into the Niger Delta Basin started in the third depositional cycle in the Cenozoic (Late Eocene) to the present, and this has been attributed to regressive delta sequence. The stratigraphy of the Niger Delta is closely tied to the structural and sedimentary cycles of the Benue Trough. The Niger Delta Basin is divided into three lithostratigraphic units, namely: Akata Formation (marine), Agbada Formation (transitional) and Benin Formation (continental) [10,19]. Three environments of deposition are recognised in the Niger Delta namely: (a) the continental consisting of Bende/Ameki Group, coastal plain sand and deltaic plain (Eocene – Oligocence); (b) the transitional consists of meander belt, backswamp, and mangrove swamps (Oligocence – Miocence) and marine comprises Estuaries, Beach ridges and bars (Miocence – Pliocence) [19]. An outline of the geological map of the Cenozoic Niger Delta Basin is shown in Fig. 1. Details of the geological setting of the Cenozoic Niger Delta Basin have been discussed [6,10,16].

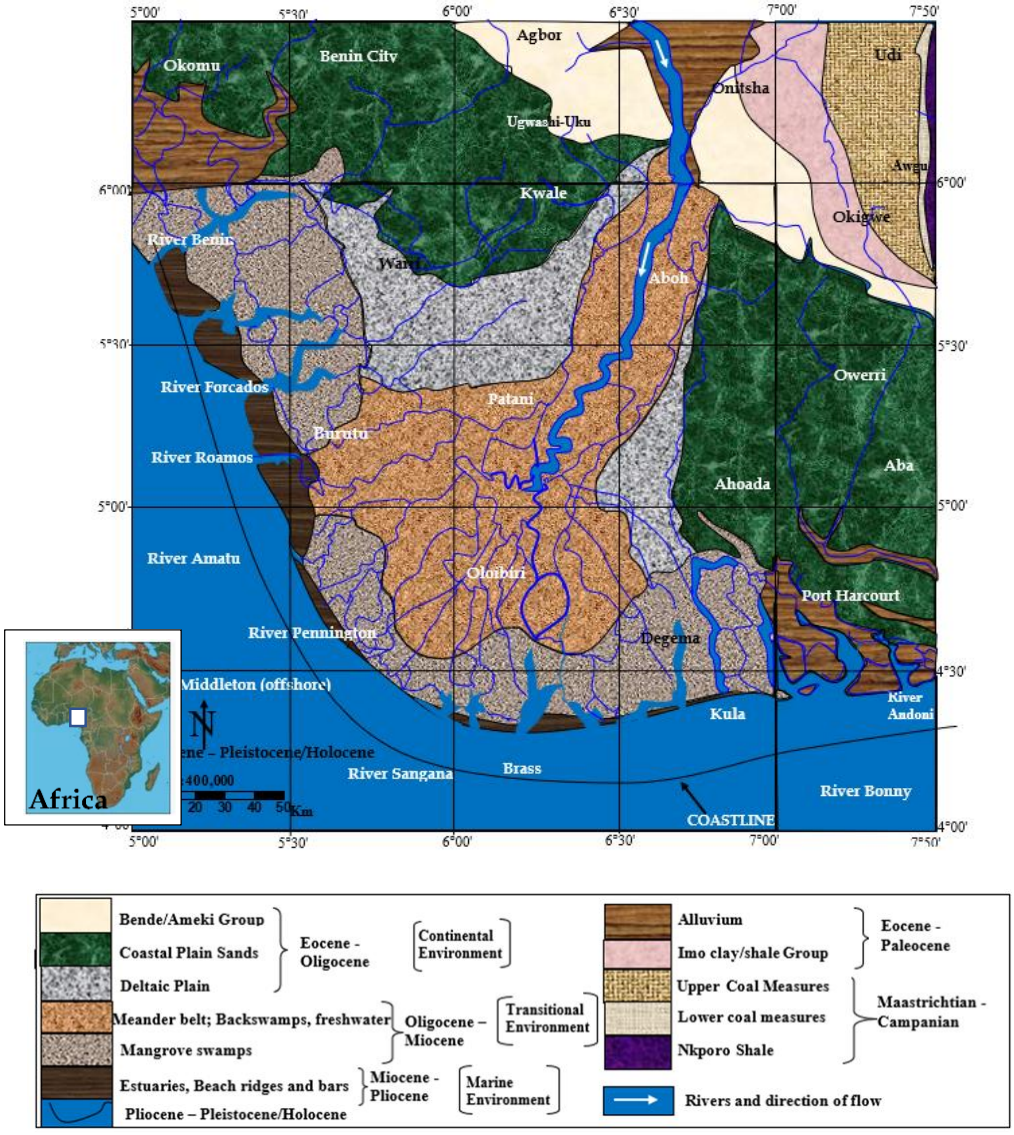

Fig. 1. Outline of the geological map of the Cenozoic Niger Delta Basin (*modified from NGSA 1964 and 2003; Frankl and Cordry, [19]*)

3. Niger Delta depobelt province

The development of the Niger Delta took place in discrete structural units (depobelts) that act as sub-basins, and this was as a result of the activity of large growth faults and clay diapers [21]. Doust and Omotola [16] described three prominent depobelt provinces based on geological structure namely: (a) the Northern delta depobelt province that overlies relatively shallow basement, with the oldest generally rotational growth faults that are evenly spaced and increasing in steepness seaward; (b) the Central Delta depobelts province, characterised by well-defined structures with successive deeper rollover crests that shift seaward for any given growth fault; and (c) the Distal Delta depobelt province, characterised by complex structures due to internal gravity systems on the modern continental slope.

The three prominent depobelt provinces can be divided further into seven depobelts based on age [16]: (i) the Northern Delta depobelt, (ii) Greater Ughelli depobelt, (iii) Central Swamp I depobelt, (iv) Central Swamp II depobelt, (v) Coastal Swamp I depobelt, (vi) Coastal Swamp II depobelt, and (vii) Offshore depobelt (Table 1). Other studies identified five depobelts in

the Niger Delta by grouping them as Northern, Greater Ughelli, Central Swamp, Coastal Swamp and Offshore depobelts [10,22].

Table 1. The seven prominent depobelts of the Niger Delta Basin based on age (*modified from Doust and Omatsola* [16])

Depobelts	Paralic sequence	Alluvial sands
Northern Delta	Late Eocene to Oligocene	Early Miocene
Greater Ughelli	Oligocene to Early Miocene	Early Miocene
Central Swamp I	Early to Middle Miocene	Middle Miocene
Central Swamp II	Middle Miocene	Middle Miocene
Coastal Swamp I	Middle to Late Miocene	Late Miocene
Coastal Swamp II	Middle to Late Miocene	Late Miocene
Offshore	Late Miocene/Pliocene	Late Miocene/Pliocene

The Cenozoic Niger Delta Basin is one of the world's major hydrocarbon basins with proven reserve of over 37.2 billion barrels of recoverable hydrocarbon (2.93% of the world reserve) at the end of 2011, ranking Niger Delta Province the twelfth largest hydrocarbon province in the World [10,23]. With an estimated 41.4 years at the present rate of production of over 2,457 barrels per day (BP, 2012 report). The Basin has been explored for over 50 years after over 47 billion barrels have been produced [24] and exploration activities are still ongoing. A schematic diagram showing various hydrocarbon prolific areas in the Niger Delta is shown in Fig. 2.

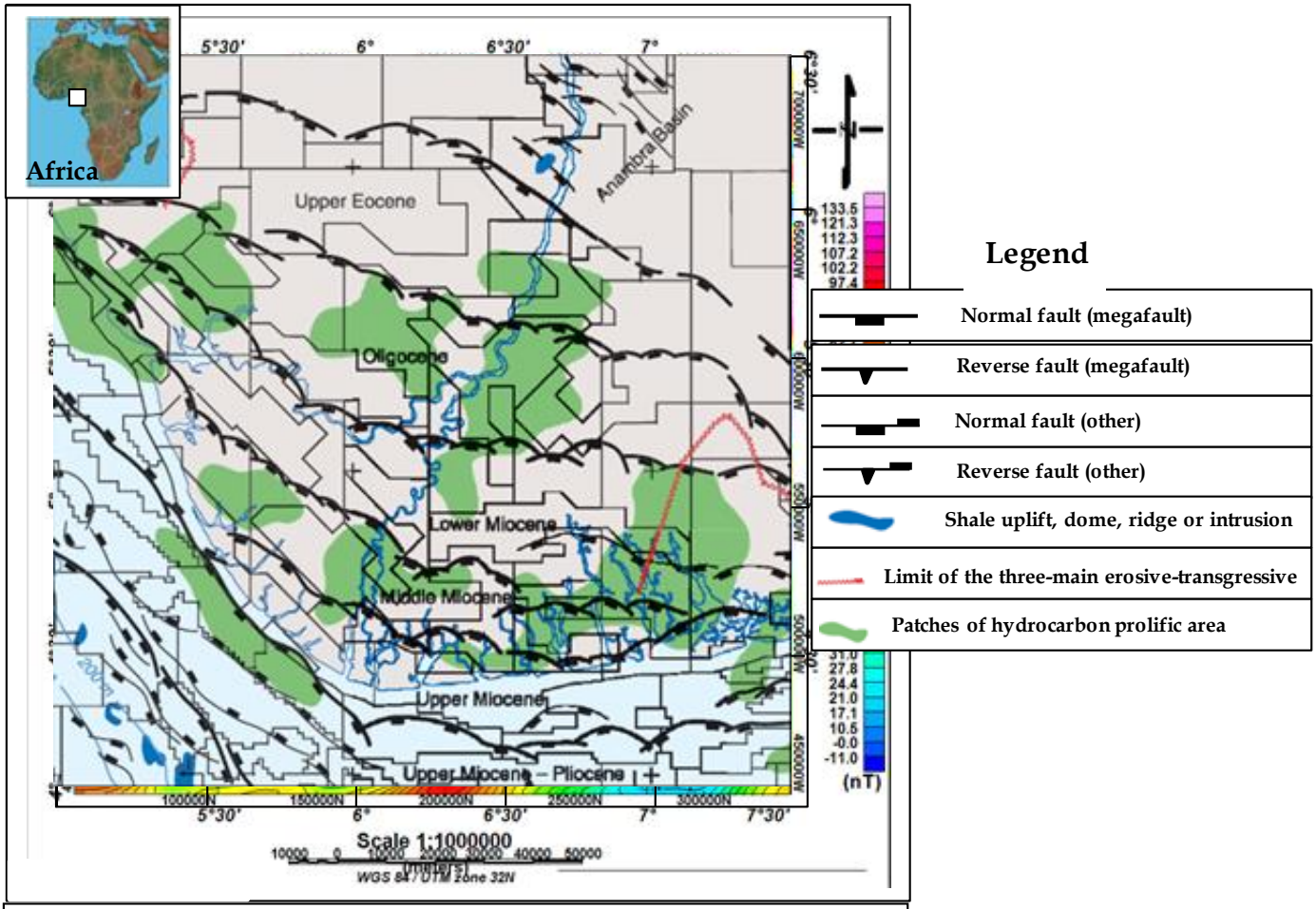

Fig. 2. Schematic diagram showing the location of Niger Delta hydrocarbon prolific areas in green *(extracted from Stacher* [39]*; Saugy and Eyer* [40]*)*

4. Background

As discussed in previous studies [25-28], sedimentary basins, salt diapirs, granite structures and grabens are characterised by negative gravity anomalies (also called gravity lows or gravity minima) while positive gravity anomalies (also called gravity highs or gravity maxima) are characterised by horsts, uplifts and mafic rock materials. The magnetic susceptibility varies from less than 10^{-4} emu/cm^3 for sedimentary rocks to between 10^{-3} and 10^{-2} emu/cm^3 for iron-rich basic igneous rocks [28]. In general, basic igneous rock has high magnetic susceptibility due to their relatively high magnetite content. Acidic igneous rocks and metamorphic rocks have intermediate magnetite content while sedimentary rocks have low magnetic susceptibility due to low magnetite content. However, there are some exceptional cases; some sediment might have high magnetic content. For example, laterites containing maghemite or remanently magnetized hematite [29] or marine sediment with complicated magnetic mineral assemblages [30]. In this study, it was however assumed that there were no exceptional cases and the interpretations will be based on the principles outlined by Sharma [27] and Telford *et al.* [28].

5. Data and processing sequence

Most corrections, in particular drift, latitude, Free-air and Bouguer corrections had already been applied to the gravity data. Therefore, we will focus on their applications rather than acquisition. A high-resolution aeromagnetic data of the Niger Delta was acquired between 2009 and 2010 by Fugro Airborne Survey Ltd, with preliminary interpretation carried out by Patterson Grant and West (PGW) Consultants Canada. The high-resolution Bouguer gravity anomaly data used for this study, cover most part of the onshore Niger Delta area while the high-resolution aeromagnetic data covers the onshore Niger Delta with adjacent offshore (Figs. 3a and b). The acquisition procedures have been discussed by Paterson et al. [31] and Reford et al. [32]. The magnetic data, post-processed and presented in this section, relate to the distribution of magnetic minerals within the sub-surface of the Niger Delta area. The new aeromagnetic data were gridded using a bi-directional gridding technique since the data were acquired along parallel lines. To enhance the geological features, due to deeper magnetic sources, various low-pass phase filters were applied to the aeromagnetic data. The essence of the filters is to eliminate the effects of shallow wavelength anomalies or noise. The two main filters applied included: (i) reduction to equator (RTE) of the magnetic data and (ii) upward continuation of the magnetic data. In this study, the magnetic data were reduced to magnetic equator using an average geomagnetic inclination of -16°.5' and an average geomagnetic declination of -2°.25'. The main purpose of this filter is to position the magnetic data above their causative sources. The data were also upward continued to 2000 m to suppress the effects of cultural noise from the area especially pipeline network or effects of shallow sources and the map was presented in Fig. 3a. Many filters were not applied in this study to avoid the possible attenuation of the geological information that in this case seem to be unnecessary for this interpretation.

6. Procedure

In this study, gravity and magnetic data were used to qualitatively map various sub-basins within the Niger Delta area using Oasis Montaj software. The procedure for identifying sub-basins and hydrocarbon prolific areas are outlined below:

a. identify areas with gravity lows and magnetic lows within the Niger Delta Basin. This is important because regions with negative gravity anomalies or negative magnetic anomalies are often associated with sub-basins or sedimentary basins.
b. superimpose gravity map on magnetic map or vice versa using Oasis Montaj. This is important due to areas where both maps display similar negative anomaly characteristics and were marked as sub-basins and could be related to areas of potential hydrocarbon prolific zones.
c. compare the superimposed maps with sediment thickness distribution map in the same area.
d. compare the results obtained with previously identified prolific belts/centres.

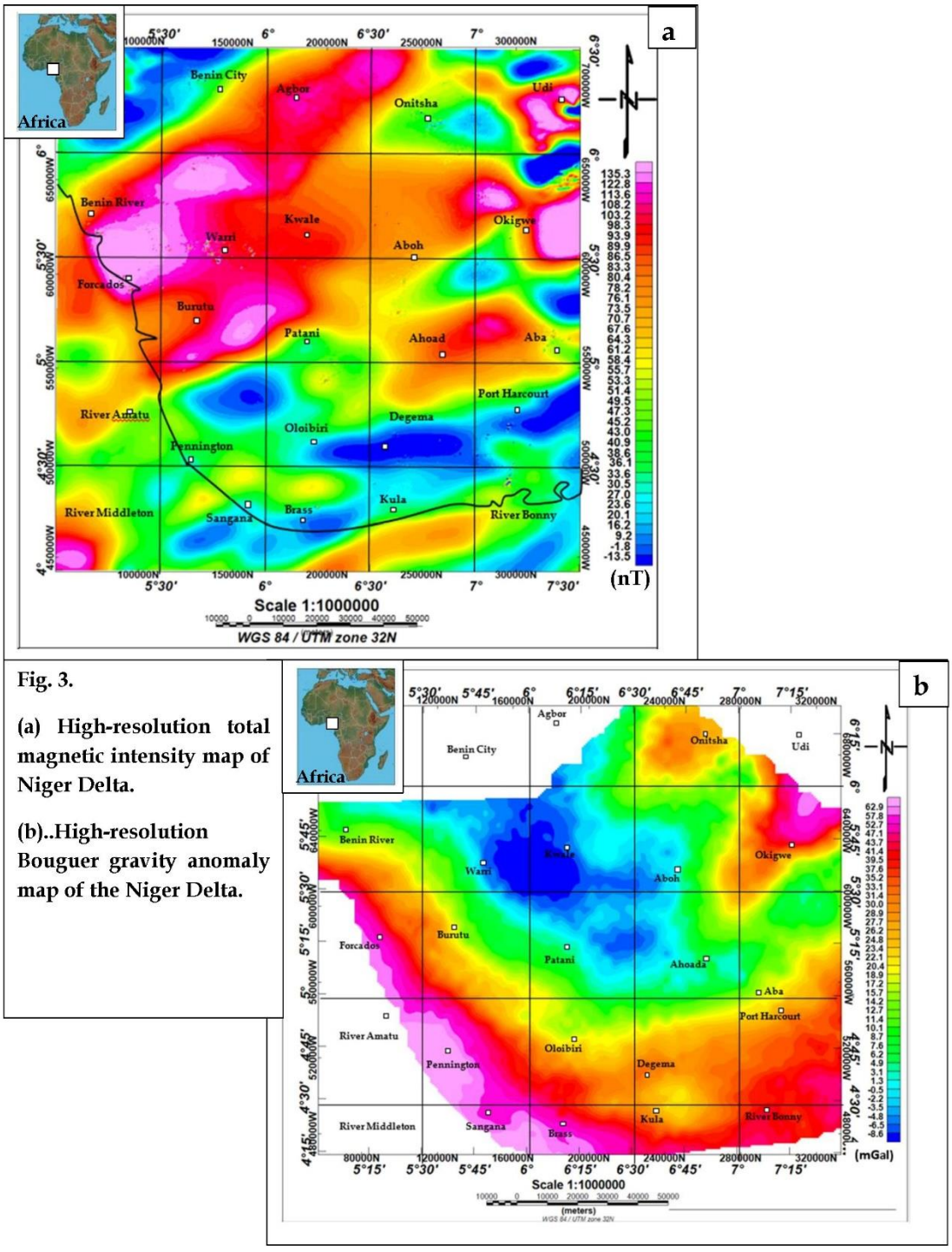

Fig. 3.

(a) High-resolution total magnetic intensity map of Niger Delta.

(b)..High-resolution Bouguer gravity anomaly map of the Niger Delta.

7. Results and discussion

7.1. Sub-basins within the Niger Delta

Within the Niger Delta Basin, nine (9) major magnetic lows were recognised from magnetic map, namely: Sangana magnetic low, Brass magnetic low, Bonny magnetic low, Oloibiri-Pennington magnetic low, Degema magnetic low, Port-Harcourt magnetic low, Ahoada magnetic

low, Owerri-Aba magnetic low, and Okigwe-Udi magnetic low (Fig. 4). The magnetic lows recognised are associated with areas of low magnetic anomalies that may represent sedimentary rocks, and in some cases intermediate anomalies that may be associated with granitic rocks. The magnetic lows may be caused by intra-basement faulting and were speculated to represent sub-basins within the Niger Delta Basin.

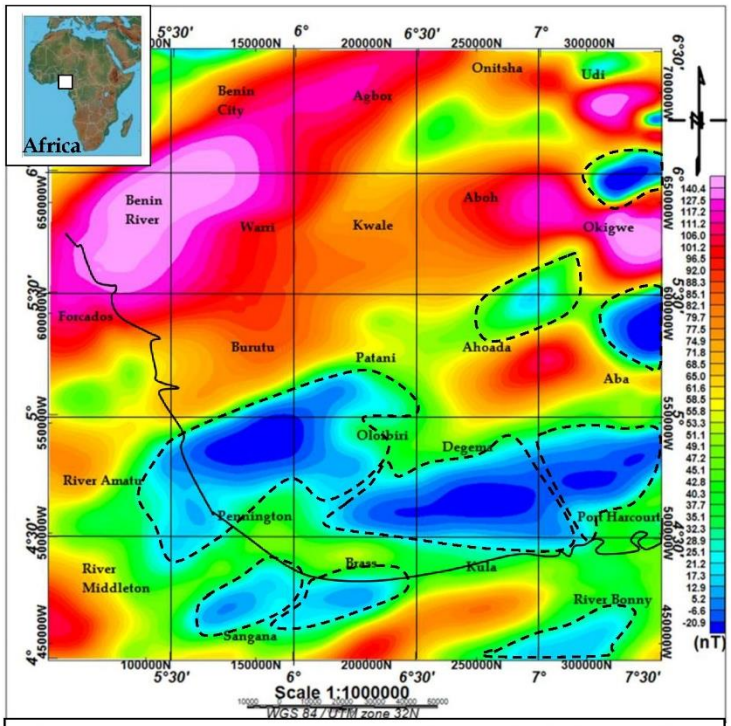

Fig. 4. Magnetic anomaly map of the Niger Delta Basin showing nine (9) major magnetic lows in blue colour.

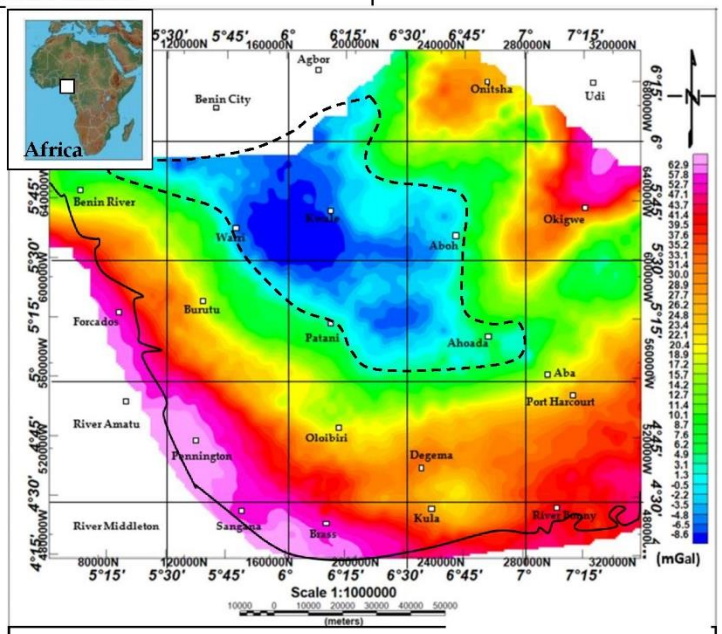

Fig. 5. Gravity anomaly map of the Niger Delta Basin showing a major gravity low in blue colour.

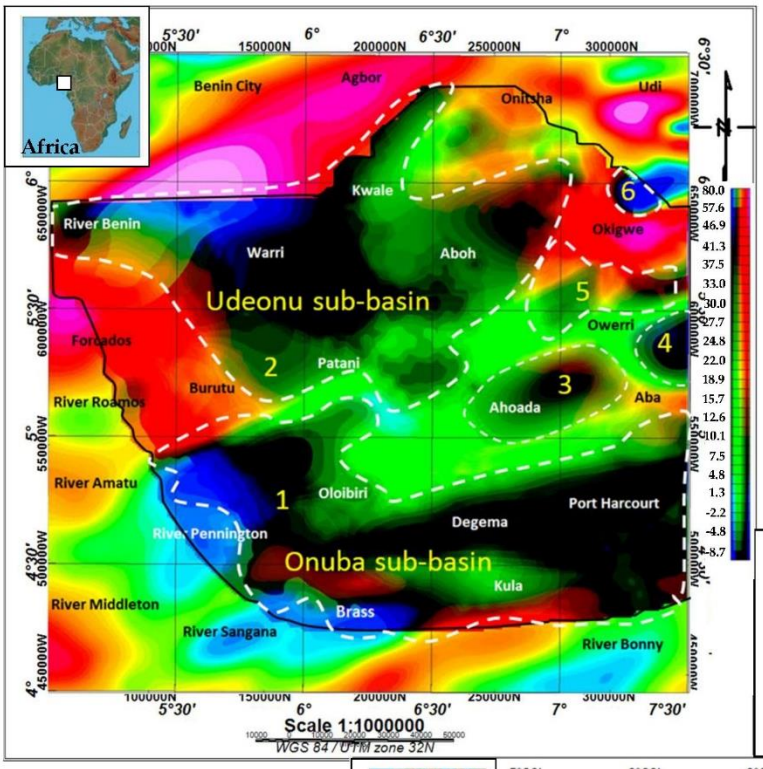

Fig. 6. The super-imposed gravity low map on magnetic low map of the Niger Delta indicating six sub-basins assumed to be related to hydrocarbon prolific areas (black colour).

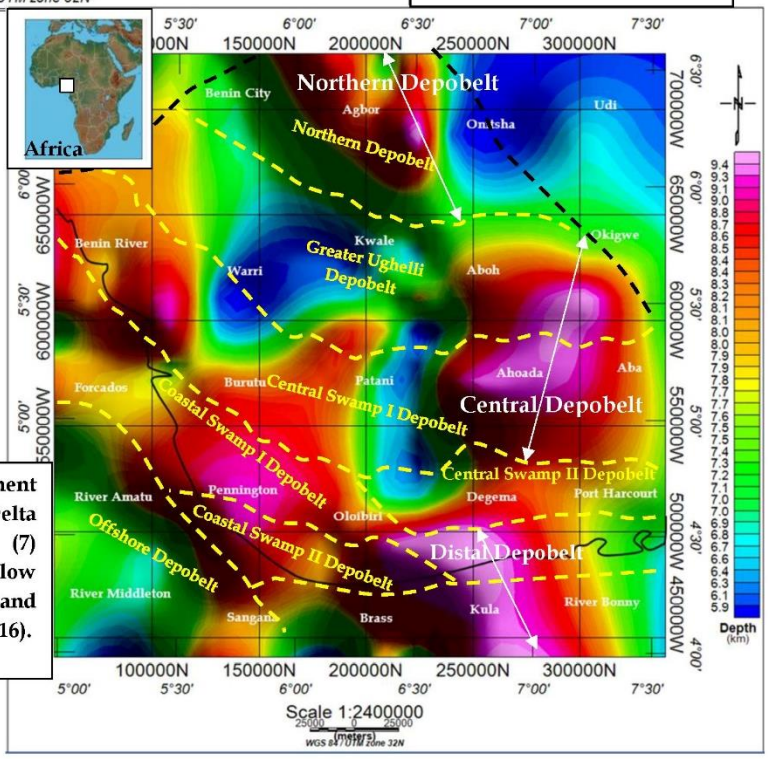

Fig. 7. The thickness of sediment map of the Niger Delta highlighting the seven (7) depobelts in broken yellow colour (modified from Doust and Omotola, 1989 and Onuba, 2016).

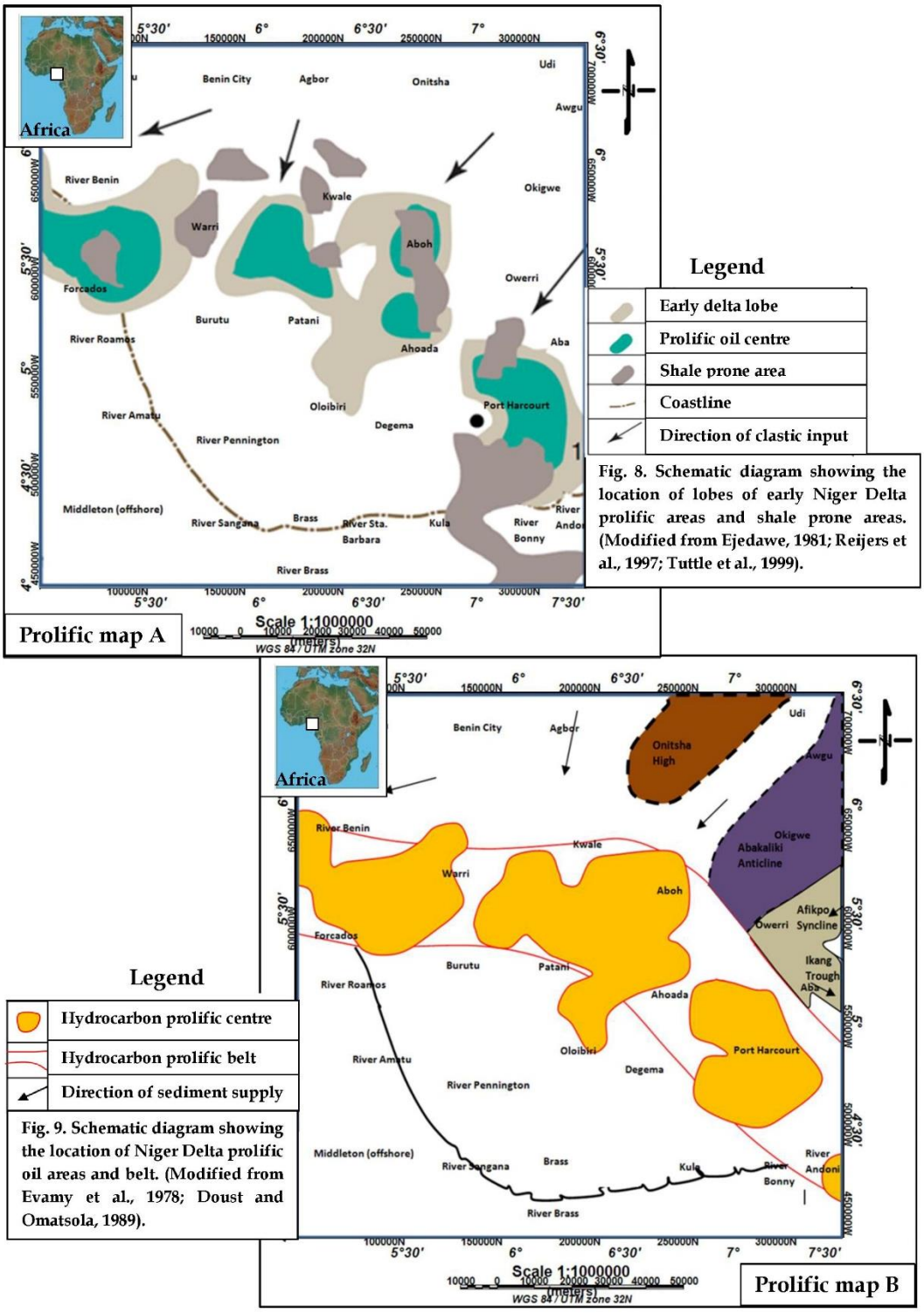

Fig. 8. Schematic diagram showing the location of lobes of early Niger Delta prolific areas and shale prone areas. (Modified from Ejedawe, 1981; Reijers et al., 1997; Tuttle et al., 1999).

Fig. 9. Schematic diagram showing the location of Niger Delta prolific oil areas and belt. (Modified from Evamy et al., 1978; Doust and Omatsola, 1989).

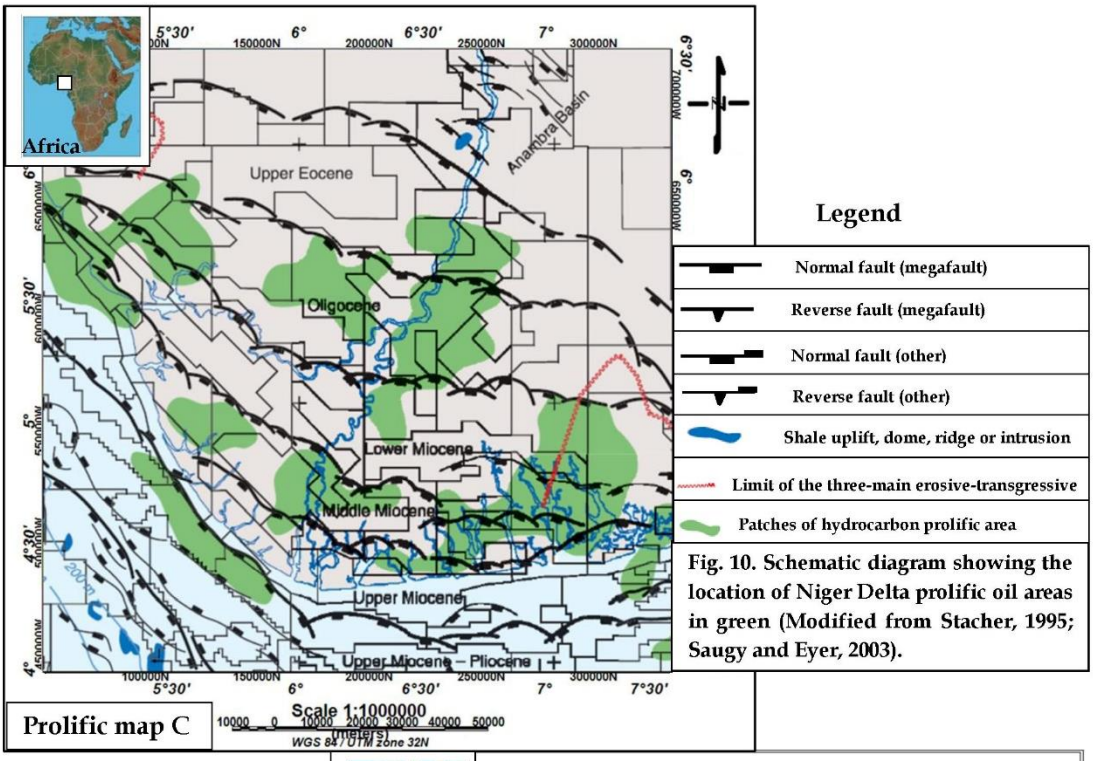

Fig. 10. Schematic diagram showing the location of Niger Delta prolific oil areas in green (Modified from Stacher, 1995; Saugy and Eyer, 2003).

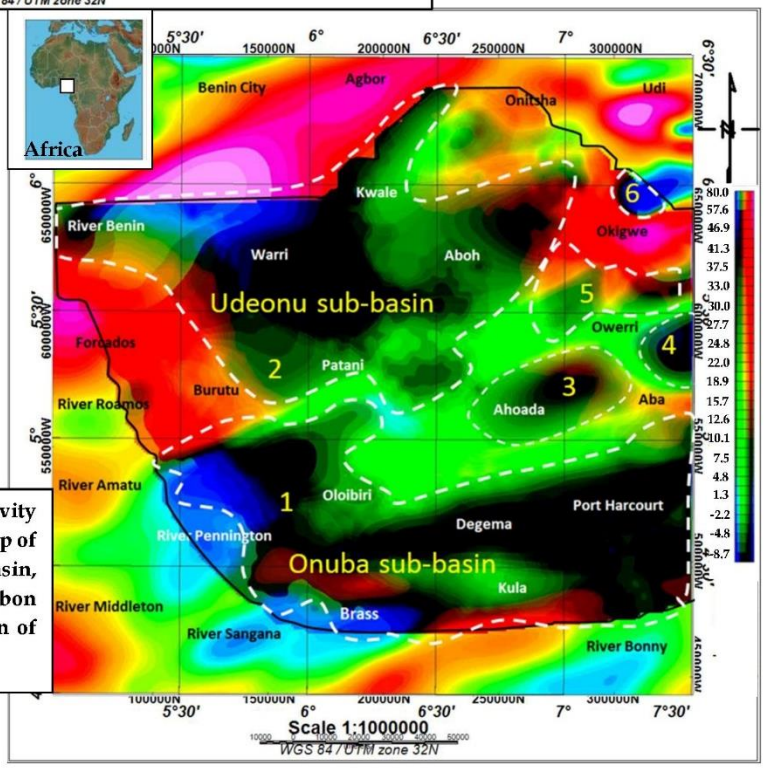

Fig. 11. Super-imposed gravity low map on magnetic low map of the Niger Delta Basin, highlighting some hydrocarbon prolific areas in dark portion of the map.

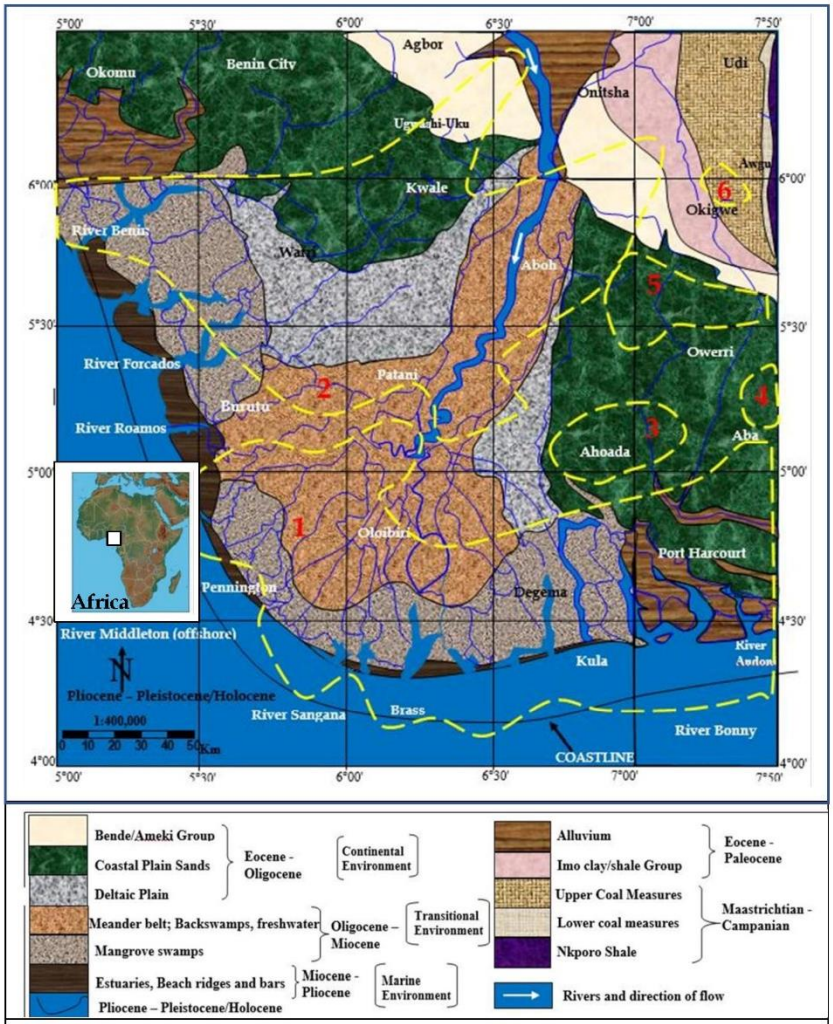

Fig. 12. Outline of the geological map of the Niger Delta indicating hydrocarbon prolific areas in yellow circle (modified from NGSA 1964, 2003 and Frankl and Cordry, 1967)

Six (6) sub-basins were recognised within the Niger Delta Basin by superimposing the gravity low map on the magnetic low map using Oasis Montaj (see Fig. 6). Among the sub-basins recognised, two of them are larger than the other four sub-basins. The two large sub-basins were named: the Onuba sub-basin (1) and the Udeonu sub-basin (2). The areas covered by Onuba sub-basin include: the Sangana, Brass, Kula, Bonny, Pennington, Oloibiri, Degema and Port-Harcourt areas while the areas covered by Udeonu sub-basin include: Burutu, Patani, River-Benin, Warri, Kwale, Aboh and Agbor areas. Other sub-basins include: Ahoada sub-basin (3), Aba sub-basin (4), Owerri sub-basin (5) and Okigwe sub-basin (6).

The Udeonu sub-basin lies mainly within the central part of the Delta depobelt and partly in the Northern Delta depobelt. The Central Delta depobelt is characterised by well-defined structures with successive deeper rollover crests that shift seaward for any given growth fault [16]. The Northern Delta depobelt is underlain by shallow basement and has the oldest generally rotational growth faults that are evenly spaced and increase in steepness seaward [16]. While based on age, the Udeonu sub-basin lies mainly within the Greater Ughelli, Northern and Central Swamp (I and II) depobelts. The Onuba sub-basin on the other hand lies within the distal part of the Delta depobelt province and is characterised by complex structures due

to internal gravity systems on the modern continental slope as suggested by Doust and Omotola [16]. While based on age, the Onuba sub-basin lies within Offshore, Coastal Swamp I, Coastal Swamp II, and Central Swamp II depobelts.

The major hydrocarbon prolific areas show some resemblance to the recognised Onuba and Udeonu sub-basins, and these were compared to the thickness of sedimentary unit in the Niger Delta Basin (obtained from Onuba, [34]) and presented in Fig. 6. The results show that most of the prolific areas occur in places where sediments thickness varies from more than 4 km to about 10 km. This implies that these prolific areas have sufficient thickness of sediment to potentially allow hydrocarbon to form [35-37]. It is therefore speculated that the sub-basins identified might act as depocentres for the major hydrocarbon discoveries within the onshore Niger Delta Basin and these sub-basins may be characterised by higher net-to-gross reservoirs depending on sediment provenance and delivery mechanisms [38]. The Onuba and Udeonu sub-basins are hereby suggested to be associated with the major hydrocarbon prolific areas within the onshore Niger Delta Basin and adjacent offshore [16,39-40].

7.2. Hydrocarbon prolific areas of the Niger Delta Basin

In this study, two main hydrocarbon prolific areas were identified at the distal and the central part of the delta (Figs 6 and 7). The two hydrocarbon prolific areas were compared to the three (3) previously identified hydrocarbon prolific maps namely: (i) Prolific map A [8-10], (ii) Prolific map B [6, 16] and (iii) Prolific map C [39-40]. The results obtained indicate that all the prolific maps (A, B, C and the present study) lie within the central part of the delta (see Figs. 8, 9, 10 and 11) and cut through the Northern depobelt and the Central Swamp (I and II) depobelts (Early Eocene to Middle Miocene). In addition, the evidence from the same results further suggest that only prolific map C and that of the present study lie considerably within the distal part of the Niger Delta (Figs 10 and 11). This implies that the prolific map C and the one recognised from the present study cut across the Central Swamp II, the Coastal Swamp (I and II) and the Offshore depobelts (Middle Miocene to Pliocene). Omotsola [24] argued that of the major depobelts within the Onshore Niger Delta, the Coastal Swamps (I and II) are the most productive depobelts. If this is true, it could imply that the distal part of the delta could be more productive than the central part of the delta. This study is also in agreement with previous study suggesting that the most hydrocarbon prolific system of the Niger Delta was attributed to the Eocene–Miocene marine shale source rocks and Oligocene–Miocene turbidite reservoir sands [18].

The reservoir properties and source rock characteristics of the Onuba and Udeonu sub-basins within the onshore Niger Delta Basin are highlighted. The known reservoir rock of the onshore Niger Delta mainly comprises sandstone and unconsolidated sands of the Agbada Formation of predominantly Eocene to Pliocene age [6]. Studies suggest that the major reservoirs are observed mainly as the Miocene paralic sandstones with porosity of 40% and Darcy's permeability of 2 and a thickness of 100 metres [41]. The quality and shape of the reservoir rock is attributed to point bars of distributary channels and coastal bars that often cut intermittently by sand-filled channels [42]. The source rock of onshore Niger Delta Basin was suggested to have originated from marine shale of Akata Formation and intercalated shale of paralic sandstone of Agbada Formation [43]. The source rock contains land plant material and is capable of generating hydrocarbons [44]. Ejedawe et al. [45] using maturation models suggested that Agbada shale act as source rock for oil while the Akata shale act as source rock for gas at the central part of the delta. This cuts through the Udeonu sub-basin, Ahoada sub-basin, Aba sub-basin and Okigwe sub-basin. While at the distal part of the delta (the Onuba sub-basin), both Agbada and Akata Shales act as source rock for oil.

The Udeonu sub-basin (Eocene–Miocene) lies mainly within the central part of the onshore Niger Delta Basin that falls within the central prolific map similar to prolific maps A and B. The Udeonu sub-basin of the onshore Niger Delta is characterised by a gravity low and this is may be related to granite structures or grabens with accumulated sediment thickness ranging from 7 km to about 9 km. The magnetic anomaly amplitudes beneath the Udeonu sub-basin range

from less than 100 nT to 10s nT. The area with amplitude of less than 10 nT were suggested to be related to sedimentary magnetization contrasts while the area with amplitude of 10s nT were suggested to be related to acidic igneous rocks or deep metamorphic basement [25]. It is thereby suggested that the Udeonu sub-basin is most likely to be underlain by thin continental or transitional crust rather than oceanic crust as previously suggested [6,8,16]. Ejedawe [8], using cumulative probability plot of oil reserve density (ORD) argued that the central Niger Delta hydrocarbon prolific area (Fig. 8), marks the transition zone between oceanic and continental crusts and this zone of weakness was also attributed to the tectonic zone of active subsidence [6,16]. Evamy et al. [6] further suggested that continent-ocean boundary (COB) within the Niger Delta area may serve as a major depobelt where the delta attains a dominant zone of crustal instability.

The Onuba sub-basin (Miocene-Pliocene) lies mainly within the distal part of the onshore Niger Delta Basin. It is underlain by gravity high of some tens of mGal and this may be related to intermediate rocks or uplifts associated with basement fault or anticlinal faults. The magnetic anomaly amplitudes beneath the Onuba sub-basin range from less than 10 nT to 10s nT. Most of the areas with amplitudes of less than 10 nT were related to sedimentary magnetization contrasts within the basin and the areas of 10s nT may be underlain by acidic igneous rocks or deep metamorphic basement due to no strong magnetic anomaly amplitude in this area [25-28]. Based on the above observation, it is hereby suggested that the Onuba sub-basin may likely be underlain by continental crust rather than transitional/COB as previously suggested [6,8,47].

Haack et al. [38] examined the position of the hydrocarbon prolific area in the Niger Delta with respect to oil prone marine source rock deposited adjacent to the central prolific belt. They suggested that source rock accumulation was influenced by pre-Cenozoic structures related to basement structures. This influence may have conditioned the major boundary fault to separate the Niger Delta Basin into (depobelts) that serve as main breaks in the regional dip of the delta [6]. The depobelts have been linked with the activity of large growth faults and clay diapers [21]. These features reflect the very common trapping mechanism for hydrocarbon accumulation in the Niger Delta Basin. Most oil and gas fields in the Niger Delta are characterised by these features. Fig. 12. highlights the geological map of the Niger Delta, indicating hydrocarbon prolific areas.

8. Summary and conclusions

This study was a cursory attempt to map sub-basins and relate them to major hydrocarbon prolific areas within the onshore Cenozoic Niger Delta Basin using magnetic and gravity data. In this study, nine (9) major magnetic lows were recognised from the magnetic map, and they could have been caused by intra-basement faulting. On the other hand, one major extensive gravity low was recognised and may perhaps reflects low density rocks within the Niger Delta Basin.

Based on that, six (6) sub-basins were then mapped by super-imposing gravity low map on the magnetic low map namely: the Onuba sub-basin, the Udeonu sub-basin, Ahoada sub-basin, Aba sub-basin, Owerri sub-basin, and Okigwe sub-basin. Among the sub-basins recognised, two of them are quite extensive with Onuba sub-basin covering Sangana, Brass, Kula, Bonny, Pennington, Oloibiri, Degema and Port-Harcourt areas and the Udeonu sub-basin covering Burutu, Patani, River-Benin, Warri, Kwale, Aboh and Agbor areas. The six sub-basins were suggested to lie within the hydrocarbon prolific areas.

The Udeonu sub-basin lies mainly within the Central delta depobelt cutting across the Greater Ughelli depobelt, the Northern depobelt and the Central Swamp (I and II) depobelts (Early Eocene to Middle Miocene). While the Onuba sub-basin lies within the Distal Delta depobelt province cutting across the Central Swamp II, the Coastal Swamp (I and II) and the Offshore depobelts (Middle Miocene to Pliocene). Out of the major Onshore Niger Delta depobelts, Omotsola [24] argued that the Coastal Swamp (I and II) are the most productive depobelts. If this is true, it could imply that the distal part of the delta that lies within the Onuba sub-basin could be more productive than the central part of the delta.

Insights obtained from this study, if combined with other non-geophysical data and deep drilling operations, might help to identify precise hydrocarbon targets, which could lead to a reduction in operational risks, cost, and time. This idea requires further investigation to understand the nature of the hydrocarbon prolific areas.

References

[1] Allaby M. A dictionary of geology and earth sciences. Oxford University Press, 2013.
[2] Kearey P. The new Penguin dictionary of geology. Penguin Books, 1996.
[3] Sprague A, Garfield T, Goulding F, Beaubouef R, Sullivan M, Rossen C, Campion K, Sick Afoose D, Abreu V, and Schellpeper M. Integrated slope channel depositional models: the key to successful prediction of reservoir presence and quality in offshore West Africa. CIPM, cuarto E-Exitep, 2005; 1-13.
[4] Lays P, Chavagnac P, and Tenepalli S. Hydrocarbon migration and trapping mechanism in lake Albert Basin, Uganda. Africa: Success in Rift, Sag and Passive Margin Settings edn. Wembley Stadium, London: The 12th PESGB/HGS Africa Conference on Africa E & P, September 2013.
[5] Gay P. Mapping Geologic Structure of Basement and Role of Basement in Hydrocarbon Entrapment. (AAPG Search and discovery), 2002.
[6] Evamy B, Haremboure J, Kamerling P, Knaap, W, Molloy F, and Rowlands P. Hydrocarbon habitat of Tertiary Niger delta. AAPG Bulletin, 1978; 62(1): 1-39.
[7] Dailly GC. Pendulum Effect and Niger Delta Prolific Belt: GEOLOGIC NOTES. AAPG Bulletin, 1976; 60(9): 1543-1550.
[8] Ejedawe J. Patterns of incidence of oil reserves in Niger Delta Basin. AAPG Bulletin, 1981; 65(9): 1574-1585.
[9] Reijers T, Petters S, and Nwajide C. The Niger delta basin. Sedimentary Basins of the World, 1997; 3: 151-172.
[10] Tuttle ML, Charpentier RR, and Brownfield ME. The Niger Delta Petroleum System: Niger Delta Province, Nigeria, Cameroon, and Equatorial Guinea, Africa. US Department of the Interior, US Geological Survey, 1999.
[11] Daly M. Africa's oil and Gas resources and the potential of its Sub-saharan Cratonic Basins. Africa: Success in rift, sag, and passive margins. edn. Wembley Stadium, London: The 12th PESGB/HGS Conference on Africa E & P, 2013.
[12] Huc AY. September. African rifts and source rocks. Africa: Success in rift, sag, and passive margins. edn. Wembley Stadium, London: The 12th PESGB/HGS Conference on Africa E & P, 2013.
[13] Grant NK. South Atlantic, Benue Trough, and Gulf of Guinea Cretaceous Triple Junction. Geological Society of America Bulletin, 1971; 82(8), 2295-2298.
[14] Haack RC, Sundararaman P, Diedjomahor JO, Xiao H, Gant NJ, May ED, and Kelsch K. AAPG Memoir 73, Chapter 16: Niger Delta Petroleum Systems, Nigeria, 2000.
[15] Short K, and Stauble A. Outline of geology of Niger Delta. AAPG Bulletin, 1967; 51(5), 761-779.
[16] Doust,H, and Omatsola E. Niger Delta, in, Edwards, J. D., and Santogrossi, P.A., eds., Divergent/passive Margin Basins, AAPG Memoir 48: Tulsa, American Association of Petroleum Geologists, 1989; 239-248.
[17] Obiora S, Lambert-Aikhionbare D, and Ai O. Field measurements in descriptions of igneous and metamorphic rocks, Proceedings of Field Mapping Standardization Workshop, Ibadan University Press, 2009.
[18] Liu J, Pan X, Ma J, Tian Z, Chen Y, and Wan L. Petroleum geology and resources in West Africa: An overview. Petroleum Exploration and Development, 2008; 35(3): 378-384.
[19] Frankl E, and Cordry E. The Niger Delta oil province: Recent developments onshore and offshore, 7th World Petroleum Congress, 1967.
[20] He S, and Middleton M. Heat flow and thermal maturity modelling in the northern Carnarvon basin, north West Shelf, Australia. Marine and Petroleum Geology, 2002; 19(9): 1073-1088.
[21] Knox GJ, And Omatsola EM. Development of the Cenozoic Niger Delta in terms of the 'Escalator Regression'model and impact on hydrocarbon distribution. Coastal Lowlands. Springer, 1989; 181-202.
[22] Obaje NG. Geology and mineral resources of Nigeria. Springer, 2009.
[23] BP Report. BP Statistical Review of World Energy, pp. bp.com/statistical review, June 2012.

[24] Omotsola EBI. The Niger Delta is not a mature basin. Africa oil and gas report (http://africaoil-gasreport.com/2013/06/oil-patch-sub-sahara/the-niger-delta-is-not-a-mature-basin-omatsola/), June, 2013.
[25] Bird D. Primer: interpreting magnetic data. AAPG Explorer, 1997; 18(5), 18-21.
[26] Kearey P, Brooks M, and Hill I. An introduction to geophysical exploration. John Wiley & Sons, 2002.
[27] Sharma PV. Geophysical methods in geology. Elsevier Science Pub. Co., Inc., New York, NY, 1985.
[28] Telford WM, and Sheriff RE. Applied geophysics. Cambridge university press, 1990.
[29] Milsom J. Field geophysics. 3rd edition edn. John Wiley and Sons, 2003.
[30] Horng C, and Chen K. Complicated magnetic mineral assemblages in marine sediments offshore of southwestern Taiwan: possible influence of methane flux on the early diagenetic process. Terrestrial Atmospheric and Oceanic Sciences, 2006; 17(4), 1009.
[31] Paterson, Grant and Watson Limited. Technical assistance for the interpretation of airborne geophysical surveys for sustainable Management of Mineral Resources Project, Ministry of Mines and Steel Development Nigeria, 2009; 1-18.
[32] Reford SW, Misener JD, Paterson P, Ugalde HA, Gana JS, and Oladele O. Nigeria's Nationwide High-resolution Airborne Geophysical Surveys. SEG Denver 2010 Annual Meeting, 2010; 1835-1839.
[33] Hospers J. The geology of the Niger delta area. HM Stationery Office, 1971.
[34] Onuba LN. A preliminary analysis of the crustal structures of the Cenozoic Niger Delta Basin: insights from potential field data. PhD Thesis, University of Aberdeen, UK, 2016.
[35] Dow WG. Petroleum source beds on continental slopes and rises. AAPG Bulletin, 1978; 62(9): 1584-1606.
[36] Cornford C. Source rocks and hydrocarbons of the North Sea. Petroleum Geology of the North Sea: Basic Concepts and Recent Advances, Fourth Edition, 1998; 376-462.
[37] Gluyas J, and Swarbrick R. Petroleum geoscience. John Wiley & Sons, 2005.
[38] Haack R, Sundararaman P, and Dahl J. Niger Delta petroleum system (abs.): AAPG/ABGP Hedberg Research Symposium. Extended Abstracts Volume, Rio de Janeiro, Brazil, 1997.
[39] Stacher P. Present understanding of the Niger Delta hydrocarbon habitat. Geology of Deltas, AA Balkema, Rotterdam, 1995; 257-267.
[40] Saugy L, and Eyer JA. Fifty years of exploration in the Niger Delta (West Africa), in M.T. Halbouty, ed., Giant oil and gas fields of the decade 1990 – 1991, AAPG Memoir 78, 2003; 211-226.
[41] Edwards JD, Santogrossi PA. Summary and conclusions, in, Edwards JD, Santogrossi PA., eds., Divergent/passive Margin Basins, AAPG Memoir 48: Tulsa, American Association of Petroleum Geologists, 1990: 239-248.
[42] Kulke H. Nigeria, in, Kulke, H., ed., Regional Petroleum Geology of the World. Part II: Africa, America, Australia and Antarctica: Berlin, Gebrüder Borntraeger, 1995; 143-172.
[43] Mattick RE. Assessment of the petroleum, coal, and geothermal resources of the Economic Community of West African States (ECOWAS) region, 1982.
[44] Girard O. Petroleum geology of the Niger Delta. Report on petroleum resources of the Federal Republic of Nigeria.US Dept. of Energy, Washington, DC, 1979; B1–B29.
[45] Ejedawe J, Coker S, Lambert-Aikhionbare D, Alofe K, and Adoh F. Evolution of oil-generative window and oil and gas occurrence in Tertiary Niger Delta Basin. AAPG Bulletin, 1984; 68(11): 1744-1751.
[46] Okereke C, and Ananaba S. Deep crustal lineament inferred from aeromagnetic anomalies over the Niger Delta, Nigeria. Journal of Mining and Geology, 2007; 42(2): 127-131.

To whom correspondence should be addressed Dr. Leonard N. Onuba, Department of Geology, Chukwuemeka Odumegwu Ojukwu University PMB 02, Uli, Nigeria

Petroleum and Coal

Article **Open Access**

BURNING CHARACTERISTICS AND FUEL PROPERTIES OF OBOMKPA, IHIOMA, AND OGBOLIGBO LIGNITE COALS FROM NIGERIA

Bemgba Bevan Nyakuma[1,2]

[1] *Hydrogen and Fuel Cell Laboratory, Centre of Hydrogen Energy, Universiti Teknologi Malaysia, 81310 Skudai, Johor Bahru, Malaysia*
[2] *School of Chemical and Energy Engineering, Faculty of Engineering, Universiti Teknologi Malaysia, 81310 Skudai, Johor Bahru, Malaysia*

Received December 1, 2018; Accepted January 18, 2019

Abstract

Coal utilisation currently accounts for 40% of electricity generation worldwide. With energy demand projected to rise by 50% by 2042, coal-fired power is expected to expand particularly in nations with vast coal deposits such as Nigeria. However, limited scientific data on coal fuel properties and other socio-economic and political factors have hindered progress in Nigeria. Therefore, this study seeks to examine the burning (combustion) characteristics of Obomkpa (BMK), Ihioma (IHM), and Ogboligbo (OGB) lignite coals. It presents insights into the physicochemical properties, thermal degradation behaviour, and characteristic temperature profiles of the coals. The results showed that BMK contains high carbon, hydrogen, heating value but low oxygen compared to IHM and OGB whereas IHM showed the highest volatile matter but the lowest fixed carbon. However, OGB showed poor physicochemical qualities compared to BMK and IHM. The oxidative thermal analyses of the samples resulted in high mass losses and low residuals. The characteristic temperature profiles revealed IHM is more reactive, ignitable, and thermally efficient compared to the BMK and OGB lignite coal samples. Hence, IHM is a good feedstock for gasification, whereas BMK is suited for combustion and OGB for coke formation or coal blending.

Keywords: *Oxidative Characterization; Fuel Characteristics; Lignite Coal; Nigeria.*

1. Introduction

Coal is the most abundant and extensively dispersed fossil fuel worldwide [1]. It is also considered a reliable fuel for the supply of affordable base load energy and offers significant benefits that other fuels cannot currently accomplish around the globe [2]. As a result, coal has become critical to the global energy mix, which presently accounts for over 38% or 8000 TWh of electricity generated from coal-fired power plants [3]. Given this, the coal power industry provides the energy required by billions of consumers worldwide, thereby stimulating socio-economic growth and development as seen in India and China over the years [2,4]. With the demand for energy projected to soar by 50% by the year 2042, coal-fired power generation is expected to expand particularly in nations like Vietnam, Mozambique, and Nigeria. It is predicted that the astronomic growth in energy demand in these nations will expand coal-fired power in the years to come. The discovery of vast new deposits of coal particularly in Nigeria has revived interest in the energy generation. According to estimates, Nigeria has 640 million tons of proven resources and 2.8 billion tons of coal reserves strategically located across Nigeria. The vast majority of Nigeria's coal is located in the lower, middle and upper regions of the Benue trough which extends from the SW to NE of Nigeria's sedimentary basin. Therefore, the establishment of coal power plants in the various geopolitical zones within these sedimentary basins will greatly augment Nigeria's epileptic power supply.

The recent discovery of vast coal deposits in Obomkpa (BMK) in Aniocha-North Local Government Area (Delta State), Ihioma (IHM) in Orlu Local Government Area (Imo State), and Ogboligbo (OGB) in Igalamela-Odolu Local Government Area (Kogi State) have further increased the prospects of coal-fired power generation in Nigeria. Preliminary studies on BMK, IHM, and OGB have revealed the samples are low-ranked coals (LRC) or lignite [5-6] with potential for energy production. Other studies have basically provided estimates of deposits [7-9], physicochemical and mineralogical assessment [10-12], petroleum source rock potential [13-16], or other applications [17]. As a result, there is limited scientific data on the burning (combustion) characteristics and oxidative thermal properties of these lignite coals in literature. Therefore, this study seeks to examine the burning (combustion) characteristics of Obomkpa (BMK), Ihioma (IHM), and Ogboligbo (OGB) lignite coals from Nigeria's sedimentary basin. It will also present comprehensive data on the physicochemical, calorific values, thermal degradation behaviour and characteristic temperature profiles of the samples under mild oxidative conditions. It is envisaged that the findings will provide valuable insights into the fuel properties and possible applications of the lignite coals for the future design, operation and optimisation of coal-fired power or chemical plants in Nigeria.

2. Experimental

The rock samples were acquired from Obomkpa (BMK) in Aniocha-North Local Government Area (Delta State), Ihioma (IHM) in Orlu Local Government Area (Imo State), and Ogboligbo (OGB) in Igalamela-Odolu Local Government Area (Kogi State) all in Nigeria. The samples were subsequently crushed, ground, and sieved into 250 μm sized particles for physicochemical characterisation and thermal analysis. Next, the samples were characterised by ultimate, proximate, and calorific value analyses. The ultimate analyses were performed according to ASTM D5291-16 on the CHNS Elemental analyser (Model: vario MACRO Cube™ GmbH, Germany) to determine the elemental compositions of the samples. Next, the proximate fuel properties were determined through thermogravimetric (TG) analysis according to procedures reported in the literature [18]. The calorific value analysis was performed according to ASTM standard D2015 for determination of higher heating value (HHV) through bomb calorimetry using the combustion calorimeter (Model: IKA C2000, USA).

Next, the burning (combustion) characteristics and thermal degradation behaviour were examined by thermogravimetric analysis (TGA). The TG runs were performed under mild oxidative conditions and controlled by an air flow/purge rate at 20 mL/min through the non-isothermal heating programme of the TG analyser (Model: Shimadzu TG-50 analyser, Japan). For each test, approximately 10 mg of coal was weighed and placed in alumina crucible before the samples were heated at 20 °C/min from 30°C to 800°C. In the end, the TG analyser was cooled down, the raw data retrieved and processed on the Shimadzu Workstation (Version: TA-60WS). Next, the mass loss (%), and derivative mass loss (%/min) was plotted against temperature to obtain TG-DTG plots for the oxidative thermal analysis of the coals. The plots were then analysed, to examine the burning characteristics through its degradation behaviour, thermal reactivity and temperature profile characteristics (TPC), according to the procedures in the literature [19-20]. The TPCs examined in this study are; ignition (T_{ons}), midpoint (T_{mid}), and maximum decomposition (T_{max}), and burnout (T_{off}) temperatures along with mass loss rate (%/min) and residual mass (R_M, %).

3. Results and discussion

The objective of this study is to critically examine the burning characteristics of the lignite coal samples; Obomkpa (BMK), Ihioma (IHM), and Ogboligbo (OGB) from Nigeria. The results are presented in terms of its fuel and burning characteristics.

3.1. Fuel properties

Table 1 presents the fuel properties of BMK, IHM, and OGB lignite coals from Nigeria. The terms; C, H, N, S, O denote the elements carbon, hydrogen, nitrogen, sulphur, and oxygen,

respectively. However, M, VM, A, FC, and HHV denote the proximate properties; moisture, volatile matter, ash, fixed carbon and higher heating value, respectively.

Table 1. Fuel characteristics of Nigerian lignite coals

Fuel characteristics	Symbol/Unit	BMK	IHM	OGB
Ultimate analysis	C (wt. %)	50.38	46.80	37.48
	H (wt. %)	5.62	5.39	3.51
	N (wt. %)	0.59	0.64	0.80
	S (wt. %)	0.96	1.52	2.33
	O (wt. %)	42.45	45.64	55.88
Proximate analysis	M (wt. %)	3.63	4.75	3.12
	VM (wt. %)	58.05	69.52	51.43
	A (wt. %)	11.73	2.43	1.03
	FC (wt. %)	26.61	23.30	44.41
Calorific analysis	HHV (MJ/kg)	19.66	19.40	15.55

As observed in Table 1, the coals contain high compositions of C, H, N, O, and S. The highest compositions of C, H and the lowest O were observed for BMK which explains its comparatively higher calorific value (HHV) of 19.66 MJ/kg. Similarly, BMK contains the lowest N and S content which indicates a potentially lower risk of pollutant emissions such as NO_x, SO_x and NH_x during combustion. However, BMK contains the highest ash content of all the lignite coals examined in this study. This could result in significant ash deposition along with the concomitant problems of ash disposal, fouling and agglomeration during combustion. In contrast, the highest N and S content was observed in OGB. The sample also exhibited the lowest C, H, but the highest O which accounts for its low HHV of 15.55 MJ/kg compared to BMK (19.66 MJ/kg) and IHM (19.40 MJ/kg). Lastly, the fuel characteristics of IHM were found to be mid-way between BMK and OGB as observed in the elemental compositions. However, IHM contains the highest and lowest concentrations of VM and FC, respectively. The results indicate IHM is a suitable for coal gasification due to its VM, M and relatively low ash content.

3.2. Burning characteristics

The TG and DTG plots for the oxidative thermal analysis of Obomkpa (BMK), Ihioma (IHM), and Ogboligbo (OGB) lignite coals are presented in Figures 1 and 2.

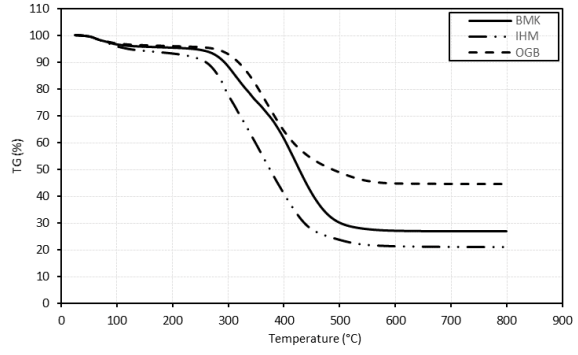

Figure 1. TG plots for oxidative, thermal analysis of Nigerian lignites

As observed in Figure 1, the BMK and IHM coals experienced signification mass loss as evidenced in the downward sloping curves compared to OGB during thermal analysis from RT to 800°C. This demonstrates the burning characteristics, and thermal degradation behaviour was significantly influenced by temperature which resulted in a mass loss during TG analysis. The magnitude of the mass loss for the coals was examined from the temperature profile characteristics (TPCs). The TPCs for the coals deduced from the TG plots in Figure 1 are presented in Table 2.

As observed from Table 2, the T_{ons} for the coals ranged from 250.10°C to 309.45°C. The T_{ons} is the lowest temperature in which a sample undergoing thermal analysis begins to decompose or experience mass loss. The lowest and the highest values for T_{ons} were observed

for IHM and BMK, respectively. This indicates that IHM is ignited or begins to thermally decompose at lower temperatures compared to BMK. Hence, it can be surmised that IHM is more reactive (less thermally stable) compared to OGB and BMK based on the reactions conditions examined in this study. The greater reactivity of IHM can be ascribed to its high VM (volatile matter) and lower FC (fixed carbon) as earlier presented in Table 1.

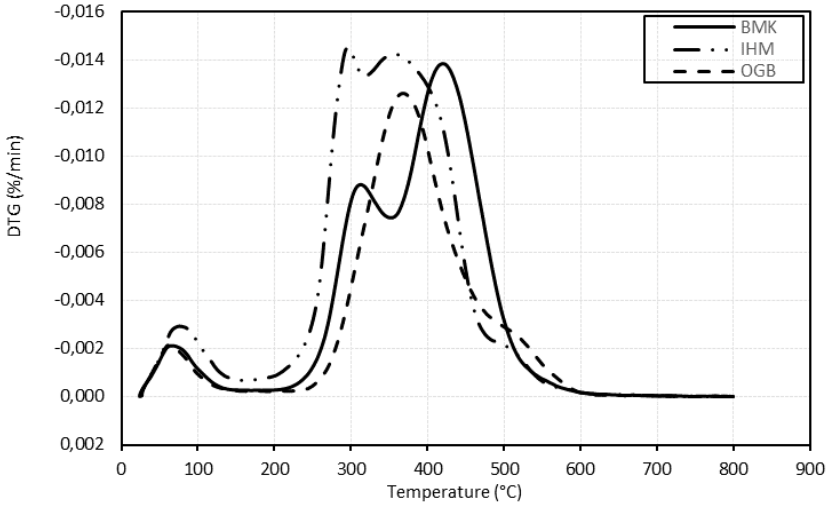

Figure 2. DTG plots for oxidative thermal analysis of Nigerian lignites

Table 2. TG-TPCs for BMK, IHM and OGB lignite coals

TPC Parameter	Symbol, Unit	BMK	IHM	OGB
Onset	T_{ons} (°C)	309.45	250.10	296.37
Mid-point	T_{mid} (°C)	394.32	347.29	375.99
Offset	T_{off} (°C)	480.59	436.53	454.37
Mass loss	(M_L, %)	73.18	78.94	55.51
Residual mass	(R_M, %)	26.82	21.06	44.49

Next, the T_{mid} values for the coals were examined. The T_{mid} is the intermediate temperature of the TG plot during thermal degradation of the sample. As observed, the T_{mid} ranged from 347.29 °C to 394.32 °C. Similarly, the lowest and highest values were observed for IHM and BMK, respectively. Lastly, the burnout temperatures or T_{off} ranged from 436.53°C to 480.59°C. The T_{off} is the temperature in which devolatilization or thermal degradation of volatiles is finalised during TGA. The lowest and highest T_{off} were observed for the IHM and BMK, respectively. Based on the TG-TPCs, IHM is the most reactive coal compared to OGB and BMK.

The mass loss (M_L, %) and residual mass (R_M, %) for the coals were also examined in this study. The M_L (%) is the mass of the sample lost or thermally degraded during TG analysis, whereas the R_M (%) is the mass of the sample remaining at the end of the process. The M_L of the coals was in the range 55.51% to 78.94%. The highest mass loss (M_L, %) was observed for IHM coal whereas the lowest was OGB. However, the R_M ranged from 21.06% to 44.49% for the coals. The highest R_M was observed for OGB whereas the least was for IHM. The results confirm that IHM is the most reactive coal whereas OGB is most thermally stable.

Next, the DTG plots for the oxidative thermal analyses of the coals were deduced as presented in Figure 2. As observed, the DTG plots showed a set of small peaks for derivative mass loss (DTG, %/min) below 200°C for all the coal samples examined in the study. The peaks, denoted as DyP (drying peak), in this range are typically ascribed to drying (or loss of moisture) during thermal analysis. The largest DyP was observed for IHM, BMK, and OGB in decreasing order of magnitude. The size of the IHM drying peak is due to its higher moisture content (4.75 wt.%) compared with BMK (3.63 wt.%) and OGB (3.12 wt.%).

Furthermore, the DTG plots showed another set of larger peaks, denoted as devolatilization peaks 1 and 2 (DvP_1 and DvP_2), in the range 200°C to 600°C for the thermal degradation of the coals examined in the study. The thermal analysis of the OGB coal resulted in one symmetric peak whereas BMK and IHM showed two peaks with different decomposition temperatures. Based on this, the TPCs were deduced to examine the decomposition mechanism of coals based on the DTG peaks as presented in Table 3.

Table 3. DTG-TPCs for BMK, IHM and OGB lignite coals

Parameter	Unit	BMK	IHM	OGB
Drying peak	DyP, °C	64.70	75.87	63.72
Devolatilization peak 1	DvP_1, °C	312.99	295.74	368.50
Devolatilization peak 2	DvP_2, °C	420.14	356.00	No peak

As observed in Table 3, the maximum temperature of the drying peaks (DyP) for the coals ranged from 63.72°C to 75.87°C. The highest DyP was observed for IHM which as earlier stated is due to its higher moisture (M) content compared to BMK and OGB. Due to its higher M, higher energy is required to dry the sample during thermal analysis which accounts for the larger size of its DyP compared to the other samples. Next, the DvP_1 peaks for the coals ranged from 295.74°C to 368.50°C. The DvP_2 peaks observed for only BMK and IHM were between 356.00°C and 420.14°C. In both cases, the lowest peak values were observed for IHM whereas the highest was observed in OGB. Overall, the results confirm that IHM is more reactive compared to the other coals examined based on the TPCs deduced from the thermal analysis. Furthermore, the reactivity of coals was examined from the mass loss during the various stages of the thermal analysis. Based on the DTG peaks and degradation temperatures, the oxidative thermal analysis of the coals occurred in three stages. The range of temperatures was; 25 – 110°C, 110 – 600°C, and 600– 800°C. The corresponding mass losses (M_L, %) during each stage is presented in Table 4.

Table 4. Mass loss during coal decomposition stages

Temperature range (°C)	Stage	Thermal process	BMK (%)	IHM (%)	OGB (%)
25 – 110	I	Drying	3.75	4.65	3.30
110 – 600	II	Devolatilization	69.24	73.99	51.98
600 – 800	III	Coke formation	0.19	0.29	0.23

The mass loss (M_L, %) in stage I ranged from 3.30% for OGB to 4.65% for IHM. As observed, the highest mass loss during the drying stage was for IHM. In comparison, the M_L for the samples is in good agreement with the moisture content in Table 1. In stage II, the M_L ranged from 51.98% (OGB) to 73.99% (IHM). The value observed for BMK is to some degree equivalent to its volatile matter (VM=51.43%) reported in Table 1. However, the M_L values for BMK and IHM observed in Table 4 differ by 11.19% and 4.47% from their VM. The higher values observed for the M_L may be ascribed to degradation or loss of other coal components during thermal analysis. Lastly, M_L during stage III ranged from 0.19 in BMK to 0.29% in IHM. Overall, it can be surmised that the reactivity of the coals is in the order IHM>BMK>OGB based on the M_L data deduced and presented in Table 4.

4. Conclusion

The paper presented new findings on the temperature profile characteristics of three newly discovered lignite coals; BMK (Obomkpa), IHM (Ihioma) and OGB (Ogboligbo) from Nigeria. The coal samples were characterised by physicochemical, calorific value, and non-isothermal oxidative thermogravimetric analyses. The physicochemical analysis results showed that BMK contains high C, H, HHV and low O compared to IHM and OGB. The BMK sample also exhibited

the lowest N and S but significantly high ash. The IHM contained the highest VM but the lowest FC. However, OGB showed poor physicochemical coal qualities with comparatively lower values to BMK and IHM. Overall, the oxidative thermal analysis of the coals resulted in a significant mass loss but low residual mass. Based on the temperature profile characteristics (TPC), IHM is more reactive, ignitable, and thermally efficient compared to BMK and OGB. Due to its properties, IHM is a potentially good candidate for energy recovery through gasification. However, BMK will be suitable for combustion whereas OGB is best suited for coke formation or blending with other coals.

Acknowledgement

The author wishes to acknowledge the support and technical assistance of the Centre of Hydrogen Energy, Universiti Teknologi Malaysia (Skudai Campus) for the TGA. Furthermore, many thanks accrue to the National Centre for Petroleum Research and Development (Abubakar Tafawa Balewa University, Bauchi Nigeria) and National Metallurgical Research and Development Centre (Jos, Nigeria) for supplying the coals.

References

[1] McGlade C, and Ekins P. The geographical distribution of fossil fuels unused when limiting global warming to 2 C. Nature, 2015; 517(7533): 187.
[2] Kellow, G. Technology: The Common ground solution toward low-carbon energy. World Coal, 2017; 10(10): 10-11.
[3] Coal Industry Advisory Board, The Global Value of Coal. 2012; IEA Headquarters: Paris, France.
[4] Shearer C. Mathew-Shah N. Myllyvirta L. Yu A, and Nace T. Tracking the global coal plant pipeline. Boom and Bust 2018 9th June, 2018]; Available from: https://bit.ly/2MdLCl6.
[5] Nyakuma BB, Oladokun O, Jauro A, and Nyakuma DD. Fuel Characterization of Newly Discovered Nigerian Coals. IOP Conference Series: Materials Science and Engineering, 2017; 217(1): 012012.
[6] Nyakuma BB, Oladokun O, Jauro A, and Nyakuma DD. Evaluating the Energy Recovery Potential of Nigerian Coals under Non-Isothermal Thermogravimetry. IOP Conference Series: Materials Science and Engineering, 2017; 217(1): 012013.
[7] Nwasike OT, and Gregory O. Opportunities and Challenges of an Integrated Energy Policy for Nigeria-Perspectives from a competing Energy Product. in Nigeria Annual International Conference and Exhibition. 2003. Society of Petroleum Engineers.
[8] Ohimain EI. Can Nigeria generate 30% of her electricity from coal. International Journal of Energy and Power Engineering, 2014; 3(1): 28-37.
[9] Emodi NV. The Energy Sector in Nigeria, in Energy Policies for Sustainable Development Strategies. 2016; Springer. p. 9-67.
[10] Nwoko C, Onyedika G, Nkwoada A, and Anyanwu G. Mineralogical and Physicochemical Assessment of Ihioma Coal in Imo State of Nigeria. IOSR Journal of Applied Chemistry (IOSR-JAC), 2016; 9(12): 42-46.
[11] Ogala JE. The geochemistry of lignite from the neogene ogwashi-asaba formation, niger delta basin, southern nigeria. Earth Sciences Research Journal, 2012; 16(2): 151-164.
[12] Hannan M, Oluwole A, Kehinde L, and Borisade A. Determination of oxygen, nitrogen, and silicon in Nigerian fossil fuels by 14 MeV neutron activation analysis. Journal of radioanalytical and nuclear chemistry, 2003; 256(1): 61-65.
[13] Akande SO, Hoffknecht A, and Erdtmann BD. Rank and petrographic composition of selected upper cretaceous and tertiary coals of Southern Nigeria. International Journal of Coal Geology, 1992; 20(3): 209-224.
[14] Ogala J. Source rock potential and thermal maturity of the Tertiary lignite series in the Ogwashi-Asaba Formation, Southern Nigeria. Asian Journal of Earth Sciences, 2011; 4(3): 157.
[15] Akande SO, Adeoye MO, and Erdtmann BD. Petroleum Source Rock Potential Assessment of the Oligocene-Miocene Ogwashi Asaba Formation, Southern Anambra Basin, Nigeria. 2015.
[16] Ogala J, Siavalas G, and Christanis K. Coal petrography, mineralogy and geochemistry of lignite samples from the Ogwashi–Asaba Formation, Nigeria. Journal of African Earth Sciences, 2012; 66: 35-45.
[17] Eligwe CA and Okolue NB. Adsorption of iron (II) by a Nigerian brown coal. Fuel, 1994; 73(4): 569-572.

[18] Donahue CJ and Rais EA. Proximate Analysis of Coal. Journal of Chemical Education, 2009; 86(2): 222.
[19] Nyakuma BB and Jauro A. Physicochemical Characterization and Thermal Decomposition of Garin Maiganga Coal. GeoScience Engineering, 2016; 62(3): 6-11.
[20] Nyakuma BB and Jauro A. Chemical and Pyrolytic Thermogravimetric Characterization of Nigerian Bituminous Coals. GeoScience Engineering, 2016; 62(3): 1-5.

To whom correspondence should be addressed Dr. Bemgba Bevan Nyakuma, Hydrogen and Fuel Cell Laboratory, Centre of Hydrogen Energy,Universiti Teknologi Malaysia, 81310 Skudai, Johor Bahru, Malaysia

Petroleum and Coal

Article **Open Access**

AN ASSESSMENT OF THE EFFECT OF COAL BLENDING ON HARDGROVE GRINDABILITY INDEX

Niaz Muhammad Shahani

School of Mines, China University of Mining & Technology, Xuzhou, 221116, China

Received December 2, 2018; Accepted January 18, 2019

Abstract

Hardgrove Grindability Index (HGI) is a determining factor of energy consumption during grinding. The current study is aimed at investigating the influence of the blending behavior on HGIs of two dissimilar coal samples.

In this study, one local coal sample is taken from Lakhra coal deposits and second sample is extracted from Indonesian coal reserves for empirical experiment and analysis. The total number of nine blends with different blending ratios based on the Net Calorific Value (NCV) was made. In addition, the samples were further tested for proximate and ultimate analysis, Gross Calorific Values and HGI respectively. The ASTM D409-D409M standard Hardgrove grindability tester was used for the determination of HGI of cited two coal samples. The main purpose of this study is to determine the blends that specify the optimum results those are appropriate for power sectors and cement industries. According to the above study, the blend no 2 and 3 demonstrate the optimum results for cement factories with approximately HGI 46 and 49 with sulphur content 1.01 and 1.17, whereas blend no 4 and 5 are appropriate for power sectors with approximately HGI 52 and 54 with sulphur content 1.37 and 1.58.

Furthermore, the value of the blends for HGI and moisture content shows the inverse relation, as the moisture content increases HGI value decreases. Similarly, research results also determine that there is also inverse relationship between the blend value of volatile matter and total carbon with HGI. Additionally, the GCV also exhibits inverse relationship while ash and fixed carbon reveal direct relationship with the value of blends for HGI. In the same manner, sulfur also exhibits direct relation with HGI value..

Keywords: *Coal blending; Gross calorific value; Hardgrove grindability index; proximate analysis; Ultimate analysis.*

1. Introduction

Among fuel, coal has the key standing in meeting the energy needs around the globe. It's extensively leading source of energy accessible to world economy nowadays [1].

The HGI is intended to conclude ease through which coal can be ground. It evaluates the grindability of coal and is a confidential measure of coal. It delivers the knowledge of grinding power consumption and comminuting extents. HGI of coal can be contingent on the composition of coal. It's extensively utilized by the industries so as to measure power need throughout the process of comminution [2-5]. Typically, harder coals have low HGI and softer coals have higher HGI contents [6-10]. A number of the physical properties of coal like stiffness, tenacity, and rupture are often indicated by it as similarly [11-13].

Generally, coal grindability is classified into two terms: first is work index that measures overall energy consumption for obtaining product quality fineness is determined; second is grindability index through that fineness of absolute product is measured for same grinding work of standard samples. As work index is time and labor cost consuming factor, therefore, Hardgrove grindability index (HGI) is mostly preferred for projecting the behavior of coal and energy consumptions requirements of mill [14]. It is very important to discuss that multiple physical and chemical properties of coal put impact on the value and measurement of HGI,

including particulars of moisture, ash, volatile matter and fixed carbon. In addition to that, presence and exact proportion of multiple macerals and microlithotypes and composition and supply of mineral substance. Coal blending is also a compulsory parameter that affects the HGI grindability of assumed coal. Usually, coal blending doesn't indicate any additive relation among the Hardgrave grindability index results of separate constituent coals [15].

This study deals with the assessment of HGI of two dissimilar coal blends related to their chemical properties.

Various countries around the globe depend on different sectors that play role in the strength of economy. Some countries rely on agriculture and other on their mineral resources. The Pakistan is one among those countries that rely on agriculture, though preserves adequate potential to distract the economic dependence on her mineral capitals that have been asking for the consideration. Little attention to the coal sector can not only increase the severe energy crisis the country is dealing, but it can also influence economy.

Figure 1. Hardgrove grindability index machine [19]

Energy deficiency in Pakistan is a biggest problem and it can be utilized by the local coal as a solid fuel for power generation and if its use is given top priority by the industrialists [16].

As matter of coal-fired is concerned, it is usual practice to make convenient blend of local coals apart from separate coals within Pakistan. Generally, coals and blends are ground before use for burning.

The coal grindability is usually influenced by the blending factor, as stated in the literature [17- 18]. A few studies have revealed some confident result on grindability because of its blending. The current research has been assumed to investigate the effect of coal blending on the HGI grindability of local and foreign coal.

2. Factors affecting the Hardgrove grindability values

The HGI is mostly affected by the petrographic structure of coal. Usually, grindability grows as the content of volatile matter rises of about 30%, on the far side that the grindability declines. Likewise, with the increment in carbon content, the HGI value will increases as well and the grindability then decrease quickly with the carbon value greater than about 92%. The coal with the classification of lithotype having comparable percentages of volatile matter comprise variance in the HGI results. Durite is also labeled as dull coal is a lithotype attribute by low HGI and is usually the hardest. Classification fusite is considered by means of lithotype with the principal value of HGI is uncertain as a result of its highest fragility is affected by initiation of substantial quantity of pulverized portions rather through screening and grinding in the investigating tool [20]. Glittering vitrinite is another type of lithotypes in black coal that have considerably greater HGI values as compared to the durites in the identical coal classification. The variance in grindability of distinct lithotypes permits for particular grinding. It is usually effective with the existence of vitrinite in coal raises the value of HGI, however, the liptinite and micronite macerals decline the grindability.

3. Materials and methodology

Approximately 10 kg of coal sample from Indonesia was provided by Engineer Faisal Raza traders from their coal stores located in Karachi and 10 kg of Lakhra coal was directly taken from

the mining region of Lakhra. Each sample of 10 kg was thoroughly mixed in order to ensure homogeneity as far as possible. The two coals selected for the present studies were such that one coal had the low HGI (Indonesian coal) while the other coal had high HGI (Lakhra coal).

The experiments were carried out on two dissimilar coal samples with their unary and binary blends. The standard ASTM D409-D409M was followed for the determination of HGIs. For a realistic study, two normal reference coals were conjointly used. The results of these experiments are given in Tables 1 to 4.

The proximate and ultimate analysis was also achieved on each blended coal sample in agreement with ASTM standards. All experiments were carried out on air-dried origin. Total carbon and sulfur were measured with Carbon-Sulfur analyzer ASTM-D-5016-08 standard.

The process, for the determination of HGI, was as follow;

The 50 mg sample of prescribed size -75+3350 mesh was taken in the ball mill of HGI machine along with 8 iron balls with diameter 25.4±0.003 mm. The mouth of the ball mill was closed and was set to rotate for exactly 70±0.25 revolutions. After the requisite rotation was achieved, the machine stopped automatically. The sample left within the ball mill was later collected along with any pulverized material holding on to the surface of the HGI machine with the assistance of a brush.

This sample was after placed in a 75μ size of sieve and was shivered approximately for 10 minutes. The sample which passed through 75μ size and retained on 3350μ size was weighed on the balance. The HGI value is determined by the given experimental formula [21]:

$$HGI = 13 + 6.93W \quad (1)$$

where: W is weight of the test sample passing through 75μ sieve after grinding in the HGI machine.

4. Calculation for the determination of the percentage of coal blends

The blends of two dissimilar coal samples on thermal based on NCV were prepared by using the following calculation [22]; Suppose the total heat to be obtained from the blend is 100,000 kJ. If the 90 % heat is required from Indonesian coal than heat required from it is 90,000 kcal. Then, heat required from Lakhra coal is 10 % which total to 10,000 kcal.

kg coal of Indonesian coal required for 90,000 kcal = $\frac{90{,}000\ kcal}{NCV\ of\ Indonesian\ coal\ kcal/kg} = \frac{90{,}000}{6483}$

Hence, kg coal of Indonesian for 90,000 kcal =13.88 kg coal.

Similarly, kg coal of Lakhra coal required for10, 000 kcal = $\frac{10{,}000\ kcal}{NCV\ of\ Lakhra\ coal\ kcal/kg} = \frac{10{,}000}{4877}$

Hence, kg coal of Lakhra for 10,000 kcal = 2.05 kg coal

Percentage (%) of Indonesian coal by weight = $\frac{13.88}{(13.88+2.05)} \times 100 = 87.131\ \%$

Percentage (%) of Lakhra coal by weight = $\frac{\text{kg coal of Lakhra}}{(\text{kg coal of Indonesian} + \text{kg coal of Lakhra})} \times 100$

$= \frac{2.05}{(13.88+2.05)} \times 100 = 12.868\ \%$

The thermal percentages of other blends were calculated in similar way and their results are presented in Table 2.

The Net calorific value (NCV) and hydrogen (%) was determined by the following formula;

$$NCV = GCV - \left[(0{,}089.H) + \frac{TM}{100}.587\right] \quad (2)$$

$$H = 0{,}069.\frac{GCV}{100+VM} - 2.86 \quad (3)$$

where: GCV is the Gross calorific value in kcal/kg; H is Hydrogen content present in the coal in %; TM is the Total Moisture in %; VM is the volatile matter.

Table 1. Analysis of coal samples and their HGI values as received basis

Sample	TM (%)	Ash (%)	VM (%)	FC (%)	GCV (kcal/kg)	NCV (kcal/kg)	TC (%)	S (%)	H (%)	HGI value
Indonesian	11	13	37.9	34.5	6 420	6 483	65.90	0.80	10.58	44
Lakhra	8.6	15	41.5	38.9	4 828	4 877	55.78	5.68	6.99	66

TM- total moisture; VM- volatile matter; FC-fixed carbon; GCV-gross caloric value; NCV-net caloric value; TC-total carbon; S-sulfur; H-hydrogen, HGI- Hardgrove grindability index

Table 2. Calculated percentage of each assumed sample

Blend ratios (%)	Thermal blending ratio (%)		Weight blending ratio (%)	
	Indonesian	Lakhra	Indonesian	Lakhra
1	100	0	100	0
2	90	10	87.131	12.858
3	80	20	74.938	25.061
4	70	30	63.695	36.304
5	60	40	53.008	46.991
6	50	50	42.928	57.071
7	40	60	33.401	66.598
8	30	70	24.378	75.621
9	20	80	15.811	84.188
10	10	90	7.703	92.296
11	0	100	0	100

Table 3. Measured analysis of the binary blends of two dissimilar coal samples

Blend ratios	TM (%)	Ash (%)	VM (%)	FC (%)	GCV (kcal/kg)	NCV (kcal/kg)	TC (%)	S (%)	H (%)	HGI value
1	11	13	37.9	34.5	6420	6 483	65.90	0.80	10.58	44
2	10.80	13.2	38.3	35	6 360.64	6 423	64.04	1.03	10.42	46
3	10.58	13.5	38.9	35.44	6 279.24	6 340	62.22	1.17	10.19	49
4	10.32	13.7	39.2	35.82	6 097.48	6 156	60.38	1.37	9.79	52
5	10.1	14	40.10	36.28	5 916.44	5 956	58.54	1.58	9.33	54
6	9.87	14.3	40.3	36.73	5 735.04	5 792	58.08	2.46	8.94	57
7	9.6	14.4	40.6	37.14	5 553.64	5 608	57.62	3.20	8.55	59
8	9.73	14.6	41	37.59	5 372.24	5 426	57.16	3.82	8.14	62
9	9.13	14.7	41.1	38.01	5 190.84	5 243	56.70	4.44	7.76	63
10	8.88	14.9	41.3	38.48	5 009.44	5 060	56.24	5.18	7.38	64
11	8.6	15	41.5	38.9	4 828	4 877	55.78	5.68	6.99	66

Table 4. Calculated analysis of the binary blends of two dissimilar coal samples

Blend ratios	TM (%)	Ash (%)	VM (%)	FC (%)	GCV (kcal/kg)	NCV (kcal/kg)	TC (%)	S (%)	H (%)	HGI value
1	11	13	37.9	34.5	6 420	6 483	65.9	0.80	10.58	44
2	10.91	13.4	38.6	35.02	6 261	6 163.1	64.44	0.996	10.19	47
3	10.46	13.7	38.8	35.5	6 012	6 016.2	63.98	1.064	9.65	50
4	10	13.8	39.1	35.97	5 943	5 868.3	63.52	1.105	9.48	51
5	9.76	14.1	39.6	36.42	5 784	5 704.4	64.06	1.477	9.10	53
6	9.52	14.3	40	36.86	5 635	5 576.5	60.38	2.228	8.76	55
7	9.48	14.5	40.2	37.29	5 466	5 428.6	58.54	2.992	8.40	57
8	9.25	14.6	40.5	37.72	5 307	5 283.7	57.15	3.29	8.05	60
9	8.90	14.7	41	38.14	5 148	5 135.8	56.23	4.267	7.68	61
10	8.78	14.8	41.2	38.54	4 951	4 988.9	56.01	4.89	7.26	62
11	8.6	15	41.5	38.9	4 828	4 877	55.78	5.68	6.99	66

TM- total moisture; VM- volatile matter; FC-fixed carbon; GCV-gross caloric value; NCV-net caloric value; TC-total carbon; S-sulfur; H-hydrogen, HGI- Hardgrove grindability index.

5. Results and discussion

The overall results those have been extracted from the study are discussed here in the aspect of relative grindability of ease of pulverization of the local as well as international coals.

In case of comparison with the grindability of low-rank coals, it was observed that some cases regarding low-rank coals within other countries have similarities with the coal found in Pakistan.

Results of this research work are presented together in tabular and as well as in graphical order. Table 1 to 4 represents the proper investigation of two dissimilar coal samples with different grade and their unary and the binary blends comprising the determined data of their HGI contents.

5.1. Effect of coal blending on Hardgrove grindability index

The current research determines the HGI of coal blends of different heating ratios arranged from two different coals. One from Indonesia hard coal having HGI 44 and second local coal from Lakhra having HGI 66. The experimentally measured HGI values of different blends ranged between 46 and 64 whereas the weighted average calculated values ranged between 47 and 62 as given in Table 3 and 4.

On the other hand, the weighted average calculated values of HGI are lesser by 1 to 2 compared to the experimentally determined HGI values for blending ratios having 60 % to 10 % of Indonesian coal as indicated in table 4.

The consequences of current work are supported by related work conducted in past research on coal as following;

The results of this study specify that experimentally measured HGI values of coal blends varied by about 1 to 2 with the weighted average calculated values [23]. Moreover, he added that the influence of moisture and coal blending on HGI of Western Australian coal where it has been perceived that measured HGI values of binary and tertiary blends resembled sound with the weighted average values of HGI within ±2.

Contrary to the above-cited conclusions of researchers, results of [24] state that even though coals with the same HGI mixed together, the measured HGI values of blends determines smaller than the calculated values, in certain conditions poorer than either blended constituents. Consequently, it was determined that there is no other technique except experimentally measured method for the determining of the HGI of the different coal blends.

5.2. Effect of chemical properties of coal blending on Hardgrove Grindability Index of coal samples

5.2.1. Proximate analysis

5.2.1.1. Moisture

The calculated moisture contents found to be marginally higher related to the experimentally determined contents for all blending ratios of Indonesian coal in Lakhra coal. The contrast between the measured and calculated values ranges 0.25 % to 1%.

Thus, the consequences have exposed advancement of moisture contents in blends within the range 0.25 % to 1 %. These results are supported by the reflection [25] who specified that to any form of moisture content comprising only internal and surface moisture constituent, advancement should apply.

5.2.1.2. Volatile matter

The change between experimentally measured and calculated values was found and ranges 0% and 2.6 %. The experimentally measured values conclude higher than the calculated values for total blending ratios. The results of the present study are supported by the results of [25] and [26].

5.2.1.3. Ash

The experimentally measured ash content values of different blends ranged between 18 % and 40 % whereas the weighted average calculated values ranged between 15.9% and 39.1% as mentioned in Table no 3 and 4. The experimentally measured values always conclude higher than the calculated values for total blending ratios [26-27].

5.2.1.4 Fixed carbon

There is no any method to determine the fixed experimentally, hence it is determined by using the following formula;
FC = 100 - Moisture + ash + volatile matter; where FC is the fixed carbon.

The progression of fixed carbon content can be determined with the addition of the other three components i.e. moisture content, volatile matter content and ash content. It is affected by mistakes in their determination. It has been perceived that the calculated values are always higher than the measured values of fixed carbon.

5.2.2 Partial ultimate analysis

5.2.2.1 Total carbon

The results clearly indicate that the blends of total carbon seem to be an additive property. These evaluations of the present work are equivalent to the results of [27-28].

5.2.2.2 Sulfur

The experimentally measured total sulfur values of different blends ranged between 1.08 % and 5.18 % whereas the weighted average calculated values ranged between 0.996 % and 4.89 % as shown in Table 3 and 4 representing a variance from 0.034% to 0.29%. The results of the current study are supported by the opinion of [28].

5.2.2.3 Hydrogen content

The reason for a difference between the measured and calculated values of hydrogen content may be because of the volatile matter value and the gross calorific value rises or reduces steadily. The Syler's equation has been used for the determination of hydrogen value when GCV was in kJ/kg.

6. Conclusion

The industrial sector in Pakistan, particularly the cement sector is consuming blends of high sulfur local coal and low sulfur imported coals. The two coals are blended together to carry the sulfur content of the blend to a limit of about 2% acceptable in the cement industry. The pulverization characteristics of imported coal and local coal are completely dissimilar.

This study was conducted to experimentally measure the pulverization characteristics which are measured by HGI and it was concluded that the blends of two dissimilar coals indicate the prime consequences and are acceptable for power plants and cement industries.

In addition, it was concluded that;

- Out of the 9 potential blends, the blend 2 & 3 show the prime results which are in good agreement for the cement industries about 46 & 49 HGI value with sulfur content 1.01 & 1.17.
- Although blend 4 & 5 are meet for power plants about 52 & 54 HGI value with sulfur content 1.37 & 1.58.

The blends value for HGI and moisture content indicates the opposite relation, as the moisture content rises HGI value decreases instantly. Past studies revealed that coal with high moisture content noted as a hard coal though it may include the small HGI values on grinding but talking about the Lakhra coal which shows uniqueness with low moisture content is 8.6 and HGI value is high 66 nearly. It is because of the maceral present in the Lakhra coal that is vitrinite. It is commonly valid that the existence of vitrinite in coal increases the HGI value, though the micronite and liptinite macerals diminish the grindability.

Moreover, it is also confirmed that the blends value of moisture content and volatile matter (VM) demonstrates the opposite relation with HGI. As the HGI value increases the value of moisture content and volatile matter decreases. Similarly, the total carbon also show the opposite relation with HGI. However, the value of ash and fixed carbon shows the direct relation with the blends value for HGI. Likewise sulfur also show the direct relation with the HGI.

Acknowledgment

The first and topmost thanks are due to the School of Mines, China University of Mining and Technology (CUMT) to providing experimental facilities. In addition, the author is also thankful to Local traders in Karachi for providing such assistance to collect the Indonesian coal sample and Lakhra coal mines to accomplish this research study.

References

[1] Sanders GJ, Ziaja D, Kottmann J. 2002. Cost efficient beneficiation of coal by ROMJIGs and BATAC Jigs. Coal Preparation, 2002; 22: 181-197.
[2] Dejene DY. The Utilization of Indigenous Coal as Energy Substitute in Cement Industry, p. 8. PhD Thesis Addis Ababa University Faculty of Technology 2004.
[3] Isherwood B. Carbon Connections PL, Newcastle, Australia. (June 2014) Personal communication
[4] Gutscher R. Vienna, Austria, EVN (2014) Personal communication.
[5] Sloss LL. Blending of coals to meet power station requirements, © IEA Clean Coal Centre 2014, 978–92–9029–559-4.
[6] Qzbayoglu G, Ozbayoglu MA, and Ozbayoglu EM. Estimation of Hardgrove grindability index of Turkish coals by neural networks. International Journal of Mineral Processing, 2008; 85: 93–100.
[7] Beran RR. Coal Hand Book. New York: Marcel & Dekker 1981.
[8] International Organization for Standardization (ISO). 1994. Hard Coal-Determination of HGI, ISO 5074: Geneva, Switzerland: ISO.
[9] Majid A. Handbook for Cement Engineers. Lahore, Pakistan: Inst. Of Professional Advancement 2002.
[10] Speight JG. Handbook of Coal Analysis. Hoboken, NJ: John Wiley & Sons 2005.
[11] Dutkiewicz RK, Scieszka SF, and Fintel RHV. A study of the energy-size reduction relationship in impact crushing of coal. Power Technology, 1986; 49(1): 83–86.
[12] Tiryaki B. Technical note practical assessment of the grindability of coal using its hardness characteristics. Rock Mechanics & Rock Engineering, 2005; 38(2): 145–151.
[13] ACARP Report, Hargrove Grindability Index, 1998. Australian Coal Association Research Program. PO Box 7148 Riverside Centre Qld 4001 Australia.
[14] Tichánek F. Contribution to Determination of Coal Grindability using Hardgrove Method. Geo-Science Engineering, 2008; LIV, 27-32.
[15] Vuthaluru HB, Brooke RJ, Zhang DK, Yan HM. Effects of Moisture and Coal Blending on Hardgrove Grindability Index of Western Australian coal. Fuel Processing Technology, 2003; 81 67-76.
[16] Wahab A, Nawaz S, Shahzad K, Akhtar J, Kanwal S, Munir S, Sheikh N. Desulfurization and Demineralization of Lakhra Coal by Molten Caustic Leaching, Energy Sources, Part A: Recovery, Utilization, and Environmental Effects, 2015; 37:11, 1219-1223.
[17] Vuthaluru HB, Brooke RJ, Zhang DK, and Yan HM. Effects of moisture and coal blending on hardgrove grindibility index of Western Australian coals. Fuel Processing Technology, 2003; 81(1): 67–76.
[18] Rubiera F, Arenillas A, Fuente E, Miles N, and Pis JJ. Effect of grinding behavior of coal blends on coal utilization for combustion. Power Technology, 1999; 105: 351–356.
[19] Tichánek F. 2008. Contribution to determination of coal grindability using Hardgrove method. GeoScience Engineering, 2008; LIV(2): 27-32.
[20] Speight JG. The Chemistry and Technology of Coal. New York 1994: Marcel & Dekker.
[21] Trimble AS, Hower AC. Studies of the relationship between coal petrology and grinding properties, International Journal of Coal Geology, 2003; 54: 253– 260.
[22] Aroosh K. Effects of coal blending on Hardgrove grindability index. Masters Thesis 2014.
[23] Vuthaluru HB, Brooke RJ, Zhang DK, Yan HM. 2003. Effects of moisture and coal blending on Hardgrove Grindability Index of Western Australian coal, Fuel Processing Technology, 2003; 81: 67– 76.
[24] Ashley C, Phill B. Evaluate combustion behavior of Australian export and overseas low rank coal blends; Project Number: C3097, 2012< www.acarp.com.au/abstracts.aspx.
[25] Wall T, Elliott L, Sanders D, Ashley C. Technology Assessment Report 14, 2001, Cooperative Research Centre For Black Coal Utilisation, NSW Australia, p. 22.
[26] Riley JT, Gilleland SR, Forsythe RF, Graham HD, Hayes FJ. Non-additive analytical values for coal blends, Proceedings of the 7th international conference on coal testing, Charleston, WV, USA, 21-23 Mar. 1989. Ashland, KY, USA, Coal Testing Conference, Standards Laboratories, Technical Services Division, pp. 32-38.

[27] Carpenter MA. Coal blending for power stations, IEA Coal Research Report IEACR/81 1995.
[28] Su S. 2001. Combustion behaviour and ash deposition of blended coals, PhD Thesis, The University of Queensland 1999, Brisbane.
[29] Su S, Pohl JH, Holcombe D, Hart JA. Techniques to determine ignition, flame stability and burnout of blended coals in p.f. power station boilers. Progress in Energy and Combustion Science, 2001; 27, 75–98.

To whom correspondence should be addressed: Niaz Muhammad Shahani, School of Mines, China University of Mining & Technology, Xuzhou, 221116, China, Email: shahani.niaz@cumt.edu.cn

Petroleum and Coal

Article **Open Access**

PREPARATION AND EVALUATION OF N-ALKYL METHYLACRYLATE-VINYL ACETATE - METHACRYLIC ACID TERPOLYMERS AS POUR POINT DEPRESSANT FOR FUEL

T. T. Khidr

Egyptian Petroleum Research Institute, Nasr City Cairo, Egypt

Received December 10, 2018; Accepted January 18, 2019

Abstract

A variety of techniques have been employed in order to reduce problems caused by the crystallization of paraffin during the production. Four different alkyl chain length of n-alkyl methacrylate-vinyl acetate-methacrylic acid terpolymers were prepared and characterized by the infrared spectrometer, and the molecular weight of the prepared additives was determined by using gel permeation chromatography analysis. The performance of the prepared terpolymers as pour point depressants additives for fuel oil. The efficiency of the prepared compounds on pour point depressants for fuel oil increases by increasing the concentration of these additives and the alkyl chain length of n-alkyl methacrylate. The X- ray diffractometer patterns of wax in the absence and presence of investigated additives were studied. Comparison of morphologies and structures of waxy crystals in fuel oil beneficiated with and without a pour point depressant was made by micro photographic studies which show the modification in wax morphology due to the additive.

Keywords: *Terpolymers; Fuel oil; Pour point depressants; Wax modification.*

1. Introduction

Hydrocarbon fuel oils, for example, petroleum distillate fuels, contain n-paraffin waxes that tend to be separated from the oil in low temperature [1-2] The waxes generally crystallize as an interlocking network offine sheets, thereby entrapping the remaining fuel in cage like structures [3] and causing the cold flow problems such as blockage of fuel lines and filters in engine fuel system. Studies have shown that the network waxes amounting to as little as 1–2wt% of the sample are still capable of causing low temperature fluidity and operability problems in distillate fuels [4-5]. Highly waxy crude oils are characterized by a high pour point, viscosity, and yield stress, and exhibit non-Newtonian flow behaviour below pour point temperature [6-8] The flow properties of crude oil play a great role in its production storage, transport, and refining [9-11] pour point depressants (PPDs) to improve the cold flow properties of oils has been proven to be an effective and economical way [12]. In general, these additives have a wax-like paraffin part which provides the interaction between the additive and paraffin and a polar segment that is responsible for modifying the morphology of wax crystals [13-14].

Some characteristics of the additives should be considered: there should be a sufficient number of pendant alkyl groups with sufficiently long hydrocarbon chains, there should be an appropriate distance between the hydrocarbon pendant chains and there should be a suitable ratio of monomers for copolymer additives [15-16]. Many experimental and theoretical studies have been performed to reveal the pour point depressant mechanism and many hypothetical mechanism theories have been formed, in which adsorption, co-crystallization, nucleation, and improved wax solubility are the most widely accepted view points [17-18].In the present study, we have synthesized four alkyl methacrylate-vinyl acetate-methacrylic acid terpolymers with different long-chain alkyls by free radical polymerization and evaluated their influence on the flow properties of fuel oil.

2. Experimental

2.1. Materials

The following chemicals were used, methacrylic acid, dodecyl alcohol, hexadecyl alcohol, octadecyl alcohol, two linear saturated long chain alcohol blends NAFOL 20+A, and NAFOL 1822 B were supplied from Condea Chemical Company, the typical analysis is listed in Table 1. Vinyl acetate was purchased from Aldrich and distilled under reduced pressure before use. P-toluene sulphonic acid, dibenzoyl peroxide, and other common chemicals used were of laboratory grade reagents.

Table 1. Typical analysis of linear long-chain alcohol blends (NAFOL)

Properties	NAFOL 20+A	NAFOL 1822 B	Properties	NAFOL 20+A	NAFOL 1822 B
	Composition, wt %		Density g/cm^3 at 80°C	0.803	0.802
C16-OH	0.9	0.2	Solidification point,°C	56-60	63-65
C18-OH	24.3	15.0	Ester No. mg KOH/g	9.9	0.16
C20-OH	24.4	14.8	Acid No. mg KOH/g	0.05	0.01
C22-OH	38.2	69.8	Water, wt%	0.06	0.04
C24-OH	9.9	0.2	Flash point,°C	208	204
C26-OH	2.3	-	Iodine No. mg/100 mg	8.2	0.23
			Average carbon number (calculated)	C_{av}= 20	C_{av}= 22

2.2. Middle distillate fuel oil composition

Middle distillate fuel oil (FO) derived from the waxy western desert crude oil with physico-chemical characteristics given in Table (2) was used for evaluation of the performance of the synthesized additives. The n-paraffin content of the fuel oil tested was determined by urea adduction [19]. The fuel oil was subjected to gas liquid chromatographic analysis to determine the average carbon number and carbon number distribution.

Table 2. Physical characteristics of fuel oil

Properties	Methods	Result
Specific gravity at 60/60°F	IP 160/87	0.8412
Kinematics viscosity at 40°C (cSt)	IP 71/80	3.7
Cloud point (cp), °C	IP 219/82	24
Pour point (pp), °C	IP 15/67(80)	15
Sulfur content (wt%)	IP 266/87	0.231
Flash point, °C	IP 34/82 (87)	123
Total paraffins content (wt%)	Urea adduct	20.3
n-paraffin (wt%)	GLC	19.9
Iso-paraffins (wt%)	GLC	0.40

2.3. Synthesis additives

2.3.1. Synthesis of n-alkyl methacylate

The methacrylic acid mono-esters were prepared by reacting 1 mole of methacrylic acid with 1.1 mole of a series of n-alkyl alcohols which having increasing number of carbon atoms dodecyl alcohol, hexadecyl alcohol, two linear saturated long chain alcohol blends NAFOL 20+A (C_{av}=20) and NAFOL 1822 B(C_{av}=22) using p-toluene sulphonic acid as catalyst, toluene as a solvent (100ml) and hydroquinone to avoid polymerization. The reaction mixture was conducted for 24 hours at the reflux temperature. Water was separated azeotropically using Dean-Stark apparatus. The excess of the residual alcohol was removed through distillation under vacuum; then the reaction mixture was extracted with n-hexane, washed several times with water to remove unreacted methacylic acid and the catalyst, and then dried under vacuum at 40C.

2.3.2. Synthesis of terpolymers

The above synthesized alky methacrylate, vinyl acetate and methacrylic acid dissolved in toluene in a 1:1:1 mol ratio were taken in a four-necked flask. In the beginning, the contents were subjected to nitrogen flushing for twenty minutes, then gradually heated to 95 °C. When the temperature of the reaction reached 95°C, benzoyl peroxide dissolved in toluene as an initiator was added drop by drop. The whole content was refluxed for 8 h. Finally, the thick slurry was distilled under reduced pressure, followed by precipitation in excess ethanol and vacuum dried for 24 h [20]. The prepared additives are named as MVM-12, M VM-16, MVM-20, and MVM-22, respectively.

2.4. Characterization of the prepared terpolymers

Infrared spectra for esters n-alkyl methacrylate and their terpolymers with vinyl acetate and metacrylic acid were recorded on FTIR spectrophotometer (Genesis Series) using the traditional transmission technique for KBr pellets.

Molecular weights and polydispersity of terpolymers were determined by using gel permeation chromatographic analysis (GPC) with a refractive index detector using column styragel HR THF 7.8X300 mm, equipped with a water 515 HPLC pump. THF was used as an eluent at a flow rate of 1ml/min. Aliquots (1ml) of each sample were diluted with an appropriate amount of THF and were shaken vigorously, then passed through a filter and injected into the GPC for analysis.

2.5. Evaluation tests

2.5.1. Pour point measurements

Pour points were measured by following the ASTM D97 method. An appropriate quantity of additive (250–2000 ppm) in 1 mL toluene was added to 50 ml fuel oil in a cylindrical test jar and the mixture was first heated to 45°C. The test jar was then placed in a digital pour point cooling bath, and the sample was cooled at a specified rate and examined at intervals of 3°C for flow characteristics. The lowest temperature at which the movement of the specimen is observed is recorded as the pour point. The results are presented as pour point reduction in relation to the pour point of the fuel oil. The pour point reduction was calculated from the following equation: pour point reduction: $\Delta pp = pp_{pure} - pp_{add}$;
where PP_{pure} is the pour point of the pure fuel oil, and PP_{add} is the pour point of the fuel oil containing the additive.

2.5.2. X-Ray diffraction spectroscopy

The structure of the wax isolates from fuel oil and wax + 1500 ppm (MVM-22), and wax + 1500 ppm (MVM-12) were characterized using X-ray powder diffract meter, PANalytical X'Pert PRO MPD (Netherland). Cu Kα radiation with wave length= 1.5418Å was used at a rating of 40 kV, 40 mA. The diffraction patterns were recorded at room temperature in the angular range of 4-70º (2θ) with step size 0.02º (2θ) and scan step time 0.4 (s). The crystalline phases were identified using the ICDD-PDF database.

2.5.3. Microscopic Studies

An Olympus polarizing microscope model BHSP fitted with an automatic camera with a 35mm format was used to study the wax crystals of untreated and additive treated fuel oil at a temperature of -5°C below the pour point. The temperature of the tested lube oil sample was controlled on the microscope slide by an attached cooling thermostat. The adopted magnification was 100X.

3. Results and discussion

3.1. Chemical structure and characterization of the prepared terpolymers

By analyzing the most important signals in the FTIR spectra, it was confirmed that the four terpolymers share the same profile. According, the spectrum of compound acrylic acid which

illustrates the O-H stretching band of the carboxylic group which appeared as a small broad band at 3443 cm^{-1}. It can be clearly seen the characteristic CH_3 and CH_2 of the alkyl group adsorption peaks at 2925 and 2854 cm^{-1}, the characteristic C = O stretching peaks of methacrylate at 1727 cm^{-1}, and the characteristic, and we can see the intensity of CH_3 and CH_2 bands increases with the increase of the length of alkyl groups [21]. The characteristic C =C is stretching vibration peak at 1639 cm^{-1} almost vanishes completely. This indicates that there exist alkyl chain moiety, methacrylate moiety, and vinyl acetate moiety in the prepared terpolymer.

The molecular weights and polydispersity index of the four terpolymers were determined using a gel permeation chromatograph the results are given in Table 3.

Table 3. Characterization of the synthesized terpolymer additives alkyl methacrylate-vinyl acetate-methacrylic acid

Additive designation	Composition	M_w (g/mol)	Poly dispersity index
MVM-12	Terpolymer (dodecyl methacrylate-vinyl acetate – methacrylic acid)	11350	1.70
MVM-16	Terpolymer (hexadecyl methacrylate- vinyl acetate – methacrylic acid)	15660	2.03
MVM-20	Terpolymer (NAFOL 20+A methacrylate-vinyl acetate - methacrylic acid)	20351	2.42
MVM-22	Terpolymer (NAFOL 1822 B methacrylate- vinyl acetate – methacrylic acid)	22980	3.09

3.2. Pour point

The pour point of the fuel oil sample is 15°C. The reduced extent of the four terpolymers with different n-alkyl chain lengths MVM-12, MVM-16, MVM-20 and MVM-22 at various concentrations to pour point is shown in Table 4 and Figure 1. It can be seen from Figure 1, the n-alkyl chain length and concentration of PPDs have very important effects on the reduction extent of pour point.

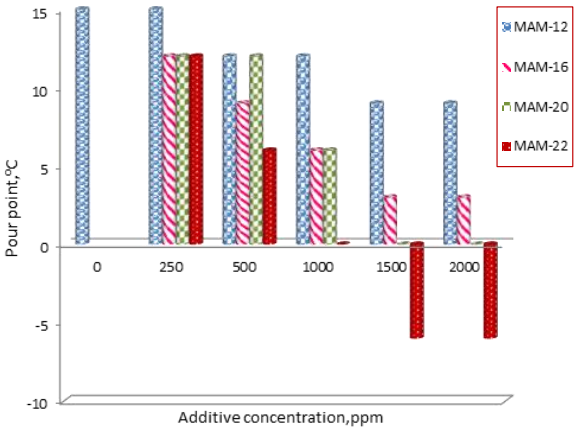

Figure 1. Relation between additive concentration and pour point depressant for fuel oil

The influence of n-alkyl chain length of terpolymers is closely related to the content of the corresponding n-alkane in the fuel oil, especially for their influence on the PP. The effects of the PPDs on reducing PP sometimes are in consistent, because PP is closely related to the formation of the three-dimensional network. MVM-22 exhibits the best considerable reduction on PP. At a concentration of 1500ppm, MVM-22 reduces the PP by -6°C and (reduces the PP by 21°C) and has a better effect on reducing PP with MVM-20 (reduces the PP by 15°C). In the pour point tests that were conducted with various samples methacrylate terpolymers, we note that for a given size of a pendant hydrocarbon group, an increase in the proportion of these groups increases the performance of the additive. Also, for a given terpolymers composition, increasing the size of the alkyl group improves the performance of the additive. The effect of the four terpolymer additives MVM-12, MVM-16, MVM-20 and MVM-22 on pour point for sample fuel oil are shown in Table 4. With increasing the concentration of the additives an increase in their activity was observed and as a result, a great depression of pour point was achieved. This means that at these concentration ranges the additives may co-crystallize with the paraffins and modify their crystals, at higher concentrations of additives, the side way growth becomes more difficult for the wax crystals (4).

Table 4. The effect of additives on the pour point of fuel oil

Additives designation	n-alkyl side chain	Additive concen-tration, ppm	PP, °C	ΔPP, °C
MAM12	12	0	15	0
		250	15	0
		500	12	3
		1000	12	3
		1500	9	6
		2000	6	6
MAM16	16	0	15	0
		250	12	3
		500	9	6
		1000	6	9
		1500	3	12
		2000	3	12
MAM20	20	0	15	0
		250	12	3
		500	12	3
		1000	6	9
		1500	0	15
		2000	0	15
MAM22	22	0	15	0
		250	12	3
		500	6	9
		1000	0	15
		1500	-6	21
		2000	-6	21

PP = pour point ΔPP = pour point depression

3.3. X-Ray diffraction measurements

X-Ray diffraction investigation of wax in the absence and presence of prepared additives (1500 ppm). The particle size of wax with in the presence of 1500ppm MVM-22 and wax with 1500ppm from MVM-12 were determined by using the Scherer equation [22].

$d = \frac{B\lambda}{\beta cos\theta}$, where d is the mean particle diameter; B is Scherer constant (0.89); λ is wave length of the x- ray beam = 1.5405Å; β is full -width half maximum FWHM of diffraction lines, and θ is the diffraction angle.

The computed values of particle size Table 5 showed increasing the order of wax with 1500 ppm of MVM-22 = 4.47 < wax with 1500 ppm of MVM-12= 5.88 < Wax = 9.41.

Table 5. X-Ray Diffraction results of the wax and wax with additives

Sample	Pos, [2θ]	FWMH(o)	d-spacing, [Å]	Rel. intensity, [%]
Wax	21.4033	0.2952	4.17095	100.00
	22.2754	0.1574	3.75442	31.60
Wax+MVM22	21.4305	0.3129	4.1522	100.00
	23.7275	0.3346	375044	31.45
Wax+MVM12	21.2772	0.2952	4.17596	100.00
	19.1588	0.2362	4.63264	31.6

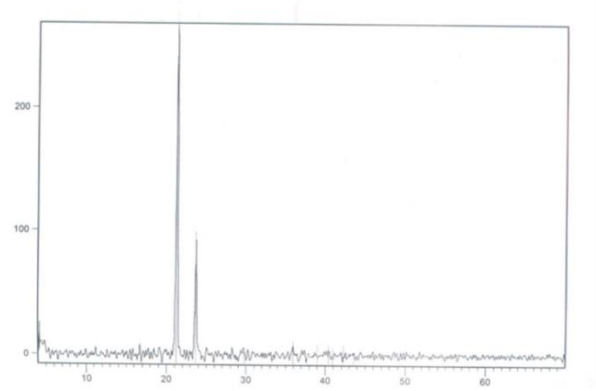

Figure 2. XRD spectra for wax in presence of 1500ppm from MVM-22

The PPD additives are considered to be well in the primitive molecular orientating and nucleating process. MVM-22 is considered more efficient than MVM-12. Figure 2 represents the XRD spectrogram for MVM-22 additives. The PPD molecules will get into the lattice part of wax crystal cells causing a change in the surface properties of the wax crystals. It will also bring the n-alkane molecules to deposit on the surface of the wax crystals. Adsorption can also decrease the plane density, but the changes of the surface properties of the wax crystal are different from those with co- crystallization.

3.4. Mechanism studies

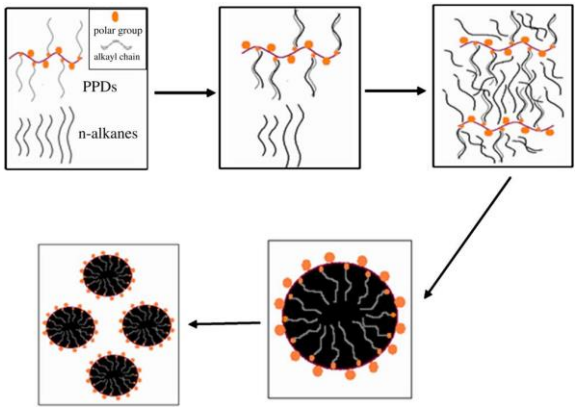

Figure 3. Schematic drawing of operating mechanism of terpolymers in fuel oil

The probable mechanism is shown in Figure 3 At wax appearance temperature, the alkyl chain of the PPDs co-crystallized with the corresponding n-alkanes in the fuel and became the nuclei of wax growth. With the temperature decrease, other n-alkanes in the fuel oil gradually precipitated out in the nuclei and the PPD molecules in a closer position combined with each other through n-alkanes. Thus wax crystals gradually grow. The polar groups of the PPD molecules play a very important impact on the morphology of wax crystals. Due to the strong polarity of the polar group on the methacrylic acid, wax crystals are easy to form sphere or ellipsoid, which has a smaller specific surface. The system has low surface energy and is more stable. As the polar groups distributed on the surface of wax crystals, wax crystals are difficult to bond together to form a three-dimensional network. But when the size distribution of wax crystals is very uneven, the smaller particles tend to get together with the bigger ones. The system is more stable.

3.5. The effect of terpolymer additives on wax crystal modification

The photomicrography of waxy fuel oil without treatment showed a column large wax crystal (PP=15^{o}C), Figure 4(a) to compare with The photomicrography of treatment the fuel oil with 1500 ppm from MVM-12, MVM-16, MVM-20 and MVM-22 terpolymer additives illustrated in Figure 4(b, c, d, e) respectively. From in section of this Figure 4, it can be observed that the wax crystals configurations have been modified to involve many fine dispersed crystals as shown in Figure 4(d, e). In this case, the wax modification in the order MVM-22 > MVM-20 > MVM-16, i.e. from these obtained data it can be concluded that there is a correlation between wax modification and measured flow parameters.

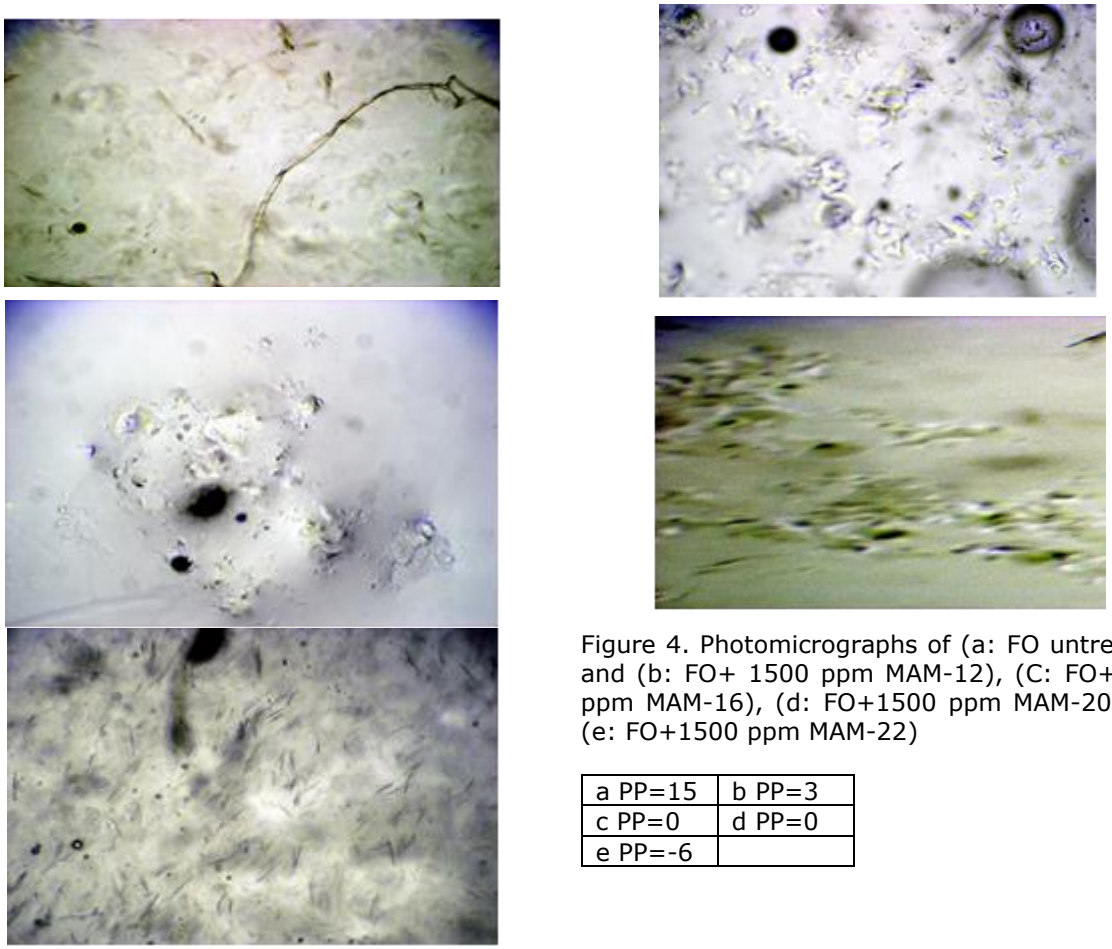

Figure 4. Photomicrographs of (a: FO untreated) and (b: FO+ 1500 ppm MAM-12), (C: FO+1500 ppm MAM-16), (d: FO+1500 ppm MAM-20) and (e: FO+1500 ppm MAM-22)

a PP=15	b PP=3
c PP=0	d PP=0
e PP=-6	

4. Conclusions

Four alkyl methacrylate – vinyl acetate- methacrylic acid terpolymer additives with different alkyl groups from C_{12} to C_{22} and different were prepared, purified and characterized by FTIR and GPC their effects on pour point properties of the fuel oil were investigated.

In the pour point tests that were conducted with various samples of n- alkyl methacrylate –vinyl acetate- methacrylic acid terpolymers, we note that for a given size of a pendant hydrocarbon group, an increase in the proportion of these groups increases the performance of the additive. Also, for a given terpolymer composition, increasing the size of the alkyl group improves the performance of the additive.

With increasing the concentration of the additives, an increase in their activity was obtained, and as a result, a great depression of pour point was achieved.

Study X-ray diffraction of wax and wax with different additives. Photomicrographic analysis showed that a clear effect of the terpolymer additives on the wax crystal modification which is in agreement with the above results

References

[1] Coutinho JAP, Mirante F, Ribeiro JC, Sansot JM and Daridon JL. Cloud and pour points in fuel blends. Fuel.,2002; 81(7): 963–967.

[2] Petifjean D, Pierre M, Hubert N, Bouroukba M and Dirand M. Influence of addition of pure components on the structural state of multi-n-alkane mixtures. Fuel., 2001; 80(14):2007–2011.

[3] Wu CJ, Zhang JL, Li W and Wu N. Molecular dynamics simulation guiding the improvement of EVA-type pour point depressant. Fuel., 2005; 84(16): 2039–2047.

[4] Al-Sabagh AH, El-Hamouly S H, Khidr TT, El-Ghazawy A and Higazy S A. Synthesis of phthalimide and succinimide copolymers and their evaluation as flow improvers for an Egyptian waxy crude oil. Egyptian J. Pet., 2013; 22:381–393.
[5] Khidr TT. Synthesis of some Additives and Study Effect of Gas Oil Composition on Flow Properties. J. Dispers. Sci. Technol., 2008;29:184–192.
[6] El-Gamal MI and Gad MAE. Low temperature rheological behavior of Umbarka waxy crude and influence of flow improver. Rev Inst Fr Pet.,1997;52:369–79
[7] van Engelen PG, Kaul LC, Vos B and Aranha PH. Study of flow improvers for transportation of Bombay high crude oil through submarine pipelines oil through submarine pipelines. J. Technol December1981:2539–2544.
[8] Uhde A, Kopp G. Pipeline problems resulting from the handling of waxy crudes. J Inst Petrol.,1971; 57:63–73.
[9] Al-Sabagh A M, Kafrawy A F, Khidr, TT, El-Ghazawy RA and Mishrif MR. Synthesis and Evaluation of Some Novel polymeric Surfactants Based on Aromatic Amines used as wax dispersion for Waxy Gas Oil. J. Dispers. Sci. Technol., 2007; 28:976–983.
[10] Ahmed SM, Khidr TT and Ismail DA. Journal of Dispersion Science and Technology., 2017;39 (8): 1160-1164.
[11] Al-Sabagh AM, Noor El-Din MR, Morsi RE, and Elsabee MZ. Styrene-Maleic Anhydride Copolymers Ester Evaluate as Flow Improvers for Waxy Crude Oil. J. Pet. Sci. Eng., 2009; 65:139–146.
[12] Han S, Song YPand Ren TH. Impact of alkyl methacrylate-maleic anhydride copolymers as pour point depressant on crystallization behavior of diesel fuel, Energy &Fuels.,2009; 23: 2576–2580.
[13] Khidr TT and El-Shamy AA. Synergistic Effect between ethoxylated surfactants and commercial additives the decrease pour point distillate fuel oil. J. Petroleum and Coal., 2018; 60(1) 99-105.
[14] Hafiz A A. and Khidr TT. Hexa-Triethanolamine Oleate Esters as Pour Point Deperessant for Waxy Crude Oils. J. Petrol. Sci. Eng., 2007;56:296–302.
[15] Jung KM, Chun BH, Park SH, Lee CH and Kim SH. Synthesis of methacrylate copolymers and their effects as pour point depressants for lubricant oil, Journal of Applied Polymer Science., 2011; 120:2579–2586.
[16] Chen WH, Zhang XD, Zhao ZC, and Yin CY. UNIQUAC model for wax solution with pour point depressant, Fluid Phase Equilibria., 2009;280: 9–15.
[17] Fang L, Zhang XD, Ma JH and Zhang BT. Investigation into a pour point depressant for Shengli crude oil, Industrial and Engineering Chemistry Research., 2012;51: 11605–11612.
[18] Khidr TT, Doheim MM and El-Shamy OAA. Effect of Ethoxylate on Pour Point Depressant of Fuel Oil. Energy Sources, Part A: Recovery, Utilization and Environmental Effects., 2015; 37:1697-1703.
[19] Marquat JR, Dellow GB, and Freitas ER. Determination of normal paraffins in petroleum heavy distillates by urea adduction and gas chromatography. Anal. Chem.,1968 40:1633–1637.
[20] Deshmukh S and Bharambe DP. Synthesis of polymeric pour point depressants for Nada crude oil (Gujarat, India) and its impact on oil rheology, Fuel Processing Technology., 2008; 89: 227–233.
[21] Al-Sabagh AM, Sabaa MW, Saad GR, Khidr TT and Khalil TM. Synthesis of polymeric additives based on itaconic acid and their evaluation as pour point depressants for lube oil in relation to rheological flow properties, Egyptian Journal of Petroleum., 2012; 21: 19–30.
[22] Cullity XBD. Element of X-Ray Diffraction 3rd ed., Addison – Weesley, 1967.

To whom correspondence should be addressed: Prof. Dr. T. T. Khidr, Egyptian Petroleum Research Institute, Nasr City Cairo, Egypt

Petroleum and Coal

Article **Open Access**

ANALYSIS OF RHEOLOGICAL PROPERTIES OF BITUMEN IN RELATION TO PHYSICAL PROPERTIES

Eva Remišová, Viera Zatkalíková*

Department of Highway Engineering. Faculty of Civil Engineering. The University of Žilina. Department of Materials Engineering. Faculty of Mechanical Engineering. The University of Žilina. Univerzitná 8215/ 1. 010 26 Žilina. Slovak Republic

Received December 18, 2018; Accepted February 3, 2019

Abstract

The bituminous binders used in road constructions are characterized by empirical tests as penetration, softening point and breaking point without characterizing the elastic-plastic response. This now appears to be inadequate mainly in the case of polymer modified bitumen. The objective of this work was to investigate the rheological properties of non-modified and polymer modified bitumen binders in dynamic shear rheometer by complex shear modulus and phase angle. The complex shear modulus values of non-modified bitumen are lower than the polymer modified bitumen at higher temperatures throughout the frequency range. The phase angle values of non-modified bitumen are significantly higher over the temperature and frequency test range. This is caused by lower elasticity compared to polymer-modified bitumen. Comparison of penetration results with complex shear modulus at 25°C showed that the bitumen is harder, the penetration is lower, and the complex shear modulus is higher.

***Keywords**: bitumen binder; rheology; complex modulus; phase angle; empirical properties.*

1. Introduction

Bitumen is one of the basic building materials, which is mainly used in road construction. Research works on bituminous binders, and asphalt mixtures were based on the assumption that bitumen can be characterized and sorted by empirical tests such as softening point, penetration or break point. These tests determine the stiffness and consistency of the binder without characterizing the elastic-plastic response. Especially in the case of polymers modified bitumen [1], these tests cannot adequately describe the complex rheological behavior of bitumen binders.

The development of the use of bitumen binders in road construction also leads to the development of new test methods that best describe their physical properties. One of the most important features is the behavior of bituminous binders at low temperatures, where there is a risk of breakage of the road with frost cracks. Further detection of high-temperature resistance where there is a risk of permanent deformations. This corresponds to the high-temperature sensitivity of the bituminous binder, which can be described by the viscosity dependence on the temperature as noted in [2-5]. Last but not least, it is important to evaluate the fatigue properties of the material or to characterize the resistance to loss of cohesion. The development of new testing methods according to [6], functional tests, have focused on characterizing the visco-elastic behavior of bitumen to better prediction of binders behaviour in asphalt mixtures, especially in critical conditions of failure - rutting, low temperature cracking and fatigue cracking in asphalt pavement roads. These methods include characterization in the dynamic shear rheometer DSR, the rotary viscometer or the bending beam rheometer BBR.

2. Bitumen rheology

At present, the most commonly used method of fundamental rheological testing of bitumen properties is dynamic mechanical analysis usually by means oscillatory-type testing. Rheological tests, compared to classical empirical tests, allow the properties of materials to be evaluated against loads, temperature intervals, frequencies and time at different loads. It allows to investigate the dynamic development of materials over time and to model the deformation properties of substances that are influenced by external forces. The basic methods of rheological measurement can be divided according to the load mode as rotation tests, oscillatory tests, creep tests, relaxation tests.

Bitumen binders behave in part as an elastic material (the deformation after loading is reversible, at a very low temperature) and partly as a viscous fluid (deformation due to load is irreversible, at high temperature). The dynamic mechanical analysis (DMA) of rheological properties allows characterization of the viscous and elastic behavior of bitumen binder at service temperatures. The sample of the binder is located between the two plates, the bottom plate is firm, and the upper one oscillates over the sample and creates shear stress. DMA is performed on a fresh binder, bitumen after short-term aging RTFOT and bitumen after long-term aging PAV using dynamic shear rheometer (DSR). The DSR test allows quantifying both elastic and viscous properties. This enables the bitumen binder to be characterized in the temperature range during the road pavement using in service.

At the University of Žilina, the rheological properties are measured on the Physica MCR 301 oscillatory rheometer with convection heating device CTD 450 by Frequency Sweep (FS) test method. FS test method uses a parallel plate system (PP), a set of two parallel plates, the bottom plate is stationary, upper is shear, performing the oscillatory motion. The distance between the plates (shear interval) *h* is exactly defined (Figure 1). The FS test is performed at a constant temperature, and for the viscoelastic materials, it is controlled by shear strain in the form of a sinusoidal oscillation function:

$$\gamma(t) = \gamma_A . sin\omega t \quad (1)$$

Testing the viscoelastic materials, the resulting stress and presetting the strain are not in phase, the strain delays behind the stress by a phase angle. If the oscillatory shear is sinusoidal, following [7-8] the shear stress τ is expressed:

$$\tau(t) = \tau_A . \sin(\omega t + \delta) = \tau_A . (cos\omega t + i . sin\omega t) \quad (2)$$

where τ_A is the stress amplitude (Pa), ω is the angular frequency (rad/s), $\omega = 2\pi f$, t is the time (s) and δ is the phase angle of the measured material response specified in degrees.

The complex shear modulus G^* expressing the resistance of the bitumen binder to deformation when subjected to repeated stress [7], is calculated using the equations:

$$G^* = \frac{\tau(t)}{\gamma(t)} \quad (3)$$

Parameters resulting from oscillation processes are written in the complex form:

$$|G^*| = \sqrt{(G')^2 + (G'')^2} \quad (4)$$

The storage modulus G' represents deformation energy stored by the sample. After unloading the stored energy acts reversible deformation process and the material behaves elastically. The loss modulus G'' is the amount of deformation energy consumed by the sample during the shear process. A part of this energy heats the sample, there are frictional forces between the molecules, frictional heat occurs, and the residue is released as heat to the environment. The sample with the high loss modulus exhibits irreversible deformation and indication of the relative size of the reversible and irreversible deformation and the expression of the displacement or the delay between the applied shear load and the resultant shear conversion. The complex shear modulus or resistance to deformation of bitumen increases with the addition of polymers [8]. The character of the cross-linked polymers (elastomer example used in polymer modified bitumen) is more or less flexible, soft or relatively rigid solid.

The values of parameter G^* and δ are dependent on temperature and load frequency of bitumen binder. At high temperatures, the binders behave as viscous liquids without the ability

to return to their original shape. In this case, the viscous component prevails, with the phase angle *δ* approaching 90°. At low temperatures, bitumen behaves as elastic materials that return from deformation completely. This property is represented by the elastic component, and the phase angle δ is approaching 0°.

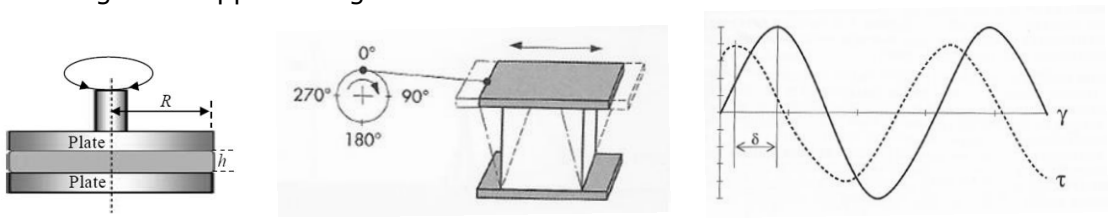

Figure 1. FS test [7]

A bitumen is considered as a liquid with high viscosity. Highly viscous materials usually have a higher temperature dependence compared to low-viscosity fluids. When heating non-crystalizing materials, a transition takes place from a rigid, solid consistency with $G' > G''$. In this case, the glass transition temperature is reached at the maximum of the G'' curve and the melting temperature occurs at the intersection of curves of G' and G'' [7]. The temperature susceptibility of binder decreases significantly with the polymer modification which makes binder more suitable to use in extreme climatic regions as mentioned in [9] and [10].

3. Experimental program

The scope of the research study was to evaluate the rheology properties of various bitumen binders in relation to physical properties, in terms of showing a better behavioral characterization as well as differences between unmodified and modified bitumen. Bitumen modified by the addition of macromolecular substances such as synthetic polymers, change their thermo-viscous and elasto-viscous properties. Polymers reduce the temperature sensitivity of bitumen (harder at high summer temperatures, reduce brittleness at low temperatures), extend the plasticity range to 80°C, increase elasticity, aging resistance, extend service life. The qualitative level is related to the type of modifier and its quantity in bitumen (usually 2 to 12 %), the type of bitumen and its chemical composition, the technological process especially the way of homogenization.

The experimental study covered paving grade bitumen of 50/70 and 35/50 gradation and polymer modified bitumen PMB 45/80-75 and PMB 25/55-60. The purpose of the research related to analyzing of rheological properties in relation to empirical properties was divided into two stages. First, the physical properties of bitumen binders, that are the most frequent indicators of their behavior in practice were determined by empirical tests including the needle penetration at 25°C according to EN 1426 and a softening point (the Ring and Ball Test) according to EN 1427. The measured results of the samples are shown in the following Table 1.

Table 1. Bitumen physical properties

	Penetration at 25°C [0.1mm]	Softening point [°C]	Dynamic viscosity at 135°C [mPa.s]	Dynamic viscosity at 165°C [mPa.s]
35/50;A11	44.8	56.2	855.0	203.75
50/70;A1	64.1	49.8	470.44	118.22
50/70;A4	61.0	48.0	516.31	126.3
50/70;A7	54.3	51.0	500.08	128.31
PMB 45/80-75;M2	54.6	80.8	2236.0	553.75
PMB 45/80-75;M3	74.3	75.4	1572.5	383.75
PMB 45/80-75;M4	60.5	78.4	1825.0	417.5
PMB 25/55-60;M11	35.8	62.0	2725.0	585.0

Second, the rheological properties were determined by dynamic-mechanical analysis according to EN 14770. Using the dynamic shear rheometer (Figure 2), the values of the complex shear modulus and the phase angle were determined under the selected test conditions:
Mode of loading: controlled-strain, amplitude γ_A = 5%
Temperatures: range 25 to 80°C
Frequencies: range 0,1 to 10 Hz.

Bitumen binder sample is sandwiched between two circular parallel plates (PP system) with 25 mm diameter and distant from each other to a thickness of 1 mm. The lower plate is fixed while upper plate oscillates back and forth across the sample at a different frequency to create shearing action. This measuring method [7] enables simultaneous monitoring of rheological parameters *G′*, *G″* and η^* in the chosen interval of angular frequencies.

Figure 2. Dynamic shear rheometer Physica MCR301 (left), SW for the test and results (right)

4. Results and analysis

The method of "FS test" allows observing the rheological parameters (η^*, *G′, G″*) depending on the angular frequency ω at a constant temperature. If the intersection of the curves *G′, G″* can be observed, the molecular weight changes (length and branching of hydrocarbon chains) and degradation of the material can be assessed. The test data record at a certain temperature and for each angular frequency contains values of parameters storage modulus, loss modulus, complex viscosity, shear stress, shear rate, and torque.

The rheological data for the tested bitumen are presented as standard in the form of master curves of complex modulus *G** and phase angle δ at a reference temperature. Master curves represent the viscoelastic behavior of bitumen binder at a given temperature for a range of frequencies, bigger than that tested. It is based on the principle of the time-temperature superposition system. The experimental curves can be superimposed by shifting all curves to one selected as the base curve [7]. Temperature dependence of this shift is expressed by the function $log a_T(T)$. Temperature shift factor a_T can be expressed by any standard method. In this study the Williams-Landel-Ferry equation according to [11] and [12] was used:

$$log a_T = \frac{-C_1(T-T_{ref})}{C_2+(T-T_{ref})} \quad (5)$$

where *T* is temperature, T_{ref} is the reference temperature, C_1 and C_2 are taken as constants.

This method is found in [12] to be applicable to bitumens. The results of tested bitumen are shown in Figure 3 and 4.

Samples of the same grade bitumen exhibit similar values of the complex modulus as seen in both non-modified and modified bitumen binders. At all test temperatures in the observed range of angular frequencies, the highest values of the complex shear modulus were determined in the case of harder bitumen, namely samples PMB 25/55-60; M11 and 35/50; A11; and the lowest values 50/70 paving grade bitumen samples. At higher test temperatures (e.g., 70 and 80°C), the shear modulus values of 35/50 bitumen get closer to the values of PMB 45/80-75 bitumen samples.

At higher load frequencies and pavement service temperature, the shear modulus values of paving grade bitumen are higher than PMB 45/80-75 bitumen samples. From Figure 3 and

Figure 4 it can be noted that the change in bitumen stiffness with a change of loading frequency is more markedly in the case of paving grade bitumen compared to the modified bitumen. That is also confirmed by the values of the loss and storage modulus. The values of the loss modulus of non-modified bitumen are significantly higher than the storage modulus at all tested frequencies and temperatures. The polymer component in modified bitumen, mainly at higher temperatures, increases the storage modulus, acts the reversible deformation process and the material behaves elastic.

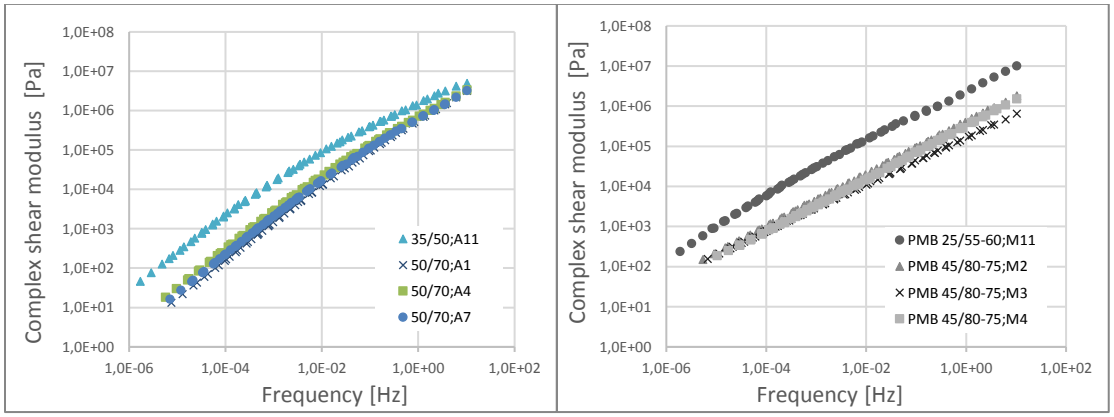

Figure 3. Complex modulus of non-modified (left) and modified (right) bitumen samples at 25°C reference temperature

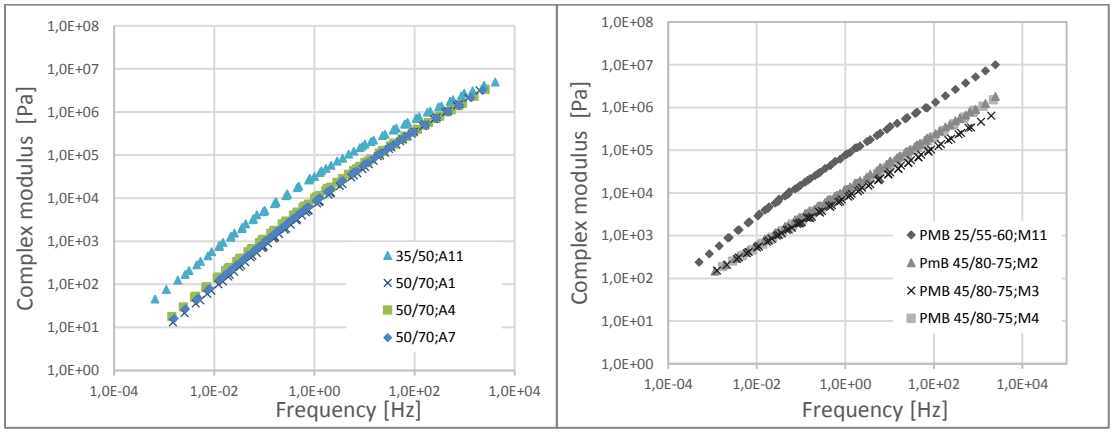

Figure 4. Complex modulus of non-modified (left) and modified (right) bitumen samples at 50°C reference temperature

Through the master curves, it has been shown that the same grade bitumen (paving grade and modified bitumen) have approximately the same values of the complex shear modulus across the frequency range. The master curves of the paving grade bitumen modulus are parallel. Lower penetration bitumen have higher values of the complex shear modulus; the master curve is shifted to higher values. Higher values of the complex modulus indicate that the binder has greater resistance to deformations at repeated loads.

The phase angle δ determines the time lag between the induced shear strain and the required shear stress in a controlled strain test. Phase angle δ can be described as an indicator of the relative magnitude of reversible and irreversible deformation. By comparing the values of phase angle (Figure 5), it can be stated that the phase angle of paving grade bitumen is in the range of 70° to 90°, while for modified bitumen it is from 50° to 70°. The phase angle of modified bitumen is significantly lower; the bitumen behaves elastic because of the polymer component in the bitumen.

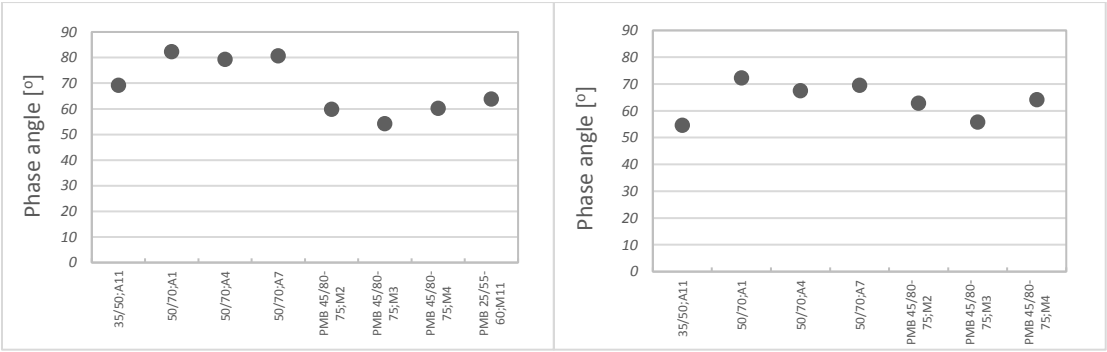

Figure 5. Values of phase angle from the DSR test at 50°C (left) and 25°C (right)

The results of rheological measurements of bitumen binders were compared with the basic properties determined by the empirical tests. The bitumen stiffness at 25°C represented by the penetration was compared with a stiffness modulus set at 25°C and a load frequency of 1.59 Hz, based upon an equivalent vehicle speed of 80 km.h^{-1} (Figure 6). Comparison of penetration results with complex shear modulus values at 25 °C showed that the harder bitumen is, the lower penetration and the higher complex shear modulus are. The relationship between the stiffness as penetration and complex modulus (DSR at 25 °C) was expressed by [13] as *logG*=2.923-1.9*logPen* and confirmed according to [14] dependence between $G^*\sin\delta$ at 25 °C and penetration.

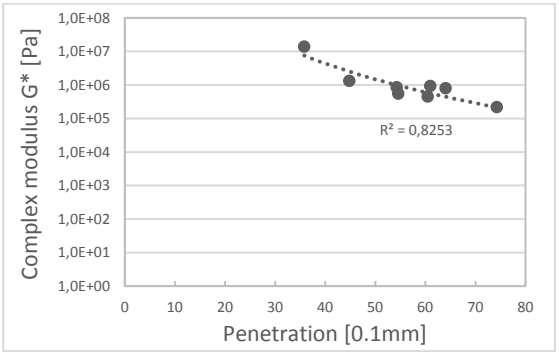

Figure 6. Relation between the penetration at 25°C and complex modulus at 25°C and frequency 1.59 Hz

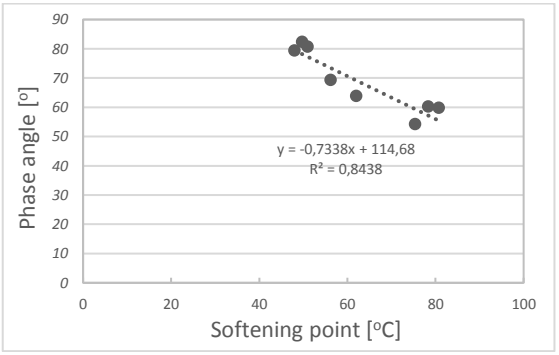

Figure 7. Relation between the softening point and phase angle at 50°C and frequency 1.59 Hz

With increasing temperatures (50°C or 60°C) the complex modulus values decrease. This is a representation of the loading of bitumen in the summer season. The modified bitumen PMB 25/55-60 shows the highest value at both temperatures (50°C or 60°C), next bitumen 35/50, and the other bitumen show significantly lower values. It is evident that the harder bitumen in terms of penetration has higher values of the complex shear modulus. The modulus is reduced by increasing penetration. Relatively high dependence has been shown in Figure 7 between the softening point and phase angle.

5. Conclusion

The main objective of this work was to investigate the rheological properties of bitumen in DSR. The obtained data are graphically presented as isochrones, isotherms, and master curves of the complex shear modulus and phase shift angle. Using the complex shear modulus G^* and the phase angle δ, it is possible to characterize the viscoelastic behavior of bitumen at different temperatures and load frequencies.

By comparing the values of tested paving grade (35/50, 50/70) and modified (PMB 45/80-75, PMB 25/55-60) bitumen, it was determined that the complex shear modulus values of

non-modified bitumen are lower than those of the polymer modified bitumen at higher temperatures throughout the frequency range. The phase angle values of non-modified bitumen are significantly higher over the temperature and frequency test range. This is caused by lower elasticity compared to polymer-modified bitumen.

Comparison of penetration results with complex shear modulus at 25 °C showed that the harder bitumen is, the lower penetration and the higher complex shear modulus are. This dependence applies to both paving grade and modified bitumen.

Acknowledgment

The research was supported partially by Scientific Grant Agency of Ministry of Education, Science and Sport of Slovak Republic and Slovak Academy of Science grant VEGA No. 1/0300/17 Research of performance related and rheological properties of bituminous binders.

References

[1] Bari J, Witczak MW. New Predictive Models for Viscosity and Complex Shear Modulus of Asphalt Binders: For Use with Mechanistic-Empirical Pavement Design Guide. Transportation Research Record: Journal of the Transportation Research Board 2007; No.2001(-1); p.9-19.

[2] Haider SW,Mrza MW, Thottempudi AK, Bari J, Baladi GY. Effect of test methods on viscosity temperature susceptibility characterization of asphalt binder for the Mechanistic-Empirical Pavement Design Guide, T&DI Congress ASCE 2011: 482-492.

[3] Holý M, Remišová E. Routine testing of bitumen binders, Civil and Environmental Engineering 2017; 13(2): 125-133.

[4] Remišová E, Zatkalíková V. Evaluation of bituminous binder in relation to resistance to permanent deformation, Procedia Engineering,2016; 153: 584-589.

[5] Hrušková L, Kiselová B, Daučík P. Criteria for evaluation of unmodified and modified bitumens, Pet Coal 2015; 57(6): 650-660.

[6] Yusoff NIMd, Shaw MT, Airey GD. Modelling the linear viscoelastic rheological properties of bituminous binders, Construction and Building Materials, 2011; 25(5): 2171-2189.

[7] Mezger TG. The Rheology Handbook. 3rd revised Ed., Hanover Germany: Vincentz Network, 2011.

[8] Kahovec J. Rheology of Polymer Systems, Wiley-VCH, Praha 2007; p.182.

[9] Javid MA. Effect of Polymer Modification on Rheological Properties of Asphalt, Journal of Civil Engineering Research 2016; 6(3): 55-60.

[10] Bahia HU, Hanson DI, Zeng M, Zhai H, Khatri MA, Anderson RM. Characterization of Modified Asphalt Binders in Superpave Mix Design, NCHRP Report 459, National Academy Press Washington, D.C. 2001.

[11] Malkin AY, Isayev A. Rheology: Concepts, Methods, and Applications, 2nd edition, ChemTec Publishing 2011.

[12] Yusoff NI, Chailleux E, Airey GD. A Comparative Study of the Influence of Shift Factor Equations on Master Curve Construction, International Journal of Pavement Research and Technology, 2011; 4(6): 324-336.

[13] Saal RNJ, Labout JWA. Rheological properties of Asphalts, Rheology (Ed. Eidrich), Vol II, Ch. 9, Academic Press Inc., 1958; 363-400.

[14] Lee MG, Chiu ChT, Kan YCh, Chen KCh. Comparison of Results of SHRP and Conventional Binder Tests on Paving Asphalts", International Journal of Applied Science and Engineering, 2004; 2(3): 245-256.

[15] Hoštáková M. Bitumen rheology properties (in Slovak), Diploma thesis, University of Žilina, 2018, p.80.

To whom correspondence should be addressed: Eva Remišová, Department of Highway Engineering. Faculty of Civil Engineering. The University of Žilina. Department of Materials Engineering. Faculty of Mechanical Engineering. The University of Žilina. Univerzitná 8215/1. 010 26 Žilina. Slovak Republic,
eva.remisova@fstav.uniza.sk

Petroleum and Coal

Article **Open Access**

STUDIES ON SULFUR RECOVERY PLANT PERFORMANCE USING ASPEN HYSYS SULSIM SIMULATIONS

Nagamalleswara Rao K[1], Juma Haydary[2]*

[1] Centre for Disaster Mitigation and Management, Vellore Institute of Technology, Vellore, Tamilnadu, India - 632014
[2] Institute of Chemical and Environmental Engineering, Slovak University of Technology, Bratislava Slovakia

Received December 8, 2018; Accepted February 8, 2019

Abstract

Sulfur recovery is a core process in both midstream and downstream oil and gas industries. Changing the feed composition, temperature, and pressure, degrading the equipment and catalysts, suboptimal operations due to inadequate control of temperature, pressure and air flow rate are some of the obstacles which reduce the performance of the sulfur recovery units. Low performance of sulfur recovery units creates the issues of safety and environmental problems. The objective of work is improving the performance of sulfur recovery unit in a gas plant. Aspen HYSYS V10 sulsim modified Claus three stage simulation model is used to mimic the behavior of a real sulfur recovery unit and it is considered as the base case. The performance of the base case is 93.89%. Base case process is optimized by controlling the air demand percent and the adjusting the sulfur dew point margin. These changes improved the performance to 98.60%. The performance of the plant is tested for a challenging feed composition case and this change reduced the performance to 96.39%. Arranging the selective oxidation converter improved the performance to 99.14%. Adding the tail gas section with the recycle stream and replacing the alumina catalyst with titania catalyst improved the performance to 99.92%. The simulation procedure developed in this work is useful to process engineers to smoothly handle the sulfur recovery unit in challenging situations.

***Keywords**: Alumina catalyst; Challenging feed; Sulfur recovery unit; Sulsim; Titania catalyst.*

1. Introduction

Natural gas contains H_2S, CO_2, SO_2, NH_3, mercaptans and other sulfur-containing compounds. Presence of these contaminants in natural gas degrades the quality of sales gas, corrodes the equipment, pipelines and causes acid rains [1]. Sulfur-containing natural gas is named as sour gas if it contains ammonia and it is called as acid gas if ammonia is not present. Acid gas must be treated: to meet safety considerations and environmental regulations, to reduce corrosion and protect equipment, to improve quality of liquid products and to improve heating value of sales gas. The most commonly used method for acid gas cleaning is done using regenerative amine solvents. In this process, acid gas is passed through the aqueous amine solution. H_2S and CO_2 are absorbed by amines and they are separated from the natural gas and the gas is sweetened [2]. The mixture of amines and contaminants can then be regenerated with heat, and the amines can be reused in the process.

In gas plants, after the acid gas cleaning, sulfur is removed. Based on H_2S content in acid gas, acid gas is classified as lean acid gas and rich acid gas. H_2S content in rich acid gas is greater than 50% and in lean acid gases, H_2S content is less than 50%. From the inception, Claus process is the most practiced process industrially for recovery of sulfur [3]. In Claus process, sulfur recovery from acid gases is a challenging task because of operational parameters and feed stock changes [4]. Process challenges can be handled by process modifications.

Process modification studies need the knowledge of thermodynamics and kinetics of chemical species involved in the process. Various studies on process modification and optimization are available to the sulfur recovery. Some of them are: A review for process modification technologies [5], Selectox process for lean acid gases processing [6], studies on effect of reaction parameters on the quality of captured sulfur [7], reaction with adsorption in a reaction furnace itself to overcome the Claus reaction equilibrium limitations [8], super Claus process using selective oxidation catalyst [9], designing new alumina catalysts with specific properties [10-11] and structures [12], lanthanum oxide based catalysts [13], ammonia pyrolysis and oxidation technique [14], benzene destruction technique [15], new tubular Claus catalytic reactor heat exchanger unit filled with a heat transfer enhancement medium [16], Claus recycle with double combustion process [17], reaction kinetic studies to reduce CS_2 formation [18], BTX oxidation by SO_2 in a BTX destruction unit placed between Claus furnace and catalytic units [19], toluene destruction using oxygen enriched air [20], maintaining suitable operating conditions in the reaction furnace for the presence of toluene and carbon dioxide [21], feasibility studies for lean acid gas feed containing mercaptans [22], coupled modification of GTU and SRU processes [23], thermal insulation to avoid thermal damage of Claus reaction chamber [24], reducing number of catalytic stages by following guidelines for the design of thermal section [25], introducing high temperature air combustion technology [26].

In the Claus process maximum possible sulfur is recovered from the thermal and catalytic sections. For a two-stage Claus process the maximum sulfur recovery is 95% and for a three-stage Claus process sulfur recovery is 98% [4]. These recovery efficiencies are not sufficient to meet the stringent environmental regulations. The new regulations demands, 100% recovery of sulfur from acid gases. To meet the new environmental standards tail gas treatment units are attached to the sulfur recovery units. In tail gas treatment the remaining sulfur is recovered. Various technologies available for tail gas cleaning in literature are Beavon sulfur removal process [27], in which the tail gas is treated in two-steps. Sulfur contaminants are first catalytically hydrolysed and/or hydrogenated to hydrogen sulfide and the hydrogen sulfide is then converted to elemental sulfur and recovered, The Shell Claus Off-gas Treating (SCOT) Process [28], use of Cu- and Ag-exchanged Y zeolites as selective adsorbents for hydrogen sulfide [29], temperature swing adsorption systems for Claus tail gas clean up units [30], use of a re-generable solid sorbent [31].

Performance of the Claus units depends on thermodynamics and kinetic factors of the process [32]. Using thermodynamics and kinetic data models for the Claus process can be developped [25, 33-35]. These models are useful for the simulation of Claus process and its unit operations [36], Genetic algorithms [37], model-based optimization techniques [38], modeling and multi-optimization of thermal section [39] are some the techniques used for the improved performance of sulfur recovery units. The advantage of the simulations is one can predict the response of the process for challenging conditions and for operational changes [40-42].

The above studies motivated the present simulation work to improve the performance of the sulfur recovery plant with tail gas treating section. Results of this work are useful for process modification studies to recover the desired quantity of sulfur from acid gases without changing the process equipment.

2. Process description

Acid gas feed to the modified Claus three- stage process contains H_2S, CO_2, CH_4, C_2H_6, C_3H_8. Feed gas composition is given in Table 1. Acid gas is processed for sulfur recovery using the Aspen HYSYS Sulsim Claus three-stage process with tail gas treatment section and incinerator.

Table 1. Feed gas composition of sour gas

Component	Mole fractions	Component	Mole fractions
CO_2	0.242	C_2H_6	0.002
H_2S	0.75	C_3H_8	0.001
CH_4	0.005		

In general the Claus plant contains two sections. Section one is the thermal section by containing the main burner, reaction furnace, and waste heat boiler. Section two is the catalytic section by containing two or three catalytic converters in series. Catalytic converter contains a catalytic reactor with a catalyst layer and a condenser. In between catalytic reactors, re-heaters are present to provide the necessary heat for the catalytic reactions. Schematic diagram for Claus three-stage process is shown in Figure 1. At the entrance of the thermal section main burner is placed. The role of the main burner is to burn the impurities (i.e. hydrocarbons, ammonia and mercaptans) present in the acid gas stream from the acid gas cleaning unit. For this reaction, external air stream is supplied. Adjacent to the main burner, reaction furnace is present. In reaction furnace, 1/3rd of the H_2S is converted to elemental sulfur. Corresponding reactions are the reaction (1) and reaction (2).

$$3H_2S + \frac{3}{2}O_2 \rightarrow SO_2 + 2H_2S + H_2O \quad (1)$$

$$2H_2S + SO_2 \leftrightarrow 3S + 2H_2O + heat \quad (2)$$

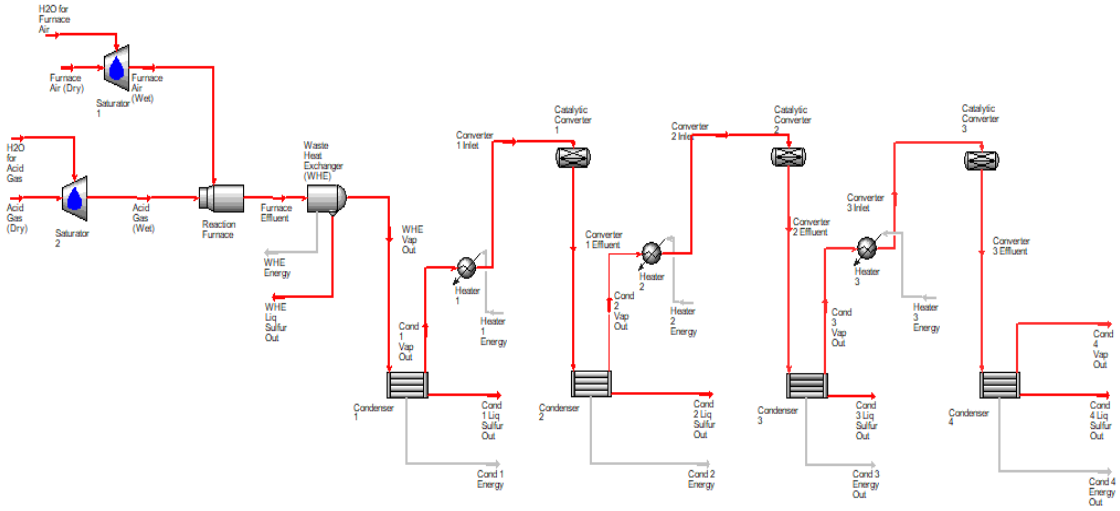

Figure 1. Process flow diagram for the base case three stage Claus process

Remaining 2/3rd of the H_2S is converted into elemental sulfur in catalytic converters followed by the thermal section. The overall Claus reaction is given by reaction (3).

$$2H_2S + SO_2 \rightarrow \frac{3}{n}S_n + 2H_2O \quad (3)$$

Due to the combustion reaction at the reaction furnace, some impurities are also formed. Impurities formed are COS and CS_2. These impurities lower the sulfur recovery efficiency and these can be handled at catalytic converters only by hydrolysis reactions. Hydrolysis reactions are the reaction (4) and reaction (5).

$$COS + H_2O \leftrightarrow CO_2 + H_2S \quad (4)$$

$$CS_2 + 2H_2O \leftrightarrow CO_2 + 2H_2S \quad (5)$$

Reaction (4) and (5) takes place at high temperatures and in the presence of the catalyst. In thermal furnace reactions (1) and reaction (2) takes place in about 2 seconds at 1000^0C - 1400^0C. The elemental sulfur formed in the reaction furnace is cooled in the waste heat boiler and it is separated by condensation. By absorbing the heat from the reaction furnace gases, steam is generated from the waste heat boiler. The remaining unconverted gases are sent to the re-heater. Re-heater acts as a link between the thermal section and catalytic section. Re-heater outlet stream is connected to the catalytic converter. In catalytic converters, the reaction to form sulfur is continued. This step improves the further sulfur recovery. Catalytic reactors operate at temperatures above the sulfur dew point. From the process gases, at each

catalytic converter, elemental sulfur is condensed and collected in the condensers. In general alumina catalyst and titania catalysts are used as catalysts in catalytic converters. The gaseous effluent from the last catalytic stage condenser is low in sulfur-containing compounds but may require some additional treating to meet flare gas specifications. This gas is sent to tail gas treating processing, which can contain unit operations such as hydrogenation bed, reducing gas generator, quench tower, amine absorber, incinerator, and flare. The amount of sulfur recovery needed depends on the tail gas treating system installed. The recycle gas stream will be recycled back to the reactor furnace. The process gas containing the low sulfur compounds is directed to the incinerator and flare.

3. Process simulation

Acid gas stream from the amine regenerator unit in the acid gas cleaning unit is connected to the sulfur recovery unit as feed gas stream. The tail gas stream is connected to the outlet of the Sulsim sub-flow sheet. After the convergence of the Aspen HYSYS V10 Sulsim, sub-flow sheet cumulative sulfur recovery of the unit is checked. If the initial overall performance is not satisfactory a couple of modifications are performed to improve the performance of the sulfur recovery unit.

In the simulation, the main parameters considered are reaction furnace empirical model, H_2S to SO_2 ratio, the temperature of catalytic converters, incinerator checker wall kinetic parameters. Base case simulation uses the straight through acid gas empirical model. Selection of the empirical model depends on the percentage of the H_2S present in the feed gas. Here, straight through amine acid gas empirical model is selected and this option is suitable for feed containing the more than 50% of the H_2S. For further improvement in sulfur recovery, it can be tested with other empirical models available in Aspen HYSYS. Optimum H_2S to SO_2 ratio can be maintained by arranging air demand analyzer (ADA) and adjust operations as shown in Figure 2. ADA is connected between the last condenser and the reaction furnace. Air demand analyzer (ADA) is useful in adjusting the air to fuel ratio and Adjust block is useful to adjust the converter temperature. To meet the tail gas specifications air demand analyzer controls air flow to the reaction furnace. To do this, in ADA internal options, tail gas is selected as the sample stream, target variable is selected as air demand percent and air demand target value is set as zero percent (it corresponds to the ratio of H_2S and SO_2 as 2). For convergence, it needs more iteration. After re-converging, performance will be improved.

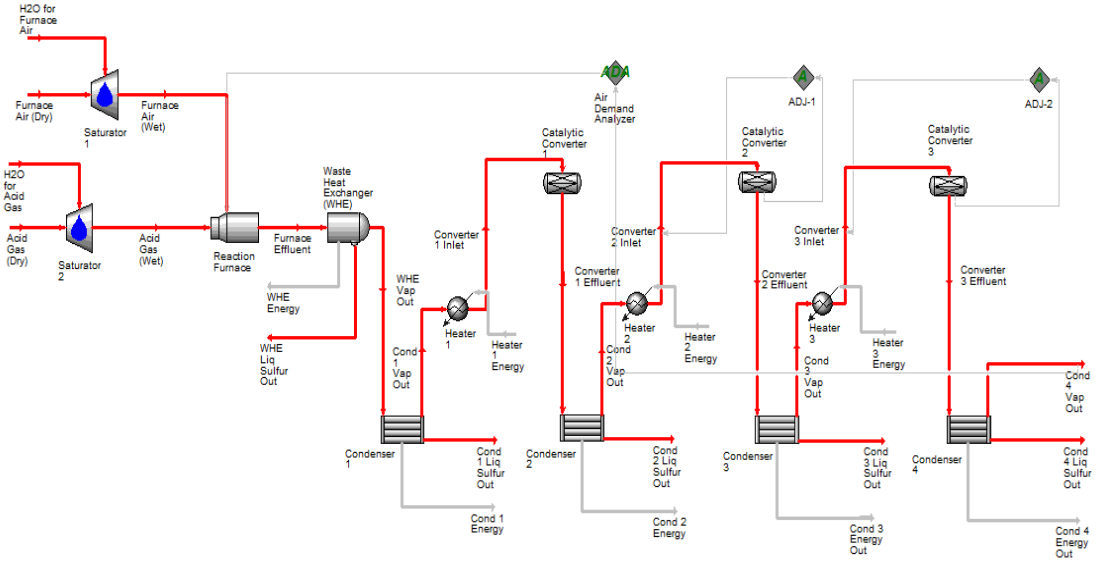

Figure 2. Sulfur recovery unit with air demand analyser and adjust operations

Adjust operations are arranged at catalytic converter 2 and catalytic converter 3, these can be seen in Figure 2. Adjust operations are added to decrease the outlet sulfur dew point margin. Initially, it is 24.52°C for the second catalytic converter. For catalytic converter operations, these temperatures should be as low as possible without depositing sulfur on the catalyst. A good target is 10°C. This value can be adjusted using the adjust unit operation. Second catalytic converter target variable is outlet sulfur dew point margin. 10°C is specified as the specified target value of outlet sulfur dew point margin. In parameters specifications, minimum temperature specified as 135°C and the maximum temperature specified as 500°C. Process re-converges and improvements in the performance of sulfur recovery are observed. For further recovery of sulfur selective oxidation section is added.

Selective oxidation converter is connected to the vapor outlet stream from the last condenser attached to the catalytic converter 3. It can be seen in Figure 3.

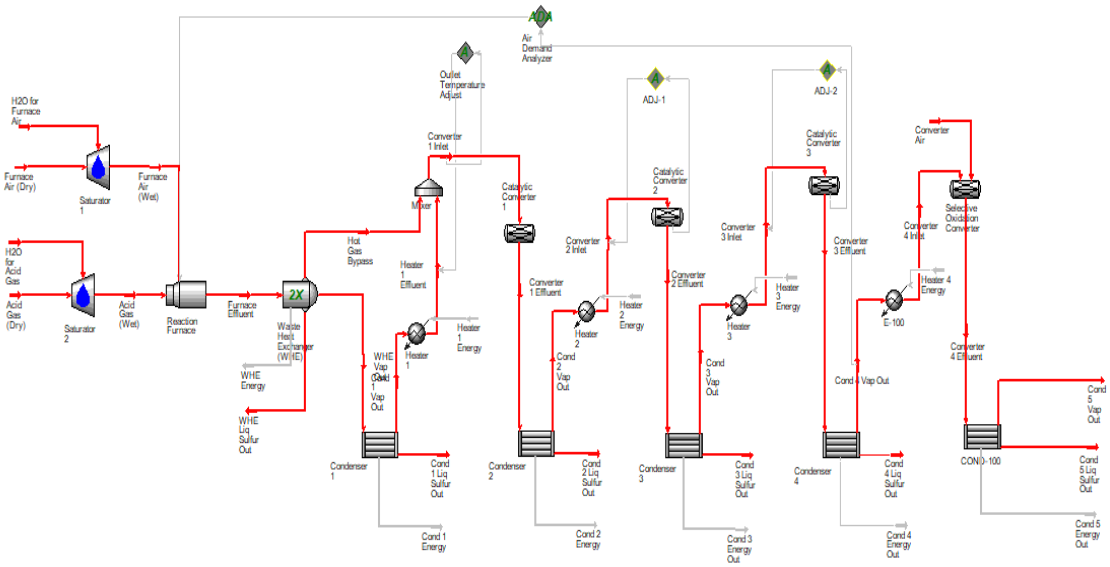

Figure 3. Sulfur recovery unit with selective oxidation converter

Feed composition fluctuations are common in sulfur recovery units. To handle challenging situations in this study, simulations are performed for low percentage composition of H_2S in the feed stream. The same optimization procedure is followed as in the above sections to handle the challenging situation to maintain the same sulfur compounds compositions in tail gas without changing the process equipment.

In Figure 4, the tail gas section is attached. It contains the reducing gas generator, hydrogenation bed, quench tower and simple amine absorber. In reducing gas generator mention burn stoichiometry as 85% and Steam to fuel ratio 85 mass%. Similarly RGG Air, RGG Fuel Gas, and RGG Water streams also defined. Adjust block is added (ADJ-3) to adjust RGG Fuel Gas Flow to achieve an RGG Effluent temperature of 285°C. The next the data for hydrogenation bed is given. For quench tower set the pressure drop 3 kPa and the outlet temperature to 35°C. Data for simple amine absorber also provided.

Finally, sulfur recovery efficiency is tested by varying the alumina catalyst with titania catalyst and the improvements in performance are noted.

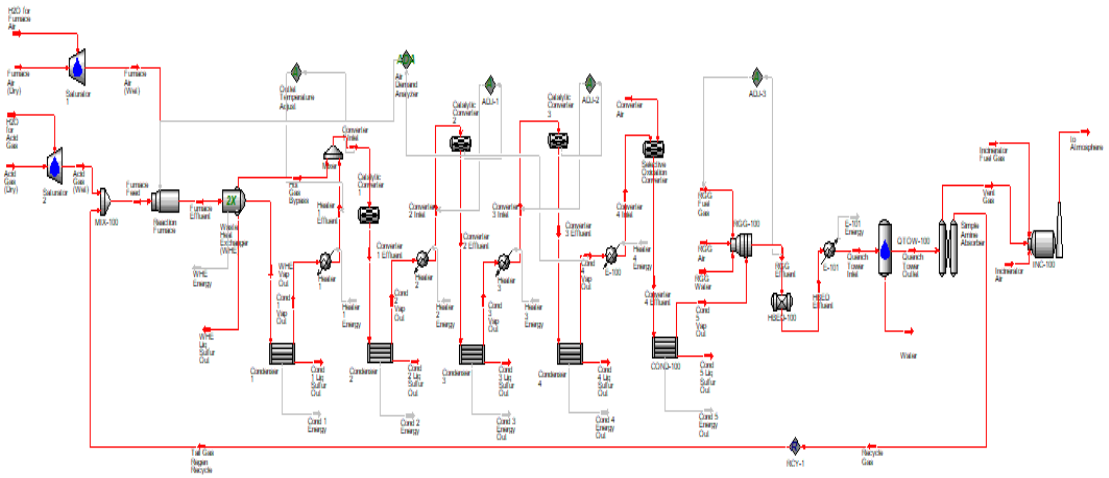

Figure 4. Sulfur recovery unit with tail gas treating section, incinerator and recycle stream

4. Results and discussion

Acid gas feed composition (mole fractions) to sulfur recovery unit is: CO_2 0.242, H_2S 0.75, CH_4 0.005, C_2H_6 0.002, C_3H_8 0.001, Simulations are conducted to improve the cumulative sulfur recovery of the three- stage Claus process. Main parameters concentrated for simulation are H_2S/SO_2 ratio, outlet sulfur dew point temperature, catalytic converter inlet stream temperatures, incinerator temperature. Since improvements in sulfur recovery are possible by improving the hydrolysis reaction (i.e. reactions (4) and (5)) to achieve this at first catalytic converter influence of temperature increase on sulfur recovery is tested while maintaining the second and third catalytic converters at low temperatures (operating the last two stages at low temperatures favours the Claus reaction). For further improvements of cumulative sulfur recovery or to improve the hydrolysis reaction performance Titania catalyst is selected which is available in catalytic converter unit operation.

In sulfur recovery plants (SRUs) sometimes processes are challenging due to changing feed slates. For changing feed conditions current process configurations does not meet the desired specifications. To meet the current process configurations process optimization conducted and the optimum process parameters calculated.

4.1. Effect of H_2S/CO_2 ratio

Performance of the SRU decreases due to incomplete oxidation, losing catalytic activity and lowering temperatures of the furnace. The base case process cumulative sulfur recovery efficiency obtained is 93.89% (Table 2).

Table 2. Sulfur recovery efficiency summary for base case process

Stage	Thermal reaction furnace	Catalytic converter 1	Catalytic converter 2	Catalytic converter 3
Conversion percent	68.25	47.02	53.85	24.28
Cumulative conversion percent	68.25	83.17	92.21	94.10
Sulfur recovery percent	99.73	98.76	97.88	89.90
Cumulative sulfur recovery percent	68.08	82.98	92.02	93.89
COS hydrolysis percent	---	97.37	74.38	60.56
CS_2 hydrolysis percent	---	93.93	43.98	28.80
Overall recovery efficiency percent	---	---	---	93.89

To increase the sulfur recovery around 98.5% operational changes are needed. To meet the flare specifications, it is also mandatory to maintain the concentration of sulfur-containing compounds in the tail gas less than 1 kmole/hr. These changes (i.e. improving the sulfur recovery percent) can be made with no equipment changes. Adjust block is added to adjust the converter temperature, Air demand analyzer is added to adjust air to fuel ratio. Air demand analyzer targeted the last condenser vapor outlet stream in the catalytic section. First catalytic temperature is at 340^0C to ensure CS_2 and COS destruction. Second and third catalytic converters are maintained at minimum sulfur dew point margin of at least 10^0C so that no liquid sulfur will not deposit on the catalyst surface. Deposition of liquid sulfur on the catalyst surface decreases the overall recovery percent of sulfur.

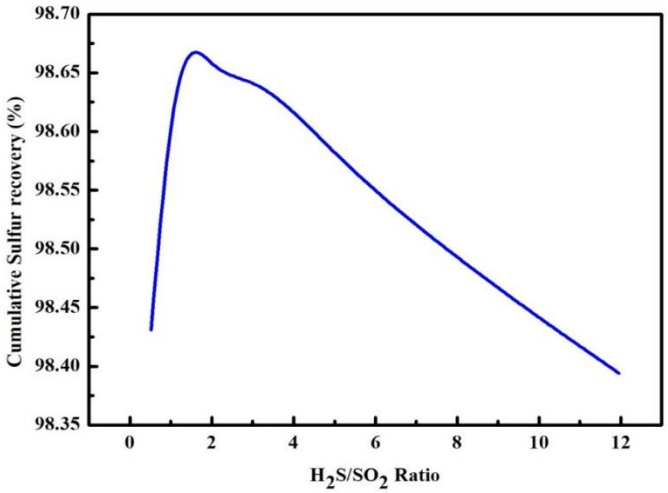

Figure 5. Variation of cumulative sulfur recovery percent with H_2S/SO_2

H_2S/SO_2 ratios (air demand %) and their effect on sulfur recovery are shown in Figure 5. Based on Claus reaction i.e. reaction (3) more closeness of the H_2S/SO_2 ratio to number 2 leads to better performance and more sulfur recovery efficiency for the catalytic section. At low zero percent air demand (i.e. the ratio between H_2S to CO_2 is 2:1) the cumulative percent recovery of sulfur is maximum and the value is from the 98.6%. (Table 3)

Table 3. Sulfur recovery unit performance summary for optimized process

Stage	Thermal reaction furnace	Catalytic converter 1	Catalytic converter 2	Catalytic converter 3
Conversion percent	68.56	48.61	80.79	62.73
Cumulative conversion percent	68.56	83.83	96.86	98.80
Sulfur recovery percent	99.75	98.84	98.58	90.61
Cumulative sulfur recovery percent	68.39	83.65	96.67	98.60
COS hydrolysis percent	N/A	97.19	36.05	12.31
CS_2 hydrolysis percent	N/A	94.33	9.974	2.213
Overall recovery efficiency percent	---	---	---	98.60

4.2. Effect of outlet sulfur dew point margin

To know the effect of outlet dew point temperature adjust block is added at the second catalytic converter. Outlet sulfur dew point temperature is varied by adjusting the target variable values and the corresponding variations in sulfur recovery are shown in Figure 6. It is observed that at lower sulfur dew point temperature margin, percent sulfur recovery is more. Very low temperatures are also not favorable for catalysts. The temperatures between 5°C and 10°C are identified as favorable dew point temperature margins.

4.3. Effect of temperature

At reaction furnace, because of side reactions, by-products like COS and CS_2 are formed. Presence of these compounds reduces the efficiency of sulfur recovery. To destruct these compounds increased temperatures at first catalytic converter are required. From Figure 7 it

is evident that the temperature increasing from 250°C to 340°C cumulative percent recovery of sulfur increased from 98.35 to 98.6%. This is because of additional decomposition of COS and CS_2 at first catalytic converter. At very high temperatures percent sulfur recovery is too low this may be due to decreasing activity of catalyst because of deposition of sulfur on the catalyst surface.

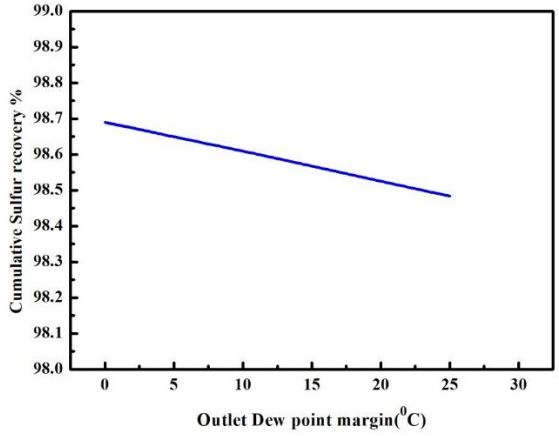

Figure 6. Variation of cumulative percent recovery of sulfur with outlet dew point temperature margin at catalytic converter two

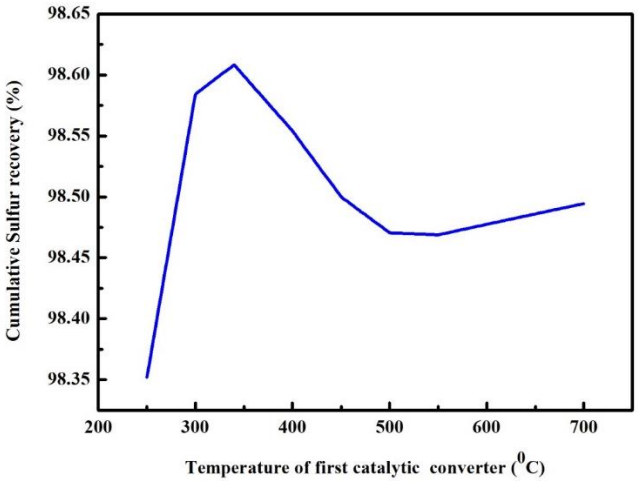

Figure 7. Variation of cumulative percent recovery of sulfur with varying temperature of first catalytic converter (for additional destruction of COS and CS_2)

4.4. Process for challenged feed

In the base case, the sulfur recovery percent obtained is 98.61% corresponding to a flow rate of about 4.2774 kmol/hr of sulfur-containing compounds in the tail gas. However, the refinery is looking to increase the amount of low-cost heavy sour crude in the crude slate, which contains a greater concentration of sulfur. The composition of the new feed in mole fraction is H_2S 0.8, CO_2 0.05 and it is given in Table 4. When the new feed simulated to the SRU in HYSYS, the feed change increased the amount of sulfur -containing compounds in tail gas to 43.377 kmole/hr, which is above the 4.2774 kmol/hr target. To meet the target specifications we need to investigate the options.

The first option is installing a bypass around the WHE at next turnaround. Single-pass option is changed to double pass for the WHE. By-pass split fraction is varied from 0 to 0.15. Zero bypass fraction means we are not bypassing any gas from the WHE to the first stage. Then we are not saving any operational expenses on heater 1 duty. Outlet temperature adjust target value is from 335°C to 355°C. To see the effect of both parameters i.e. bypass fraction and catalytic converter 1 temperature on cumulative sulfur recovery sensitivity analysis is done. With an increase in bypass fraction, the amount of sulfur in tail gas increased. It is shown in Figure 8.

Table 4. Feed Gas Composition of acid gas for challenging case

Component	Mole fractions	Component	Mole fractions
CO_2	0.05	C_2H_6	0.02
H_2S	0.80	C_3H_8	0.01
SO_2	0.05	n-C_4H_{10}	0.005
CH_4	0.06	i-C_5H_{12}	0.005

The increase is very small i.e in the order of about 0.02 kmol/hr for a bypass up to 15%. This can be reduced with the additional efficiency of the selective oxidation converter. If we completely bypass the preheater of the first catalytic converter saved reheater duty costs (up to 29,000 kJ/h) with a minimal impact on increasing sulfur in the tail gas. The second option

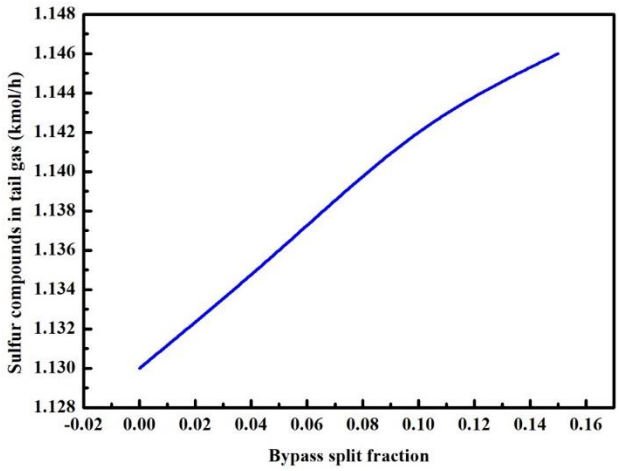

Figure 8. Effect of bypass split fraction on tail gas sulfur compounds

is adding an additional catalytic stage with a selective oxidation converter at next turnaround. This will help to improve the overall recovery efficiency. The optimal operating temperature at the first catalytic converter inlet is around 340°C for a bypass fraction of zero. This is due to higher destructions of COS and CS_2 in the first catalytic stage at higher temperatures.

To know the effect of the selective catalytic converter on cumulative sulfur recovery sensitivity analysis was done by varying the inlet temperature of the fourth selective catalytic converter. Temperature range is from 160°C to 340°C. The new recovery efficiency is 99.14% (Table 5). This corresponds to 0.5548 kmol/hr of sulfur-containing compounds in the tail gas, which should enable us to meet the flare specifications.

Table 5. Sulfur recovery unit performance for three stage Claus process with selective catalytic converter

Stage	Thermal reaction furnace	Catalytic converter 1	Catalytic converter 2	Catalytic converter 3	Selective catalytic oxidation converter
Conversion percent	71.32	34.66	81.12	63.12	59.64
Cumulative conversion percent	71.32	81.25	96.44	98.67	99.45
Sulfur recovery percent	70.76	99.20	98.33	88.88	71.12
Cumulative sulfur recovery percent	50.47	81.01	96.18	98.39	99.14
COS hydrolysis percent	---	96.48	33.51	11.34	----
CS_2 hydrolysis percent	----	90.65	8.66	1.96	----
Overall recovery efficiency percent	---	---	---	---	99.14

4.5. Tail gas treating

The tail gas section further reduces the sulfur content to meet the flare specifications. Recycle stream redirected from the tail gas regenerator to the SRU furnace inlet for further cleaning of the tail gas, this step decreases the overall sulfur recovery. An incinerator is added to investigate the value of installing a checker wall. Benefits of installing checker wall on eliminating breakthrough of $COS+CS_2+H_2S+SO_2$ to the flare is to be evaluated. Simulation goal is to maintain the target of < 0.8 kmol/hr of sulfur-containing compounds to the tail gas section, including the recycle, and to evaluate the impact of the incinerator upgrade will have on stack composition. Recycle stream arrangement effect can be observed in condenser 5 vapour outlet. In condenser 5 vapor outlet, sulfur compound flow increased from 0.45 kmol/hr to 0.58 kgmol/hr. This is due to additional sulfur is recycled to the furnace. It is still below the 0.8 kmol/hr target from the base case. Incinerator parameters kinetic value 4(a factor of incinerator geometry and it implies good mixing in the existing system), residence time 1.5 seconds, stack value 1 second. Corresponding COS + CS_2 + H_2S at Exit is 3.94 ppm total, which is fairly low compared to a typical flare spec of 50 ppm.

Effect of installing a checker wall (better mixing in the incinerator) is checked by changing its kinetic value from 4 to 8. Corresponding $COS+CS_2+H_2S$ concentration is 1.973 ppmmol, this value is exactly half the original value.

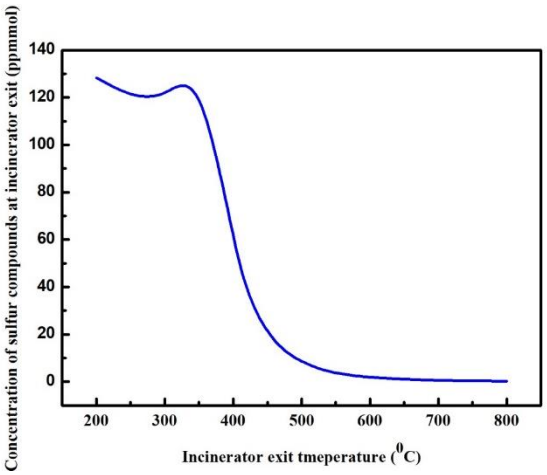

Figure 9. Variation of concentration of sulfur containing compounds (ppmmol) at incinerator exit with incinerator exit temperature

Effect of incinerator temperature on sulfur compounds at the exit of incinerator is shown in Figure 9. For increasing temperatures, sulfur compounds concentrations are decreasing at the exit of the incinerator. The optimum temperature observed is 410^{0}C and the corresponding concentration is 49 ppm mol. These results are useful whether or not to invest the additional capital to install a checker wall at the next turnaround.

4.6. COS and CS_2 hydrolysis percentage at each unit operation

When acid gas is burned in the reaction furnace, some undesirable reactants like COS and CS_2 are created due to the side reaction between CO_2, hydrocarbon and H_2S. These sulfur compounds reduce the percent sulfur recovery. Their concentrations should be minimized. COS and CS_2 can be reduced by hydrolysis reaction take place at catalytic converters especially at the first catalytic converter. Hydrolysis is the reaction between COS and H_2O or CS_2 and H_2O which is turning back that reactant to H_2S. H_2S is then can participate in Claus reaction which is a desired main reaction in the sulfur reactor. In Figure 10 CS_2 hydrolysis percentages at each unit operation are given. CS2 hydrolysis conversion at converter 1 is 92%, at converter 2 is 5.32% and at converter 3 is 1.24%. These results show that CS_2 hydrolysis conversion is more at converter 1. Similarly, COS hydrolysis conversion at each converter is given in Figure 11. It is observed that at converter 1 hydrolysis conversion is 97% and the conversion values decrease from converter 1 to converter 3. These observations are useful in taking the better process design decisions.

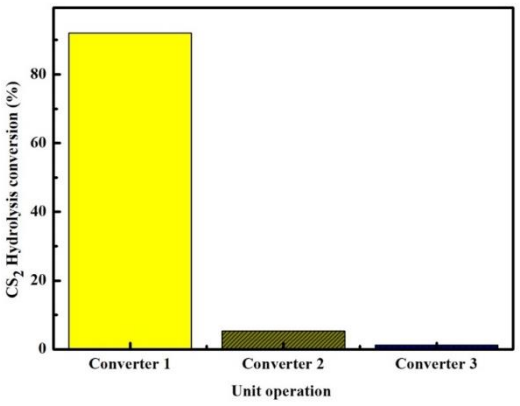

Figure 10. Variation of CS_2 hydrolysis conversion for catalytic converters

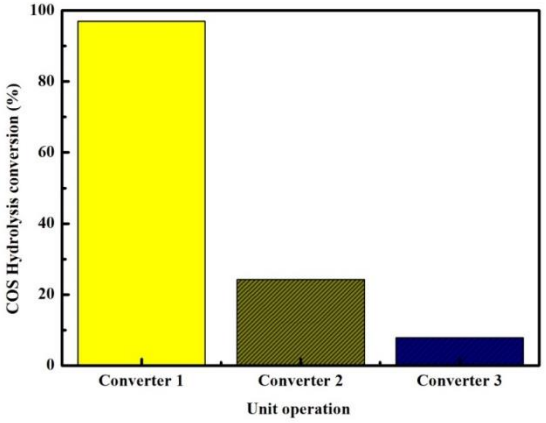

Figure 11. Variation of COS hydrolysis percentage with unit operations

4.7. Percent sulfur conversion and cumulative percent sulfur recovery at each unit operation

Optimizing the entire Claus process is possible by knowing the percent conversion and percent recovery of sulfur at each stage of the process. To know these effects variation of

percent sulfur conversion at each unit operation and variation of cumulative percent sulfur recovery at each unit operation are shown in Figure 12 and in Figure 13 respectively. From Figure 12 it is evident that percent conversion of sulfur is more at converter two (It is well matched with the statement that 1/3rd of the H_2S is converted into elemental sulfur at the reaction furnace and the remaining 2/3rd of H_2S is converted at the remaining stages of the process). In Figure 14 outlet concentrations of sulfur compounds at each unit operation is shown. From Figure 13 cumulative percent recovery of sulfur is increasing progressively. From Figure 14 it is known that the concentration of sulfur compounds are decreasing at the unit operations in the order of furnace to the incinerator.

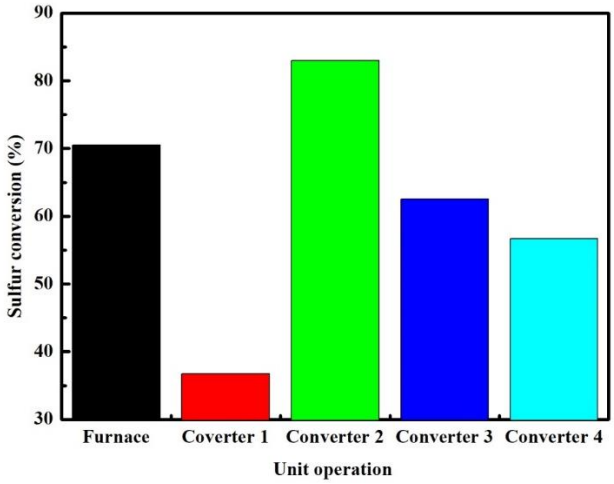

Figure 12. Stage wise sulfur conversion

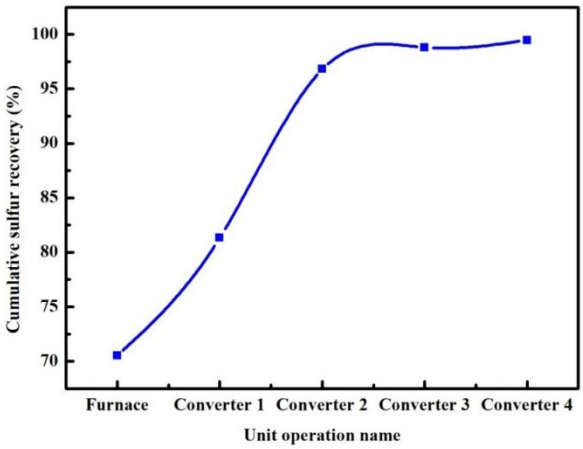

Figure 13. Cumulative percent recovery of sulfur for unit operations

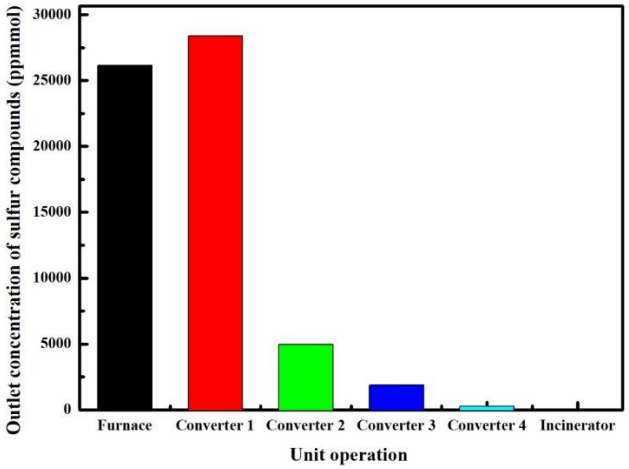

Figure 14. Variation of outlet concentrations of sulfur components (ppmmol) with unit operations

4.8. Catalyst selection

For alumina catalyst case the overall performance is 99.92% (Table 6). Sulfur recovery percentage for Titania catalyst is given 99.93%. By the selection of titania catalyst for the first stage catalytic converter hydrolysis reaction performance is improved. Catalyst change option improved the performance slightly. Space velocity and catalyst bed volumes are necessary for Titania catalyst. Space velocity is 1000 hr^{-1} and catalyst bed volume is 10.42 m^3. The reason for higher performances of Titania catalyst may be its high hydrolysis reaction while keeping Claus reaction.

Table 6. Sulfur recovery performance summary for sulfur recovery unit attached with tail gas section and incinerator

Stage	Thermal Reaction furnace	Catalytic converter 1	Catalytic converter 2	Catalytic converter 3	Selective catalytic oxidation converter
Conversion percent	70.50	36.71	82.96	62.53	56.69
Cumulative conversion percent	70.50	81.32	96.80	98.79	99.47
Sulfur recovery percent	99.44	96.14	96.98	77.52	45.74
Cumulative sulfur recovery percent	70.11	80.89	96.32	98.24	98.80
COS hydrolysis percent	---	97.04	24.19	7.836	---
CS_2 hydrolysis percent	---	92.04	5.33	1.243	----
Overall recovery efficiency percent	---	---	---	---	99.92

Acknowledgement

Authors are grateful to Vellore Institute of Technology (VIT University), India for providing the necessary facilities for the successful completion of this research work and Slovak University of Technology, Bratislava Slovakia, for supporting this work via Grant APVV-15-0148 provided by the Slovak Research and Development Agency.

References

[1] Moore CW, Zielinska B, Petron G, Jackson RB. Air impacts of increased natural gas acquisition, processing, and use: a critical review, Environmental science & technology, 2014; 48(15): 8349-8359.
[2] Aaron D, Tsouris C. Separation of CO_2 from flue gas: a review, Separation Science and Technology, 2005; 40(3): 321-348.
[3] Paskall HG. Capability of the modified-Claus process; Western Research and Development, 1979.
[4] Bohme G, Sames J. The seven deadly sins of sulfur recovery. In Sulfur Conference, Calgary, Alberta, Canada,1999.
[5] Hyne JB. Recent developments in sulfur production from hydrogen sulfide-containing gases. ACS syposium series, 1982,183:37-56.
[6] Beavon D, Kouzel B, Ward J. Claus processing of novel acid gas streams. In ACS symposium series, 1982; 183: 57-68. 1155 16th ST, NW, Washington, DC 20036 USA: ACS.
[7] Selim H, Gupta AK, Al Shoaibi A. Effect of reaction parameters on the quality of captured sulfur in Claus process, Applied energy, 2013, 104: 772-776.
[8] Elsner MP, Menge M, Müller C, Agar DW. The Claus process: teaching an old dog new tricks, CatalysisToday, 2003; 79: 487-494.
[9] van Nisselrooy PFMT, Lagas JA. Super Claus reduces SO_2, emission by the use of a new selective oxidation catalyst, Catalysis today, 2003; 16(2): 263-271.
[10] Nedez C, Ray JL. A new Claus catalyst to reduce atmospheric pollution, Catalysis today, 1996; 27(1-2):49-53.
[11] Pearson MJ. Alumina catalysts in low-temperature Claus process, Industrial & Engineering Chemistry Product Research and Development, 1997; 16(2): 154-158.
[12] Tong S, Dalla Lana IG, Chuang KT. Effect of catalyst shape on the hydrolysis of COS and CS_2 in a simulated Claus converter. Industrial & engineering chemistry research, 1997; 36(10): 4087-4093.
[13] Baglio JA, Susa TJ, Wortham DW, Trickett EA, Lewis TJ. Lanthanum oxide-based catalysts for the Claus process, Industrial & Engineering Chemistry Product Research and Development, 1982; 21(3):408-415.
[14] Monnery W.D, Hawboldt K.A, Pollock A.E, Svrcek W.Y. Ammonia pyrolysis and oxidation in the Claus furnace, Industrial & engineering chemistry research, 2001; 40(1): 44-151.
[15] Sinha S, Raj A, Al-Shoaibi AS, Alhassan SM, Chung SH. Benzene destruction in Claus process by sulfur dioxide: a reaction kinetics study, Industrial and Engineering Chemistry Research, 2014; 53(26):10608-10617.
[16] Keller AE, Ramani S, Allison JD, Lusk SE, Hatcher NA, Swinney LD, Shaver RS. ConocoPhillips Co. 2009. Increased capacity sulfur recovery plant and process for recovering elemental sulfur. U.S. Patent 7,501,111.
[17] El-Bishtawi R, Haimour NM. Claus recycle with double combustion process. Fuel Processing Technology, 2004; 86(3):245-260.

[18] Karan K, Behie LA. CS_2 formation in the Claus reaction furnace: a kinetic study of methane - sulfur and methane - hydrogen sulfide reactions, Industrial & engineering chemistry research, 2004; 43(13):3304-3313.
[19] Raj A, Sinha S. Reaction mechanism for the oxidation of aromatic contaminants present in feed gas to Claus process, Energy Procedia, 2015; 66: 61-64.
[20] Ibrahim S, Al Shoaibi A, Gupta AK. Toluene destruction in thermal stage of Claus reactor with oxygen enriched air, Applied Energy, 2014; 115: 1-8.
[21] Ibrahim S, Rahman RK, Raj A. Effects of H_2O in the Feed of Sulfur Recovery Unit on Sulfur Production and Aromatics Emission from Claus Furnace, Industrial & Engineering Chemistry Research, 2017; 56(41): 11713-11725.
[22] Mahdipoor HR, Ashkezari AD. Feasibility study of a sulfur recovery unit containing mercaptans in lean acid gas feed, Journal of Natural Gas Science and Engineering, 2016; 31: 585-588.
[23] Asil AG, Shahsavand A, Mirzaei S. Maximization of sulfur recovery efficiency via coupled modification of GTU and SRU processes, Egyptian Journal of Petroleum, 2017; 26(3): 579-592.
[24] Chidambaram S. Thermal Damage of Sulfur Processed Chamber under Claus Operating Reaction Conditions-A Case Study, Case Studies in Construction Materials, 2018; 8: 517-529.
[25] Ibrahim S, Raj A. Kinetic simulation of acid gas (H_2S and CO_2) destruction for simultaneous syngas and sulfur recovery, Industrial & Engineering Chemistry Research, 2016; 55(24): 6743-6752.
[26] Sassi M, Gupta AK. Sulfur recovery from acid gas using the Claus process and high temperature air combustion (HiTAC) technology, American Journal of Environmental Sciences, 2008; 4(5):502.
[27] Beavon DK, Fleck RN. Beavon. Sulfur Removal Process for Claus Plant Tail Gas, Advances in chemistry. 1975.
[28] Swaim CD. The Shell Claus Offgas Treating (SCOT) Process, Advances in Chemistry, 1975.
[29] Sung CY, Al Hashimi S, McCormick A, Tsapatsis M, Cococcioni M. Density functional theory study on the adsorption of H_2S and other Claus process tail gas components on copper-and silver-exchanged Y zeolites, The Journal of Physical Chemistry C, 2012; 116(5): 3561-3575.
[30] Al Wahedi Y, Torres AI, Al Hashimi S, Dowling NI, Daoutidis P, Tsapatsis M. Economic assessment of temperature swing adsorption systems as Claus tail gas clean up units, Chemical Engineering Science, 2015; 126:186-195.
[31] Buchanan JS, Stern DL, Nariman KE, Teitman GJ, Sodomin JF, Johnson DL. Regenerable solid sorbents for Claus tail gas cleanup: A treatment process for the catalytic removal of SO_2 and H_2S, Industrial & engineering chemistry research, 1996; 35(8): 2495-2499.
[32] Khudenko BM, Gitman GM, Wechsler TE. Oxygen based Claus process for recovery of sulfur from H_2S gases, Journal of environmental engineering, 1993; 119(6): 1233-1251.
[33] Nabikandi NJ, Fatemi S. Kinetic modelling of a commercial sulfur recovery unit based on Claus straight through process: Comparison with equilibrium model, Journal of Industrial and Engineering Chemistry, 2015; 30:50-63.
[34] Jones D, Bhattacharyya D, Turton R, Zitney SE. Rigorous kinetic modeling and optimization study of a modified Claus unit for an integrated gasification combined cycle (IGCC) power plant with CO_2 capture, Industrial & Engineering Chemistry Research, 2012; 51(5): 2362-2375.
[35] Rahman RK, Raj A, Ibrahim S, Khan MI, Al Muhairi NO. Reduction in natural gas consumption in sulfur recovery units through kinetic simulation using a detailed reaction mechanism, Industrial & Engineering Chemistry Research, 2018; 57(5): 1417-1428.
[36] Mohammed S, Raj A, Al Shoaibi A. Effects of fuel gas addition to Claus furnace on the formation of soot precursors, Combustion and Flame, 2016; 168: 240-254.
[37] Ghahraloud H, Farsi M, Rahimpour MR. Modeling and optimization of an industrial Claus process: Thermal and catalytic section, Journal of the Taiwan Institute of Chemical Engineers, 2017; 76: 1-9.
[38] Manenti F, Papasidero D, Bozzano G, Ranzi E. Model-based optimization of sulfur recovery units, Computers & Chemical Engineering, 2014; 66:244-251.
[39] Kazempour H, Pourfayaz F, Mehrpooya M. Modeling and multi-optimization of thermal section of Claus process based on kinetic model, Journal of Natural Gas Science and Engineering, 2017; 38: 235-244.
[40] Zughbi HD, Razzak SA. Simulation of flow and chemical reactions in a Claus sulfur converter, Industrial & engineering chemistry research, 2005; 44(26): 9828-9839.

[41] Sinha S, Raj A, AlShoaibi AS, Alhassan SM, Chung, SH. Toluene destruction in the Claus process by sulfur dioxide: a reaction kinetics study, Industrial & Engineering Chemistry Research, 2014; 53(42):16293-16308.
[42] Sinha S, Raj A, Al Shoaibi AS, Chung SH. Reaction mechanism for m-xylene oxidation in the Claus process by sulfur dioxide, The Journal of Physical Chemistry A, 2015; 119(38): 9889-9900.

To whom correspondence should be addressed: Dr. Nagamalleswara Rao K, Centre for Disaster Mitigation and Management, Vellore Institute of Technology, Vellore, Tamilnadu, India – 632014

Petroleum and Coal

Article **Open Access**

CFD ANALYSIS OF CATALYST SHAPE EFFECTS ON HYDRODYNAMIC AND HEAT TRANSFER CHARACTERISTICS OF FIXED BED REACTORS

Yaghoub Behjat, Afshin Ziyari, Majid Kakavand

Process Development and Equipment Technology Division, Research Institute of Petroleum Industry, Tehran, Iran

Received December 10, 2018; Accepted February 18, 2019

Abstract

In this research, the effects of cylindrical catalyst shape on hydrodynamic and heat transfer characteristics of fixed bed reactors have been investigated by means of CFD analysis. In the developed model, the catalyst particles have been considered as porous media whose thermal conductivity are associated with the heat transfer from the reactor wall to bed. The computational model was validated using corresponding experimental data to predict the spherical catalyst heat transfer rate to the bed center. Comparison between the CFD model results with experimental radial temperature profile reveals that the computational model is able to predict the rate of the heat transfer with acceptable accuracy. The validated computational model has then been used to investigate the effects of ten types of cylindrical catalyst shapes on hydrodynamic and heat transfer characteristics of a fixed bed reactor with bed-to-particle diameter ratio (N) of 2 and 4. The results obtained from the CFD model indicate that due to the catalysts configuration and their contact points, there would be a complicated flow field around the catalysts. Comparing the bed heat transfer and pressure drop amounts for two cases (N=2 and 4) indicates that the optimum catalyst shape for increasing the heat transfer ratio to the bed center and lowering the pressure drop along the bed for the two cases (N= 2 and 4) is the same. On the other hand, CFD simulation results show that increase of the number of the holes in catalysts considerably decreases the bed pressure drop, while it has a minor effect on decreasing the heat transfer rate to the bed center.

Keywords: *Fixed Bed Reactor; Hydrodynamic; Heat Transfer; Catalyst Shape; CFD Simulation.*

1. Introduction

Catalysts with complex shapes such as punching tablets are widely used in industrial steam reforming processes. Formed catalysts are used to increase the effective mass transfer, increase the heat transfer and decrease the pressure drop. Although simulation of the steam reforming process by means of one-dimensional and two-dimensional models have been widely reported in the literature but optimization of the catalysts dimensions and shapes, as well as development of certain relations for prediction of heat transfer characteristics, have been little cited. Researches on CFD simulation of fixed bed reactors have been generally done by limited research groups, mainly focusing on the rate of heat transfer in these beds.

Dixon and his colleagues in their first research activities in this field determined the turbulence model as well as the required parameters for CFD simulation of fixed bed reactors by means of some simple experiments. Their experiment was an investigation of the heat transfer amount to a column having a diameter of 2 inches and a length of 18 inches with boundary condition of a steady temperature at the walls. In this bed, spherical catalysts with a diameter of 1 inch had been used [1].

Some other researchers simulated the system with different shape of catalysts to study the effects of catalyst shapes on the hydrodynamic and heat transfer characteristics of the bed. The main goal of these simulations was to investigate the effects of the catalyst shape on the

heat transfer characteristics near the walls and also study the influence of the catalyst holes and empty spaces on the heat transfer. The results of these simulations showed that the shape of the catalyst has a minor impact on the heat transfer near the walls, but in the bed center it has a major influence. The reported results showed that under a steady pressure drop the temperature of the reactor and walls increases if non-porous catalysts are applied [2].

Dixon and his colleagues in the second stage of their researches simulated the effects of the catalyst shape on the reaction inside the bed. This study was done with a spherical catalyst. The results indicated that the assumption of steady temperature and steady catalyst particle concentration will remain satisfied for catalyst particles far from the walls, but for those near the walls, it will be violated. With no more simulations, they concluded that the same results will be maintained for non-spherical catalysts [3].

In their third research activities, Dixon and his colleagues investigated the effects of catalysts shape on the pressure drop and heat transfer in fixed bed reactors. In this research 5 different catalyst shapes were simulated with the bed by means of CFD. The results showed that the cylindrical catalyst with 4 holes yields the minimum pressure drop and heat transfer ratio. The filled catalyst (without holes) particles resulted in maximum pressure drop and heat transfer ratio. In this study, the effects of the catalyst thermal conductivity have not been investigated [4].

Guardo and his colleagues investigated the effects of the turbulence model in CFD analysis of the fixed beds in their first research work. In this study turbulence models with one and two equations models have been applied and the pressure drop value deducted from the simulation has been compared with experimental and semi-experimental data. In all simulated cases, canalization has occurred near the walls and in the empty spaces of the catalyst particles. All the results of these simulations have been compatible with those of the magnetic photography experiments [5]. In their second research works, Guardo and his colleagues have investigated the effects of the heat transfer from the fluid to the catalyst particles. In this work, the heat transfer coefficient between the gas and the catalyst particles inside the bed has been computed. It is observed that adequate mesh has not been considered in the contact points of the catalysts which have resulted in a considerable error in the numerical solution of the equations [6].

Heat transfer of single cylindrical particle affected by wall has been investigated numerically and experimentally for limited Reynolds number. The heat transfer in two different orientations (axial and cross flow over the particle) considered by Hashemabadi *et al.* Influence of wall on heat transfer of particle in different bed-to-cylinder diameter ratio discussed [7]. Hashemabadi *et al.* studied experimentally and computationally the flow and heat transfer characteristics of regularly arranged cylindrical particles in a bed with a bed-to-particle diameter ratio of 2.65 in two different arrangements of particles [8]. Hashemabadi et al. in the other research investigated numerically and experimentally the heat transfer of a multi-lobe particle (tri-lobe, tetra-lobe, and penta-lobe) affected by the wall in cross and axial-flow was. The heat and mass transfer analogy was applied for gaining the Nusselt number for each particle in axial and cross flow [9].

In literature, minor attention has been paid to the shape of catalysts, and they have usually been considered to be spherical in simulations. Also, the effects of catalyst shapes on hydrodynamic and heat transfer characteristics have not yet been studied comprehensively with precise optimum computational grids. In this research, the effects of catalyst shapes on hydrodynamic and heat transfer characteristics for a fixed bed reactor with bed-to-catalyst particle ratio of 2 has been studied. In addition to the spherical catalyst, 10 different cylindrical catalyst shapes with bed-to-catalyst particle ratio of 2 and 4 have been also incorporated in CFD simulations to be studied for their effects on the hydrodynamic and temperature profile inside the bed.

2. Governing equations and modeling

The general form of the equation used for mass conservation law (continuity equation) is as follows [2,10,11]:

$$\frac{\partial \rho}{\partial t} + \nabla.\left(\rho\,\vec{v}\right) = 0 \quad (1)$$

Momentum and energy conservation equations are as followings:

$$\frac{\partial}{\partial t}\rho\,\vec{v} + \nabla.\left(\rho\,\vec{v}\,\vec{v}\right) = -\nabla P + \rho g + \nabla.\overline{S} + S_i \quad (2)$$

$$\rho C_P\left(\frac{\partial}{\partial t}T + \vec{v}\,.\nabla T\right) = -\nabla.\left(k_{eff}\nabla T\right) \quad (3)$$

Turbulence equations are also incorporated in the computational model as the velocity of the gas phase in industrial steam reforming process is very high (Reynolds number = 25000). RNG k-ε turbulence model has been incorporated as it can be used to analyze swirl flows as well as the flows on high curvature surfaces because of the additional terms it has got in ε equation. Also for modeling of the turbulence near the reactor walls, the standard wall function model has been used [12-13].

$$\rho\frac{\partial k}{\partial t} + \rho v k = \left(\mu + \frac{\mu_t}{\sigma_k}k_j\right) + G - \rho\varepsilon \quad (4)$$

$$\rho\frac{\partial \varepsilon}{\partial t} + \rho v \varepsilon_j = \left(\mu + \frac{\mu_t}{\sigma_\varepsilon}\varepsilon_j\right) + C_1\frac{\varepsilon}{k}G - C_2\rho\frac{\varepsilon^2}{k} - \frac{C_\mu\eta^3\left(1-{}^{\eta}/_{\eta_0}\right)}{1+\beta\eta^3}\frac{\varepsilon^2}{k} \quad (5)$$

In this research, the heat transfer phenomena inside catalyst particles have been simulated considering each catalyst particle as porous media. Porous media modeling includes experimental determination of flow resistance. Porous media is simulated by adding a momentum well to the standard flow field equation. This momentum includes viscous and inertial resistance as indicated in the following equation [10].

$$\mathrm{S_i} = -\left(\sum_{\mathrm{j=1}}^{3}\mathrm{D_{ij}}\mu\,\upsilon_\mathrm{j} + \sum_{\mathrm{j=1}}^{3}\mathrm{C_{ij}}\frac{1}{2}\rho|\upsilon|\upsilon_\mathrm{j}\right) \quad (6)$$

$\mathrm{S_i}$ is the cumulative momentum for part i (x,y) of momentum equation, $|\upsilon|$ is the velocity order and C and D are some defined matrixes. This momentum well is the cause of pressure gradient and accordingly a pressure drop proportional to fluid velocity (velocity into power 4) in a porous cell. For a homogenous porous medium we have:

$$\mathrm{S_i} = -\left(\frac{\mu}{\alpha}\upsilon_\mathrm{i} + \beta\frac{1}{2}\rho|\upsilon|\upsilon_\mathrm{i}\right) \quad (7)$$

where α is the permeability and β is the inertial resistance coefficient. For a slow flow in a porous medium, the pressure drop is usually proportional to velocity. Pressure drop in all directions (x,y,z) derived using the following relation:

$$\Delta\mathrm{p_i} = \sum_{\mathrm{j=1}}^{3}\frac{\mu}{\alpha_\mathrm{ij}}\upsilon_\mathrm{j}\Delta\,\mathrm{n_i} \quad (8)$$

Permeability and inertial resistance in relation (7) can be computed using the following equations:

$$\alpha = \frac{\mathrm{d^2_m}}{150}\frac{\phi^3}{(1-\phi)^2} \quad (9)$$

$$\beta = \frac{3.5}{\mathrm{d_m}}\frac{(1-\phi)}{\phi^3} \quad (10)$$

Pore size distribution (d_m) in the catalyst particles whose mean value has been considered 3792 Angstrom has been adopted from experimental data. Considering the pore size and the volume fraction of the catalyst particles because of the porous medium, β and $1/\alpha$ are computed as $\beta = 40562086.37$ and $\frac{1}{\alpha} = 2.34572 \times 10^{15}$ respectively.

3. CFD simulation

To generate an adequate geometry for the simulations, different shapes of the catalyst have to be randomly placed in the reactor. The main issue is to place the catalyst in the reactor in a manner to firstly avoid flow canalization and secondly produce a high quality mesh in the contact point of catalyst particles with each other and with the reactor wall. If the catalysts are tangent, it would be impossible to generate an adequate computational grid in contact points, and so the following approaches have been proposed for generating the required geometry.

- The catalyst particles volumes become greater up to the point that the contact point between them becomes a circle with a very small radius.
- The catalyst particles volumes become smaller up to the point that the contact point between them makes a small space in which suitable grids can be generated. It shall be noted that the catalyst sizes shall not be so much small to let the fluid flow between their contact points.

Considering that in this research the heat transfer is modeled as the thermal conductivity of the catalyst particles, an increase of particles volumes will cause the formation of an integrated catalyst volume inside the bed and hence increases the error. The increase of catalyst volume is not an adequate approach for generating a proper geometry. Accordingly, it was found better to reduce the catalyst volumes whose main challenging issue is the selection of the proper amount of this reduction. The decrease of catalyst volumes shall be up to a point to firstly avoid the flow of the fluid between the contact points and secondly increase considerably the amount of computation volume. It was found that a reduction of more than 1% in catalyst particles radiuses will cause a flow of the fluid between the contact points. The particles radiuses were decreased by 0.5%, and the simulations were carried out. The results showed that with this amount of catalyst volume reduction, no fluid will flow between the contact points of catalyst particles even up to Reynolds number of 70000.

To validate the computational model, an experimental bed with spherical catalyst was implemented using available experimental geometry and computational mesh data [1]. In this stage, the complete 360 degrees of the bed geometry was implemented, and the optimum computational grid was achieved for catalyst particles inner parts and surrounding fluid flow. The implemented bed contained 44 catalyst particles in 22 layers. The diameter of the bed was 2 inches while that of the catalyst particles was 1 inch. The center to center distance between two adjacent catalysts along the bed axis was$\sqrt{2}R$. So for placing the catalysts inside the bed, the catalysts of each layer are placed at a distance of$\sqrt{2}R$ long the bed axis from the previous layer and each layer is rotated 90 degree about the bed axis. The computational grid in this simulation is tetragonal which has been selected because of its geometry complexity. At least two computation cells have been considered in contact points of the catalysts with each other and with the reactor walls. Figure (1) illustrates the achieved computational grid of this bed with spherical catalysts. Figure (2) depicts 10 different cylindrical catalysts which have been simulated in this study.

Because of the catalysts random arrangement in the bed and hence the implementation of complex geometry, development of a proper computational cell in contact points of the catalyst particles is very difficult and time-consuming. Table (1) shows the boundary conditions of the achieved simulation.

Table 1. Boundary conditions of the simulated bed

Input, Velocity Constant	Velocity=14.3m/s, Temperature=600K, Turbulence=10%
Wall	No Fluid Slip, Temperature=1000K
Output	Constant Pressure

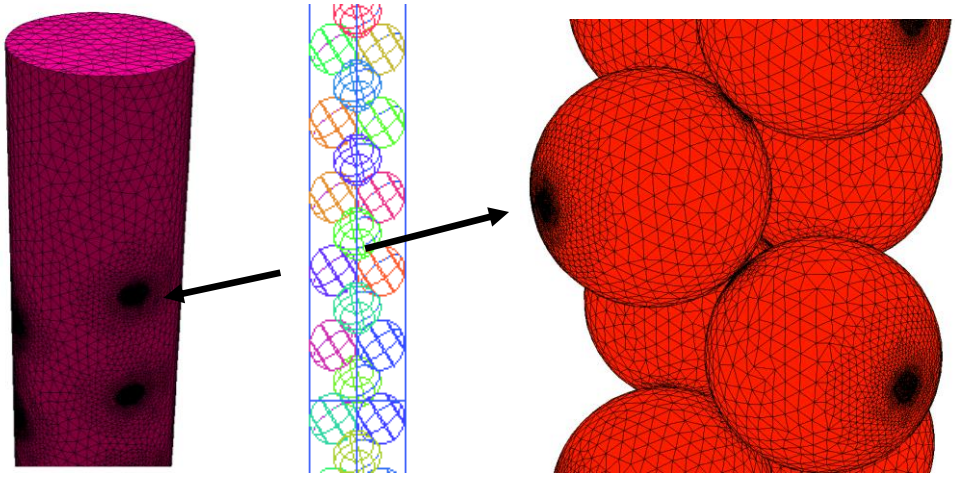

Figure 1. Schematic of the computational grid used for a bed with spherical catalysts

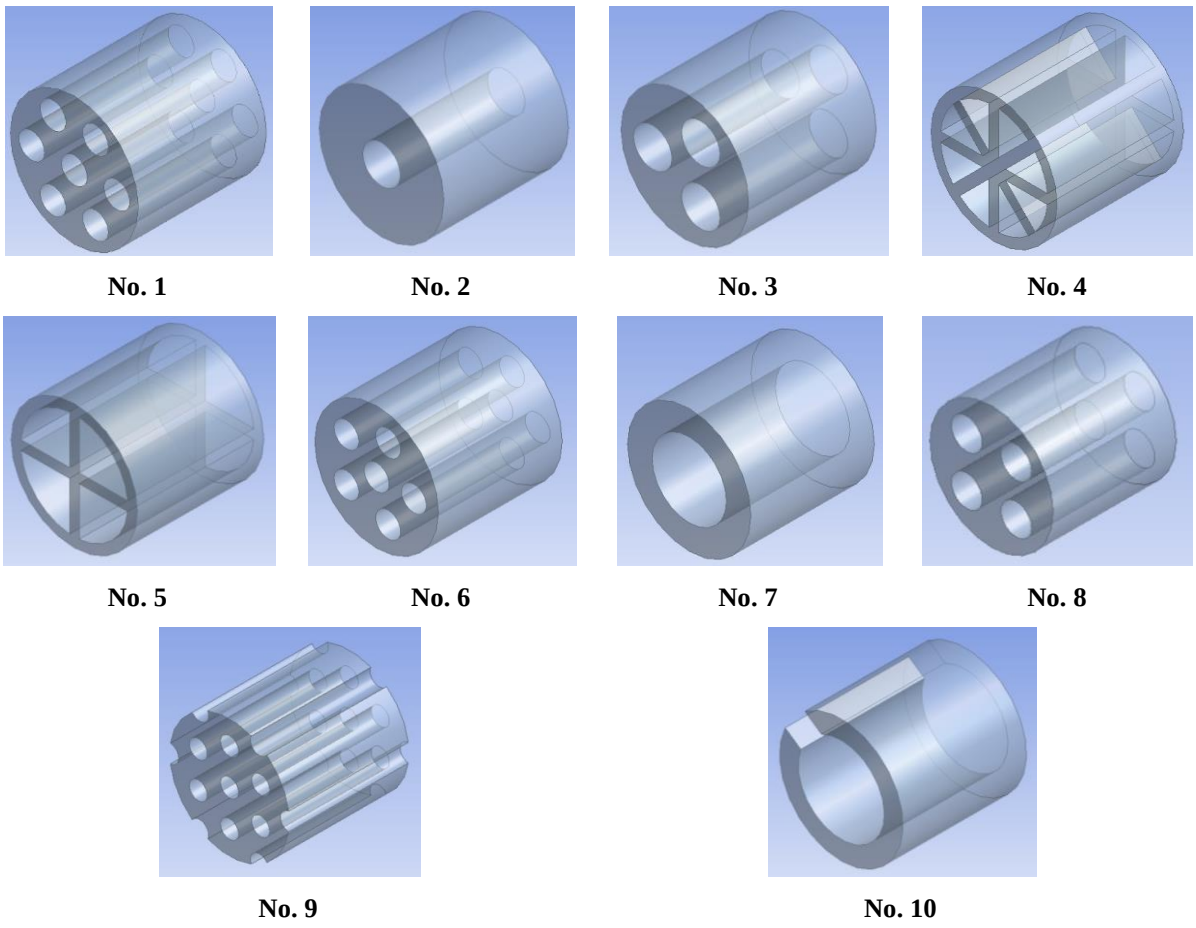

Figure 2. Ten different shapes of simulate cylindrical catalysts

Considering that the arrangement of the cylindrical catalysts inside the bed cannot be easily predicted and taking into account that this arrangement can extremely influence the results, it was decided to use two glass cylinders with internal diameters of 2 and 4 inches and cylindrical catalysts with diameter and height of 1 inch. For the bed with a bed to catalyst diameter ratio of 2, 10 pieces of catalysts were randomly placed in the glass cylinder of 2 inch diameter. Then geometry similar to the implemented bed was developed, and the meshing of the inner

parts of the catalysts, as well as the catalyst particle surrounding fluid flow, was achieved. Figure (3) illustrates the real bed, implemented bed geometry and developed computational grids for three types of catalysts (No. 3, No. 4, No. 9) for a bed with a bed to catalyst diameter ratio of 2 (N=2).

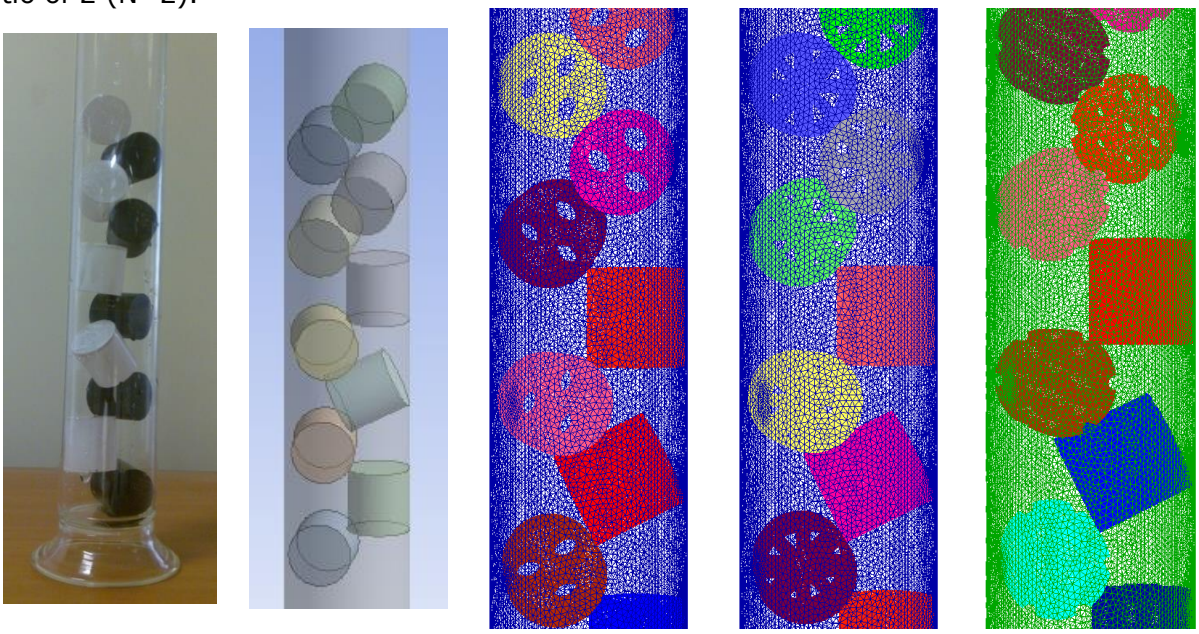

Figure 3. Real bed, catalysts geometry and developed grids for some catalysts

In next step, catalysts geometry was developed for a bed with a bed-to-catalyst diameter ratio of 4 (N=4) and random arrangement of 48 pieces of catalysts in 6 layers (8 pieces of catalyst in each layer). Because of the random arrangement of these catalysts and development of complex geometry, implementation of suitable computational cells for contact points of catalysts particles was very difficult and time-consuming. In figures (4) and (5) a sample of the developed grids and catalysts arrangements for layers two and three and for two different types of catalysts (No. 3, No. 4) has been shown. Figure (6) showed a schematic of the catalysts arrangement and implemented meshing in some layers for two different shapes of cylindrical catalysts in a bed having a bed-to-catalyst diameter ratio of 4 (N=4).

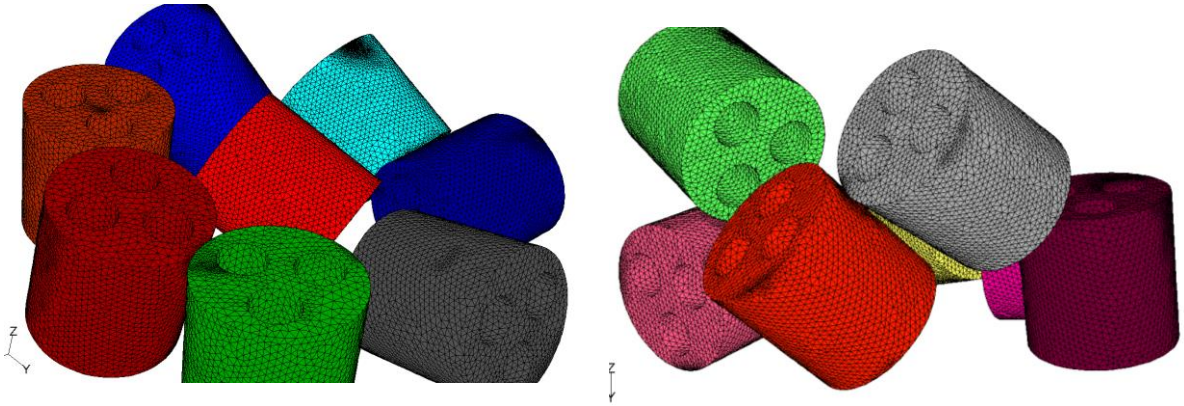

Figures 4. Arrangement of No. 3 catalyst in N=4 bed

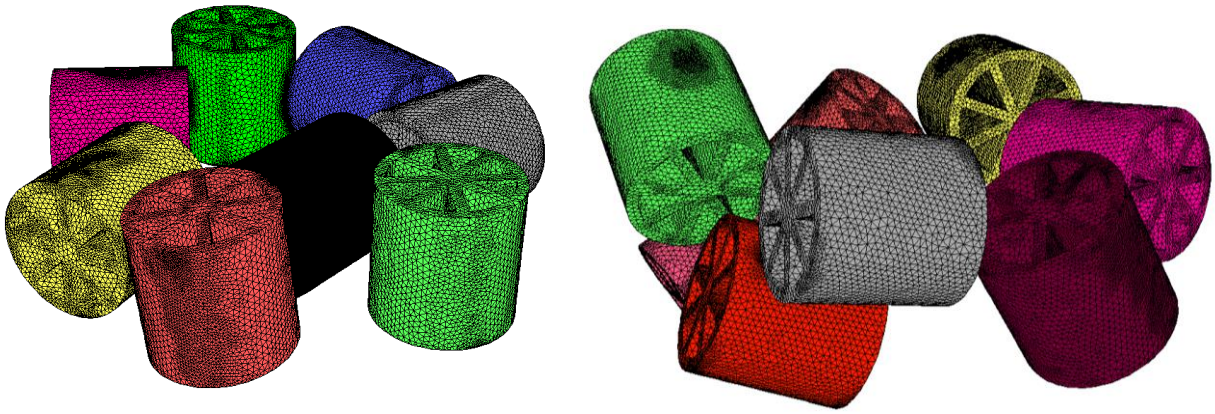

Figure 5. Arrangement of No. 4 catalyst in N=4 bed

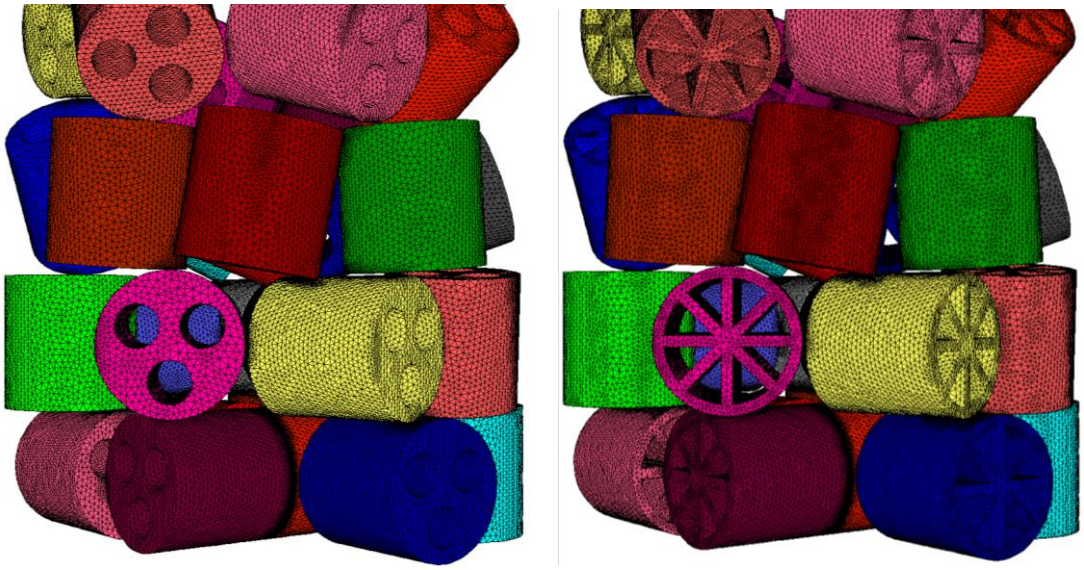

Figure 6. Schematic of catalyst arrangement for 2 catalyst types in N=4 bed

4. Results and discussions

4.1. Validation of the developed computational model

For validation of the developed computational model, experimental data in literature has been used to estimate the heat transfer rate from the walls to the center of the bed. In figure (7) the CFD simulation results have been compared with experimental results [1] adopted from the measurement of the bed temperature radial distributions at two different bed heights. As illustrated in this figure, the results taken from the developed model has got a little deviation from those of the experimental ones. The amount of the error at a bed height of Z = 0.42 m is shown to be 8.52% which is quite acceptable.

4.2. Study of the hydrodynamic parameters and spherical catalysts heat transfer

Figure (8) illustrates the gas flow around the catalyst particles for experimental and industrial conditions with Reynolds numbers of 986 and 25000 respectively. It is shown that there is a complex hydrodynamic around the catalyst particles. It is observed in this figure that the nature of the gas flows for these two Reynolds numbers are diversely different. In high Reynolds number, the separation occurs around the catalyst center while for the low Reynolds number, the phenomenon occurs in last one third of the catalyst. It is also shown in this figure

that the radial mixing of the flows occurs more in low Reynolds number and as the Reynolds number increases, the radial flow mixing decreases.

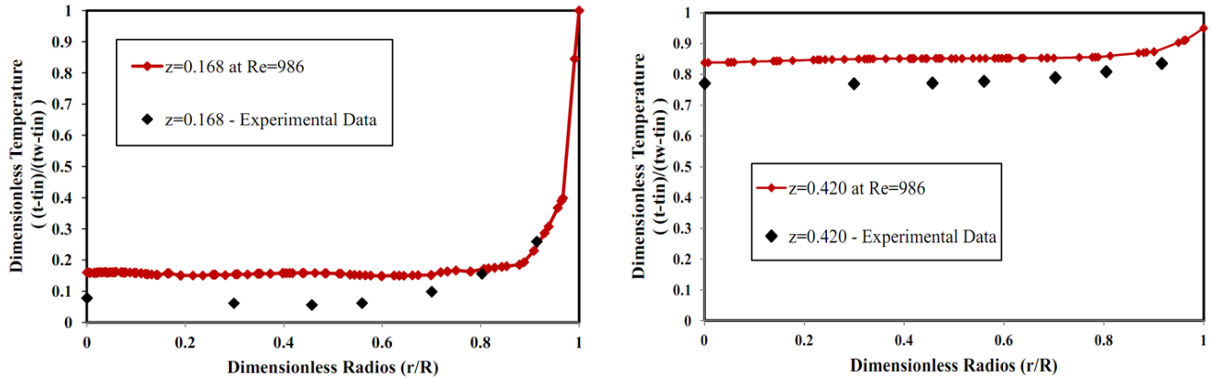

Figure 7. Temperature radial distribution at two different bed heights

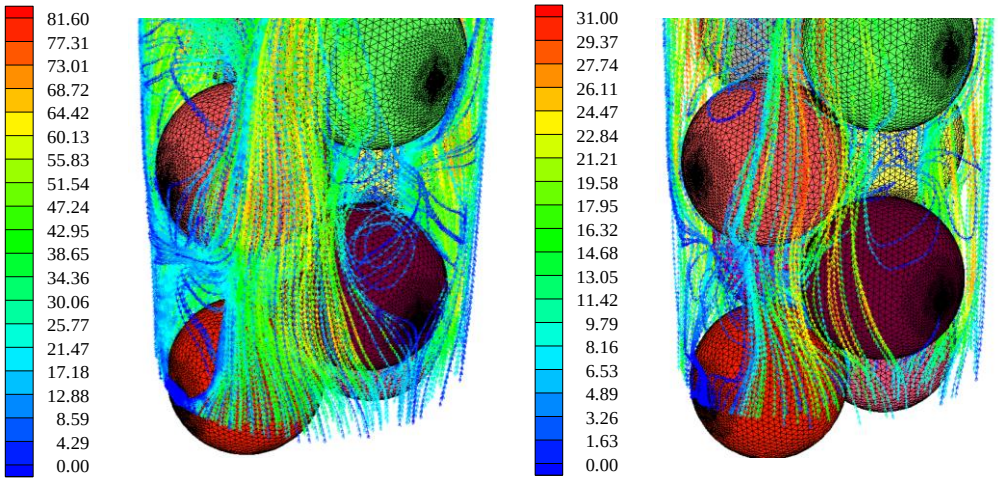

Figure 8. Fluid flow path line around catalysts particles

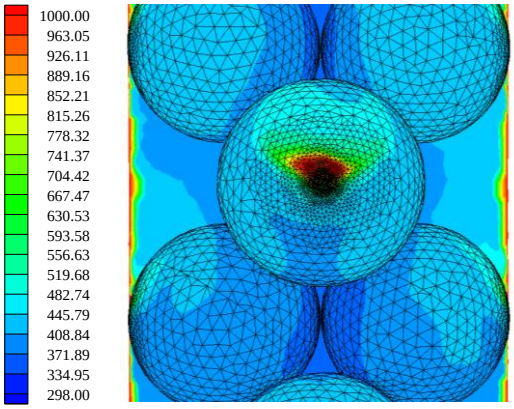

Figure 9. The thermal profile of spherical catalyst particles

Figure (9) demonstrates the thermal profile and the heat transferred from the bed walls to the inner parts of the catalyst particles. It is observed from this figure that the temperature is high near the bed walls and the contact points of the catalysts with the walls but in a little distance from the bed walls, the heat transfer to the bed decrease drastically. According to the thermal profile depicted in figure (9), it is noticed that the temperature penetration from the bed wall to its internal is very low which has a negative impact on reforming reactions and so to increase the efficiency of the reactor, the heat transfer to the bed internal shall get increased.

4.3. CFD simulation of fixed bed reactors with cylindrical catalysts

The main goal of this simulation is to determine the best catalyst geometry and shape that can result in an effective heat transfer and a decrease of pressure drop in beds with bed-to-catalyst diameter ratios of 2 and 4. The governing equations of the gas phase and porous medium have been simultaneously discretized in the form of algebraic equations by applying finite volume numerical method and first and second order upwind discretization scheme. These discretized equations have been solved by means of an upgraded algorithm of SIMPLE [14-15].

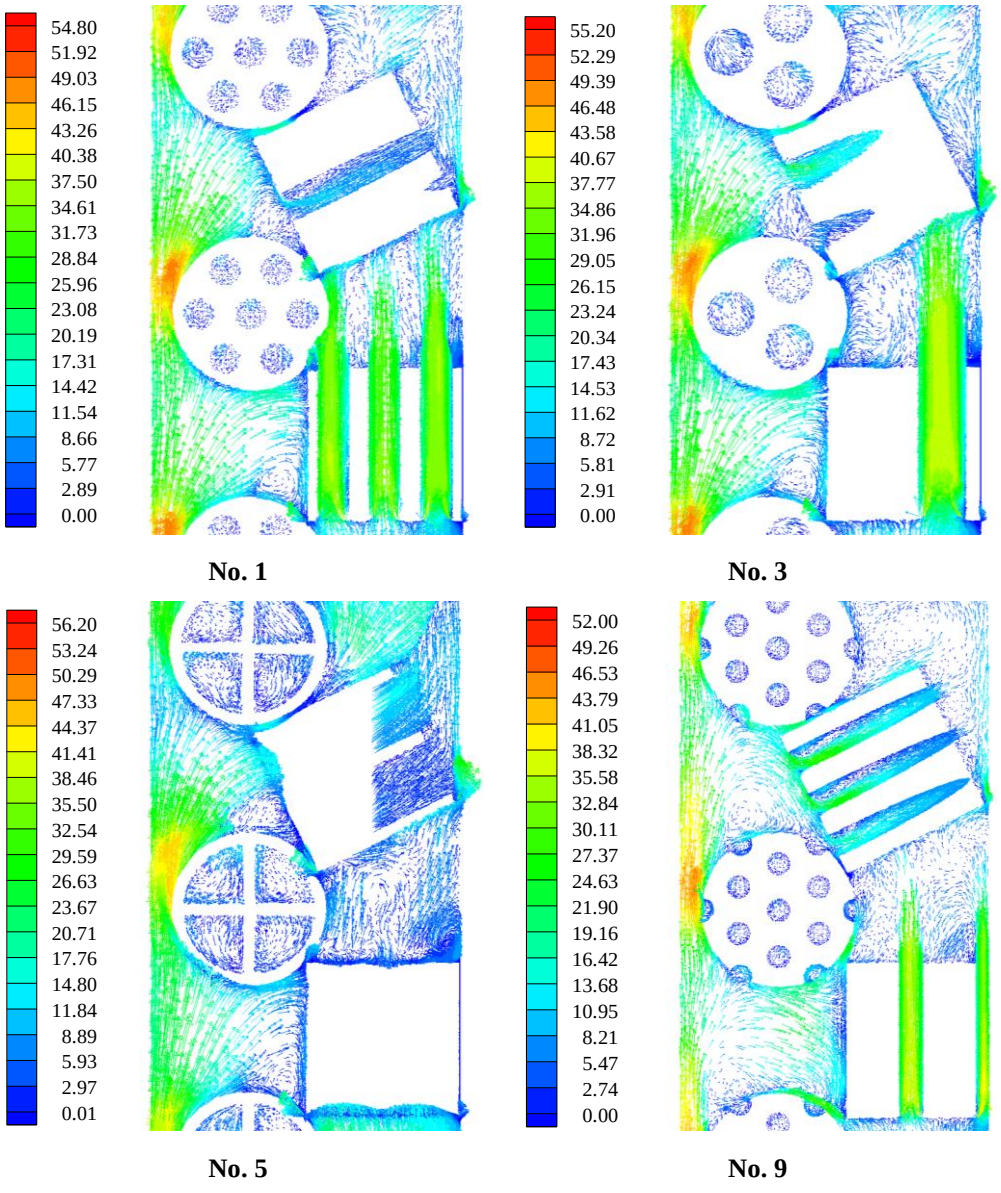

Figure 10. Gas phase velocity vectors around catalyst particles for N=2.

As discussed earlier, there is a complex hydrodynamic around catalysts because of their layout inside the bed and their contact points with the bed walls. Because of this complexity and interaction of the catalysts, the hydrodynamic of the flow and heat transfer is very complex and needs special approaches and optimum computational networks to achieve convergence in CFD simulation. Gas phase velocity vectors around catalyst particles for four different shapes (No. 1, No. 3, No. 5, No. 9) in a specific height of the bed in two cases of bed-to

catalyst ratios of 2 and 4 have been depicted in figures (10) and (11). It is observed from these figures that there is a complex hydrodynamic around catalyst particles which are dependent on their shapes and layout. Also, the results of the CFD simulation show that the maximum gas velocity occurs near the bed walls and the gas near this area gets canalized because of the empty spaces a so leaves the bed without any catalytic reforming reaction. Because of the existence of pseudo plug flows in bed, an optimum layout and shape have to be selected for catalysts to increase radial flows in order to increase the heat transfer and reforming reactions rates and hence improve the efficiency of the synthesis gas conversion.

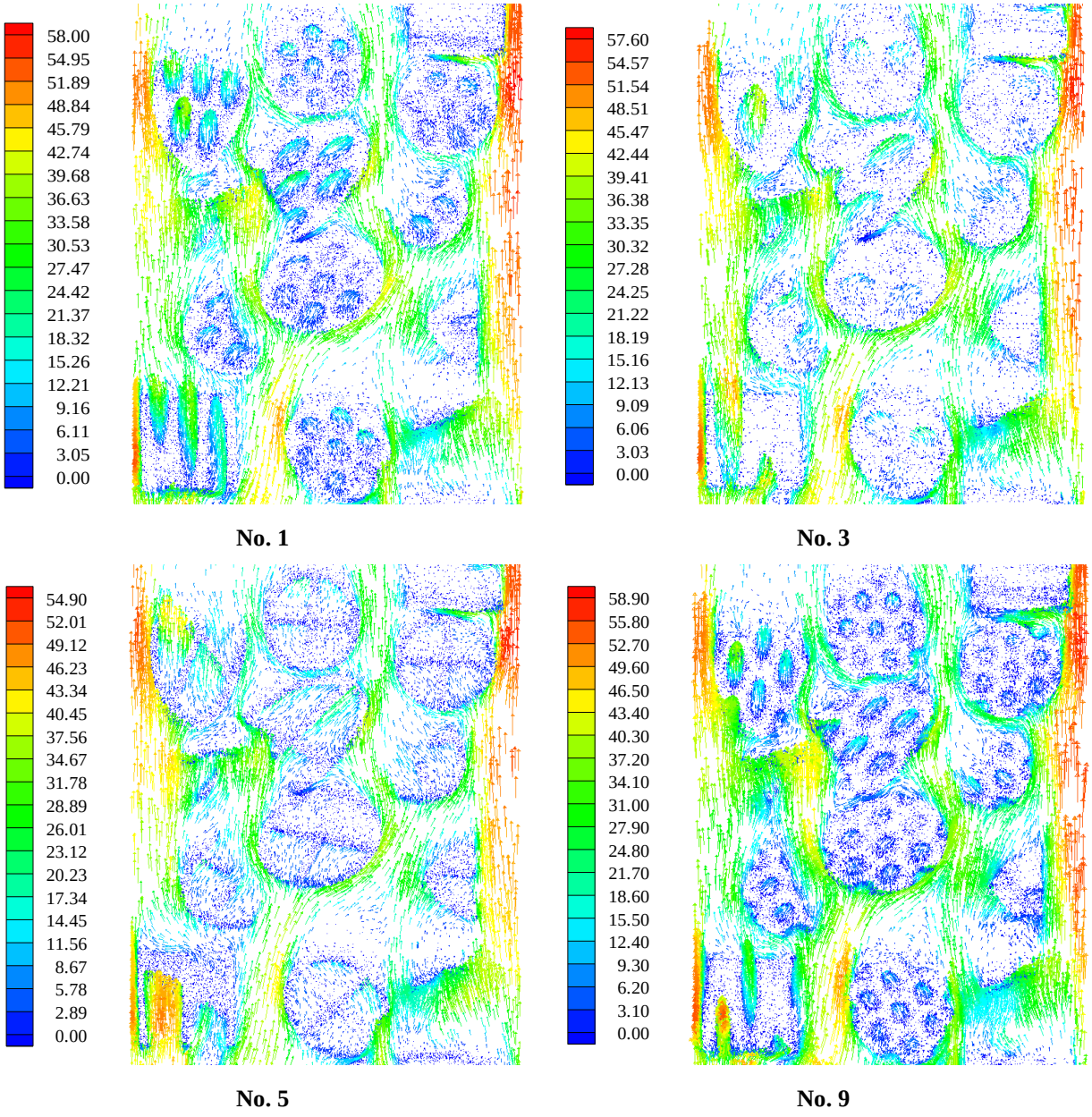

Figure 11. Gas phase velocity vectors around catalyst particles for N=4

The pressure drop amounts for each type of catalyst in bed for N=2 and N=4 at Reynolds number of 12500 and also the mean values of fluid temperatures at bed output have been shown in tables (2) and (3) respectively.

Table 2 Pressure drop and mean fluid temperature at bed outlet for N=2

Catalyst number	Temperature at bed outlet	Pressure drop across bed (Pa)
No. 1	651.4	1285.5
No. 2	660.9	1343.9
No. 3	651.5	1297.6
No. 4	656.1	294.6
No. 5	654.9	292.1
No. 6	659.5	318.71
No. 7	658.2	308.2
No. 8	659.52	300.5
No. 9	656.42	317.5
No. 10	655.4	286.3

Table 3. Pressure drop and mean fluid temperature at bed outlet for N=4

Catalyst number	Temperature at bed outlet	Pressure drop across bed (Pa)
No. 1	628.36	2932.9
No. 2	629.56	3320.1
No. 3	628.66	2871.3
No. 4	627.5	2684.6
No. 5	627.33	2374.9
No. 6	628.83	2999.8
No. 7	629.41	2586.6
No. 8	628.79	2946.1
No. 9	629.55	3068.2
No. 10	626.45	2048.9

It is observed from these tables that the maximum pressure drop and maximum heat transfer to the bed are occurred for catalyst No. (2). It is also noticed from these tables that the rate of pressure drop is coincident with that of the temperature increase of the bed. This happens because in all simulation cases the main reason for pressure drop is the deviation of the fluid from its direct trajectory resulting in radial flows. Radial flows cause an increase of the heat transfer to the bed center. On the other hand, the results given in tables (2) and (3) show that the minimum pressure drop and heat transfer occurs for catalyst No. (10). Also comparing the results of pressure drop and heat transfer rate for two beds (N=2 and 4) reveals that the bed-to-catalyst ratio hasn't got a considerable effect on hydrodynamic and heat transfer characteristics. So it can be deducted that catalyst No. (2) which resulted in the maximum heat transfer can be also suitable for industrial reactors (N=8). Also considering the results taken from CFD simulations and hydrodynamic and heat transfer characteristics, it can be concluded that increase of the catalyst holes and their sizes (an increase of the porosity) has a major impact on system pressure drop and minimum effect on the heat transfer rate to the bed center. It shall be noted that the selection of the best catalyst geometry is dependent on simultaneous simulation of the reforming reactions with flow fields and heat transfer.

5. Conclusion

Although there has been a wide range of researches carried out on steam reforming processes in literature, little studies have been done on catalyst shape and their effects on heat transfer characteristics. In this research, the effects of catalyst shapes on hydrodynamic and heat transfer characteristics were studied using CFD technique. Considering the catalyst particles as porous media, the effect of their thermal conductivity on the heat transfer from the walls to the bed center was investigated. To validate the computational model, experimental data for prediction of heat transfer rate from spherical catalysts to bed centers cited in literature were used. Comparing the results taken from simulation with those of the experimental data on temperature radial profile at different heights of the bed, it was observed that the

mean relative error resulted from the computational model at the height of Z=0.42 m was 8.52%. Regard to the obtained error, it was concluded that the developed computational model could well predict with an acceptable error the hydrodynamic and heat transfer characteristics of a bed with spherical catalysts. In next stage of this study, the validated model was used to investigate the effects of 10 different shape of cylindrical catalysts on hydrodynamic and heat transfer characteristics of a fixed bed reactor with bed-to-catalyst diameter ratios of 2 and 4 (N=2 and 4). The results taken from CFD simulations showed that there is a complex hydrodynamic around catalyst particles because of their layout and the contact points between them and the bed walls. The results showed that the trend of the pressure drop increase was coincident with that of the bed temperature increase and this occurred because the main reason of pressure drop increase was actually deviation of the fluid flow from direct trajectory forming radial flows. On the other hand, the existence of radial flows in bed caused an increase of the heat transferred to the bed center. Comparing the amounts of the heat transfer and pressure drop for two beds of N=2 and 4 showed that increase of the bed-to-catalyst diameter ratio didn't have much impact on the hydrodynamic and heat transfer characteristics. So catalyst No. 2 which had the highest amount of heat transfer to the bed center was concluded to be also suitable for the industrial case (N=8). The results of the CFD simulations as well as hydrodynamic and heat transfer characteristics indicated that increase of the hole numbers as dimensions on the catalyst particles (an increase of the catalyst particles porosity) has a major effect on pressure drop reduction while it plays a minor role in the decrease of the heat transfer to the bed center. Considering the results adopted from the developed model, it was observed that the maximum pressure drop across the bed and the maximum heat transfer to the bed center were obtained from the cylindrical catalyst having a single hole with a small diameter.

Nomenclature

C_{ij}: *Prescribed matrices in porous media*
C_{P}: *Specific heat*
$C_{1,2,\mu}$: *RNG k- ε constant*
d_m: *Pore size*
D_{ij}: *Prescribed matrices in porous media*
G: Production of turbulent kinetic energy
k: Turbulent kinetic energy
k_{eff}: *Effective conductivity*
N: bed-to-particle diameter ratio
No: Catalyst shape number
S: Stress tensor
P: Pressure:
Re: Reynolds number
S_i: *Cumulative momentum*
T: Thermodynamic temperature
t: Time
v: Velocity

Greek symbols

α: Permeability
β: Inertial resistance coefficient
σ: Turbulent Prandtl number
ϕ: Void fraction in porous media
μ: Viscosity
Δn: Thickness of porous media in each direction
ρ: Density
ε: Turbulent dissipation rate

References

[1] Nijemeisland M. Influences of catalyst particle geometry on fixed bed reactor near-wall heat transfer using CFD, Ph.D. Thesis, Worcester Polytechnic Institute, 2003.

[2] Nijemeisland M, Dixon AG, Stitt EH. Catalyst design by CFD for heat transfer and reaction in steam reforming. Chemical Engineering Science, 2004; 59: 5185–5191.

[3] Dixon AG, Taskin ME, Stitt EH, Nijemeisland M. 3D CFD simulations of steam reforming with resolved intraparticle reaction and gradients. Chemical Engineering Science, 2007;62: 4963–4966.

[4] Dixon AG, Taskin ME, Nijemeisland M, Stitt EH. Wall-to-particle heat transfer in steam reformer tubes: CFD comparison of catalyst particles. Chemical Engineering Science, 2008; 63: 2219–2224.

[5] Guardo A, Coussirat M, Larrayoz MA, Recasens F, Egusquiza E. Influence of the turbulence model in CFD modeling of wall-to-fluid heat transfer in packed beds. Chemical Engineering Science, 2005; 60: 1733–1742.

[6] Guardo A, Coussirat M, Recasens F, Larrayoz MA, Escaler X. CFD study on particle-to-fluid heat transfer in fixed bed reactors: Convective heat transfer at low and high pressure. Chemical Engineering Science,2006; 61: 4341–4353.
[7] Mirhashemi FS, Hashemabadi SH, Noroozi S. CFD simulation and experimental validation for wall effects on heat transfer of finite cylindrical catalyst. International Communications in Heat and Mass Transfer, 2011; 38(8): 1148–1155.
[8] Mirhashemi FS, Hashemabadi SH. Experimental and CFD study of wall effects on orderly stacked cylindrical particles heat transfer in a tube channel. International Communications in Heat and Mass Transfer, 2012; 39(3): 449–455.
[9] Zare M, Hashemabadi SH. Experimental study and CFD simulation of wall effects on heat transfer of an extrudate multi-lobe particle. International Communications in Heat and Mass Transfer, 2013; 43: 122–130.
[10] Ranade VV. Computational Flow Modeling for Chemical Reactor Engineering, Academic press, London 2002.
[11] Ahmadi Motlagh AH, Hashemabadi SH. 3D CFD simulation and experimental validation of particle-to-fluid heat transfer in a randomly packed bed of cylindrical particles. International Communications in Heat and Mass Transfer, 2008; 35: 1183–1189.
[12] Hinze JO. Turbulence, Second editions, McGraw-Hill, 1975.
[13] Wilcox DC. Turbulence modeling for CFD, Second editions, DCW Industries, California, 1994.
[14] Patankar SV. Numerical heat transfer and fluid flow, Washington, DC, Hemisphere Publishing Corp., 1980.
[15] Versteeg HK, Malalasekera W. An Introduction to Computational Fluid Dynamics: The Finite Volume Method, Prentice Hall, 1996.

To whom correspondence should be addressed: Assistant professor Dr. Yaghoub Behjat, Process Development and Equipment Technology Division, Research Institute of Petroleum Industry (RIPI), Tehran, Iran

Petroleum and Coal

Article **Open Access**

PRODUCTION OF PLASTIC LUBRICANTS ON THE BASIS OF WASTE LUBRICATED OILS

Andrey Grigorov[1], Oleg Zelenskii[1, 2], Leonid Saienko[3], Svitlana Zhyrnova[1]

[1] *National Technical University «Kharkov Polytechnic Institute», Kharkov, Ukraine*
[2] *Ukrainian State Coal-Chemistry Institute, Kharkov, Ukraine*
[3] *Kharkiv National University of Civil Engineering and Architecture, Kharkov, Ukraine*

Received December 11, 2018; Accepted February 18, 2019

Abstract

The results of studies of used lubricating oils, various functional purposes and greases obtained on their use as a thickener 5 wt % of secondary low-pressure polyethylene have been presented. Depending on the operating conditions in the samples of waste oils, the content of water and mechanical impurities varies in the range of 0.03-0.3 wt %, 0.08-1.30 wt %. Heating the oils to a temperature of 230°C showed that in the area of heating to a temperature of 200°C, the mass loss and decrease in viscosity are not significant, however, if this temperature is exceeded, an intensive process of destruction of oil hydrocarbons begins, and it will negatively affect the quantitative yield and performance properties of the lubricant. The obtained results showed that the lower the viscosity of the base oil from which the grease is made, the less stable it is during storage and operation, the worse its adhesive properties. Waste motor and transmission gear oils are advisable to use in the production of antifriction greases while hydraulic and industrial plastic lubricants are better to use in the production of protective greases.

***Keywords**: Plastic grease; thickener; polyethylene products; base oil; quality indicators.*

1. Introduction

Plastic lubricants (greases) today are one of the most popular petroleum products, which, due to their operational properties, are widely used in various industries.

Current trends that have emerged in the global oil refining and petrochemical industries are such that most of the manufacturers of plastic lubricants, to ensure competitiveness, are forced to go the way of reducing the final cost of their products while maintaining their quality.

The main directions in choosing such a path are the improvement (optimization) of the technological process of production and the expansion of the raw material base due to the involvement of new, cheaper materials in the technological process.

2. The purpose and objectives of the research

In general, the composition of any grease can be represented in the form of a structural block diagram shown in Fig.1.

The main component in the composition of greases is base oils (not less than 70 wt %) of mineral or synthetic nature [1-2].

Mineral oils, distillate or residual, are high-boiling fractions (boiling point > 350°C) obtained in primary oil refining plants by distilling fuel oil or tar under vacuum. Further, these fractions are cleaned using selective solvents from high-boiling paraffin hydrocarbons and tar-asphaltene substances.

Synthetic oils have better viscosity-temperature properties and higher stability against oxidation, compared to mineral oils. They are obtained by special directed synthesis in the presence of catalysts, which makes them more expensive than mineral oils. In view of what, they

are used in the manufacture of special types of lubricants for use in harsh environments. Synthetic oils include polyolefins, esters of carboxylic, phosphoric and silicic acids, polyglycolic esters and siloxane oils.

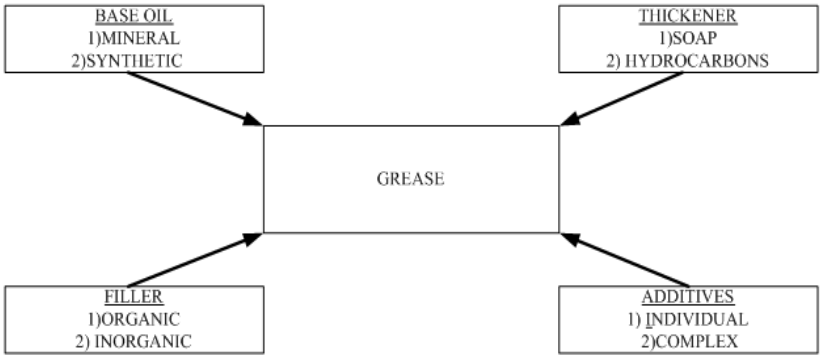

Fig. 1. The composition of the grease

The main property of base oil, both mineral and synthetic, on which many physical properties and tribological characteristics of plastic lubricants depend, is considered to be viscosity [3-4].

Thus, choosing cheaper basic components of grease – base oil and a thickener, you can significantly reduce the cost of the final product. In this regard, recently a number of works have appeared in the technical literature in which it is proposed to use waste oil as base oil - lubricating oils of various functional purposes. Under this approach, on the one hand, the expansion of the resource base of the technological process is gained and, on the other hand, the reduction of the harmful environmental impact of toxic industrial waste is achieved [5].

In the works [6-7], on the basis of waste oil, from which mechanical impurities, oxidation products of hydrocarbon oil and decomposition of additives, and a thickener – sodium and calcium soaps, obtained on the basis of bottom synthetic fatty acid residues were extracted, and the general-purpose antifriction lubricant was obtained. Also, as a base for the production of greases, besides used motor oils, purified waste vegetable oils can also be used [8].

A common drawback of the works cited above is the need for deep cleaning of the base oil, which is a very time-consuming, a multi-stage process that requires significant material costs for its implementation. This is mainly due to the softening effect of the detergent-dispersant additives found in the waste oil on the formation of the structure of lubricants thickened with metal soaps. Also, the oxidation products of hydrocarbons in the base oil have a negative effect on the process of structure formation of the grease during its production, and, as a result, the surface properties of commercial grease [6-7, 9].

At the same time, the additives found in the waste oil possess anticorrosive properties, and the oxidation products of hydrocarbons are surface-active substances, which ultimately will help to improve the tribological characteristics of plastic lubricants based on them.

The most rational approach in the development of technology for the production of greases based on used oils may be the search for a new type of a thickener, for the application of which it is not necessary to carry out a deep cleaning of the base oil.

Taking into account that temperature properties of the use of greases depend on the properties of the thickener, we will propose to use secondary high-density or low-pressure polyethylene for this purpose. The use of polyethylene as a thickener has a number of positive aspects: lubricants containing polyethylene have high rheological properties [10], polyethylene has a rather high melting point (more than 100°C) and, finally, recycled polyethylene is a harmful household waste, and its recycling allows to significantly improve the global environmental situation.

Therefore, in the future, we will consider the possibility of using various used lubricating oils, without their deep purification, for the production of plastic lubricants, in which the thickening agent is the secondary polyethylene.

3. Results and discussion

At the first stage of the laboratory study, the following used lubricating oils were taken: engine oil SAE5W-40 (sample No. 1), engine oil SAE10W-40 (sample No. 2), transmission oil SAE90W-140 (sample No. 3), hydraulic oil HLP 46 (sample No. 4), industrial oil I-40 (sample No. 5). In all the samples, the kinematic viscosity at 100 °C, the content of water and mechanical impurities, and the corrosive effect on metals: copper and steel plates were determined (Table 1).

Table 1. Results of laboratory research waste oils

Indicator name	Sample number				
	1	2	3	4	5
Kinematic viscosity at 100°C, mm^2/s	14.75	12.31	29.92	6.74	7.74
Water content, wt %	0.3	0.2	0.1	0.05	0.03
The content of mechanical impurities, wt %	0.11	0.09	1.3	0.10	0.08
Corrosive effect on the copper plate in the liquid phase, points	2	2	1	Not available	
Corrosive effect on the copper plate in the vapor phase, points	1	1	2	Not available	
Corrosive effect on the steel plate in the liquid phase, points	Not available				
Corrosive effect on the steel plate in the vapor phase, points	Not available				

Taking into account the data obtained, we note that the corrosive effect on metals in some samples is absent or varies in the margin from weak (1 point) to moderate impact (2 points), and the oils themselves do not need additional anti-corrosion treatment. The content of water and mechanical impurities, practically in all samples, also fluctuate in a rather narrow range of values and can be removed to the required level without the use of any special equipment, but only due to the sedimentation of oils when heated, on average, to 100-110 °C.

The exception, from the considered samples, is transmission oil with the content of mechanical impurities of more than 1 wt %, which is quite explicable by the conditions of its operation. In this case, it will be possible to apply centrifugation to the oil purification, or taking into account the nature of mechanical impurities and magnetic cleaning.

Further, the behavior of the oils under investigation was studied when they were heated in the temperature range up to 230 °C, with exposure at each fixed sample temperature for 30 minutes (Fig. 2).

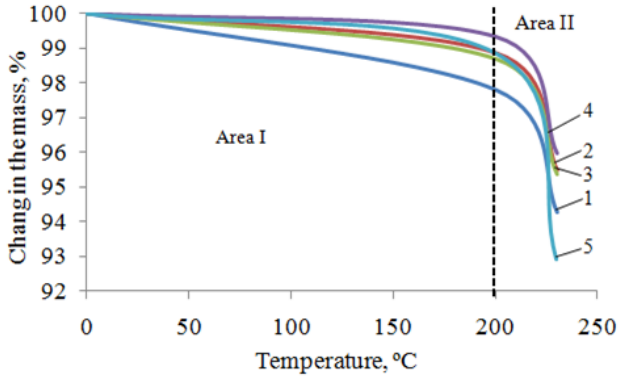

Fig. 2. The change in the mass of oil samples when heated: 1, 2, 3, 4 and 5 – sample numbers

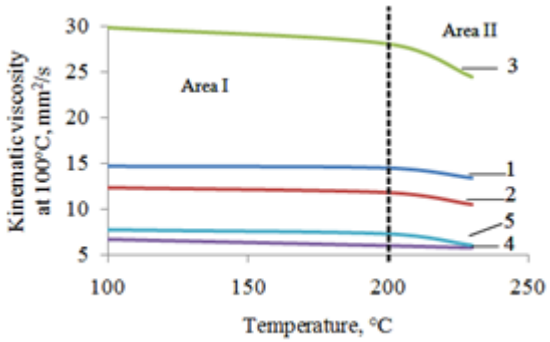

Fig. 3. The change in kinematic viscosity of oil samples when heated at 100°C: 1, 2, 3, 4 and 5 – sample numbers

When samples of waste oil are heated to a temperature of 200°C (Fig. 1), which corresponds to the area I, there is a gradual loss of sample mass, which is associated with evaporation of water and light hydrocarbon fractions, which can be formed during the operation of oil. After 200ºC, area II, there is a more significant loss of mass of the samples, which indicates the beginning of the destructive processes of oil occurring with hydrocarbons, which will deepen with increasing temperature. In this regard, the temperature of about 200ºC can be recommended as the final one during the heat treatment stage of the grease.

It is possible to judge the destructive processes occurring during the heating of oil samples by the rate of change of the kinematic viscosity, which is determined at 100°C (Fig. 3).

Thus, in the area I for all oil samples there is a slight decrease in the kinematic viscosity relative to the initial value. This change can be quantitatively characterized by the rate of viscosity change from temperature (by 1ºC): sample No. 1 v^{100}/t = 0.0020 (mm^2/s); sample No. 2 v^{100}/t = 0.0051 (mm^2/s); sample No. 3 v^{100}/t = 0.0180 (mm^2/s); sample No. 4 v^{100}/t = 0.0070 (mm^2/s); sample No. 5 v^{100}/t = 0.0044 (mm^2/s).

In area II, destructive processes of hydrocarbon raw materials occur and the same rates for each oil sample take higher values (by 1ºC): sample No. 1 v^{100}/t = 0.0037 (mm^2/s); sample No. 2 v^{100}/t = 0.041 (mm^2/s); sample No. 3 v^{100}/t = 0.122 (mm^2/s); sample No. 4 v^{100}/t = 0.0080 (mm^2/s); sample No. 5 v^{100}/t = 0.0413 (mm^2/s).

The next stage of the laboratory study involved obtaining, on the basis of the studied samples of used lubricating oils, plastic greases containing up to 5 % of a complex additive, in which thickened secondary low-pressure polyethylene acted as a thickener, in an amount of 5 wt % for raw materials.

In the resulting grease samples, some quality indicators (Table 2) were determined that were directly related to the viscosity of the base oil.

Table 2. Indicators of the quality of the resulting greases

Indicator name	Grease on the base oil				
	No. 1	No. 2	No. 3	No. 4	No. 5
Evaporation, wt %	0.16	0.22	0.12	0.25	0.34
Colloidal stability, wt %	7.10	8.23	5.90	9.65	11.96
Penetration at 25ºC, mm·0.1	224	237	219	324	308
Adhesive properties, discharge in a centrifuge, rpm	3000	3000	3500	2000	2000
Corrosive effects on metals (copper, steel)	Not available				

The obtained results showed that the lower the viscosity of the base oil from which the grease is made, the less stable it is during storage and operation, and the worse its adhesive properties are.

4. Conclusion

Used lubricating oils of various functional purposes, today, can be used as a raw material in the production of plastic lubricants. The use of such raw materials has a number of positive aspects: low cost, the presence of residual potential of additives and disposal of hazardous industrial waste.

However, it should be noted that when using metal soaps as a thickener, it is necessary to perform a deep cleaning of the oil from additives and products of aging, and this, in turn, affects the increase in the cost of the final product. In this case, effective thickeners, which allow obtaining high-quality greases with minimal cleaning costs while preserving the residual potential of the additives in the oil, are secondary polymers, in particular, low-pressure polyethylene.

The best raw materials for the production of anti-friction grease are engine and gear oils. The lubricant obtained on the basis of the oils has high stability and good adhesive properties during storage and operation. It makes most senses to use hydraulic and industrial oils in the

production of lubricants used in assemblies at relatively low rotational speeds or protective lubricants.

References

[1] NIIR Board of Consultants & Engineers. Modern Technology of Petroleum, Greases, Lubricants & Petro Chemicals, 2nd ed.; NIIR Project Consultancy Services, 2015; p. 704.

[2] Rizvi SQA. A Comprehensive Review of Lubricant Chemistry, Technology, Selection, and Design; ASTM International, 2009; p. 665.

[3] Casserly E, Langlais T, Springer SP, Kumar A. The effect of base oils on thickening and physical properties of lubricating greases. The European Lubricants Industry Magazine. 2018; 144: 32-37.

[4] De Laurentis N, Kadiric A, Lugt PM, Cann PM. The influence of bearing grease composition on friction in rolling/sliding concentrated contacts. Tribol. Int. 2016; 94: 624-632.

[5] Boughton B, Horvath A. Environmental assessment of used oil management methods. Environmental Science & Technology. 2004; 38(2): 353-358.

[6] Kornev AY, Ostrikov VV, Vigdorovich VI, Shihalev IN. Obtaining the greases based on waste oils. Science in Central Russia. 2013; 4: 11-14.

[7] Shihalev IN. A method for obtaining a dispersion medium of lubricants based on used motor oils and evaluating the performance of a grease in a friction unit. Science in Central Russia. 2015; 17(5): 98-104.

[8] Rajvanshi A, Pandey PK. Lubricating Grease from Waste Cooking Oil and Waste Motor Sludge. International Journal of Chemical and Molecular Engineering. 2016; 10(9): 1220-1223.

[9] Skobeltsin AS, Nemets VL. Study of the possibility of using used motor oils as a dispersion medium of soap greases. Oil Refining and Petrochemistry. 2005; 10: 32-36.

[10] Dixena R, Sayanna E, Badoni R. Recycled and Virgin HDPEs as Bleed Inhibitors and Their Rheological Influences on Lubricating Greases Thickened with PP and mPP. Lubricants. 2014; 2: 237-248.

To whom correspondence should be addressed: Dr. Andrey Grigorov, National Technical University «Kharkov Polytechnic Institute», 61002, 2 Kirpichova str., Kharkov, Ukraine, grigorovandrey@ukr.net

Petroleum and Coal

Article **Open Access**

EXPERIMENTAL AND CMG STUDY OF ASPHALTENE PRECIPITATION UNDER NATURAL DEPLETION AND GAS INJECTION CONDITIONS

Reza Hashemi[1], L. K. Kshirsagar[1], Somnath Nandi[2]*, P. B. Jadhav[1], Elias Ghaleh Golab[3]*

[1] Department of Petroleum Engineering, Maharashtra Institute of Technology, Paud Road, Kothrud, Pune - 411038, India
[2] Department of Technology, Savitribai Phule Pune University, Ganeshkhind, Pune - 411007, India
[3] Department of Petroleum Engineering, Omidiyeh Branch, Islamic Azad University Omidiyeh , Iran

Received December 12, 2018; Accepted February 18, 2019

Abstract

Problems associated with asphaltene deposition are key challenges for the upstream industry. In this research work, systematic experimental studies of asphaltene precipitation were conducted for two different Iranian crude reservoirs. Though gas injection in the reservoir enhances the crude productivity, it leads to higher precipitation of asphaltene compared to the natural depletion conditions. State of the art software tool namely CMG was utilized to predict the performance of the reservoirs for natural depletion condition as well as at high gas injection conditions. The CMG based predictions matched well with the experimental observations for both the reservoirs with reasonable accuracy.

Keywords: *Asphaltene precipitation; Gas injection; CMG; Simulation; Enhanced oil recovery.*

1. Introduction

Crude oil trapped in reservoir rock matrix is a complex mixture of hydrocarbons of various molecular weights, though sometimes other organic compounds containing small quantities of hetero atoms like nitrogen, oxygen, and sulfur are also present. The composition of crude varies based on its location as well as its maturity. Main constituents of crude oil are saturated hydrocarbons, aromatics, resins and asphaltenes (SARA). Asphaltenes are heterocyclic unsaturated macromolecules consisting primarily of carbon, hydrogen, and a minor proportion of hetero elements such as oxygen, sulfur, and nitrogen. It is really difficult to measure the molecular weight of asphaltene accurately due to its complex composition and the chemical association behavior [1]. Apart from causing the reservoir formation damage, asphaltene deposits could also result in reversal of the rock wettability to oil-wet, which leads to a lower recovery factor [2].Deposition of asphaltenes in oil wells, pumps, flow lines, pipelines, and production facilities can reduce well productivity, damage pumps, restrict or plug flow line and pipelines and foul production handling facilities [3-4].The precipitation phenomena can change the wetability of the formation of rock from water wet to oil wet which hinders the oil recovery efficiency [5]. Precipitated asphaltenes may also build-up in the near wellbore, reservoir rock and clog the porous matrix of the reservoir during drilling and chemical treatment [6].Injection of miscible or partially miscible gases is a promising enhanced oil recovery technique for many reservoirs. However,earlier studies indicated that the injection of gases namely carbon-dioxide (CO_2), nitrogen (N_2) and hydrocarbons like methane (CH_4), etc. changes the solubility of heavy components in the reservoir oil and causes asphaltene instability [7-9].Knowledge of asphaltene thermodynamic behavior is essential to understand the deposition characteristics. For the effective performance of a producing reservoir and to optimize the production, it is necessary to have accurate predictions of the amount of asphaltene precipitation as a function of the amount of solvent, temperature, and pressure, etc. [10]. The paper deals with a systematic investigation of asphaltene deposition for two reservoirs in Iran. A simulation study based on

Computer Modeling Group (CMG) WinProp module is also conducted in order to predict the asphaltene deposition at various operating conditions.

2. Experimental

Crude samples were taken from two south Iranian oil reservoirs Rag Sefid and Aghajari field, their properties are reported in Table 1. Reservoir fluid compositions and other basic properties were determined by means of the GC-MS (Gas-Chromatography Mass-Spectroscopy) technique and differential liberation tests. The samples were also determined for weight percent's of saturates, aromatics, resins, and asphaltenes. The compositions of the crude samples and the SARA analysis are presented in Tables 2 and 3 respectively.

Table 1. Properties of crude oil samples

Sample	Unit	Aghajari	Rag Sefid
Reservoir temperature	°F	158	212
Saturation pressure	PSIA	2715	2853
Solution GOR	SCF/STB	560	479
API gravity of residual oil	°API	25	22
Reservoir pressure	PSIA	4890	4158

Table 2. Composition of oil samples

Component	Mole percent		Component	Mole percent	
	Aghajari	Rag Sefid		Aghajari	Rag Sefid
H_2S	0.47	2.4	C_6	4.55	5.4
N_2	0.12	0.11	C_7	4.46	3.7
CO_2	2.33	4.94	C_8	3.85	4.28
C_1	38.83	24.01	C_9	2.27	2.87
C_2	6.06	6.89	C_{10}	2.41	2.73
C_3	5.9	5.51	C_{11}	2.56	2.68
i-C_4	1.04	0.9	C_{12+}	19.36	28.18
n-C_4	2.83	2.87	MW of C_{12} fraction	498	432
i-C_5	1.33	1.22	MW of reservoir oil	115	152
n-C_5	1.63	1.31	SG. of C_{12+} fraction @60/60°F	0.961	0.981

Table 3. SARA analysis

Sample	Unit	Aghajari	Rag Sefid
Saturated	wt%	59.58	32.90
Aromatic	wt%	26.12	39.85
Resin	wt%	6.3	12.02
Asphaltene	wt%	8.9	14.4

2.1. High Pressure High Temperature System (HPHT)

Asphaltene weight precipitation change by pressure is detected by High Pressure High Temperature (HPHT) Filtration device and associated IP143 tests [11]. An HPHT filtration system was available to perform natural depletion and with an injection of various gases namely nitrogen (N_2), carbon dioxide (CO_2), and methane (CH_4) injection tests under reservoir temperature. The system can provide reliable result until the pressure range of 10000 psi and temperature up to 482°F. The experimental set up, as represented by Fig.1, comprises of a Pressure-Volume-Temperature (PVT) cell, shaker, hydraulic pump, high pressure metal filter, oven, pressure transducer, high pressure sampler, pressure gauges, and recombination cell system, micron metal filter for the separation of asphaltene particle from original fluid sample in PVT cell.

In these sets of experiments, a conventional pressure depletion process was performed at the reservoir temperature for natural depletion. The experimental procedure in this step is described as follows:

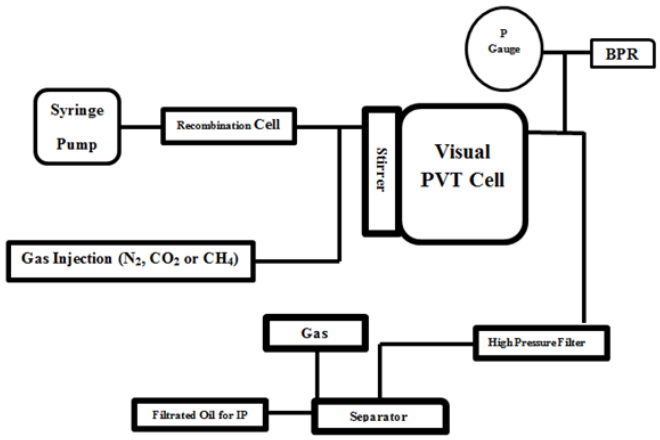

Figure 1. Schematic of the experimental setup

The equilibrium cell was carefully and properly cleaned and set at reservoir temperature. For RagSefid reservoir, the temperature is 212°F, and for the Aghajari reservoir, the temperature is 158°F. The intended oil was first filtered through a proper filter paper to separate any solids present in the oil and then inject into the cell under single phase conditions at reservoir pressure. A magnetic stirrer was used to shake the oil sample for 24 hr and speed up the equilibrium process. The cell pressure was lowered in subsequent predefined steps; at each stage, a high pressure filtration process was performed with a 0.5 filter paper. A limited volume of the sample around 10 ml for each pressure step was allowed to flow into the filter manifold at constant pressure and temperature. In order to avoid alteration of the asphaltene solubility, only a small dropping pressure should be applied around the filter. High pressure helium was applied to sustain a back-pressure on the downstream of the filter so that the fluid sample can flow gently through the filter with only a small pressure drop.

The oil which filtered injected in a separator and the asphaltene amount of the remaining oil is measured by standard IP143 procedure. The difference between the amount of asphaltene of the original sample and the filtered oil at each pressure determines the weight percent of precipitated asphaltene. The weight of precipitated asphaltene is then divided by the weight of the oil sample that is used in the IP143 procedure to give the weight percent of precipitated asphaltene. Since the experimental procedure is set to determine the amount of asphaltene of the filtered fluid, the asphaltene deposition problems in the equilibrium cell and the connection flow lines do not affect the precision of the experiments, and trustworthy data could be collected. Result for natural depletion is represented in Figures 2 and 3 for the crude sample from Rag Sefid and Aghajari oil fields respectively.

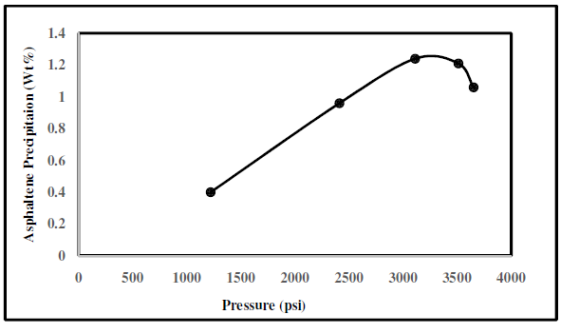

Figure 2. Natural depletion in Rag Sefid sample at its reservoir temperature, 212°F

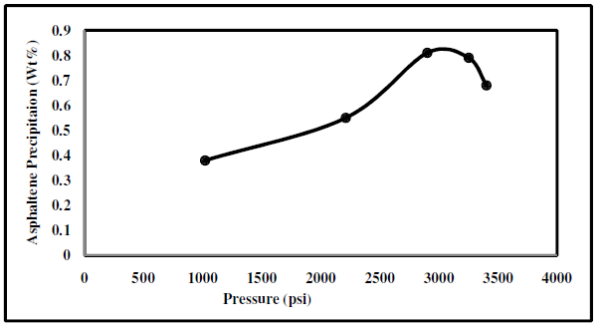

Figure 3. Natural depletion in Aghajari Sample at its reservoir temperature, 158°F

2.2. Gas injection

In this stage, a set of experiments were carried out to study the effect of different agents on the asphaltene precipitation behaviour of oil samples through the gas injection process. In these experiments, N_2, CO_2, and CH_4 gases were used systematically for infusion in miscible conditions. A known volume of new oil was injected into the equilibrium cell at the reservoir temperature while the cell pressure is set above the mixture saturation pressure to avoid phase separation during fluid transfer and recombination of oil and gas samples. In the present investigation, a small amount of gases (N_2, CO_2, or CH_4) was injected separately into the cell

under isothermal conditions. The mixture was permissible to equilibrate and settle down for 24 h to ensure full asphaltene precipitation. A high pressure filtration was presented to quantify asphaltene precipitation as a function of pressure. The sampling, filtration, and estimation processes were similar to natural depletion experiments.

3. Results and discussion

To test the effect of nitrogen injection on asphaltene instability, 10 mole percent of N_2 was recombined with Rag Sefid reservoir oil sample at a reservoir temperature of 212ºF. N_2 injection was repeated for the same sample with 15 and 20 mole percent of N_2 at the reservoir temperature of 212ºF. In the similar lines, to understand effects of nature of gas on asphaltene precipitation, other gases namely CO_2 and CH_4 injection were carried out at 10 mol %, 15 mol %, and 20 mol % concentrations. The observations are reported in Figures 4, 5 and 6. It has been observed that with an increase in gas injection, asphaltene precipitation increased. The same procedure was performed with the Aghajari field oil sample with the injection of 10, 15, 20 mole percent at the reservoir temperature of 158ºF. The respective results are reported in Figures 7, 8 and 9 respectively. As evident from these figures, increased gas injection enhances asphaltene precipitation, and it has also been observed that the precipitation is maximum with CO_2 injection and least with methane (CH_4) gas injection (please refer to Figures 4 – 9).

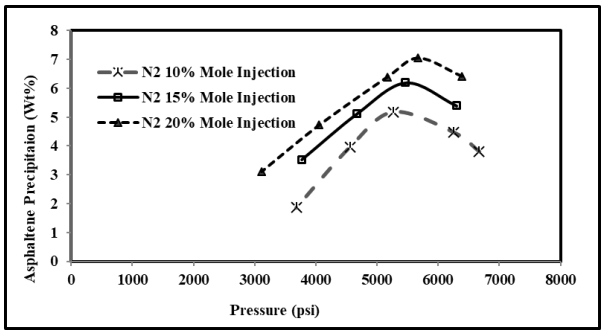

Figure 4. Effect of N_2 injection on asphaltene precipitation for Rag Sefid sample

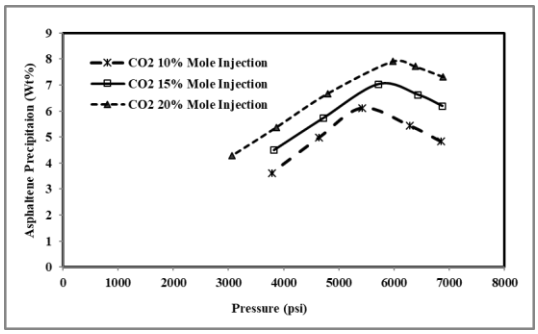

Figure 5. Effect of CO_2 injection on asphaltene precipitation for Rag Sefid sample

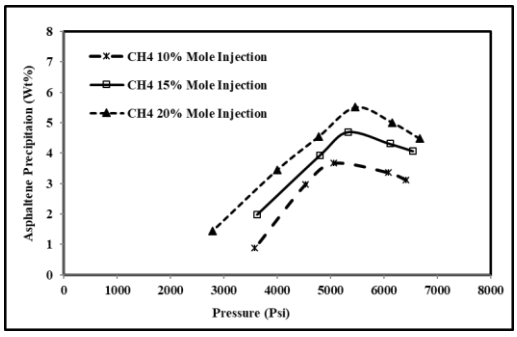

Figure 6. Effect of CH_4 injection on asphaltene precipitation for Rag Sefid sample

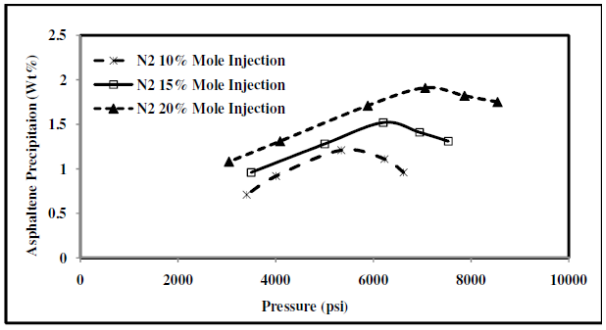

Figure 7. Effect of N_2 injection on asphaltene precipitation for Aghajari sample

Results of Figures 4, 5, 6 indicates that at lower pressures than bubble point pressure, the asphaltene re-dissolution decreases with increasing concentrations of gases and this is due to the formation of complex cluster structures of asphaltene molecules. With increasing pressure, at a pressure below the critical point pressure, the amount of precipitate in the constant concentration of gas increases, and with increasing concentrations of injected gas, this amount of precipitate will be increased. When the injection pressure reaches the point of the bubble point, the maximum amount of asphaltene precipitation will take place, and this precipitation will increase with the increased mole percentage of the gases as evident from Figures 4 for N_2 injection for the Rag Sefid reservoir sample. The identical trend is observed for CO_2 and CH_4

injections as evident from Figures 5 and 6. At higher pressures than that of the bubble point pressure, the amount of deposition is reduced, as the solubility of asphaltene is increased and hence the amount of precipitation will be reduced [5].

But it should be kept in mind that the total precipitate generated will not be disolved again, and this amount of precipitate will be greater than the amount of precipitate produced at the lowest pressure from the bubble pressure. With increasing pressure below the bubble point, the number of precipitate increases, since under these pressures, cluster deposits with complex compounds are created and increase with increasing pressure, preventing the dissolution of precipitates in oil. At the bubble point pressure, the highest precipitate concentration is generated for all the gas concentrations of 10, 15, 20 mole percent injections. It needs to be mentioned that with the increased amount of injected gas to the initial crude sample, the composition will be changed causing an increase in bubble point pressure (P_b). Therefore, with enhanced gas injection, the composition changes leading to the greater amount of asphaltene precipitation. But at higher pressures above the bubble point, the amount of dissolution of the precipitates increased due to the breakdown of the complex cluster structure formed at lower pressures [9].

With the lowering of the reservoir temperature, the mobility of asphaltene molecules in the system will be reduced, and therefore there will be less likelihood of the collision of the asphaltene molecules in the solution. Hence, the rate of clustering of the asphaltene molecules and, consequently, their precipitation will be decreased; it is evident from Figures 2 and 3 as the temperature is reduced, asphaltene precipitation is reduced from 1.3% to 0.8% for normal depletion conditions. The same trend is observed for gas injection conditions also, as evident from comparison of Figures 6 and 9, both with methane (CH_4) injection, while for Rag Sefied field asphaltene precipitation is almost 6% with 20 mol% gas injection vis-à-vis only 1.5% precipitation for Aghajari reservoir which operates at much lower temperature.

4. Simulation study

It will always be beneficial for operational purpose if a mathematical model is available which can predict the asphaltene precipitation with sensible precision. The WinProp module of CMG software was utilized to model and predict the asphaltene precipitation based on experimentally obtained data. CMG group has employed a pure solid model [12], and it can predict the asphaltene precipitation for the natural depletion condition and that for different gas injection conditions. The CMG WinProp package computes fugacity of asphaltene – expressed as pure, dense solid phase represented by Eqn. 1:

$$\ln f_s = \ln f_s^* + \frac{v_s(P - P^*)}{RT} \quad (1)$$

The prediction is valid for isothermal reservoir conditions of normally depleting reservoirs as well as for the enhanced oil recovery mechanisms via gas injections. As per guidelines [13], the heaviest oil fraction is to be spitted into two components one will be precipitating while the other one is a non-precipitating component. Though they have identical properties but these sub-fractions behave differently with light components, the precipitating fraction has higher interaction coefficient with light hydrocarbons. At the onset pressure for a given temperature as noticed experimentally, fugacity of the precipitated fraction is obtained utilizing equation of state (EOS). This fugacity is considered to be the reference fugacity of precipitation in Eqn. 1. Subsequently, the mole fraction of the precipitating fraction is obtained using Eqn. 2:

$$x_{Asph} = \frac{w_{Asph} \times MW_{Crude}}{MW_{Asph}} \quad (2)$$

where w_{Asph} denotes weight fraction of asphaltene present in the crude sample having molecular weight MW_{Crude}, the molecular weight of asphaltene is represented by MW_{Asph} and x_{Asph} is the mole fraction of asphaltene precipitated.

For modeling, the used matching parameters are solid molar volume and interaction coefficients between precipitating component and light end components of crude oil. Solid molar

volume affects the amount of precipitation at bubble point; higher molar volumes result in higher precipitation values. Interaction coefficients between precipitating and light end hydrocarbons control the precipitation and re-dissolution of asphaltene at pressures below the saturation pressure. Modeling results for natural pressure depletion experiments for both the reservoirs are represented in Figures 10 and 14 respectively. Results of asphaltene precipitation modeling for 20% nitrogen, 20% carbon dioxide, and 20% methane for the Rag Sefid reservoir are provided in Figures 11, 12 and 13. In all these plots, experimental values are provided for effective comparison; it is evident that almost all cased CMG simulation able to pick up the trend well. Similarly, CMG simulations for Aghajari oil samples were performed, and the trend obtained are represented along with the experimental observations in Figures 15, 16 and 17, though there are some deviations, the overall trend is picked up. The significant observation is that the CMG simulation can able to correctly predict the trend of the highest amount of asphaltene precipitation for CO_2 gas injection and the least one for methane injection as observed experimentally (kindly refer to Figures 16 and 17).

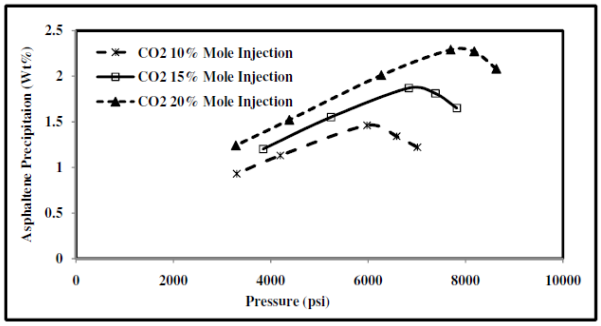

Figure 8. Effect of CO_2 injection on asphaltene precipitation for Aghajari sample

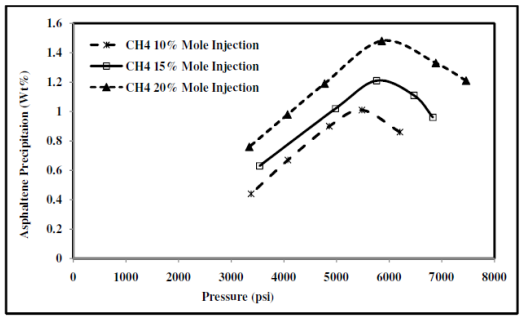

Figure 9. Effect of CH_4 injection on asphaltene precipitation for Aghajari sample

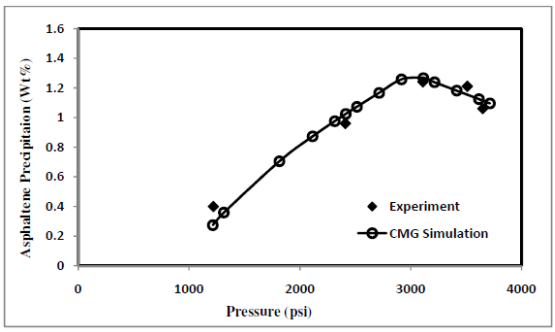

Figure 10. CMG WinProp predictions for natural depletion process in Rag Sefid sample

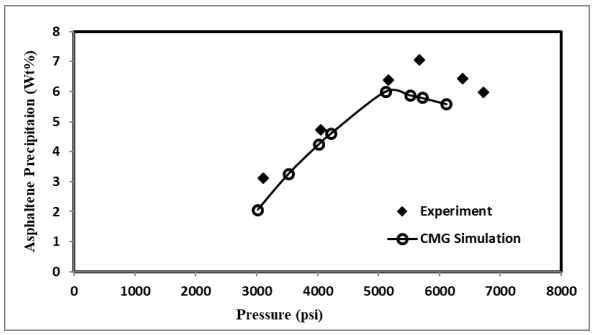

Figure 11. CMG WinProp predictions for 20% N_2 gas injection process in Rag Sefid sample

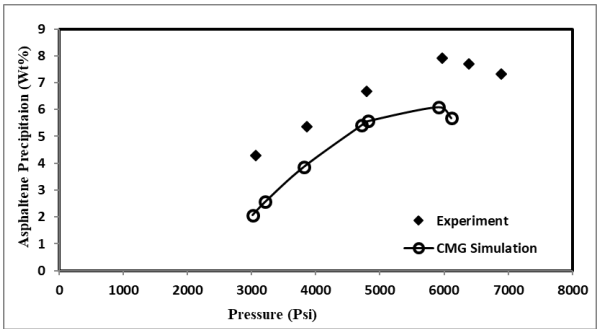

Figure 12. CMG WinProp predictions for 20% CO_2 gas injection in Rag Sefid sample

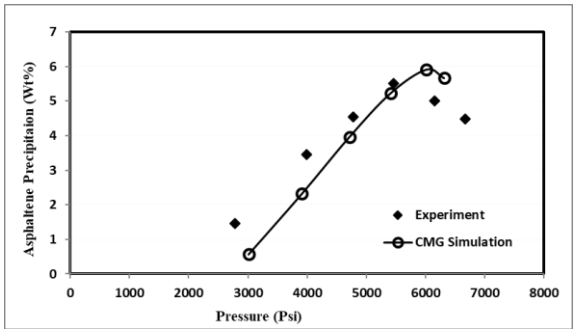

Figure 13. CMG WinProp predictions for 20% CH_4 gas injection in Rag Sefid sample

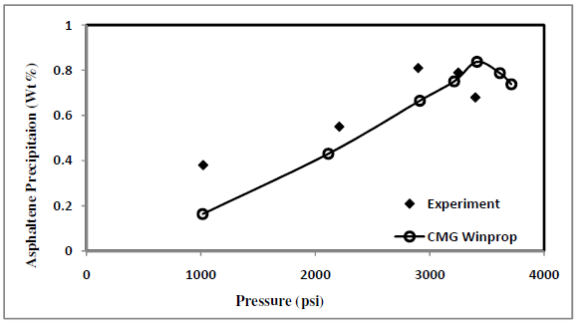

Figure 14. CMG WinProp predictions for natural depletion process in Aghajari sample

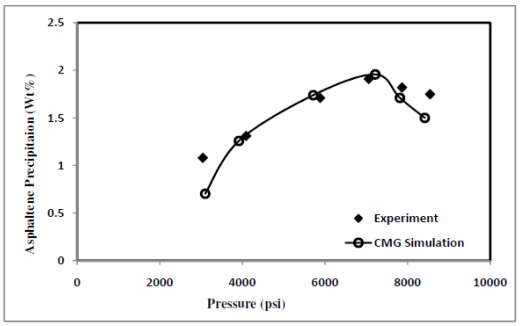

Figure 15. CMG WinProp predictions for 20% N_2 gas injection in Aghajari sample

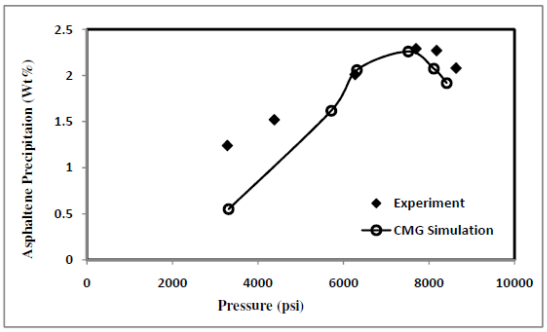

Figure 16. CMG WinProp predictions for 20% CO_2 gas injection in Aghajari sample

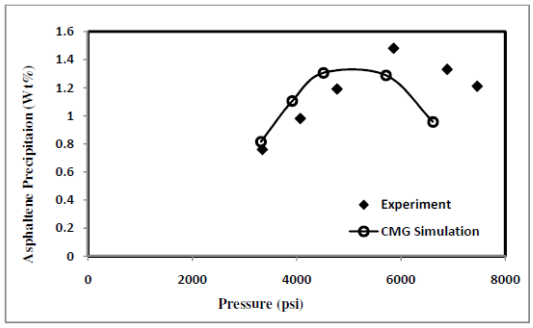

Figure 17. CMG WinProp predictions for 20% CH_4 gas injection in Aghajari sample

5. Conclusion

While the crude reservoirs are injected with CO_2, N_2 and CH_4 gases for enhanced oil recovery, the maximum amount of asphaltene precipitation is reported with CO_2 injection, and minimum amount of asphaltene precipitation is noticed with CH_4 gas injection. Increase in the concentration (mole percent) of gas injection caused an increased amount of asphaltene precipitation for both the crude samples. The experimental observation was well supported by CMG simulations. Below the bubble point pressures, the amount of asphaltene precipitation increased with the increasing pressure. Whereas, above the bubble point pressure the amount of asphaltene precipitation decreases with increasing pressure. A detailed and systematic study of Rag Sefid reservoir and Aghajari reservoir oil samples were conducted in the presence of gas injection. The study will be beneficial in designing the enhanced oil recovery mechanism of the fields using gas injection techniques.

Symbols

API	*Crude specific gravity*	*(°API)*
f_s	*fugacity*	*kPa*
f_s*	*Reference fugacity*	*kPa*
MW	*Molecular weight*	*g/mol*
P	*Pressure*	*psi*
P_b	*Bubble point pressure*	*psi*
R	*Gas constant*	*8.314 J/mol. K*
T	*Absolute temperature*	*K*
v	*Molar volume*	*m^3/mole*
w	*Weight fraction of asphaltene precipitated*	*(-)*
x	*Mole fraction*	*(-)*

Subscripts

Asph Asphaltenes Crude Crude sample

References

[1] Andersen SI, and Speight JO. Thermodynamic models for asphaltene solubility and preci-pitation. J. Pet. Sci. & Eng., 1999; 22: 53-66.

[2] Yan J, Plancher H, Morrow NR. Paper No. SPE 37232. SPE International Symposium on Oilfield Chemistry, Houston, (1997).

[3] Cimino R, Correra S, del Bianco A, and Lockhart TP. Solubility and phase behavior of asphaltenes in hydrocarbon media. in Asphaltenes: Fundamentals Applications; Editors: Sheu, E. Y., Mullins, O. C.; Plenum Press, New York, Pages 97-130, (1995).

[4] Saniere A, Hénaut I, and Argiller JF. Pipeline transportation of heavy oils, a Strategic, economic and technological challenge. Oil & Gas Sci. Technol. – Rev. IFP, 2004; 59(5): 455-466.

[5] Buckley JS, and Wang J. Crude oil and asphaltene characterization for Prediction of wetting alteration. J. Pet. Sci. & Eng.,2002; 33: 1889–1893.

[6] Leontaritis KJ, Amaefule JO, and Charles RE. A systematic approach for preventionand treatment of formation damage caused by asphaltene deposition. SPE Prod. Facil., 1994; 9(3): 157-164.

[7] Srivastava RK, Huang SS, and Dong M. Asphaltene deposition during CO_2 flooding, SPE Prod. Facil., 1999; 14(4): 235.

[8] Jamaluddin AKM, Joshi N, Iwere F, and Gurpinar O. An Investigation of asphaltene instability under nitrogen injection. Paper SPE 74393, Presented at the SPE International Petroleum Conference and Exhibition, Mexico, 10-12 February (2002).

[9] Negahban S, Bahamaish JNM, Joshi N, Nighswander J, and Jamaluddin AKM. An experimental study at an Abu Dhabi Reservoir of asphaltene precipitation caused by gas injection. SPE Production & Facilities, 2005; 20(2): 115-125.

[10] Agrawala M, Yarranton HW. An Asphaltene association model analogous to linear polymerization. Ind. Eng. Chem. Res., 2001; 40: 4664-4672.

[11] ASTM, Standard Test Method for Determination of Asphaltene (Heptane Insoluble In Crude Petroleum and Petroleum Products. 2000.

[12] Nghiem LX, Hassam MS, and Nutakki R. Efficient modeling of asphaltene Precipitation. in: SPE Ann. Tech. Conf. and Exh.,3–6 October (1993), Houston, Texas.

[13] CMG Group (2015) Win Prop Manual.

To whom correspondence should be addressed: Dr. Somnath Nandi, Department of Technology, Savitribai Phule Pune University (formerly University of Pune), Ganeshkhind, Pune – 411007, INDIA

Petroleum and Coal

Article **Open Access**

SEDIMENTARY RESPONSE TO SALT RELATED TECTONICS AND ITS HAZARDS IN A HYDROCARBON FIELD, KWANZA BASIN, ANGOLA

O. A. Anyiam[1], B. A. Jolly[2], and S. M. Harry[3]

[1] *Department of Geology, University of Nigeria, Nsukka, Nigeria*
[2] *Department of Geology, Ahmadu Bello University, Zaria*
[3] *Belemaoil Producing Ltd, Port Harcourt*

Received August 20, 2018; Accepted February 18, 2019

Abstract

The presence of extensive Aptian salt basin underlying the south Atlantic passive margin has in so many ways influenced the pattern of tectonics and its sedimentary response during the Cretaceous. Aptian salt in the Kwanza Basin was deposited in two sub-basins separated by a margin-parallel chain of platforms on which salt is either small or absent. Salt withdrawal and dissolution during the mid-Cretaceous led to the formation of a series of north-south trending salt ridges and associated depo-centres that provided, and controlled the accommodation space for the deposition of marine sediments. The post-salt marine deposition was controlled by the subsidence of sediment packages into synforms between salt walls initiated by extension of the underlying Aptian salt. Thermal subsidence was locally enhanced by halokinesis in the vicinity of the salt horizon, creating sediment down-building which led to the initiation of prominent salt domes. These thick salt-bearing successions in the basin form sealing hydrocarbon traps with abnormally high fluid pressures (AHFP). Forecasting of AHFP in evaporates is difficult due to the absence of transition zones in salts. Such poor pressure forecast and risk evaluation in an oil field can result in well kicks and subsequent blow-outs. Better seismic imaging and interpretation of the subsurface reduces the risk of possible blow-out hazard in such hydrocarbon field.

Keywords: *Salt-related tectonics; sedimentary response; abnormal fluid pressure; blow-out*

1. Introduction

The Kwanza Basin (south Atlantic passive margin) is characterized by predominantly Cretaceous sedimentary section with both pre-salt lacustrine and post-salt marine sediments. A thick section of Aptian salt divides the lacustrine section from the overlying marine section. The good seismic image of the Kwanza Basin allows a completely chaotic and bumpy horizon to be displayed. Careful seismic interpretation revealed a series of salt ridges and their associated depo-centres that provided the accommodation space for marine sediments. The basin is more than 300 km wide, from the onshore exposures of the Precambrian Congo craton to the Angola abyssal plain [1].

This paper focuses on the sedimentary response to the Aptian salt- related tectonics in the Kwanza Basin (Fig. 1) and the abnormally high fluid pressure associated with thick salt sequences that form sealing complexes in many oil regions. A better understanding of these salt related seals in a basin helps to reduce the risk of well-bore kicks and eventual blow-outs in the oil field.

2. Regional geological settings

The Kwanza Basin was formed during the Early Cretaceous opening of the South Atlantic Ocean [1-3]. The basin's fill started with a continental regime in the early Cretaceous (Neocomian) and ended in Tertiary with the marine regime (Fig. 2).

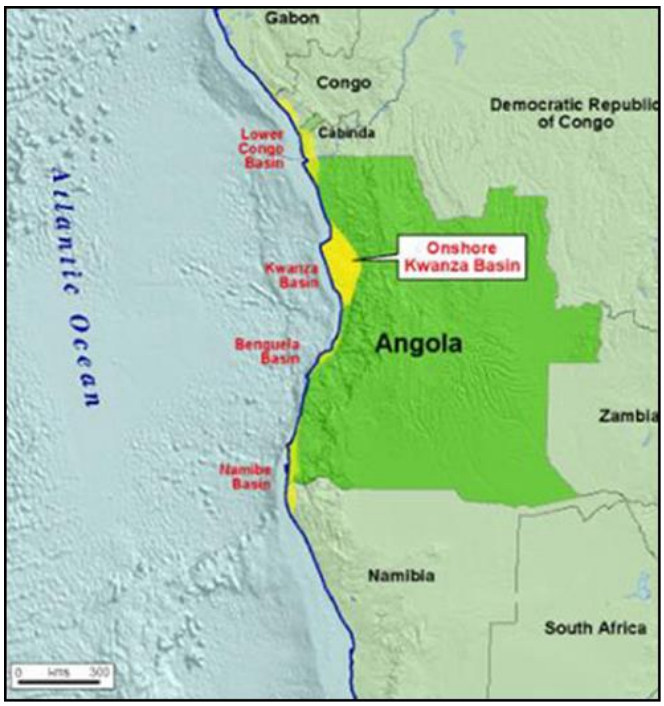

Fig.1. Map of Africa showing the location of Kwanza Basin in the south Atlantic passive margin [11]

Early Cretaceous time witnessed the splitting of the huge continent named Pangea, which gave rise to two continents known as South America and Africa. This break up process corresponds to the rifting phase. Huc [4] stated that this separation was initiated by the thinning and dislocation of mainly granitic crust. The crustal thinning was caused by the local uprise of partially melted igneous rocks from underlying asthenosphere. The resulting rifts were then occupied by large lakes such as the East Lakes of the East African Rift, and thick lacustrine sediments were deposited in those lakes.

The next process was an ocean opening in which the asthenospheric magma began to be emplaced at the mid-oceanic ridge, where basaltic oceanic magma was generated to make up the floor of the ocean that is being formed [5].

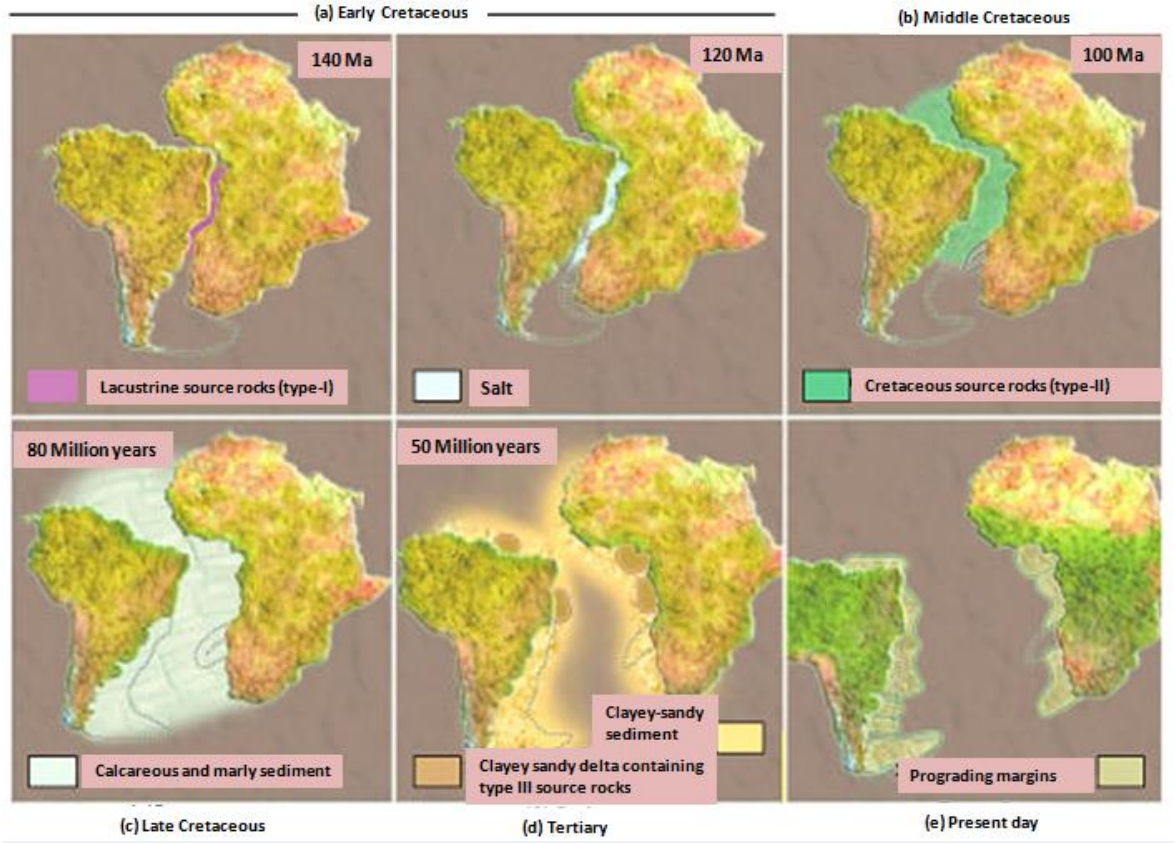

Fig.2.a-e. Schematic evolution of coastal basin in areas around south Atlantic passive *margin (modified from [4])*

This is the drift phase. As the ocean basin continues to open, the oldest oceanic crust, close to the continental margins, become progressively colder with increasing density which led to warping under the effect of their weight. During the opening process, in Aptian, the pathway gave way to oceanic basin of irregular depth and moderate width. The basin underwent periodic isolation from the ocean circulation which then started evaporation process resulting in the accumulation of large quantities of salt. These salt layers covered the pre-salt lacustrine sediments. The confinement of the differ-rent sub-basins at that time led to the regional deposition of organic rich sediments. The ope-ning of the ocean still continued in the late Cretaceous. So the ocean became ventilated, thus interrupting the conditions favourable for the accumulation of organic rich source rocks [5]. In the Tertiary, thick layers of terrigenous sediments were accumulated as deltas, to fill the available space produced by the down warping of the margin.

3. Methodology

The study of the "chaotic bump" seismic volume involves the review of the geological settings of the Kwanza Basin from some related published studies. The 3-D seismic volume (Vertical range: - 594 ms to -2488 ms) was then loaded on Petrel software for 3D geological interpretation (Fig.3). It is a methodology-based approach, which specifically involves data management, seismic data viewing and structural interpretation. These specific actions were achieved using the imaging and interpretations of terminations and horizons, faults, facies, geobodies (salt, channels, mud diapirs) etc. The top and bottom horizons of the volume were picked and gridded to observe the topographic lows and highs. Then, the seismic volume was realized and most of the attributes (chaos, variance with smoothing, phase shift, RMS amplitude, instantaneous frequency, local structural dip and rendered volume) and surface picks were done on a cropped volume with a vertical range of -756 ms to -1424 ms. An analogue basin with similar sedimentary response to salt-related tectonics was used to analyze and interpret the data from Kwanza Basin. The seismic reflections are dull and discontinuous (chaotic) in some places, thereby making it difficult to pick the horizons as continuous reflectors. As a result, horizon misties were encountered which necessitated the imposition of geologic interpretations on the seismic using manual tracking method.

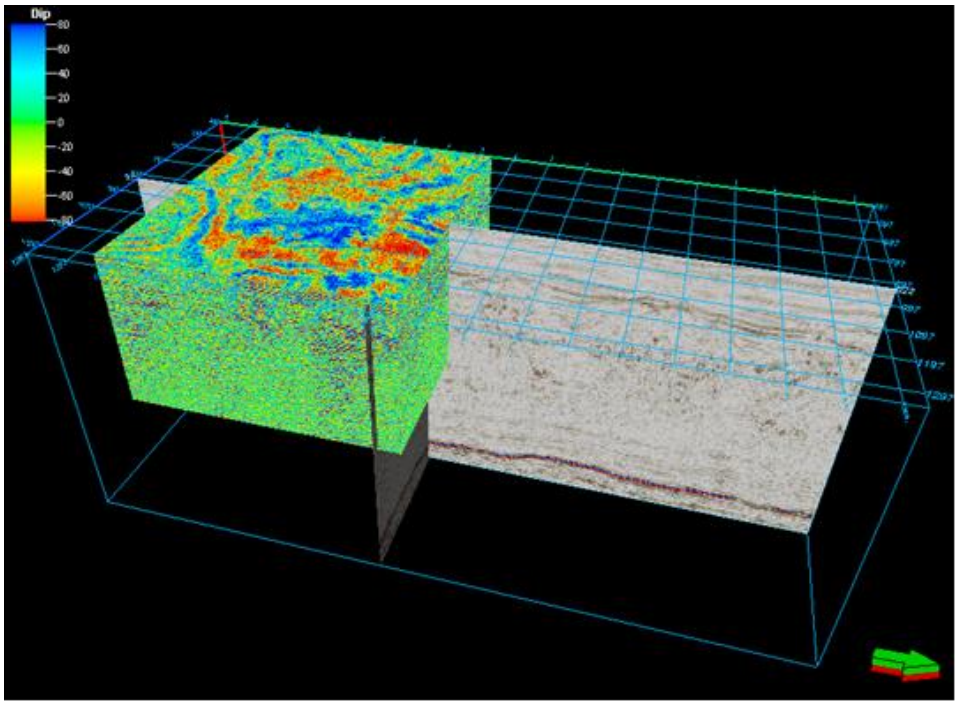

Fig.3. The raw-data (3D-Seismic Volume – Inline and Xline with a cropped volume of the study area)

4. Results and discussions

The result of the seismic volume shows a series of sediment packages 'pods' that have subsided into synforms (furrows) between salt walls (Figs. 4 & 5), initiated by the extension of the underlying Aptian salt.

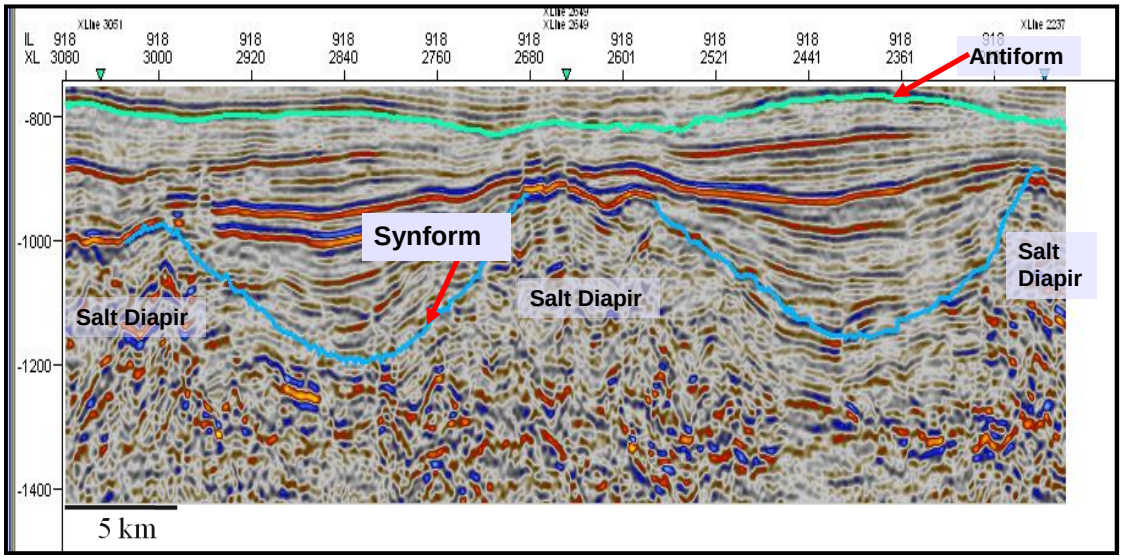

Fig.4. In-Line 918 showing the structural styles in the "Chaotic_Bumps" seismic volume

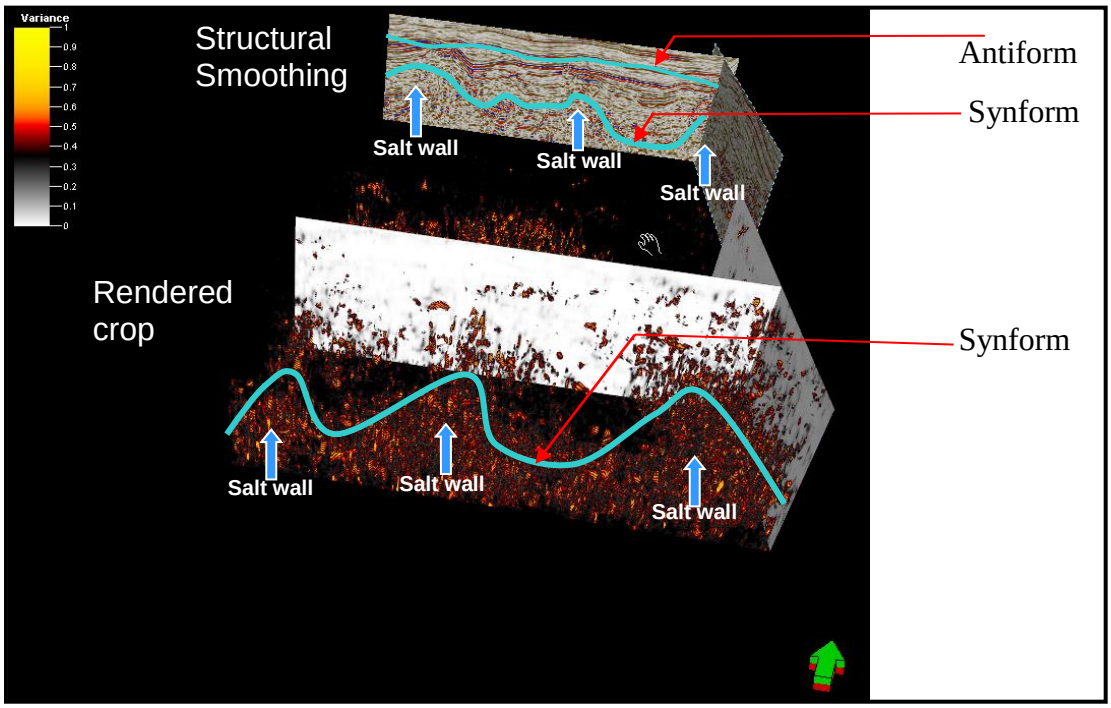

Fig.5. Rendered crop volume and structural smoothing Inline/Xline, showing the synform and antiform structural style and the salt dome withdrawal

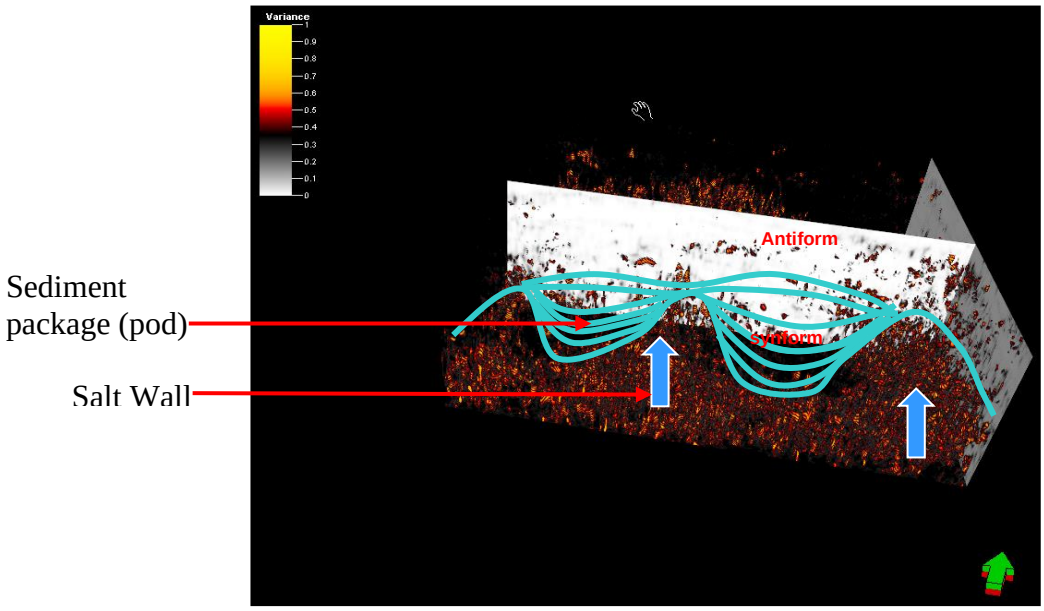

Fig.6. Rendered crop volume with Inline/Xline, showing sediment packages (pods) between chaotic salt walls

This observed sediment synforms and salt walls (antiforms) confirm the model for the evolution of salt walls and sediments by Hodgson et al. [6]. Such salt tectonics is strictly tied to regional extensional deformation because salt is weak and does not undergo compaction. In this kind of setting, salts can rapidly rise to the surface through the space created by thinning and separation of the fault blocks by passive diapirism and spread over the sediments as allochthonous salts. The salt observed in this study did not form sheets, but formed salt walls that separated the sediment pods. The topographic lows are infilled with post- salt marine sediments which progressively displaced the salt under the pods (Fig. 5). The pod subsidence ceased when the salt has been completely displaced (salt welds) and the pods no longer provide accommodation at the surface. This observation agrees with those of Jackson and Talbot [8], in their work in the Gulf of Mexico, where these grounding surfaces were also observed. The displacement of these salts was as a result of salt withdrawal downdip; to build other salt walls as crustal extension continues. Salt dissolution could also cause salt withdrawal in this type of basin [9]. As the salt continued to withdraw downdip, the old pods became relative highs as synforms form over collapsing salt walls. Series of these sediments as seen in Figures 4-6 form bumpy horizons, with the antiforms having the usual trapping attributes of anticlines.

4.1. Hazards associated with salt-bearing sequences

Thick salt-bearing sequences like those encountered in the study area form sealing complexes in many oil and gas regions of the world. Such sedimentary basins have accumulations of hydrocarbons and brine with abnormally high fluid pressure (AHFP) [6-7]. Mapping of these evaporate sequences and prediction of their over-pressured intervals are indeed a challenging problem. This is because of the absence of transition zones in evaporates, unlike what is obtained in typical clastic seals. As a result, there are no indications of approaching over-pressured intervals, as can be observed in clastics. So, reservoir pressure within these formations changes abruptly, with no gradual transition [10]). Another complicating factor in such evaporate seals is their non-uniform gas saturation, which gives an erroneous information on the amount of gas build up within the salt interval [10].

Over-pressured fluid accumulations are usually encountered immediately underneath the salt section, which is drilled easily and at a high rate. It is rather very difficult in such an environment to observe an increase in drilling rate caused by a decrease in the rock strength or by a decrease in differential pressure between the borehole and the reservoir.

Because of the peculiar physical and chemical nature of salts relative to the surrounding sediments, all indirect techniques should be utilized in the abnormal pressure forecast. Such indirect methods must afford to establish patterns of the geologic evolution of regional or local structures and associated hydrocarbon accumulations. For reliable AHFP forecast, it is necessary to delineate the salt plugs, walls, and sheets, with their corresponding depths using 3-D seismic interpretation software as applied in this study. This will enable the wellsite geologist to apply appropriate mud pressure within these delineated intervals to keep the formation fluid in check during drilling. The predictive precursors of the AHFP include the evidence of vertical gas migration along flanks of salt plugs and associated fracture zones (and faults); the appearance of "gas clay" in circulating mud (i.e., plastic greenish-grey and brown clay with gas bubbles).

Currently, the available techniques for the identification of over-pressured zone are based on well logs obtained during drilling (MWD). This means that an abnormally high pressure zone is identified within the localized vertical wellbore; with an unknown areal extent. This prevents the undertaking of protective measures in the nearby wells drilled subsequently. As a result, unexpected abnormal high pressure can be encountered at different stages of hydrocarbon exploration and development. However, we can mitigate this problem if a detailed seismic analysis has been undertaken to identify the salt bodies and their geometries. For instance, where the salt forms large canopies – there is a higher tendency for anomalously high fluid pressure beneath; and if it is more of salt walls – the impact may be less than that of canopy although that could lead to compartmentalization of pressure. In essence, by accurately analysing the architecture and geometry of the salt bodies, in addition to delineating their depth of occurrence as we have done in this study; can serve as the first step in predicting the potential hazards.

5. Conclusion

The salt- related tectonics in the Kwanza Basin is principally influenced by crustal extension, which allows salt to flow laterally from areas of high load to areas of lower load, restricted only by friction on the edges of the salt and the weight of the overburden. This load gradient was as a result of the regional extension, lateral variations in the weight of overburden and temperature gradients in salts which cause dissolution and subsequent salt withdrawal.

Aptian salt was progressively displaced from under the sediment pod to form salt walls and ridges, while the intervening topographic lows were filled up with marine sediments. Because these salt layers formed efficient regional decollements, they, therefore, controlled the style of sedimentation and deformation in the Kwanza Basin. On the other hand, thick salt-bearing sequences like that in the Kwanza Basin form hydrocarbon sealing complexes with abnormally high fluid pressure. Proper delineation of these salt intervals in a basin leads to better forecasting of the subsurface pressure build up, which invariably reduces the risk of well kicks and subsequent blow-out. This requires special seismic imaging techniques to enhance better high pressure forecast.

References

[1] Hudec MR, and Jackson MPA. 2004. Regional restoration across the Kwanza Basin, Angola: Salt tectonics triggered by repeated uplift of a metastable passive margin. AAPG Bulletin, 2004; 88(7) 971-990.

[2] Brink AH. Petroleum geology of Gabon basin: AAPG Bulletin, 1974; 58: 216-235.

[3] Karner GD, Driscoll NW, McGinnis JP, Brumbaugh WD, and Cameron NR. Tectonic significance of syn-rift sediment packages across the Gabon–Cabinda continental margin. Marine and Petroleum Geology, 1997; 14: 973-1000.

[4] Huc AY. Petroleum in the South Atlantic. Oil and Gas Science Technol. Rev. IFP, 2004; 59(3): 243-253.

[5] Nombo-Makaya NL, and Han CH. 2009. Pre-Salt Petroleum System of Vandji-Conkouati Structure (Lower Congo Basin), Republic of Congo. Research Journal of Applied Sciences, 2009; 4(3): 101-107.

[6] Hodgson NA, Farnsworth J, and Fraser AJ. Salt-related tectonics, Sedimentation and hydrocarbon plays in the Central Graben, North Sea, UKCS. *In:* R. F. P. Hardman (ed.) 1992. Exploration Britain: Geological insights for the next decade. Geological Society Special Publication, 69:31-63.
[7] Zilberman VI, Serebryakov VA, Gorfunkel MV, Chilingar GV, and Robertson-JR JO. Prediction of Abnormally High Pressure in Petroliferous Salt-bearing Sections. Journal of Petroleum Science & Engineering, 2001; 29(1):17-27.
[8] Jackson MPA, and Cramez C. Seismic recognition of salt welds in salt tectonic regimes. Tenth Annual Research Conference, Gulf Coast Section, Society of Economic Paleontologists and Minerologists Foundation, Programs and Abstracts, 1989; 66-71.
[9] Jackson MPA, and Talbot CJ. Salt Canopies. Tenth Annual Research Conferene, Gulf Coast Section, Society of Economic Paleontologists and Minerologists Foundation. Programs and Abstracts, 1989;72-78.
[10] Hudec MR, and Jackson MPA. 2007. Terra infirma: Understanding salt tectonics. Earth Science reviews, 2007; 8 (1-2): 1-28.
[11] www.rpsgroup.com/Angola.aspx

To whom correspondence should be addressed: Dr. Okwudiri. A. Anyiam, Department of Geology, University of Nigeria, e-mail: okwudiri.anyiam@unn.edu.ng

Petroleum and Coal

Article **Open Access**

DISTINCT METHODOLOGIES TO ASSESS THE CONDITIONS OF PETROLEUM RESERVOIRS WITH RESPECT TO ONSET OF SAND PRODUCTION

Mohammad M. Ghiasi[1], Mohammad F. Ghasemi[2], Vahid Heidaripour[3], Amir H. Mohammadi[1]**

[1] *Discipline of Chemical Engineering, School of Engineering, University of KwaZulu-Natal, Howard College Campus, South Africa*
[2] *Schmidt Institute of Physics of the Earth, Russian Academy of Sciences, Bolshaya Gruzinskaya, 10-1 Moscow 123242, Russia*
[3] *Department of Computer Science, Kharazmi University, Tehran, Iran*

Received December 27, 2018; Accepted February 18, 2019

Abstract

Handling such problem as sanding in the petroleum industry leads to safe and more economic access to the required energy for development. With the objective of making strategy in order to deal with sanding the results of assessing the conditions at which sand production takes place in petroleum reservoirs have been reported in this communication. In this work, CART-Decision Tree, Random Forest and Extremely Randomized Tree (Extra Tree) have been employed to conduct the classification for the first time. The dominating variables in sanding including total vertical depth, transmit time, cohesive strength of the formation, water and gas flow rates, bottom hole flowing pressure, drawdown pressure, effective overburden stress, shut per foot, and perforation interval have been introduced into the employed approaches for obtaining the best models. The modeling process was performed on the basis of the gathered field data from the literature. All the developed models classify the sanding conditions with 100% accuracy. The performance of the presented models proves their capability in determining the possible sand production in a real petroleum field. Hence, the presented methodologies will pave the way for effective sand control plan.

Keywords: *Sand production; classification; modeling; reservoir; decision tree.*

1. Introduction

1.1. Energy security and Sand production phenomenon

In view of growth in population and advancement in standards of living as well, the energy consumption is increased. According to the U.S. Information Administration (EIA) [1], the increase in the world energy consumption is fully expected to happen for the upcoming decades. Hence, a lot of importance is attached to energy security and conservations.

The growth in the world economy can be attributed to the advances in technologies since the 1750s. It is clear that development of new technologies/ methodologies, leading to efficient utilization of energy resources, is crucial for sustainable development. Nowadays, large share of energy demand of the world is provided by petroleum fluids. Indeed, fossil fuels, especially crude oil and natural gas, play a significant role in supplying the energy demand [2]. Hence, solving/ handling the petroleum production, processing, and transportation problems provides safe and more economic access to the required energy for development.

The sand production is a costly phenomenon that brings substantial damages and problems to the petroleum industry. In the petroleum industry, sand production is known to be the coexistence of solid particles with the produced reservoir fluid. It is believed that about 70% of the hydrocarbons exist in oil and gas reserves are in not well-consolidated reservoirs [3-4]. Because of initiation of drilling and starting hydrocarbon production from a well, leading to

redistributing the pore pressure and stresses around the production cavity, the hydro-mechanical equilibrium of the sandstone formation is disrupted. Consequently, the sand particles travel from the reservoir into the production well [5-7]. Based on the field observations, the sand volumetric concentration in systems of oil pipe ranges between 1% and 40% [8-9].

Various problems are associated with the sand production. Further to the damages of sanding on production facilities, this phenomenon is responsible for the instability of the wellbore and production cavities [10-12]. As a result, production losses increase. Additional costs may also be imposed owing to depositional of waste sand [3,13]. This can be the reason for the increase in costs of maintenance and operation. Equipment erosion indicates another problem caused by sanding [14]. It should be noted that the limited sand production might noticeably increase the productivity of the well in conventional reservoirs [11]. In view of the aforementioned facts, implementation of strategies for sand control and management is highly crucial. To achieve this, the potential of the defined reservoir to sand production is extremely beneficial.

1.2. Literature review

Great efforts have been made in the study of sand production by many researchers. Since the sand arches have been observed in the field around each hole in the casing of well, several researchers employed the phenomenon of sand arching for identifying the possibility of production of sand [15-17]. In 2001, the sand arches behavior, stability, and morphology were evaluated by Bianco and Halleck [3]. In 1989, Morita *et al.* [18] studied the effects of different variables using an analytical approach. Based on the reported results, stress and pressure distribution of wellbore around well, drag forces induced by fluid flow, formation rock strength, perforation geometry and shot density, and history of cyclic loading are the main parameters that affect sanding. In 1991, analyses of five common sand problems in the field were provided by Morita and Boyd [19]. More works on the subject of sand production is reviewed by Ranjith *et al.* [7].

In 2014, the permeability evolution law within process of sand production of weak sandstone was investigated by Nie *et al.* [20]. In another work, a coupled numerical approach was presented on the basis of Lattice Boltzmann Method and Discrete Element Method by Ghassemi and Pak [21]. The proposed model was then employed for simulating the sand production. More recently, Jiang *et al.* [22] studied the ureolytic activities of purified urease enzyme and Bacillus megaterium in both oxic and anoxic conditions for their promising use in control of subsea floor production.

Several models including numerical, empirical, and theoretical are available in the literature for sand prediction [5,17,23-24]. In 2000, Doan *et al.* [25] presented a numerical model for sand gravitational deposition in a horizontal well in heavy oil reservoirs. Similar to other fields of petroleum and natural gas engineering, the algorithms developed based on the artificial intelligence (AI) have been employed in investigating the sand production. In 1999, a neural-based method was proposed by Kanj and Abousleiman [26] for estimating the sanding onset for Northern Adriatic Basin gas wells. Further to the above, Azad *et al.* [27] presented another neural network model for predicting the critical bottom hole flowing pressure inhibiting sanding. Recently, Khamehchi *et al.* [28] presented two models including back-propagation neural network and particle swarm optimization neural network to estimate the critical total drawdown as an indicator of sanding in gas and oil wells.

2. Objective of the study

In 2016, Gharagheizi *et al.* [29] developed a model based on the least square version of support vector machine (LS-SVM) classification method for predicting the sand production onset in reservoirs. It was shown that the LS-SVM classification approach can successfully be employed for prediction of conditions under which sand production occurs. To the best of our knowledge, there is no other published work in this area.

The high performance of the SVM methodology in classification problems has been approved [30]. However, direct understanding of the rules obtained by SVM approach is hard.

Furthermore, they are costly in computation [31]. In view of this, the aim of this study was applying CART-decision trees, Random Forest, and Extra Trees for the application of interest and exploring their performances in classification. Decision trees present several benefits. For example, the background is easy to understand and interpret; they are convertible to set of if-then rules, and there is no need to know about the nature of the data [32].

In this work, three classification methods including CART-Decision Tree, Random Forest and Extremely Randomized Trees (Extra Trees) are utilized to identify the sanding conditions. These algorithms are used for the first time for the application of interest.

The used data in this study for classification include a databank of 31 wells of Northern Adriatic Basin [14]. Amongst the investigated wells, 23 wells are reported as problematic wells with respect to the production of sand; the other wells are considered to be sand free [14]. According to the work of Moricca *et al.* [14] the following parameters are main variables that affect the production of sand: effective overburden stress (EOVS), bottom hole flowing pressure (BHFP), total vertical depth (TVD), transmit time (TT), drawdown pressure (DD), cohesive strength of the formation (COH), shut per foot (SPF), water and gas flow rates (Qw & Qg), perforation interval (Hperf). Before introducing the collected data points into the aforementioned classification algorithms, the data points were tested for incomplete data. Consequently, two sets of gathered databank were removed. Table 1 gives the finalized data points used for the modeling process. In the last column of Table 1, entitled field data, 1 means sand production is observed and 0 means sand production is not observed.

To achieve the goal, the rest of the work is pursued as follows: first, the background of Decision Tree, Random Forest and Extremely Randomized Trees (Extra Trees) are introduced. Second, the development of models for predicting the possibility of the sand production is presented. Finally, the developed models and their results are investigated and discussed.

3. Theory

3.1. Decision tree

As one of the most well-known algorithms for classification, decision trees can be utilized for extraction of classification rules from the data [33]. Decision trees have highly flexible hypothesis space and their theory is easy to understand. Commonly, the obtained results by decision trees are comparable or higher than the outputs of the available methods of classification [34]. In the development of decision trees, there is no need to tune a large number of variables [35].

Decision trees are categorized as non-parametric methods of supervised learning that employ the strategy of divide and conquer. There is no need of assumptions regarding the distributions of the input data. A decision tree is consisting of a root node, internal nodes and terminal (leaf) nodes. Classification in decision tree starts at the root node and each non-leaf node (non-terminal node) asks a question about some features and has N children, where N is the number of possible answers. According to the answer, this process continues to the subtree of one child, while a leaf node is met.

For example, if in a decision tree all features have binary values (in other words all question have "yes" or "no" answer) the algorithm of prediction is like this:

```
Algorithm DecisionTreePredict(tree, test point)
if tree is of the form Leaf(guess) then
    return guess
else if tree is of the form Node(f, left, right) then
    if f = yes in test point then
        return DecisionTreePredict(left, test point)
    else
        return DecisionTreePredict(right, test point)
    end if
end if
```

Table 1 Gathered field data for investigating the sand production from petroleum reservoir

No.	TVD	TT	COH	Q_g	Q_w	BHFP	DD	EOVS	SPF	H_{perf}	Field observed
1	319	105	22	42.3	5672	133.2	27.8	651	4	14	1
2	3182	105	21.9	51.2	68	140.4	16.6	642	4	16	1
3	3366	100	24.7	66.9	157	156.2	18.9	601	4	6	1
4	3647	100	29.6	80.6	85	153.8	57.8	670	8	20	1
5	4548	85	53.2	48	886	209.1	58.9	823	4	18	1
6	4088	85	39.5	72.7	116	147	44	781	2	17	1
7	2100	115	10.8	28.5	724	160.1	8.9	300	4	15.5	1
8	1930	132	9.7	27.5	695	175.5	11.2	245	4	11.5	1
9	2139	112	11.1	36.8	280	185.5	6.1	283	4	10.5	1
10	2380	110	13	23	42	113	47.4	413	6	11	1
11	1122	150	5.7	108	0	107	8	115	12	10.5	1
12	1340	130	6.6	51	52	126.6	14.4	140	12	6.5	1
13	1070	170	5.5	82	70	103.8	0.7	111	4	9	1
14	1920	130	9.6	111	0	248	82	153	4	9	1
15	2530	100	14.3	58	68	302.2	97.8	242	4	4.5	1
16	1640	145	8	94	1260	189	46.8	150	12	10	1
17	2130	120	11	86	112	268.3	31.7	179	4	3.5	1
18	3655	100	19.8	69.8	1780	287.6	9.1	553	4	21	1
19	3668	100	30	75.8	150	272.3	9.2	571	4	21	1
20	1503	125	7.3	139.5	35	152.3	2.2	177	4	11.5	1
21	3170	100	21.7	48	2823	222.1	6.4	485	4	16	1
22	3197	95	22.1	73	273	184.6	48.6	535	2	12	0
23	3230	105	22.6	117	68	210	10	517	27	4	0
24	3684	95	30.3	108.7	36	266.6	59.7	581	1	12	0
25	3005	93	19.5	55	91	67	1	615	33	4	0
26	3790	85	32.5	93.4	77	217.2	124.4	654	8.5	12	0
27	2750	98	16.5	125.8	75	251.8	3	372	8.5	4	0
28	2983	98	19.2	48	28	102	6.1	581	12	4	0
29	3175	100	21.8	30.3	1.698	216.1	17.1	492	20	4	0

The traditional decision trees can be classified into several methodologies as follows:

- Decision trees: such algorithms as Iterative Dichotomiser 3 (ID3) [33] and C4.5 [36] are the examples. ID3 creates a multi-way tree, finding for each node (i.e. in a greedy manner) the categorical feature that will yield the largest information gain for categorical targets. Trees are grown to their maximum size and then a pruning step is usually applied to improve the ability of the tree to generalize to unseen data. C4.5 is very similar to ID3 but features do not need to be categorical. It dynamically defines discrete intervals of continues values to achieve this. C4.5 converts the trained trees into sets of rules in the format of if-then. This accuracy of each rule is then evaluated to determine the order in which they should be applied. Pruning is done by removing a rule's precondition if the accuracy of the rule improves without it [36].
- Fuzzy decision trees: like fuzzy ID3. This algorithm is on the basis of a fuzzy implementation of the aforesaid ID3 method [37-38].
- Oblique decision trees: Classification and Regression Trees (CART) [39] is an example of oblique decision trees. It is similar to C4.5. CART uses a generalization of the binomial variance called the Gini index while C4.5 uses entropy for its impurity function. CART constructs binary trees using the feature and threshold for continue data.

CART algorithm selects the most important and significant parameters and eliminates non-significant parameters and is impervious to transformations that means if some parameters change to their logarithm or square root the structure of tree will not change. CART isolates the outliers in a separate node and finally it can easily handle noisy data. With this advantages and scalable complexity and also ease of implementation, CART method seems a reasonable

to choose. Hence, in this work, among various algorithms for decision tree, the CART method was employed for the application of interest.

3.2. Ensemble methodologies

Ensemble methods of classification use multiple different classifiers and aggregate their result by voting instead of using a single classifier. The main principle behind ensemble methods is that a set of weak classifiers can form a strong classifier if they come together in a right way. Every error is possible to make by a minority of classifiers and aggregate theme can achieve the optimal classification. Random Forest and Extra trees (Extremely Randomized Trees) are both ensemble methods that are used in this work. The following sections introduce these types of ensemble approaches.

3.2.1. Random forest

Random Forest is an ensemble of trees grown using some form of randomization and have a structure like the decision tree. In test and prediction phase, an instance is classified by sending it down every tree and aggregating the results.

In growing trees, training data are divided into some random subsets and each tree is grown using a different subset. Also, randomness can be injected in the selection of features at each node to determine the split. A well-known procedure namely Forest-RC is introduced for growing random forest [40]. There is also other algorithms for this purpose in the literature [39,41]. In Forest-RC, the split at each node is based on linear combinations of features rather than one single feature. This allows dealing with cases with only a few inputs supplied and a small set of train data, which is our main motivation to use it. And another advantage is that a Random forest does not over-fit [42] and we can run as many trees as we want.

General training procedure of L trees is as follows:

1. N Sample cases at random with replacement to create a subset of the data. The subset size is 2/3 of all samples.
2. At each node:
   - m predictor variables are selected at random from all the predictor variables.
   - The predictor variable that provides the best split, according to some objective function, is used to do a binary split on that node.

Different m values result in different systems for Random forest: m << number of predictor variables. More details about the theoretical background of random forest classifiers are documented elsewhere [42].

3.2.2. Extra trees

In 2006, Geurts *et al.* [43] introduced the extremely randomized trees. This method is similar to the random forests algorithm in the sense that it is based on selecting at each node a random subset of K features to decide on the split and trees are built using complete samples without partitioning [44]. In other words, the same input training set is used to train all trees. In fact, the difference between random forest and an extra tree is where the randomness injected.

In this method, each tree grows as follows:

- At each node K of random splits including random choice of variable xi, and random choice of threshold t, will be selected and kept among these the one which maximizes the score to grow a tree. More details of score measure are available elsewhere [45].
- Growing of trees continues until all subsamples at all leaves are pure in terms of outputs or there are less than nmin learning samples in them.
- When a tree is grown, each leaf Lj is labeled with a prediction y ˆ_j defined as the local sample average of the output variable, given by (|Lj| is the number of learning cases that reach leaf Lj).

- $\hat{y}_j = \frac{1}{|L_j|} \sum_{(x^i, y^i) \in x^i} y_i$ (1)

Extra Tree also handles the probable outlier effect on the models induced and its computational complexity is N log N; where N is the size of training data set. There is a more formal description of the algorithm and a detailed discussion of its main features in the literature [43].

4. Development of models

Every time we used decision tree in this work, training was done with CART algorithm described above. Here is CART pseudo-code for GUIDE classification tree construction [39]:

1. Start at the root node.
2. For each ordered variable X, convert it to an unordered variable X by grouping its values in the node into a small number of intervals. If X is unordered, set X = X.
3. Perform a chi-squared test of independence of each X variable versus Y on the data in the node and compute its significance probability.
4. Choose the variable X∗ associated with the X that has the smallest significance probability.
5. Find the split set {X∗ ∈ S∗} that minimizes the sum of Gini indices and uses it to split the node into two child nodes.
6. If a stopping criterion is reached, exit. Otherwise, apply steps 2–5 to each child node.
7. Prune the tree with the CART method.

In Ensemble making, injection of randomness is in the classifier construction and the prediction of the ensemble is given as the averaged prediction of the individual classifiers. This is applied for both Random Forest and Extra Tree classifiers.

For developing the models including CART-decision tree, random forest, and extra tree models, the gathered databank was randomly separated into two sub data sets: training dataset (about 80%) and test dataset (about 20%). The allocated data points for training were employed in the development process. On the other hands, the assigned data points for the test were used for evaluation of the capability of the constructed model in predicting the unseen data.

5. Results and discussion

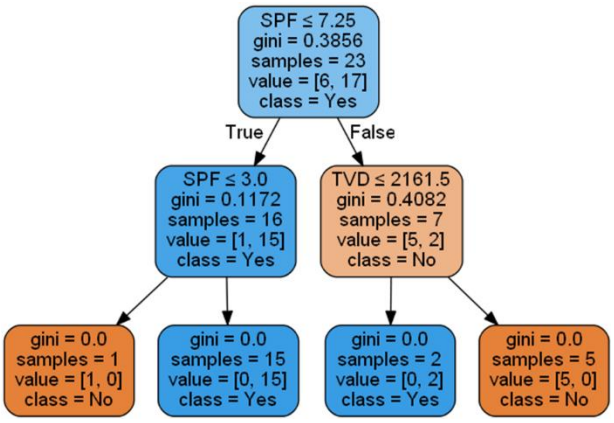

Figure 1. The presented CART model for assessing the conditions of petroleum reservoirs with respect to onset of sand production

As mentioned earlier, 23 data points were used for training and 6 data points were employed as test examples. The obtained model for investigating the sand production status employing CART classifier is shown in Figure 1. Based on the obtained results, the presented CART model reproduces all 23 training samples and 6 test examples same as corresponding field data points. Hence, the accuracy of the proposed CART algorithm is 100%.

The procedure of obtaining the output through the proposed CART model is illustrated using two examples as follows: for the first example, consider the case 22 from Table 1.

According to Figure 1, we start with the root; the SPF of the selected data point is less than 7.25, and this is true. Hence, we go to the left subtree. The SPF is again the criteria in the second stage; SPF of the data is equal to 2 and is less than 3.0 and again this is true. So we

go to the left leaf and the class is No. this means there is no sand production. With accordance to the real data, the result is correct.

For the second example, the case 1 from Table 1 is chosen. Start with the root node, the SPF for this case is 4; compare it with the root node, and, in this case, it is less than 7.25. Hence, we go to the left subtree. Again, compare SPF with SPF in this node and is bigger than 3.0; and we go to the right leaf and the class is Yes, i.e. the sand production is observed. According to the real data the predicted result is correct.

As can be seen from Figure 1, among the main parameters including EOVS, BHFP, TVD, TT, DD, COH, SPF, Q_w, Q_g, and H_{perf} only SPF and TVD are considered in the CART model. Indeed, the built CART model is able to forecast the conditions at which sand production is occurred by introducing these two parameters. It may be concluded that these two parameters are the most important variables for investigation of the sand production using CART algorithm.

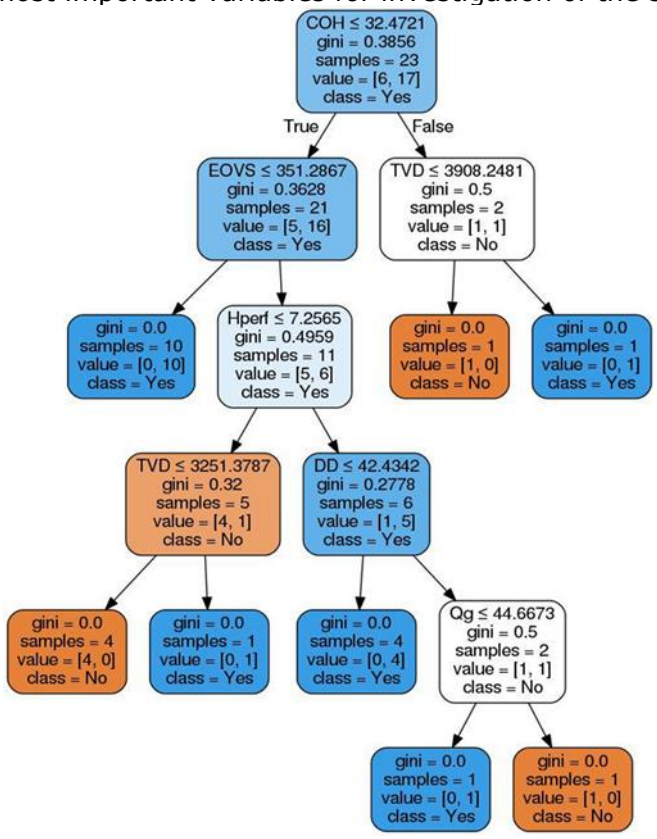

Figure 2. The presented Extra Tree model for assessing the conditions of petroleum reservoirs with respect to onset of sand production

The constructed Extra Tree model for studying the sand production is shown in Figure 2. The proposed Extra Tree model provides the accuracy of 100% for both training and test subdata. As aforesaid before, this type of classifier has extremely randomized behavior. As a result, multiple runs can generate various structures. Similar to the previous model, the procedure of the developed Extra Tree model is clarified using two examples. For the first case, the first data row from Table 1 is selected. The root says that if COH is less than 32.4721, then go to the left subtree; the COH in the first row is 22. Consequently, we are in the left subtree. This stage says if EOVS is less than 351.2867, then go to the left, else go to the right; EOVS is 651. So, we go to the right subtree. In this level, the H_{perf} must be considered. H_{perf} is 14 and is greater than 7.2565; hence, the next node is the root of the right subtree. DD is 27.8 and is less than 42.4342 and we go to the left subtree. Finally, the last leaf is reached and it says that the class is Yes.

As another sample, from Table 1, we chose a case in row 29. COH is 21.8 and is less than 32.4721; so, we go to the left subtree and EOVS is 492 which is greater than 351.2867. Hence, we go to the right subtree; considering the Hperf, we must go to the left subtree. In this stage, we compare the value of TVD; TVD is 3175 and is less than 3251.3787 and is true; and again we go to the left leaf. Based on the model, the class is No.

As it depicted in Figure 1, the presented Extra Tree model considers more parameters as compared to the built CART model. Indeed, in the case of sand production from petroleum reservoirs, decision making via the developed Extra Tree needs the values of EOVS, TVD, DD, COH, Q_g , and H_{perf}.

The third algorithm for studying the sand production is based on Random Forest. The developed Random Forest model consists of 10 weak classifiers. The forest aggregates their votes to predict the final result. All trees of the proposed forest are shown in Figure 3.

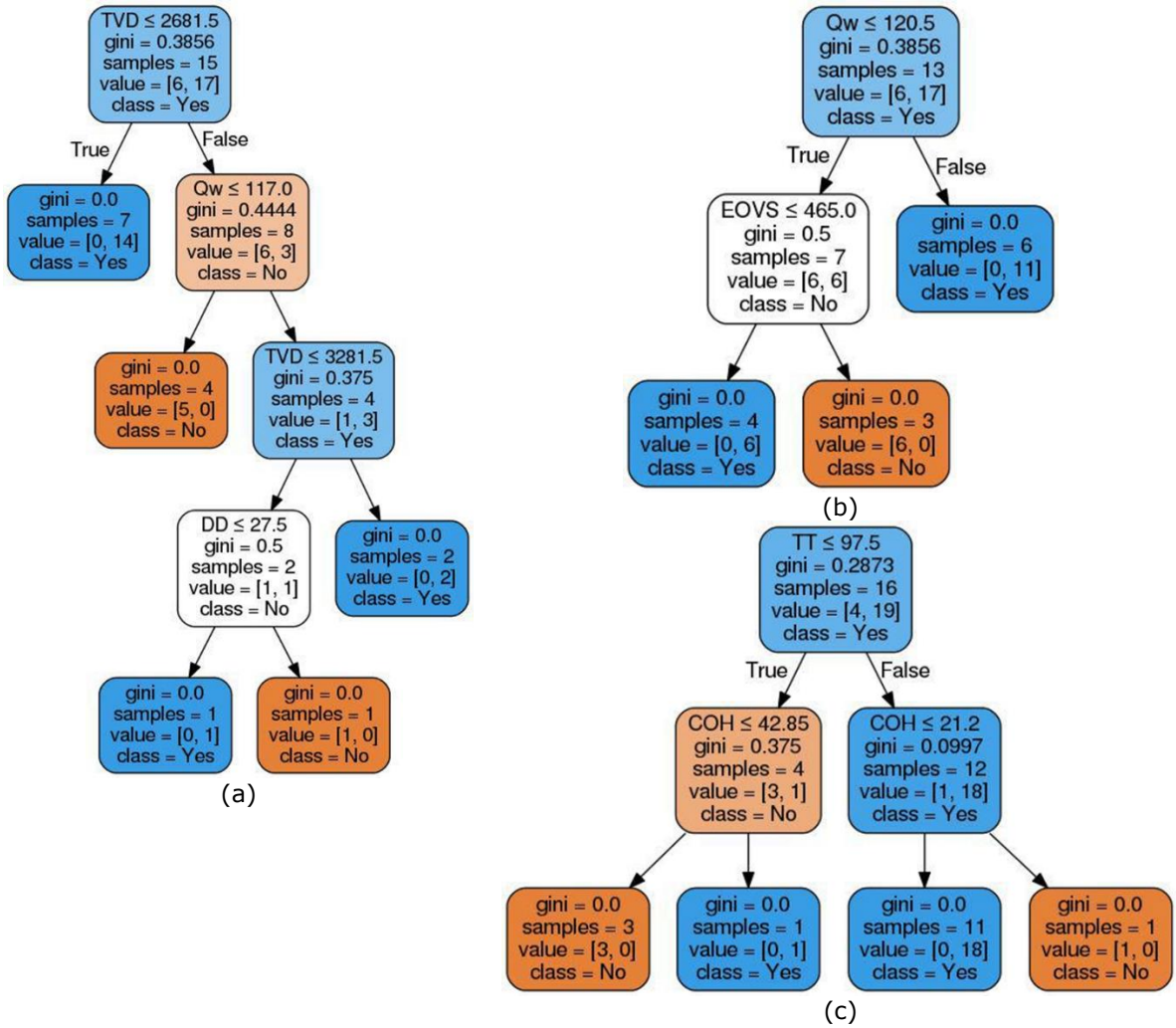

Figure 3. The trees of the presented Random Forest model for assessing the conditions of petroleum reservoirs with respect to onset of sand production (a-c)

For showing the procedure of using the developed Random Forest algorithm, Figure 3 and data in row 8 from Table 1 were employed. The root of Figure 3a says that compare TVD; and the TVD number in this case is 1930 and is less than 2681.5. Hence, we go to left and class is Yes. Based on the next tree of the presented Random Forest model, shown in Figure 3b, if Q_w is less than or equal to 120.5, the left is selected. In the data, Q_w is 724 and is greater than 120.5; this means that the right leaf must be selected. Finally, the class is Yes. Pursuing the procedure, the class obtained by remaining trees of the proposed Random Forest model, shown in Figure 3c to 3j, is Yes. As explained, all the trees in the model present the class of Yes. Hence, the final result of the built Random Forest model for the selected data shows that the sand production is observed.

Demonstrated in this section, all the presented models in this work including CART, Extra Tree, and Random Forest models are capable to predict the right conditions for sand production phenomenon. However, in view of the fact that the available databank for modeling purpose is not extensive and the number of test samples are not adequately enough, the presented models may have low generalization capability on the new and unseen data points.

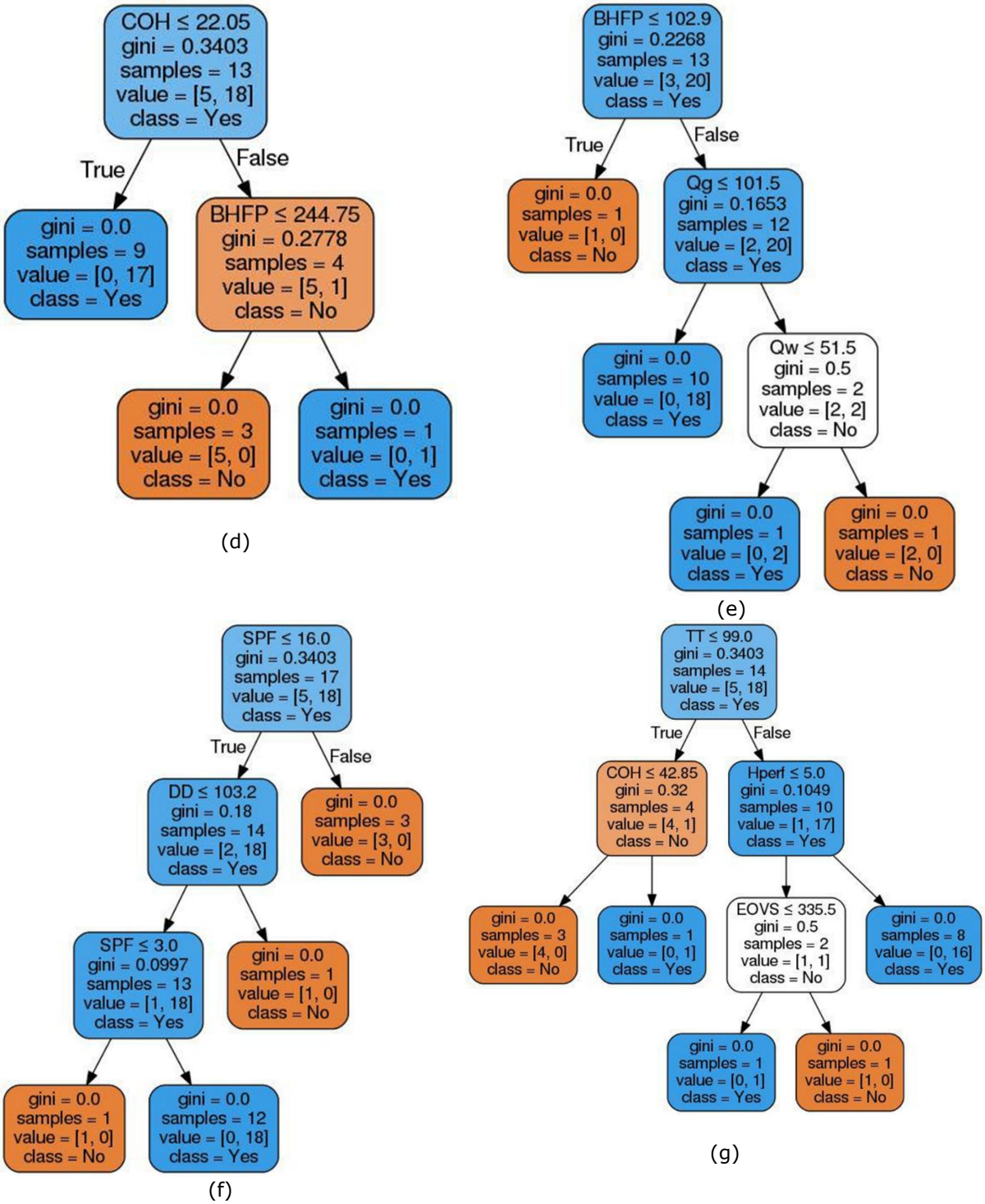

Figure 3. The trees of the presented Random Forest model for assessing the conditions of petroleum reservoirs with respect to onset of sand production (d-g)

Further to the above, since the CART classifier considers only two parameters, it may have the minimum generalization ability amongst the presented models. It should also be noted that introducing a databank with more reliable data points to the aforementioned algorithms may result in obtaining different structures for the models.

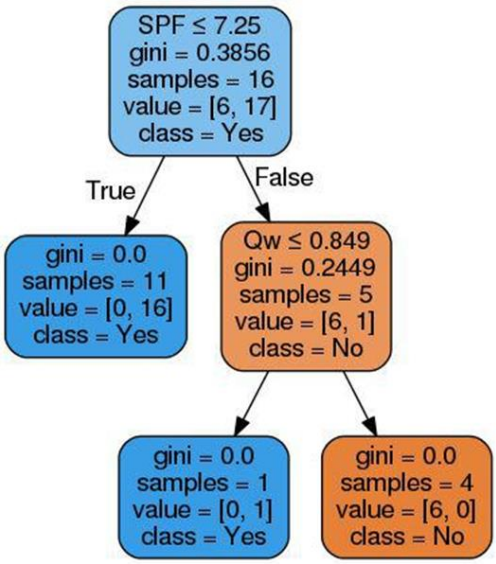

(h)

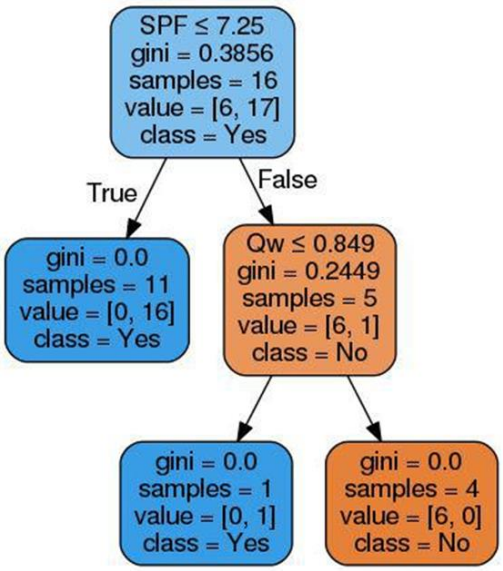

(i)

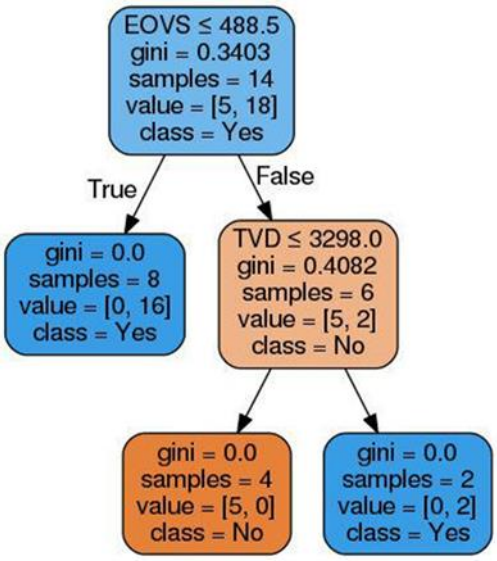

(j)

Figure 3 The trees of the presented Random Forest model for assessing the conditions of petroleum reservoirs with respect to onset of sand production (h-j)

From a computational complexity point of view, the CART classifier is the simplest model and the Random forest algorithm is the most complex model. However, in view of the fact that the Random Forest approach is not been over fitted, as explained before, it is suggested to use this model for the application of interest. For predicting the sanding through the proposed Random Forest model, all the investigated parameters are required.

6. Conclusion

Presented in this communication, CART-Decision Tree, Extra Tree, and Random Forest algorithms were utilized for developing models capable to determine the possible sand production in a real petroleum field. To achieve this goal, the models were developed employing a total number of 23 field data points. The performance of the constructed models in classifying the unseen data was evaluated using 6 field data.

Based on the obtained results, all the proposed models have excellent classification power in identifying the petroleum reservoir conditions with respect to sanding. Indeed, the built models provide 100% accuracy for the application of interest. It should be noted that more

robust models can be developed if more reliable data points are available. The proposed methodologies in this study can be implemented for facilitating the strategies for sand control plan. However, as it described in the previous section of the work, it is recommended to employ the Random Forest algorithm for investigating the sand production in petroleum reservoirs.

The proposed techniques in this work can play a vital role in the investigation of sand production in various oil and natural gas industrial applications. Indeed, utilizing the presented algorithms will pave the way for sand-control decision making. Consequently, secure energy production can be achieved.

Acknowledgement

The first author acknowledges the help of Mr. Farid D. Maleki from Kharazmi University, Tehran, Iran and Mr. Mohammad Mahmoudi from TU Wien, Wien, Austria who have made a contribution to improve the paper.

References

[1] International energy outlook 2013 Washington, DC 20585, U.S. Energy Information Administration.
[2] Ghiasi MM, Arabloo M, Mohammadi AH, and Barghi T. Application of ANFIS soft computing technique in modeling the CO_2 capture with MEA, DEA, and TEA aqueous solutions. Int J Greenhouse Gas Control, 2016; 49: 47-54.
[3] Bianco LCB, and Halleck PM. Mechanisms of Arch Instability and Sand Production in Two-Phase Saturated Poorly Consolidated Sandstones. Society of Petroleum Engineers 2001.
[4] Nouri A, Vaziri H, Belhaj H, and Islam R. Comprehensive Transient Modeling of Sand Production in Horizontal Wellbores. Society of Petroleum Engineers 2003.
[5] Nouri A, Vaziri H, Kuru E and Islam R. A comparison of two sanding criteria in physical and numerical modeling of sand production. J Petr Sci Eng., 2006; 50(1): 55-70.
[6] Ranjith PG, Perera MSA, Perera WKG, Wu B, and Choi SK. Effective parameters for sand production in unconsolidated formations: An experimental study. J Petr Sci Eng., 2013; 105: 34-42.
[7] Ranjith PG, Perera MSA, Perera WKG, Choi SK, and Yasar E. Sand production during the extrusion of hydrocarbons from geological formations: A review. J Petr Sci Eng., 2014; 124: 72-82.
[8] Almedeij JH, and Algharaib MK. Influence of sand production on pressure drawdown in horizontal wells: Theoretical evidence. J Petr Sci Eng., 2005; 47(3–4): 137-145.
[9] Talaghat MR, Esmaeilzadeh F.and Mowla D. Sand production control by chemical consolidation. J Petr Sci Eng., 2009; 67(1–2): 34-40.
[10] Willson SM, Moschovidis ZA, Cameron JR and Palmer ID. New Model for Predicting the Rate of Sand Production. Society of Petroleum Engineers 2002.
[11] Wang J, Settari AT, Walters D and Wan R. An integrated modular approach to modeling sand production and cavity growth with emphasis on the multiphase and 3D effects. American Rock Mechanics Association 2006.
[12] Fattahpour V, Moosavi M and Mehranpour M. An experimental investigation on the effect of rock strength and perforation size on sand production. J Petroleum Sci Eng., 2012; 86–87: 172-189.
[13] Sanfilippo F, Ripa G, Brignoli M and Santarelli FJ. Economical Management of Sand Production by a Methodology Validated on an Extensive Database of Field Data. Society of Petroleum Engineers 1995.
[14] Moricca G, Ripa G, Sanfilippo F and Santarelli FJ. Basin scale rock mechanics: Field observations of sand production. Society of Petroleum Engineers 1994.
[15] Hall CD Jr., and Harrisberger WH. Stability of Sand Arches: A Key to Sand Control. J. Pet. Technol., 1970; 22(7):
[16] Tippie DB, and Kohlhaas CA. Effect of Flow Rate on Stability of Unconsolidated Producing Sands. Society of Petroleum Engineers 1973.
[17] Bratli RK, and Risnes R. Stability and Failure of Sand Arches. Society of Petroleum Engineers Journal, 1981; 21(2):236-248 1981.
[18] Morita N, Whitfill DL, Fedde OP and Levik TH. Parametric Study of Sand-Production Prediction: Analytical Approach. 1989; SPE Production Engineering 4 (01), 25-33.
[19] Morita N, and Boyd PA. Typical Sand Production Problems Case Studies and Strategies for Sand Control. Society of Petroleum Engineers 1991.
[20] Nie X, Yang S, Ding J, Cao L, Zhou F, Ma Q and Qiu Z. Experimental investigation on permeability evolution law during sand production process of weak sandstone. J Nat Gas Sci Eng., 2014; 21: 248-254.

[21] Ghassemi A, and Pak A. Numerical simulation of sand production experiment using a coupled Lattice Boltzmann–Discrete Element Method. J Petr Sci Eng., 2015; 135: 218-231.
[22] Jiang N-J, Yoshioka H, Yamamoto K and Soga K. Ureolytic activities of a urease-producing bacterium and purified urease enzyme in the anoxic condition: Implication for subseafloor sand production control by microbially induced carbonate precipitation (MICP). Ecol Eng., 2016; 90: 96-104.
[23] Coates GR, and Denoo SA. Mechanical Properties Program Using Borehole Analysis And Mohr's Circle, Society of Petrophysicists and Well-Log Analysts. SPWLA 22nd Annual Logging Symposium, 23-26 June 1981, Mexico City, Mexico
[24] Weingarten JS, and Perkins TK. Prediction of Sand Production in Gas Wells: Methods and Gulf of Mexico Case Studies. Journal of Petroleum Technology, 1995; 47(7):596-600.
[25] Doan QT, Doan LT, Ali SMF and Oguztoreli M. Sand Deposition Inside a Horizontal Well-A Simulation Approach. Annual Technical Meeting, June 8 - 10, 2000,Calgary, Alberta
[26] Kanj MY, and Abousleiman Y. Realistic Sanding Predictions: A Neural Approach, Society of Petroleum Engineers 1999.
[27] Azad M, Zargar G, Arabjamaloei R, Hamzei A and Ekramzadeh MA. A New Approach to Sand Production Onset Prediction Using Artificial Neural Networks. Petr Sci Tech., 2011; 29(19): 1975-1983.
[28] Khamehchi E, Rahimzadeh Kivi I and Akbari M. A novel approach to sand production prediction using artificial intelligence. J Petr Sci Eng., 2014; 123: 147-154.
[29] Gharagheizi F, Mohammadi AH, Arabloo M, and Shokrollahi A. Prediction of Sand Production Onset in Petroleum Reservoirs Using a Reliable Classification Approach. Petr., 2017; 3(2): 280-285.
[30] Bishop C. Pattern Recognition and Machine Learning. Singapore. Springer 2006.
[31] El-Telbany ME, and Warda M. (2016) An Empirical Comparison of Tree-Based Learning Algorithms: An Egyptian Rice Diseases Classification Case Study. Int J Adv Res Art Intel 5(1): 22-26.
[32] Zhao Y, and Zhang Y. Comparison of decision tree methods for finding active objects. Adv Space Res., 2008; 41(12): 1955-1959.
[33] Quinlan JR. Induction of decision trees. Mach Learn, 1986; 1(1): 81-106.
[34] Lim T, Loh W and Shih Y. An empirical comparison of decision trees and other classification methods. Technical Report, Department of Statistics 1997, University of Wisconsin.
[35] Gehrke J, Ganti V, Ramakrishnan R.and Loh W-Y. BOAT-optimistic decision tree construction. Proceedings of the 1999 ACM SIGMOD international conference on Management of data. Philadelphia, Pennsylvania, USA, ACM: 169-180.
[36] Salzberg SL. C4.5: Programs for Machine Learning by J. Ross Quinlan. Morgan Kaufmann Publishers, Inc., Mach Learn, 1993; 16(3): 235-240.
[37] Weber R. Fuzzy ID3: a class of methods for automatic knowledge acquisition. Proceedings of the 2nd International Conference on Fuzzy Logic and Neural Networks 1992, Iizuka, Japan.
[38] Umano M, Okamoto H, Hatono I, Tamura H, Kawachi F, Umedz S and Kinoshita J. Fuzzy Decision Trees by Fuzzy ID3 algorithm and its Applications to Diagnosis System. Proceedings of the third IEEE Conference on Fuzzy Systems 1994, Orlando.
[39] Breiman L, Friedman J, Stone CJ, and Olshen RA. Classification and Regression Trees, Taylor & Francis 1984.
[40] Breiman L. Random Forests. Mach Learn, 2001; 45(1): 5-32.
[41] Robnik-Sikonja M. Machine Learning. ECML 2004 Proceedings, Berlin, Springer.
[42] Breiman L. RANDOM FORESTS--RANDOM FEATURES. CA, Statistics Department, University of California Berkeley 1999.
[43] Geurts P, Ernst D and Wehenkel L. Extremely randomized trees. Mach Learn, 2006; 63(1): 3-42.
[44] Geurts P, and Louppe G. Learning to rank with extremely randomized trees, JMLR: Workshop and Conference Proceedings, 2011; 14: 49-61.
[45] Wehenkel L, Ernst D and Geurts P. Ensembles of extremely randomized trees and some generic applications. RTE-VT workshop 2006. Paris.

To whom correspondence should be addressed: Professor Dr. Amir H. Mohammadi, Discipline of Chemical Engineering, School of Engineering, University of KwaZulu-Natal, Howard College Campus, King George V Avenue, Durban 4041, South Africa

Petroleum and Coal

Article **Open Access**

INVESTIGATION OF ASPHALTENE PRECIPITATION IN BANGESTAN RESERVOIR, KUPAL OIL FIELD, SW OF IRAN

Hossein Tabatabaei, Sasan Dadgar, Hadis Deimar*

Department of Petroleum Engineering, Islamic Azad University, Gachsaran Branch, Gachsaran, Iran

Received January 23, 2019; Accepted February 19, 2019

Abstract

One of the most important problems is the production of asphaltene sedimentation is in oil reservoirs. Enclosure in the porous environment of the oil field, well heads and processing plants is a serious problem in the production of asphaltene oil. The complex composition of deposited materials is proportional to the type of crude oil composition, well depth, formation temperature, and pressure drop and production process. These factors will disrupt the chemical equilibrium in the reservoir and result in the formation of asphaltene sedimentation. The main purpose of this study is to investigate the causes of asphaltene sedimentation in the Bangestan reservoir of Kupal oil field. The results showed that despite the existence of a single source rock for productive reservoir layers, the oil wells of the reservoir of Bangestan lacked the peripheral and perpendicular continuity of the reservoir during the reservoir, and were based on independent production areas. The values of asphaltene colloidal instability index (CII) (0.93-1.26) indicated that this oil field is prone to precipitation of asphaltene. The study of our data in the Bangestan reservoir showed that temperature has no direct or indirect effect on sedimentation. The evaluation of pressure – time diagram showed that when the production increased, the reservoir pressure decreased and the asphaltene sedimentation was formed. Finally, it can be prevented from the formation of asphalt precipitation by the principled production of the reservoir.

Keywords: *Kupal oil field; Bangestan reservoir; Asphaltene Precipitation; SARA test.*

1. Introduction

One of the most important problems in the production of oil reservoirs is the formation of asphaltene sedimentation [1]. Reducing the permeability of the rocky reservoir, the formation of sedimentation in the well and reducing the recovery of petroleum products are among the major problems encountered by asphalting reservoirs. One of the most important factors affecting the sedimentation of asphaltene in oil reservoirs is the change of pressure and injection of solvent [2]. Asphaltene is generally heavy compounds found in crude oil. According to laboratory studies, part of the asphaltic compounds is thought to be solved and partly different in the form of colloids in oil. The sedimentation of asphaltene in reservoirs depends on changes in pressure, temperature, and composition of the oil. These factors will disrupt the chemical equilibrium of the reservoir and result in the formation of asphaltene sedimentation [3].

Asphaltene is either soluble in oil or as a colloidal suspension, which is found in oil that is absorbed by resins on their surface in a state of equilibrium [4]. Asphaltenic is a cut of an oil or other carbon-based material that is soluble in paraffinic solvents with a low boiling point (such as normal heptane) and in benzene.

The disparity in the components of the oil components due to environmental and operational factors will cause many problems and issues [5-6]. The most important consequences of this type of instability in the system of equilibrium of oil compounds are the formation, growth, and sedimentation of heavy organic compounds. The most important of these sedimentations are the problems associated with sedimentation of asphaltene components [7].

In the primary and secondary phases of oil production, due to changes in the thermodynamic conditions of hydrocarbon fluids, such as the change in the composition of oil, temperature and fluid pressure, the stability equilibrium of the thermodynamics of organic asphaltene is disrupted and asphaltene sedimentations are formed by various mechanisms and due to moving through porous medium of the formation, enclosures are created in the wells as well as in oil transportation and processing facilities [8].

The sedimentation of asphaltene causes a lot of problems in the recovery, transfer and refining of oil. For example, sedimentation of asphaltene on the porous surfaces of the reservoir rock causes changes in oil reservoir wettability. Also, this process during the exploitation of well will stop production [9]. Due to the fact that the financial damage caused by this phenomenon is significant, how to produce from such wells has become an important place.

Reservoir quantities, oil composition, resin and asphaltene concentrations in oil, pressure, temperature and flow characteristics will be effective in the formation of asphaltene sediment in the reservoir [8,10].

In Iran, many reservoirs have the problem of depositing heavy compounds such as asphaltene. For example, the formations of the Bangestan group which include oil fields of Ahwaz, Marun, Ramshir, Rag-e-Safid, Aghajari, and Gachsaran. Asphaltene sedimentation in oil reservoirs reduces the permeability and changes the reservoir wettability and, finally, reduces the production of oil, which has become a major problem in the production from Bangestan reservoirs (Illam and Sarvak). To study the sedimentation behavior of asphaltene in a different light and heavy oils as well as to predict the best method of preventing or remedy this problem, a research study was conducted. Asphaltene is precipitated by increasing the viscosity of the fluid, changing the properties of the cement and the blocking pores and flow paths causes damages to the reservoir.

2. Geological properties of Bangestan reservoir of Kupal oil field

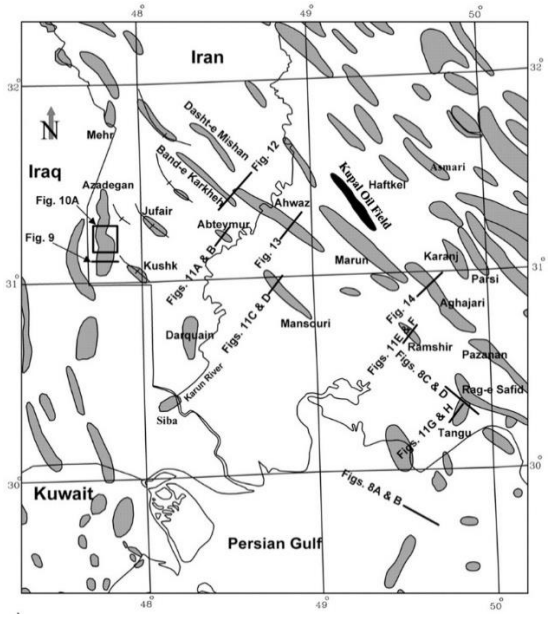

Figure 1. Location of the Kupal oil field and the wells selected for sampling

The data from the study of wells drilled in the Bangestan reservoir of Kupal oil field (Fig.1) indicated that the reservoir is less productive than those in the vicinity of Ahwaz, due to factors such as salt production, low porosity, and high saturation. The Bangestan group varies in a sedimentary environment in the northwest in the Lurestan region to the continental shelf in the south-east of Fars. In these areas, more than 800 meters of shallow neritic limestone, along with fluctuations in the margin of sedimentation, is also reported. Limestone of Kupal oil field has a special distribution. In the northwest, it is found in shallow, intertidal and enclosed seas, and in the south-east, limestone of free seas are observed.

The Bangestan reservoir in the Kupal oilfield [11], like the Asmari reservoir, is an anticline sinus whose length is 32 km and its width is 4.5 km. The geophysical information of the Bangestan reservoir in Kupal oil field showed the presence of a thrust fault in the southeastern part of the field, suggesting that if the intersection of such a fault was associated with a normal fault, it could lead to the formation of a fracture system with abundant production. Based on studies, the Bangestan reservoir of this oilfield is divided into nine zones that consisted of four reservoir zones, of which porous carbonates were separated by the denser

carbonate layers [12]. The most amount of in place oil of this field is located in the highest part of the Sarvak formation, which is the main productive zone of this field. The aforementioned zone is bounded by two discontinuity planes of early Cenomanian - late Turonian at the base and a nonconformity plane of the early Turonian-late Santonian from the top.

3. Zones susceptible to precipitation of asphaltene

Asphaltene is deposited in oil wells due to changes in well pressure or changes in other reservoir quantities, including temperature and composition crude oil. Some wells are at the beginning of the asphaltene sedimentation problem, but in the later phases of production, this problem will arise. Therefore, for this study, the zones susceptible to precipitation of asphaltene in the reservoir should first be identified.

Increasing the amount of asphaltene sedimentation is due to reduced solvent solubility and its ability to maintain the suspension of asphaltene-resin clusters. To determine the zones susceptible to sedimentation of asphaltene, a 7 number of samples of crude oil wells were selected. Subsequent samples were then analyzed by column chromatography and, for each individual sample, the saturated, aromatic, resin and asphaltene portion (SARA) are specified for samples and zones susceptible to asphaltene sedimentation were identified (Tab.1). The Colloidal Instability Index (CII) of asphaltene can be measured using SARA Laboratories (Tab.2).

Table 1. Geochemical data and gross chemical composition of oils

Sample No.	Well No.	Saturated	Asphaltene	Resin (N.S.0)	Aromatic
1	4	45.5	1.8	14.9	27.2
2	26	37	1.6	14.6	26.7
3	71	38.2	2.2	13.2	29.3
4	23	46.6	2.3	14.7	36.3
5	44	54.9	0.9	15.1	29.1
6	32	49.7	1.2	12.2	36.9
7	8	46.5	1.9	11.8	29.3

Table 2. CII data of Bangestan reservoir oils in Kupal oilfield

Sample No.	1	2	3	4	5	6	7
CII	1.12	0.93	0.95	0.95	1.26	1.03	1.17

This index is known and calculated as the ratio of total amounts of saturated and asphaltene to the sum of aromatics and resins. If the CII value is less than 0.7, asphaltenic oil is stable in the formation of heavy sediments, while asphaltenic oil is unstable for values of 0.9-0.7 and is released under the conditions of the oil system. For asymmetric values of more than 0.9, the asphaltenic oil will be completely unstable. On the basis of this, it was observed that the indices of colloidal instability in hydrocarbon fluids were more than 0.7. Therefore, the desired oils are instable due to the formation of asphaltene sediment (Fig. 2).

Also, in order to determine the asphaltene stability in the reservoir, the ratio of the Saturated/Aromatic components to the ratio of Asphaltene/Resin was used. According to this, most of the oil samples from the Bangestan reservoir are located in the instable zone (instable zone of Middle East). This illustration clearly shows that one of the main factors of asphaltene sedimentation in these wells is the low content of resin and aromatic components in oil (Fig. 3). Study of the ratio of CII and resin ratio to asphaltene that wells are instable, so that the CII values change from 0.7 to 0.9 are high. An examination of the quantities considered in the Bangestan reservoir of Kupal oil field indicated that all of them were susceptible to sedimentation of asphaltene, but this phenomenon was observed in wells studied.

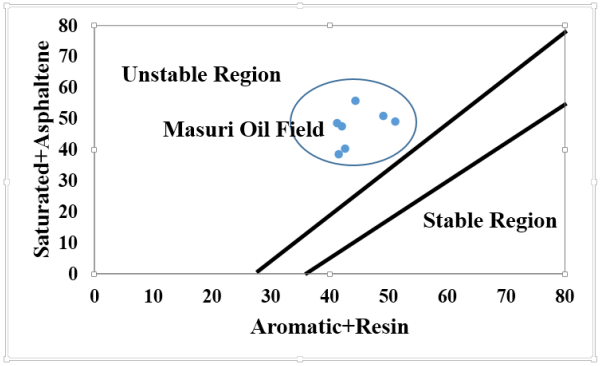

Figure 2: Study of the CII index in reservoir samples indicates that samples are placed in a stable range [13].

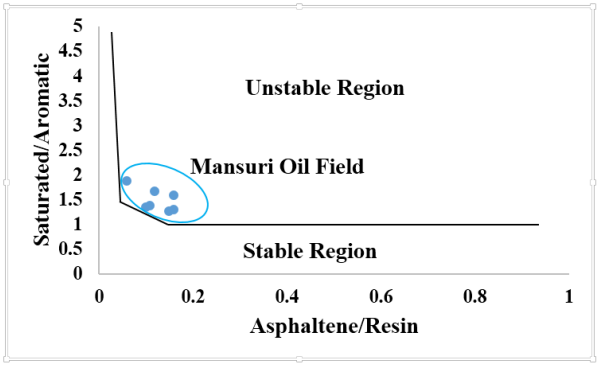

Figure 3. Changes in the Saturation/Aromatics ratio versus Asphaltene/Resin ratio in the samples of oil in the Bangestan oil reservoir show that all of the impurities are in a stable range [13]

4. Variation in oil composition

The methods used in the geochemistry for determination of oil properties, determination of the distribution of hydrocarbon and the presence of various compounds, including normal alkaline and isoprenoids such as pristane (Pr) and phytane (Ph), are used for gas chromatography (Tab.3). Using the data derived from this method, one can determine the type of organic facies, the type of kerosene, the type of sedimentation environment, thermal maturation and the effect of biodegradation and leaching on samples [14].

Evidence such as the single modal pattern of gas chromatograms in samples, the normal frequency of light alkanes (nC_{12}-nC_{20}), the values of the Carbon Preference Index (CPI) near one, and the low ratios of normal alkanes to isoprenoids imply that the studied oils have the same origin rock and belongs to the environment with organic material of algae type [15]. The results of the gas chromatography analysis of the samples showed a spectrum of carbon C_{11} to C_{36} and also showed that light hydrocarbons have a high frequency of C_9 to C_{26} and hydrocarbons heavier than C_{20} have a low frequency (Fig. 4).

Table 3. Isotopic and Pr/Ph data of Bangestan reservoir oils in Kupal oilfield

Sample No.	4	8	32	23	71	44	26
Pr/Ph	0.84	0.91	0.88	0.77	0.9	0.94	0.86
$\delta^{13}C$	-25.6	-25.4	-.25.6	-25.5	-25.5	-25.6	-25.5

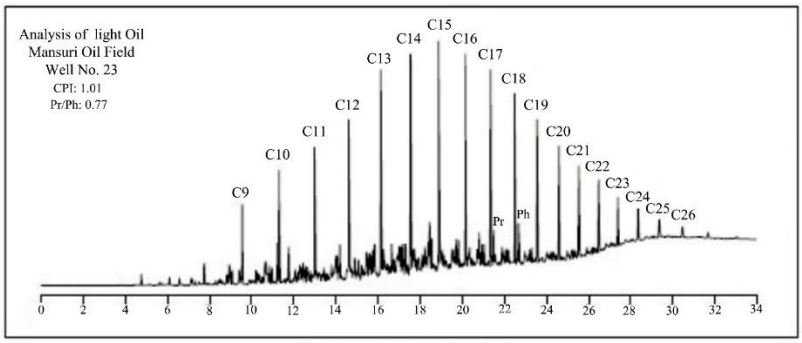

Figure 4. Chromatogram obtained from gas chromatography analysis of saturated samples of oils from Bangestan reservoir in Kupal oil field

A star diagram is used to indicate the ratio of the odd to even normal alkanes [16]. Using this figure, it was determined that the values of the normal ratio of alkanes with very clear overlapping represent the origin of the rock that they derive from [17-18](Fig. 5).

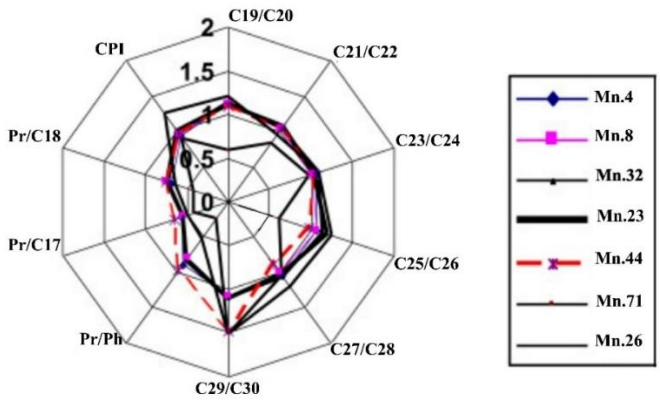

Figure 5. Star diagram was drawn to determine the same origin for samples of oil from the Bangestan reservoir via the results of gas chromatography

Using the pristane/phytane ratio (Pr/Ph) for a sample of studied oils, this ratio was found to be less than one (at least 0.77 and a maximum of 0.94) in all samples. This could indicate the sedimentary rocks of the origin of the Bangestan oil in a reduction environment. Of course, this result should be compared with other quantities [19].

With a high frequency of quantities of light normal alkanes, high molecular levels of oil, as well as any other alteration process, such as leaching and biodegradation, were established. The Pr/Ph ratio is calculated for reservoir oil (less than 2), which can be used to indicate the formation of crude oil from an organic-rich marine-reduction carbonate rock.

The diagram of carbon isotope values variation $\delta^{13}C$ by Pr/Ph ratio can be used in order to determine the age and lithology of origin rock of oil in rethe servoir of Bangestan oilfield) (Chung, 1992). Based on this diagram, it was discovered that high crude oil was produced from Mesozoic Age carbonate origin rock (Fig. 6).

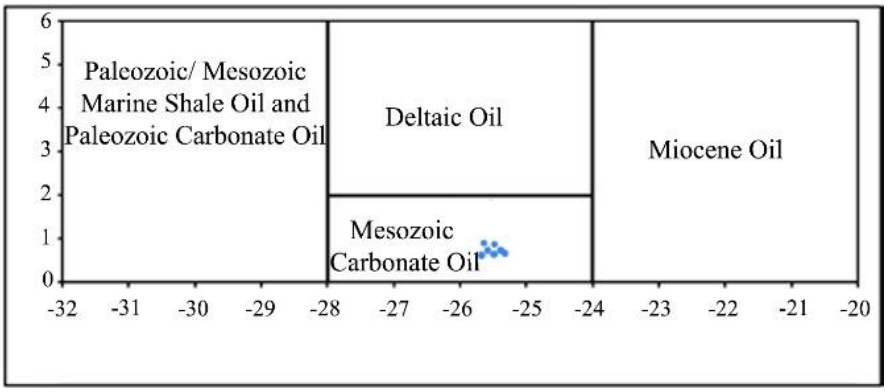

Figure 6. Changes of carbon-13 isotope of crude oil ($\delta^{13}C$) relative to Pr/Ph ratio to determine the age and lithology of the origin rock in sampled oils from Bangestan reservoir of Kupal oilfield (*adapted from* [20])

5. Effect of pressure

One of the most important factors in the formation of asphaltene sediment is reservoir oil pressure variation. Changing pressure is usually accompanied by a change in temperature. These changes cause physical and chemical instability and eventually the formation of asphaltene in crude oil. The change in pressure alone can also cause sedimentation of asphaltene [21]. By decreasing the pressure to reach the bubble point, the crude oil solubility decreases, which is due to the loss of crude oil density. In order to investigate the pressure variations in the formation, data from the repeated layer tests and hydrostatic pressure of the well was used.

Abnormal pressure is defined as changes in formation fluid pressure gradient relative to the hydrostatic pressure gradient. This pressure is caused by the presence of one or a number of impermeable layers that interfere with layers fluid [22]. Interpretation of pressure in a multilayered reservoir is made to examine the lateral and perpendicular continuity and estimate the gradient of the pressure [23].

Time is an important factor in controlling changes in the pressure of oil reservoirs [24], so that if the pressure decreases or increases in a few million years, the fluids will have more time to

disperse and the pressure is slightly offset from the equilibrium state and vice versa, if pressure is increased in less time, fluids of different pressure can be generated [25]. This causes the pressure to be offset from equilibrium. In this case, the pressure changes caused the asphaltene to be removed from the oil and reduce its solubility and sedimentation in the reservoir.

Different studies are necessary to obtain the information on reservoir rock performance from the beginning to the end of production. In reservoirs with high pressure zones, the increase in temperature will be consistent with increasing pressure. Increasing the pressure reduces the molecular volume and increases the solubility of the hydrocarbon fluids. Also, under bubble point, the higher pressure from the gas (hydrocarbon gases) in the crude oil is solved, and it decreases the solubility [26]. The lowest solubility of asphaltene in crude oil occurs at the bubble point, which is associated with the maximum amount of asphaltene sedimentation. In an underground reservoir in general, with increasing pressure, the stability and degree of solubility of the asphaltene (constant temperature and constant volume of gas) increase.

Investigation of asphaltene sedimentation in the reservoir showed that the highest amount of asphalt sediment was observed around one of the wells. Asphalt sedimentation is due to changes in the equilibrium condition of asphaltene in the reservoir. A study of the reservoir pressure observed in a 40-year period indicated that the production pressure of the reservoir is reduced by increasing the reservoir pressure. Therefore, with decreasing pressure in the reservoir, it seems that there is a direct relationship with increasing asphaltene precipitation (Fig. 7). The study of the number of wells that faced deposited in a ten-year period indicated that with increasing production from the Bangestan reservoir, the number of these wells has increased, so that between1980-2015, the number of these wells is increased from 2 to 12 wells.

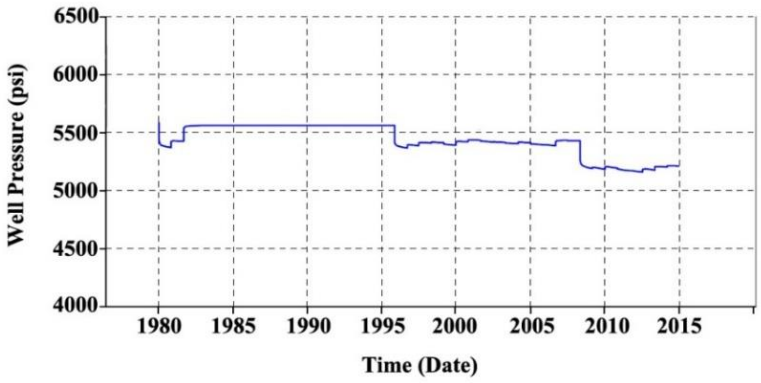

Figure 7. In Bangestan reservoir, pressure varies in the pressure-time graph, and pressure data is staggered relative to time

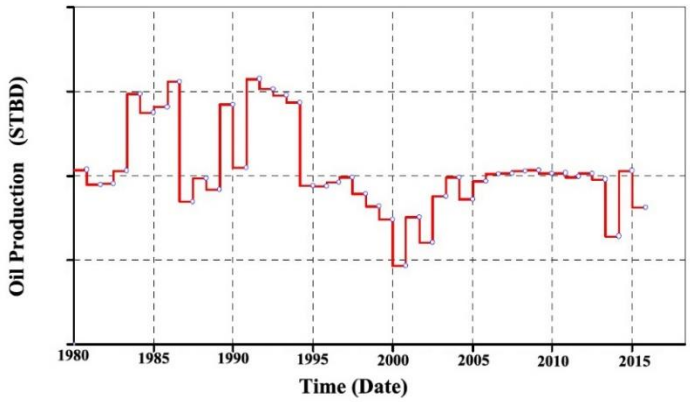

Figure 8. Chart of production to time in well No.23, and changes over a period of approximately 40 years, and production decline over time

6. Temperature drop

The temperature drop is the most common reason for wax sedimentation [27] because the solubility of wax in oil decreases with decreasing temperature. Regarding precipitation of asphaltene, temperature changes are less effective than the effect of pressure and oil composition [28-30].

As the temperature of the system increases, the resins are dissolved, and thus a kind of balance of electrical charge between the particles occurs, because the solubility of the oil depends on the resin in the asphaltene. In other words, because of the effect of the temperature on both the evaporation and the density of the liquid, the temperature changes in these properties, and this ultimately leads to a decrease in the solubility of crude oil. Asphaltene sediment is therefore observed at low temperatures.

There are many observations relating to the effect of temperature variations on the frequency of asphaltene. According to Andersen and Beardy [31], the asphaltene sedimentation rate increases with increasing temperature. In explanation of this phenomenon, it can be said that with increasing temperature and molecular mobility, the probability of collision and bonding of particles increased and eventually lead to asphaltene sedimentation. But generally, in addition to the above factors, the increase in temperature causes an increase in the movement or in other words the Brownian motion of the molecules of oil, which increases the probability of collisions of particles with each other and the absorption of particles of resin by particles of asphaltene which finally decreases the probability of formation of asphaltene sediment [4].

Usually, the drop in pressure is accompanied by a drop in temperature. The temperature is generally considered as a direct factor in the precipitation of asphaltene, which is due to the instability of dependent forces that are caused by the change in temperature. The temperature may affect the solubility of maltenes and the resins, and a temperature drop will lead the system to the production of paraffin deposits. This change of temperature may also occur with the expansion of carbon dioxide gas.

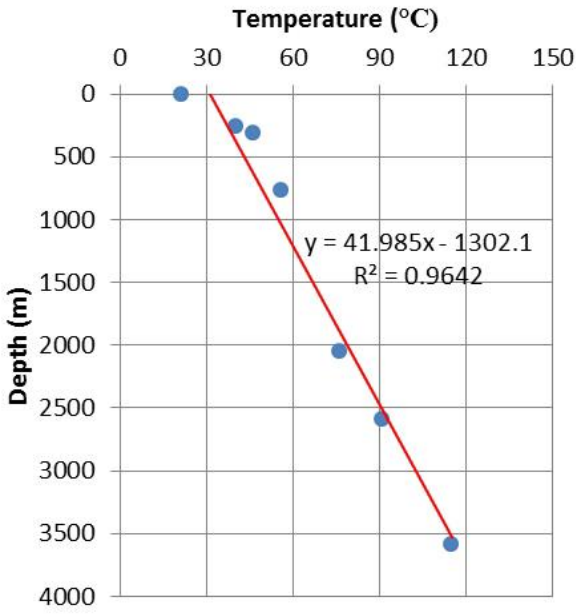

Figure 9. To determine the geothermal gradient of the area, temperature data of 7 wells were used

To study the effect of temperature and determine the geothermal gradient of the field, 7 wells were selected throughout the field. Using the temperature data of the wells, the geothermal gradient of the area was drawn.

According to the Andersen and Beardy [31], asphaltene sedimentation began to decrease with increasing temperature to more than a certain temperature (about 60 degrees), which caused it to overcome the kinetic energy that applied the system to the adherence of asphaltene particles to be bonded. Investigations indicated that the depth of the asphaltene was 2100-3000 meters, which would have a temperature between 60°-80°C with respect to the geothermal gradient (Fig. 9). By studying the temperature data of the Bangestan reservoir of Kupal oil field, the temperature variation cannot be considered as a direct factor in the sedimentation of asphaltene.

7. Conclusion

The carbon preference index was determined in samples from C_{10} to C_{26}. This determines the marine origin of the organism and the organic materials and indicates the origin of rocks belonging to reducing environments, saline waters along with evaporative sequences. The results of the oil fingerprinting method indicate that the studied samples from the wells of Bangestan reservoir in Kupal oilfield were different from the viewpoint of the considered variables that were plotted by stars. Therefore, it can be concluded that in the Bangestan reservoir of Kupal oil field, drilled wells in the study area are not related to reservoir continuity, and the reservoir has independent production sections.

By studying the temperature data from the reservoir, the temperature cannot be considered as an indirect or indirect effect on the formation of asphaltene sedimentation. The analysis of changes in pressure data in reservoir layers confirms that the pressure of different zones was different and had different trends. As a result, there seems to be no pressure relationship between the reservoir zones. As pressure from the reservoir increases, production of oil pressure decreases and therefore, it seems that there will be a direct relationship between pressure drop and sedimentation of asphaltene in the reservoir, so that in the wells with deposited asphaltene, the pressure was reduced. Finally, principled production from the reservoir can lead to prevention of pressure drop and consequent the asphaltene precipitation.

References

[1] Almehaideb RA. Asphaltene precipitation and deposition in the near wellbore region: A modeling approach. Journal of Petroleum Science and Engineering, 2004; 42: 157– 170.

[2] Vafaie Seft M, Mousavi-Dehghani SA. Application of association theory to the prediction of Asphaltene deposition: Deposition due to natural depletion and miscible gas injection processes in petroleum reservoirs. Fluid phase equilibria, 2006; 247., 182-189.

[3] Kamari A, Safiri A, Mohammadi AH. A compositional model for estimating asphaltene precipitation conditions in live reservoir oil systems. J. Dispers. Sci. Technol., 2015; 36: 301-309.

[4] Soulgani BS, Tohidi B, Rashtchian D, and Jamialahmadi M. Modelling of Asphaltene Precipitation in well Column of Iranian Crudes: Kupal Case Study. Canadian International Petroleum Conference, Calgary, June 2008.

[5] Leontaritis KJ, and Mansoori GA. 1987 Asphaltene flocculation during oil recovery and processing: a thermodynamic-colloidal model, Proceedings of the SPE Symposium on Oil Field Chemistry. Society of Petroleum Engineers 1987, Richardson, TX, SPE 16258.

[6] Mosavi-Dehghani SA, Riazi MR, Vafaie-Sefti M, Mansoori GA. An analysis of methods for determination of onset of asphaltene phase separation. Journal of petroleum science and theology, 2004; 42: 145-156.

[7] Zendehboud, S, Rajabzadeh AR, Bahadori A, Chatzis I, Dusseault MB, Elkamel A, Lohi A, Fowler M. 2014, Connectionist model to estimate performance of steam-assisted gravity drainage in fractured and un-fractured petroleum reservoirs: enhanced oil recovery implications. Ind. Eng. Chem. Res., 2014; 53: 1645-1662.

[8] Leontaritis KJ. Asphaltene near-wellbore formation damage modeling. Presented at the 1998 SPE Formation Damage Control Conference held in Lafayette, Louisiana, February 18-19, 1998, SPE 39446, (1998).

[9] Davudov D, Moghanloo RG. Impact of pore compressibility and connectivity loss on shale permeability. Int J Coal Geol., 2018; 187: 98-113.

[10] Kawanaka S, Park SJ, and Mansoori GA. The role of asphaltene deposition in EOR gas flooding. Presented at the 1988 SPE/DOE Symposium on Enhanced Oil Recovery, Richardson, TX, Feb 15-17, paper SPE 17376.

[11] Tabatabaei H, Motamed A, Mosavian SS. Geochemical studies of Pabdeh formation in Kupal oil field and determination of oil production. The 1st International Applied Geological Congress, Department of Geology, Islamic Azad University Mashhad Branch, Iran, 26-28 April 2010.

[12] Speers RG. The geology of the Bangestan Reservoir in Marun field (P-3541). NISOC, geology department 1978.

[13] Verdier SCR. Experimental Study and Modelling of Asphaltene Precipitation Caused by Gas Injection., PhD Thesis, IVC-SEP - Centre for Phase Equilibrium and Separation Processes

Department of Chemical Engineering 2006, Technical University of Denmark, Lyngby, Denmark, 284p.
[15] Peters KE, Moldowan JM. The Biomarker Guide. Interpreting Molecular Fossils in Petroleum and Ancient Sediments. Prentice- Hall 1993, Englewood Cliffs, New Jersey.
[16] Kaufman RL, Ahmed AS, Elsinger RJ. Gas chromatography as a development and production tools for ngerprinting oils from individual reservoirs: applications in the Gulf of Mexico. In: GC SSEPM Foundation Ninth Annual Research Conference Proceedings, October 1, 1990, pp. 263–282.
[17] Alizadeh B, Adabi MH, Tezheh F. Oil-Oil Correlation of Asmari and Bangestan Reservoirs using Gas Chromatography (GC) and stable isotopes of carbon and sulfur in Marun Oilfield, S.W. Iran. Iranian Journal of Science and Technology, 2007; 31(A3): 241-253.
[18] Alizadeh B, Alipor M, Hossinee SH, Jahangard AA. 2011. Paleo environment reconstruction using biological marker for the Upper Triassic- middle Jurasic sedimentary succession in Tabas Basin, Central Iran. Organic Geochemistry,2011; 42: 431–437.
[19] Powell TG, McKirdy DM. 1973. The effect of source material, rock type and diagenesis on the n-alkane content of sediments. Geochemical ET Cosmochimica Act, 1973; 35: 523-633.
[20] Chung HM, Rooney MA, Toon MB, Claypool GE. Carbon isotope composition of marine crude oils. American Association of Petroleum Geologists Bulletin, 1992; 76: 1000-1007.
[21] Akbarzadeh K, Eskin D, Ratulowski J, Taylor SD, 2011 Asphaltene Deposition Measurement and Modeling for Flow Assurance of Subsea Tubing's and Pipelines. OTC Brazil.
[22] Jamialahmadi M, Soltani B, Müller-Steinhagen H, Rashtchian D. Measurement and prediction of the rate of deposition of flocculated asphaltene particles from oil. International Journal of Heat and Mass Transfer; 2009; 52(19):4624-34.
[23] Jackson RR, Carnegie A, and Dubost FX. Pressure Measurement and Pressure Gradient Analysis: How Reliable for Determining Fluid Density and Compositional Gradients. Annual International Conference and Exhibition held in Abuja, Nigeria, 6-8 August 2007.
[24] Andersen SI, Speight JG. Observations on the critical micelle concentration of asphaltene. Fuel, 1993; 72, 1343.
[25] Hunt JM. Petroleum Geochemistry and Geology. 2nd Edition. W.H. Freeman and Company 1996, New York. 743 p.
[27] Shen Z, Sheng JJ. 2017, Investigation of asphaltene deposition mechanisms during CO_2 huff-n-puff injection in Eagle Ford shale. Pet Sci Technol, 2017; 35(20):1960–6.
[28] Mansoori GA, Jiang TS, Kawanaka S. Asphaltene Deposition and its Role in Petroleum Production and Processing, Chicago 1988, Illinois 60680, USA.
[29] Mansoori GA, Vazquez D. Identification and Measurement of Petroleum Precipitates. J. of Petroleum Sci. and Eng., 2000; 26: 49- 55.
[30] Soulgani BS, Jamialahmadi M, Rashtchian D, and Tohidi B. A New Thermodynamic Scale Equation for Modelling of Asphaltene Precipitation Form Live Oil. Canadian International Petroleum Conference 2009, Calgary.
[31] Andersen SI, and Birdi KS. Influence of Temperature Solvent on the precipitation of Asphaltene. Fuel Science and Technology, 1990; Int. 8: 593-615.

To whom correspondence should be addressed: Dr. Hossein Tabatabaei, Department of Petroleum Engineering, Islamic Azad University, Gachsaran Branch, Gachsaran, Iran

Petroleum and Coal

Article **Open Access**

GEOPHYSICAL LOGS ANALYSIS FOR FORMATION EVALUATION: A CASE STUDY OF "ODOKOKO" FIELD, COASTAL SWAMP DEPOBELT, NIGER DELTA

Daniel Ayodele[1], Mode Ayonma Wilfred[1], Onimisi Martins[2]

[1] Department of Geology, University of Nigeria, Nsukka, Nigeria
[2] Faculty of Geology and Mining, University of Rwanda, Kigali, Rwanda

Received July 4, 2018; Accepted September 21, 2018

Abstract

The logs were used to identify the sand intervals which are potential commercial hydrocarbon bearing reservoirs. A cut off of 43 API was used for sand, 65API for shaly sand and 85 for sandy shale in the Cross plotting technique and the unsupervised neural network process of Petrel. Four sands of possible reservoir quality were identified. Their porosities range from 23% to 34%, permeability from 2104 to 16361 md and hydrocarbon saturation from 66 - 98 percent. The shale volume was found to be in the range of 3 - 31 percent and net to gross from 0.69 - 0.97. The porosity- permeability relationship is near perfectly logarithmic with correlation coefficients (R^2) ranging from 0.98 to 0.99. The Bulk Volume Hydrocarbon (BVH) was found to be a good hydrocarbon indicator and also has a strong quadratic relationship with the acoustic impedance at the wells with correlation coefficients (R^2) ranging from 0.553 to 0.837. The sands studied are potential high quality reservoirs.

Keywords: *Geophysical logs; porosity; permeability; Bulk Volume hydrocarbon; Acoustic impedance; reservoirs.*

1. Introduction

The "Odokoko" field in the Coastal Swamp depobelt of the Niger Delta, Basin consists of-sands and shale formations.The mostly unconsolidated formations consist of sands ranging from fluvial(channel) to fluvio-marine (Barrier Bar sands), while shales are generally fluvio-marine or lagoonal. Formation evaluation is mostly based on geophysical logs [1]. Petrophysical parameters like lithology, fluid content, porosity, water saturation, hydrocarbon saturation and permeability are derived using geophysical welllog data. It is usually done to delineate the reservoir sands and asses their commercial viability by evaluating petrophysical parameters and consequently the volume of hydrocarbon in place and its producibility. In the work of [2], it was demonstrated that petrophysical parameters such as porosity (φ), permeability (K) and saturation (S), for any given rock type are controlled by pore sizes and their distribution and interconnection. He stated that a broad relationship exists between porosity and permeability of a formation. He stated that a broad relationship exists between porosity and permeability of a formation. The goal of reservoir characterization is to predict the spatial distribution of such petrophysical parameters on a field scale. This paper presents the results of studies of the petrophysical evaluation of the "Odokoko" field in the Coastal Swamp Depobelt of the Niger Delta Basin, and determining the porosity permeability relationship of the field using geophysical well log data. It presents a detailed qualitative and quantitative estimation of the reservoir and the fluids in it. This includes the lithology, porosity, permeability and hydrocarbon saturation. The Bulk Volume Hydrocarbon (BVH) is the product of effective porosity and hydrocarbon saturation. Its usefulness as a hydrocarbon indicator and relationship to acoustic impedance was determined in this study. These are results useful for locating and estimating the economic prospects of the reservoir(s) intercepted by the wells.

2. Geology and Stratigraphy of the Niger Delta

The Niger Delta consists of three major lithostratigraphic units: the Akata, Agbada and Benin formations. The Oligocene- Holocene Benin Formation is a loose fresh water bearing sand with occasional lignite and clay goesdown to a depth of 2,286 m. The Agbada Formation is made up of alternating sands and shales. The sands are mostly encountered at the upper parts while shales are found mostly at the deeper parts. The Agbada Formation is thickest at the centre of the Delta and is over 3700m and are Eocene-Holocene [3]. This is the seat of most known oil reservoirs in the Niger Delta. The Akata Formationthought to be at the base of the delta is Palaeocene- Holocene facies of marine origin and composed of thick shale sequences (potential source rock), turbidite sand (potential reservoir in deep water) and minor amounts of clay and silt. It is estimated that the formation is up to 7000m thickin the central part of the delta. The marine shale is typically over pressured [4].

The Niger delta oil province is characterized by approximately east-west trending syn-sedimentary faults and folds. These syn-sedimentary faults are called growth faults and the anticlines associated with them are called roll-over anticlines [5].

3. Materials and methods

Suites of Five geophysical well logs were obtained from SPDC in Nigeria, recorded at various locations within the "Odokoko" field, Niger Delta basin. A sample of these well logs is shown in Fig.2. Petrel® software: the Petrel software is a Schlumberger owned window PC software application designed to analyse oil reservoir data from multiple sources.

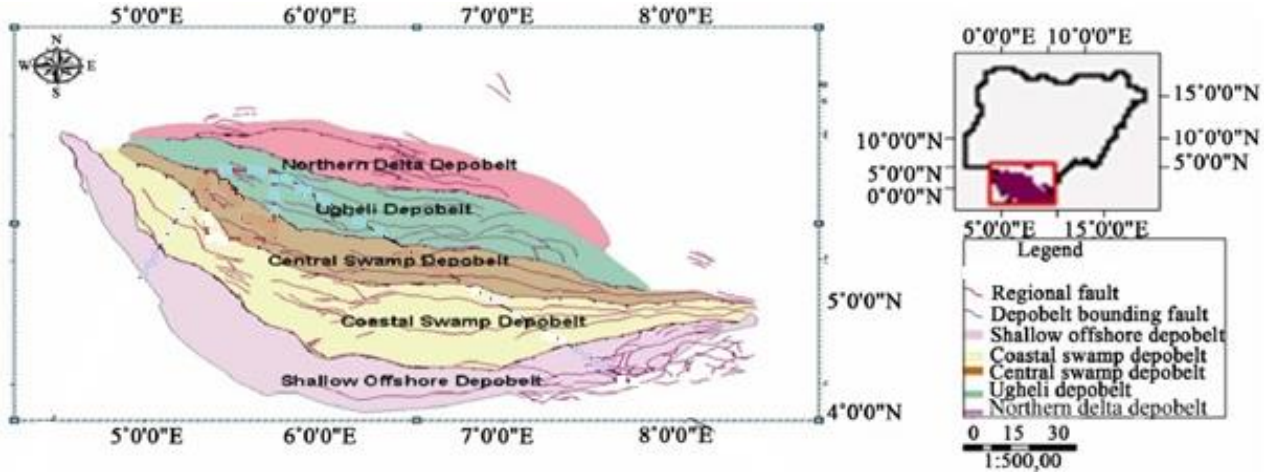

Fig 1 Map of Nigeria showing depobelts in the Niger Delta [6]

3.1. Qualitative analysis

The suite of geophysical well logs were evaluated to determine sand/shale lithology pattern, differentiate the hydrocarbon/non-hydrocarbon zones of the area penetrated by the wells.

3.1.1. Sand/shale lithology

Sand and shale bodies were delineated from the gamma ray log signatures. Sand bodies were identified by deflection to the left due to the low concentration of radioactive minerals in it and shale to the right due to the high concentration of radioactive minerals in it. This enables differentiation between sand, shaly sand, sandy shale and shale using the train estimation model process of Petrel to generate the lithology log. This is indicated by yellow for sand, orange for shaly sand, light grey for sandy shale and dark grey for shale colourations. The cross plot technique was also used for lithologic identification. A cut off of 80API gamma ray was used for classification of sands and shales and cross plotted with sonic, density and neutron porosity logs respectively.

3.1.2. Differentiation of hydrocarbon and non-hydrocarbon bearing zones

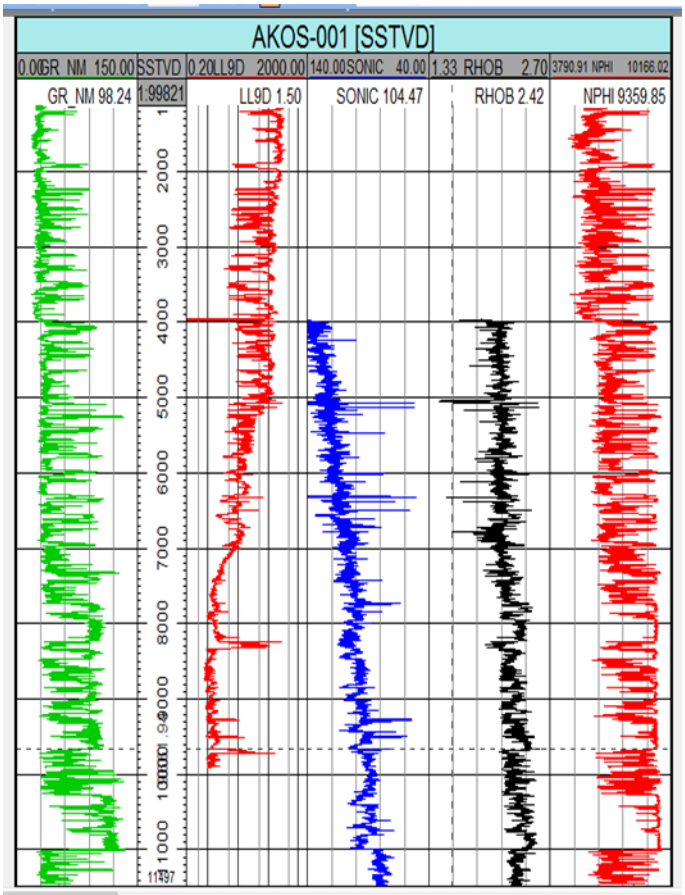

A combination of the gamma ray and resistivity logs were used to differentiate between the hydrocarbon and non-hydrocarbon bearing units. The resistivity and gamma ray logs are shown in tracks 1 and 2 of Fig. 2 respectively. The scale increases from left to right, the values depending on the log type and scale of data acquisition. The gamma ray log is used to indicate the sand and shale bodies within the formation. Hydrocarbon saturated zones in the sand bodies were identified by the deflection on the Laterolog Deep resistivity log. It is a well established fact that hydrocarbon is more resistive than formation waters. Increase in resistivity is indicated by deflections to the right on the resistivity log. Crossplots of BVH vs Acoustic (Impedance AI), porosity vs AI and water saturation vs AI were also performed.

Fig. 2. Typical suite of well logs in Odokoko field
GR_NM- Gamma Ray Log; LL9D-Resistivity Log; SONIC-Sonic log; RHOB-Density Log; NPHI-Neutron-Porosity Log

3.2. Quantitative interpretation

This involves the use of empirical formulae to estimate the petrophysical parameters such as porosity, permeability, volume of shale and hydrocarbon saturation.

3.2.1. Determination of volume of shale (V_{sh})

The gamma ray log was used to calculate the volume of shale in a porous reservoir. The first step in determining the volume of shale from a gamma ray log is the calculation of the gamma ray index using equation 1:

$$I_{GR} = \frac{GR_{log} - GR_{min}}{GR_{max} - GR_{min}} = \quad (1)$$

where: I_{GR} = Gamma ray index; GR_{log} = Gamma ray reading of the formation; GR_{min} = minimum gamma ray (clean sand); GR_{max} = maximum gamma ray (shale). All these values are read off within a particular reservoir.

Having obtained the gamma ray index, the volume of shale is calculated using the [7] formula (equation 2),

$$V_{sh} = 0.083(2^{3.7 \times I_{GR}} - 1.0) \quad \text{(Tertiary consolidated sand)} \quad (2)$$

3.2.2. Determination of porosity (Ø)

Porosity is defined as the percentage of voids to the total volume of rock. The Formation density log was used to determine Formation porosity. The Formation porosity was determined by substituting the bulk density readings obtained from the density log and volume of shale within each reservoir into equation 3 [7]

$$Ø_{eff.} = \frac{\rho_{ma} - \rho_b}{\rho_{ma} - \rho_{fl}} - V_{sh}\left(\frac{\rho_{ma} - \rho_b}{\rho_{ma} - \rho_{fl}}\right) \quad (3)$$

where: $Ø_{eff}$ is the effective porosity; ρ_{ma} is the matrix density = 2.65gm/cm^3 (sandstone); ρ_{fl} is the fluid density = 1.1gm/cm^3 (fluid density); ρ_b = formation bulk density.

The criteria for classifying porosity given is:
Ø <0.05= Negligible, 0.05< Ø<0.1= Poor, 0.1 Ø<0.15= Fair, 0.15< Ø<0.25%= Good, 0.25<Ø<0.30 = Very good, Ø>0.30 = Excellent.

3.2.3. Determination of compressional velocity (V_p)

This is the velocity of compressional seismic waves within a rock, ie velocity of acoustic wave in rock. It is estimated from the sonic log

$$V_p = 10^6/\Delta T\ (\mu sec/ft) \quad (4)$$

where: ΔT=corrected conic travel time in μsec/ft.

3.2.4. Determination of acoustic impedance

The Acoustic impedance values of the lithologies intercepted by the wells were calculated using the equation below.

$$AI = V_b * \rho_b \quad (5)$$

where: V_b =velocity of acoustic wave in rock = $10^6/\Delta T$ (μsec/ft); ρ_b = Density log value in gm/cc.

3.2.5. Estimation of water saturation

Water saturation of the un-invaded zone was determined using the [2] equation;

$$S_w{}^2 = \frac{F \times R_w}{R_t} \quad (6)$$

But $$F = \frac{R_o}{R_w} \quad (7)$$

Thus, $$S_w{}^2 = \frac{R_o}{R_t} \quad (8)$$

where: S_w= water saturation of the un-invaded zone; R_o= resistivity of formation at 100% water saturation; R_t= true formation resistivity (log readings); F = formation factor.
Irreducible water saturation is determined using [9]

$$S_{wirr} = \sqrt{\frac{F}{2000}} \quad (9)$$

3.2.6. Hydrocarbon saturation (S_h)

This is the percentage of pore volume in a formation occupied by hydrocarbons. It is obtained by subtracting the value obtained for water saturation from 100%.

i.e., $S_h = (100 - Sw)\ \%$ [2] (10)

where: S_h = hydrocarbon saturation; S_w = water saturation.

3.2.7. Permeability (K)

The ability of a rock to transmit fluid is referred to as permeability. It is related to porosity but not always dependent on it. It is controlled by the size of the connecting passages (pore throats or capillaries) between pores. It is measured in darcies or millidarcies. The permeability is obtained from the equation given by the Wyllie and Rose in [8].

$$k = \left[\frac{250 \times Ø^3}{S_{wirr}}\right]^2 \quad (11)$$

where S_{wirr} is the irreducible water saturation

A practical oil field rule of thumb for classifying permeability:
poor to fair = 1.0 to 14 md, moderate = 15 to 49 md, good = 50 to 249 md, very good = 250 to 1000 md, >1 darcy =excellent.

3.2.8. Determination of bulk volume hydrocarbon (BVH)

The BVH is the product of hydrocarbon saturation and effective porosity. It is an aggregate of three well log properties; gamma ray, density and resistivity logs. These logs enable the determination of lithology, porosity and water saturation. Accurate determination of these properties enables determination of good reservoir prospects as well as reliable reservoir characterisation. The BVH combines the strengths of these properties in order to deploy the synergy which exists among them for more accurate and reliable reservoir prediction and characterisation.

$$BVH = \emptyset_{eff.} \times S_h \quad (12)$$

BVH values >0.15 =good reservoir.

4. Results and discussion

The results of the study are presented in figures (3-8) and tables (1 -3) while the interpretation of results is presented both qualitatively and quantitatively.

4.1. Qualitative interpretation

For the log interpretation shown in Fig. 2, its litho-stratigraphic correlation furnishes knowledge of the general stratigraphy of the study field. Four lithologies were identified using the gamma ray log; **sand, shaly sand, sandy shale and shale**. The colour code for the lithology log are, yellow for sand, orange for shaly sand, light grey for sandy shale and dark grey for shale.

Correlating sand bodies of potential reservoir interest in this field was an uphill task. The gamma ray, resistivity, sonic, density and neutron logs showed great variations between wells even for those very close to each other. This is probably because the wells are located in areas with complicated faulting. The absence of some sands in some of the wells also indicate an unconformity in the area.

4.2. Well Correlation/Reservoir identification

Correlation was necessary to determine lateral continuity or discontinuity of reservoir facies in the field in order to properly delineate reservoir extent. Reservoir identification was done using gamma ray log signatures as markers and lithology indicators with a shale volume cut off of 20% and Laterolog Deep resistivity was used to identify potential reservoirs. The reservoir correlation panel is displayed in Fig 3. The alternation of sands and shale in various proportions and thicknesses within the evaluated depth conforms to that of the Agbada formation. The evaluated depth and the thicknesses of the various overlaying shale units, suggest a comfortable room for accumulation of matured hydrocarbon-prospective sequence in the studied area. From the correlation panel, there are stratigraphic discontinuities which may have been caused by faulting and or pinchouts in the area.

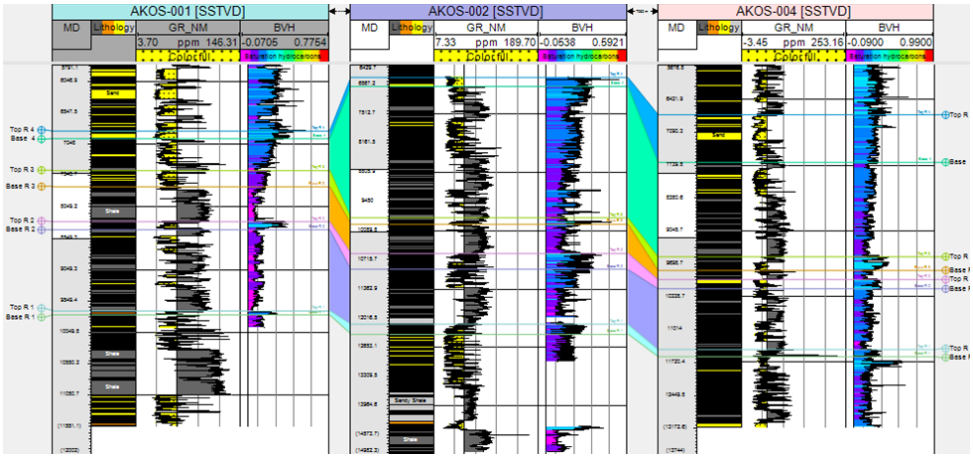

Fig.3. Well correlation panel showing the Top and Base of the interpreted reservoir sands.

4.3. Porosity - permeability relationship

The permeability of the Formations were determined using equation (11). It ranged from 2104 - 16361 md. The permeability values show excellent permeability. Figs. 4a-care sample porosity - permeability plots. It shows a perfectly correlated logarithmic relationship between the porosity and permeability. Permeability was found to be highest in Akos 001 and least in Akos 004. This may be as a result of more clay volumes present in the sand at well Akos 004.

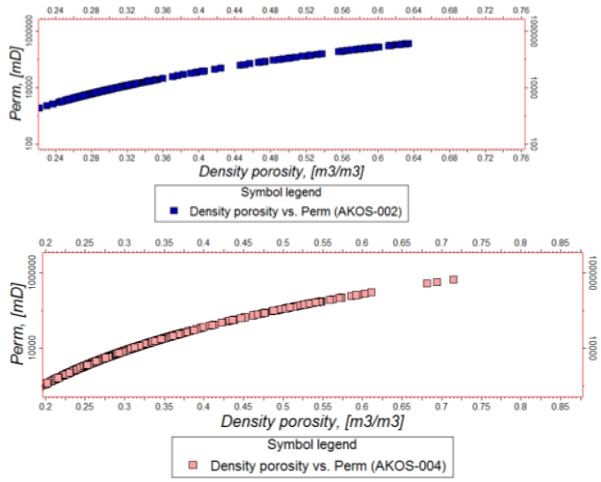

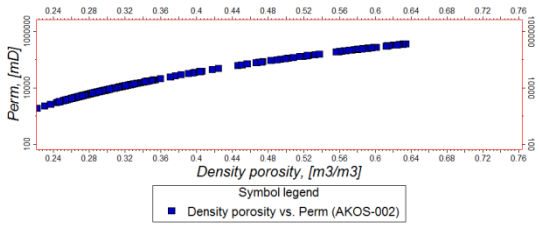

Fig 4 (a-c). Porosity permeability relationship in Akos 001,002 and 004

Table 1. Porosity Permeability relationships of the wells in the study area

Wells	Porosity-permeability relation-ship	Correlation coefficient (R^2)
AKOS 001	Log K=5.59 φ + 2.31	0.99
AKOS 002	Log K=5.36 φ + 2.30	0.99
AKOS 004	Log K=6.17 φ + 2.07	0.98

4.4. BVH-AI relationships of the wells in the study area

The BVH was determined using equation 12.

Table 2. Comparison of correlation coefficients of the crossplots of AI vs porosity, AI vs water saturation and AI vs BVH

	Correlation coefficient, R^2			
Parameter	Akos 001	Akos 002	Akos 004	Average
Acoustic Impedance (Z) vs porosity	-0.76	0.033	-0.63	-0.4533
Acoustic Impedance (Z) vs Water saturation	0.81	0.04	0.25	0.367
Acoustic Impedance (Z) vs BVH	0.837	0.553	0.714	0.701

The impedance tends to increase with decreasing BVH and increasing shaliness probably due to decreasing effective porosity as seen in figure 5.

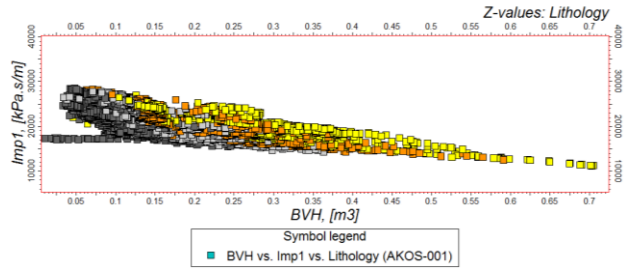

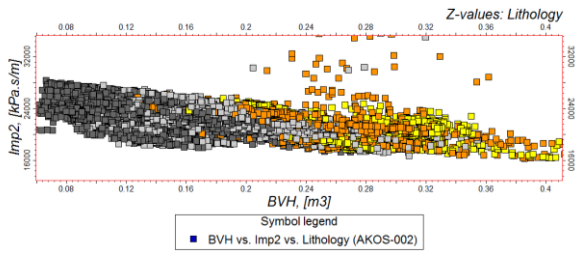

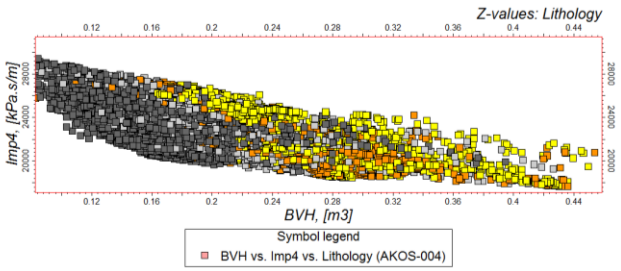

Figure 5. Crossplots of BVH and P-impedance colored by lithology

Table 3. BVH-AI relationships of the wells in the study area

Wells	BVH-Acoustic impedance relationships	*R2*
AKOS 001	AI=26056.1-32230.9BVH +1588.7BVH2	0.837
AKOS 002	AI= 27218.7-40537.9 BVH + 1283.3 BVH2	0.553
AKOS 004	AI= 30775.5-48787.2BVH + 466417.1 BVH2	0.714

The correlation coefficients, R^2, values displayed in Table 3 shows clearly that the BVH and acoustic impedance, AI, have a strong quadratic relationship.

4.5. BVH as hydrocarbon indicator

Figures 6 displays the results of petrophysical analysis. The BVH shows a potential as a good hydrocarbon indicator. It corroborates gamma ray, resistivity and Poisson ratio logs indicating hydrocarbon presence in sand D_2000. As can be seen in Fig. 7, intervals of high BVH coincides with sand and shaly sand lithologies, high effective porosity, high permeability, low water saturation, low shale volume, and low Poisson ratio. All these are indicative of good reservoir prospect sands in the three wells displayed.

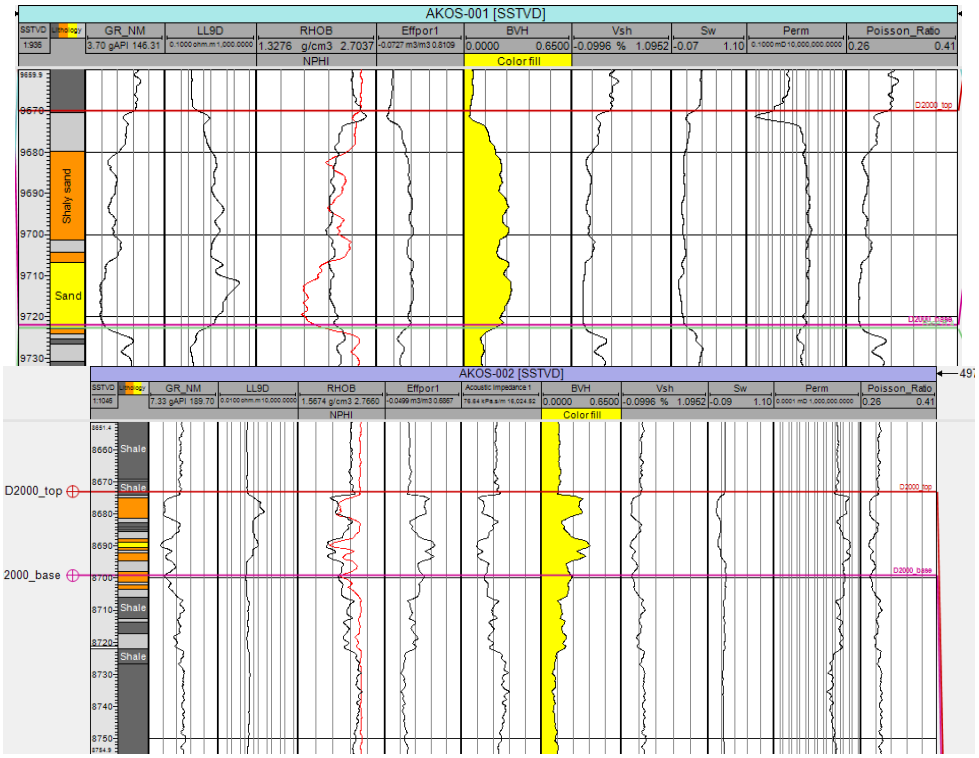

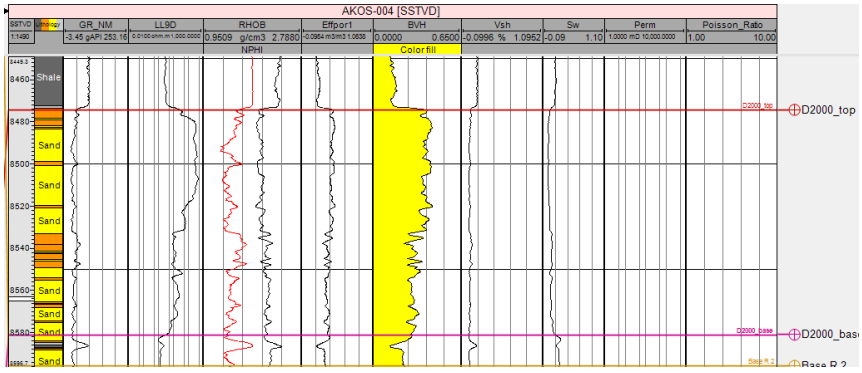

Fig 6. Results log for the D_2000 reservoir showing the BVH as a hydrocarbon indicator in agreement with Gamma ray, resistivity and poisson ratio logs, BVH values averaging 0.26 in Akos 001, 0.27 in Akos 002 and 0.29 in Akos 004

4.6. Quantitative interpretation

Following is a description of key petrophysical parameters for each reservoir intercepted by the wells arranged in stratigraphic order.

4.4.1. Reservoir 4

Table 4 shows the result of some computed petrophysical parameters for reservoir 4 It has a gross thickness ranging from 87 to 730 feet and the average net-gross ratio (N/G) is 0.94.

The average porosity in the three wells which intercept reservoir 4 is 0.31. This is an excellent porosity value. The average permeability is 10655md, an excellent value that permits the free flow of fluid within the reservoir. The hydrocarbon saturation is 0.89 on average, hence reservoir 1 is a hydrocarbon saturated reservoir with potential for high recovery factor. It has an average BVH of 0.26. This implies that sands having BVH of 0.26 or greater are potentially good reservoirs in the study area.

4.6.2. Reservoir 3

Some computed petrophysical parameters for reservoir 3 are shown in Table 4. It has a gross thickness ranging from 98 to 301 feet and the average net-gross ratio (N/G) is 0.93.

The average porosity across the three wells within which reservoir 3 is encountered is 0.29. This is a very good porosity value. The average permeability is 5366 md, an excellent value that permit the free flow of fluid within the reservoir. The hydrocarbon saturation indicates a high proportion of hydrocarbon (0.87 average) to the quantity of water within the reservoir. Hence reservoir 2 is a hydrocarbon saturated reservoir. It has an average BVH of 0.24. This implies that BVH of 0.24 or greater are potentially good reservoirs in the study area and that reservoir 3 has less than reservoir 4 if they have the same areal extent.

4.6.3. Reservoir 2

Table 4. show the result of some computed petrophysical parameters for this reservoir. It has a gross thickness ranging from 104 to 134 feet, and the average net to gross ratio (N/G) is 0.94.

It has an excellent porosity value averaging 0.32. The average permeability is 13.312 darcies, an excellent value. The hydrocarbon saturation indicates a high proportion of hydrocarbon (0.94 average) to the quantity of water within the reservoir. It has an average BVH of 0.28. This implies that reservoir 2 has greater potential than reservoir 4and 3 if they have the same areal extent.

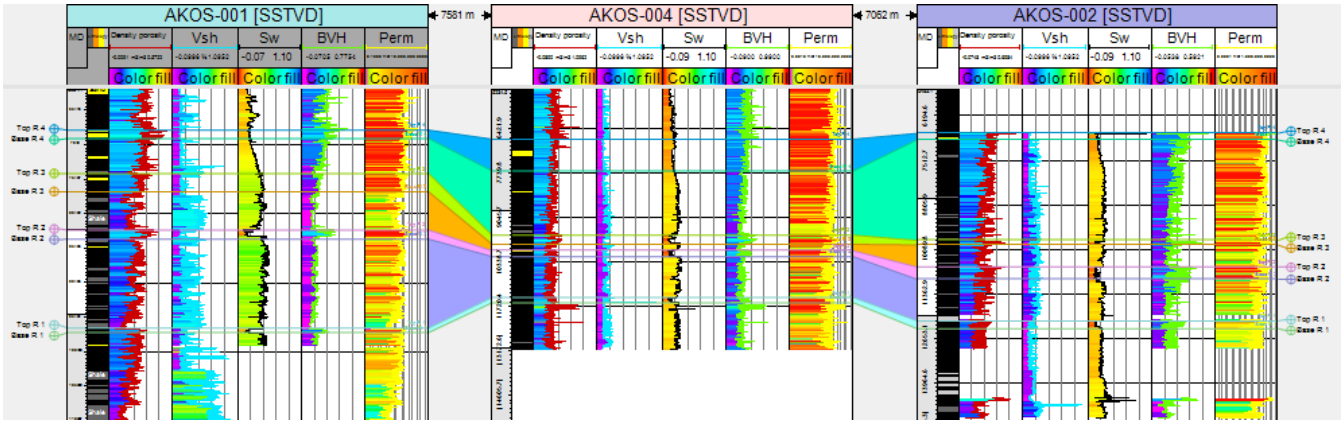

Fig. 7. Typical results logs including lithologic section for "Odokoko"field, Niger Delta. Quantity of water within the reservoir.

4.6.4. Reservoir 1

Some computed petrophysical parameters for reservoir 1 are displayed in table 2. It has a gross thickness ranging from 58 to 174 feet, and the average net to gross ratio (N/G) is 0.96.

The average porosity across the three wells incepting reservoir 1 is 0.31. This is an excellent porosity value. The average permeability is 12.168 darcies, indicating free flow of fluid within the reservoir. The hydrocarbon saturation of 0.95 average, to the quantity of water within the reservoir implies reservoir 1 is a hydrocarbon saturated reservoir. It also has an average BVH of 0.28.

Table 4 Petrophysical Analysis of 'Odokoko' field showing field average values.

	THICKNESS (ft)				NET TO GROSS				POROSITY (Φ)				Shale volume (Vsh)				Water saturation (Sw)				Hydrocarbon Saturation (Sh)				Bulk volume Hydrocarbon (BVH)				Permeability (k)			
WELLS	R4	R3	R2	R1	R4	R3	R2	R1	R4	R3	R2	R1	R4	R3	R2	R1	R4	R3	R2	R1	R4	R3	R2	R1	R4	R3	R2	R1	R4	R3	R2	R1
AKOS 001	132	301	104	58	0.94	0.86	0.87	0.97	0.30	0.23	0.33	0.31	0.06	0.14	0.13	0.03	0.13	0.34	0.11	0.05	0.87	0.66	0.89	0.95	0.2453	0.13055	0.25552	0.28567	9848	2104	14242	9836
AKOS 002	87	98	282	174	0.97	0.97	0.98	0.96	0.31	0.32	0.34	0.31	0.03	0.03	0.02	0.04	0.09	0.03	0.02	0.04	0.91	0.97	0.98	0.96	0.2736	0.30109	0.32654	0.2857	9677	1694	16361	10528
AKOS 004	730	206	134	99	0.92	0.96	0.97	0.96	0.31	0.32	0.29	0.3	0.08	0.04	0.03	0.04	0.11	0.03	0.04	0.05	0.89	0.97	0.96	0.95	0.2538	0.29798	0.27005	0.2736	12440	12300	9332	16141
AVERAGE	316	202	173	110	0.94	0.93	0.94	0.96	0.31	0.29	0.32	0.31	0.06	0.07	0.06	0.04	0.11	0.13	0.06	0.05	0.89	0.87	0.94	0.95	0.26	0.24	0.28	0.28	10655	5366	13312	12168

4.7. Crossplot analysis

The cross plots in fig.8(a-i) show that clay proportions were increasing from Akos 001 to 002 and 004 having the highest clay volume. From the relative positions of the wells, the clay volume is increasing westwards. This may indicate that the sediments are transported from the east and deposited westwards becoming finer with depth.

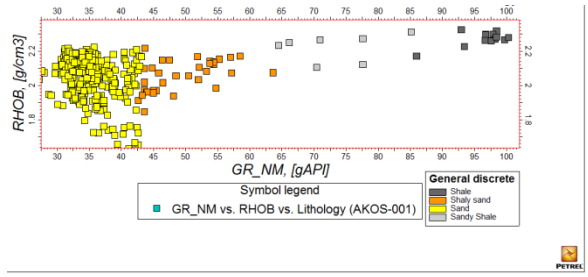

a. Gamma ray - density cross plot for Akos 001

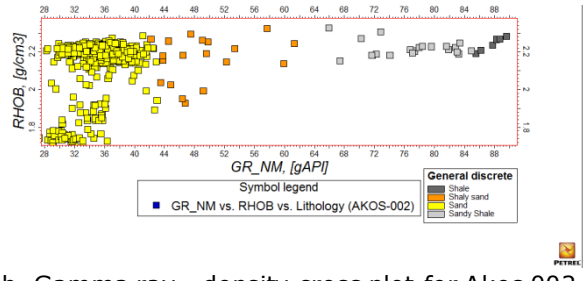

b. Gamma ray - density cross plot for Akos 002

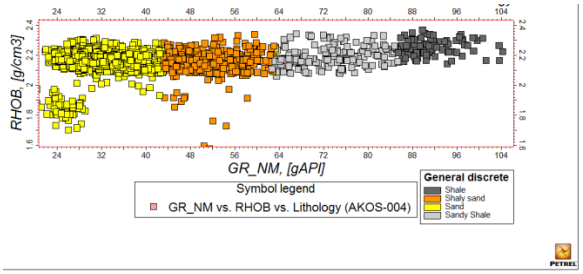

c. Gamma ray - density cross plot for Akos 003

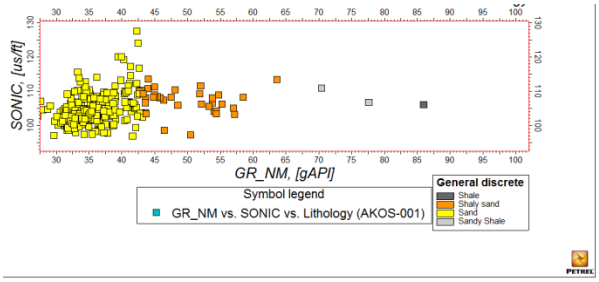

d. Gamma ray - Sonic cross plot for Akos 001

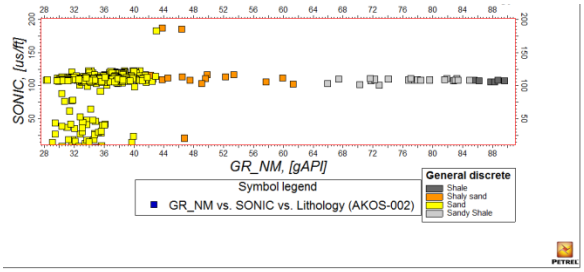

e. Gamma ray - Sonic cross plot for Akos 002

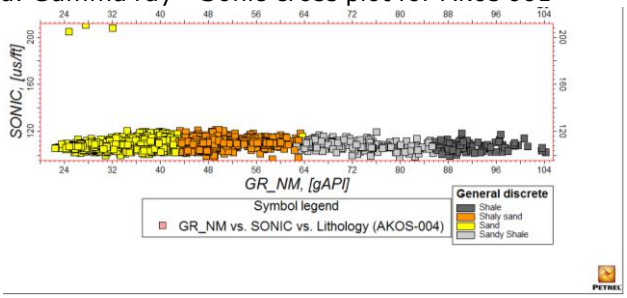

f. Gamma ray - Sonic cross plot for Akos 003

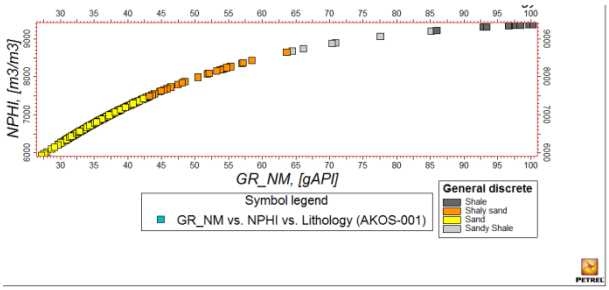

g. Gamma ray - NPHI cross plot for Akos 001

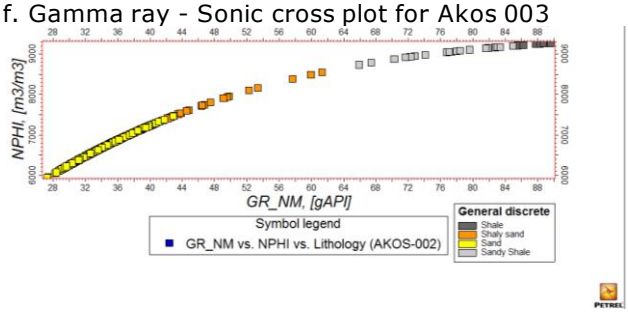

h. Gamma ray - NPHI cross plot for Akos 002

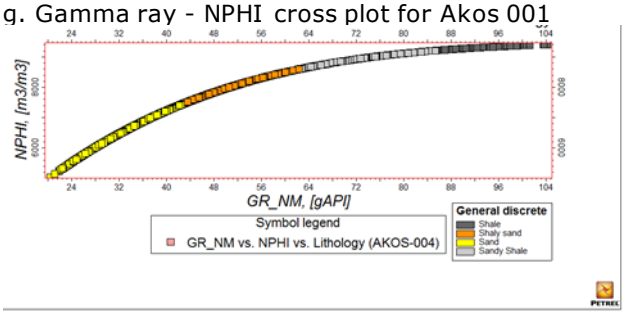

i. Gamma ray - NPHI cross plot for Akos 003

Fig. 8 (a-i) Cross plot technique for lithologic identification for Odokoko field for Akos 001, 002and 004 wells

5. Conclusion

All the reservoirs encountered have excellent porosity and permeability values. Their gross thicknesses range between 110 and 316 feet, net to gross values greater than 0.80, and high hydrocarbon saturation greater than 0.89 on average, implies excellent hydrocarbon pore volume for hydrocarbon accumulation in commercial quantity. The permeability values were of excellent value. The BVH is found to have a strong quadratic relationship with acoustic impedance and is a good hydrocarbon indicator. Based on this study, the "Odokoko" field contains high quality reservoirs.

References

[1] Aigbedion I, and Iyayi SE, Formation Evaluation of Oshioka Field Using Geophysical Well Logs. Middle-East Journal of Scientific Research, (2007), Vol. 2 (3-4) pp 107-110,

[2] Archie GE. The electrical resistivity log as an aid in determining some reservoir characteristics, Transactions of American Institute of Mineralogy, Metallurgy and Petroleum Engineering., (1942), Vol.146, p.54-62.

[3] Mode AW, Adepehin EJ, Anyiam OA, Petrophysical Effects of Clay Heterogeneity on Reservoirs' Properties: Case Study of "Brown Field, Niger Delta, Nigeria. NAPE Bulletin, (2013), Vol.25 No 1, pp. 61-67

[4] Doust H, and Omatsola E.:Niger Delta, In, Edwards,J.D., and Santogrossi, P.A., Eds., Divergent/Passive Margin Basins, AAPG Memoir 48: Tulsa, American Association of Petroleum Geologists, (1990), pp. 239-248.

[5] Evamy DD, P. Hammering, WA Kmoap and P. Rowlands, Hydrocarbon habitat of the tertiary Niger Delta,American Association of Petroleum Geologist Bulletin, (1978), Vol.62 No.(2) pp 1-10.

[6] Onyekuru SO, Ibelegbu EC, Iwuagwu JC, Akan Godfrey Essien, A.G.,and Akaolisa, C.Z., Sequence Stratigraphic Analysis of "XB Field", Central Swamp Depobelt, Niger Delta Basin, Southern Nigeria, International Journal of Geosciences, (2012), Vol. 3, pp 237-257

[7] Dresser Atlas, (1979) Log Interpretation Charts (Houston, Texas, Dresser Industries Inc. p. 107.

[8] Asquith G and Krygowski D Relationships of Well Log Interpretation in Basic Well Log Analysis Method in Exploration Series, American Association of Petroleum Geologists, (2004) No 3.pp.102.

To whom correspondence should be addressed: Daniel Ayodele, Department of Geology, University of Nigeria, Nsukka

Petroleum and Coal

Article **Open Access**

THE SUITABILITY OF EGG SHELL AND SNAIL SHELL WASTE FOR PH AND MUD WEIGHT ENHANCEMENT OF WATER BASED DRILLING MUD

Rita U. Onolemhemhen, Olugbenga Olamigoke, Abdul-Quadri O. Kaka

Department of Chemical and Petroleum Engineering, University of Lagos

Received November 29, 2018; Accepted January 18, 2019

Abstract

In this study, the effect of two food waste materials, egg shell, and snail shell as local environmentally-friendly additives, on the pH and mud weight of water based mud was evaluated. The water based mud samples were formulated using bentonite, barite, distilled water with egg shell and snail shell in varying weight proportions. Mud weight and pH measurements were taken at 25ºC. The results showed that egg shell and snail shell increased the pH value by 8.4% and 29.9% respectively due to the addition of 30g of each additive. The pH value was however increased by 54.9% when 15g of each additive in equal amounts was added to the mud. Correspondingly, the mud weight was increased by 12.6% and 8.4% due to the addition of 30g of egg shell and snail shell respectively. The mud weight was however increased by 28.9% when 15g of each additive in equal amounts was added to the mud. It was concluded that the combination of a snail shell and egg shell has a high potential for pH enhancement with a reduced potential for the mud weight increase. Snail shell is more effective as a pH enhancer while egg shell is more effective in increasing mud weight.

Keywords: *Water based mud; pH enhancer; local additives; egg shell; snail shell; weighting agent.*

1. Introduction

There are a plethora of additives for drilling fluids. These drilling mud additives are chemicals added to drilling mud in order to change the mud properties and composition. However, many efforts have been devoted to drilling mud formulation mainly to enhance the quality and function of drilling muds, as well as to comply with the more stringent laws on environmental pollution or marine contamination. Some are used for pH control-that is, for chemical-reaction control (inhibit or enhance) and drill-string-corrosion mitigation [1-2]. While synthetic additives are currently in use, several researchers have investigated the use of natural products as additives to these chemicals.

The potential of cocoa pods, plantain peels, rice husks, and groundnut shells as corrosion inhibitors was investigated. Cocoa pod extracts exhibited high corrosion inhibition potential when compared to the synthetic KOH. Cocoa pod extract was also found to be more stable thermally and very effective in filtration loss reduction at high temperatures. However, it showed a thinning tendency with the mud requiring additional viscosifier to improve its rheology [3]. An experimental investigation into the use of burnt plantain and banana peels in water based drilling local mud as corrosion control additives revealed that though plantain peels were more effective than banana peels for increasing the pH both local additives increased mud pH to between 9.5 to 12.5 which compared suitably to imported sodium hydroxide [4].

Properties of mud formulated with variable concentrations of cellulose processed from corn cob were compared with that of a standard mud formulated from Polyanionic Cellulose (PAC). The results showed that the pH, mud density, specific gravity of the mud formulated from corn cob cellulose are higher than that of the standard mud, but rheology of the prepared mud was lower than that of the standard mud. The results show that cellulose processed from corn

cob can significantly reduce fluid loss in a water based drilling mud, suggesting cellulose as a good fluid loss control agent [5]. Grass added to the bentonite drilling fluid improved the rheological properties such as apparent and plastic viscosities and gel strength. The filtration characteristics of the bentonite drilling fluid were also enhanced because lower filtration losses were observed for all samples. However, the test carried out on the pH indicated that the addition of grass decreased the pH of the drilling fluid [6].

The aim of this paper is to investigate the suitability of egg shell and snail shell as local additives to enhance and improve the pH and density of water based mud, as both materials are biodegradable and easily accessible.

1.1. The composition of food waste additives

The main component of snail shell includes more than 95% calcium carbonate in the form of aragonite ($CaCO_3$), a small number of shells hormone (organic matter and trace elements) and trace amounts of K, Na, Zn, Sr, Fe, Mg but with no trace of sulfur [7]. The pH value of snail shell in solution is 8.84, which shows that its solution is alkaline, which may result from the presence of Calcium carbonate and protein as some of the composition of the shell [8].

The microstructure of the egg shell powder reveals that the powder consists of porous irregular shaped powder. The Energy-dispersive X-ray spectroscopy of egg shell particles reveals that the particles contain Ca, Si, O, C. These elements confirm that, the egg shell powder consists of calcium carbonate in the form of calcite ($CaCO_3$), tilleyite ($Ca_5Si_2O_7(CO_3)_2$), *etc.* [9]. The composition of hen eggshell has been reported to be 94 to 96 kg calcium carbonate, 1 kg magnesium carbonate, and 1 kg calcium phosphate per 100 kg eggshell with a minor amount of organic matter [10]

2. Experimental section

2.1. Materials

The influence of snail shell powder and egg shell powder on pH and mud weight of water based drilling mud was investigated.

2.1.1. Egg shell (ES) powder

Egg shell was extracted from boiled eggs. After the extraction, it was then broken into smaller sizes to provide a large surface area for effective drying. The egg shell was naturally dried under the sun for about 2 days because it has low water content. It was then grinded, using a manual grinder and pulverized using 250mm spaced sieve and then transferred into a clean petri-dish for storage.

2.1.2. Snail shell (SS) powder

Snail shells were obtained from de-shelled cooked snails. The snail species is *Archachatina marginata*. The shells were dried naturally under the sun for about 3 days because snail shell has high water content compared to the egg shell. The snail shell was then grinded using a manual grinder after which it was pulverized using 250mm spaced sieve. The pulverized sample was transferred into a petri-dish container for storage.

2.1.3. Drilling mud

Non-inhibitive water based mud was prepared (the composition of the control mud sample is shown in Table 1).

Table 1. Composition of control mud sample

Constituents	Concentration	Function
De-ionized Water	350 ml	Base fluid
Barite	90 grams	Weighting agent
API Bentonite	25 grams	Viscosifier

2.2. Methods

2.2.1. Mud balance

A pressurized mud balance was used to determine the mud weight of each sample. The mud balance was calibrated using distilled water. The balanced cup was cleaned, dried and filled to the brim with the mud sample to be measured. The lid was placed on the cup as some mud flowed out of the hole on the lid to ensure that there was no trapped air in the cup. The cup and lid were wiped to dry off any mud on the surface in order to obtain accurate measurement as the knife edge was placed on the fulcrum and the rider adjusted until the cup content and the rider was at equilibrium. The density of the mud sample was read on the calibrated arm of the mud balance.

2.2.2. pH Meter

The pH meter was calibrated using deionized (distilled) water and the mud sample to be measured was poured into a glass beaker. The pH meter probe was immersed in the mud sample and at steady pH value indicated on the meter. This was recorded as the pH value of the mud sample.

2.3. Procedure

Nineteen water based mud samples were prepared to have varying masses of egg shell and snail shell in additional to the constituents given in Table 1. The first sample (Sample A) is the control mud without the local additives. Samples B to G have egg shell concentration ranging from 5g to 30g with the concentration increasing by 5g across samples. Samples H to M have snail shell concentration ranging from 5g to 30g with the concentration increasing by 5g across samples. Both egg shell and snail shell were blended into samples N to S in equal amounts ranging from 2.5g to 15g of each local additive. The corresponding pH and mud density for each were measured using mud balance and pH meter respectively. The effect of the local additives on the properties of the water based drilling mud was compared to that of the standard API values.

3. Results and discussion

3.1. The effect of the local additives on mud weight

The mud weight of the control mud sample before the addition of either egg shell or snail shell was 9.50 ppg. Figure 1 shows the effect of the local additives on mud weight. On addition of 5 g of each local additive to different samples of the control mud, snail shell increased the mud weight by about 0.63% while egg shell increased the mud weight by 1.89%, with egg shell having the more obvious effect on the mud weight of the drilling fluid. With the addition of 10 g of each local additive to different samples of the control mud, the mud weight of egg shell gave 9.73 ppg which is an increase of 2.42% due to the egg shell, and that of snail shell gave 9.64 pgg which is an increase of 1.47%.

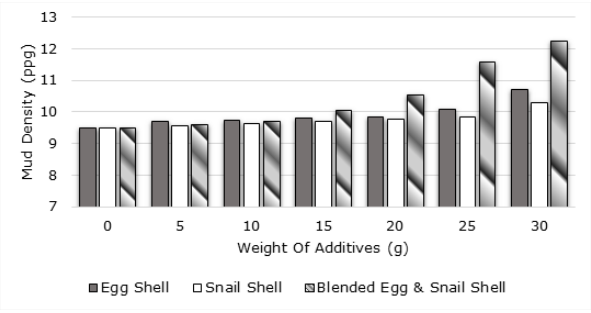

Figure 1. Effect of additives (individual and combined) on mud density

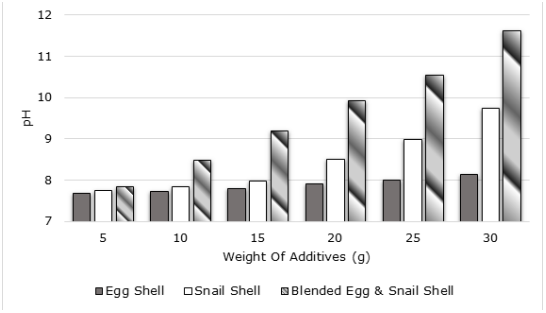

Figure 2 Effect of additives (individual and combined) on pH of mud samples

The mud weight was increased by 12.6% and 8.4% due to the addition of 30 g of egg shell and snail shell respectively to separate control mud samples.

Both local materials (egg shell and snail shell) were combined in weight proportions with the control mud which contains 350ml of de-ionized water, 90 g of barite and 25 g of bentonite. With the addition of 2.5 g of egg shell and 2.5 g of a snail shell, the mud weight increased by 1.05%. With the addition of 5 g of each local material combined in the mud, the mud weight increased by 2.1%. As shown in Figure 1, the effect of the combined local additives on mud weight is less than the individual effect of egg shell at 5 g and 10 g weight proportion. However, on the addition of 7.5 g of each local material combined in the mud which gives a total weight of 15 g, the weight increased by 5.8% as compared to 3.16% and 2.2% due to the addition of 15 g of egg shell and snail shell respectively. The effect of combining both egg shell and snail shell increases with increasing weight proportion in the water based drilling mud, as shown in Figure 1. The mud weight increased by 28.9% due to the addition of 15 g of both egg shell and snail shell (total local additive weight of 30 g) while the weight by 12.6% and 8.4% due to the addition of 30 g of egg shell and snail shell respectively.

A statistical correlation for mud weight estimation was developed from the mud weight measurements obtained from the addition of egg shell powder and snail shell powder to water based drilling mud.

$$MW = 9.46 + 0.020547SS + 0.001254ES^2 + 0.009679(ES)(SS) \quad (1)$$

The correlation has $R^2 = 0.969$ (Adjusted $R^2 = 0.963$ and Standard error of 0.139853). The correlation is a non-linear regression equation with a significant two-way interaction term (ES)(SS). The correlation is applicable for less than 30 g of the local additive; egg shell, snail shell or combined additives.

3.2. The effect of the local additives on the pH

The pH is defined as the negative log of the activity of the hydrogen ion in an aqueous solution. Solutions with less pH less than 7 are said to be acidic, and solutions with a pH greater than 7 are basic or alkaline. It was expected that both egg shell and snail shell would significantly enhance the pH of drilling mud because of their high calcium content. The pH measurements taken are shown in Figure 2.

The incremental additions of egg shell gave a minimal change in pH of mud while additions of snail shell enhanced pH value. Figure 2 shows that as the mud weight increased the pH value also increased due to the additional additives added to the drilling mud. It can be clearly observed that snail shell is a better pH enhancer than an egg shell. The combination of both local material (i.e. egg shell and snail shell) further enhanced the pH values of the drilling mud.

The initial pH value of the control mud sample was 7.65. As shown in Figure 2, the pH increased by 1.31% to 29.9% due to the additional of 5 g to 30 g of snail shell respectively. The addition of 5 g of egg shell increased the pH by only 0.52% while the pH increased by 8.4% on the addition of 30 g of the egg shell to the control mud. Significant pH enhancement was observed with both egg shell, and snail shell was added to the control mud. With the addition of 2.5 g of egg shell and 2.5 g of a snail shell, the pH increased by 2.61%. On the addition of 15 g of each local material combined in the mud which gives a total weight of 30 g, the pH was increased by 54.9%.

A statistical correlation for pH estimation was also developed from the pH measurements obtained by the addition of egg shell powder and snail shell powder to water based drilling mud.

$$pH = 7.7035 + 0.01259ES + 0.002131SS^2 + 0.001538(ES)(SS) \quad (2)$$

The correlation has $R^2 = 0.977$ (Adjusted $R^2 = 0.973$ and Standard error of 0.175104). From the measurements, pH strongly correlates with both the square of the snail shell weight and with the two-way interaction term (ES)(SS). However, pH correlates weakly with the egg shell added. The correlation is also applicable for less than 30 g of the local additive; egg shell, snail shell or combined additives.

Drilling fluids perform better in pH range between 9.5 and 12.5 for water-base mud. If the pH of the mud is low, below 7.0, it becomes acidic and can corrode the drilling equipment and also pollute the environment [11]. The results gave an average pH value between 7.69 and 12.25 which is within the stipulated API standard of 9.5 – 12.5.

This results confirm that snail shell is effective as a pH enhancer. It measures up to caustic soda in its pH enhancing quality, and the incremental addition of the additives increase the pH of the mud. Furthermore, the combination of egg shell and snail shell can be used for pH enhancement.

4. Conclusions

Egg shell powder has a higher potential to enhance water based drilling mud weight as compared to snail shell powder. Snail shell powder is effective in enhancing the pH of water based drilling mud. The effect of snail shell compared favourably to sodium hydroxide the widely used pH enhancer in the drilling industry. Egg shell minimally enhanced the pH as compared to a snail shell.

The effect of combined egg shell and snail shell blended into the drilling mud for enhancing drilling mud is not significant below 7.5 g/350 mL. However, above this threshold, the combined additive is more effective than egg shell in enhancing the mud weight.

Egg shell and snail shell blended into water based drilling mud are recommended for enhancing the pH. Similar pilot studies can be guided by the statistical correlations for mud weight and pH using egg shell and snail shell independently in combination.

Recommendation

Based on these results and conclusions of the experimental research study, the following recommendations are suggested for future work:

- The effect of egg shell and snail shell on the rheology of water based mud is imperative.
- The potential of egg shell for mud weight enhancement should be investigated without barite as the weighting agent and compared to industrial calcium carbonate.

Acknowledgements

The authors would like to thank all the technical staff at the Drilling Fluids Laboratory in the Department of Chemical and Petroleum Engineering at the University of Lagos.

References

[1] Eustes III AW. Fundamentals of Drilling Engineering, 1st ed.; Mitchell, RF., Miska, S. Ed.; Society of Petroleum Engineers, 2011; Vol. 12, p. 95.

[2] Husin H, Elrais KA, Choi HJ, Aman Z. Influence of Graphene Nanoplatelet and Silver Nanoparticle on the Rheological Properties of Water-Based Mud. Appl. Sci. 2018; 8(1): 1-13.

[3] Aremu MO, Arinkoola AO, Salam KK, Ogunmola EO. Potential of Local pH Control Additives for Corrosion Inhibition in Water Base Drilling Fluids. Pet Coal 2017; 59(5): 611-619.

[4] Adebowale AOJ, Mnape MMR, Jamiudeen KR. Local content supplements As an Alternative to Imported Corrosion Control Additives for Drilling Mud Treatment. Proceedings of the International Academic Conference for Sub-Sahara African Transformation & Development 2015; 3(4): 1-8.

[5] Nmegbu CGJ, Bekee B. Evaluation of Corn Cob Cellulose and its Suitability for Drilling Mud Formulation Int. Journal of Engineering Research and Applications. 2014; 4(5): 112-117.

[6] Hossain EM, Wajheeuddin M. The use of grass as an environmentally friendly additive in water based drilling fluids. Pet. Sci. 2016; 13(1): 292–303.

[7] Zhang Y, Liu S, Wu H. Experiment study on the decomposition properties of snail shell. BTAIJ, 2014; 9(8): 303-307.

[8] Jatto OE, Asia IO, Medjor WE. F. Proximate and Mineral Composition of Different Species of Snail Shell. The Pacific Journal of Science and Technology. 2010; 11(1); 416-419.

[9] Aigbodian VS, Edokpia RO, Asuke F, Eke MN. Development of Egg Shell Powder Solution as Ecofriendly Reagent: for Chemical Treatment of Natural Fibers for Polymer Composites Production J. Mater. Environ. Sci., 2018; 9(2): 559-564.

[10] Garnjanagoonchorn W, Changpuak A. Preparation and Partial Characterization of Eggshell Calcium Chloride. International Journal of Food Properties, 2007; 10: 497–503.
[1] Okorie OM, Offia US. Basic Petroleum Production Technology. 1st Ed., COEWA Publishers, Warri, p. 215-265.

To whom correspondence should be addressed Dr. Olugbenga Olamigoke, Department of Chemical and Petroleum Engineering, University of Lagos, oolamigoke@unilag.edu.ng

Petroleum and Coal

Article **Open Access**

ECONOMIC MODEL AND RISK ANALYSIS FOR NATURAL GAS PLANT IN A DYNAMIC GAS PRICING SYSTEM IN NIGERIA

G. Okechukwu Ani, and S. Sunday Ikiensikimama

Petroleum and Gas Engineering Department, University of Port Harcourt, Nigeria

Received January 5, 2019; Accepted March 15, 2019

Abstract

The monetization of natural gas in Nigeria, rather than its wrong usage to alter the natural state of the environment via flaring, has taken the front stage of the investment portfolio. However, investors should be well informed of the profitability of the investment. This paper seeks to valuate the viability of investment in the natural gas plant from the source to consumers. Developing economic and cash flow model, determination of economic/profitability indicators, and sensitivity analysis are the stages adopted for this work. The sensitivity analysis is in two parts: deterministic and stochastic sensitivities. CAPEX, OPEX, LPG percentage recovery, wellhead gas, dry gas and LPG prices (input variables) and NPV, IRR, and PI (forecast variables) were selected for the sensitivity analysis. In the stochastic analysis, Monte Carlo Simulation was carried out using @RISK software. Results obtained shows that the estimated deterministic economic indicators, are NPV: $3889.5, IRR: 58.3% (real) and 84.86% (nominal, PI: 3.59 and payback time: 1.46 years, which meet the criteria for viable investment in the gas processing plant. The stochastic values show that the NPV is $3674.22 million, IRR is 82.23% (nominal) and 55.75% (real), and PI is 3.462, and the likelihood is 58.91%, 59.92%, and 58.27%, indicating 40% uncertainty in achieving these values. The sensitivity analysis reveals that this uncertainty is the risk imposed by the CAPEX, OPEX and wellhead gas price. The LPG price and percentage recovery have a high positive impact on the forecast variables. This work will enable decision makers to make an informed decision before investment.

Keywords: *Monetization; Risk and Uncertainty; @RISK, Forecast; Monte Carlo; Profitability indicators; Gas infrastructure.*

1. Introduction

The drive for a cleaner source of energy is inevitable, to reduce environmental pollutants, sustain the natural state of the ecosystems and natural gas has been a cleaner source of energy when combusted. Nigeria has over 180 Tcf of natural gas reserves [1-3]. The total natural gas reserve in Nigeria is 192.065 Tcf. This total gas reserve has a breakdown of 97.208 Tcf Associated Gas (AG) reserves and 94.857 Tcf Non Associated Gas (NAG) reserves [4]. According to [1] and [2], (between 2008 and 2014), natural gas has under gone utilization in Nigeria, but not optimal utilization. The recent discovery of new oil and gas fields may have to increase Nigeria natural gas reserves to 192 Tcf, as stated by [3] and [4] (Figure 1).

Nigeria natural gas reserve is enormous but it is under-utilize, and gas flaring activities have taken advantage of this under-utilization which is as a result of poor gas infrastructural development. Nigeria's economy can have a boost if this enormous natural gas reserve is monetized via the different monetization options (Gas-To-Liquid (GTL), Compressed Natural Gas (CNG), Natural Gas Liquid (NGL), Liquefied Petroleum Gas (LPG), and Liquefied Natural Gas (LNG)) [5]. Each of these monetization options utilizes natural gas as the feedstock.

Presently, many homes in Nigeria utilize Liquefied Petroleum Gas (LPG) for domestic cooking and heating, because of its clean nature when burnt. Many more homes are bracing up to join the numbers. Industries that use heavy machinery in production drive their machinery with power generated from natural gas (main methane) and these industries are continuously

investing more on their production systems. In addition, the Gas to Power industry is another consumer of natural gas. Therefore, there is every tendency that natural gas utilization will increase in the future through the expansion of the market for its products. These are pointers for potential investors in the natural gas downstream sector.

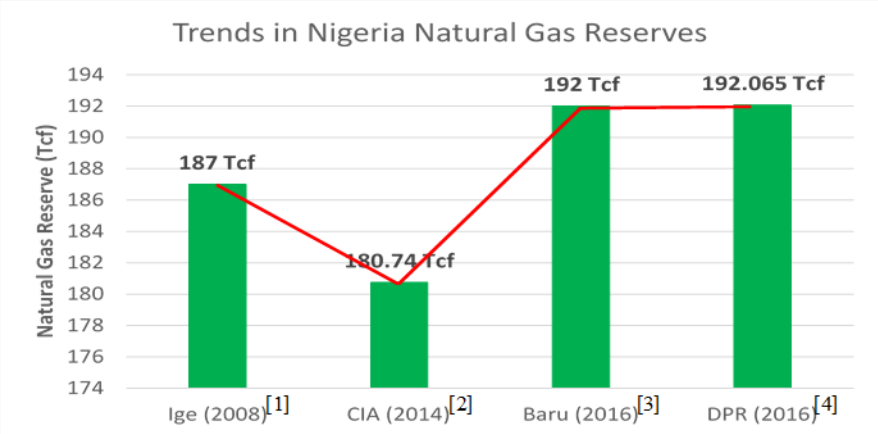

Figure 1. Natural gas reserve status in Nigeria

In Nigeria, there are fewer investors (XEN Energy - 25MMScfd, PNG Gas - 30MMScfd, Greenville - 80MMScfd, Niger Delta (Ogbele Gas Processing Plant) - 100MMScfd and Giga Gas - 140MMScfd), in the natural gas business, thus monetization is not optimal, possibly due to "lack of willingness of oil producers to mobilize funds to monetize what is essentially seen as a low value by-product compared to oil"[6]. In addition, lack of information about the economics (financial implication and returns) and risk associated with the business, will hamper investor's interest. Therefore, this work seeks to bring to bear an economic model and analysis of the profitability, risk, and uncertainty for investment in natural gas plant, via cash flow model development and sensitivity analysis, with LPG and dry natural gas as target products.

2. Literature review

2.1. Natural gas processing and infrastructure

The development of natural gas fields requires gas developers to make the right decision in terms of siting a gas plant, gas infrastructure and long term economic benefit of the processing plant. In this way, the gas developers will be able to predict and control capital spending, while maximizing the value of their natural gas and Natural Gas Liquids (NGLs) [7].

Making the right decisions during the initial stages of a gas processing plant project is important for the ultimate business outcome and long term survival in the gas business. These decisions can include "technology selection, plant configuration, plant sizing, and site selection together with determining the optimal contracting and construction strategies." [8] The development of gas processing systems can require considerable infrastructure decision and sound economic judgment, which can maximize cost recovery. Figure 2, shows a typical configuration in the block flow diagram of the natural gas processing plant, and whatever type of configuration, the Capital Expenditure (Capex) and Operating Expenditure (Opex) depend on the compositions, components, and extent of processing of the natural gas.

Construction and project cost can come under control via two essentials aspect of any project: feasibility studies and project oversight in-house, and that proper design, accurately modelled facility performance, and identifying optimal operating strategies can reduce operating cost to a minimum [10].

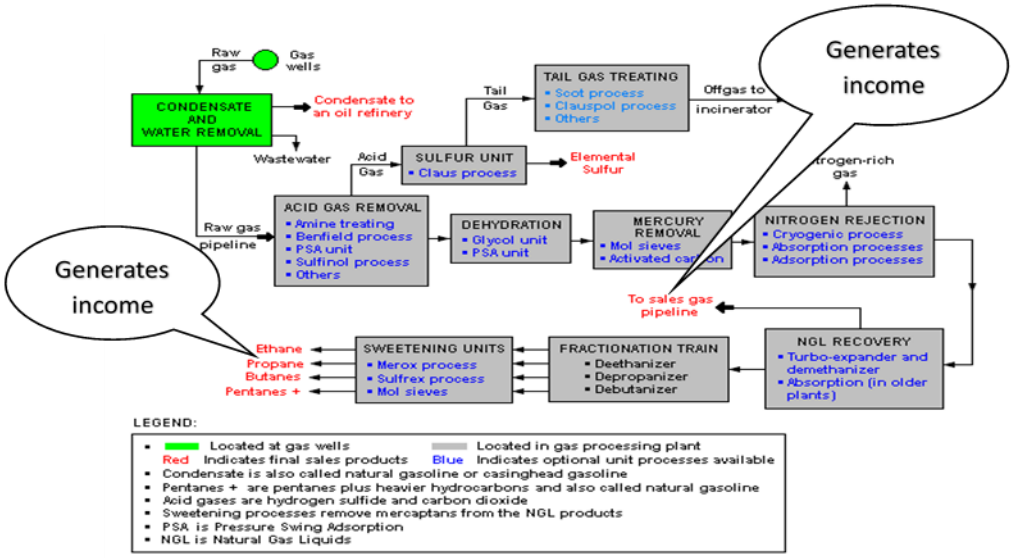

Figure 2. Block flow diagram of a natural gas processing plant [9]

2.2. Natural gas and product price dynamics

The dynamic of demand and supply of natural gas is dictated by its market price, which (in this paper) is divided into two parts: wellhead gas price (producer price) and product price (consumer price). The price of natural gas is not stable because of dwindling oil price and demand for natural gas during winter and summer (in polar region). Countries like Nigeria, demand natural gas and LPG depends on the number of residents and companies that are available to use it.

However, "depending on market condition, either the consumers' or the producers' perspective tends to dominate the pricing decision, and a number of alternative pricing mechanisms have emerged in the market." [11]

Simple Regression (Equation 1) by regressing West Texas Index (WTI) and Henry Hub Spot Price, using weekly price information, was developed by [12].

$$P_{HH} = -0.1104 + 0.1393P_{WTI} \quad (1)$$

The Henry Hub sports price is dependent on short-term price. Hence, any change in demand and supply will affect the natural gas price, thereby, making it more volatile. For the year 2017, the average spot price for natural gas is \$3.01/MMBtu (\$3.10/MScf).

Nigeria National Petroleum Corporation (NNPC) report, February 2017, quoted the price of natural gas as \$2.9/MScf, which is almost the same with the Henry Hub natural gas spot price of \$2.85/MMBtu (\$2.92/MScf), at the same month and year. The price of dry natural gas (from processing plant) supplied to industries and power generation companies (Gas-to-Power), was reviewed and approved by Nigeria National Petroleum Corporation (NNPC), from \$1.5/MScf to \$2.5/MScf. Transportation tariff of \$0.8/MScf was added to this price, making a total of \$3.3/MScf price of gas supplied to the industries and power sector.

Reports by [13], shows that one truck of LPG (20 metric tonnes) was valued at N3.5 millions at the second halve of 2016. At this time, the official currency exchange rate was \$1/N190. The report also reveals that, when the official rate hiked to above \$1/N300 in the first quarter of 2017, 20 metric tonnes of LPG increased to above N5 millions. The attendant effect of this price dynamics is the hike in the retailer's price.

Recent data from [14] shows that, the average price of refilling LPG of 12.5kg cylinder, increased by 2.64% monthly and by 33.11% yearly, from N4, 830.22 in April 2017 to N4, 957.88 in May 2017. The hike in natural gas and product prices has resulted in a push in the inflation rate in Nigeria. The Consumer Price Index (CPI), which measures the inflation rate,

reveals that gas prices and other commodities have increase Nigeria's inflation rate to 18.55% in December 2017 [14].

2.3. Natural gas processing economics

The natural gas industry is bedeviled with risk and uncertainties, in terms of market structure, the available market for the products, dynamics of demand and supply for wellhead gas and the products, price dynamics for wellhead gas and the products, infrastructure, government policies and working fiscal regimes. These risk and uncertainties call for careful decision making before investing in natural gas infrastructure.

Data from various liquefaction projects were used by [15] to calculate the average cost breakdown by plant area and by category for natural gas liquefaction processes and found that the liquefaction and refrigerator systems require about 50% of the total plant cost.

CAPEX), OPEX, and natural gas price are intrinsic parameters in developing an economic and cash flow models. These parameters are used to determine useful economic indicators (NPV, IRR, PI, PVR, GRR, and payback time) on which decision making is relied on, to determine the viability of investing in a natural gas infrastructure project. However, to enhance decision making, further economic analysis such as Monte Carlos Simulation (stochastic Analysis) should be done.

Economic model and analysis on the development of Nigerian offshore marginal fields using Probabilistic approach were presented by [16]. Economic yardsticks (payback time, NPV, IRR, PI, PVR, and profit to investment ratio) were investigated and Monte Carlo Simulation (using Crystal Ball) was used to perform sensitivity analysis which shows that NPV, IRR, and payback time are more sensitive to changes in oil price, gas price and tax rate. However, the economic model for natural gas as a separate unit was not developed in their work.

The economic model for exploiting stranded natural gas in Niger Delta Offshore fields, using two natural gas monetization options: Gas-to-Liquid and Liquefied Natural Gas with pipelines and gas processing were developed by [17]. The NPV for both monetization options, shows that, at a lower price of oil and gas, the LNG monetization option is more attractive, but as the natural gas price increases, both monetization options becomes less attractive for investment. However, sensitivity analysis to further determine the option that poses more risk to investors was not done.

An engineering economic technique for valuation of the viability of marginal oil and gas fields' project in Nigeria using Financial Simulation Analysis was adopted by [18]. Like the sensitivity analysis done by [16] using Crystal Ball, [18] also, carried out sensitivity analysis using Crystal Ball, the input variables are "oil price per barrel, development/capital cost, real discount rate, operating cost, abandonment cost, total field production, Petroleum Profit Tax (PPT) and royalty", and the forecast variable was Post-tax NPV. Among the input variables, [18] found out that PPT, oil price, and royalty have much more impact on the NPV. Again, like the work done by [16], Natural gas processing unit was not considered in the economic model and analysis.

3. Materials and method

Cash flow models are unique to a particular investment in the oil and gas business. It is unique in the sense that, the target product(s) determines the facilities that form the entire plant and it also determines the capital and operating expenditure for a project. However, the process of economic valuation is the same including the natural gas plant considered in this paper. Therefore, the materials used in this work are Excel spreadsheet and @RISK software, and the method adopted was divided into three stages.

3.1. Stage one: Developing the economic and cash flow model

The economic model for the natural gas processing plant was developed using an excel spreadsheet. Figure 2 shows the entire process from which the economic and cash flow model was developed.

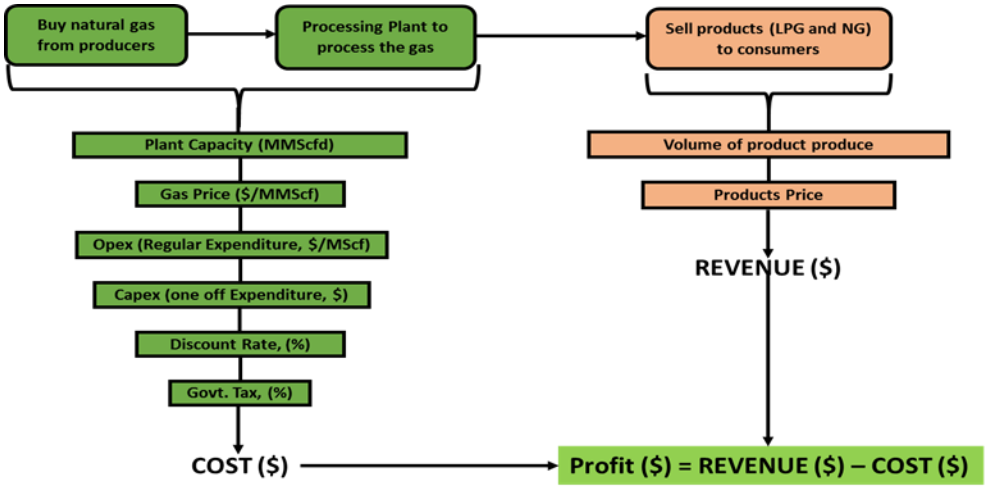

Figure 3. Simplified schematic of the entire process

The natural gas processing plant of interest has a design capacity of 70 MMScfd and an operating capacity of 60 MMScfd. However, the operating capacity was used in the development of the cash flow model. In addition, 356 operating days, 20 years operation of the natural gas processing plant, inflation rate of 17% and straight-line depreciation for 5 years were assumed. Table 1, shows a summary of the input parameters and assumptions.

Table 1. Summary of input parameters and assumptions

Plant capacity (Operating)		60	MMScfd
Wellhead gas price	P_{wg}	4	$/MScf
Discount rate (Real)	r_R	15	%
Government tax	CIT	30	%
Operating days		356	days
No. of years forecasted	t	20	year
depreciation method	SLD	5	year
Products	**Symbol**	**Price**	**Unit**
Natural gas	P_{NG}	3.3	$/MScf
LPG	P_{LPG}	280	$/mt

In developing the cash flow model, Equation 2 was modeled using LPG production data from a major gas processing plant, to estimate the volume of LPG recovered from the NGL, which was extracted from the feed gas.

$$V_{LPG} = 153.53\beta\alpha_r q \quad (mt/day) \qquad (2)$$

where: β is the mole fraction of C_3/C_4 recovered from the NGL; α_r is the percentage of NGL recovered from the feed gas and, q is the operating capacity of the plant (MMScfd).

The q is dependent on the source of the feed gas while β and α_r are dependent on the treatment plant recovery process and are cash flow model parameters.

3.2. Stage two: Determination of profitability indicators

The process of decision making on the viability of oil and gas property requires estimation of profitability indicators, which are summarized in Table 2.

Net Present Value (NPV)

The NPV is the surplus of cash resulting from the present value, and it is the difference between the present value of cash inflows and the present value of cash outflows at a company's or investor's hurdle rate (or discount rate).

Internal rate of return (IRR)

The "Internal rate of return (IRR) has been a popular managerial indicator since the 1950s, and it is still widely used today"[19]. The IRR is the discount rate that produces zero NPV. In addition, is the discount rate such that the present value of cash outflows is equal to the present value of cash inflows, and it determines the maximum borrowing cost of capital to make the investment viable. The IRR is measured in percentage.

Profitability index (PI)

The screening of investment by the use of NPV may be very attractive, especially when it passes the screening test, but it does not take into account the size of the investment. To take care of the weakness of NPV, the PI was introduced to measure the total return for every dollar invested in a project

Present value ratio (PVR) and Growth rate of return (GRR)

The PVR and GRR are investment screening indicators and are a function of PI and discount rate. The PVR measures the gain per dollar invested, and the GRR measures the capability of reinvestment of capital at the prevailing discount rate. PVR must be greater than zero, and the GRR must be greater than the discount rate for viable investment.

Payback period

The payout measures the time to recoup an investment. At this point, the cumulative net cash loss is exactly equal to the cumulative net cash gain (break-even point).

Table 2. Economic indicators for managerial decision making process

S/N	Indicators	Equation
1	Net Present Value (NPV) (nominal)	$NPV^N = \sum_{t=0}^{n} \frac{(NCF^N)_t}{(1+r_N)^t}$
2	Internal Rate of Return (IRR) (nominal)	$NPV^N = \sum_{t=0}^{n} \frac{(NCF^N)_t}{(1+r_N')^t} = 0$
3	Profitability Index (PI)	$PI = 1 + \frac{NPV^N}{I_o}$
4	Present Value Ratio (PVR)	$PVR = \frac{NPV^N}{I_o}$
5	Growth Rate of Return (GRR)	$RR = (PI)^{\frac{1}{t}}(1+i) - 1$
6	Payback Time	Time (years) at which CummNCF = 0
7	Unit Technical Cost (UTC)	$UTC = \frac{Discounted\ Cost\ (CAPEX + OPEX)}{Discounted\ Reserves\ /Production}$
8	Nominal Discount Rate (r_N)	$r_N = (1+i_r)r_R + i_r$

where r_R is the real discount rate, r_N is the nominal discount rate (which is as a result of inflation) and i_r is the inflation rate, $r_N' = IRR^N$, is the nominal IRR, $r_R' = IRR^R$ is obtained by substituting r_N' for r_N and calculating r_R', I_o is the present value of Capital Expenditure (CAPEX) at the given discount rate r_R, used in discounting NPV.

3.3. Stage three: Deterministic and stochastic sensitivity model of the variables

Two methods of determining the sensitivity (deterministic and stochastic) of the forecast variables to changes in the input variables were presented, to capture risk and uncertainty in the natural gas project.

The deterministic sensitivity is a single point model of one input variable and one forecast variable. The input variable is price, and the forecast variable is NPV, with these two single point variables, an NPV profile was generated, using Equations 3.

$$NPV_d = f(P) \quad (3)$$

where NPV_d is the Net Present Value under deterministic sensitivity; P is the price for wellhead gas, dry natural gas, supplied to industries and LPG price for domestic purpose.

Stochastic sensitivity involves Monte Carlo simulation using @RISK software, such that, more than one decision variable in the investment model will be varied at the same time, to

determine their different level of impact on a forecast variable. Each input variable (wellhead gas, dry gas *and* LPG prices, Opex, Capex and percentage recovery of NGL), is described by a Probability Distribution Function (PDF). The PDF for the gas prices is Lognormal Distribution. The lognormal PDF has lower boundary but no upper boundary, and this inform its choice for the gas prices, because, the price of gas can never be zero as time passes. Opex and Capex are Uniform Distribution, since it is uncertain about the most likely Opex and Capex for the gas plant. The PDF for percentage recovery of NGL is triangular. The choice for this distribution was based on the maximum (most likely) recovery of the LPG from the NGL, which is dependent on the plant design and target product.

4. Results and discussion

Table 3, shows the economic indicators estimated from the cash flow model.

Table 3. Economic indicators before and after income tax

Indicators	Before income tax	After income tax	Unit
NPV	6 199.3	3 889.5	$MM
IRR	112.86	84.86	%
PI	5.13	3.59	
PVR	4.13	2.59	
GRR	46.02	43.44	%
Payout Time	1.08	1.46	year

The indicators, before income tax, are greater than the indicators after income tax, except payout time. This is because of the impact of income tax, and the essence of depreciating the asset is for the income tax purpose. The estimated NPV of the cash flow after income tax is positive ($3889.5 million > 0), which indicates viable investment. The estimated IRR in Table 3 are the nominal values, the real IRR was calculated to be 0.583 (58.3%) after income tax, and it is greater than the discount rate, 0.15 (15%). The implication is that, at 58.3%, the NPV is zero indicating the maximum borrowing cost of capital to make the project of investment viable. Above this value, the investment starts to generate negative NPV. Also, the IRR must not go below the cost of capital. Therefore, it is profitable if the company hurdle rate is between the discount rate and the IRR (15% < hurdle rate of ≤ 58.3%). The GRR estimated from the cash flow, meets the criteria (Table 4), but can be used in decision making, only when the investment has the capability that capital from this project can be re-invested at the prevailing discount rate.

The PVR measures the gain per capital invested. Thus, the estimated PVR (2.59), indicates that there is $2.95 gain for every $1 invested, thereby making the gas processing plant viable for investment. The estimated PI (3.59) after income tax, indicating that the natural gas processing plant will return a total of $3.59 for every $1, where $2.59 is gain for every $1 invested. The estimated payout time after income tax is 1.46 years. Although, the work done by [16] was based on oil and gas marginal field, but gave a payout time of 1.42, which agrees with the value obtained in this work.

Table 4 Summary of profitability measures and decision rules

	Decision rules	
Profitability measure	Accept if	Reject if
Payback period @ d	≤ Desired	≥ Desired
Net present value (NPV) @ d	> 0	< 0
Internal rate of return (IRR) @ d	> d	< d
Profitability index (PI) @ d	> 1	< 1
Present value ratio (PVR) @ d	> 0	< 0
Growth rate of return (GRR) @ d	> d	< d
Unit technical cost @ d	< Average Product Price	> Average Product Price

4.1. Deterministic sensitivity analysis

Market forces of demand and supply of natural gas, are dynamic in nature, and they dictate the prices of wellhead gas and its products. Using Equations 3, NPV profile of Figures 4 and 5 were generated for wellhead gas and LPG prices respectively.

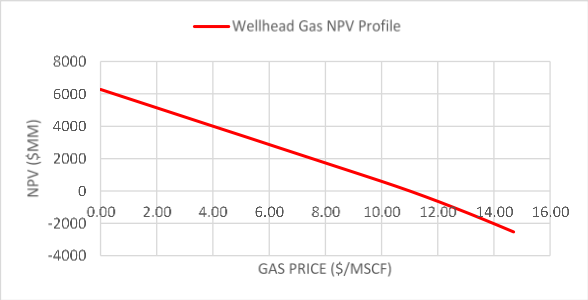

Figure 4. Wellhead Gas NPV sensitivity profile

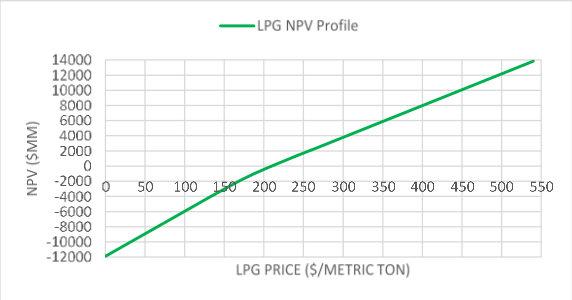

Figure 5. LPG NPV sensitivity profile

The maximum price to buy wellhead gas from the producer so that the investment continues to generate positive income was $10.99/MScf, and this value is the Break-even price of the wellhead gas (Figure 4). Above this price, the investment starts to generate negative NPV, and as the price decreases, the NPV increases, which favours the investors. In transfer pricing, increasing the wellhead gas price favours the producer, but becomes a loss to the gas processing company, vice versa. The minimum amount at which the LPG can be sold was $210.42/ metric ton (Figure 5). This is the Break-even price for the LPG. Below this price, the NPV becomes negative, indicating a loss to the investors. This price is an important parameter to be monitored such that it does not fall below a unit production cost. The break-even price for the dry natural gas on the cash flow model was very low (less than $0.2/MScf), indicating the favourable market for dry natural gas down to a price as low as $0.2/MScf.

Unit Technical Cost (UTC) indicates what the product is costing to develop the processing plant and to produce the product. The UTC is calculated when $NPV = 0, PI = 1.0,$ and discothe unt rate is the IRR. Therefore, the UTC is the same as the minimum price at which the product can be sold, but its screening criteria is that, it must be lower than ($210.42/mt < $280/mt) the proposed product price or the prevailing market price of the product (LPG).

4.2. Stochastic sensitivity analysis: @RISK base simulation

The Monte Carlo Simulation using @RISK was done with 5,000 iterations. From Figures 6 and 7, the Monte Carlo simulations show that the NPV and IRR are lognormal distributed with a mean (expected) value of $3672.22 million and 82.05% (nominal) with a standard deviation of $1176.50 million and 18.62%. The likelihood of these values is 0.5891 (58.91%) and 0.5992 (59.92%), indicating 40% uncertainty in getting the expected NPV and IRR (Figures 6 and 7). This uncertainty poses a risk on the cost of capital; once there is an escalation in gas price, procurement and installation costs.

Figure 8 shows that of the PI, which measures the size of the project, with an expected value is 3.462, which is well above 1.0, indicating that for every $1 million dollars invested, there is $3.462 million total return, with the likelihood of 58.27% (i.e. probability of 0.5827). This implies that investors are 58.27% certain that the investment will return $3.462 million, the rest is the risk associated with the investment due to uncertainty in price escalation.

Figures 9, 10, and 11, shows the sensitive response of the NPV, IRR, and PI from the input variables. The chances of achieving their expected values are above 50%. This culminates from the individual impact of the input variables. For the three forecast variables, the LPG price and percentage recovery have the highest positive impact on them, indicating that, increasing these values will increase their output and vice versa. The dry gas price has the least positive effect on the forecast variables, indicating that more returns will be achieved if the processing company focuses on increasing LPG production.

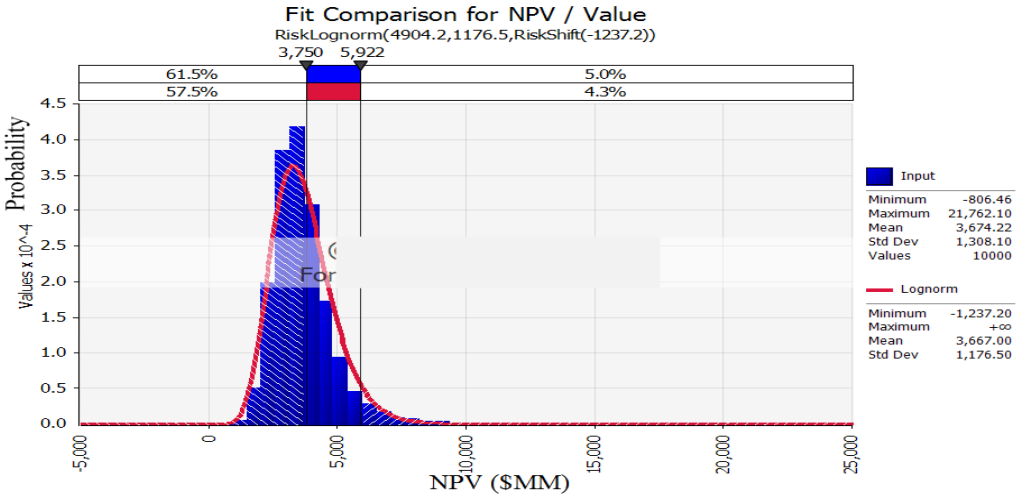

Figure 6. Simulated NPV fitted with normal distribution function

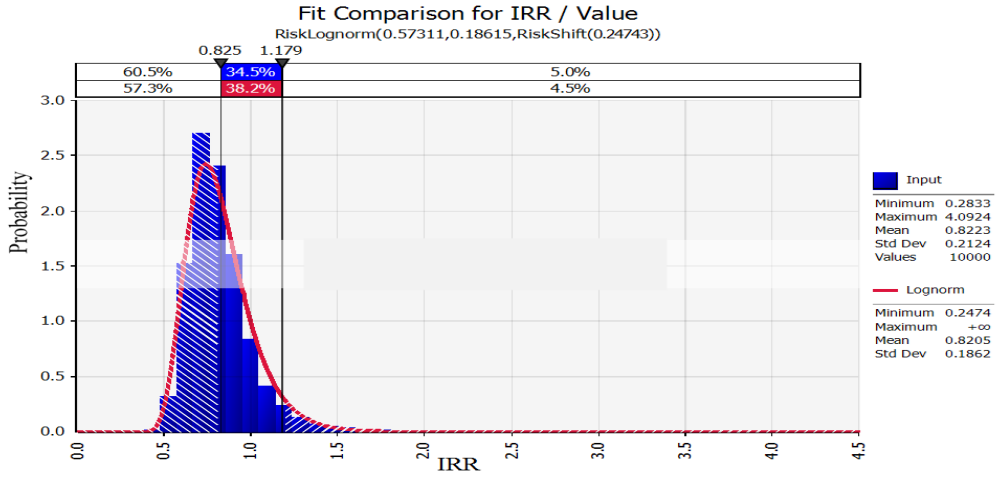

Figure 7. Simulated IRR fitted with normal distribution function

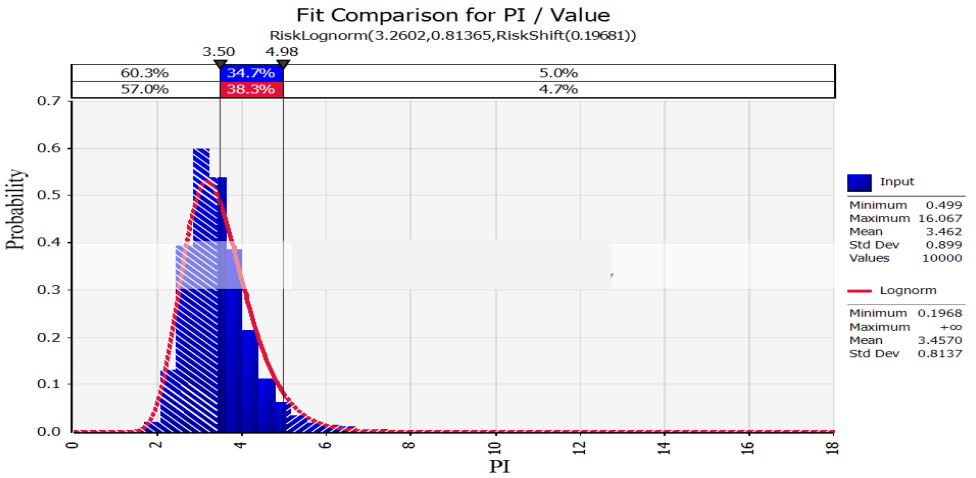

Figure 8. Simulated PI fitted with normal distribution function

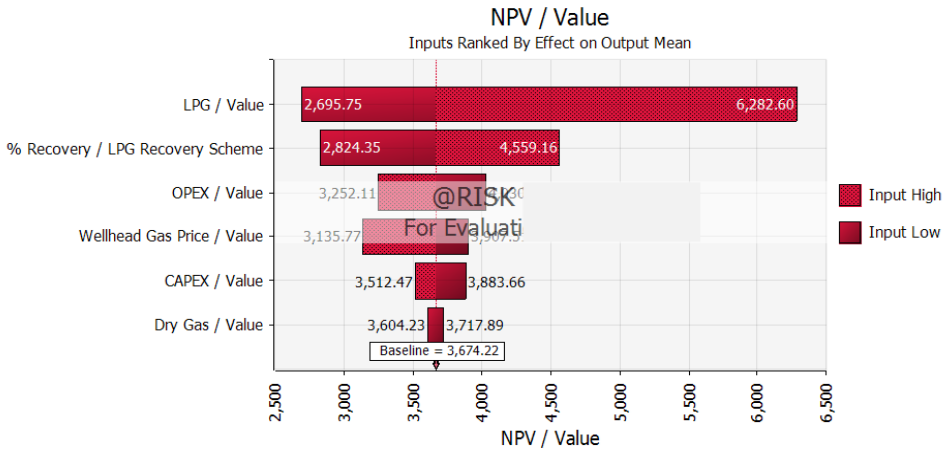

Figure 9. Tornado diagram of the NPV response based on effect of output mean

The OPEX has the highest negative impact on the NPV and IRR, (Figure 9 and 10). Therefore, the gas plant should be designed to maximize recovery of LPG (this is where the percentage recovery in Equation 2, comes in) and minimize OPEX, thereby minimizing the negative effect of the OPEX on the NPV and IRR.

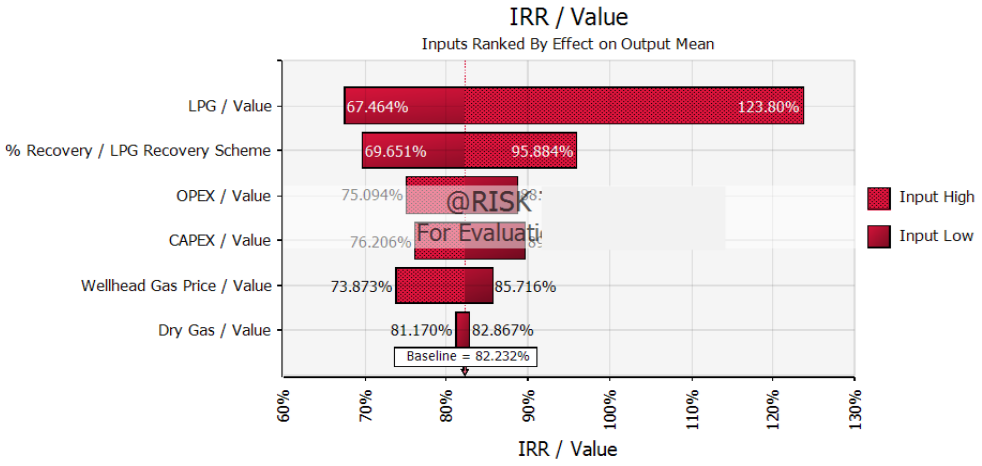

Figure 10. Tornado diagram of the IRR response based on effect of output mean

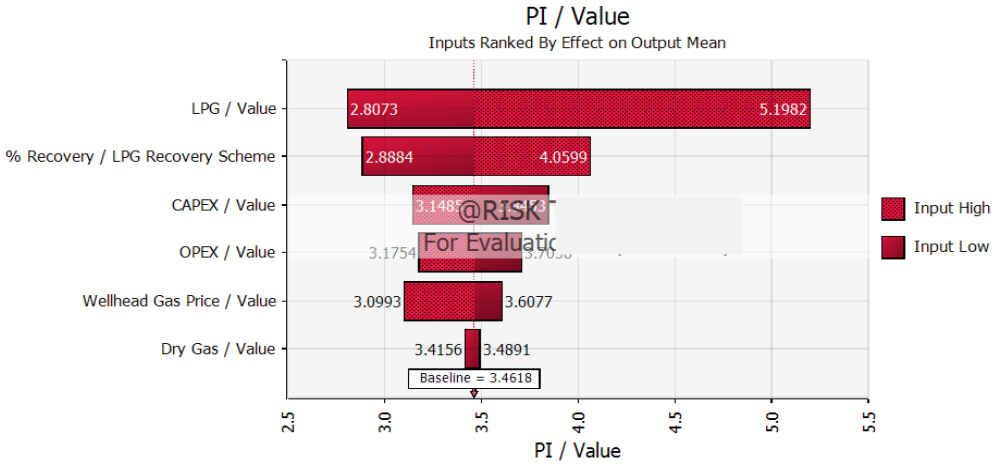

Figure 11. Tornado diagram of the PI response based on effect of output mean

The negative effect of the OPEX and CAPEX on the NPV and IRR imposes a risk on the cost of capital in the midst of inflation. When there are an inflation and price escalation, the nominal discount rate will increase (Table 2), thereby reducing the expected values and the chances of achieving them. Figure 11 shows that the CAPEX has an impact that is more negative on the PI.

The negative impact of CAPEX, imposes a risk on the investment, indicating that increasing the CAPEX will reduce the likelihood of getting the expected PI. However, since the CAPEX is a one-off cost, the risk will come in the form of the delay in completing the installation of the gas processing facilities, commissioning and startup operations. During this delay, cost of procurement and installation might escalate, as stated by [15], and in the process, escalate the CAPEX and payback time, thereby decreasing the likelihood of achieving the expected return from the investment. Timely completion and startup operation will minimize the risk imposed by the CAPEX on the PI.

Figures 12, 13 and 14 are the spider charts of the sensitivity analysis. The chart shows the sensitive response of the forecast variables, which is dependent on the steepness of the input variables.

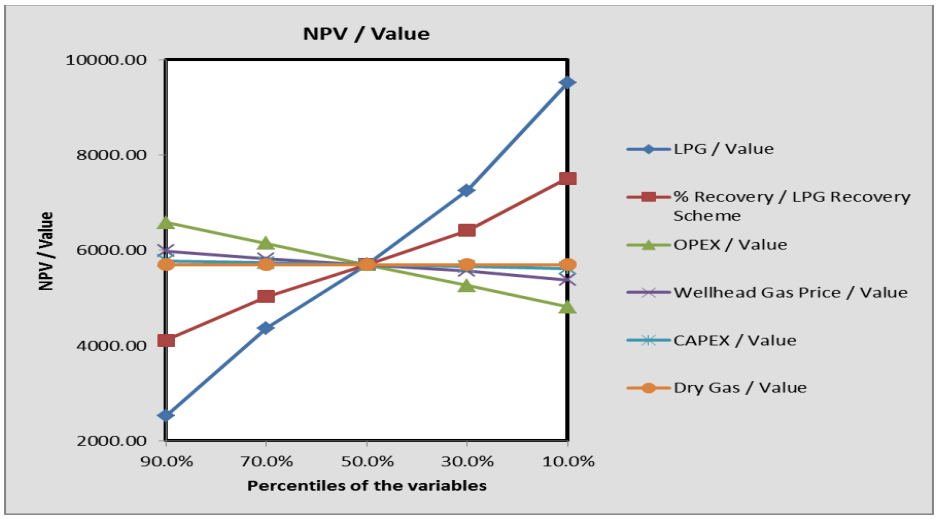

Figure 12. Stochastic spider diagram for the NPV

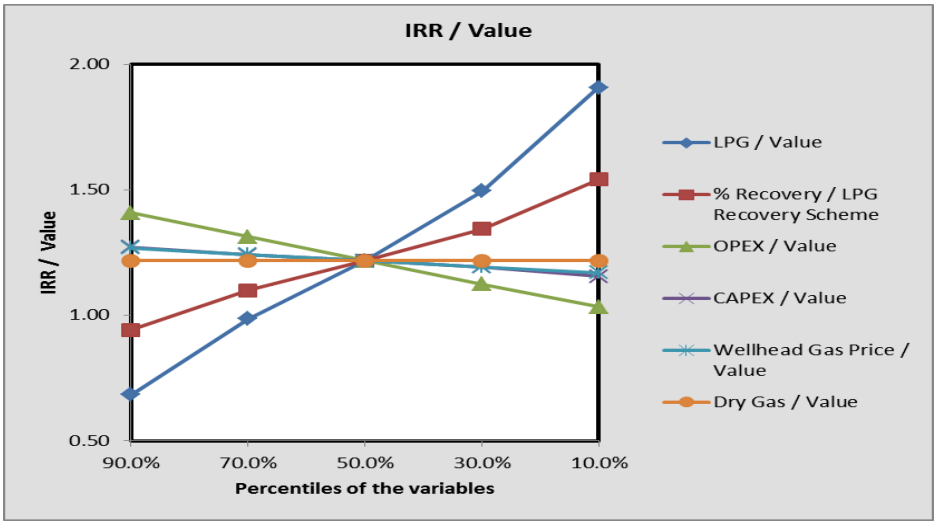

Figure 13.Stochastic spider diagram for the IRR

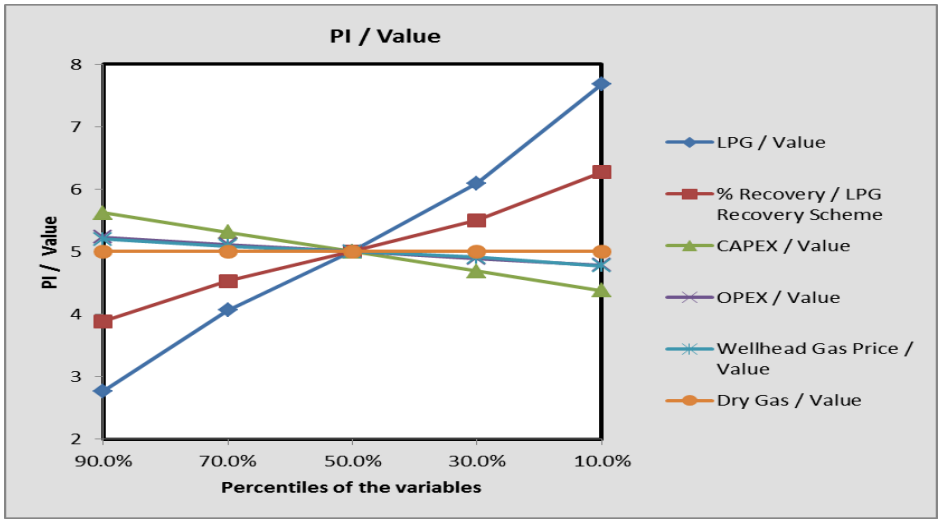

Figure 14. Stochastic spider diagram for the PI

Figures 12 to 14, show that LPG price and percentage recovery, have the most positive steepness and thus increases the value of the forecast variables. CAPEX, OPEX and wellhead gas price have negative steepness, indicating an inverse relationship with the forecast variables.

These findings, are in agreement with the stochastic analysis done by [16,18], which shows that CAPEX has a more negative impact on forecast variables, and the dry gas price has a positive effect on the forecast variables.

5. Conclusions

The starting point for economic valuation of oil and gas project is the development of cash flow (which is unique to a particular project) to determine the viability of the project using economic indicators. The analysis of the cash flow shows that the expected stochastic values of the indicators are less than the deterministic (best average) values, because of the risk associated with the project. The stochastic values are $3674.22 million, 82.05% (0.8205) and 3.462, while the deterministic values are $3889.5 million, 84.86% (0.8486) and 3.59 for NPV, IRR, and PI respectively.

Investment in natural gas infrastructure is viable, but decision makers must pay more attention to the instability of wellhead gas price, product price and investment capital in the midst of inflation and escalation of the cost of procurement and installation of plant facilities. These input parameters pose risk and uncertainty on the parameters that define the profitability of the investment. Therefore, decision makers should advice investors based on stochastic values rather than deterministic values, because the stochastic values are associated with risk and uncertainty.

References

[1] Ige DO. The Nigerian Gas Master Plan: Investor Road-show. Nigeria National Petroleum Corporation 2008, Abuja, Nigeria.
[2] Central Intelligence Agency (CIA), USA, World Fact Book, 2014
[3] Baru M. (2017) Nigeria Natural Gas Reserves Hit 192 Tcf. Nigeria National Petroleum Corporation (NNPC) Bulletin 2017.
[4] Department of Petroleum Resources, Oil and Gas Annual Report, 2015.
[5] Ubani CE, and Ani GO. (2016), Natural Gas Utilization and its Effect on Nigeria's Economic. International Journal of Scientific Engineering and Technology, 2016; 5(12): 532-536.
[6] Antoine J. Outlook for Flare Reduction in Nigeria. Technical Report No. 34, Agence Française de Développemnet 2017, France.
[7] Gas Processing: Modular Gas Processing Plants. UOP LLC, Honeywell Company, East Algonquin, USA, 2016.

[8] Worley P. Gas Processing: Capability and Experience. Resources and Energy. EcoNomics 2015, Houston, USA.
[9] Milton RB. Natural Gas Processing: A Schematic Flow Diagram of a Typical Large Natural Gas Processing Plant.,2013 http://chemengineering.wikispaces.com.
[10] Beck R. Improve Gas Processing Assets with Innovations in Process Modelling. Special Report: Gas Processing and NGL 2014, Hydrocarbon Processing, Gulf Publishing.
[11] Subhes CB. Energy Economics: Concept, Issues, Markets, and Governance. Springer 2011, London.
[12] Brown SP, and Yucel MK. What Drives Natural Gas Prices? Working Paper 0703, Federal Reserve Bank of Dallas 2007, Dallas, Texas, USA.
[13] Alike E. How International Pricing of Cooking Gas Escalated Domestic Price. This day news paper 2017.
[14] National Bureau of Statistics (NBS), 2017.
[15] Brian S. LNG Plant Cost Escalation. OIES Papers 2014, Oxford Institute for Energy Studies, USA.
[16] Adamu MA, Ajienka JA, Ikiensikimama SS. Economic Analysis on the Development of Nigerian Offshore Marginal Field using Probabilistic Model. Journal of Advances in Petroleum Exploration and Development, 2013; 6(1): 11-21.
[17] Nweke IF, and Adewale D. Economic Model in Exploiting Stranded Natural Gas in Niger Delta Offshore Field. International Journal of Engineering Research and Development (IJERD), 2015; 11(04): 12-18.
[18] Yusuf OA, and John-Felix KA. Economic Evaluation of Nigerian Marginal Oil and Gas Field using Financial Simulation Analysis. International Journal of Energy Economics and Policy (IJEEP), 2016; 6(3): 563-574.
[19] Wright DJ. Petroleum Economics: Petroleum Engineering Handbook. General Engineering, Vol. 1, Society of Petroleum Engineers 2007, Norwest Questa, 767-807.

To whom correspondence should be addressed: G. Okechukwu Ani, Petroleum and Gas Engineering Department, University of Port Harcourt, Nigeria

Petroleum and Coal

Article **Open Access**

WAYS OF IMPROVING THE EQUIPMENT FOR PRIMARY PETROLEUM REFINING

Nabil Abdul Sater[1], Andrey Grigorov[1], Alena Tulskaya[1], Tatiana Ovsiannikova[1], Alexey Sytnik[2]*

[1] *National Technical university "Kharkiv Polytechnic Institute", Kharkiv, Ukraine*
[2] *Ukrainian State Coal-Chemistry Institute, Kharkiv, Ukraine*

Received January 7, 2019; Accepted March 19, 2019

Abstract

The general ways of improvement the primary petroleum refining rigs have been described in this article. It has been proposed to consider the operational control of primary petroleum refining processes as the most perspective branch of petroleum industry due to its comparatively cheap implementation. Operational control has a significant influence on the safe operation of equipment, products quality and amount of harmful emissions. Electrical conductivity and relative permittivity have been defined as the specific parameters for effective operational control.Primary oil refining rigs are the most important part of any petroleum refinery. Despite the Nelson complexity index which is only 1,0 for refineries it should be considered that they have a strong impact on the secondary refining rigs. That's why one of the most important task in the petroleum refining industry worldwide is improvement of primary oil refining rigs.

Keywords: *primary petroleum refining processes; relative permittivity; electrical conductivity; control parameter; level of separation; fraction; emulsion; salts.*

1. Introduction

Primary petroleum refining equipment, as a rule, include the following technological parts: raw material treatment (removing of salts, water and mechanical admixtures), gasoline fraction separation, distillation, vacuum treatment of fuel oil. All these parts are in strong connection. So improvement of one or several parts affect the general equipment efficiency.

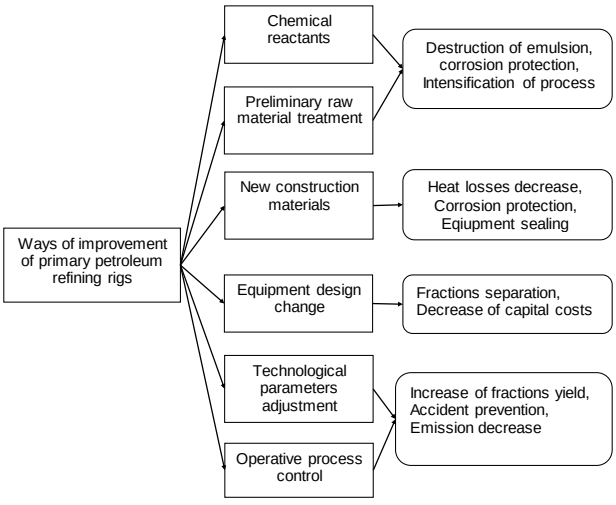

Fig.1. Structural model of improvement the primary petroleum refining process

One of the most significant criterion of efficiency for primary petroleum refining rigs evaluation is depth of separation of light fractions and refining of heavy fractions. According to [1] fuel oil vapor contains about 5 % of diesel hydrocarbons and tar contains about 10 % of vacuum distillate fraction [2]. Very important performance measure of equipment is durability which is caused by corrosion protection and harmful emission decrease.

General directions of improvement the primary petroleum refining equipment, that can provide its long durability and decrease of harmful emissions, may be performed in Fig. 1. Each of these directions will be observed in details below.

2. Results and discussion

Addition of various chemical demulsifiers is widely used in petroleum refining industry and mainly at electro desalting and electro dehydrating rigs. The following demulsifiers are most popular in Ukraine and Russia:
- Dissolvan 4411 and Separol 25 (Germany);
- NALCO EC, Basorol E2032 and L-1632 (USA);
- R-11 and X-2647 (Japan);
- Servo 5348 (Holland);
- Kemelix 3448x (Great Britain)

But search of the most effective and comparably cheap demulsifiers has not been finished yet. The examples of researches devoted to the current problem ale presented below.

For dehydration of crude oil from Basra, Iraq there have been applied demulsifiers based on industrial foundry oil. There has been compared the efficiency of two types of demulsifies: industrial RP/6000 and ammonium sulphonate from castor oil. The best results for the separation of emulsion (15 % of water, 3 % of NaCl) were obtained at the highest pH rate and highest concentration of ACS demulsifier [3].

Authors of [4] have described the research devoted to the application of different water-soluble and low-soluble demulsifiers for oil and water separation. Etoxylate of fatty alcohol, triethanolamine have been considered as the most effective from the water-soluble group and Basorol E2032, Basorol PDB 9935 and TOMAC from low-soluble group.

It has been found out that increase of demulsifier concentration, salt content and temperature up to 350 K encourages the separation degree at pH 5-9.

It has been also found out that the most effective composition that provides almost 90 % separation of oil and water, consists of triethanolamine – 16%, etoxylate of fatty alcohol – 20%, Basorol E2032 – 6 %, Basorol PDB 9935 – 8 %, TOMAC – 12 % and aromatic dissolvent – 39 %. Besides this new composition was more effective than industrial demulsifiers (VZB 1413 provides 65 % separation and VZB 1414 – 72 % separation). Moreover, addition of light hydrocarbon dissolvent encourages the destruction of oil-water emulsion and reduces the viscosity [5]. Authors of [6] proposed the new composition of demulsifiers that contain 25 – 48 % of surfactant "Sinterol" («Синтерол»), 3-8 % of modifying additives and dissolvent (methanol – aldehyde fraction). Level of oil dehydration with the proposed demulsifier can be raised up to 96 %. To protect the industrial equipment from corrosion destruction there has been proposed to add the following chemical reactants: amides, aliphatic amines and, in particular, nitrogen-containing inhibitor – polyhexamethylenguanidine – hydrate (5 – 20 g per 1 ton of raw material). Current inhibitor provides the 95-98 % protection [9]. To prevent the corrosion of equipment at oil and gas fields, pipelines and refining systems there should be applied an inhibitor of metal corrosion that contains 70 – 99,9 % of synthetic oil (as a by-product of benzene hydration and further oxidation of cyclohexane by air and dehydration of cyclohexanol) and 0,1 -30 % of carbamide [10].

Chemical reactants are widely used for preparation of crude oil and gas condensate for transporting. Authors of [11] recommend to perform the preparation of sulfur-containing crude oil through its low-pressure separation or in additional separation column at 300 – 350 K and 0.1 – 0.5 MPa. The aim of proposed method is to reduce the acidity and corrosion activity of crude oil. In [12] there has been described numerous compounds that may be applied as the corrosion inhibitors for steel in acidic solutions. It has been shown that acetylene alcohol is the most active component for corrosion protection.

Design change for refining equipment is one of the most complicated direction for improvement the primary petroleum refining rigs which demands considerable investments. At the same time, there are two determining factors of effective separation of petroleum fractions – design of contact devices and constant temperature gradient in distillation column. Bubble-cap trays and valve collars are the most widely used devices in atmospheric distillation columns [13]. Replacement of bubble-cap trays with ejection trays provides the increase of tray efficiency up to 20 % [20]. Replacement of grooved tray with ejection valve trays encourages

the decrease of distillate fractions content in fuel oil by 7 % in average [15]. According to [16] the regular structured nozzles by "Sulzer" are the most effective comparing to tray contact devices. Replacement of trays with stationary valves with regular structured nozzle "Sulzer" provides the increase of equipment productivity and decrease the content of C_7 –hydrocarbons in low-boiling fraction 350 K down to 0.43 %. In [17] authors describe the varying of sections diameter in packed columns. This approach allows to decrease energy costs for separation in distillate columns.

Methods of pretreatment of raw material aim the increase the yieldt of light fractions, encourages the destruction of oil-water emulsions and can be implemented for the preparation of oil before the electrodesalter and electrodehydrator. In [18] there have been presented the results of activation of viscous crude oil by rotary pulsating apparatus by waves from infrasound to ultrasound. As a result – the content of gasoline fraction raised up to 10 % comparing to unprocessed crude oil.

In [19] there has been described a research devoted to desalting and dehydration of crude oil with pretreatment in electromagnetic field at 0,1375 Tl and linear flow speed 1 m/s which has shown the increase of dehydration level by 5-30 % and 2 times decrease of emulsifier consumption comparing to traditional technologies.

Implementation of technological refining of crude oil includes the exploitation of equipment under extremely hard conditions, i.e. wide temperature and pressure rate, corrosion destruction etc. Thus, construction materials of pipes, heaters, coils, valves and pumps play the crucial role. There are widely used different types of steel that contain Cr, Mo, Mn, Si, Ti, Ni etc. These components improve strength and hardenability and corrosion resistance of steel. Nowadays the most popular types of steel are produced by JFE Steel Company [21]. Also there are widely used metal and non-metal matrices with the specific location of hardeners. One of the most promising construction sealants in petroleum refining industry is expanded graphite [22]. Due to its high adsorption capacity expanded graphite can be applied for removing of fuel oil, heavy metals and other organic substances from water. The main benefit of expanded graphite is its self-regeneration. 1 gram of expanded graphite can adsorb up to 80 grams of organic substances [23]. Carbon materials can be applied for production of complicated high-temperature heaters including flexible pipes, high-temperature heat shields etc. [24]

Technological parameters of primary oil refining such as temperature, pressure and infinite reflux can be considered as the powerful tools to improve the production efficiency [25]. Each type of raw material, that is supposed to be processed at refinery, has a considerable level of technological parameters. For example, boiling point is the crucial factor for construction materials choose. Heat balance of equipment depends on the temperature of raw materials and refining products. Pressure has the huge influence on boiling point of liquids and on separation of liquid and gas fractions in separators. Infinite reflux is an important factor that defines temperature range of column. Also temperature and pressure have an influence on construction materials, design of refining equipment and environmental safety.

Operational control of refining processes is the developing branch of petroleum industry. Nowadays the operational control at most of the refineries in Ukraine and Russia is based on laboratory analysis of samples, taken from the definite key points of rig. In this case there should be defined around 3-5 quality parameters which are supposed to be defined as soon as possible. Ideally there should be a specific integral parameter to characterize the composition and structure of raw material and products. Specific conductivity (δ) and relative permittivity (ε) have been proposed as the specific integral parameter [26-27]. Choose of parameter should be based on origin of analyzed material. Thus, primary oil refining field can be divided into two areas (Fig. 2). Preparation area includes the separation of water, salts and mechanical admixtures from crude oil. Refining area includes stabilization of oil and fractional separation in distillate column.

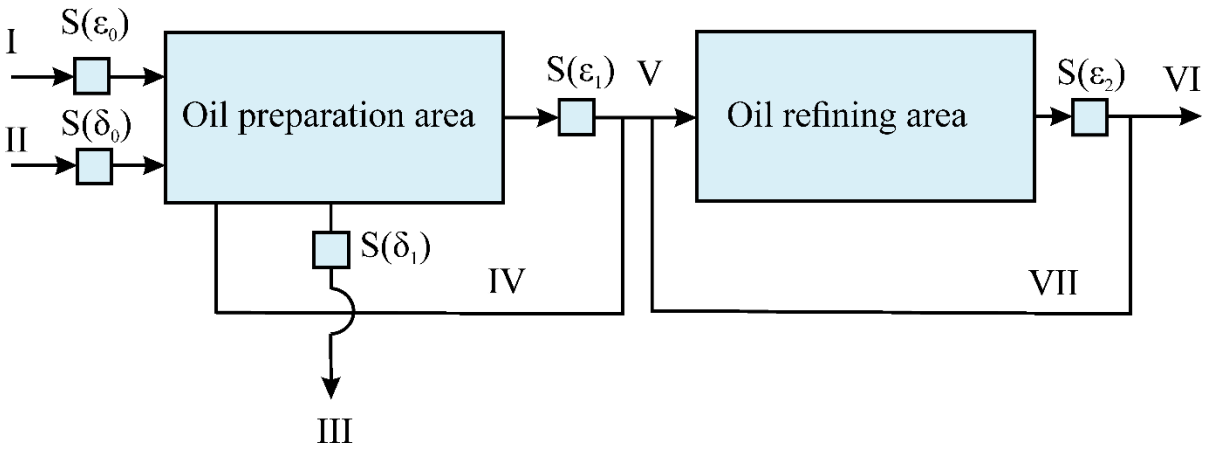

Fig 2. Structural scheme of primary petroleum refining:
I – crude oil, II – fresh water, III – waste water, IV – insufficiently prepared crude oil, V – prepared oil, VI – final product, VII – substandard product

Considering the fact that crude oil and products of it refining are non-polar dielectrics, it is quietly reasonable to control these substances by permittivity ε. For this purposes on I, V and VI fields there have been located the sensors $S(\varepsilon_0)$, $S(\varepsilon_1)$, $S(\varepsilon_2)$ to measure this parameter. Also, parameter ε may be used for determination of water in prepared crude oil. Since the increase of boiling point of petroleum fractions leads to increase of relative permittivity, sensor $S(\varepsilon_2)$ may be used to get the reliable information about the level of fractions separation.

Considering the electric conductivity it should mentioned that its value always depends on the amount of conductive components that are removed with water in preparation area (flow III). In this case salts and mechanical admixtures are conductive components that have been removed from crude oil. In the preparation area the proportion $\delta_1 > \delta_0$ is always constant so to control the removal of salts and admixtures in II and III flow there have been set special sensors $S(\delta_0)$, $S(\delta_1)$.

Based on sensors $S(\varepsilon_1)$ and $S(\delta_1)$ readings if the prepared oil is unfit for further refining and refining, it should be taken back to preparation area. Similarly, for refining area – if the high level of separation has not been reached, the products should be mixed with crude oil for repeated refining.

3. Conclusion

The general ways of improvement of primary petroleum refining rigs were presented. In our opinion, one of the most perspective directions is operative process control. This system is based on primary diagnostic information received from sensors that have been set at the general material flows of the rigs. The operating principle of sensor is based on the measuring of electrical conductivity and relative permittivity in different areas. The presented scheme provides the realibility of equipment exploitation, reduces the harmful emission and minimize the time for correction of technological parameters.

References

[1] Akhmetov SA. Tehnologiya glubokoy pererabotki nefti i gaza, Moscow, 2002, 217 p.
[2] Kapitonova OV. Nalozhenie neftyanyih fraktsiy pri razdelenii mazuta pod vakuumom. Vestnik tehnologicheskogo universiteta. 2015. Vol.18, №20: 88-90.
[3] Ali HAAR. Preparation and evaluation of demulsifiers agents for Basra crude oil. Applied Petrochemical Research. 2012; 1(1-4): 29–33.
[4] Hajivand P. Optimization of demulsifier formulation for separation of water from crude oil emulsions. Brazilian Journal of Chemical Engineering, 2015; 32(01): 107 – 118.
[5] Salam KK. Improving the Demulsification Process of Heavy Crude Oil Emulsion through Blending with Diluent. Journal of Petroleum Engineering, 2013; 1: 96 – 102.

[6] Yasakov E. Issledovanie svoystv izvestnogo i razrabotannogo deemulgatorov dlya obezvozhivaniya i obessolivaniya vodoneftyanyih emulsi. Neftegazovoe delo, 2010; 2: 1-13.
[7] Fazulzyanov RR. Primenenie reagentov na ustanovkah pervichnoy pererabotki nefti. Vestnik Kazanskogo tehnologicheskogo universiteta, 2013; 6: 192-195.
[8] Farhutdinova AR, Mukatdisov NI, Elpidinskiy AA, Grechuhina AA. Sostavyi ingibitorov korrozii dlya razlichnyih sred. Vestnik Kazanskogo tehnologicheskogo universiteta, 2013; 4: 272- 276.
[9] Tomin VP. RF Patent 2108409, C23F11/173, 10.04.1998.
[10] Moiseeva LS. RF Patent №2151818, C23F11/12, 27.06.2000.
[11] Fahriev AM. RF Patent №2529677, C10G19/02, C10G29/06, 20.09.2006.
[12] Finšgar M. Application of corrosion inhibitors for steels in acidic media for the oil and gas industry: A review. Corrosion Science, 2014; 86: 17-41.
[13] Skoblo AI. Protsessyi i apparatyi neftegazopererabotki i neftehimii, 3rd ed.; Nedra-Biznestsentr: Moscow, 2000; 677 p.
[14] Bogatyih KF. Konstruktivno-tehnologicheskiy podhod k vyiboru kontaktnyih ustroystv dlya realizatsii resurso-energosberegayuschih tehnologiy. Aktualnyie problemyi tehnicheskih, estestvennyih i gumanitarnyih nauk: materialyi Mezhdunarodnoy nauchno-tehnicheskoy konferentsii. UFA, May 2005: 65-68
[15] Almabekov OA. Sovershenstvovanie kontaktnyih ustroystv rektifikatsionnyih kolonn. Almatyi tehnologiyalyi, 2014; 2: 16-19.
[16] Kagan AM. Sravnenie tarelchatyih i nasadochnyih kontaktnyih ustroystv kolonnyih apparatov. Himicheskoe i neftegazovoe mashinostroenie, 2007; 1: 9 - 10.
[17] Churakova SK. Razrabotka resurso-energosberegayuschih tehnologiy fraktsionirovaniya na osnove konstruktivno-tehnologicheskogo podhoda. Tehnologii nefti i gaza, 2013; 4(87): 8-14.
[18] Hamidullin RF. Uvelichenie vyihoda svetlyih distillyatov pri pomoschi aktivatsii neftyanogo syirya. Himiya i tehnologiya topliv i masel, 2016; 6(598): 29-34.
[19] Takaeva MA. Intensifikatsiya protsessa podgotovki i pererabotki groznenskih neftey. Materialyi mezhdunarodnoy nauchno-tehnicheskoy konferentsii «Aktualnyie problemyi tehnicheskih, estestvennyih i gumanitarnyih nauk». UFA: UGNTU, 2010: 47-50.
[20] Brand AE. Gidrodinamicheskaya kavitatsionnaya obrabotka kak sposob snizheniya vyazkosti vyisokovyazkih neftey i povyisheniya effektivnosti transportirovki. Sovremennyie problemyi nauki i obrazovaniya, 2015; 2-3: 1-5.
[21] Masamura Katsumi Steel Products for Energy Industries. JFE Technical report No. 18, March 2013: 1-11.
[22] Burleshin M. Grafit prihodit na smenu asbesta. Vestnik Mosenergo, 2001; 9: 3-4.
[23] Inagaki M. Exfoliation of graphite via intercalation compounds. Chemistry and physics of Carbon, 2004; 29: 1-69.
[24] Leng Y. Influences of density and flake size on the mechanical properties of flexible graphite. Carbon. 1998; 36: 875- 881.
[25] Golden SW. TECHNOLOGY Temperature, pressure measurements solve column operating problems. Oil & Gas Journal, 1995; 93: 45- 49.
[26] Peinado-Guevara H. Relationship between chloride concentration and electrical conductivity in groundwater and its estimation from vertical electrical soundings (VESs) in Guasave, Sinaloa. Cienc. Inv. Agr., 2012; 39(1): 229-239.
[27] Ajienkaa JA. Measurement of dielectric constant of oilfield emulsions and its application to emulsion resolution. Journal of Petroleum Science and Engineering, 1993; 9(4): 331-339.

To whom correspondence should be addressed: Professor Alena Tulskaya, National Technical University "Kharkiv Polytechnic Institute", Kharkiv, Ukraine

Petroleum and Coal

Article **Open Access**

PREDICTION OF ASPHALTENE ONSET PRESSURES DURING NATURAL GAS AND CARBON DIOXIDE INJECTIONS

Oguamah Ifeanyi[1] Isehunwa Sunday[2], and Udeagbara Stephen[3]*

[1] *Department of Petroleum Engineering, Federal University of Technology, Owerri, Nigeria*
[2] *Department of Petroleum Engineering, University of Ibadan, Nigeria*
[3] *Department of Chemical and Petroleum Engineering, Afe Babalola University, Ado Ekiti, Nigeria*

Received December 3, 2018; Accepted February 8, 2019

Abstract

Asphaltene precipitation is one of the challenges encountered during the production of heavy crude oils. Precipitation may also be pronounced during gas injection operations performed to improve production of such heavy crudes. Many of the reported models used for predicting Asphaltene Precipitation in order to achieve the best reservoir and production management practices are rather complex for routine applications. This study was designed to develop a simple but accurate model for predicting Asphaltene precipitation onset during gas injection into oil reservoirs. The parameters for the equation were obtained by tuning to experimental PVT data to obtain pressure-temperature phase profiles. Upper Asphaltene Onset Pressures (UAOP) were predicted under carbon dioxide gas injection and natural gas injection. Results were validated using published data, and compared with the Perturbed Chain Statistical Associating Fluid Theory (PCSAFT) Equation of State. The predictions matched experimental data. Generally, UAOP increased with an increasing proportion of injected gases and varied with reservoir fluid and type of injected fluid. This shows that as much as possible, injections of gases into heavy oils reservoirs should be done at the highest possible pressures.

Keywords: *Asphaltene precipitation; Reservoir fluid modelling; Gas injection operations.*

1. Introduction

Asphaltenes are very complex solid component part petroleum fluids; they are usually high boiling materials with metals contents and heteroatoms like oxygen and sulphur while Nitrogen exists in various heterocyclic types including pyridine, aniline, quinolin, and pyrrole [1] it also exhibits polymer characteristics being derived from basic hydrocarbon units. Asphaltene precipitation poses challenges in petroleum production and storage systems, reservoir, wellhead, pipelines and process facilities [2-5] and understanding behavior of asphaltene has been a major challenge to the oil industry [6-7]. Numerous studies have been done in areas of asphaltene thermodynamics, structural characteristics, depositional behaviour, mitigation and economics, These studies, however, do not effectively give solutions to the asphaltene problem, [8], observed a rise in the quantity of precipitated asphaltene with temperature increase, although the reverse is the case for asphaltene dispersed in paraffin solutions. Leontaritis [9] suggested the asphaltene precipitation envelope (APE) describe the conditions under which asphaltene precipitation can occur; the asphaltene precipitation envelope shows the region in which precipitation occurs in a temperature-pressure or temperature-composition diagram, the upper asphaltene onset conditions fall within the points on the APE. Studies described asphaltene molecules as undergoing self-association or association with resins, while the resin-to-resin association is not possible, asphaltene-resin association causes asphaltene stability in mixtures. Leontaritis and Mansoori [10] later suggested the steric colloidal model for predicting the onset of flocculation of colloidal asphaltene in oil mixtures based on the phenomenon that

Resin particle are very important in Asphaltene stability and that a streaming potential develops during oil flow, this contains charged colloidal particles which causes the flocculation and precipitation of asphaltene particles.

The thermodynamic behaviour of asphaltene in solution is usually described by the molecular solution theory, which suggests that the stability of asphaltene in oil as a solution and the separation of the oil (solvent) and asphaltene (solid) phase when asphaltene precipitation occurs. This approach has found use in different literature, which includes the Flory-Huggins-(FH) theory, Flory-Huggins-Goldstein theory, Scatchard-Hildebrand equation, Statistical Association Fluid Theory (SAFT) and thermodynamic colloidal Theories. Most models in literature are based on a combination of these theories, for instance, the micellar approach suggests that Asphaltene in aromatic solvents, crudes, and aromatic/alkane mixtures form micelles [11]. This approach suggests that the micelles formed by asphaltene molecules remain stable in crude oil and it can precipitate upon the attainment of a critical concentration when the concentration of asphaltene monomers reaches a critical concentration which causes the solubility of the monomer concentration to be lower than the solubility of the asphaltene micelles, [12]. Studies have shown that asphaltene micelles form when crude oil contains excess hydrocarbon. Priyanto [13], described different stages in asphaltene association, suggesting that at concentrations above CMC asphaltene in solution will self-associate, as concentration further increases the self-associated Asphaltene will form a coacervate, and a continuous increase in concentration will result in the formation of asphaltene aggregates. Asphaltene micelle formation shares structural similarity with surfactant systems [14].

There are other approaches used to study the thermodynamic behaviour of associating fluids these approaches include, the Perturbation theory, Tangent Sphere model, Lattice model, Hole model, Molecular simulation, Scaled Particle theory, and Partition function theory. The Cell and Lattice models provide different adaptations of the compressible lattice model of solid polymers while incorporating compressibility in a different manner. The hole model combines both methods of incorporating compressibility introduced by cell and lattice fluid, it assumes that molecular sized holes exist in a solid state and an increased number of holes will confer fluid like properties to the solids, also during compression vacant holes are replaced by molecules, thereby causing gas to act as a liquid. Perturbation theory is a useful tool in many branches of physics and statistical mechanics of classical fluids. In perturbation theory, the fluid structure is characterised by a set of distribution functions brought about by expanding a fluid about the same properties of its reference fluid. One of the earliest applications of perturbation theory can be seen in the assignment of parameters to VDW EOS in order to account for the two major interacting components namely, the high-density repulsion and the low-density attraction.

Perturbation theory has been widely applied to classical associating fluids in other to understand their thermodynamic behaviours [15]. Wertheim further suggested the Statistical Associated Fluid Theory (SAFT), for describing the thermodynamic behaviour of associating fluids. The basis for the development of the SAFT model was the sequential expansion of the Helmholtz energy about an integral molecular distribution function and the inherent association capability [16]. This resulted in an association between the excess Helmholtz energy of association, the energy formed because of the formation of adjacent molecular chains and a function related to the segment-to-segment interaction.

Where, is the residual energy contribution as a result of the interaction of adjacent segments, refers to contribution due to the formation of adjacent chains, refers to site-site interaction of segments while refers to the association energy contribution.

In recent time, the association theory has been widely used to model asphaltene behaviour, but it is rather complex and used many parameters that are difficult to define. Kontogeorgis and Folas [17] introduced the cubic plus association equation of state, combining the classical equation of state with an association term, in order to describe complex mixtures and hydrocarbon.

The focus of this study will be on the formulation of a simple equation of state to study the asphaltene onset pressure during CO_2 gas injection in oil reservoirs.

2. Methodology

We suggest an expression in the form:

$$P = \frac{RT}{(V-b)} - \frac{a}{v(v+b)} - \frac{c}{(v+b)} \quad (1)$$

The parameter "a" terms represents the attractive term, while parameter "b" is the volume parameter, and "c" the non-physical force term.

The equation can be simplified to the form:

$$P = \frac{RT}{v-b} - \frac{(a+cv)}{v(v+b)} \quad (2)$$

The fugacity coefficient was calculated from the following thermodynamic equation:

$$\varphi_i = \frac{1}{RT}\int_v^{\infty}\left[\left(\frac{\partial P}{\partial n_i}\right)_{T,n,V,n_i} - RT/V\right]dV - \ln Z \quad (3)$$

where:

$$P = \frac{RT}{V-b} - \frac{a(T)}{V(V+b)} - \frac{c(T)}{V+b} \quad (4)$$

The derivation of the fugacity equation for the equation of state formulation is achieved by incorporating, equation (2) in equation (4) to obtain.

$$ln\,\varphi = (Z-1) - ln\,Z + \frac{1}{RT}\left[-\frac{1}{RT}\,ln\,\frac{V}{V-b} + \frac{a}{b}\,ln(V+b) + c\,ln(V+b)\right]_{\infty}^{V} \quad (5)$$

Simplifying further gives:

$$ln\,\varphi = (Z-1) - ln\,Z - ln(Z-B) + \frac{A}{B}ln\left(1+\frac{B}{Z}\right) + C\,ln(Z+B) \quad (6)$$

The phase liquid-solid phase equilibrium is given in terms of fugacity as

$$\varphi_i^L = \varphi_i^V. \quad (7)$$

where L, S indicate the liquid and solid phases respectively, and i represent the specie.

For a liquid- solid phase formulation at equilibrium, the fugacity of the i^{th} component in the liquid and solid phase can be expressed as.

$$ln\left(\frac{\theta_V}{\theta_L}\right) = Z_V - Z_L - ln\left(\frac{Z_V}{Z_L}\right) - ln\left(\frac{Z_V-B}{Z_L-B}\right) - \frac{A}{B}\left(\frac{Z_V+B}{Z_L+B}\right)\left(\frac{Z_V}{Z_L}\right) - C\,ln\left(\frac{Z_V+B}{Z_L+B}\right) \quad (8)$$

For each n component in a mixture, the equation of state can be expressed in terms of fugacity as:

$$ln\,\varphi = (Z-1)B' - ln\,Z - ln(Z-B) + \frac{A}{B}\left(A_i' - B_l'\right)ln\left(1+\frac{B}{Z}\right) + C\,ln(Z+B) \quad (9)$$

where,

$$A' = \left(1/2\sum_{i,j=1}^{N}(1-k_{ij})(a_i a_j)^{\frac{1}{2}}\right) \quad (10);\; B' = \frac{b_i}{b};\; C_i' = \frac{c_i}{c} \quad (11)$$

A fitting procedure as suggested by Kontogeorgis and Folas [17] was used to determine the parameters of the equation The parameters were fitted to the vapour pressure and liquid density using the Generalised Reduced Gradient (GRG) non-linear minimization program, the objective function minimized in this study is the root sum of squares errors function defined by the expression:

$$\text{Objective function} = \sqrt{\sum_{j=1}^{k\Sigma}\sum_{j=1}^{m\Sigma}\left(x_{ij}^{exp\,est}\,()^2\right)} \quad (12)$$

where: i=data point number with a group; j=Measured variables for a data point; k=total number of a point in a data group; m=Number of points in a data group; x is the measured or calculated variable.

Reservoir fluid Data from the studies done by Arya et al. [18] and a model oil mixture developed by Marcano *et al.* [19], designated as Fluid-1, and Fluid-2, respectively were investigated. In order to model Asphaltene precipitation in the test petroleum fluid samples, the fluid volume was assumed constant. The Crude oil composition and properties used for the study is shown in Table 2 and Table 3 respectively.

2.1. Determination of molar volume

The molar volume used for the equation was derived from a simple adjustment procedure done in excel software, which can be summarised by the expression:

$$V = V_{fitted} - V_{adjusted} \quad (13)$$

where: V_{fiited} is the volume fitted from experimental data; $V_{adjusted}$ is the adjustment.

Fluid-1 was used by Al-Hammadi et al. [20] (2015) and Arya et al. [18] (2016), the PC SAFT results were obtained by an approach similar to Panuganti [21] (2012), while Fluid-2 has been was used by Jamaluddin et al. [22] (2002), under nitrogen gas injections of 5, 10 and 20wt%.

Table 1. Crude oil compositions gas phase

Component	Fluid 1 (Mol %)	Fluid 2 (Mol %)	Component	Fluid 1 (Mol %)	Fluid 2 (Mol %)
N_2	0.163	0.490	Iso-butane	1.885	0.810
H_2S	1.944	3.220	n-Butane	5.671	3.710
CO_2	0.000	11.370	Iso-pentane	2.993	1.220
Methane	33.600	27.360	n-pentane	2.980	1.980
Ethane	7.673	9.410	C6+	38.236	34.280
Propane	7.282	6.700			

Table 2. Properties of crude oil samples

Properties	Fluid-1	Fluid-1
Saturates (wt. %)	57.4	66.26
Aromatics (wt. %)	30.8	25.29
Resins (wt. %)	10.4	5.25
Asphaltenes (wt. %)	1.40	2.80
MW of C_{6+}	-	208.08
Res. fluid MW (g/mol)	102.04	97.50
STO Density (g/cm^3)	0.906	0.823
GOR (scf/stb)	900	787

3. Results and discussion

Equation (3) represents a 3-parameters equation of state (EOS), it is different from the most commonly used EOS. While parameter "a" is a function of temperature for most equations of state, in this study, parameter "b" is a function of temperature as given in Table 3.

Figures 1-3 show the UAOP and bubble point pressures of Fluid-1 under natural gas injection scenarios of 0, 15, and 30 wt% result of comparison between the PC SAFT model results and this study with respect to experimental model, for the gas injection scenarios showed agreement with experimental data and PC-SAFT data for the bubble point pressures and UAOP at different values of pressure and temperature. The model predicted both the Saturation pressures and Upper Asphaltene onset pressure (UAOP) of the reservoir fluids shown in Tables 2 and 3. The deviations between the PC-SAFT and this study was less pronounced for the saturation pressure especially at a lower temperature, while the deviation for UAOP increased at higher pressures. The result also showed an increase in the gap between the saturation pressure line and the upper Asphaltene onset UAOP as injection increased from 0 to 30wt%. This may be due to an increase in interaction between Asphaltene and STO and increased precipitation as a result of a change in fluid composition during gas injection.

Figures 4-6 show the UAOP and bubble point pressures for Fluid-2 under CO_2 gas injections of 0, 10 and 20wt%. The model prediction shows agreement with the experimental data and

PC SAFT results at 0wt% gas injection, but noticeable deviations were observed at 10 wt% and 20wt% Co2 gas injections, there is also an increase in the difference between UAOP and the saturation pressure with an increase in the amount of injected gas. This agrees with the findings of Gonzalez *et al.* [23]. The "a" and "c" parameters for the model equation were obtained by a parameter fitting procedure while a temperature based correlation was used to obtain the b parameter as shown in Table 3. Generally, the study showed slight deviations in the UAOP as the injected gas increased from 0 wt% to 30 wt% natural gas injection for Fluid-1; 10 and 10 wt% to 20 wt% CO_2 gas Injection for Fluid-2, this shows that changes in the composition of crude oil will affect the asphaltene behavior. These deviations were also proportional to the changes in the values of the liquids volume used in the model equation. The liquid volume also decreased with an increase in the gas injection for Fluid-1, Fluid-2. This may be due to the formation of Asphaltene precipitation in petroleum fluids. Formation of Asphaltene precipitation in the petroleum

Table 3. Fitted parameters used

Fluid	a	b	c
Fluid-1	0.999	$0.0036T^2$-3.760T+1002.9	0.964
Fluid-2	0.998	$0.0128T^2$-9.118T+1588.0	0.918

Table 4. SAFT parameters correlations for saturates (Gross and Sadowski [24])

M	0.0253MW+0.9263
σ	$3.369MW^{0.0271}$
ε/k	$132.11MW^{0.1221}$

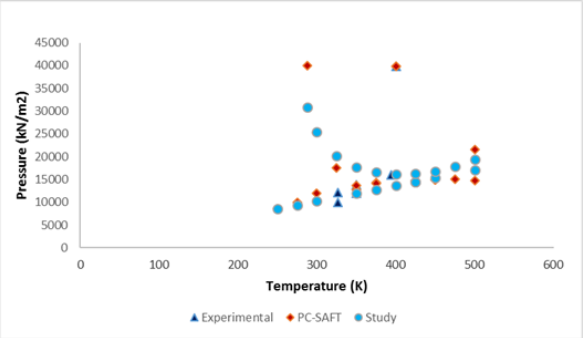

Figure 1. UAOP and Bubble point pressures for Fluid-1 at 0 wt% natural gas injection

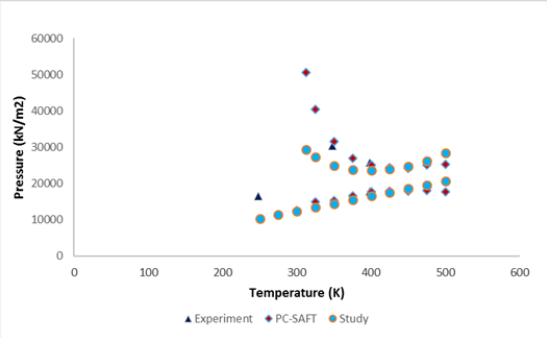

Figure 2. UAOP and Bubble point pressures for Fluid-1 at 15wt. % natural gas injection

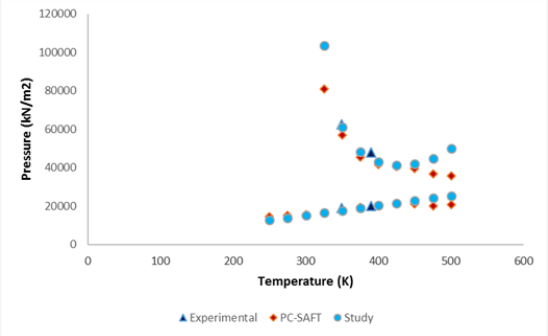

Figure 3. UAOP and Bubble point pressures for Fluid-1 at 30 wt. % natural gas injection

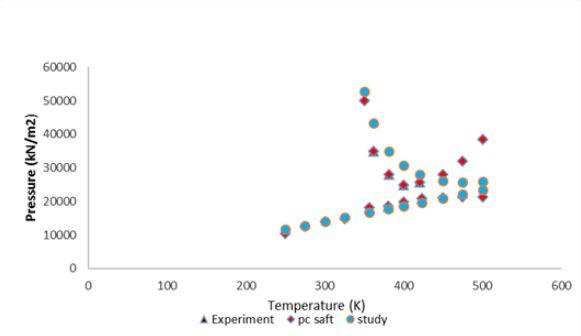

Figure 4. UAOP and Bubble point pressures for Fluid-2 at 0wt. % CO_2 gas injection

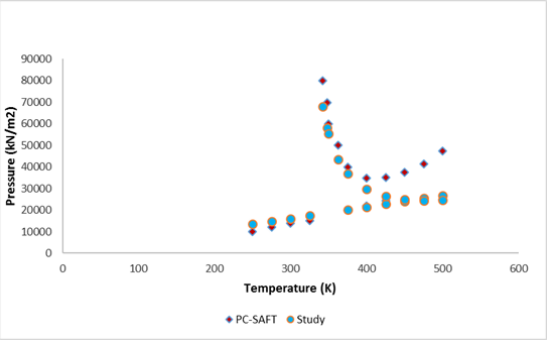

Figure 5. UAOP and Bubble point pressures for Fluid-2 at 10wt. % CO_2 gas injection

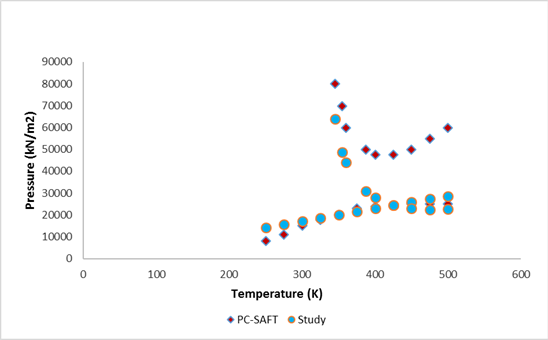

Figure 6. UAOP and Bubble point pressures for Fluid-2 at 20wt. % CO_2 gas injection

4. Conclusion

A simple method was used to predict phase envelopes of heavy crude and determine their upper asphaltene onset pressure. Application to carbon dioxide and Natural gas injection led to the following conclusion:

1. The Upper Asphaltene Onset Pressures UAOP occurred at high pressure and temperature which indicates that asphaltene will form at the reservoir regions rather than at the surface.
2. As gas injections increased, the Upper Asphaltene Onset Pressure increases will little change in temperature.
3. Changes in the composition of crude oil during gas injection will affect the asphaltene behaviour in crude oil.

Acknowledgment

We acknowledge the support of the management and Staff of The Petroleum Engineering Department of the Federal University of Technology Owerri in the writing of this article.

References

[1] Zuo P, and Shen W. Identification of Nitrogen-Polyaromatic Compounds in Asphaltene from Co-Processing of Coal and Petroleum Residue Using Chromatography with Mass Spectrometry. Int. J. Coal Sci. Tech., 2017; 2095-8293.

[2] Carpentier B, Wilheims A, Mansoori GA. Reservoir Organic geochemistry: Processes and application J. Pet. Sci. and Eng., 1997; 56: 341-343.

[3] Mansoori GA. Asphaltene Deposition: An Economic Challenge in Heavy Petroleum Crude Utilization and Processing. OPEC Review, 1998; 103-113.

[4] Pineda-Flores G, Mesta-Howard AM. Petroleum Asphaltene: Generated Problematic and Possible Biodegradation Mechanism. Rev Lat. Microbiologia, 2001; 43(3): 143-150.

[5] Vaider S. Experimental Study and Modelling of Asphaltene Precipitation Caused by Gas Injection. PhD. diss., Technical University of Denmark 2006.

[6] Chen Z, Zhang L, Quan S, Sh, Q, and Xu C. Molecular Structure and Association Behavior of Petroleum Asphaltene. In: Xu C., Shi Q. (eds) Structure and Modelling of Complex Petroleum Mixture. Structure and Bonding, Springer 2015, 168: 1-38.

[7] Oh K, and Deo MD. Near Infrared Spectroscopy to Study Asphaltene Aggregation in Solvents. In: Mullins, O.C.; Sheu, E.Y., Hammami, A.; Marshall, A.G. (eds) Asphaltenes, Heavy Oils, and Petroleomics. Springer 2007: 469-488.

[8] Ali LH, and Al- Ghannam KA. Investigation into Asphaltenes in Heavy Crude Oils: 1. Effect of Temperature on Precipitation by Alkane Solvents. Fuel, 1981; 60: 1045.

[9] Leontaritis KJ. The Asphaltene and wax Deposition Envelopes. Fuel Science and Technology International, 1996; 14(1-2): 13-39.

[10] Leontaritis KJ, Mansoori GA. Asphaltene Flocculation during Oil Production and Processing: A thermodynamic Colloidal Model. In SPE International Symposium on OilField Chemistry, Society of Petroleum Engineers: San Antonio, Texas, USA. February 1987.

[11] Pan H, and Farozabadi A. Thermodynamic Micellization Model for Asphaltene Precipitation Inhibition. AICHE J., 1999; 991516-KB-314.
[12] Wu J, and Prausnitz JM, Firoozabadi A. Molecular Thermodynamics of Asphaltene Precipitation in Reservoir Fluids. AICHE J., 2000; 46(1): 197-209.
13 Priyanto S, Mansoori GA, and Suwono A. Measurement of Property Relationships of Nano-Structure Micelles and Coacervates of Asphaltene in Pure Solvent. Chemical Engineering Science, 2001; 56: 6933-6939.
[14] Sheu EY, and Mullins OC. Editors. Asphaltene: Fundamentals and Applications. Plenum Publishing Co.: New York, 1995.
[15] Wertheim MS. Fluids with Highly Directional Attractive Forces. I. Statistical Thermodynamics. J. Stat. Phys., 1983, 35: 19-34.
[16] Chapman NG, Gubbins KE, Jackson G, and Radosz M. SAFT: Equation of States Solution Model for Associating Fluids. Fluid Phase Equilibria, 1989; 52: 31-35.
[17] Kontogoergis GM, and Folas GK. Thermodynamic Models for Industrial applications: from Classical and Advanced Mixing Rules to Association Theories. John Wiley& Sons: West Sussex 2010, U.K.
[18] Arya A, Liang X, von Solms N, and Kontogeorgis GM. Modelling of Asphaltene Onset Precipitation Conditions with Cubic Plus Association (CPA) and Perturbed Chain Statistical Associating Fluid Theory (PC-SAFT) Equation of State. Energy& Fuels, 2016; 30(8): 6835-6852.
[19] Marcano F, Ranaudo AM, Chirinos J, Daridon JL, and Carrier H. Study of Asphaltene Aggregation in Toluene/n-Heptane/CO_2 Mixtures under High-Pressure Conditions. Energy& Fuels, 2013; 27(8): 4598-4603
[20] Al-Hammadi AA, Vargas FM, and Chapman WG. Comparison of Cubic Plus-Association and Perturbed-Chain Statistical Associating Fluid Theory Methods for Modelling Asphaltene Phase Behaviour and Pressure-Volume-Temperature Properties. Energy Fuels, 2015; 29(5): 2864-2875.
[21] Panuganti SR. Asphaltene Behaviour in crude oil system. Ph.D. Thesis Submitted to Rice University 2013.
[22] Jamaluddin AKM, Josh, N, Iwere F, and Gurpina O. An Investigation of Asphaltene Instability under Nitrogen Injection. SPE International Conference and Exhibition, Mexico, February 2002; SPE 74393
[23] Gonzalez DL, Hirasaki GJ, Creek J, and Chapman WG. Modelling Asphaltene Precipitation Due to Changes in Composition Using the Perturbed Chain Statistical Associating Fluid Theory. Energy and Fuels, 2007; 21: 1231- 1242.
[24] Gross J, Sadowski G. An Equation of State Based on a Perturbation Theory of Chain Molecules. Ind. Eng. Chem. Res. 2001; 40: 1244-1260.

To whom correspondence should be addressed: Oguamah Ifeanyi, Department of Petroleum Engineering, Federal University of Technology, Owerri, Nigeria, E-mail uchelex@gmail.com

Petroleum and Coal

Article **Open Access**

WAY TO INCREASE THE ENERGY EFFICIENCY OF THE DISTILLATION UNIT AT ETHYLBENZENE MANUFACTURING TECHNOLOGY

*Elena S. Khlebnikova[1], Elena N. Ivashkina[2], Andrey V. Volf[2], Irena O. Dolganova[2]**

[1] Los Alamos National Laboratory, Los Alamos 87545, USA
[2] National Research Tomsk Polytechnic University, Tomsk 634050, Russia

Received January 13, 2019; Accepted March 19, 2019

Abstract

The object of research is the installation of rectification columns for benzene, ethylbenzene, and polyalkylbenzenes. The purpose of this work is an optimization of rectification technological modes and energy efficiency increasing of distillation in the technology of ethylbenzene production by replacing of the used in reboilers vapor at 4 MPa by vapor at 2 MPa. The proposed optimization option of the rectification unit is efficient since the implementation of the proposed technical solution will be achieved using Vapor 2 with increased efficiency of the process, namely a reduction of vapor consumption. The total consumption of vapor after the upgrade will be 2.751 Gcal / hour, which is 2168 Gcal per year less than the current vapor load.

Keywords: *ethylbenzene; distillation; simulation; column; optimization.*

1. Introduction

The process of mixtures rectification is one of the most energy-intensive processes and is widely used in enterprises. Mass transfer columns have a complicated design, large metal content and high energy consumption as heating and cooling agents. Energy consumption is largely dependent on units design, that is, the efficiency of contact devices used in columns. From the theory and operation of rectification, it is known that the lower the efficiency of contact devices, the larger reflux flow rate (reflux ratio) and the vapor stream (vapor number) are required, therefore, increasing the costs of heating agent in a column reboiler and cooling agent in a dephlegmator.

Nowadays the main problem of rectification is the high power demand of installations [1]. Therefore, the process continues to occupy a leading position in energy consumption in the petrochemical and refining industries.

The purpose of this work is an optimization of rectification technological modes and energy efficiency increase of distillation in benzene with ethylene alkylation technology by replacing the used vapor at 4 MPa by vapor at 2 MPa.

Process modeling is a useful tool to optimize the operation of industrial plants [2–11]. Different models can solve and prevent various problems and emergencies as they are developed with due consideration of physicochemical reactor process. This makes them sensitive to changes in raw material composition and performance properties of the catalysts.

2. Object and methods of research

Ethylbenzene (EB) is used as an intermediate in the production of synthetic rubber and styrene [12-13]. Rectification unit of one of the ethylbenzene and dry benzene production enterprises (Fig. 1) includes three distillation columns K-52, K-62, and K-72. Column K-52 is designed for stripping of recycled benzene from alkylate, column K-62 is designed to separate ethylbenzene, and column K-72 is designed to separate polyalkylbenzenes (PABs) from resin.

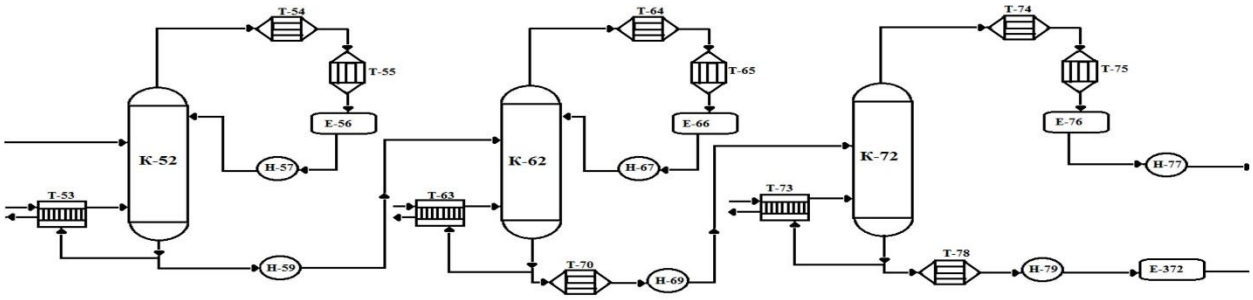

Figure 1. Rectification unit of one of the ethylbenzene and dry benzene production enterprises

For this study, the input data were parameters of technological regime obtained from the installation of ethylbenzene production for one of the petrochemical industries. Tab. 1 shows the structural characteristics of the existing columns.

Table 1. The design parameters of distillation columns

Column parameter	K-52	K-62	K-72
Inner diameter, mm	2000	2200	1400
Number of trays	60	80	37
Trays distance	450	450	400

Tab. 2 shows thermobaric performance characteristics of distillation columns, according to the current regulations of technology.

Table 2. Operating modes of columns

Column operating mode	K-52	K-62	K-72
Overhead vapor pressure, kPa	100	100	130-220
Bottom liquid pressure, kPa	120-160	120-170	5.3-21.3
Overhead vapor temperature, °C	75-100	125-139	not standardized
Bottom liquid temperature, °C	145-165	175-200	160-195

Distillation columns K-62 and K-72 consume heat which is supplied by vapor P = 2.8 MPa throttled from vapor P = 4 MPa through reboilers T-63 and T-73, the heat to the distillation column K-52 is fed by vapor P = 2 MPa through T-53 reboiler. For the operating mode of rectification columns, it requires vapor at about 200°C. According to the thermal power plant (TPP) that produces vapor with P = 2 MPa, T = 300°C and P = 4 MPa, T = 340°C, but due to the long-haul pipeline (about 10 km), the vapor parameters are significantly reduced. As a result, the necessary temperature for columns K-62 and K-72 with required operating modes can be ensured only by vapor P = 4 MPa.

The feasible option of optimization mode is the bottom temperature reducing, which will allow using Vapor 2 for the temperature difference between coolants (this option does not require significant overhaul). The lower temperature of Vapor 2 is determined as 194°C. The temperature reduction of the column bottom is possible by reducing the pressure in the column, which in turn will lead to boiling temperatures reduction of the component and a separated mixture of evaporated liquid in reboiler.

Calculations for determination of the columns optimal mode were carried out using a universal Aspen HYSYS simulation system. Simulation process was performed on purpose the flows compositions, top and bottom temperatures of the columns were as close as possible to those columns regime parameters presented in Tab. 2.

The basis of the program is the general principles of material and heat balances calculations. The connection of elements provides a flowsheet simulation with relevant transformations in the system. Calculation of hydrocarbon systems was carried out using the Peng-Robinson equation of state.

3. Results and discussions

As a result, calculations were made to determine the optimal operation of the processing circuit in order to increase the efficiency of the distillation process, ethylbenzene and the establishment of the possibility of reducing the temperature of the bottoms of the columns.

Aspen HYSYS simulation environment [14-15] allows to define the optimal parameters of the distillation columns, and reboilers with requirements to the production technology and assess the energy efficiency. The following basic formulas are required for the material heat balance of distillation column:

$$F = P + W \quad (1)$$

where F – the mass flow of feed mixture, *kg/s*; D – the mass flow of overhead products, *kg s*; W – the mass flow of bottom products, *kg/s*.

For continuous operation of the column taking into account heat losses:

$$Q_{reboiler}+Q_f+Q_r=Q_w+Q_d+Q_{losses} \quad (2)$$

As a result of technological calculations using the parameters of the technological regime material balances of columns, compositions of product and feed streams were obtained (Tab. 3). Further confirmatory analysis for reboilers was performed; the results are shown in Tab. 4.

Table 3. Material balance of columns

	Units		K-52		K-62		K-72	
Flow		Feed	Overhead vapor	Bottom liquid	Overhead vapor	Bottom liquid	Overhead vapor	Bottom liquid
Flow rate	kg/h	20070.00	10366.43	9699.57	5953.61	3745.96	3545.51	200.44
Temperature		95	72.3	151	74	174	81.5	132.7
Pressure	kPa	140	80	130	60	100	4	12
Reflux rate	kg/h	6740			8930		1060	
				Composition				
Paraffins	mass fractions	0.0055	0.0106	0.0000	0.0000	0.0000	0.0000	0.0000
Benzene	mass fractions	0.5093	0.9857	0.0000	0.0000	0.0000	0.0000	0.0000
Toluene	mass fractions	0.0027	0.0036	0.0017	0.0028	0.0000	0.0000	0.0000
Ethylbenzene	mass fractions	0.3013	0.0000	0.6234	0.9961	0.0310	0.0327	0.0000
p-Xylene	mass fractions	0.0000	0.0000	0.0001	0.0001	0.0000	0.0000	0.0000
m-Xylene	mass fractions	0.0001	0.0000	0.0002	0.0003	0.0001	0.0001	0.0000
o-Xylene	mass fractions	0.0000	0.0000	0.0001	0.0001	0.0001	0.0001	0.0000
Cumene	mass fractions	0.0017	0.0000	0.0034	0.0006	0.0079	0.0084	0.0000
i-Bbenzene	mass fractions	0.0050	0.0000	0.0103	0.0000	0.0268	0.0283	0.0000
sec-Bbenzene	mass fractions	0.0025	0.0000	0.0052	0.0000	0.0134	0.0142	0.0000
tret-Bbenzene	mass fractions	0.0025	0.0000	0.0052	0.0000	0.0134	0.0142	0.0000
1,3,5-Ethylbenzene	mass fractions	0.0026	0.0000	0.0053	0.0000	0.0137	0.0032	0.2001
1,3-Ethylbenzene	mass fractions	0.0947	0.0000	0.1959	0.0000	0.5072	0.5350	0.0150
1,2-Ethylbenzene	mass fractions	0.0324	0.0000	0.0671	0.0000	0.1736	0.1830	0.0081
1,4-Ethylbenzene	mass fractions	0.0324	0.0000	0.0671	0.0000	0.1736	0.1809	0.0460
Resin	mass fractions	0.0073	0.0000	0.0151	0.0000	0.0391	0.0000	0.7308

Table 4. Results of confirmatory calculation for reboilers

	Temperature, °C	Pressure, kPa	Flow rate, kg/h	Technical features
Flow	Reboiler T-53			
Hot vapor P=2	194.0	1300.0	3800.0	A=182 m^2, D=1470 mm, H=4516 m, $P_{tube-side}$=1 MPa, $P_{shell-side}$=1.4 MPa
Cooled Vapor P=2	154.8	1250.0	3800.0	
EB	151.0	130.0	22420.1	
Hot EB	178.0	90.0	22420.1	
	Reboiler T-63			
Hot vapor P=2	196.0	1300.0	2500.0	A=182 m^2, D=1000 mm, P=4805 mm, $P_{tube-side}$=0.55 MPa, $P_{shell-side}$ =3.5 MPa
Cooled Vapor 2	180.4	1250.0	2500.0	
PABs	174.0	100.0	15539.6	
Hot PABs	191.2	90.0	15539.6	
	Reboiler T-73			
Hot Vapor 2	195.0	1300.0	435.0	A=61 m^2, D=630 mm, H=4830 mm, $P_{tube-side}$ =4 MPa, $P_{shell-side}$ =4 MPa
Cooled Vapor 2	134.5	1250.0	435.0	
Resin	132.7	12.0	2396.9	
Hot resin	189.2	2.0	2396.9	

According to calculations (Tab. 5), if under defined conditions the boiling point of the bottom liquid in column K-62 is about 174°C, it allows using Vapor 2 as a coolant in the reboiler of the column.

The column K -72 operates under vacuum. The boiling point of the bottom liquid under calculated conditions (Tab. 4) is 132.7°C. Thus, for the heating of the bottom liquid Vapor 2 can be used.

Based on the analysis of results it can be concluded that the proposed optimization option of rectification unit is efficient since the implementation of the proposed technical solution will be achieved using Vapor 2 with increased efficiency of the process, namely a reduction of vapor consumption. This option does not require substantial reconstruction (replacements of units or contact devices, etc.) and is quite cheaper.

In addition, condensers and reboilers loads with an average annual production ethylbenzene capacity of 35600 t/year were defined. Based on the obtained results, the thermal balance (Tab. 5) was defined.

Table 5. Heat balance

	Before modernization		After modernization	
№	Flow	Gcal/h	Flow	Gcal/h
	The use of vapor heat			
1	Vapor 2 in T-53	1.321	Vapor 2 in T-53	1.321
2	Vapor 4 in T-63	1.546	Vapor 2 in T-63	1.200
3	Vapor 4 in T-73	0.155	Vapor 2 in T-73	0.230
	Total	3.022		2.751

Thus, the total consumption of vapor after the upgrade will be 2.751 Gcal/hour, which is 2168 Gcal per year less than the current vapor load.

4. Conclusions

In this study optimization calculations for the rectification flowsheet of ethylbenzene and dry benzene from the reaction mass were conducted. Based on the results the optimized parameters of a technological mode that will improve the efficiency of the process are suggested.

In Aspen HYSYS environment calculations have shown the ability to operate temperatures decreasing in columns K-53, K-62 and K-72 from operating temperatures to the parameters supplied by Vapor 2 from the reboiler to the column bottom. This upgrade will allow using Vapor 2 instead of Vapor 4 and reducing the flow of consumed vapor.

Acknowledgments

The work was financed by subsidy for state support to the leading universities of the Russian Federation in order to increase their competitiveness among the world's leading research and educational centers. This work was also supported by the Grant of the President of Russia [MD-4620.2018.8].

References

[1] Yadav GD, Doshi NS. Synthesis of Linear Phenyldodecanes by the Alkylation of Benzene with 1-Dodecene over Non-Zeolitic Catalyst. 2002; 6(3): 23.
[2] Kiss AA, Ignat RM, Landaeta SJ F, de Haan AB. Intensified process for aromatics separation powered by Kaibel and dividing-wall columns. Chem. Eng. Process. Process Intensif., 2013; 67: 39–48.
[3] Vorobev A. Boussinesq approximation of the Cahn-Hilliard-Navier-Stokes equations, Phys. Rev. E - Stat. Nonlinear, Soft Matter Phys., 2010; 82: 056312.
[4] Dolganova IO, Buryhina ES, Ivashkina EN, Bekker AV. Simulation of the high-octane alkylates manufacturing considering the process unsteadiness. Pet. Sci. Technol. 2018; 36(7): 514–519.
[5] Ivanchina E, Ivashkina E, Dolganova I, Frantsina E,. Dolganov I Influence of alkylaromatic hydrocarbons on the efficiency of linear alkylbenzene sulfonic acid synthesis. Chem. Eng. J., 2017; 329: 250–261.
[6] A.K. Coker. Modeling of Chemical Kinetics and Reactor Design; 2001.
[7] Modeling N. Numerical Modeling for Fluid Flow, Heat Transfer, and Combustion, Steam Its Gener. Use. 2005; 114: 383–393.
[8] Dym CL. Principles of Mathematical Modeling; Academic Press 2004. ISBN: 9780122265518
[9] Bockhorn H.Ullmann's Encyclopedia of Industrial Chemistry, Chapter: Mathematical modeling; John Wiley & Sons; 2003 ISBN 3527303855.
[10] S. Heinz, Mathematical Modeling; Springer-Verlag GmbH Germany, part of Springer Nature 2014. Hardcover ISBN 978-3-642-20310-7
[11] Chianese A, Annesini MC, de Santis R, Marrelli L. A model of a pilot bubble column reactor for benzene alkylation by ethylene. Chem. Eng. J., 1981; 2: 151–158.
[12] Berenblyum AS, Katsman EA, Berenblyum RA, Hommeltoft SI. Modeling of side reactions of isobutane alkylation with butenes catalyzed by trifluoromethane sulfonic acid. Appl. Catal. A Gen,. 2005; 284: 207-214.
[13] Jana AK. Heat integrated distillation operation. Appl. Energy. 2010; 218: 1477–1494.
[14] Bellussi G, Pazzuconi G, Perego C, Girotti G, Terzoni G. Liquid-phase alkylation of benzene with light olefins catalyzed by β zeolites. J. Catal., 1995; 157: 227–234.
[15] Al-Matar A. Selecting Fluid Packages for HYSYS Process Simulator. ResearchGate; 2015; 10.13140/RG.2.1.3461.4487.
[16] AspenTech Inc, Hysys 2004 .2: Dynamic Modeling, AspenTech; 2005.

To whom correspondence should be addressed: Dr. Irena O. Dolganova, National Research Tomsk Polytechnic University, Tomsk 634050, Russia,

Petroleum and Coal

Article **Open Access**

EXPERIMENTAL INVESTIGATIONS ON THE PERFORMANCE AND EMISSION CHARACTERISTICS OF A COMPRESSION IGNITION ENGINE USING BLENDS OF TIRE PYROLYSIS OIL AND DIESEL

N. Kapilan, L. J. Naik

Department of Mechanical Engineering, Nagarjuna College of Engineering and Technology, Bengaluru, India

Received January 13, 2019; Accepted March 19, 2019

Abstract

Most of the countries are facing the problem in the disposal of scrap tires and tubes. This problem can be overcome by the production of tire pyrolysis oil (TPO) from these materials. The calorific value and other properties of the TPO are similar to the fossil diesel, and hence in this work, it was used as a partial replacement to the diesel. The fuel blend (DTPO20) was prepared by mixing 20% of TPO with 80% of diesel and properties of this blend was determined and compared with the diesel. The engine tests were carried out on a single cylinder, four strokes, naturally aspirated compression ignition engine with the fuel blend, DTPO20. From the engine tests, it is observed that the engine gives lower thermal efficiency and higher engine exhaust emissions with this blend. Hence, the compression ratio of the engine was increased from 16.5:1 to 17.5:1 and engine tests were carried out again, and results of this engine tests were compared with the compression ratio of 16.5:1.

Keywords: *Alternative fuel; tire pyrolysis oil; blend, engine tests; compression ratio.*

1. Introduction

A tire is a strong, flexible and ring-shaped component that surrounds a wheel's rim and provides a gripping surface for traction of a moving vehicle. The natural rubber is the main raw material used in the manufacturing of tires. The other materials such as fabric, steel wire, carbon black and chemical compounds such as antioxidants and antiozonants are used to prepare the tires [1]. It is reported that approximately 1.5 billion tires are produced each year [2]. The USA is the largest producer of tires and India accounts for about 6-7% of the global waste tire. Also, the scrap tire arising in Europe increases every year [3]. The developed and developing countries are facing problems in disposal of the waste tire, and this problem can be solved by converting it into fuel. The scrap tires can be converted into liquid fuel by pyrolysis process, and this fuel (tire pyrolysis oil) can be used as a substitute for the diesel in the compression ignition engines.

In recent years, the search for alternative fuels is significant due to stringent norms of emission, depletion of fossil fuels and fluctuating cost of the petroleum products. Finding suitable alternative fuel will be the solution to this problem. The fossil fuel depletion has been identified as a future challenge, and it is important to understand that the fossil energy problem and the anthropogenic climate change problem are tightly connected [4]. The depletion studies for individual fuels are relatively abundant and fewer studies include the demand of the socio-economic system [5].

The TPO has long hydrocarbon chains with a high heating value, and hence TPO can be used as an alternative fuel for diesel engines. India is the second largest producer of reclaimed rubber, and hence it has the potential for the production of the TPO [6]. The scrap tires can be converted into fuel through a pyrolysis process. In this process, the scrap tires and tubes are shredded, and the reaction takes place at a higher temperature in an oxygen-free atmosphere.

The higher reaction temperature breaks down the rubber polymers and these smaller molecules vaporize and condensed to get liquid fuel called TPO. The yield of the pyrolysis process is affected by the type of raw materials, reactor types and type of catalysts. G. Lopez *et al.* results show that 475°C is an appropriate temperature for the pyrolysis of waste tires. Also, they suggested that the quality of the oil is optimum at this temperature and an increase in temperature to 575°C reduced the TPO yield to 53.9 %. However, it substantially changes the chemical composition by increasing the aromatic content [7].

The hydrodesulfurized waste TPO mainly composed of a light naphtha fraction [8]. The pyrolytic oil is a complex liquid mixture, composed mainly of aromatic compounds and olefins. It is reported that the pyrolytic oil has higher detonation resistance in relation to the conventional fuels and the tire pyrolysis oil is miscible with diesel in the entire concentration range [9].

Few researchers reported that the properties of the TPO are similar to fossil diesel and hence it can be used as a substitute for the diesel [10]. The integration of solar thermal energy, via concentrated solar power systems, into the pyrolysis process will reduce the operating cost [11]. MN Islam and MR Nahian reported that the distilled TPO is similar to diesel fuel and able to replace diesel fuel in the small engine. They observed that the brake specific fuel consumption of fuel blend of diesel and TPO is close to the specific fuel consumption of diesel and suggested that the fuel blend can be directly utilized in diesel engine [12]. Hürdoğan *et al.* carried out engine tests on a four-stroke, four cylinders, naturally aspirated, direct-injected diesel engine running with various blends of waste tire pyrolysis oil (WTPO) with diesel fuel and the experimental results showed that WTPO–diesel blends indicated similar performance with diesel fuel in terms of torque and power output of the test engine. They suggested that the blends of pyrolysis oil of waste tire WTPO10 can efficiently be used in diesel engines without any engine modifications [13]. Hürdoğan *et al.* carried out engine tests on a six-cylinder, compression ignition, turbocharged, heavy-duty engine with and without an intercooler, at two different engine speeds and at various loads. The engine results indicate that TPO can be efficiently used in turbocharged non-intercooled compression ignition engines at high loads, which opens its use in power generation [14]. The engine tests conducted on a single cylinder compression ignition engine with the mixture of biodiesel and TPO as fuel indicates that the TPO can be used as a partial substitute for the diesel with higher fuel injector nozzle opening pressure [15].

In this work, we prepared the fuel blend of diesel and TPO and used this fuel blend as fuel in the compression ignition engine to reduce the operating cost as TPO is cheaper as compared to the diesel. Also, we studied the effect of compression ratio on the performance and emissions of a compression ignition engine fueled with the blends of diesel and TPO.

2. Materials and methodology

In this work, TPO available in the local market was purchased and used as fuel for the engine tests. The TPO was filtered using filter paper to remove the impurities. The fuel blend was prepared by mixing diesel and TPO, with a ratio of 80:20 (volume basis) and is named as DTPO20. The properties of the diesel, TPO and blend were determined by ASTM and BIS methods. The blend DTPO20 was used as fuel in the diesel engine

The engine tests were carried out on a single cylinder naturally aspirated direct injection compression ignition engine with diesel and DTPO20 blend. The technical details of the engine and experimental setup is given in Table 1. The engine load was varied from no load to full load using an eddy current dynamometer. The compression ratio was varied to study its impact on engine performance and emissions. An AVL make gas analyzer was used to measure the engine exhaust emissions, and necessary instrumentations were provided to measure the engine performance parameters such as airflow, fuel flow, temperature, and load measurement. Figure 1 shows the experimental setup.

Table 1 Technical details of the engine and experimental setup

Engine	Single cylinder,4-Stroke, Naturally Aspirated Diesel Engine
Make	Kirloskar
Rated speed	1500 rpm
Maximum brake power	3.5 kW at 1500 rpm
Displacement	661 CC
Load sensor	Load cell, type strain gauge, range 0-50 Kg
Dynamometer	Eddy Current Dynamometer
Thermocouple sensor	Type RTD
Thermocouple range	0 – 1200 Degree C

Figure 1. Engine experimental setup

3. Results and discussion

The homogenous blend was prepared by mixing TPO and diesel vigorously and was used as fuel in the compression ignition engine. The fuel properties of the DTPO20, TPO, and diesel were determined, and the results are shown in Table 2. From the table, it is observed that the properties of DTPO20 are close to diesel.

Table 2. Properties of fuels

Property	Diesel	TPO	DTPO20
Viscosity (mm^2/s)	2.5	3.2	2.7
Calorific value (MJ/kg)	42.04	41.2	41.7
Density (kg/m^3)	845	885	853
Flash Point ($^\circ C$)	65	42	50
Fire Point ($^\circ C$)	59	46	57
Carbon residue (%mass)	0.06	0.75	0.19
Pour point ($^\circ C$)	4.2	6.1	4.6

The engine tests were conducted successfully with the blend of TPO and diesel and studied the effect of compression ratio on engine performance and emissions of the diesel engine. The term brake thermal efficiency indicates the effectiveness of conversion of heat energy possessed by the fuel into mechanical energy. Figure 2 shows the brake thermal efficiency (BTE)

of the engine at different loads with various compression ratios. From the figure, we observe that as the load increases the brake thermal efficiency of the engine increases due to the increase in fuel consumption at higher loads. From the figure, it is observed that the BTE of the engine with a higher compression ratio of 17.5:1 results in higher BTE. This may be due to the increase in combustion chamber temperature at a compression ratio which results in better atomization and spray formation of the fuel blend as compared to lower compression ratio.

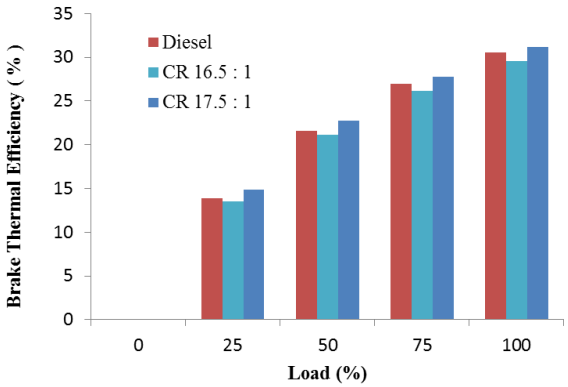

Figure 2. Effect of compression ratio on brake thermal efficiency at different loads

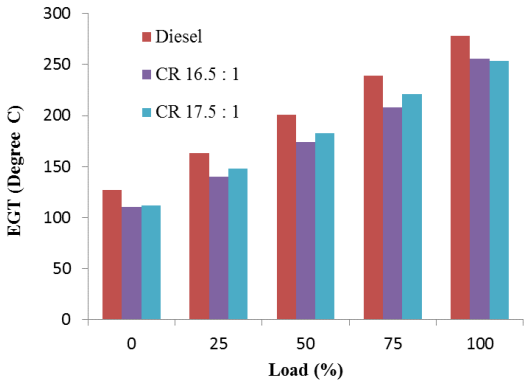

Figure 3. Effect of compression ratio on EGT at different loads

Figure 3 compares the engine exhaust gas temperature (EGT) of the diesel and TPO blend at different loads with different compression ratio. The consumption of the fuel increases with increase in the load, and hence the EGT of the engine increases with the load. The EGT of the diesel is higher than the TPO blend. However the higher compression ratio of 17.5:1 results in higher EGT as compared to the compression ratio of 16.5:1 and this is due to better combustion of the blend. A slight variation in EGT of the engine was observed at different compression ratios.

The carbon monoxide (CO) and unburnt hydrocarbon (HC) emissions of the engine indicates the combustion quality of the fuel inside the combustion chamber. The main reason for the formation of CO emission is due to a lack of sufficient oxygen and oxidization temperatures. The poor combustion of the fuel results in higher CO emission. The CO emission of the engine with diesel and TPO blend and at different compression ratio is shown in Figure 4.

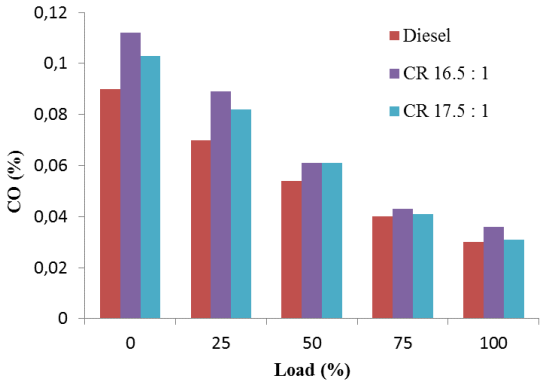

Figure 4. Effect of compression ratio on CO emission at different loads

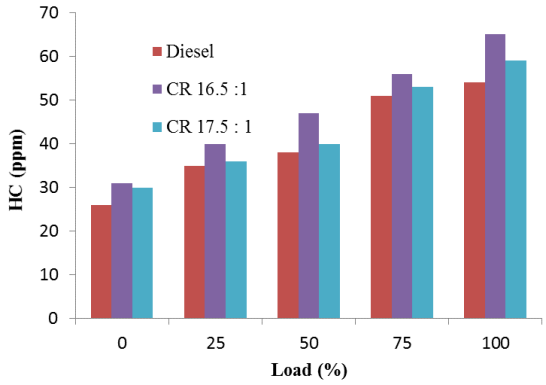

Figure 5. Effect of compression ratio on HC at different loads

From the figure, it is observed that the engine emits lower CO emission with the diesel as compared to the TPO blend. The compression ratio of 16.5:1 results in higher CO emission as compared to the compression ratio of 17.5:1. This is due to higher aromatic content of the

TPO which results in higher CO emission. However, the higher compression ratio with TPO blend results in higher combustion chamber temperature and better oxidation of the fuel which causes lower CO emission. The variation in CO emission is low at higher loads, and this may be due to higher combustion chamber temperature and lower ignition delay at higher loads.

Figure 5 shows the hydrocarbon (HC) emission of the diesel engine at different loads with different fuels and at different compression ratios. From the figure, it is observed that the TPO blend results in higher HC emission as compared to diesel. The HC emission is lower with the higher compression ratio of 17.5:1 as compared with the compression ratio of 16.5:1. The higher compression ratio results in lower ignition delay and hence the HC emission of the 17.5:1 is lower than the 16.5:1.

The oxides of nitrogen (NOx) emissions of the diesel engine depend upon the combustion temperature. The NOx emission of the engine with different fuels and at different loads is shown in Figure 6. From the figure, it is observed that the NOx emission of the engine with diesel results in lower NOx emission as compared to the TPO blend with the compression ratio of 17.5:1. The NOx emission of the engine with the compression ratio of 16.5: 1 is lower than the other compression ratio and diesel. The higher compression ratio of 17.5:1 results in higher combustion chamber temperatures and pressure which results in better combustion and causes higher NOx emission.

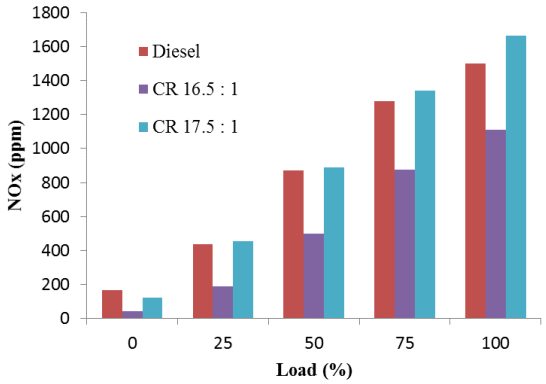

Figure 6. Effect of compression Ratio on NOx at different loads

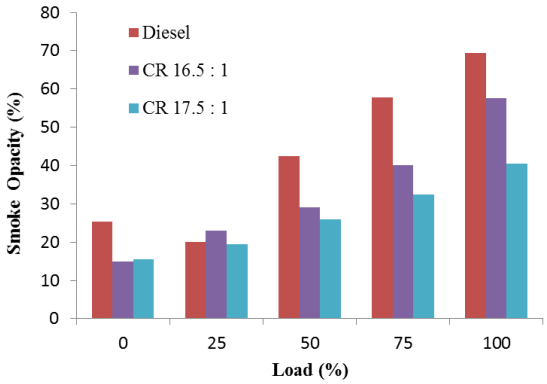

Figure 7 Effect of compression ratio on smoke opacity at different loads

One of the major emissions of the diesel engine is smoke emission and is an incomplete combustion product. Generally, it is formed in the rich mixture in the combustion chamber. The engine smoke emission with different fuels at different compression ratios and loads is shown in Figure 7. From the figure, it is observed that as the load increases the smoke emission also increases and this is due to a reduction in air-fuel ratio. The diesel results in higher smoke emission as compared to TPO blend at higher loads. The compression ratio of 16.5:1 results in higher smoke emission as compared to the compression ratio of 17.5:1. The compression ratio of 17.5:1 results in lower smoke emission is due to higher combustion chamber temperature which results in better oxidation and combustion of the fuel.

4. Conclusion

The pyrolysis of scrap tire and tubes is one of the effective methods of disposal of scrap tires and tubes. Also, the pyrolysis oil can be used as a partial substitute for the diesel in the compression ignition engines as the properties of the TPO are similar to the diesel. The engine tests were carried out with the blends of TPO and diesel and studied the effect of compression ratio on the performance and emissions of the engine. From this work, we observe that the higher compression ratio results in better brake thermal efficiency and lower CO, HC and smoke emissions. However, it results in higher NOx emissions. This is due to higher combus-

tion chamber temperature which results in better combustion and lower engine exhaust emissions. From this work, we suggest that the fuel blend of diesel and TPO can be used as fuel in the compression ignition engine with a higher compression ratio.

References

[1] https://www.ustires.org/whats-tire-0 (Accessed on 21st November 2018).
[2] Williams PT, Besler S. Pyrolysis-thermogravimetric analysis of tires and tyre components. Fuel, 1995; 74: 1277-1283.
[3] Williams PT. Pyrolysis of waste tyres: a review, Waste Management, 2013; 33(8): 1714 - 1728.
[4] Höök M, Tang X. Depletion of fossil fuels and anthropogenic climate change—A review. Energy Policy, 2013; 52: 797-809.
[5] I Capellán-Pérez, Mediavilla M, de Castro C, Carpintero Ó, Miguel LJ. Fossil fuel depletion and socio-economic scenarios: An integrated approach. Energy, 2014; 77: 641-666.
[6] https://weibold.com/etrmas-statistics-on-scrap-tire-collection-and-recycling-in-europe/(Accessed on 21st November 2018).
[7] Lopez G, Alvarez J, Amutio JM, Mkhize NM, Olazar M. Waste truck-tyre processing by flash pyrolysis in a conical spouted bed reactor. Energy Conversion and Management, 2017; 142: 523-532.
[8] Jantaraksa N, Prasassarakich P, Reubroycharoen P, Hinchiranan N. Cleaner alternative liquid fuels derived from the hydrodesulfurization of waste tire pyrolysis oil. Energy Conversion and Management, 2015; 95: 424-434.
[9] Umeki ER, de Oliveira CF, Torres RB, RGes dos Santos. Physico-chemistry properties of fuel blends composed of diesel and tire pyrolysis oil. Fuel, 2016; 185: 236-242.
[10] Alvarez J, Lopez G, Amutio M, Mkhize NM, Olazar M. Evaluation of the properties of tyre pyrolysis oils obtained in a conical spouted bed reactor, Energy, 2017; 128: 463-474.
[11] Zeaiter J, Azizi F, Lameh M, Milani D, Ismail HY, Abbas A. Waste tire pyrolysis using thermal solar energy: An integrated approach. Renewable Energy, 2018; 123: 44-51.
[12] Islam MN, and Nahian MR. Improvement of Waste Tire Pyrolysis Oil and Performance Test with Diesel in CI Engine. Journal of Renewable Energy, 2016; Article ID 5137247: 1- 8.
[13] Hürdoğan E, Ozalp C, Kara O, Ozcanli M. Experimental investigation on performance and emission characteristics of waste tire pyrolysis oil–diesel blends in a diesel engine. International Journal of Hydrogen Energy, 2017; 42(36): 23373-23378.
[14] Vihar R, Seljak T, Oprešnik SR, Katrašnik T. Combustion characteristics of tire pyrolysis oil in turbo charged compression ignition engine, Fuel, 2015; 150: 226-235.
[15] Kapilan N, Naik J. Studies on Improvement of Performance of Compression Ignition Engine Fuelled with Mixture of Honge Biodiesel and Tire Pyrolysis Oil. Strojnícky casopis–Journal of Mechanical Engineering, 2018; 68(1): 15-24.

To whom correspondence should be addressed: Dr. N. Kapilan, Department of Mechanical Engineering, Nagarjuna College of Engineering and Technology, Bengaluru, India

Petroleum and Coal

Article **Open Access**

MATHEMATICAL MODELING OF THE PROCESS CATALYTIC ISOMERIZATION OF LIGHT NAPHTHA

Emiliya D. Ivanchina[1], Vyacheslav A. Chuzlov[1], Nikita R. Ivanchin[2], Anatoli Borissov[3], Gaini Zh. Seitenov[4], Rizagul' M. Dusova[1]*

[1] *Tomsk Polytechnic University, Russia*
[2] *Tomsk State University, Russia*
[3] *General Vortex Energy Inc., Missouri City, USA*
[4] *S. Toraighyrov Pavlodar State University, Kazakhstan*

Received January 10, 2019; Accepted March 19, 2019

Abstract

The aim of this work is to study the process of catalytic isomerization of light naphtha by the method of mathematical modelling. The influence of temperature and feedstock flow rate on octane number and yield of the product (branched alkanes) was studied depending on the feedstock composition. The temperature mode of the process was optimized depending on the composition and feedstock flow rate.

Keywords: *catalytic isomerization; branched alkanes; octane number; method of mathematical modelling.*

1. Introduction

Motor fuel is one of the most demanded products of the oil refining industry. The demand for motor fuel is constantly increasing all over the world [1-5]. Currently, the tendency towards increasing the demand for motor fuel of meeting EURO standards is observed [6-10]. Isomerization of gasoline fractions is the process of obtaining a high-octane component of gasoline fuels by converting linear hydrocarbons into isomers. The studies on oil refining processes using the method of mathematical modelling are relevant these days. The models, developed based on the thermodynamic and kinetic regularities of the processes, allows making recommendations for control of the technological parameters of industrial processes, which ensures meeting specifications for product quality and achieving an optimal yield of the product in the conditions of constantly changing the composition of the feedstock. The aim of this work is to study the process of catalytic isomerization by the method of mathematical modelling.

2. Object and method of research

The object of the current research is the industrial process of catalytic isomerization, which is aimed to produce gasoline fuel of meeting EURO standards.

Development of new and intensification of existing catalytic processes is effectively performed by the method of mathematical modeling, the methodology and foundations of which were described in the classical works of the Academician of the Russian Academy of Sciences GK Boreskov and the Corresponding Member of the Russian Academy of Sciences MG Slinko in 1960-1970s [11] at the Boreskov Institute of Catalysis Siberian Branch of the Russian Academy of Sciences (Boreskov and Slinko [12-14]).

Further works of Slinko [15] are devoted to the theory of catalytic reactions, processes and reactors. Significant contribution to the development of mathematical modeling of catalytic processes and reactors was made by the followers of MG Slinko: VS Beskov [16], Matros [17],

GS Yablonsky [18], AS Noskov [19], ED Ivancina [20-24], and foreign researchers: R Aris [25], GF Froment [26].

The feedstock for the process of catalytic isomerization light naphtha passes through two successive reactors with a catalyst, then enters the stabilization column. The sequential arrangement of the reactors allows the process to be carried out continuously, while in one reactor the catalyst regeneration takes place; in the second one, the isomerization process takes place. This method of operation allows for economical use of the catalyst without interrupting production. This scheme is the simplest variant of isomerization. To describe the process of isomerization by mathematical modeling, the following steps are required:

- thermodynamic analysis of the process;
- evaluation of the kinetic parameters of the possible reaction;
- model of the reactor;
- construction of the technological scheme.

Isomerization reactions are reversible processes in which the system tends to a thermodynamic equilibrium between n-paraffins and isoparaffins. The main reactions occurring in the reactor are shown in Fig. 1 with the indication of octane numbers according to the research method.

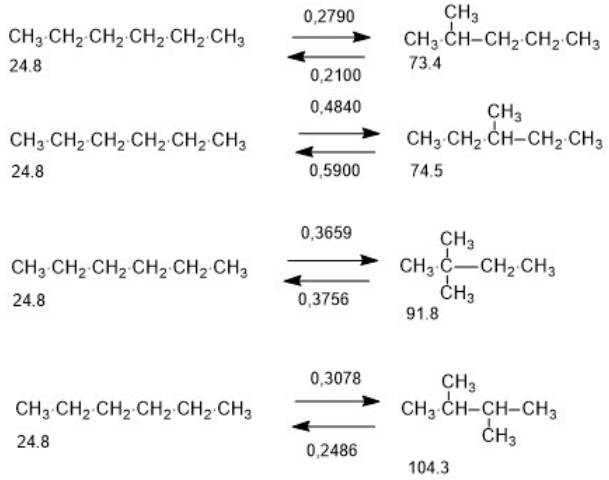

Figure 1. Main reactions of the isomerization process at T = 130°C, P = 3 MPa, on Pt/$SO^{4-}ZrO_2$ catalyst

Experimental data of industrial run of the isomerization unit were used in the construction of a mathematical model. Changes in the composition of raw materials used for the calculation are shown in Table 1.

Such change in the feedstock composition requires constant correction of the mode of the isomerization reactor operation, determination and maintenance of optimal technological parameters for the exact feedstock composition in order to obtain the maximum yield of the product meets required quality. In this work, the influence of temperature and feedstock flow rate on the yield was studied, as well as a technological mode for the two variants of unit operation was optimized using the developed mathematical model.

Table 1. Changes in raw material composition

Component	wt. %	Component	wt. %
isopentane	7.3 – 15.4	3- methylpentane	6.7 – 13.3
n-pentane	14.9 – 28.9	n-hexane	7.1 – 17.1
2,2 - dimethylbutane	0.3 – 1.1	Methylcyclopentane	2.6 – 11
cyclopentane	5 – 13.3	Benzene	0.7 – 1.6
2,3- dimethylbutane	1.6 – 3.1	Cyclohexane	0.4 – 7.2
2- methylpentane	13.9 – 20.7		

The model is written as a system of material and heat balances as follows:

$$\begin{cases} G \cdot \frac{\partial C_i}{\partial z} + G \cdot \frac{\partial C_i}{\partial V} = \sum_{j=1}^{m} a_j \cdot W_j \\ G \cdot \frac{\partial T}{\partial z} + G \cdot \frac{\partial T}{\partial V} = \frac{1}{\rho \cdot C_p^m} \sum_{j=1}^{m} Q_j \cdot a_j \cdot W_j \end{cases} \quad (1)$$

Initial and boundary conditions are as follows: z=0: C_i=$C_{i,0}$; T=T_0; V=0: C_i=$C_{i,0}$; T=T_0, where z is the volume of refined feedstock from the moment of fresh catalyst load, m^3; G is the feedstock flow rate, m^3/h; $z = G \cdot t$ (t is the catalyst operating time from the moment of fresh catalyst load, h); C_i is the content of i^{th} component, mol/l; V is the catalyst bed volume, m^3; a_j is the catalyst activity in j^{th} reaction; ρ is the density of mixture, kg/m^3; C_p^{mix} is the specific heat capacity of the mixture, J/(kg·K); Q_j is the heat effect of j^{th} reaction, J/mol; T is the temperature, K; W_j is the rate of j^{th} reaction, mol/(l·s); m is the number of reactions. In the above system of equations, the residence time of the reagents in the reaction zone, which depends on the hourly flow rate of the feedstock G and the volume of the catalyst V, under the conditions of the unstable load of the industrial plant for feedstock is replaced by the "reduced time" z = G·t, equal to the total volume of the processed feedstock during the time t.

The system of differential equations is solved by the difference method and is implemented in the object-oriented Delphi environment.

3. Experimental

3.1. Studying the influence of temperature on the izomerization process

The process of isomerization of light gasoline is equilibrium, and the quality of the resulting product depends on the equilibrium position between the target and side reactions. At low temperatures, the process slows down the kinetic factor due to the low values of the isomerization rate constants of normal alkanes. At high temperatures manifests the thermodynamic factor of the deceleration of the process: because isomerizes normal paraffins are favorable to low temperature because of its exothermic. The results of predictive calculations are shown in Fig. 2.

An increase in the isomerization temperature above the optimum (138-142°C for raw materials with a low content of naphthenic and aromatic hydrocarbons, 145-147°C for raw materials with a high content of naphthenic, 148-155°C for raw materials with a high content of aromatic and naphthenic hydrocarbons) leads to a decrease in the yield of isomerizate due to an increase in the contribution of adverse reactions.

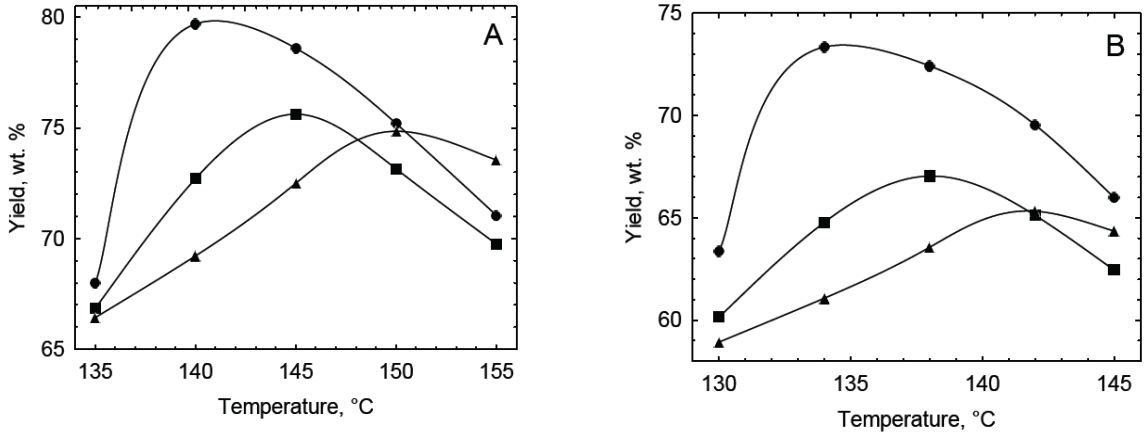

A-sulfated catalyst B-chlorinated catalyst

Figure 2. Yield of C5-C6 isoalkanes depending on temperature: (●) – composition No. 1, (■) – composition No. 3, (▲) – composition No. 6

3.2. Studying the influence of feedstock flow rate on the izomerization process

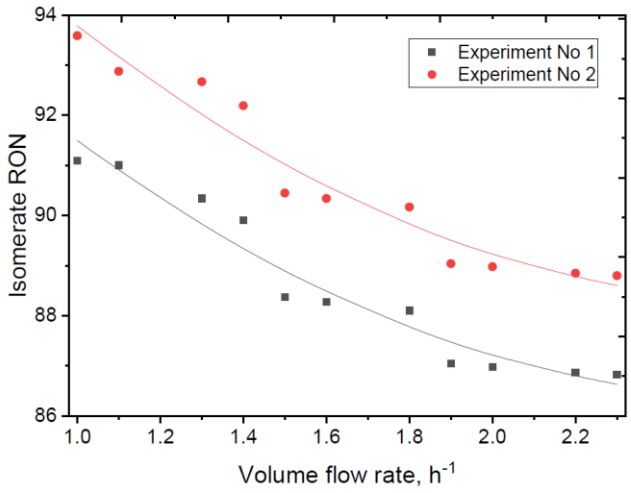

As the load on the raw material increases on the isomerization reactor unit, the contact time of the raw material with the catalyst decreases, and the octane number of the isomerizate obtained decreases. The forecast is based on models of the influence of feed loading on the octane number of the isomerized product to the isomerization with recycling of n-C_5-C_6 and the low-branched hexanes presented in Fig. 3.

Figure 3 Octane number(RON) isomerizate depending on the volumetric feed rate of raw materials for isomerization technology with n-C_5-C_6 recycle and low-branched hexanes

4. Conclusions

The influence of temperature and feedstock flow rate in the rages 320–360 C and 290–330 m^3/h respectively on the cold flow properties and yield of the product (diesel fuel) was studied depending on the feedstock composition. The temperature mode of the process was optimized depending on the composition and feedstock flow rate.

The optimal temperature range in reactors is determined by the technological mode of the process, the composition of the processed raw materials, as well as the hardware design of the process. The high content of naphthenic and aromatic hydrocarbons in raw materials leads to inhibition of transformation of normal alkanes into isoalkanes. Depending on the type of catalyst, the optimum temperature lies in the range of 138-142°C for raw materials with a low content of naphthenic and aromatic hydrocarbons, 145-147°C for raw materials with a high content of naphthenic, 148-155°C for raw materials with a high content of aromatic aR

References

[1] Hegab A, La Rocca A, Shayler P. Towards keeping diesel fuel supply and demand in balance: Dual-fuelling of diesel engines with natural gas. Renewable and Sustainable Energy Reviews, 2017;70: 666–697

[2] Kholod N, Evans M. Reducing black carbon emissions from diesel vehicles in Russia: An assessment and policy recommendations. Environmental Science & Policy, 2016;56: 1–8

[3] Wadud Z. Diesel demand in the road freight sector in the UK: Estimates for different vehicle types. Applied Energy, 2016; 165: 849–857

[4] Barla P, Gilbert-Gonthier M, Kuela J-RT. The demand for road diesel in Canada. Energy Economics,2014; 43: 316–322

[5] Melikoglu M. Demand forecast for road transportation fuels including gasoline, diesel, LPG, bioethanol and biodiesel for Turkey between 2013 and 2023. Renewable Energy,2014; 64: 164–171

[6] Boldushevskii RE, Kapustin VM, Chernysheva EA, Gulyaeva LA, Grudanova AI, Stolonogova TI. Studying of the efficiency of a catalytic dewaxing process utilizing zeolite-based catalyst with an iron additive. Catalysis in Industry, 2015; 7(4): 301-306

[7] Grudanova AI, Gulyaeva LA, Krasil'nikova LA, Chernysheva EA. A catalyst for producing diesel fuels with improved cold flow characteristics. Catalysis in Industry, 2016; 8(1): 40-47

[8] Zhao Zh, Xue Y, Xu G, Zhou J, Lian X, Liu P, Chen D, Han S, Lin H. Effect of the nano-hybrid pour point depressants on the cold flow properties of diesel fuel. Fuel, 2017; 193: 65–71

[9] Andreassen N. Arctic energy development in Russia – How "sustainability" can fit? Energy Research & Social Science, 2016; 16: 78–88

[10] Hintsala H, Niemela S, Tervonen P. Arctic potential e Could more structured view improve the understanding of Arctic business opportunities. Polar Science, 2016;10: 450–457.

[11] Slinko MG. Dynamics of chemical processes and reactors. Industry & Chemistry 1979; 11: 27–31.
[12] Slinko MG. Foundations and principles of mathematical modeling of catalytic processes, Novosibirsk, Russia: Boreskov Institute of Catalysis, 2004.
[13] Slinko MG. Kinetic model as a basis of mathematical modeling of catalytic processes. Theor Found Chem Eng 1976; 10(1): 137–146.
[14] Slinko MG. Kinetic studies is a basis of mathematical modeling of processes and reactors. Kinet Catal 1972; 13(3): 566-580.
[15] Slinko MG. History of development of mathematical modeling of catalytic processes and reactors. Theor Found Chem Eng 2007. 41(1): 16–34.
[16] Beskov VS, Flokk V. Modeling of catalytic processes and reactors, Moscow, Russia: Khimiya, 1991. *(in Russian)*
[17] Zagoruiko AN, Matros YS. Mathematical modelling of Claus reactors undergoing sulfur condensation and evaporation. Chem. Eng. J., 2002; 87: 73–88.
[18] Gorban AN, Yablonsky GS. Extended detailed balance for systems with irreversible reactions. Chem. Eng. Sci., 2011; 66: 5388–5399.
[19] Zagoruiko AN, Belyi AS, Smolikov MD, Noskov AS. Unsteady-state kinetic simulation of naphtha reforming and coke combustion processes in the fixed and moving catalyst beds. Catalysis Today, 2014; 220-222: 168-177
[20] Belinskaya NS, Ivanchina ED, Ivashkina EN, Sejtenova G. Studying patterns of synthesis of low freezing distillates from atmospheric gasoil by means of mathematical modelling. Current Organic Synthesis, 2017; 14(3): 365-371
[21] Ivanchina ED, Ivashkina EN, Frantsina EV, Dolganova IO, Ivanov SY. Increasing the selectivity of synthesis stages for linear alkyl benzenes. Current Organic Synthesis, 2017; 14(3): 342-352
[22] Belinskaya NS, Frantsina EV, Ivanchina ED, Popova NV, Belozertseva NE. Determination of optimal temperature of catalytic dewaxing process for diesel fuel production. Pet Coal, 2016; 58(7): 695-699
[23] Khlebnikova ES, Dolganova IO, Ivashkina EN, Koshkin SA. Modeling of Benzene with Ethylene Alkylation. MATEC Web of Conferences, 2016;49: 1-5
[24] Dmitriev VM, Gandga TV, Dolganov IM, Pisarev MO, Dolganova IO, Sizova EN, Ivashkina E. N. Structure of network simulator for training and retraining of operators of controlled technological objects of oil and gas industry. Petroleum and Coal, 2015; 57(6): 691-695.
[25] Aris R. The mathematical theory of diffusion and reaction in permeable catalysts, Oxford, Great Britain: Claredon Press, 1975.
[26] Froment G. On fundamental kinetic equations for chemical reactions and processes. Curr. Opin Chem Eng., 2014; 5: 1–6.

To whom correspondence should be addressed: Dr. Vyacheslav A. Chuzlov, National Research Tomsk Polytechnic University, Engineering school of natural resources, Division for Chemical Engineering, Lenin Avenue, 30, Tomsk, 634050, Russia, e-mail: chuva@tpu.ru

Petroleum and Coal

Article **Open Access**

GEOCHEMISTRY AND MULTIVARIATE STATISTICAL EVALUATION OF MAJOR OXIDES, TRACE AND RARE EARTH ELEMENTS IN COAL OCCURRENCES AND DEPOSITS AROUND KOGI EAST, NORTHERN ANAMBRA BASIN, NIGERIA

E. G. Ameh

Earth Sciences Department, Faculty of Natural Sciences, Kogi State University, Anyigba, Nigeria

Received January 7, 2019; Accepted March 19, 2019

Abstract

The Cretaceous Mamu Formation coal samples located within the Northern Anambra Basin were collected, analysed and interpreted using a multivariate statistical approach to determine the major, trace and rare elements association with a view to determining the source of the terrestrial rocks, palaeo-weathering/climatic conditions and tectonic setting. The dominant oxides such as SiO_2, Al_2O_3, Fe_2O_3, TiO_2, and CaO were identified in the coal to suggest terrigenous origin. The ratio of SiO_2/Al_2O_3 of 4.8 suggests that the coal was formed from low land peat associated with freshwater continental marine or blackish water with low salinity as indicated by Sr/Ba and $CaO+MgO/K_2O+Na_2O$ ratios. The major oxides also revealed the stable condition of deposition, a low degree of tectonic setting but constant subsidence in the basin. The condition of deposition was acidic in nature as indicated by TiO_2/Zr plot. Based on the abundance of Zr, Zn, Ba, Ni, Co, Sr, V, and Y, moderate salinity, sub-oxic to oxic bottom water condition was prevalent and also an indication of marine influence. Based on the ratios of La/Yb; La/Sm and Gd/Yb, LREE has higher enrichment than HREE. Humid climatic conditions were observed at the coal formation stage while weak laterization to kaolinization was also evidence.

Keywords: *Kogi East; Multivariate; Factor and Cluster; Varimax; Eucledean.*

1. Introduction

Coal is a carbon-rich, combustible, stratified organic sedimentary rock composed of altered and/or decomposed plant remains of non-marine origin combined with varying minor amount of inorganic materials [1]. The Anambra Basin, located in the Lower Benue trough is a major coal producing basin in Nigeria. Coal is a complex organic rock comprised of mainly decayed plants conditioned by syngenetic, diagenetic, epigenetic and detrital inorganic elements [2]. The Anambra Basin contains important coal measures in the Mamu and Nsukka Formations [3]. The mining of this sub-bituminous coal occurred in the Mamu Formation. Total coal reserves in the north-south trending coal belt were assed to be about 1.5billion tons. Lignite deposits occur in numerous seams in an east-west belt to the southwest [3]. A number of studies [4-8] have been conducted on the stratigraphic succession, organic and inorganic geochemistry of coal, distribution, and abundance of coal in Anambra Basin. Previous work has also been carried out on the trace elements in coal in the study area [2,9-13].

Nigeria is endowed with abundant coal reserves of the required quality suitable for power generation and other by products that are waiting to be tapped [3].

The objectives of this current study are to present the inorganic characteristics of Okaba coal using the multivariate statistical approach with a view to determining the oxides/elements association, the provenance of terrigenous components of coal deposits, palaeoclimate/weathering environments and tectonic settings.

2. Geological setting

Anambra basin, located in the Lower Benue Trough is a major coal producing basin in Nigeria (Figure 1). Anambra basin, a near triangular basin is located in the eastern part of Nigeria. The basin is bounded in the west by the Okitipupa ridge, in the south by the Niger Delta Basin, to the northwest, it directly overlies the Basement complex and inter fingers the Bida Basin [14]. Anambra basin lies between longitudes 6.3°E and 8.0°E and latitudes 5.0°N and 8.0°N. This basin is delimited in the north by the Basement complex, the Middle Benue Trough, and the Abakaliki Anticlinorium. Authors such as Akande and Erdtmann, [15]; Obaje *et al.* [4] have considered the basin as the lower Benue Trough, a NE-SW trending, folded, aborted rift basin that runs obliquely across Nigeria. Its origin was linked to the tectonic processes that accompanied the separation of the African and South American plates in the Early Cretaceous. This rift model is supported by evidence from structural, geomorphic, stratigraphic and paleontological studies [16-18]. The evolution of Anambra Basin represented the third cycle in the evolution of the trough and its associated basins when the Abakaliki Trough was uplifted to form the Abakaliki Anticlinorium while the Anambra platform was downwarped to form the Anambra Basin resulting in the westward displacement of the trough's depositional axis [18-20].

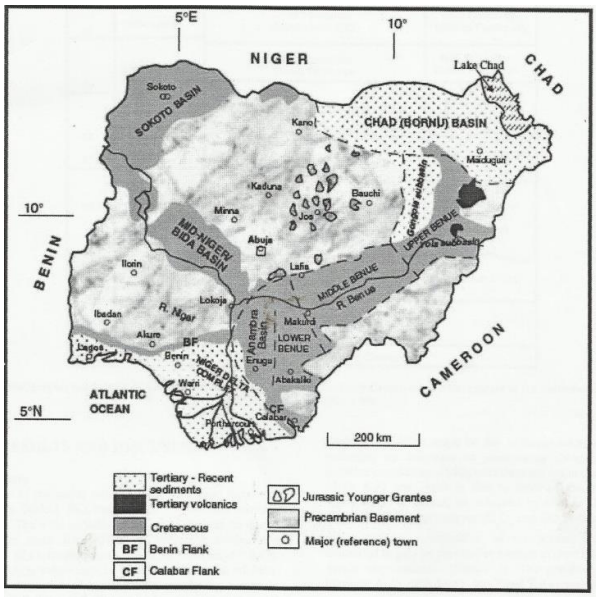

Figure 1. General geology of Nigeria *(after Obaje et al. [24])*

The basin is a sedimentary succession that directly overlies the facies of the Lower Benue trough and consists of Campanian to early Palaeocene lithofacies [20]. Several works on the Palaeoenvironment, palaeogeography, sedimen-tary tectonics, coal deposits and lithostratigraphy have been carried out ([2-3,7-8,13,20,23]). Sedi-ments deposition within the Anambra Basin started during the Campanian, with Nkporo and Enuge shales constituting the basal beds of the Campanian period. The Campanion was a period of short marine transgression and regression, where the shallow-sea later became shallower due to subsidence [23]. This resulted in a regressive phase during the Maastrichtian which deposited the flood plain sediments and deltaic foresets of Mamu Formation regarded as the Lower coal measures. The Mamu Formation is overlain by the Ajali sandstones which also overlain by Nsukka Formation [23].

2.1. Lithostratigraphy of study area

Nkporo Formation. This is the basal sedimentary unit deposited during the Santonian folding and inversion in south eastern Nigeria and indicates a late Campanian age [25]. The formation is poorly exposed but has been described as a coarsening upward deltaic sequence of shale and interbed of sands and shale with occasional thin beds of limestones [25].

Enugu shales. This consists of carbonaceous grey, black shales and coals with interbeds of very fine sandstones/siltstones deposited in lower flood plain and swampy environment. The bedding planes are poorly defined with early diagenetic minerals such as pyrite and siderites. The Enugu shale is assigned Campanian to Lower Maastrichtian [25].

Mamu Formation. This formation overlies the Enugu shales conformably and contains sandstones, shale, mudstone, sandy-shale with coal seams in various horizons. The sediment pile ranges from 75m to over 100m. These deposits are an estuarine flood plain, swamp and flat flood [25].

Ajali Sandstones. This Formation (Middle Maastrichtian) overlies the Mamu Formation and has Middle to Upper Maastrichtian age. It has a thickness range of less than 300m to over 1000m at the Centre of the basin. This formation is made up of texturally mature sand facies [25].

Nsukka Formation. The Nsukka Formation is Upper Maastrichtian to Danian in age. It consists of alternating sandstones, sandy shales, and mudstones with interbedded coal seams. The marine shales of the Nsukka Formation were deposited in the Palaeocene, overlain by the tidal Nanka sandstones of Eocene age which constitute the Tertiary succession [2].

3. Materials and methods

Eighteen samples were collected from six locations scattered around Kogi east, Northern Anambra Basin, Nigeria. These eighteen representative samples were pre-prepared by washing, cutting and bagging and sent to Acme Laboratory Canada for sample preparation and analysis. All samples were analyzed at the Acme Analytical Laboratories Ltd, Canada for major, minor and trace element geochemistry. The ICP-mass spectrometer (Perkin-Elmer, Elan 6000) and inductively coupled plasma-mass spectrograph were used for the analysis. The samples were digested by weighing 0.2g aliquot in a graphite crucible mixed with 1.5g lithium metaborate/tetraborate ($LiBO_2/LiB_4O_7$) to form flux. The crucibles were placed in an oven and heated up to 980oC for 30 minutes. The cooled bead was dissolved in 5% HNO_3 (ACS grade nitric acid diluted in demineralized water). Calibration standards and reagent blanks were added to sample sequences. The basic package that consists of thirty-four elements (Ba, Co, Cs, Ga, Hf, Nb, Rb, Sn, Sr, Ta, Th, U, V, Y, Zr, La, Ce, Pr, Nd, Sm, Eu, Gd, Lu) was determined. A second 0.5g split sample was digested in Aqua Regia and analysed by ICP-MS to determine Au, Ag, As, Bi, Cd, Cu, Hg, Mo, Ni, Pb, Sb, Se, and Zn. An ICP-emission spectrograph (Spectro Ciros Vision or Varian 735) was also used for determination of major oxides and some trace elements (SiO_2,Al_2O_3, Fe_2O_3, CaO, MgO, TiO_2, P_2O_5, Cr_2O_5, Ba, Nb, Ni, Sr, Sc, Y, and Zr). Loss on ignition (LOI) was determined by the weight loss upon heating 1g split sample at 95°C for 90 minutes.

The multivariate technique was applied to reveal hidden affinities within the database and undetectable by other means [26]. This method helps in extracting information about the similarities or dissimilarities among parameters. Latent factors in data sets were identified, and variables responsible for the variations observed explained the structure of the data set [26]. This is the basis for factor and cluster analyses which themselves are based on correlation coefficient relationships.

Factor analysis through a linear dependence model constructed in an abstract space called factor score space was used. It searches for correlations among measured variables that characterized a set of geochemical data [27]. Factor analysis reduces space dimensionality to obtain a better grouping of variables and determine relations between major components and variables analysed [29]. Elements association obtained from factor analysis is mathematically independent. The factor solutions provide information on loadings; communalities and eigenvalues [30].

Cluster analysis was also performed to classify elements of different geochemical sources on the basis of similar chemical properties. Hierarchical cluster analysis was used to find the true group of data. Cluster analysis using dendograms was used to identify relatively homogeneous groups of variables with similar properties [28]. Each cluster group shows similar and specific groups with respect to the source and geochemical characteristics. Data for cluster analysis were standardized to equalize the influence of the geochemical variables.

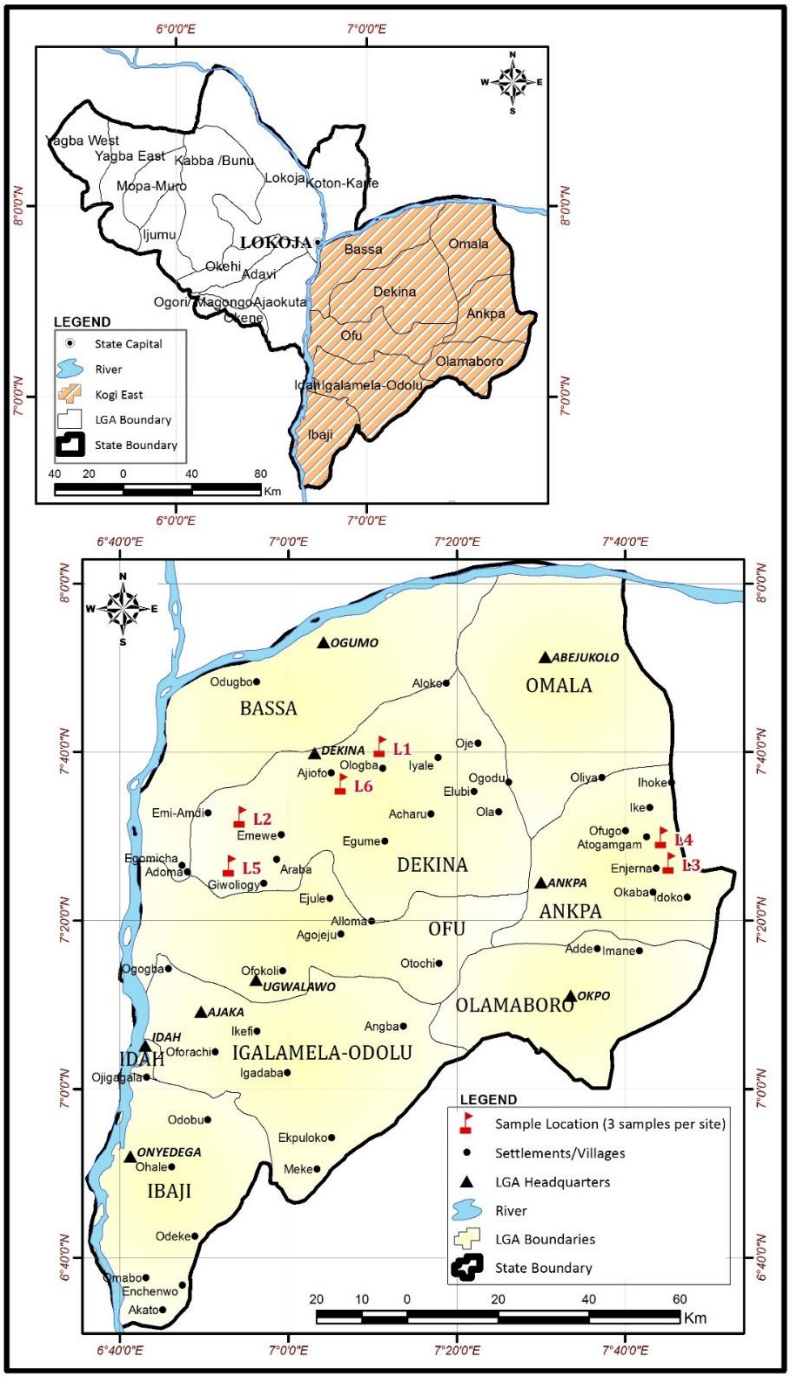

Scale: 1: 25,000

Figure 2. Sample location map of the study area (*modified after Ameh, 2019)*

4. Results and discussion

4.1. Evidence from major oxides

The oxides, trace and rare elements are present in coals in inorganic forms. Many elements in coal are derived from the detrital inputs to the precursor swamp and many chalcophile elements associated with sulphide minerals [2]. The inorganic elements present in the coals suggest that these elements were sourced from terrigenous origin [31].

The result of the dominant coal major oxides shows average mean weight% of SiO_2 (16.36); Al_2O_3 (3.5); Fe_2O_3 (1.20); TiO_2 (0.44) and CaO (0.14) respectively. The rest oxides have significantly low mean weight percentages. The percentage weight of LOI is 78.06 (Table 1). The low Al_2O_3 could imply limited supply of detrital materials in peat and low level of weathering in the source area and coal seams [32]. On the basis of the concentrations of CaO; Na_2O and MgO, this coal may have been formed under continental freshwater conditions and low salinity environment. The major source of K in coal could be detrital, from coal intrusive and volcanic rocks which were clearly absent here. Also, the low Ti concentration observed may be due to the limited supply of Ti in peat and high in situ nature of inorganic matter [32].

Table 1. Descriptive statistics of major oxides in shale

Major oxides	Minimum	Maximum	Mean	SD	Std. error Mean	t-square	95% Confidence interval of the difference Lower	Upper
SiO_2	3.94	62.00	16.36	22.55	9.20	1.77	-7.30	40.02
Al_2O_3	1.53	8.26	3.57	2.67	1.09	3.27	0.76	6.37
Fe_2O_3	0.18	2.22	1.20	0.73	0.30	4.01	0.43	1.97
MgO	0.00	0.07	0.03	0.02	0.00	3.40	0.00	0.05
CaO	0.01	0.32	0.14	0.11	0.04	3.06	0.02	0.26
Na_2O	0.00	0.01	0.00	0.00	0.00	2.08	0.00	0.01
K_2O	0.01	0.08	0.04	0.02	0.012	3.80	0.01	0.07
TiO_2	0.12	1.51	0.44	0.52	0.21	2.07	0.10	1.00
P_2O_5	0.00	0.03	0.01	0.01	0.00	2.55	0.00	0.02
MnO	0.00	0.04	0.01	0.01	0.00	2.22	0.00	0.03
Cr_2O_3	0.00	0.01	0.00	0.00	0.00	3.28	0.00	0.00
LOI	26.70	92.80	78.06	25.55	10.43	7.48	51.25	104.88
Total	32.49	167.35	99.86	52.19	21.28	38.99	44.31	154.68

4.2. Coal oxides ratios

The SiO_2/Al_2O_3 ratio recorded is 4.58. This low ratio shows that the coal results from low land peat. It also suggests a stable condition of deposition, a low degree of tectonic movement and slow but constant subsidence in the basin [32]. The $CaO+MgO/K_2O+Na_2O$ and the ratio of CaO/MgO revealed values of 4.25 and 4.67 respectively. These ratios show that the coals were probably associated with marine or brackish water influences, saline lakes or inorganic matter enriched in algal remains [32].

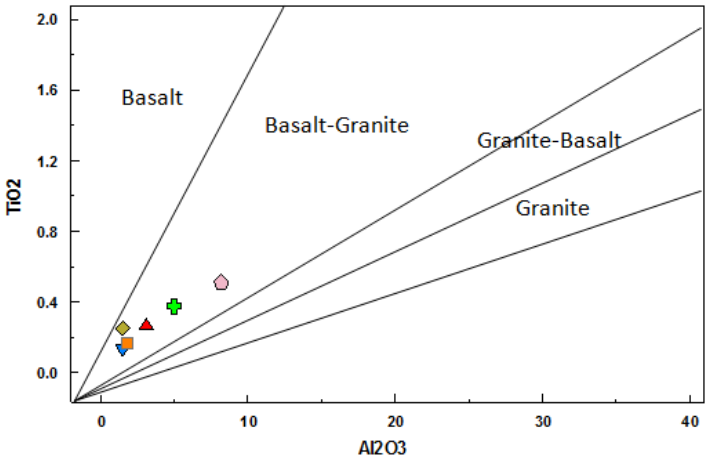

Figure 3. Provenance diagram of Al_2O_3 vs TiO_2 in coal *(after Amajor [35])*

According to Chen *et al.* [34], Al_2O_3 and TiO_2 in source rocks are preserved in the clastic sedimentary rocks because Al and Ti are not readily mobilized by weathering processes. The

ratio of Al_2O_3/TiO_2 in sandstones, mudstones, and other sedimentary rocks changed insignificantly during weathering of source rocks and subsequent transportation, deposition, and diagenesis of the sediments [35].

Based on the discriminating criterion used to distinguished different types of parent igneous rocks, the ratio of Al_2O_3 /TiO_2 in the study coal ranged from 3-10 (Figure 3). This reflects predominantly mafic igneous rocks to intermediate rocks as the source of the terrestrial sediments that form part of the coal [33,35].

4.3. Evidence from major and trace elements

The plot of TiO_2 vs Zr can be compared with earlier defined source rock fields [34,36]. From the TiO_2 vs Zr plot (Figure 4), the inorganic components of the coal around the study area falls completely in the intermediate igneous rocks. This plot, like the earlier one, showed that the terrestrial source of sediments was predominantly from intermediate igneous rocks.

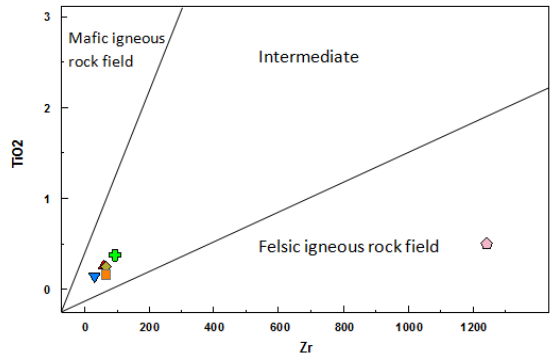

Figure 4. Provenance diagram of TiO_2 vs Zr in the study area *(after Hayashi et al. [34])*

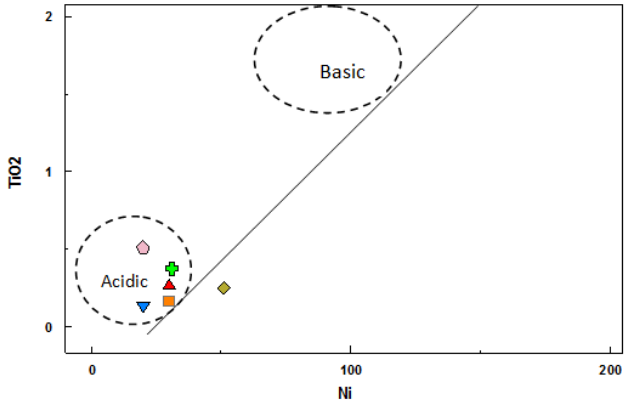

Figure 5. Provenance diagram of TiO_2 Vs Ni in coal samples *(Floyd et al. [37])*

The provenance plot of TiO_2/Ni (Figure 5) revealed that most samples plotted within the acidic field while only three samples plotted around the sandstones sedimentary trend. This is consistent with earlier plots that were predominantly basalt-granite source for the sediments.

Table 2. Correlation matrix of major oxides in coal

Major oxides	Correlation @ p= 0.01	Correlations @ P= 0.05
SiO_2	TiO_2 (0.999), LOI(0.998)	Al_2O_3 (0.907); P_2O_5(0.947; Cr_2O_3(0.958)
Al_2O_3	TiO_2(0.921); Cr_2O_3 (0.962); LOI(0.932)	Na_2O(0.887)
MgO		MnO(0.813)
CaO	MnO(0.927)	
TiO_2	Cr_2O_3(0.964); LOI(-0.999)	P_2O_5(0.956)
P_2O_5		Cr_2O_3(0.958); LOI(-0.948)
Cr_2O_3	LOI(-0.969)	

** Correlation is significant at the 0.05 level. ** Correlation is significant at the 0.01 level.*

4.4. Major oxides correlation

Given P < 0.01 (Table 2), analysis of major oxides of coal revealed strong correlation between SiO_2 and TiO_2 (0.999); SiO_2 and LOI (0.998); Al_2O_3 and TiO_2 (0.921); Al_2O_3 and Cr_2O_3 (0.962); Al_2O_3 and LOI (0.932); CaO and MnO (0.927); TiO_2 and Cr_2O_3 (0.964); TiO_2 and LOI(-0.999); Cr_2O_3 and LOI(-0.969). At P < 0.05, significant correlations were also observed between SiO_2 and Al_2O_3 (0.907); SiO_2 and P_2O_5 (0.956); SiO_2 and Cr_2O_3 (0.958); Al_2O_3 and Na_2O (0.887); MgO and MnO (0.813); TiO_2 and P_2O_5 (.956); P_2O_5 and Cr_2O_3 (0.958); P_2O_5 and LOI (-0.948).

The dominant major oxides were SiO_2; Al_2O_3 and Fe_2O_3. The likely carriers of these elements were quartz; clay minerals and pyrites [38]. The relatively high presence of TiO_2 is an indication that Ti was incorporated into the aluminosilicates structure. It could also be implied that kaolinite and TiO_2 co-precipitated or that the Ti content in sediment input to the original peat swamp from mafic basaltic rocks was probably high [38]. The high correlation between CaO-MnO (0.927) and MgO-MnO (0.813) shows that the CaO and MgO in the coals maybe associated with carbonates (calcite, dolomite, and ankerite). From Table 2, TiO_2; Cr_2O_3; LOI and Na_2O, all showed a positive correlation with Al_2O_3. This suggests that these oxides in coal were associated with aluminosilicates such as clay minerals and probably from the same source [38]. The Cr_2O_3 and LOI showed a positive relationship with P_2O_5. This affinity implies aluminophosphates minerals [38].

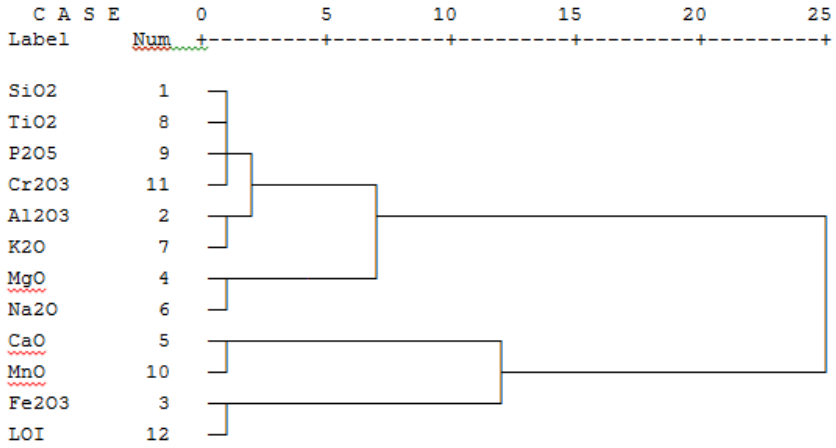

Figure 6. Cluster yield of major oxides of coal

Two clusters were extracted from the oxides of coal analysis. Cluster one consist of SiO_2, TiO_2, P_2O_5, Cr_2O_3, Al_2O_3, K_2O, MgO and Na_2O. Within this cluster, strongest similarities were observed between SiO_2, TiO_2, Cr_2O_3, K_2O, and Na_2O. A lesser degree of similarities was observed within the same cluster between P_2O_5 and Al_2O_3. Cluster two includes CaO, MnO, Fe_2O_3, and LOI. Most significant similarity was however observed between MnO and LOI (Figure 6).

While cluster one indicates mixtures of origin such as detrital quartz, clay minerals, basaltic salts of oceanic environment and some degree of carbonate affinity, cluster two suggests carbonate affinity and Fe bearing montmorillonite, chlorite and oxyhydroxides sources [32,39].

Table 3. Varimax rotated a component of major oxides of coal

Major oxides	SiO_2	Al_2O_3	Fe_2O_3	MgO	CaO	Na_2O	K_2O	TiO_2	P_2O_5
Component 1	**0.986**	**0.972**	**-0. 999**	**0.538**	-0.338	**0.729**	**0.952**	**0.989**	**0.957**
Component 2	-0.165	0.236	-0.050	**0.843**	**0.941**	**0.684**	0.307	-0.148	-0.290

Major oxides	MnO	Cr_2O_3	LOI	Eigen values	% variance	% cumulative
Component 1	-0.228	**1.000**	**-0.992**	8.685	72.378	72.378
Component 2	**0.974**	-0.013	0.128	3.315	27.622	100.00

Varimax rotated analysis extracted two factors as responsible for the 100% cumulative variance observed in the data (Table 3). Factor one consist of high factor loadings for SiO_2 (0.986); Al_2O_3 (0.972); Fe_2O_3 (-0.999); MgO (0.538); Na_2O (0.729); K_2O (0.929); TiO_2 (0.989); P_2O_5 (0.957); and LOI (-0.992). This factor has eigenvalue of 8.685 and % variance of 72.378. Factor two include high factor loadings of MgO (0.843); CaO (0.941); Na_2O (0.684); MnO (0.974). Eigenvalue of 3.315 and % variance of 27.622 was recorded.

Table 4. Descriptive statistics of trace elements in coal.

Trace elements	Minimum	Maximum	Mean	Std. Deviation	T-square	95% confidence interval of the difference	
						Lower	Upper
Ni	.00	51.00	14.20	19.28	2.89	2.67	44.66
Sc	.00	11.00	2.53	3.66	3.78	1.76	9.23
Ba	.00	122.00	69.00	43.43	5.80	44.86	116.13
Be	2.00	16.00	8.66	5.78	3.67	2.59	14.73
Co	2.50	30.50	13.75	10.62	3.17	2.60	24.89
Cs	0.00	0.30	0.06	0.10	1.74	-0.03	0.20
Ga	2.80	24.20	10.90	7.59	3.51	2.93	18.86
Hf	.80	32.40	6.71	12.59	1.30	-6.49	19.93
Nb	.00	23.50	5.24	7.35	2.45	-.38	16.12
Rb	.20	3.30	1.46	1.18	3.03	.22	2.70
Sn	2.00	2.00	2.00		1.00	-.52	1.19
Sr	.00	28.40	12.12	11.13	5.47	9.63	26.72
Ta	.10	1.60	.55	.54	2.48	-.02	1.12
Th	1.50	17.40	5.26	6.11	2.11	-1.15	11.68
U	.00	4.50	1.16	1.49	2.44	-.07	3.17
V	10.00	49.00	28.00	14.11	4.85	13.18	42.81
W	.50	1.40	.95	.63	1.36	-.27	.91
Zr	34.40	1242.50	261.20	481.13	1.33	-243.71	766.11
Y	.00	118.00	19.78	33.43	2.71	2.27	83.45
Mo	.20	0.40	0.31	0.09	7.88	0.21	0.41
Cu	7.10	30.50	14.71	8.19	4.39	6.11	23.31
Pb	2.00	10.30	5.48	3.18	4.21	2.13	8.82
Zn	7.00	504.00	118.50	192.52	1.50	-83.54	320.54
As	3.80	54.20	25.43	17.73	3.51	6.82	44.04
Cd	0.00	0.00	0.00	0.00	1.85	-0.18	1.15
Sb	0.30	1.70	0.72	0.66	1.58	-0.02	0.08
Bi	0.10	0.10	0.10	0.00	5.54	0.74	2.02
Ag	0.00	2.60	1.03	0.82	2.84	0.01	0.37
Au	0.05	0.43	0.19	0.170	2.07	-.01	0.18
Hg	0.00	0.20	0.10	0.10	2.23	0.02	0.08
Tl	0.10	0.20	0.21	0.32	1.35	0.26	0.91
Se	0.20	0.40	0.01	0.11	3.15	0.18	0.26
Total	**77.65**	**2384.03**	**630.32**	**884.96**	**97.19**	**435.49**	**1606.78**

From the rotated result (Table 3), component two is clearly a carbonate source factor while component one range from factors such as aluminosilicates, aluminophosphates, and basalts as possible sources for the variables [38].

4.5. Trace elements

The geochemical behavior of trace and rare elements in modern, organic rich sedimentary rocks such as coal has been documented and used to determine the terrestrial sediments source component of the organic rocks [20].

The trace element analysis (Table 4) indicates abundance order of: Zr>Zn>Ba>V>As>Y>Cu>Ni>Co>Sr>Ga>Be>Hf>Pb>Th>Nb>Sc>Sn. The ratio Sr/Ba of 0.176 showed that these coal occurrences were deposited on the continent. The V/(V+Ni) ratio of 0.66 is also considered as a transitional boundary from oxic to sub oxic and anoxic depositional environment [39].

The correlation (Table 5) revealed that the likely source of the trace elements was lithophilic at P=0.01.While the significant relationship was recorded between the lithophiles and the chalcophiles from trace elements such as Nb to W, it is worthy to state that this relationship occurred at P=0.005. At P=0.001 and P=0.05, from trace element Y to Sb, the chalcophile dominated the association (Table 5).

Table 5. Correlation of trace elements in coal

Trace elements	Correlation @ p= 0.01	Correlations @ P= 0.05
Ni	Z(0.993); As(0.994)	Sb (0.999); Se (0.916)
Sc	Cs(0.993); Ga (0.956); W(1.00)	V(0.819)
Ba	Sr(0.993); W(-1.00)	
Be	W(-1.00)	
Co	W(1.00); As(0.926)	Zn(0.886)
Cs	Nb(0.993); U(0.985); W(1.00); Sb(1.00); Hg(-1.00)	Hf(1.00); Zr(1.00)
Ga	W(1.00)	
Hf	Nb(0.981); Ta(0.958);Th(0.987);U(0.942); W(1.00); Zr(1.00)	
Nb	Ta(0.976); Th(0.996); U(0.988); W(1.00); Zr(0.982)	Rb(0.842); Pb(0.958)
Sr	W(1.00)	
Ta	Th(0.976); U(0.976); W(1.00); Zr(0.956)	Pb(0.812)
Th	U(0.990); W(1.00); Zr(0.943)	Pb(0.849)
U	W(1.00); Zr(0.943)	Pb(0.879); Se(-0.998)
V	W(1.00)	Mo(0.879)
W	Zr(1.00); Y(1.00); Cu(1.00); Pb(1.00); Zn(1.00); As(1.00); Sb(1.00);Hg(1.00); Tl(1.00)	
Y	Cu(0.986)	Se(-0.999)
Zn		As(0.867)
Sb	Se(1.00)	

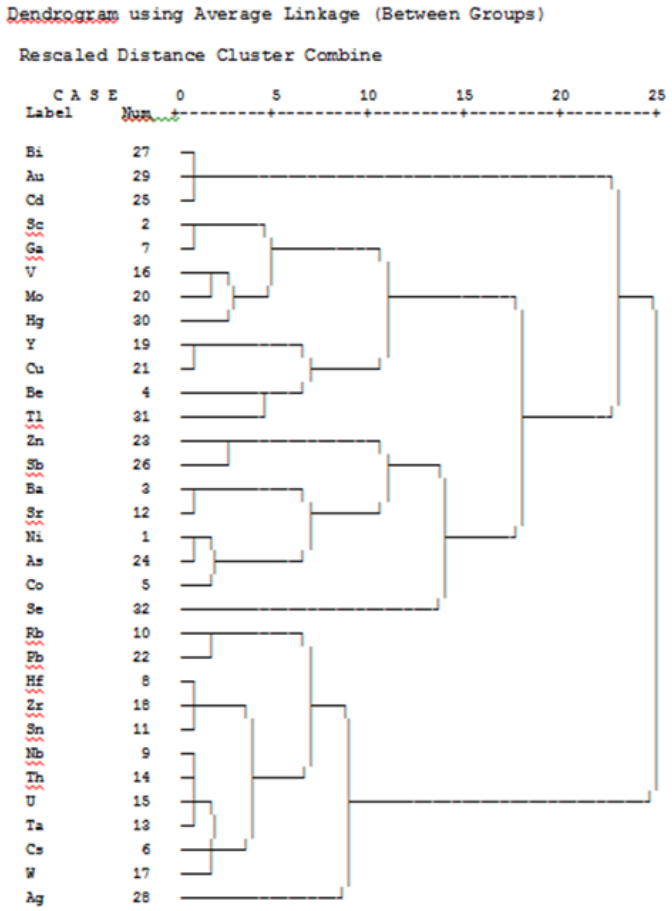

Figure 7. Cluster result of trace elements in coal

The trace element yielded four clusters (Figure 7). Cluster one (Bi, Au, and Cd) shows that all the elements were lithophilic. Cluster two is a mixture of sources. From dominantly lithophilic (Sc, V,Y,Cu, and Be) to chalcophilic (Ga,Hg and Tl) and finally the siderophile (Mo). Cluster three suggests three sources for the elements – the siderophile (Zn, Sb, Ni, Co, and Se), the lithophiles (Ba, Sr) and the chalcophiles (As). The last cluster is a mixture of two sources. These are lithophilic (Rb, Hf, Zr, Nb, Th, U, Ta, Cs and W) and the Chalcophile (Pb, Sn, and Ag).

From the above analysis, it is clear that the dominant sources for the trace elements were the lithophiles (clusters 4 and 2); Siderophile (clusters 3 and 2) and the chalcophile (clusters 1, 2, 4 and 3).

4.6. Rare earth elements

Table 6. Descriptive statistics of rare earth elements in coal

Rare Elements	Minimum	Maximum	Mean	Std. Deviation	Std. Error Mean	t-square	95% Confidence interval of the difference	
							Lower	Upper
La	4.50	48.90	21.01	17.28	7.05	2.97	2.88	39.15
Ce	9.90	94.40	42.35	31.60	12.90	3.28	9.17	75.52
Sm	.78	18.19	7.45	5.82	2.37	3.13	1.34	13.55
Eu	.15	4.40	1.72	1.42	.57	2.97	.23	3.21
Gd	.82	23.69	8.49	7.81	3.19	2.66	.29	16.70
Tb	.13	3.71	1.35	1.22	.49	2.70	.06	2.63
Dy	.78	21.00	7.67	6.93	2.83	2.71	.40	14.95
Ho	.15	4.05	1.52	1.32	.53	2.81	.13	2.90
Er	.50	10.44	4.11	3.34	1.36	3.01	.60	7.62
Tm	.05	1.38	.57	.44	.18	3.16	.10	1.03
Yb	.43	8.06	3.64	2.61	1.06	3.42	.90	6.38
Lu	.06	1.15	.53	.37	.15	3.50	.14	.92
Total	**18.25**	**239.37**	**100.41**	**80.16**	**32.68**	**36.32**	**16.24**	**369.12**

The LREE generally have higher mean concentration compared to the HREE (Table 6). The ratios of La/Yb (5.77); La/Sm (2.82) and Gd/Yb(2.33) showed that the degree of enrichment of LREE is higher than HREE. This is evidence that fractionation occurred in the LREE and HREE. The average ratio (La/Sm) n value of 2.82 indicates that some degree of fractionation also occurred among the LREE [39].

Table 7. Correlation matrix of rare earth elements in coal

Rare earth elements	Correlation @ p= 0.01	Correlations @ P= 0.05
La	Ce(0.987);	
Sm	Eu(0.983); Gd(0.982); Tb(0.985); Dy(0.988); Ho(0.994); Er(0.997); Lu(0.975);Tm(0,999); Yb(0.983)	
Eu	Gd(0.994); Tb(0.997); Dy(0.996);Ho(.994); Er(0.991); Lu(0.922);Tm(0.982); Yb(0.941)	
Gd	Tb(0.999); Dy(0.997); Ho(0.997); Er(0.993); Lu(0.918); Tm(0.978); Yb(0.933)	
Tb	Dy(0.999); Ho(0.998); Er(0.995); Lu(0.924); Tm(0.983); Yb(0.942)	
Dy	Ho(0.998); Er(0.996); Lu(0.931); Tm(0.986); Yb(0.950)	
Ho	Er(0.999); Lu(0.945); Tm(0.991); Yb(0.958)	
Er	Lu(0.958); Tm(0.996); Yb(0.969)	
Lu	Tm(0.978); Yb(0.996)	
Tm	Yb(0.987)	

*** Correlation is significant at the 0.01 level.*

At P<0.01, all the correlations recorded between Sm-Eu-Gd-Tb-Dy-Ho-Er-Lu-Tm-Yb were significant (Table 7) in both directions. Ce showed no significant relationship with any element. La also showed no significant relationship with all the elements except La and Ce (0.897). From Table 7, the REEs appeared to be generally related to primarily clay minerals and phosphates except for La and Ce that may suggest a dominantly phosphatic affinity with an organic origin.

Cluster analysis of rare earth elements yielded two clusters (Figure 8). Cluster one consists of Tb, Dy, Gd, Ho, Er, Eu, Sm, Tm, Yb, and Lu. Most significant similarities exist between Tb-Dy-Gd-Ho-Eu- Sm-Tm and Lu. Between Er and Yb was a lesser degree of similarity. Cluster two consists of La and Ce. These two elements showed the most significant similarity (Figure 8).

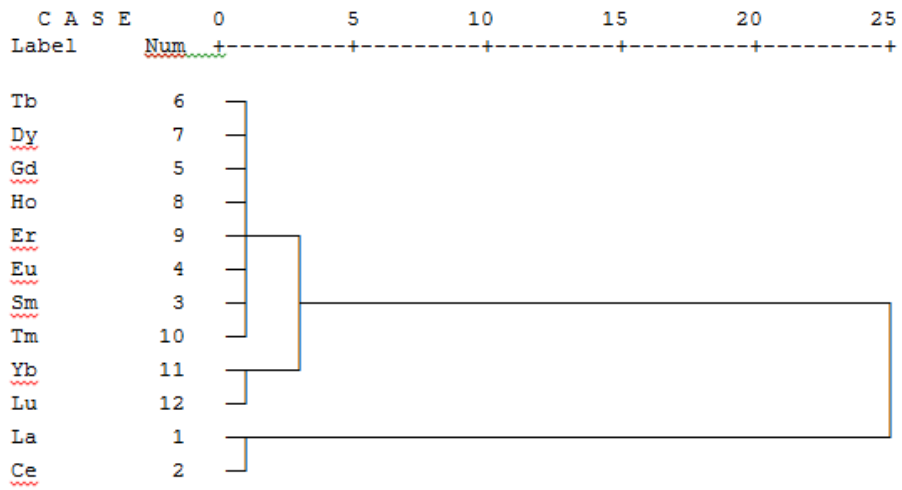

Figure 8. Rare earth element cluster analysis

From figure 8 and table 7, La and Ce appeared in the same cluster and factor component. This is an indication that these elements were from a different source and are controlled by a factor(s) different from other rare earth elements. While other REEs such as Sm, Eu, Gd, Tb, Dy, Ho, Er, Tm, Yb and Lu maybe associated with the inorganic component of the coal, the La and Ce suggests organic origin such as phosphates [38].

Table 7. Varimax rotated component matrix of rare earth elements

Rare Earth Elements	La	Ce	Sm	Eu	Gd	Tb	Dy	Ho
Component 1	0.244	0.144	**0.961**	**0.990**	**0.982**	**0.988**	**0.989**	**0.979**
Component 2	**0.967**	**0.986**	0.273	0.121	0.149	0.136	0.139	0.197

Rare Earth Elements	Er	Tm	Yb	Lu	Eigen values	% variance	% cumulative
Component 1	**0.974**	**0.960**	**0.914**	**0.885**	9.350	77.920	77.920
Component 2	0.227	0.274	0.367	0.440	2.550	21.247	99.167

The rare earth element analysis recorded two factor components (Table 7). Factor one consists of high factor loadings of .8 to .9 for all rare earth elements analysed except La and Ce. This factor has an eigenvalue of 9.350 and % variance of 77.920. Factor two consists of high factor loadings of La (0.967) and Ce (0.986) only. The % cumulative of 99.167 was enough for the variations observed (Table 7).

4.7. Palaeoweathering/climatic conditions of deposition

According to Suttner and Dutta [40], the binary plot of SiO_2 Vs (Al_2O_3 + K_2O+ Na_2O) has been used to reconstruct the climatic conditions of the source area. Based on this plot, the coal samples from the study area plotted within the humid field (Figure 9). This indicates that both weathering of source rocks/materials and conditions surrounding the coal formations occurred in humid climatic environments [33].

The Si becomes unstable in rocks due to the removal of silica rocks as weathering progresses. According to Chen *et al.* [33], the SiO_2-Al_2O_3-TFe_2O_3 (SAF) ternary diagram proposed by Schellmann [41] can be used to quantify the degree of laterization. On the basis of the SAF ternary diagram above, the coal samples from the study area may have suffered weak laterization to kaolinisation (Figure 10).

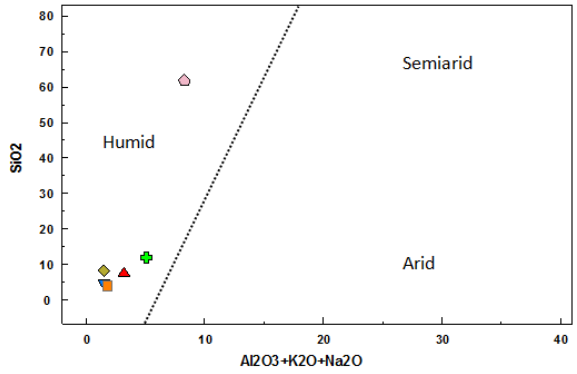

Figure 9. Paleoclimatic diagram of SiO_2 Vs Al_2O_3 +K_2O+ Na_2O *(After Suttner and Dutta, [40])*

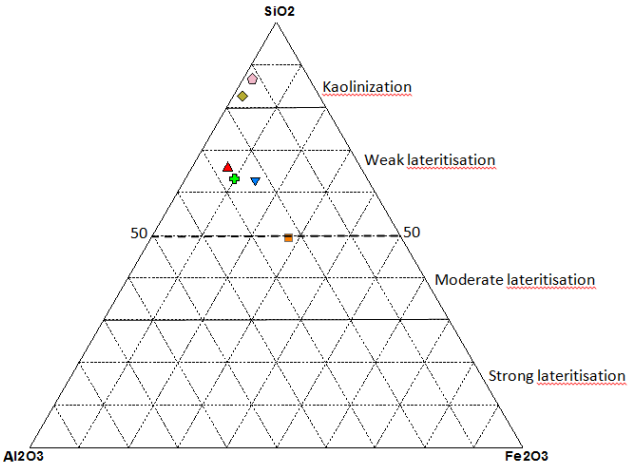

Figure 10. Triangular diagram of SiO_2-Al_2O_3-Fe_2O_3 *(after Chen et al. [33])*

5. Conclusion

From work carried out on the coal within the Northern Anambra basin, the following observations were revealed:
(a) The coal was formed from low land peat environment associated with marine or blackish water influence
(b) Stable condition of deposition, a low degree of tectonic movement but constant subsidence in the basin was observed.
(c) The transitional boundary of oxic to sub-oxic and anoxic environments was observed with an acidic and humid climate
(d) Weak laterization to kaolinization were also observed.

Conflict of interest

No conflict of interest as far as this manuscript is a concern.

References

[1] MacDonald JG, Burton CJ,Winstanley I, Lapidus DF. Collins Internet-Linked Dictionary of Geology. 2011. Learning Solutions Specialty Publications Ltd., an imprint of Rombic Concepts Ltd. Pp 480-484.
[2] Ogala JE, Omo-Irabo OO,Finekleman RB, Akaegbobi. 2010. Major oxides and trace element distribution in coal and coaly shale seams in the Enugu escarpment of south-eastern Nigeria. Global journal of geological sciences, 2010; 8(4): 175-186.
[3] Uzoegbu UM, Ekeleme IA,Uchebo UA. Oil generation capacity of Maastrichtian coals from the Anambra Basin, South eastern Nigeria. International journal of Engineering and science, 2014; 3(4): 33-46.
[4] Obaje NG, Ulu OK, Petters SW. Biostratigraphy and geochemical controls of hydrocarbon prospects in the Benue Trough and Anambra Basin, Nigeria. NAPE Bullet. 1999; 14: 18–54.
[5] Reymen, RA. Aspects of the geology of Nigeria. Ibadan 1965, Nigeria. University of Ibadan. 145p
[6] Akande SO, Hoffinecht A, Erdtmann BD. 1992. Upper Cretaceous and Tertiary coals from southern Nigeria. Composition, rank, depositional environments and their technological properties. NAPE Bull., 1992; 7: 26-38.
[7] Akande SO, Ogunmoyero IB, Petersen HI, Nytoft HP. 2007. Source rock evaluation of coals from the Lower Maastrichtian Mamu Formation, SE Nigeria. Journal of Petroleum geology, 2007; 30(40): 303-324.
[8] Okorie EO, Egila JN. 2014. Trace and major metal abundances in the shale and coal of various seams at Okaba coal mine, Kogi State, Nigeria. Int. J. Biol. Chem. Sci., 2014; 8(2): 741-754

[9] Olajire AA, Ameen AB, Abdul-Hammed M, Adekola FA. Occurrence and distribution of metals and porphyrins in Nigericoal minerals. Journal of Fuel Chemistry and Technology, 2007; 35(6): 641-647.
[10] Ndiokwere CL, Guinn VP, Burtner D. Trace elemental composition of Nigerian coal measured by neutron activation analysis. J. Radioanalytical and Nuclear Chemistry, 1983; 79(1):123-128.
[11] Sonibare OO, Ehinola OA, Egashira R, Lim K.. An investigation into the thermal decomposition of Nigerian coal. Journal of Applied Science, 2005; 5(1): 104-107.
[12] Ewa IOB. Data evaluation of trace elements determined in Nigerian coal using cluster procedures. Applied Radiation and Isotopes, 2004; 60(5): 751-758.
[13] Ogala JE, Akaegbobi MI, Omo-Irabor OO, and Finkelman RB. Statistical analysis of geochemical distribution of major and trace elements of the Maastrichtian coal measures in the Anambra Basin, Nigeria. Pet. Coal, 2009; 51(4):260-269.
[14] Adebayo OF, Akinyemi SA, Ojo AO. Palaeoenvironmental studies of Odagbo coal mine sequence, Northern Anambra Basin, Nigeria: Insight from palynomorph and geochemical analyses. International Journal of Current Research, 2015; 7(09): 20274-20286.
[15] Akande SO, Erdtmann BD. Burial metamorphism (maturation) in Cretaceous sediments of the southern Benue Trough and the Anambra Basin, Nigeria. American Association of Petroleum Geologists Bulletin, 1998; 82: 1191-1206.
[16] Reyment RA. Ammonite biostratigraphy, continental drift and scillatory transgressions. Nature, 1969; 224: 137-140.
[17] Burke KC, Dessauvagie TFJ, Whiteman AJ. Geologic history of the Benue Valley and Adjacent areas. *In*: Dessauvagie T.F. J. and Whiteman A.J. (eds), *African Geology,* Univ. Ibadan Press 1972, Nigeria, 187-206.
[18] Murat RC. Stratigraphy and paleogeography of the Cretaceous and lower Tertiary in southern Nigeria. In: African geology, University of Ibadan Press, 1972: 251-266.
[19] Weber KJ, Daukoru EM. 1975. Petroleum geological aspects of the Niger Delta. Journal of Mining and Geology, 1975; 12: 9-22.
[20] Adebayo OF, Akinyemi SA, and Ojo AO. Paleoenvironmental studies of Odagbo coal mine sequence, Northern Anambra Basin, Nigeria: Insight from palynomorph and geochemical analysis. International journal of current research, 2015; 7(09): 20274-20286.
[21] Nwajide, C.S., Reijers, T.J.A., 1996. 'Sequence Architecture in Outcrops: Examples from the Anambra Basin, Nigeria'. Nigerian Association of Petroleum Explorationists Bulletin, 11(1), pp23-32.
[22] Onyekuru, S.O., Iwuagwu, C.J., 2010. Depositional Environments and Sequence Stratigraphic Interpretation of the Campano-Maastrichtian Nkporo Shale Group and Mamu Formation Exposures at Leru-Okigwe Axis, Anambra Basin, Southeastern Nigeria. Australian Journal of Basic and Applied Sciences, 4(12), pp 6623-6640
[23] Akinyem, SA, Adebayo OF, Ojo AO, Fadipe AO, and Gitari WM. Geochemistry and mineralogy of Campanian Sandstone of Lokoja-Basange Formation, middle Niger Basin (Lokoja subbasin), Nigeria: Implications for provenance, weathering, tectonic setting and paleo-redox condition. Journal of natural sciences research, 2014; 4(16):65-89.
[24] Obaje NG, Ligouls B, Abas SI.. Petrographic Composition and depositional environments of Cretaceous coals and coal measures in the Middle Benue Trough of Nigeria. International Journal of Coal Geology, 1994; 26: 244-260
[25] Odumoso SE, Oloto IN, Omoboriowo AO. Sedimentological and Depositional Enviroment of the Mid-Maastritchtian Ajali Sandstone, Anambra Basin, Southern Nigeria. International Journal of Science and Technology, 2013; 3(1): 2224-3577.
[26] Ji-Hoon K, Byoung-Woo Y, Rak-Hyeon K, Dong-Chan K, Tae-Jin C, Jeongho L, Ho-Wan C. Application of cluster analysis for the hydrogeochemical factors of saline groundwater in Kimje, Korea. Geosciences Journal, 2003; 7(4): 313-322.
[27] Pathak JK, Mohd Alam, Shikha Sharma. Interpretation of groundwater quality using multivariate statistical technique in Moradabad City, Western Uttar Pradesh State, India. E-Journal of Chemistry, 2008; 5(3): 607-619.
[28] Praveena SM, Ahmed A, Radojevic M, Abdullah MH, Aris AZ. 2007. Factor-cluster analysis and enrichment study of mangrove sediments- An example from Mengkabong, Sabah. The Malaysian Journal of Analytical Sciences, 2007; 11(2): 421-430.
[29] Ameh EG, Imasuen IO, and Imeokparia EG. (2014): Geochemistry and Environmentic Approaches to estimate pollution impacts on soils around Okaba coal mines. British Journal of Applied Science Technology, 2014; 4(17): pp.2513-2527.

[30] Lokhande PB, Patit VV, Mujawar HA. 2008. Multivariate statistical analysis of groundwater in the vicinity of Mahad industrial area of Konkan region, India. International Journal of Applied Environmental Sciences, 2008; 3(2): 149.
[31] Yandoka BMS, Abdullah WH, Abubakar MB, Hakimi MH, Adegoke AK. Geochemistry of the Cretaceous coals from Lamja Formation, Yola Sub-basin, Northern Benue Trough, NE Nigeria: Implications for paleoenvironment, paleoclimate and tectonic setting. Journal of African Earth Sciences, 2015; 104: 56–70.
[32] Vassilev S, Vassileva C, BaxterD, Andersen LK. The relationship between chemical and mineral composition of coal and their potential applications as genetic indicators. Geologica Balcanica, 2010; 39(3): 21-41.
[33] Chen B, Liu G, Wu D, Sun R. Comparative study on geochemical characterization of the Carboniferous aluminous argillites from the Huainan Coal Basin, China. Turkish J Earth Sc., 2016; 25: 274-287.
[34] Hayashi K, Fujisawa H, Holland H, Ohmoto H. Geochemistry of approx.1.9 Ga sedimentary rocks from northeastern Labrador, Canada. Geochimica Cosmochimica Acta, 1997; 61(19): 4115-4137.
[35] Amajor LC. Major and Trace element geochemistry of Albian and Turonian shales from the Southern Benue Trough Nigeria. Journal of African Earth Science, 1987; 6: 633-641.
[36] Stone WE, Jensen LS, Church WR. Petrography and geochemistry of an unusual Fe-rich basaltic komatiite from Boston Township, Northeastern Ontario. Canadian Journal of Earth Science, 1987; 24: 2537-2550
[37] Floyd PA, Winchester JA, Park RG. Geochemistry and tectonic setting of Lewisian clastic metasediments from the early Proterozoic Loch Maree group of Gairloch, NW Scotland. Precambrian Res., 1989; 45: 203-214.
[38] Zhao L, Ward CR, French DH, Graham I. Major and Trace Element Geochemistry of Coals and Intra-Seam Claystones from the Songzao Coalfield, SW China. Minerals, 2015; (5): 870-893.
[39] Taghipour N, Marshk ZS. Geochemistry and origin of elements of Upper Triassic Olang coal deposits in Northeastern Iran. Geopersia, 2015; 5(2): 189-204.
[40] Suttner LJ, Dutta PK. Alluvial sandstone composition and Paleoclimate. L. Framework mineralogy. Journal of sedimentary petrology; 1986; 56: 329-345.
[41] Schellmann W. A new definition of Laterite. Geological Survey India. Mem., 1986; 120: 1-7

To whom correspondence should be addressed: Dr. E. G. Ameh, Earth Sciences Department, Faculty of Natural Sciences, Kogi State University, P.M.B 1008 Anyigba, Nigeria

Petroleum and Coal

Article **Open Access**

IMPROVING THE TECHNOLOGY OF PREPARING COAL FOR THE PRODUCTION OF BLAST-FURNACE COKE UNDER THE CONDITIONS OF MULTI-BASIN RAW MATERIAL BASE.
MESSAGE 3. INFLUENCE OF THE MOISTURE CONTENT OF COAL BATCH ON THE PHYSICOMECHANICAL CHARACTERISTICS OF THE COKE

V. P. Lyalyuk, E. O. Shmeltser, D. A. Kassim, I. A. Lyakhova, M.V. Kormer*

Kryvyi Rig Metallurgical Institute, Ukraine National Metallurgical Academy, 50006, Kryvyi Rig, Ukraine

Received January 25, 2019; Accepted March 26, 2019

Abstract

The packing density of the coal batch influence on the physicomechanical characteristics of the coke produced: the strength M_{25} and wear resistance M_{10}. In the absence of mechanical methods (such as ramming or partial briquetting), the packing density depends on the ash and moisture content and the degree of crushing of the coal batch. Since improvement in coke quality entails decreasing the moisture content of the coal batch, we developed a method for decreasing the moisture content directly in the silo, on the basis of osmosis and vacuum. That permits a decrease in the coal's moisture content to the optimal value, thereby boosting coke quality and improving blast-furnace performance.

Keywords: *ramming technology; bed coking; coal batch; packing density; coke quality; moisture removal.*

1. Introduction

The most important means of improving blast-furnace performance is to supply high-quality batch—in particular, high-quality coke.

In the blast furnace, coke plays a complex role. Its transformation at the tuyeres provides most of the heat required for smelting and also forms most of the reducing gas, to which gas from direct reduction is added at higher levels. Besides these functions, the coke serves as solid packing in the zone characterized by softening and melting of the iron-bearing materials: in so doing, it ensures a counterflow of batch and gas in the furnace. The coke also regulates the gas distribution over the furnace cross-section. Accordingly, coke must satisfy strict requirements.

Coke quality may be assessed in terms of physical characteristics, (strength, susceptibility to wear, and granulometric composition), chemical composition, reactivity, and post reactive strength. In terms of chemical composition, we require coke with maximum carbon content and minimum ash and sulfur content. In terms of granulometric (fractional) composition, the coke must be of uniform size, with a minimum content of the smallest (<25 mm) and largest (>80 mm) classes. High hot and cold strength is necessary.

Typical requirements were laid out at the Fifth International Congress of Blast-Furnace Specialists [1]: strength M_{25} no less than 90%; susceptibility to wear M_{10} no more than 6%; content of the >80 mm class no more than 5%; content of the <25 mm class no more than 5%; fluctuations of the moisture content no more than ±0.5%; reactivity CRI = 23—26%; and post reactive strength CSR = 70%.

Under specific conditions, classical bed coking may produce blast-furnace coke of strength M_{25} = 90% and wear susceptibility M_{10} = 6.0%. Ukrainian coke plants with M_{25} > 88.0% between 2009 and 2011 included ChAO Makeevkoks (with annual figures of 89.6, 89.1, and 88.4%), which supplies premium coke, and PAT Avdeevskii KKhZ (with annual figures of 88.5,

88.1, and 88.7%). All the other coke plants met this standard in some years but produced coke with M_{25} < 88% in other years. The coke of lowest strength was produced by PAT ArcelorMittal Krivoi Rog (with annual figures of 84.4, 83.4, and 86.6%).

In the same period, coke with M_{10} < 7% was produced at ChAO Makeevkoks (with annual figures of 7.0, 6.6, and 6.8%) and ChAO Enakievskii KKhZ (with annual figures of 7.0, 7.0, and 6.8%). These figures are considerably lower for coke from PAT Alchevskkoks (6.3, 6.4, and 5.4%); the lowest values (5.5, 5.8, and 4.1%) are observed for coke from battery 10A, which employs ramming of the coal batch and dry slaking of the coke [2].

Coke is supplied to the batch-supply bunker for blast-furnace shop 1 from coke batteries 1-4 at PAO ArcelorMittal Krivoy Rog (Table 1). This coke is produced by classical bed coking, with batch supply through charging hatches. Therefore, it remains to improve batch preparation for those blast furnaces.

Table 1. Weighted-mean characteristics of coke supplied to the blast furnaces of shop 1

Year	Characteristic, %							Content of class (mm) , %	
	W	A	S	M_{25}	M_{10}	CSR	CRI	>80	<25
2015	3,9	12,0	0,72	86,8	7,4	50,3	36,1	8,9	5,2
2016	3,8	11,5	0,60	86,5	7,8	52,4	35,2	7,4	6,4
2017	3,9	11,5	0,54	85,3	7,6	48,9	38,0	6,5	7,0

In classical coking, the rank composition and properties of the coal batch mainly determine the physico-mechanical characteristics of the coke produced, while the key factor in batch preparation for coking is the packing density of the batch. In the absence of mechanical methods (such as ramming or partial briquetting), the packing density mainly depends on the ash and moisture content and the degree of crushing of the batch. These factors, in turn, affect the thermal conditions of coking, the physico-mechanical characteristics of the coke produced, and the yield and quality of the coking products [3].

One means of improving coke quality is to increase the packing density of the coal batch before supply to the coke oven.

2. Results and discussions

The factors responsible for the poor quality of the coke produced in batteries 1-4 at PAO ArcelorMittal Krivoy Rog were analyzed in detail in [4]. Primary factors include the high moisture content of the coal batch; insufficient mixing after crushing when numerous coal concentrates are employed; and excessive crushing of batch with a high content (70-80%) of bituminous coal [5].

To investigate the influence of the granulometric composition, ash content, and moisture content of the coal batch on its packing density in the coal-preparation shop for coke production at PAO ArcelorMittal Krivoy Rog, we select samples of coal concentrates for technical analysis and also for the determination of the packing density and granulometric composition.

Table 2 presents the characteristics of these concentrates.

In Fig. 1, we plot the packing density of the coal batch supplied to coke batteries 1—4 as a function of its moisture content. The curve is parabolic, with a minimum at a moisture content of 10.3%. However, the increase in packing density is not due to a decrease in the moisture content of the batch but rather to increase in moisture content. In other words, the packing density increases as a result of an increase in the mass of water in the coal batch.

In physical terms, the influence of the moisture content on the packing density of the coal was analyzed in [6]. In the wetting of coal, the water absorbed by its particles is uniformly distributed over their surfaces, with an increase in the distance between coal particles by the thickness of the water film. That changes the packing density of the coal. With further wetting, corresponding to the minimum of the parabola, the packing density increases more sharply. This may be explained in that the free water in the batch tends to occupy the volu-me with

the minimum surface under the action of capillary forces and is concentrated in narrower intervals between the coal particles, predominantly at points of particle contact.

Table 2. Characteristics of the coal concentrates used in the batch

Supplier	Rank of coal	Moisture content W^r_t, %	Content (%) in class (mm)					Packing density, t/m³
			>6	3-6	0.5-3.0	<0.5	<3	
T34, Poland	G	9.1	38.29	15.99	32.69	13.03	45.72	0.859
Coking Coal Pardee, United States	GZh	11.0	42.65	13.76	22.24	21.35	43.59	0.870
Ukrkoks. Ukraine	Zh	14.4	12.48	13.33	41.05	33.14	74.19	0.859
Kievskaya enrichment facility, Ukraine	Zh	12.0	2.86	5.98	49.81	41.35	91.16	0.832
Krasnolimanskaya enrichment facility, Ukraine	Zh	10.5	40.56	19.74	23.10	16.60	39.70	0.871
Pechorskaya enrichment facility, Russia	2Zh	10.5	29.48	14.56	25.10	30.86	55.96	0.841
Vostochnaya enrichment facility, Kazakhstan	K + KZh	12.6	6.68	9.52	40.40	43.40	83.80	0.801
Severnaya enrichment facility, Russia	K	12.7	19.95	15.24	32.32	32.49	64.81	0.847
Ukrkoks, Ukraine	K	19.8	12.15	18.60	40.08	29.17	69.25	0.914
Alpha, United States	K	14.4	6.25	14.70	44.95	34.10	79.10	0.890
Eagle, Canada	K	12.1	14.05	12.81	34.62	38.52	73.14	0.831
Severnaya enrichment facility, Russia	K + KO + PS	17.2	14.08	12.93	34.37	38.62	72.99	0.927

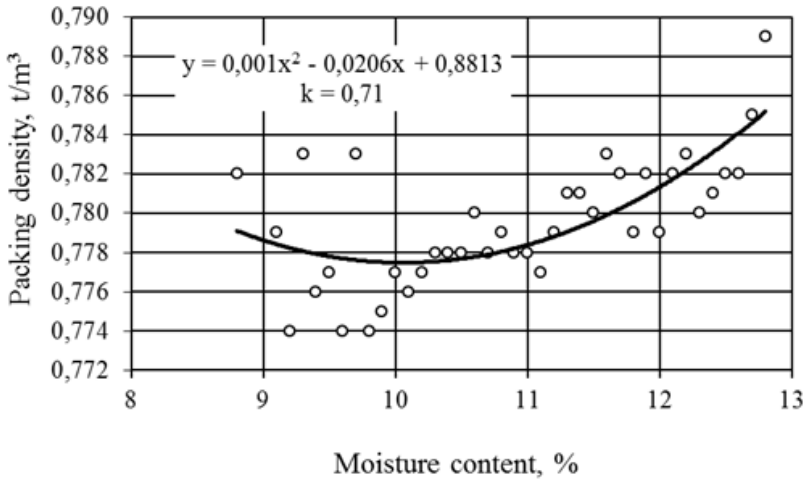

Fig. 1. Influence of the moisture content on the packing density of the coal batch (coke batteries 1—4)

The surface tension of the water around those points tends to retain the particles in place, preventing their free motion and results in denser packing on charging in the furnace chamber. This behavior is observed with an increase in the moisture content to 6— 10%. With the further increase, the capillary forces cannot retain the moisture at the contact points. Under the action of the gravitational forces, the water breaks away from the meniscus and moves into the gaps between the particles. From that point onward, the packing density of the coal batch increases on account of an increase in the water mass [6].

The moisture content of the coal batch also considerable affects the expansion pressure and the shrinkage of the coke cake. The final shrinkage of the coke cake is between 230 and 165% for a batch of moisture content between 8.1 and 14.5%.

The variation in packing density in the given period when water evaporates in the coke oven is also of interest. Recalculated for dry mass, the packing density of the coal batch (Fig. 1) is considerably less than the initial value, as indicated by Fig. 2. With an increase in the initial moisture content, we note a greater decrease in the packing density of the coal batch when the moisture evaporates in the coke oven of the battery. This will necessarily affect coke quality.

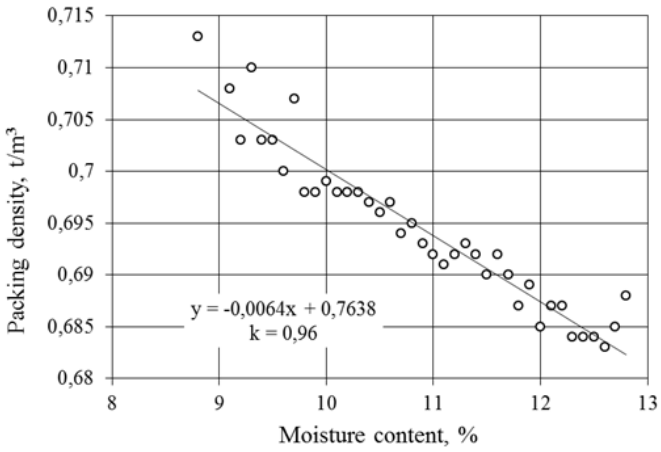

Fig.2. Influence of the moisture content on the packing density of coal batch (coke batteries 1–4), after recalculation for dry mass

It is evident from Figs. 1 and 2 that, when the mean moisture content of the coal batch is 11.2%, its mean packing density is 0.780 t/m^3. In the coke oven after evaporation of the moisture, it falls to 0.690 t/m^3 (by 11.5%).

To determine the packing density of the batch on drying (with determination of the moisture content on the basis of State Standard GOST 11041—81), we use batch of the following rank composition: 28% Zh, 41 % K, 8% K + KO+ OS, and 23% K + KO + KZh.

The granulometric composition of the batch (after crushing) is as follows (%):

>6 mm	6—3 mm	3—0.5 mm	<0.5 mm	<3 mm
1.9	8.1	42.9	47.1	90

Note that, in a batch sample containing 90% of the <3 mm class, the content of the <0.5 mm class, which impairs clinkering, is 47.1%.

In Fig. 3, we plot the dependence of the batch's packing density on its moisture content in a drying chamber. As we see, on drying coal batch with initial moisture content 11.43% and packing density 0.760 t/m^3, with a decrease in moisture content to 7.33%, its packing density increases to 0.819 t/m^3 (by 7.8%). Further drying to 5% increases the packing density of the coal batch to 0.847 t/m^3.

We also are interested in the dynamics of drying (by the method in State Standard GOST 11014—81). We find that 1g of a batch of initial moisture content 14% may be dried to 6% in 2 min; to 4% in 4 min; and to 2.4% in 8 min.

According to extensive literature data, the drying of coal batch decreases the heat consumption in coking by 15—20%; increases coke-oven productivity by 30—40%; permits increase in the content of poorly clinkering coal in the batch to 70%, without loss of coke quality (according to tests in the United States, Japan, Britain, France, Germany, and elsewhere); increases coke-plant profits by 50%; improves coke quality without change in batch composition (2.2— 2.27% increase in M_{25} and 0.8—1.4% decrease in M_{10}).

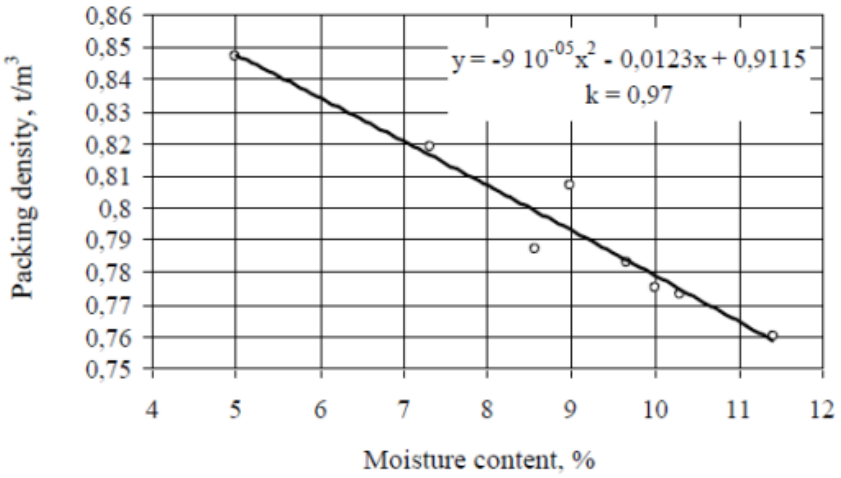

Fig. 3. Influence of the moisture content on the packing density of coal batch in a drying chamber

We also studied the influence of the content of the 0-3 mm and 0-0.5 mm classes on the packing density of the coal batch. Analyses of the results show that with a mean moisture content of 11.2%, greater crushing results in lower packing density; note the high content of 0-0.5 mm class in the batch (44—50%) and the decrease in packing density of the batch with an increase in its content.

In Fig. 4, we show the influence of the ash content on the packing density of the coal batch supplied to coke batteries 1—4 at PAO ArcelorMittal Krivoy Rog. With the increase in ash content, the packing density of the coal batch increases, because the actual density of the coal's mineral component is considerably greater than that of its organic mass. For example, the actual density of the organic mass of Donetsk Basin coal is1.16—1.39 t/m^3, depending on its metamorphic stage, while the actual density of the mineral component is more than 1.8 t/m^3 [7]. Note also that the mineral inclusions are centers of internal stress: they weaken the coke structure.

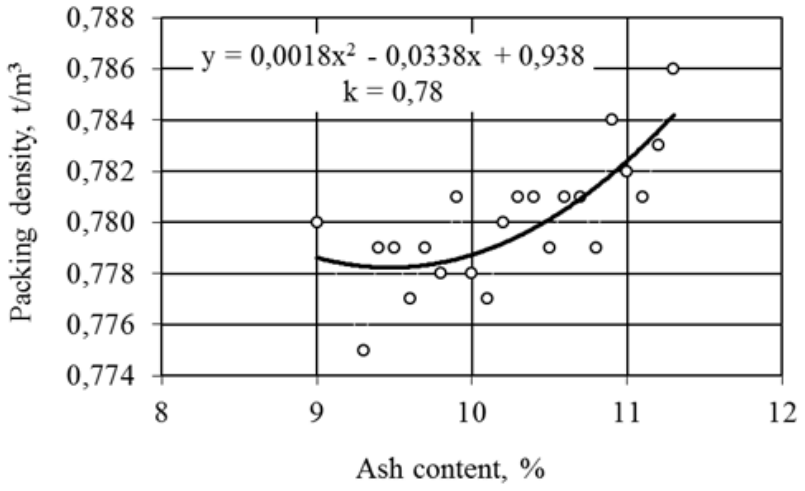

Fig. 4. Influence of the ash content on the packing density of coal batch

Analysis of the characteristics of the coal concentrates used in coking batch shows that, for the foreseeable future, the batch will contain 25—30% Karaganda Basin coal, as well as concentrates from Ukraine and Russia and other imported coal. That results in 1% increase in the mean ash content of the batch and at least 12% increase in the ash content of the coke produced [8].

To assess the aggregate effect of the moisture content, ash content, and granulometric composition (the content of the 0-3 mm and 0-0.5 mm classes) on the packing density of the coal batch, we select batch samples of the following rank composition: 10.8% G, 67.1% Zh, 14% K, 5.5% OS, and 2.6% of other ranks. Table 3 presents the characteristics of the batch samples.

Table 3. Characteristics of coal-batch samples

Sample	Packing density BD^r, t/m^3	Moisture content W^r, %	Ash content A^d, %	Content (%) of class <3 mm	Content (%) of class <0,5 mm
1	0,779	10,3	9,4	87,6	46,9
2	0,779	9,5	9,4	87,56	46,5
3	0,782	9,1	9,3	87,2	45,9
4	0,783	9	9,5	87,3	46
5	0,786	8,3	9,7	86,9	45,6
6	0,788	7,5	9,5	87,0	45,5
7	0,787	7,8	9,6	87,5	46,1
8	0,79	7,7	9,5	85,6	42,9
9	0,795	7,7	9,8	83,0	40,6
10	0,797	8,2	9,8	82,4	40,6
11	0,812	7,8	9,2	80,6	39,0
12	0,805	7,3	9,2	82,5	39,3
13	0,803	7,3	9,6	82,1	39,0
14	0,804	7,9	9,7	82,2	39,7
15	0,803	7,2	10	82,9	41,5
16	0,798	7,5	9,4	84,0	43,2
17	0,798	7,7	9,7	84,3	44
18	0,796	9	9,4	84,7	43,4
19	0,794	9,3	9,8	84,8	42,7
20	0,797	9,3	9,6	84,7	42,6

On the basis of correlation analysis, we obtain the pair correlation coefficients in Table 4. Their values indicate a close relation of the moisture content and granulometric composition of the batch with its packing density. The corresponding regression equation is as follows

$$BD^r = 1.16 - 0.00174W_t^r + 0.000553\gamma(< 0{,}5mm) - 0.00423\gamma(< 3mm) - 0.00274A^d \qquad (1)$$

Table 4. Pair-correlation coefficients

Parameter	Pair-correlation coefficients			
	W_t^r	A^d	$< 3\ mm$	$< 0.5\ mm$
Packing density BD^r of batch, t/m^3	-0,63	0,098	-0,95	-0,914

For this equation, the determination coefficient D = 92% and the correlation coefficient r = 0.96. That indicates its statistical significance.

In Figs. 5 and 6, we show the influence of the packing density on the physicomechanical characteristics of the coke produced: the strength M_{25} and wear resistance M_{10}.

On the basis of industrial tests and multifactorial correlation analysis, we may write the following regression equations for M_{25} and M_{10} as a function of the batch's packing density BD^r

M_{25} = -32.9939 +149.4599·BD^r with D = 72.4 %, r = 0.85; (2)

M_{10} = 44.46453 – 46.067·BD^r with D = 65 %, r = 0.81. (3)

The moisture content of the coal batch significantly affects the processes in the coking chamber and the coke quality, according to research at OAO Zapadno-Sibirskii Metallkurgcicheskii Kombinat [9]. The influence of the initial moisture content on the physicomechanical properties of the coke may be attributed both to change in the heat-transfer conditions within the batch over the height of the coke cake at different stages of coking and to some impairment of coke quality on account of the temperature drop due to the heat consumption in

removing the extra moisture. Experimental coking of coal batch with different rank composition and moisture content reveals significant changes in the cake conditions and hence in coke strength. Increasing the moisture content from 7.3 to 12.6% increases M_{10} from 8.6 to 10.2% and increases the content of the >80 mm class from 29.9 to 49.9%.

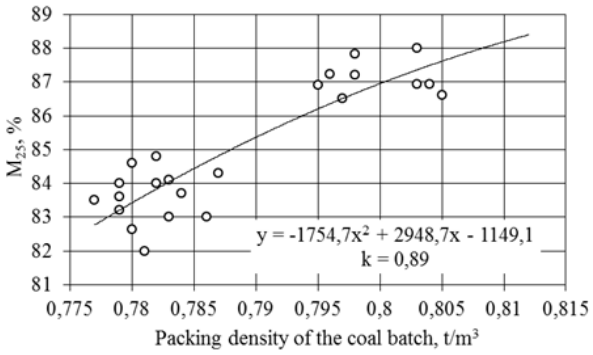

Fig. 5. Dependence of the coke strength M_{25} on the packing density of the coal batch

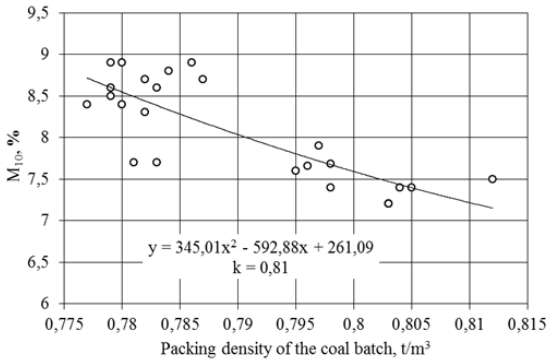

Fig. 6. Dependence of the wear resistance M_{10} on the packing density of the coal batch

Experiments at Yasinovsk coke plant with six different moisture contents of the batch also show that the coke quality declines with an increase in moisture content. Increase in moisture content from 8.1 to 14.7% reduces M_{40} from 75.8 to 73.5% and increases M_{10} from 6.7 to 8.9%. Even a small change in moisture content of the batch considerably changes the physicomechanical properties of the coke [10].

In improving the physicomechanical characteristics of coke, it is important to decrease the moisture content of the coal batch. Therefore, we need to develop a method of decreasing the moisture content directly in the silos of the coal-preparation shop.

Electroosmosis—the process in which liquid moves through capillaries or porous media under the action of an external electric field—is widely used to remove excess moisture from the soil in road and dam building, to dry peat, and also to purify water and industrial fluids. The use of electroosmosis to remove moisture from coal in storage silos is of interest [11].

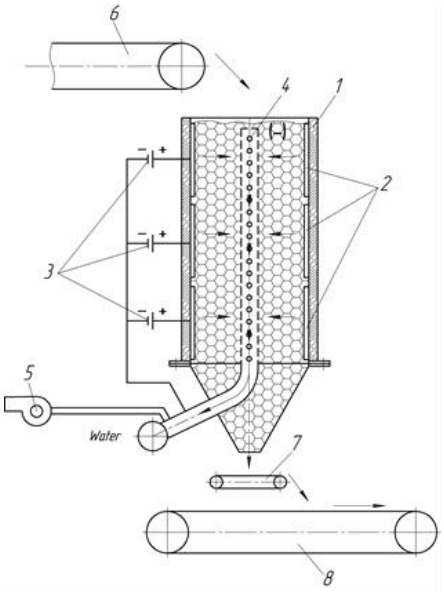

To that end (Fig. 7), a row of electrodes 2 (annular plates) connected to the positive pole of current sources 3 is positioned at the internal surface of silo wall l. In the central part of the silo, the water drain is perforated pipe 4 connected to the negative pole of sources 3. The voltage applied to annular plates 2 from sources 3 increases from the upper to the lower plates—for example, from 12 to 24 V. The number of current sources is equal to the number of annular plates.

Fig. 7. Silo in enclosed coal store:
1) silo wall; 2) electrodes (annular plates); 3) current sources; 4) perforated pipe; 5) vacuum pump; 6) conveyer belt; 7) dosing feeder; 8) output conveyer

The vacuum pump 5 creates a low-pressure zone so as to accelerate the motion of the moisture from the coal at the silo wall 1 to the center and its extraction through perforated pipe 4. Coal is charged in the silo by means of conveyor 6. Coal is discharged from the silo

onto conveyor 8 by means of dosing feeder 7 in accordance with its rank composition, so as to obtain batch for coking.

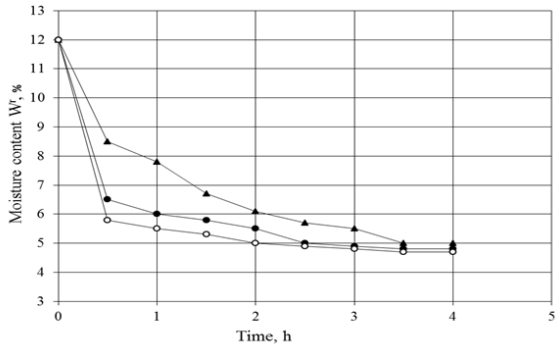

Fig. 8. Variation in coal's moisture content at pressures of 3.5 (Δ), 5 (•), and 7.5 (o) mm Hg

In Fig. 8, we show the experimental time dependence of the coal's moisture content when using osmosis in a laboratory system (height 1 m, diameter 4 m), with a voltage of1.5 V at the plates, at an internal pressure of 3.5-7.5 mm Hg. We see that, at any pressure, the loss of moisture is greatest within the first hour: after 0.5 h at 7.5 mm Hg. Thus, the laboratory tests show that electroosmosis permits a decrease in moisture content of the coal to the optimal value for coking batch. That will increase the strength of the coke and decrease its consumption in the blast furnace while improving blast-furnace performance. Thus, we have established that in the blast-furnace shops at PAO ArcelorMittal Krivoy Rog, 1% decrease in M_{10} lowers the mean coke consumption by 5.5%. With the increase in M_{25} by 1%, the mean coke consumption falls by 2.1%, on average.

3. Conclusions

Thus, the high moisture content of the batch and its significant variability has the primary influence on coke quality. The moisture content of the batch supplied to coal-preparation shops at coke plants must be no more than 6—7%. Otherwise, the plant must take measures to dry the coal. At present, in accordance with the relevant technical specifications, PAT ArcelorMittal Krivoi Rog accepts coal concentrates whose moisture content is up to 13%, with consequent loss of coke quality.

Symbols

W^r_t	*water content of the coal batch (or coke), %;*
A^d	*ash content of the coal batch (or coke) in the dry state, %;*
S_t^d	*sulphur of the coal batch (or coke) in the dry state, %;*
BD^r	*packing density of the coal batch, t/m^3*
M_{10}, M_{25}	*indices of resistance of coke abrasion and crushability, respectively, %;*
>80, <25	*content of particles more and less 80 and 25 mm in coke accordingly, %;*
CRI, CSR	*coke reactivity index and coke strength after reaction, %*

References

[1] Tovarovskii IG, and Lyalyuk VP. The V International Congress of blast furnace operators Coke Production in the Turn of Centuries. Stal', 1999; (9): 5—10.
[2] Lyalyuk VP, Lyakhova IA, Kassim DA, Shmeltser EO. Sovershenstvovovanie tekhnologii proizvodstva koksa dlya domennoi plavki (Improvement of Coke Production Technology for Blast Furnace Smelting), Krivoi Rog: Dionat, 2017.
[3] Lyalyuk VP, Uchitel' AD, Lyakhova, IA, Sokolova VP, and Kassim DA. Influence of the moisture content of coal batch on coke quality. Coke and Chemistry, 2012; 55(9): 329—334.
[4] Lyalyuk VP, Uchitel' AD, Lyakhova IA, Kassim DA, and Zaitsev GL. Preparation of coking batch. Coke and Chemistry, 2011; 54(8) 271—286.
[5] Shmeltser EO, Lyalyuk VP, Sokolova VP, Miroshnichenko DV. The using of coal blends with an increased content of coals of the middle stage of metamorphism for the production of the blast-furnace coke. Message 1. Preparation of coal blends. Pet Coal, 2018; 60(4): 605–611.
[6] Goftman MV. Prikladnaya khimiya tverdogo topliva (Applied Chemistry of Solid Fuel), Moscow: Metallurgizdat, 1963.

[7] Spravochnik koksokhimika. Tom 1. Ugli dlya koksovaniya. Obogashcheniya uglei. Podgotovka uglei k koksovaniyu (Handbook of Coke Chemist, Vol. 1: Coal for Coking. Processing of Coal. Preparation of Coal for Coking), Borisova, L.N. and Shapovalova, Yu.G., Eds., Kharkov: Inzhek, 2010.
[8] Romanyuk IV, Sikan II, Mukina NV. et al., Prospective development of the coal resource base of the ArcelorMittal Krivoy Rog coke-chemical production, Uglekhim. Zh., 2016; (3-4): 12-18.
[9] Gaineva GR. Influence of Batch Properties and the Conditions of Batch Preparation and Coking on Coke Quality. Koks i Khimiya, 2008; (10): 8—13.
[10] Bronnikov VK, and Eidel'man EYa. Influence of Batch Moisture Content on the Physicomechani cal Properties of Coke. Koks i Khimiya, 1973; (10) 12—15.
[11] Lyalyuk VP, Uchitel' AD, Shmeltser EO. et al., UA Patent 111594, Byull. Izobret., 2016, no. 21.

To whom correspondence should be addressed: Dr. E. O. Shmeltser, Kryvyi Rig Metallurgical Institute, Ukraine National Metallurgical Academy, 50006, Kryvyi Rig, Ukraine

Petroleum and Coal

Article **Open Access**

BLENDS OF LAURATE ESTER WITH MENTHOL AND CAMPHOR AS SYNTHETIC BASE FLUID

Janet Bassey Edet, Ikodiya Orji, Ozioma Achugasim*

Department of Pure and Industrial Chemistry, PMB 5323, University of Port Harcourt

Received January 5, 2019; Accepted March 26, 2019

Abstract

The preferred base fluids for formulating synthetic-based mud (SBM) for drilling problematic and sensitive oil and gas wells are usually of mineral oils origin. However, the toxic, non-biodegradable and non-renewable properties of these oils increase the cost of treating drilled cuttings prior to their discharge. This has necessitated a diversion of research interests to alternative synthetic base fluids, of which ester is one. In this work, the potential of isopropyl laurate and its blends as synthetic base fluids for oil well drilling mud formulation was investigated. The density, kinematic viscosity and flash point of the neat ester and the blends were compared with that of commercially available mineral base fluid, and API recommended values. The results obtained indicated that the additives led to an increase in the viscosity and density of the samples while lowering the flash point. Change in physical properties observed from the addition of menthol, however, was less than that from camphor. These values, however, are still within the acceptable API range for ester base fluids, the ester and its blends, therefore, possess suitable physicochemical properties appropriate for the synthetic base fluid application.

Keywords: *ester; additives; flash point; density; menthol; camphor; base fluid.*

1. Introduction

The petroleum industry utilizes a large amount of drilling mud for maximization of offshore and onshore oil and gas drilling operations [1]. Oil based mud has always been preferable in drilling operations because of their better technical performance relative to water-based drilling muds, especially when drilling through sensitive shale formations, and in the drilling of extended and deviated wells [2]. Their toxic, non-biodegradable nature, however, made them unable to meet the strict cuttings discharge requirements for aquatic environment [3-4]. Thus drill cuttings from a well drilled with mineral oil or diesel based fluid must be processed to reduce the percentage of residual base fluid to an acceptable level before disposal into aquatic ecosystems; a process that increases the overall drilling cost [5-7]. Synthetic base fluid (SBF) is a relatively new player when it comes to the formulation of oil and gas well drilling muds [8], and was introduced as a result of the search for base fluids that will combine the better technical properties of mineral oil base fluid with eco-friendliness [9-10]. Esters, together with poly alpha olefins (PAOs), internal olefins (IOs) and linear alpha olefins (LAOs) are the four major categories of SBFs that have been applied with success over the years. Esters have proved to be the most biodegradable of them all and has been employed in the drilling of several hundreds of wells since their introduction. A lot of research efforts, therefore, have been expended in the search for suitable synthetic ester base fluids, a quest that led to the investigation of natural oils like soybean and groundnut oil, biodiesel from palm and coconut oils, and esters from esterification of free fatty acids for their suitability as synthetic base fluid for drilling mud with encouraging levels of success achieved [2,8,11-13]. Working with a free fatty acid has the advantage of yielding a cleaner ester with well-defined structure instead of a cocktail of fatty acid esters as obtainable from transesterification of fats and oils.

The properties of interest for base fluid employed in formulating drilling muds for oil and gas wells include flash point, density, kinematic viscosity, thermal and hydrolytic stability, and elastomer compatibility. Ideally, an ester base fluid should have high flash point, low pour point, low viscosity, high thermal and hydrolytic stability and be compatible with existing elastomer [3]. It has been established from the literature that these physicochemical properties of esters are influenced by blending with additives like polystyrene and waste plastics [14-15]. The United States Patent Nos. 8,414,717 and 9,932,533 disclosed a method that improves the flash point of volatile organic solvents including esters and petroleum products, by blending with α-terpineol [16-17].

Camphor is a white or transparent waxy solid obtained from the essential oil distilled out of the fragrant camphor tree (*Cinnamomum camphora,L.)* and other trees from the laurel family such as basil, rosemary and sage [18-19], while menthol is a naturally occurring monoterpene found in mint plants like menthol mint (*Mentha arvensis,L.),* spearmint and peppermint **(***Mentha piperita,L.)* [20-21], These terpenoids have a long history of being used as perfumes, medicines and spices [22-23], their utilization as blends in esters, however, is a relatively unexplored area of research.

The aim of this research therefore, is to investigate the effect of blending isopropyl laurate with menthol and camphor on the physical properties of isopropyl laurate and determine the suitability of the ester and the blends as synthetic base fluid for oil drilling mud by comparing these parameters with that of a commercial base mineral fluid which serves as reference.

2. Materials and methods

The reference base fluid utilized in this study was supplied by SNEP Co. Lauric acid was esterified with isopropyl alcohol over the sulphamic acid catalyst at a temperature of 120°C for three hours according to the method reported by Orji *et al.* [12]. The Fourier Transform infra-red (FTIR) spectra of lauric acid, isopropyl alcohol, and isopropyl laurate were obtained on a Shimadzu FTIR 8400S spectrophotometer, in the range of 4000-600 cm^{-1}.

Three different blends of isopropyl ester each for menthol and camphor were prepared with 5, 10, and 15% of the additives. The kinematic viscosities of the neat ester, the blends, and the reference fluid at 40°C and 100°C were determined according to ASTM D445 method; the flash point was evaluated using Pensky-Martens closed cup method (ASTM D93) and the density determined according to ASTM D1298. Each of the samples was run in triplicates, and the average values rounded to the nearest whole number as reported.

3. Results and discussion

3.1. FTIR spectroscopic analysis of the synthesized ester

The IR spectrum of isopropyl laurate was compared with that of standards in order to assign the absorption peaks to the respective functional groups. The characteristic absorption peaks of the ester functional group were observed at 1111 and 1180 cm^{-1} (C-O), 1720 cm^{-1} (C=O), and 2924 cm^{-1} (CH). The spectrum of isopropyl laurate was also compared with the spectra of lauric acid and isopropanol. The absence of the absorption peak of the OH functional group of isopropanol and the movement of the absorbance for lauric acid carbonyl (1720 cm^{-1}) toward shorter wavelength (1697 cm^{-1}) indicate that the synthesis of isopropyl laurate was achieved. These results are summarized in Table 1, while the spectra are shown in Figures 1 through 3.

Table 1. Absorption peaks in the IR spectra of isopropyl laurate, isopropanol, and lauric acid

S/No	Functional group	Wave number (cm^{-1})		
		Isopropyl laurate	Isopropanol	Lauric acid
1	C=O	1720	-	1697
2	C-O	1180	1126	1026
		1111		1080
3	CH_2	2924	2970	2916
4	C-H	1373	1311	1350
		1350	1381	1419
			1411	
5	O-H	-	3340	-

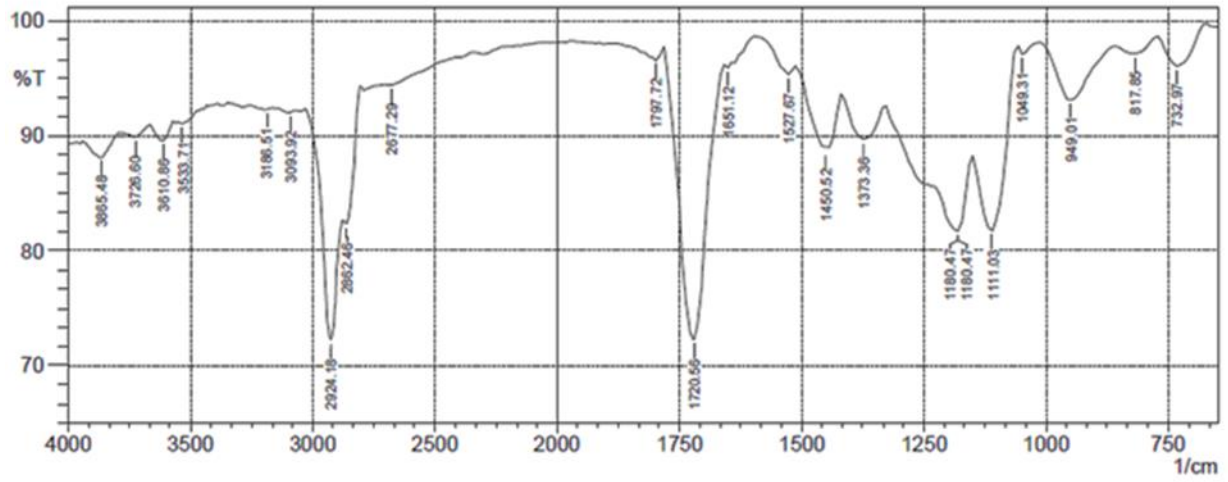

Figure 1. FTIR spectrum of isopropyl laurate (IL)

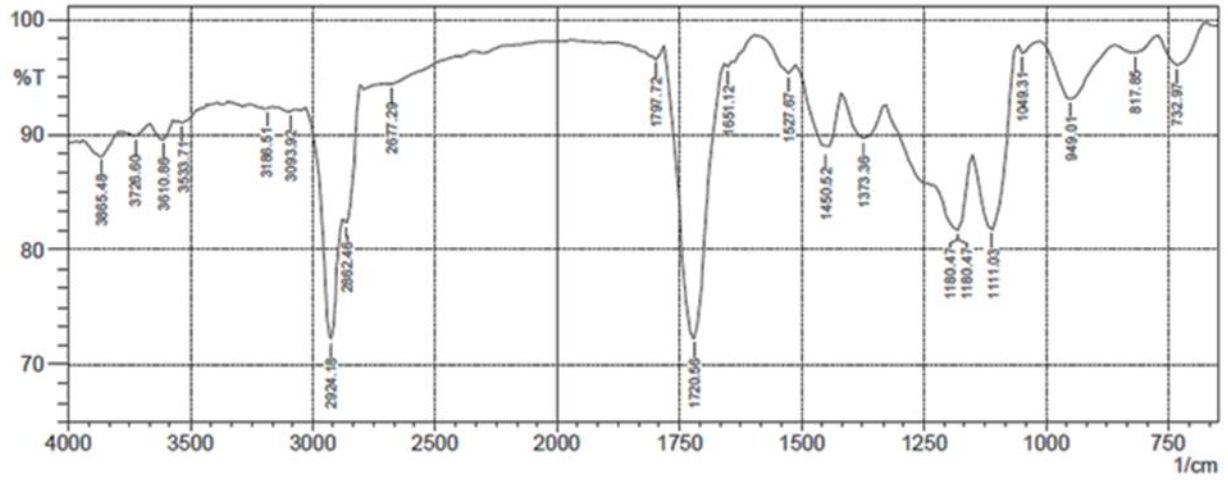

Figure 2. FTIR spectrum of lauric acid

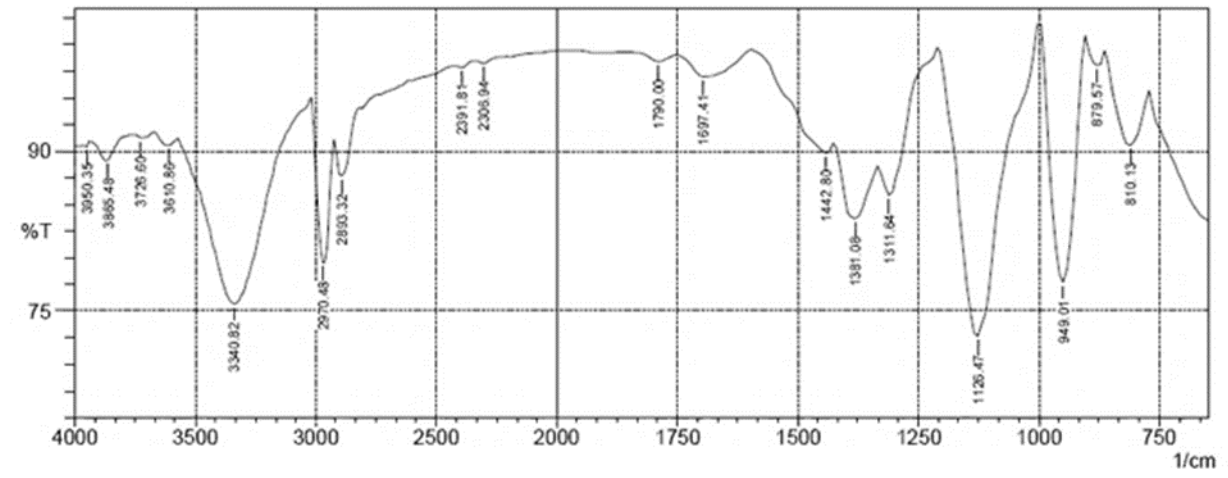

Figure 3. FTIR spectrum of isopropanol

3.2. Physical properties of the base fluids

The flash point of the reference fluid and the ester with its blends are presented in Figure 1. The flash point of a fluid is the minimum temperature at which it can generate enough ignitable vapour in the air close to its surface. A liquid with a higher flash point is relatively more difficult to ignite and therefore is safer to handle at a higher temperature. Thus, a drilling mud formulated with a base fluid with a high flash point will pose less fire hazard since less ignitable vapour is expected to accumulate above the mud. It has been suggested that the flash point of a base fluid for drilling mud application should exceed 100°C [24]. The result of the flash point determination for isopropyl laurate, its blends, and the reference indicates that the unblended isopropyl laurate has the highest flash point (118°C) whereas the blended isopropyl laurate with 20 % menthol has the lowest flash point (104°C). The isopropyl laurate with 10 % menthol exhibited a better flash point compared to the one with 15 % and 20 % menthol. The flash point of the IL and its menthol blends, however, are higher than that of the reference (103°C). Addition of camphor to IL led to a higher degree of reduction in the flash point. At 10 % addition of camphor, the flash point went as low as 61°C. The subsequent increase in the percentage of camphor; however, improved the flash point to 65°C (15%) and 79 °C (20%). The reduction in flash point on blending with additives could be attributed to the volatile nature of menthol and camphor.

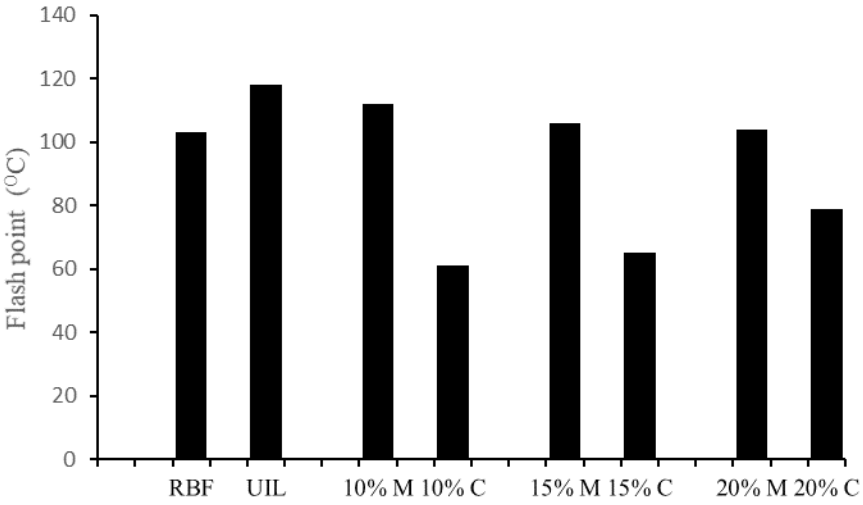

Figure 4. Flash point of isopropyl laurate and its blends

Rheological and hydraulic properties of drilling mud are affected by the kinematic viscosity of the base fluid from which it was formulated. Hence, a viscous base fluid tends to produce a viscous drilling mud which because of its poor pump-ability is more problematic to manage relative to low viscosity muds. Moreover, low viscosity base fluids when utilized in formulating drilling muds, exhibit better tolerance towards the presence of solids and water in the final formulation and increases the quantity of brine used, thereby reducing cost [25-26]. The effect of different percentage of additives on kinematic viscosity of the isopropyl ester samples at 40°C and 100°C are presented in Figure 5.

The result obtained from measuring the kinematic viscosity of the various blends indicates that inclusion of the additives led to an increase in viscosity at both temperatures. However, the highest viscosity values of 4.37 cSt at 100°C and 1.68 cSt at 40°C were recorded at 10 % menthol and 10% camphor respectively. The subsequent increase in the concentration of either additive resulted in a decrease in viscosity values. The ester and its blends recorded higher viscosity values at both temperatures relative to the reference; this is to be expected since the reference fluid is a synthetic hydrocarbon base fluid. It has been suggested that base fluid for drilling mud formulation should have viscosity values ranging from 1 to 6 cSt at 40°C [27].

Thus, the viscosity values of the ester and its blends are within acceptable values for base fluid application.

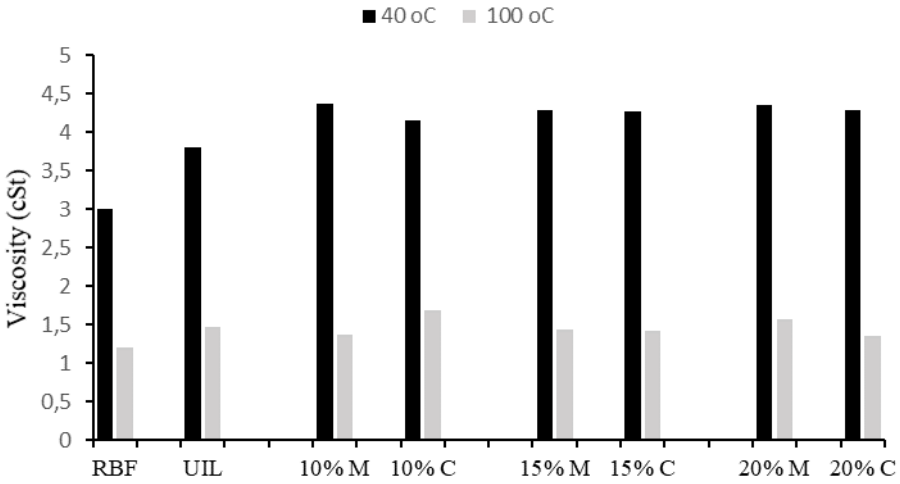

Figure 5. Kinematic viscosity of isopropyl laurate and its blends at 40°C and 100°C

The density of a base fluid affects the quantity of material required to achieve a particular standard of mud weight while formulating mud. It is required that the density of an oil base fluid be less than that of water which is 1 g/cm^3. From the result of the density determination presented in Figure 6, the RBF has the lowest value of 8.1 g/cm^3, followed by the unblended ester with 8.4 g/cm^3. It was observed that blending with menthol and camphor led to a slight increase in density. Thus the density of the ester with 10 and 15 % camphor is 0.86 g/cm^3. Increasing the percentage of camphor to 20 moved the density from 0.86 to 0.87 g/cm^3. Addition of menthol also did not bring about a significant increase in the density of the ester. The values range from 0.85, 0.85 and 0.86 g/cm^3 for 10, 15, and 20 % menthol respectively. These results are all within the recommended values for synthetic base fluid since they are all lower than the density of water.

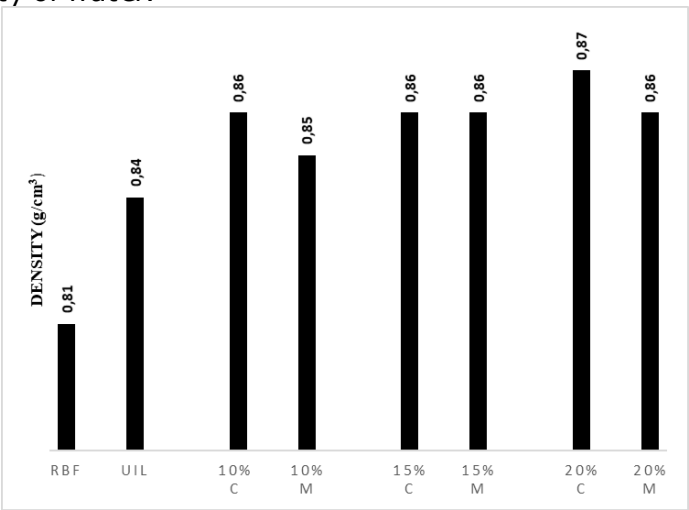

Figure 6. Density of isopropyl laurate and its blends at room temperature

4. Conclusion

From the results obtained in this work, it can be concluded that isopropyl laurate was successfully synthesized as determined proved by FTIR analysis. Isopropyl laurate has a higher flash point than the RBF.

Blending IL with camphor and menthol reduced the flash point of the ester and increased the viscosity and density marginally.

These results have demonstrated that isopropyl laurate and its blends possess properties which make them suitable for the base fluid application. It is recommended that the menthol ester blends they should be used in the formulation of inverse emulsion drilling muds for low-temperature shallow wells to avoid fire hazards since they recorded the lowest flash points of all the samples analyzed.

List of symbols

RBF	*Reference base fluid*
IL	*Isopropyl laurate*
UIL	*Unblended isopropyl laurate*
10%M	*Ester blended with 10% menthol*
10%C	*Ester blended with 10% camphor*
15%M	*Ester blended with 15% menthol*
15%C	*Ester blended with 15% camphor*
20%M	*Ester blended with 20% menthol*
20%C	*Ester blended with 20% camphor*
cSt	*Centistoke*

References

[1] Dardir MMS, Ibrahime S, Soliman M, Desouky SD, and Hafiz AA. Preparation and evaluation of some esteramides as synthetic based drilling fluids. Egyptian Journal of Petroleum, 2014; 23: 35–43.

[2] Anawe ALP, and Folayan JA. Novel synthetic-based drilling fluid through enzymatic interesterification of canola oil. International Journal of Chemical Engineering, 2018. Article ID 6418090, doi.org/10.1155/2018/6418090.

[3] Razalia SZ, Yunusa R, Rashida SA, Limc HN, and Mohamed BJ. Review of biodegradable synthetic-based drilling fluid: Progression, performance, and future prospect. Renewable and Sustainable Energy Reviews, 2018; 90: 171–186.

[4] Ali AD, Majid S, and Ehsan EM. Experimental investigation of new additive to optimize the properties of synthetic-based drilling fluid. Journal of Mining and Metallurgy, 2016; 52A(1): 37-43

[5] Growcock FB, and Patel AD. The revolution in non-aqueous drilling fluids. AADE-11- NTCE-33 AADE. National Technical Conference and Exhibition held at the Hilton Houston North Hotel, Houston, 2011; 1-8.

[6] Behnamanhar H, Noorbakhsh SS, and Maghsoudloojafari H. Environmentally Friendly Water-Based Drilling Fluid for Drilling of Water-Sensitive Formations. Journal of Petroleum and Gas Exploration Research, 2014; (4): 4: 60-71.

[7] Knez D, Gonet A, Fijał J, and Czekaj L. Trends in the Drilling Waste Management. Acta Montanistica Slovaca, 2006; 11(1): 80-83.

[8] Ekeinde E, Dosunmu A, Anyanwu C, Esop BB, and Odagme B. Rheological Characterisation of Pseudo Oil Base Mud from Local Materials. SPE-172348-MS. Society of Petroleum Engineers (SPE) Nigeria Annual International Conference and Exhibition held in Lagos, Nigeria, 2014. 1-12.

[9] Li W, Zhao X, Ji Y, Peng H, Li Y, Liu L, and Han X. An investigation on environmentally friendly biodiesel-based invert emulsion drilling fluid. Journal of Petroleum Exploration, Production and Technology, 2015; 6(3): 505–517.

[10] Sulaimon AA, Adeyemi BJ, and Rahimi M. Performance enhancement of selected vegetable oil as base fluid for drilling HPHT formation. Journal of Petroleum Science and Engineering, 2017; 152: 49–59.

[11] Agwu OE, Okon AN, and Udoh FD. A comparative study of diesel oil and soybean oil as oil-based drilling mud. Journal of Petroleum Engineering, 2015. Article ID 828451, doi.org/10.1155/2015/828451.

12 Habiba NSHA, Yunusa R, Rashidb U, Taufiq-Yap YH, Abidinam Z.Z, and Syam AM. Synthesis of palm-based ethylhexyl ester as a synthetic base oil for drilling fluids using chemical transesterification, Grasas Y Aceites, 2014;, 65: 1,

[13] Orji I, Ibezim-Ezeani MU, and Akaranta O. Synthesis of ester base fluids for drilling mud formulation using different catalysts. International Journal of Chem Tech Research, 2018; 11(9): 373-382.
[14] Morales JMV and Ordáz SL. Quality values ofna blend of expanded polystyrene dissolved in biodiesel for potential use as an alternative fuel. Energy Sources, Part A: Recovery, Utilization, and Environmental Effects, 2017; 39(6): 618-622.
[15] Mohammadi P, Nikbakht AM, Tabatabaei M, and Farhadi K. A Novel Diesel Fuel Additive to Improve Fuel Properties and to Reduce Emissions. International Journal of Automotive Engineering, 2012; 2(3): 156–162.
[16] William FR. U.S. Patent 9,932,533, 2018.
[17] Howard HW, US patent 8,414.797, 2013.
[18] Chen W, Vermaak I, and Viljoen A. Camphor: A Fumigant during the Black Death and a coveted fragrant wood in ancient Egypt and Babylon-A Review. Molecules, 2013; 18: 5434-5454.
[19] Hamidpour R, Hamidpour S. Hamidpour M, and Shahlari M. Camphor (*Cinnamomum camphora*), a traditional remedy with the history of treating several diseases. International Journal of Case Reports and Images, 2013; 4(2): 86–89.
[20] Alsharari SD, King JR, Nordman JC, Muldoon PP, Jackson A, Zhu AZX, Tyndale RF, Kabbani N, and Damaj MI. Effects of menthol on nicotine pharmacokinetic, pharmacology and dependence in mice. PLoS ONE, 2015; 10(9): e0137070.
[21] Verma RS, Rahman L, Verma RK, Chauhan A, Yadav AK, and Singh A. Essential oil composition of menthol mint (*Mentha arvensis*) and peppermint (*Mentha piperita*) cultivars at different stages of plant growth from Kumaon Region of Western Himalaya. Journal of Medicinal and Aromatic Plants, 2010; 1(1): 13-18.
[22] Zuccarini P. Camphor: risks and benefits of a widely used natural product. Journal of Applied Science and Environmental Management, 2009; 13(2): 69 – 74.
[23] Folan P, Abramova R, and Fardellone C. What is menthol? American Journal of Respiratory and Critical Care Medicine, 2017; 196, 9-10.
[24] Johanscvik C, and Grieve WR. Oil-based mud reduces bore-hole problems. Oil and Gas Journal., 1987; 4: 47-48.
[25] Eckhout D, Dolan S, Gogan R, Ledgister H, Mowat C, and Tipton P. Development process and field applications of a new ester-based mud system for ERD wells on Australia's northwest shelf. IADC/SPE Asia pacific drill. Technol. Soc. Pet. Eng., 2000. SPE-62791-MS, doi.org/10.2118/62791-MS.
[26] Dawson RB, and Carpenter JF. US Patent 5,432,152, 1995.
[27] Ellice M, Helmy S, and Shumate TG. Base oil for well-bore fluids, 1996. WO1996022342.

To whom correspondence should be addressed: Dr. Ikodiya Orji, Department of Pure and Industrial Chemistry, PMB 5323, University of Port Harcourt, Nigeria

Petroleum and Coal

Article **Open Access**

CALCULATION OF FRACTURE DENSITY VIA IMAGE LOGS AND COMPARING THE RESULTS OF MUD LOSS, GACHSARAN OIL FIELD, SW OF IRAN

Hossein Tabatabaei

Department of Petroleum Engineering, Gachsaran Branch, Islamic Azad University, Gachsaran, Iran

Received February 2, 2019; Accepted April 1, 2019

Abstract

In this study by using image logs (FMI, OBMI and UBI) of 5 wells in different sectors of Gachsaran oil field, located in SW of Iran, the number of fractures in each zone of Asmari reservoir of study well were calculated and then the fracture density chart of each zone was drawn and well No. 387 Zone 1 and 2, shows a high fracture density (5.1). Mud loss data was also converted to charts so as to be compared with fracture density chart. Base in this study, the lowest Mud loss has been related to the well No. 384 – Zone 4, and its fracture density is very low (0.2). The result showed that there was a good correlation between 2 groups of data. According to the findings of this story, although it is only image logs that are capable of showing the exact location and attitude of fractures in reservoir, but when unavailable, other data such as mud loss data can be used to predict and approximate the fracture condition in an oil well.

***Keywords**: Image log; Fracture Density; Gachsaran oil field; Mud loss; SW of Iran.*

1. Introduction

A reservoir rock is one that, in addition to high porosity to store hydrocarbons, has an appropriate permeability to drive oil fluids [1]. By this description, sandstone is commonly referred to as a good reservoir rock .However, it should be noted that more than 65 percent of the Middle Eastern hydrocarbons are located in carbonate reservoirs, and in Iran, according to the number of hydrocarbon reservoirs and regardless of the volume of hydrocarbons, about 90 percent of the large reservoirs, carbonate and 10 percent are sandy limestone. In carbonate rocks, ultimate porosity is often very low, and fracturing in these rocks is very important in increasing porosity [2], especially in permeability [3]. They are important in the carbonate reservoirs due to their high influence on the reservoir's rock properties [4-5]. Therefore, in determining the reservoir properties of carbonate rocks, fractures have a special position [6-7] and accurate determination of fractures location and determining the depths with the highest fracture rates for reservoir designation with high production potential, providing a suitable method for recycling projects, and Reconstruction, design of diversion drilling, the determination of the location of acidity and the location of the lattice operations with the completion of the well to have the highest production and also the avoidance of excessive costs in the completion of inappropriate reservoir zones has great importance [8].

In this research, by identifying zones with higher fracture density in the Asmari reservoir of the Gachsaran oil field, sections with higher production potential are introduced. Meanwhile, considering the high cost of image log, their use is limited to specific wells of a field. In the following, we have tried to find the relationship between fracture density and mud loss from studied wells, the use of these data as a substitute for estimating and predicting fractures conditions when there is no image log, are presented.

2. Geological setting

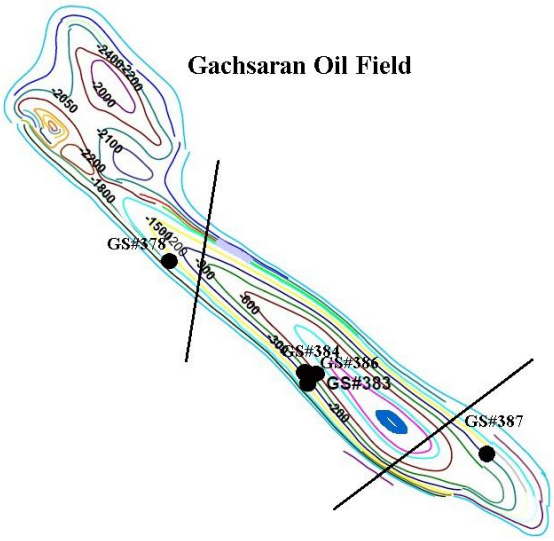

Fig.1 UGC map of Gachsaran oil field based on the upper border of the Asmari Formation and the position of the studied wells No. 378, 383, 384, 386 and 387 on it.

Gachsaran oil field is one of the most important oil fields of Iran, which is located in the southwest of Iran. This oil field has situated on Dezful Embayment. Dominant structural trends in this area are NW-SE. From tectonics view, it contains the over thrust and simple fold belts of Zagros that formed on the northeastern part of Arabian plate's passive margin. Zagros Mountains have continued to East Taurus Mountains in Turkey and have named Zagros-East Taurus hinterland. Zagros-East Taurus hinterland is external platform (fold and thrust belt) of north margin of Arabian Craton.

Gachsaran oil field is an asymmetric anticline with NW-SE trend (Fig. 1). This oil field at the Asmari horizon is 70 km in length and 11 km in width [9]. This field as a giant oil fields in Iran, consists of Asmari, Bangestan and Khami reservoirs, which were discovered in 1965 by means of seismic operation and drilling of the first well in Asmari formation. Because of tectonic activity, there are highly fractured area in this oil field, which causes upward migration of hydrocarbon [10].

3. Research method

The best methods for fracture evaluation are image logs and core. However, cores have vital limitations such as low recovery factor, being undirected, and high cost of coring [6,11]. The raw data obtained from the wellhead charts after loading in GEO FRAME-CPS3 software and performing several stages of software processing, are presented as a virtual image of the well wall. In wells drilled with a water base drill, FMI image log and in the wells where the drilling mud is based on oil, OBMI and image log UBI are used simultaneously. In this image, plate phenomena in the well wall, such as layering and fractures, are recognizable and can be compared to the direction, length, and gradient of these phenomena. In Fig. 2, for FMI image log, refers to well 387, with a scale of 1:1000 has been presented.

After plotting the image log for each of the studied wells in the Gachsaran oil field, fractures, layering and other plate phenomena were determined in it [12], and then the density of open fractures in each zone was calculated from the Asmari reservoir.

The method used in this study to calculate open fracture density is to count all open fractures in a zone or sub zone of the Asmari reservoir, and then divide the fracture number by the depth of that zone or sub zone, which is showed by 1m [13-14].

Mud loss information for wells studied in Gachsaran oil field using Excel software is presented in graphical way in different zones that comparing this chart with other information related to fractures can be about the possibility of using mud loss information to detect broken zones.

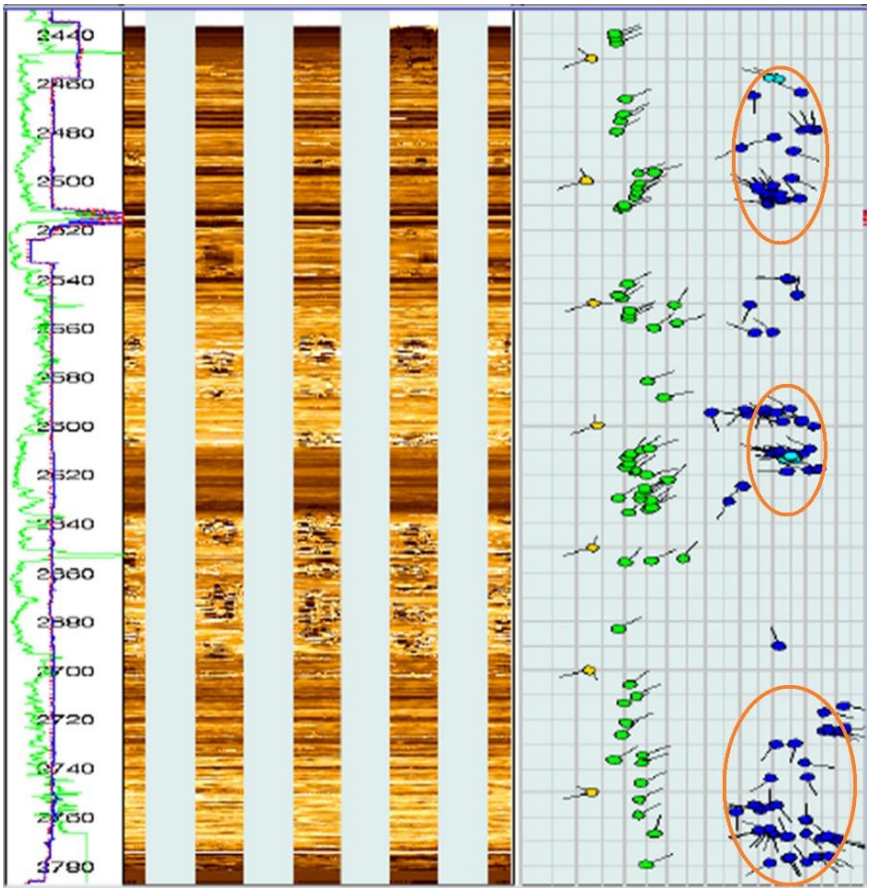

Fig. 2. The schematic representation of all the identified complications in well 378 base on FMI

4. Results and discussion

In this study FMI, OBMI and UBI image logs in wells No. 378, 383, 384, 386 and 387 were analyzed in order to identify and describe different types of fractures. The open fracture density of the oil-containing zones, the ratio of the number of open zone fractures to the drilled distance in that zone in meters was calculated in well 378, according to which zone 2, 4 and zone 7 have a fracture density of 2.7, 3.1 And 3.3 respectively that it is indicating of a high fracture density in both zones (Fig. 3). Meanwhile, as shown in Fig. 2, the depth distances from 2460 to 2510m, 2595 to 2620m, 2720 to 2780m, were described as reservoir zones with maximum fracture rates and with high production potential in well 378.

In well 383, zone 2 and zone 4, have 1.1 and 1.3 fracture potential, respectively .The fractures are roughly uniformly distributed at all depths of each zone (Fig 3). Open fracture density in zone 2 and zone 4 of wells 384 are 0.4 and 0.2, respectively, which indicates the very low fracture density in both zones and the very low production potential in this well (Fig. 3).

Based on the calculations performed in the well 386, zone 1 of this well has a fracture density of 2.1, zone 4 with a fracture density of 2.2 and zone 7 with a fracture density of 3.1. Meanwhile, in zone 5, due to the lack of log UBI information only fractures that were found in log OBMI have been seen that have a fracture density of 1.8 (Fig. 3). As can be seen, this well has a relatively high fracture density in total. In this well, the depth intervals of 2450 to 2485 meters, 2550 to 2580 meters and 2680 to 2730 meters are described as reservoir zones with maximum fracture rate and with high production potential.

The open fracture density in the well 387 shows a high fracture of this well in all depths, so that zone 1 and zone 2 each have approximately a fracture density of 5.1, sub zone 4 with a fracture density of 3.2 and zone 7 has a fracture density of 4.2, and this well has a very high

production potential (Fig. 3). Comparison of Figures 3 (Fractal Density Chart) and 4 (Mud loss Chart) shows a good correlation between fracture density and Mud loss.

The lowest Mud loss has been related to the well 384 (Fig. 4), and its fracture density is very low. Wells 378, 383, 386 having a fairly high fracture average in all depth distances, show a good correlation with the Mud loss. The well 387 has the highest fracture density among all studied wells, which is due to the under balanced drilling, the mud loss has been prohibited.

As you can see, the above shows that when number of fractures in a well increases, the greater the amount of mud can escape through them, and they can enter into the structure, which, in addition to damage to the structure, can cause problems and also for drilling operations, so that it can cause the drill string to be stuck in the space around the drill by decreasing or not circulating and preventing further drilling operations. The amount of mud loss in a particular zone of the reservoir can be a criterion for proving the presence of fractures and thus indicating reservoir zones with potential production.

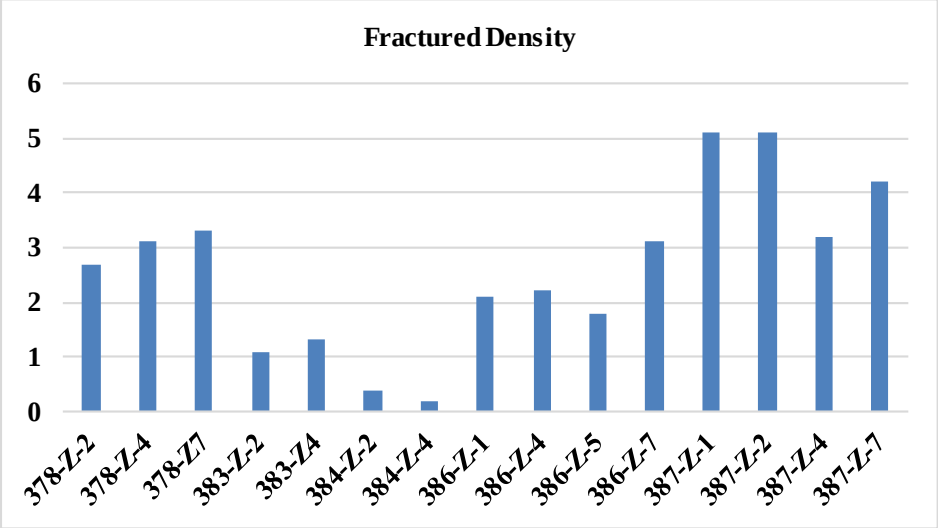

Fig. 3. Relative frequency of open fractures in different zones of Asmari structure in investigated wells base in fracture number vs. meter

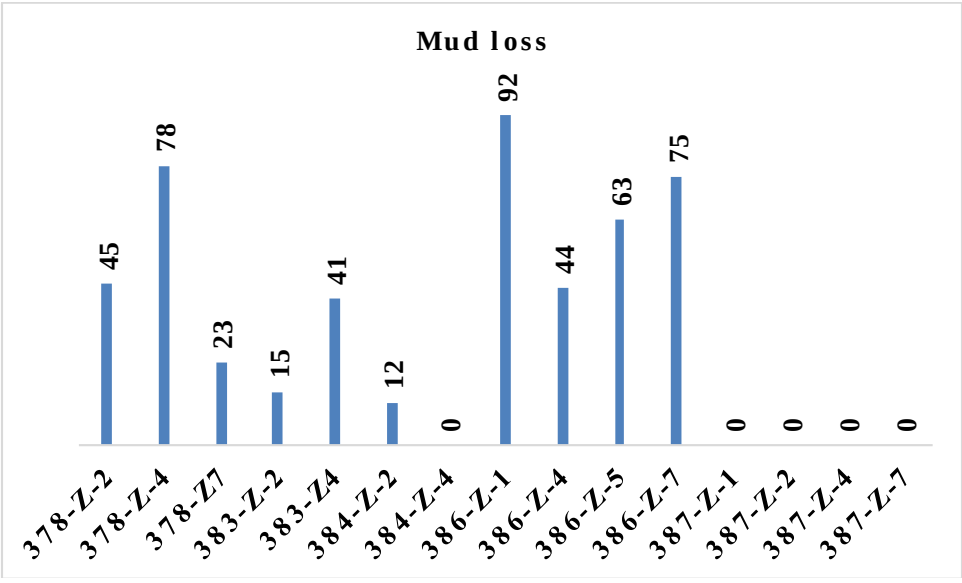

Figure 4. Mud loss average in different zones of Asmari structure from wells studied with barrel units per each hour.

5. Conclusion

Due to the fact that the Asmari reservoir characteristics are various in different parts of the Gachsaran oil field, this field is based on the characteristics of the lithology, porosity and permeability, reservoir pressure history, the amount of mud loss from each section and other reservoir properties are divided into the 3 East, Middle and West parts. This research showed that the image log is a good tool for determining the precise location and position of fractures, as well as calculating the density of fractures in order to determine the reservoir zones with high production potential. At the same time, the results of this research proved that, in the absence of image log, mud loss data can be obtained to predict and estimate the relative position of fractures can be benefit.

References

[1] El-Din ES, Mesbah MA, Kassab MA. Assessment of petrophysical parameters of clastics using well logs: the Upper Miocene in El-Wastani gas field, onshore Nile Delta, Egypt. Pet Explor Dev., 2013; 40:488–494.

[2] Abdideh M, Bahadori Birgani N, Amanipour H. Estimating the Reservoir Permeability and Fracture Density Using Petrophysical Logs in Marun Oil Field (SW Iran). Petroleum Science and Technology, 2013; 31(10): 1048-1056.

[3] Anselmetti FS, Eberli GP. The velocity-deviation log: a tool to predict pore type and permeability trends in carbonate drill holes from sonic and porosity or density logs. AAPG Bull., 1999; 83:450–466.

[4] Nelson R. Geologic analysis of naturally fractured reservoirs. Gulf Professional Publishing, 2001.

[5] Rajabi M, Sherkati S, Bohloli B, Tingay M. Subsurface fracture analysis and determination of in-situ stress direction using FMI logs: an example from the Santonian carbonates (Ilam Formation) in the Abadan Plain. Iran. Tectonophysics, 2010; 492:192–200.

[6] Khoshbakht F, Azizzadeh M, Memarian H. Comparison of electrical image log with core in a fractured carbonate reservoir. J Pet Sci Eng., 2012; 86–87:289–296.

[7] Zahmatkesh I, Aghli G, Mohammadian R. Systematic fractures analysis using image logs and complementary methods in the Marun Oilfield, SW Iran. Geopersia, 2015; 5:139–150.

[8] Tokhmchi B, Memarian H, Rezaee MR. Estimation of the fracture density in fractured zones using petrophysical logs. J Pet Sci Eng., 2010; 72: 206–213.

[9] Telmadarreie A, Shadizadeh SR, Alizadeh B. Investigation of Hydrogen Sulfide Oil Pollution Source: Asmari Oil Reservoir of Marun Oil Field in the Southwest of Iran. Iranian Journal of Chemical Engineering, 2012; 9(3): 63-74.

[10] Alizadeh B, Telmadarreie A, Shadizadeh SR, Tezhe F. Investigating Geochemical Characterization of Asmari and Bangestan Reservoir Oils and the Source of H_2S in the Marun Oilfield. Petroleum Science and Technology, 2010; 30(10): 967-975.

[11] Mohebbi A, Haghighi M, Sahimi M. Conventional logs for fracture detection & characterization in one of the Iranian field. In: International Petroleum Technology Conference, 2007.

[12] Laongsakul P, Dürrast H. Characterization of reservoir fractures using conventional geophysical logging. 33:237–246, 2011.

[13] Aghli G, Soleimani B, Moussavi-Harami R, Mohammadian R., Fractured zones detection using conventional petrophysical logs by differentiation method and its correlation with image logs. J Pet Sci Eng., 2016; 142:152–162.

[14] Nie X, Zou C, Pan L. Fracture analysis and determination of in-situ stress direction from resistivity and acoustic image logs and core data in the Wenchuan Earthquake Fault Scientific Drilling Borehole-2 (50–1370m). Tectonophysics, 2013; 593:161–171.

To whom correspondence should be addressed: Dr. Hossein Tabatabaei, Department of Petroleum Engineering, Gachsaran Branch, Islamic Azad University, Gachsaran, Iran